

THE HEAT IS ON

Burning plasma marks key step towards power from nuclear fusion

Drying up

Did a mega-drought cause chaos in the ancient world?

Team effort

Boost complex research with grass-roots collaborative networks

Relocation plans

Genomic data reveal Bronze Age migration to southern Britain

Nature.2022.01.29

[Sat, 29 Jan 2022]

- [This Week](#)
- [News in Focus](#)
- [Books & Arts](#)
- [Opinion](#)
- [Work](#)
- [Research](#)
- [Amendments & Corrections](#)

This Week

- **[India's tech innovation engines must raise their game](#)** [26 January 2022]
Editorial • The number of prestigious Indian Institutes of Technology trebled in the space of a decade. But new arrivals are struggling to establish themselves and must quickly turn things around.
- **[NASA's Webb telescope is an initial success — despite formidable odds](#)** [25 January 2022]
Editorial • Science stands to make huge gains from the James Webb Space Telescope, but there are also lessons to learn from the epic management failures that beset the project.
- **[COVID-19: endemic doesn't mean harmless](#)** [24 January 2022]
World View • Rosy assumptions endanger public health — policymakers must act now to shape the years to come.
- **[Light that never 'sees' items takes their picture](#)** [19 January 2022]
Research Highlight • Photons of different wavelengths go their separate ways to capture images.
- **[The blood markers that could help to diagnose long COVID](#)** [19 January 2022]
Research Highlight • Levels of some immune molecules are unusually high in people with persistent symptoms after infection with SARS-CoV-2.
- **[Oh elephant, what big nerves you have!](#)** [20 January 2022]
Research Highlight • The outsize nerve network running from an elephant's trunk to its brain hints at a highly developed sense of touch.
- **[Cancer cells' keratin robes keep attackers at bay](#)** [17 January 2022]
Research Highlight • Methods to strip away the keratin coat could make immune therapies more effective.
- **['Sceptres' found in ancient tomb were actually beer straws](#)** [19 January 2022]
Research Highlight • Metal tubes dating back millennia are the oldest surviving drinking straws.

- **Guided by the light, nimble nanovehicles make special deliveries** [20 January 2022]

Research Highlight • Nanometre-scale particles' asymmetrical shape makes them easier to 'drive' using near-infrared light.

- **Air pollution takes a bite out of Asia's grain crops** [21

January 2022]

Research Highlight • Ozone costs billions of dollars in yields of wheat and other staple crops in China and other East Asian nations.

- EDITORIAL
- 26 January 2022

India's tech innovation engines must raise their game

The number of prestigious Indian Institutes of Technology trebled in the space of a decade. But new arrivals are struggling to establish themselves and must quickly turn things around.



The Indian Institutes of Technology, such as IIT Delhi (pictured), are world-renowned for the quality of their students and faculty members. But India's Auditor General has expressed concerns about some of the newest institutions. Credit: Sanchit Khanna/Hindustan Times/Getty

There probably isn't a country in the world that isn't looking to build or expand billion-dollar tech corporations. The United States and China

dominate the landscape of ‘unicorns’, privately owned technology start-ups valued at US\$1 billion or more. But now some of the most rapid development is happening in India.

According to government data, India recorded 44 new billion-dollar technology companies last year, compared with 10 in 2020 and 9 in 2019 (the country has a total of 83 unicorns). Some analysts are predicting that 2022 will see another surge, with new companies in financial, agricultural and educational technology joining new life-sciences companies, games companies and online marketplaces.

A proportion of the founders and staff of these companies are graduates of the swiftly growing and prestigious Indian Institutes of Technology (IITs). There were 7 of these institutions before 2008; by 2016, the number had more than trebled, to 23. This rapid expansion is the subject of a [report by the country’s Auditor General](#), published at the end of last year. It should make for uncomfortable reading for the eight IITs assessed, which were established in 2008–09.

These IITs are criticized for not meeting targets for research and faculty- and student-recruitment. All have been hit by infrastructure delays, and in some cases students leave after enrolling. This is deeply concerning, not only for the institutions themselves, but for the richly deserved global reputation of the IIT system as a whole. Together, the national and state governments and the IITs must turn things around — and quickly.

India’s emergence as an engine in global technology innovation is entirely expected. For decades, students and staff from the first generation of IITs have excelled at US universities and in Silicon Valley companies, something that has been repeatedly acknowledged as “brand IIT” by business, political and scientific leaders, including former US president Bill Clinton, as well as Amazon and Microsoft founders Jeff Bezos and Bill Gates.

The founding vision of the first IITs in the early 1950s was to provide education and research in engineering and technology, with an additional emphasis on knowledge and skills in management and humanities subjects. The first IIT, at Kharagpur near Kolkata, opened in 1951, with 210

undergraduate students and 14 postgraduates. In 2021, more than 700,000 applicants competed for 40,000 places across all IITs.

Some graduates will no doubt want to follow in the footsteps of alumni such as Twitter chief executive Parag Agrawal, Google chief executive Sundar Pichai and IBM chief executive Arvind Krishna. But the overwhelming majority are building and working in companies at home. Although there are no publicly accessible pan-IIT data, Anurag Mehra, a chemical engineer at IIT Bombay in Mumbai, told *Nature* that “in the early years after the inception of the IITs and almost till the later 1990s, a very large fraction — sometimes as high as 60–70% — used to go abroad. Now the numbers are down to a few per cent.”

Some in India want more of the IITs and their graduates to consider careers outside technology, and to do more to address India’s socio-economic and environmental challenges. But the Auditor General’s report shows that the newer IITs are beset by problems that threaten to limit the quality of their future expansion — and therefore their potential. In 2008, a policy was set to vigorously expand the numbers of IITs; by 2016, a further 16 had been established. The funding for all IITs subsequently rose, from 49.8 billion rupees (US\$670 million) in the 2016–17 national budget to 83 billion rupees in the 2017–18 budget.

Last year’s report looked at how eight IITs performed between 2014 and 2019. Some of their areas of research include 5G, mobile sensor network technologies, metal additive manufacturing, artificial intelligence, bio-inspired engineering, catalysts, energy and health care. But at four out of the eight, research was taking place without the strategic oversight of the Research and Technology Development Councils that each IIT was supposed to establish. Five of the eight did not set PhD enrolment targets, and the three that did fell short. Five received no patents on any of their inventions or innovations during the audit period, and none attracted significant external funds (such as from businesses). The report also found that in half of the institutions, around one-third of faculty positions were unfilled during the audit period.

In addition, the report says that all of the IITs assessed are experiencing delays to infrastructure, with construction of new buildings delayed in seven

of the eight. Perhaps not surprisingly, students have not been coming. Only around one-third of an expected 19,000 students were admitted over the first 6 years of their operation.

Some of the other IITs (not assessed in the report) have taken steps to fund more multidisciplinary research, encourage start-ups and address a long-standing gender gap in recruitment of faculty members. IIT Madras in Chennai, for example, is attempting to raise \$2 million for a new endowment fund to increase the proportion of women in assistant-professor roles from 15% to 20%. And last June, IIT Bombay received funding to establish the institute's first faculty-chair position to be held by a woman. Such practices need to be shared more widely across IITs.

It is true that high-quality universities do not become high-quality institutions overnight. For example, when the Nature Index compiled a list of some of the world's leading universities under the age of 50, around 70% were at least 20 years old. But youth is not a reason for infrastructure delays, nor for failures in research governance. India's national and state governments must work with IITs to address the audit report's concerns quickly. All need to grasp the nettle so that the IITs can continue to provide science and technology leaders for India — and the world.

Nature **601**, 483-484 (2022)

doi: <https://doi.org/10.1038/d41586-022-00154-y>

This article was downloaded by **calibre** from <https://www.nature.com/articles/d41586-022-00154-y>

- EDITORIAL
- 25 January 2022

NASA's Webb telescope is an initial success — despite formidable odds

Science stands to make huge gains from the James Webb Space Telescope, but there are also lessons to learn from the epic management failures that beset the project.



Members of the Webb telescope team at the Guiana Space Centre in Kourou, French Guiana, celebrate the telescope's successful powering up on 25 December 2021. Credit: NASA/Bill Ingalls ([CC BY 2.0](#))

It was a big-science project plagued with so many problems that it seemed destined to fail. For years, the James Webb Space Telescope — an ambitious observatory planned and funded by NASA, the European Space Agency and the Canadian Space Agency — was the target of astronomy's most scathing jokes. Delayed for more than a decade owing to technical and management problems, Webb's development and operations budget ultimately ran to almost US\$10 billion, far above the initial \$1 billion estimated when the project was conceived.

Yet on 25 December 2021, an Ariane 5 rocket lifted into the skies above French Guiana and carried Webb into space. Within half an hour of launch, the telescope separated from the rocket. It subsequently embarked on an intricate dance of deployments to unfold major pieces, including a tennis-court-sized sunshield and a 6.5-metre-wide primary mirror. On 24 January, [Webb reached its ultimate destination](#), an orbit around the L2, or the second Lagrange point, some 1.5 million kilometres from Earth. Holding its sunshield behind itself like a giant umbrella to keep its mirrors and four scientific instruments in the shade, the telescope will now prepare to begin observing the Universe.

Webb was designed as a next-generation infrared telescope to succeed the Hubble Space Telescope. Between now and June — the earliest that science results are expected — the telescope will cool down to its operating temperature and start up and calibrate its instruments.

Remarkably, Webb has pulled off an essentially flawless deployment so far. Scientists and engineers are breathing huge sighs of relief. It's an apt moment to assess how other big-science projects can avoid the pitfalls that plagued Webb — and to look ahead to the astronomy that scientists hope the telescope will reveal. There are also management lessons to be learnt. For many astronomers working on an upcoming space mission, the number-one aim is probably to avoid the problems that bedevilled Webb. These boil down to two interconnected faults: the massive underestimate of the project costs and the failure to stop scientists adding a host of new technologies along the way.

NASA gave Webb the green light in 2002, expecting it to launch within a decade. But throughout the 2000s, the agency and its main contractor,

Northrop Grumman in Falls Church, Virginia, struggled to turn ambitious designs into functional hardware that could fly in space. No one had ever built anything like the enormous sunshield — made of five gossamer-thin layers that had to be folded for launch and then unfolded in space — or the similarly folded primary mirror. All had to be designed, built, tested and retested from scratch. Scientists kept asking for more capabilities, and engineers kept adding more complexity to satisfy them.

In 2010, an independent review, now a classic in the literature of project management, flagged fundamental errors, including the failure to produce multiple bottom-up estimates of the true cost of the telescope as time went on. (Even early on, few believed the initial \$1-billion estimate.) The main problem was that NASA management had accepted an unrealistically low figure and had not adjusted its thinking adequately as time went on. By 2011, Congress was fed up with cost overruns and lawmakers threatened to cancel it. Ultimately, Webb cost NASA \$8.8 billion to develop — nearly double the amount expected even in 2009. It is the most expensive telescope in history.

NASA has worked hard to try to avoid the pitfalls that afflicted Webb from affecting future missions, such as the Nancy Grace Roman Space Telescope. This is the big space telescope the agency is building to follow Webb, and should be launched in 2027. Managers on the Roman project have been relentless in their efforts to keep the mission to its cost cap, with the main extra expense so far the result of COVID-19-induced delays, which pushed costs up by almost \$400 million to \$4.3 billion. Project managers in other areas of science would do well to follow this model, and regularly acquire independent cost estimates, as well as periodic reviews as the Roman project managers have done, to be sure they remain on track.

Clearly, no one should ever build a telescope in the way NASA built Webb. But now that the observatory is in space and so close to being functional, it is time to sing its praises. Humanity has never built such an awesome machine.

With its gigantic mirror and sensitive instruments, Webb will peer at the Universe in infrared wavelengths. It will almost certainly — and immediately — smash the record for the most-distant galaxy ever observed,

and study such galaxies for clues to the evolution of the Universe. It will sniff out molecules such as carbon dioxide and water vapour in the atmospheres of exoplanets, helping scientists to understand the chances of life on these other worlds. It will reveal the secrets of star formation by peering through the dust that enshrouds stellar nurseries and prevents them from being seen with other wavelengths of light.

In line with our support for open data, *Nature* reaffirms that the journal will have no embargo on any early-release science (data from the first five months of observations); nor on the first year of science, known as Cycle 1 of the General Observers programme. We can hardly wait for the insights that the telescope will bring.

Nature **601**, 484 (2022)

doi: <https://doi.org/10.1038/d41586-022-00153-z>

This article was downloaded by **calibre** from <https://www.nature.com/articles/d41586-022-00153-z>

| [Section menu](#) | [Main menu](#) |

- WORLD VIEW
- 24 January 2022

COVID-19: endemic doesn't mean harmless



Rosy assumptions endanger public health — policymakers must act now to shape the years to come.

- [Aris Katzourakis](#) 0

The word ‘endemic’ has become one of the most misused of the pandemic. And many of the errant assumptions made encourage a misplaced complacency. It doesn’t mean that COVID-19 will come to a natural end.

To an epidemiologist, an endemic infection is one in which overall rates are static — not rising, not falling. More precisely, it means that the proportion of people who can get sick balances out the ‘basic reproduction number’ of the virus, the number of individuals that an infected individual would infect, assuming a population in which everyone could get sick. Yes, common

colds are endemic. So are Lassa fever, malaria and polio. So was smallpox, until vaccines stamped it out.

In other words, a disease can be endemic and both widespread and deadly. Malaria killed more than 600,000 people in 2020. Ten million fell ill with tuberculosis that same year and 1.5 million died. Endemic certainly does not mean that evolution has somehow tamed a pathogen so that life simply returns to ‘normal’.

As an evolutionary virologist, it frustrates me when policymakers invoke the word endemic as an excuse to do little or nothing. There’s more to global health policy than learning to live with endemic rotavirus, hepatitis C or measles.

Stating that an infection will become endemic says nothing about how long it might take to reach stasis, what the case rates, morbidity levels or death rates will be or, crucially, how much of a population — and which sectors — will be susceptible. Nor does it suggest guaranteed stability: there can still be disruptive waves from endemic infections, as seen with the US measles outbreak in 2019. Health policies and individual behaviour will determine what form — out of many possibilities — endemic COVID-19 takes.

Soon after the Alpha variant emerged and spread in late 2020, I argued that, unless infections were suppressed, viral evolution would be fast and unpredictable, with the emergence of more variants with different and potentially more-dangerous biological characteristics. Since then, public-health systems have struggled under the highly transmissible and more-virulent Delta variant, and now there is Omicron, with its substantial ability to evade the immune system, causing reinfections and breakthroughs. Beta and Gamma were also highly dangerous, but did not spread to the same extent.

The same virus can cause endemic, epidemic or pandemic infections: it depends on the interplay of a population’s behaviour, demographic structure, susceptibility and immunity, plus whether viral variants emerge. Different conditions across the world can allow more-successful variants to evolve, and these can seed new waves of epidemics. These seeds are tied to

a region's policy decisions and capacity to respond to infections. Even if one region reaches an equilibrium — be that of low or high disease and death — that might be disturbed when a new variant with new characteristics arrives.

COVID-19 is, of course, not the world's first pandemic. The fact that immune systems have evolved to cope with constant infections, and the traces of viral genetic material embedded in our own genomes from ancient viral infections, are testament to such evolutionary battles. It is likely that some viruses went 'extinct' on their own and still caused high rates of mortality on the way out.

There is a widespread, rosy misconception that viruses evolve over time to become more benign. This is not the case: there is no predestined evolutionary outcome for a virus to become more benign, especially ones, such as SARS-CoV-2, in which most transmission happens before the virus causes severe disease. Consider that Alpha and Delta are more virulent than the strain first found in Wuhan, China. The second wave of the 1918 influenza pandemic was far more deadly than the first.

Much can be done to shift the evolutionary arms race in humanity's favour. First, we must set aside lazy optimism. Second, we must be realistic about the likely levels of death, disability and sickness. Targets set for reduction should consider that circulating virus risks giving rise to new variants. Third, we must use — globally — the formidable weapons available: effective vaccines, antiviral medications, diagnostic tests and a better understanding of how to stop an airborne virus through mask wearing, distancing, and air ventilation and filtration. Fourth, we must invest in vaccines that protect against a broader range of variants.

The best way to prevent more, more-dangerous or more-transmissible variants from emerging is to stop unconstrained spread, and that requires many integrated public-health interventions, including, crucially, vaccine equity. The more a virus replicates, the greater the chance that problematic variants will arise, most probably where spread is highest. The Alpha variant was first identified in the United Kingdom, Delta was first found in India and Omicron in southern Africa — all places where spread was rampant.

Thinking that endemicity is both mild and inevitable is more than wrong, it is dangerous: it sets humanity up for many more years of disease, including unpredictable waves of outbreaks. It is more productive to consider how bad things could get if we keep giving the virus opportunities to outwit us. Then we might do more to ensure that this does not happen.

Nature **601**, 485 (2022)

doi: <https://doi.org/10.1038/d41586-022-00155-x>

This article was downloaded by **calibre** from <https://www.nature.com/articles/d41586-022-00155-x>

| [Section menu](#) | [Main menu](#) |

- RESEARCH HIGHLIGHT
- 19 January 2022

Light that never ‘sees’ items takes their picture

Photons of different wavelengths go their separate ways to capture images.



Photons of laser light (purple beams) are split into pairs, some of which create an object’s image without ever coming into contact with the item itself. Credit: Walter Oppel

Physicists have recorded images of an object using light that has never interacted with it¹.

Access options

Subscribe to nature+

Get immediate online access to the entire Nature family of 50+ journals

\$29.99

monthly

[Subscribe](#)

Subscribe to Journal

Get full journal access for 1 year

\$199.00

only \$3.90 per issue

Subscribe

All prices are NET prices.

VAT will be added later in the checkout.

Tax calculation will be finalised during checkout.

Buy article

Get time limited or full article access on ReadCube.

\$32.00

Buy

All prices are NET prices.

Additional access options:

- [Log in](#)
- [Learn about institutional subscriptions](#)

Nature **601**, 486 (2022)

doi: <https://doi.org/10.1038/d41586-022-00116-4>

References

1. 1.

Töpfer, S. *et al.* *Sci. Adv.* **8**, eabl4301 (2022).

This article was downloaded by **calibre** from <https://www.nature.com/articles/d41586-022-00116-4>

- RESEARCH HIGHLIGHT
- 19 January 2022

The blood markers that could help to diagnose long COVID

Levels of some immune molecules are unusually high in people with persistent symptoms after infection with SARS-CoV-2.



Physiotherapists in San Fernando de Henares, Spain, examine a woman with lingering health problems after a bout of COVID-19. Such long-running symptoms have been linked to immune abnormalities. Credit: Pablo Blazquez Dominguez/Getty

Scientists have identified an immune-system signature for long COVID, shedding light on the biological underpinnings of this mysterious condition¹.

As many as 30% of people infected with SARS-CoV-2 go on to be affected by long COVID, which causes debilitating symptoms — including fatigue and shortness of breath — months after an initial infection with the virus. How the pathogen wreaks sustained havoc in the body remains unclear.

Chansavath Phetsouphanh at the University of New South Wales in Sydney, Australia, and his colleagues analysed blood samples from people with long COVID and found that a SARS-CoV-2 infection elicits an immune response distinct from that of other types of coronavirus, such as those that cause the common cold.

This response persists in people experiencing long COVID. The team's analysis pointed to a collection of immune-system molecules that remained abnormally high in individuals with long COVID eight months after

infection. These molecules, such as type 1 and type 3 interferons, are usually made at the time of a viral infection. They activate immune cells called T cells and trigger inflammation.

The findings could help researchers to develop treatments for the disorder.

Nature **601**, 486 (2022)

doi: <https://doi.org/10.1038/d41586-022-00118-2>

References

1. 1.

Phetsouphanh, C. *et al.* *Nature Immunol.*
<https://doi.org/10.1038/s41590-021-01113-x> (2022).

This article was downloaded by **calibre** from <https://www.nature.com/articles/d41586-022-00118-2>

| [Section menu](#) | [Main menu](#) |

- RESEARCH HIGHLIGHT
- 20 January 2022

Oh elephant, what big nerves you have!

The outsize nerve network running from an elephant's trunk to its brain hints at a highly developed sense of touch.



A young African elephant (*Loxodonta africana*) wraps its companion in its trunk, which has a nerve cable thicker than that running from the animal's eyes to its brain. Credit: Martin Harvey/Getty

The nerve circuitry of a female elephant's trunk weighs a whopping 1.5 kilograms, thanks in part to a nerve bundle that is one of the largest known structures of its type in a living organism¹.

Access options

Subscribe to nature+

Get immediate online access to the entire Nature family of 50+ journals

\$29.99

monthly

[Subscribe](#)

Subscribe to Journal

Get full journal access for 1 year

\$199.00

only \$3.90 per issue

[Subscribe](#)

All prices are NET prices.

VAT will be added later in the checkout.

Tax calculation will be finalised during checkout.

Buy article

Get time limited or full article access on ReadCube.

\$32.00

[Buy](#)

All prices are NET prices.

Additional access options:

- [Log in](#)
- [Learn about institutional subscriptions](#)

Nature **601**, 486 (2022)

doi: <https://doi.org/10.1038/d41586-022-00114-6>

References

1. 1.

Purkart, L. *et al.* *Curr. Biol.* <https://doi.org/10.1016/j.cub.2021.12.051> (2022).

| [Section menu](#) | [Main menu](#) |

- RESEARCH HIGHLIGHT
- 17 January 2022

Cancer cells' keratin robes keep attackers at bay

Methods to strip away the keratin coat could make immune therapies more effective.

 Coloured transmission electron micrograph of a section through a ductal carcinoma of the breast

Cells from a type of breast cancer called a ductal carcinoma. Some carcinoma cells have keratin armour that protects against immune cells.
Credit: Steve Gschmeissner/Science Photo Library

Some cancer cells wrap themselves in a protein mesh that wards off immune cells — which helps to explain why treatments aimed at turning the immune system against tumours can fail¹.

Access options

Subscribe to nature+

Get immediate online access to the entire Nature family of 50+ journals

\$29.99

monthly

[Subscribe](#)

Subscribe to Journal

Get full journal access for 1 year

\$199.00

only \$3.90 per issue

[Subscribe](#)

All prices are NET prices.

VAT will be added later in the checkout.

Tax calculation will be finalised during checkout.

Buy article

Get time limited or full article access on ReadCube.

\$32.00

[Buy](#)

All prices are NET prices.

Additional access options:

- [Log in](#)
- [Learn about institutional subscriptions](#)

Nature **601**, 486 (2022)

doi: <https://doi.org/10.1038/d41586-022-00120-8>

References

1. 1.

Wang, Z. *et al.* *Proc. Natl Acad. Sci. USA*
<https://doi.org/10.1073/pnas.2119463119> (2022).

This article was downloaded by **calibre** from <https://www.nature.com/articles/d41586-022-00120-8>

| [Section menu](#) | [Main menu](#) |

- RESEARCH HIGHLIGHT
- 19 January 2022

‘Sceptres’ found in ancient tomb were actually beer straws

Metal tubes dating back millennia are the oldest surviving drinking straws.



Attendees of a Bronze Age funeral used metal straws (artist's impression) to drink beer from a communal jug. Credit: Kelvin Wilson

A 5,500-year-old set of long, thin tubes found in the northwestern Caucasus might be the oldest surviving drinking straws, an analysis of the utensils suggests¹.

Access options

Subscribe to nature+

Get immediate online access to the entire Nature family of 50+ journals

\$29.99

monthly

[Subscribe](#)

Subscribe to Journal

Get full journal access for 1 year

\$199.00

only \$3.90 per issue

Subscribe

All prices are NET prices.

VAT will be added later in the checkout.

Tax calculation will be finalised during checkout.

Buy article

Get time limited or full article access on ReadCube.

\$32.00

Buy

All prices are NET prices.

Additional access options:

- [Log in](#)
- [Learn about institutional subscriptions](#)

Nature **601**, 487 (2022)

doi: <https://doi.org/10.1038/d41586-022-00119-1>

References

1. 1.

Trifonov, V., Petrov, D. & Savelieva, L. *Antiquity*
<https://doi.org/10.15184/aqy.2021.22> (2022).

This article was downloaded by **calibre** from <https://www.nature.com/articles/d41586-022-00119-1>

- RESEARCH HIGHLIGHT
- 20 January 2022

Guided by the light, nimble nanovehicles make special deliveries

Nanometre-scale particles' asymmetrical shape makes them easier to 'drive' using near-infrared light.



Porous, nanometre-scale particles can ferry drugs that kill cancer cells.
Credit: L. Xie *et al./J. Am. Chem. Soc.*

Hollow nanoparticles shaped like acorns can act as tiny cargo carriers that move or dump their loads at the command of near-infrared light¹.

Access options

Subscribe to nature+

Get immediate online access to the entire Nature family of 50+ journals

\$29.99

monthly

[Subscribe](#)

Subscribe to Journal

Get full journal access for 1 year

\$199.00

only \$3.90 per issue

[Subscribe](#)

All prices are NET prices.

VAT will be added later in the checkout.

Tax calculation will be finalised during checkout.

Buy article

Get time limited or full article access on ReadCube.

\$32.00

[Buy](#)

All prices are NET prices.

Additional access options:

- [Log in](#)
- [Learn about institutional subscriptions](#)

Nature **601**, 487 (2022)

doi: <https://doi.org/10.1038/d41586-022-00115-5>

References

1. 1.

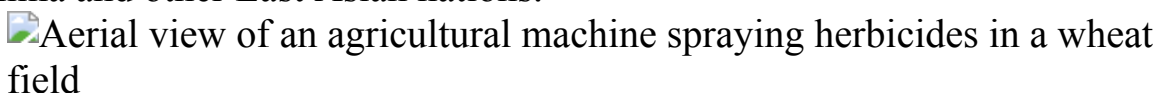
Xie, L. *et al.* *J. Am. Chem. Soc.* <https://doi.org/10.1021/jacs.1c10391> (2022).

| [Section menu](#) | [Main menu](#) |

- RESEARCH HIGHLIGHT
- 21 January 2022

Air pollution takes a bite out of Asia's grain crops

Ozone costs billions of dollars in yields of wheat and other staple crops in China and other East Asian nations.



A wheat field in Anqing, China. Ozone pollution cuts the nation's wheat production by one-third. Credit: Li Long/VCG/Getty

Farmers across East Asia lose an estimated US\$63 billion of grain annually because of ozone pollution, a by-product of fossil-fuel combustion¹.

Access options

Subscribe to nature+

Get immediate online access to the entire Nature family of 50+ journals

\$29.99

monthly

[Subscribe](#)

Subscribe to Journal

Get full journal access for 1 year

\$199.00

only \$3.90 per issue

[Subscribe](#)

All prices are NET prices.

VAT will be added later in the checkout.

Tax calculation will be finalised during checkout.

Buy article

Get time limited or full article access on ReadCube.

\$32.00

[Buy](#)

All prices are NET prices.

Additional access options:

- [Log in](#)
- [Learn about institutional subscriptions](#)

Nature **601**, 487 (2022)

doi: <https://doi.org/10.1038/d41586-022-00117-3>

References

1. 1.

Feng, Z., et al. *Nature Food* <https://doi.org/10.1038/s43016-021-00422-6> (2022).

| [Section menu](#) | [Main menu](#) |

News in Focus

- **[Tonga's huge blast and Omicron spread](#)** [26 January 2022]
News Round-Up • The latest science news, in brief.
- **[Has Biden followed the science? What researchers say](#)** [20 January 2022]
News • As the US president's first year in office ends, Nature assesses whether he's kept his promise to make evidence-based decisions.
- **[What Charles Lieber's conviction means for science](#)** [18 January 2022]
News • After Harvard chemist's trial, scientists report ripple effects for federal funding and research itself.
- **[Webb telescope reaches its final destination far from Earth](#)**
[24 January 2022]
News • The ambitious observatory has arrived at its home — near a gravitationally special spot called L2 — for a premier view of the Universe.
- **[Why scientists are racing to develop more COVID antivirals](#)** [21 January 2022]
News • The first crop of antivirals against SARS-CoV-2 is promising. But new drugs will be needed to counter the looming threat of resistance.
- **[Tonga volcano eruption created puzzling ripples in Earth's atmosphere](#)** [18 January 2022]
News • Powerful waves ringing through the atmosphere after the eruption of Hunga Tonga-Hunga Ha'apai are unlike anything seen before.
- **[Did a mega drought topple empires 4,200 years ago?](#)** [26 January 2022]
News Feature • People abandoned thriving cities in Mesopotamia, the Indus Valley and farther afield at about the same time as a decades-long drought gripped parts of the planet.

- NEWS ROUND-UP
- 26 January 2022

Tonga's huge blast and Omicron spread

The latest science news, in brief.



The Hunga Tonga–Hunga Ha'apai volcanic island as it appeared prior to the massive eruption on 15 January.Credit: Planet Labs PBC/EYEPRESS/Shutterstock

How the Tonga eruption is helping space scientists to understand Mars

NASA scientists say that the eruption of a submarine volcano in Tonga is helping them to understand how certain features formed on the surfaces of Mars and Venus.

The [unusual explosion of the Hunga Tonga–Hunga Ha‘apai volcano](#) has been calculated at more than 500 times the force of the atom bomb dropped on Hiroshima, Japan, in 1945.

Studying the volcano and its evolution in recent weeks is “important for planetary science”, says Petr Brož, a planetary volcanologist at the Institute of Geophysics of the Czech Academy of Sciences in Prague. The knowledge “might help us to reveal results of water–lava interactions on the red planet and elsewhere across the Solar System”, he says.

The volcanic island, which began to form from ash and lava expelled from an undersea volcano in early 2015, piqued the interest of researchers including James Garvin, chief scientist at NASA’s Goddard Space Flight Center in Greenbelt, Maryland, because of its similarity to [structures on Mars](#) and possibly Venus. “We don’t normally get to see islands form,” explains Garvin, but this one offered “a front-row seat”.

Volcanic islands typically last for just months before being eroded away. But Hunga Tonga–Hunga Ha‘apai survived for years, allowing Garvin’s team to use satellite observations and sea-floor surveys to study how such islands form, erode and persist. The researchers wanted to use that knowledge to understand how small conical volcanoes found on Mars might have formed in the presence of water billions of years ago.

Many volcanoes on Mars are thought to have erupted with steady flows of lava, but some could have been explosive, like Hunga Tonga–Hunga Ha‘apai, says Joseph Michalski, a planetary scientist at the University of Hong Kong.

The marine environment also mimics some aspects of the low-gravity settings on small planets such as Mars and “can shed unique light on Martian features that formed in lower gravity”, he adds.



A hospital worker in Bochum, Germany, cares for a person with COVID-19 at the start of Germany's Omicron-fuelled wave. Credit: Ina Fassbender/AFP/Getty

How does Omicron spread so fast? A high viral load isn't the answer

Around the world, Omicron has rapidly become the dominant SARS-CoV-2 strain. Now, two studies show that the variant has achieved success despite causing viral levels in the body that are similar to — or lower than — those of its main competitor, the Delta variant (J. A. Hay *et al.* Preprint at medRxiv <https://doi.org/hdgg> (2022); O. Puhach *et al.* Preprint at medRxiv <https://doi.org/hdgh>; 2022).

The results suggest that Omicron's hyper-transmissibility does not stem from the release of large amounts of virus from infected people, but from its ability to evade SARS-CoV-2 immunity caused by either vaccination or past

infection, says Emily Bruce, a virologist at the University of Vermont in Burlington. Previous research has hinted that Delta leads to a higher ‘viral load’, the amount of virus in an infected person, than other variants. This is often measured using a polymerase chain reaction (PCR) test, which provides an index of the quantity of viral RNA in the body.

To compare the variants’ viral loads, Yonatan Grad, an infectious-disease specialist at the Harvard T. H. Chan School of Public Health in Boston, Massachusetts, and his co-authors drew on test results of the staff members at the National Basketball Association, the organization responsible for professional basketball in North America. The researchers studied PCR-test results of swabs collected from infected players and personnel. Those who had Delta had a slightly higher peak viral load than did those with Omicron. “I was really not expecting to see that,” says Grad. After all, in only two months, Omicron had replaced Delta as the dominant cause of US COVID-19 cases.

Benjamin Meyer, a virologist at the University of Geneva in Switzerland, says that he, too, was stunned by Grad’s results. “Naturally, you’d think that higher transmissibility must cause a higher viral load,” he says.

Rather than measuring only viral RNA, Meyer and his colleagues assessed the number of infectious virus particles on swabs collected from a separate group of almost 150 infected people. This more stringent method found no significant difference between the viral loads of vaccinated individuals infected with Omicron and those infected with Delta.

The studies have not yet been peer reviewed.

Nature **601**, 489 (2022)

doi: <https://doi.org/10.1038/d41586-022-00156-w>

This article was downloaded by **calibre** from <https://www.nature.com/articles/d41586-022-00156-w>

- NEWS
- 20 January 2022

Has Biden followed the science? What researchers say

As the US president's first year in office ends, *Nature* assesses whether he's kept his promise to make evidence-based decisions.

- [Jeff Tollefson](#) ,
- [Max Kozlov](#) ,
- [Amy Maxmen](#) &
- [Alexandra Witze](#)



At the start of his administration, US President Joe Biden promised that he and his team would lead with science and truth.Credit: Saul Loeb/AFP/Getty

On the road to becoming US president in January 2021, Joe Biden promised to “listen to the science”. Many scientists *Nature* spoke to say he has largely made good on that pledge: the White House is no longer questioning the threat of COVID-19 and global warming, [as it did during the administration of his predecessor, Donald Trump](#). But as Biden’s first year comes to a close, researchers also say that just because the president has embraced science doesn’t mean his administration has always acted swiftly or sensibly on it.

“They’re saying the right things, and calling on programmes to do the right things on a whole range of issues,” says Andrew Rosenberg, who heads the Center for Science and Democracy at the Union of Concerned Scientists, an advocacy group based in Cambridge, Massachusetts. “But there’s an awful lot of work to do.”

Biden has scored highly with researchers [by elevating his science adviser](#), geneticist Eric Lander, to the White House’s inner circle — the cabinet — and by quickly moving to reverse many of the most stringent anti-science policies implemented by Trump. But frustrations are also mounting about how much the administration has been able to accomplish: its pandemic response has been hindered by vaccine hesitancy, misinformation and widespread mistrust of government. And its ambitious climate agenda has stalled because of political opposition in Congress.

Biden is operating in a difficult political environment, with scepticism in government institutions at an all-time high, says Susan Hyde, a political scientist at the University of California, Berkeley. Simply appointing the right people to the right positions won’t solve the problem, she adds. “How do you restore trust once a bureaucracy has been politicized? That’s an uphill battle for anybody.”

Safeguarding integrity

Biden aimed early in his administration to distinguish his science policy from Trump’s. For instance, just one week after Biden’s inauguration, he released a memorandum on “restoring trust in government through scientific integrity and evidence-based policymaking”. But it took months longer than expected to accomplish one of the most basic aims of that memorandum —

to have a task force review scientific-integrity policies across the government and recommend how they might be strengthened to safeguard against political interference.

Last week, the task force [finally released the report](#). It analysed some of the most [egregious breaches of scientific integrity](#) during the Trump administration, at agencies such as the National Oceanic and Atmospheric Administration, and concluded that the US government needs to standardize its policies across agencies and bring more accountability to those found to have violated the rules. It also recommends creating an interagency council on scientific integrity that could help to investigate violations.



In October 2020, then-president Donald Trump defiantly removed his mask upon returning to the White House, after being hospitalized with COVID-19. Before he was infected, Trump had questioned the seriousness of the disease. Credit: Win McNamee/Getty

But critics say that it does not go far enough. “While this report does a good job of setting the stage, there is also a lot more that needs to be done to actually guarantee protections for federal science,” says Lauren Kurtz, executive director of the Climate Science Legal Defense Fund in New York City. For instance, there are no details on what sort of consequences might

be appropriate for those found to have violated scientific integrity. The White House's Office of Science and Technology Policy, which led the report, says that it will be working to help implement the recommendations in the coming months.

Science watchdogs will be tracking how the White House handles this and a range of other issues, including environmental justice, nuclear weapons and thorny questions about [foreign interference in US research](#). They'll also be monitoring efforts to re-staff government agencies that lost thousands of scientists during the Trump administration. So far, those efforts have been remarkably successful at US agencies such as the Centers for Disease Control and Prevention (CDC) and the Food and Drug Administration (FDA), [according to an analysis](#) by the Union of Concerned Scientists. But other agencies, such as the Environmental Protection Agency (EPA), which shed more than 700 scientists under Trump, have struggled to make up lost ground.

Uncensoring public health

Biden's promises to restore trust in government and listen to scientists were welcome goals in January 2021, as a wave of COVID-19 infections was hitting the United States hard. The year before, Trump had contradicted recommendations made by public-health researchers at the CDC, and his administration [sidelined that agency](#) and meddled with its scientific reports.

Researchers aren't being obstructed at the CDC anymore, says Sam Groseclose, a former associate director of science at the CDC, who retired in December 2018. "They are encouraged to use science, so that's a much better environment," he says.

Still, some researchers say that in its decision-making, the CDC is neglecting what researchers have learnt from the social sciences and implementation science, which studies how health interventions are best applied in communities. For example, the CDC committed a blunder in May by recommending that vaccinated people no longer needed to mask in public places, says Helen Chu, an infectious disease specialist at the University of Washington in Seattle. The advice was sound at the time, if you had

considered virology data in a vacuum, Chu says, but it “didn’t incorporate what we know about human behaviour”. As many researchers predicted would happen, unvaccinated people also stopped wearing masks indoors, and COVID-19 cases rose before the CDC reversed its decision in late July.

Many researchers also say that the CDC has muddied the distinction between science and policy. Data can help officials to formulate policies, but policies are often based on other factors, too, such as keeping children in school and businesses running, says Kenneth Bernard, an epidemiologist and a top biodefence adviser to former presidents Bill Clinton and George W. Bush. At times, he says, CDC director Rochelle Walensky has failed to make this distinction clear to the public, which undermines trust.



CDC director Rochelle Walensky has come under fire for how the agency has communicated certain COVID-19 recommendations to the public. Credit: Jim Lo Scalzo/Getty

A prime example of this is the CDC’s guidance last month that people who test positive for COVID-19 isolate for only 5 days — down from 10 — if they don’t have ongoing symptoms. Initially, the CDC suggested that the recommendation was based on evidence about when the virus is most transmissible. But in the following days, Walensky clarified that the choice

was based on what the agency felt people would “tolerate”, and on a need to keep the country running in the face of an unprecedented surge in COVID-19 infections. “If she had said this clearly at the start, and stated that it was a trade-off of risks, people might have appreciated that,” says Angela Rasmussen, a virologist at the University of Saskatchewan in Canada. “Don’t say you’re following the science when you can’t point to the evidence.”

Former CDC director Tom Frieden agrees, suggesting that Biden might be almost too eager to show that he is not censoring science, by allowing the CDC to act independently. The White House and other agencies should not interfere with public-health science, Frieden says, but they should help to shape policies and should communicate them in a clear and unified way to avoid a flurry of confusion.

The CDC did not respond to a request for comment from *Nature*. But in an [interview this week with the Wall Street Journal](#), Walensky said she is being coached by a media consultant who will help her communicate CDC policy more clearly.

If the CDC fails to improve its handling of recommendations, researchers predict that Biden won’t be able to deliver on his promise of rebuilding trust in the government’s COVID-19 response and in the CDC.

Highs and lows for the FDA

After the Trump years, Biden also hoped to bring some normality back to the beleaguered FDA, which scientists had derided in 2020 after its controversial emergency authorizations of hydroxychloroquine and convalescent plasma as COVID-19 treatments. For the most part, Biden has returned things to how they were before, says Peter Lurie, president of the Center for Science in the Public Interest in Washington DC. Since Biden took office, the agency’s transparent review of antiviral drugs for emergency use, and its continued vigilance in monitoring for side effects from COVID-19 vaccines, serve as a model for what regulatory agencies should do in the face of a global pandemic, Lurie says.

Still, the FDA could do more to combat misinformation about vaccines and other products within the agency's purview, says Joshua Sharfstein, a vice-dean at the Johns Hopkins Bloomberg School of Public Health in Baltimore, Maryland. A deluge of misinformation about COVID-19 shots has contributed to a situation in which one-third of Americans have not been fully vaccinated. The FDA has been stuck in an “old way of communicating”, says Sharfstein, who served as the agency’s principal deputy commissioner during former president Barack Obama’s administration. It typically communicates with the public only when it is making a formal announcement, he says, and “that’s a lost opportunity”.

Erica Jefferson, the associate commissioner for external affairs at the FDA, responds that despite the agency’s efforts, “there continues to be an army of people both in the United States and abroad, that have continued to aggressively push misinformation that is inflicting significant harm”.

But experts say that Biden’s FDA will probably be remembered for a serious misstep last June, when it [approved the use of aducanumab](#) for people with Alzheimer’s disease — after an independent advisory panel had recommended that the drug be rejected because clinical-trial data had not definitively demonstrated that it could slow cognitive decline. Lurie says that the “deeply embarrassing” approval “shows that the agency is capable of making mistakes, even without the heavy hand of Trump”.

In response, Jefferson points out that the FDA used an ‘accelerated approval pathway’ for aducanumab “to allow earlier access to patients while we continue to acquire data on the drug’s benefit”. The agency required an additional clinical trial for the drug, to be completed within 9 years, as a condition of approval. “Our review has been thorough,” she adds.

Environmental protections

When it comes to the environment, Biden pledged not only to advance an ambitious climate agenda, but also [to rebuild a beleaguered EPA](#), which Trump took aim at early on in his presidency. One of the first decisions for Biden’s EPA administrator, Michael Regan, was to disband and reconstitute

the agency's main science advisory board, which had been stacked with industry-friendly scientists under the previous administration.

It was an unprecedented decision to start from scratch, says Chris Zarba, who managed that advisory board before retiring in 2018 and joining the Environmental Protection Network, an advocacy group created by former EPA employees. "They just went in and did what needed to be done."



After taking charge of the US Environmental Protection Agency under Biden, Michael Regan decided to disband the agency's main science advisory board and rebuild it. Credit: Joshua Roberts/Getty

The administration has also been busy on the rules and regulations front. For example, Regan reversed a controversial 'secret science' rule put in place under Trump that would have prevented the agency from considering non-public data when crafting regulations. Health data, such as information collected when studying the impact of air pollution on people, is often protected for privacy reasons. Many scientists say that the rule would have worked in industrial polluters' favour.

But much remains to be done. Scientists and advocacy groups say that Regan still faces challenges in rooting out improper industry influence: whistle-blowers have recently raised concerns about continued efforts to

downplay evidence of dangerous health impacts in chemical assessments, for instance. And the agency's work on climate change is just beginning. Although the administration has announced regulations targeting cars and methane emissions, the EPA has yet to address the impact of power plants, which could be crucial to meeting Biden's climate goals. The EPA did not immediately respond to *Nature*'s request for comment.

After Trump pulled the United States out of the 2015 Paris climate agreement, Biden signed an order on 19 February to bring the country back in, and made climate change [a fundamental part of his social and economic agenda](#). The administration's renewed emphasis on climate helped encourage other countries to commit to bolder emissions reductions at the United Nations summit in Glasgow in November, says Surabi Menon, a climate scientist who works with ClimateWorks Foundation, a philanthropic organization based in San Francisco, California.

Implementing Biden's domestic climate goals — [including a pledge to limit US greenhouse-gas emissions](#) to 50% of 2005 levels by 2030 — has proved more difficult. The Democrats' hallmark climate legislation — a [roughly \\$2-trillion spending bill](#) that includes hundreds of billions in proposed climate investments — is currently languishing in the US Senate. And environmentalists lamented the hypocrisy of the Biden administration authorizing oil and gas leases in the Gulf of Mexico just days after the Glasgow summit.

As is the case with creating pandemic policies at the CDC, many scientists and observers acknowledge that there is a difference between heeding climate science and crafting climate policies, which are subject to broader considerations and political pressures. "I do see the administration following the science," Menon says, "but when it comes to actual implementation, it might just take a little bit more time."

Nature **601**, 491-493 (2022)

doi: <https://doi.org/10.1038/d41586-022-00108-4>

| [Section menu](#) | [Main menu](#) |

- NEWS
- 18 January 2022

What Charles Lieber's conviction means for science

After Harvard chemist's trial, scientists report ripple effects for federal funding and research itself.

- [Andrew Silver](#)



Harvard chemist Charles Lieber leaves a courthouse in Boston, Massachusetts, during the week of his trial in December. Credit: Pat Greenhouse/*The Boston Globe* via Getty

Next week will mark two years since Harvard University chemist and nanotechnology pioneer Charles Lieber [was arrested on allegations](#) of lying to US federal authorities about his financial ties to China. Last month, a jury [convicted](#) him of making false statements, as well as related tax offences. Researchers say that the [high-profile US criminal case](#) is already having an impact on the scientific community. It marks the second time an academic researcher has been tried on accusations of hiding ties to China since the US Department of Justice (DOJ) launched its controversial ‘China Initiative’ to root out threats to national security.

“I think it makes clear to academic researchers the importance of fully and honestly disclosing the research funding they’re getting from sources to federal agencies when they’re applying for awards,” says Tobin Smith, vice-president for science policy and global affairs at the Association of American Universities in Washington DC, of which Harvard — in Cambridge, Massachusetts — is a member. “Transparency is critical to ensuring the integrity of scientific research.”

Lieber, whom Harvard placed on paid leave after his arrest, was principal investigator of a research team that received more than US\$15 million in federal grants from agencies including the US Department of Defense (DOD) and the National Institutes of Health (NIH) between 2008 and 2019. During the trial, prosecutors asserted that he had lied to or misled the DOD and the NIH about his participation in a Chinese government programme called the Thousand Talents Plan, intended to attract researchers from overseas. The prosecutors said that as part of Lieber’s Thousand Talents contract, the Wuhan University of Technology agreed to pay the scientist a salary of up to \$50,000 per month, plus living expenses and funds for starting up a laboratory. They also asserted that he didn’t report income from the Wuhan University of Technology or disclose a bank account in China with a balance exceeding \$10,000 during two calendar years to the Internal Revenue Service.

Ultimately, a federal jury found Lieber guilty on two counts of filing a false tax return, two counts of failing to file a report of foreign bank and financial accounts, and two counts of making false statements to federal authorities.

In pursuit of a Nobel

Unsurprisingly, Lieber's prosecution has had a significant impact on his laboratory and colleagues, researchers say. According to sources *Nature* spoke to, Lieber's research group has dispersed; students and postdoctoral researchers who were based in his lab at the time of his arrest have since moved to other positions. Harvard has declined to comment on the status of Lieber's team.

Anqi Zhang, a former student in Lieber's lab who is now a postdoctoral materials-science researcher at Stanford University in California, says Lieber was a good mentor and devoted scientist committed to his work. She testified as a witness for his defence during the trial and did not expect him to be convicted. "I just feel really sorry that he has to go through this," she says.

Others have been more critical. "He is a very accomplished scholar who can make very substantial contributions on the one hand, and on the other, it's a blatant abuse of federal funding and potentially encouraging threats to US prosperity and security," says Charles Wessner, an innovation-policy researcher at Georgetown University in Washington DC.

A lawyer for Lieber said in a statement to *Nature*: "Notwithstanding the verdict, Charlie Lieber should be embraced. His impact as a scientist, a researcher and a teacher is undeniable. He still has a lot more to give."

Some scientists have also pointed to the effect of the case on Lieber's research. Known for developing revolutionary nanomaterials for medicine and biology, Lieber's lab has produced innovations that include [nanoscale wires](#) that can record electrical signals from live cells such as neurons.

His research being put on hold "is a really huge loss, as he was doing cutting-edge science", says Kang-Kuen Ni, a physicist who has not

collaborated with Lieber but works in Harvard's chemistry and chemical biology department, which Lieber previously chaired.

After the trial, much was made of the fact that Lieber mentioned during an FBI interrogation that many researchers want to win a Nobel prize.

Interrogation footage shown to the jury suggested that this desire was one reason he formed links with China. Neal Lane, a science and technology policy researcher at Rice University in Houston, Texas, doubts that any prestige from a foreign talent-recruitment programme would influence the decision-making of a Nobel committee. But he says that what Lieber probably meant was that his pursuit of a prize was a rationale for accepting money and potentially other resources that could advance his research, such as facilities, equipment or employees.

Disclosing foreign ties

The DOJ launched the China Initiative in 2018 under the administration of then-president Donald Trump, and has continued it under US President Joe Biden. Researchers have called for an end to the initiative, saying that it has damaged lives because some academics are being falsely accused of crimes. Many also say that it has [led to racial profiling](#), which the US government has denied. “It signals that scientists with any connection to China — past or present — are automatically suspected of wrongdoing,” Lane says.

But there are signs that the government’s stance could be changing. In October last year, US attorney-general Merrick Garland testified before Congress that the DOJ would review the initiative.

The government is also working to clarify and simplify how scientists transmit information about foreign ties to federal funding agencies. On 4 January, the White House Office of Science and Technology Policy issued guidance on how agencies should implement improved research-security measures that Trump had called for. Trump’s measures called for better standardization of policies and reporting forms concerning conflicts of interest and commitment, and ensuring that consequences for disclosure-requirement violations were appropriate.

Smith is hopeful that the guidance will lead to increased compliance among researchers, and he says it signals that the government is working to provide more clarity about penalties, and ensure that they are appropriate. However, he thinks it might still be necessary to prosecute some researchers. “The key is to get the balance right and make sure the cases that are being brought are legitimate and strong and are really going after people who have done egregious things that are a threat to national security, or who have done things that are wrong,” he says.

Lieber’s prosecution sends a strong signal to US researchers about the importance of disclosure, and could lead them to pay more attention to whom they’re working for, or with, in partnerships with China, Wessner says.

Next steps for Lieber

After the trial, [Reuters reported](#) that Lieber’s defence team had said it “will keep up the fight”, but the lawyer in question did not respond to a request from *Nature* for further comment on the verdict. No date has been set for sentencing, according to public court records.

Gabriel Chin, a criminal-law specialist at the University of California, Davis, thinks that Lieber’s contributions to science could be taken into account into his sentencing, but says that it’s not clear whether they will be a benefit or a disadvantage. “It is not as though he was a poor person who needed the money, or that he did not have the intelligence to understand the law, or the resources to hire lawyers to comply with it,” he says. “In addition, his significant scientific contributions and expertise may make his secret association with a foreign power all the more potentially harmful.”

Meanwhile, Lieber has been unsuccessful in an attempt to sue Harvard and compel it to pay for his legal fees. Although the institution has a policy to pay defence costs for some staff members facing legal action related to their university work, one university official determined that Lieber probably violated university policy. On 10 January, the Massachusetts Supreme Judicial Court reinforced an earlier ruling by a lower court that Harvard has the right to reject Lieber’s request. However, an attorney representing Lieber

in his civil suit told university newspaper *The Harvard Crimson*: “We disagree with the court’s decision, and are assessing options as to next steps.”

Nature **601**, 493-494 (2022)

doi: <https://doi.org/10.1038/d41586-022-00107-5>

This article was downloaded by **calibre** from <https://www.nature.com/articles/d41586-022-00107-5>

| [Section menu](#) | [Main menu](#) |

- NEWS
- 24 January 2022
- Correction [25 January 2022](#)

Webb telescope reaches its final destination far from Earth

The ambitious observatory has arrived at its home — near a gravitationally special spot called L2 — for a premier view of the Universe.

- [Alexandra Witze](#)



This image of the Webb telescope was captured by cameras on board the rocket that launched it into space, just after the two separated. Credit: Arianespace, ESA, NASA, CSA, CNES ([CC BY 2.0](#))

NASA's James Webb Space Telescope has just reached its final destination — around a gravitationally special spot in space known as the second

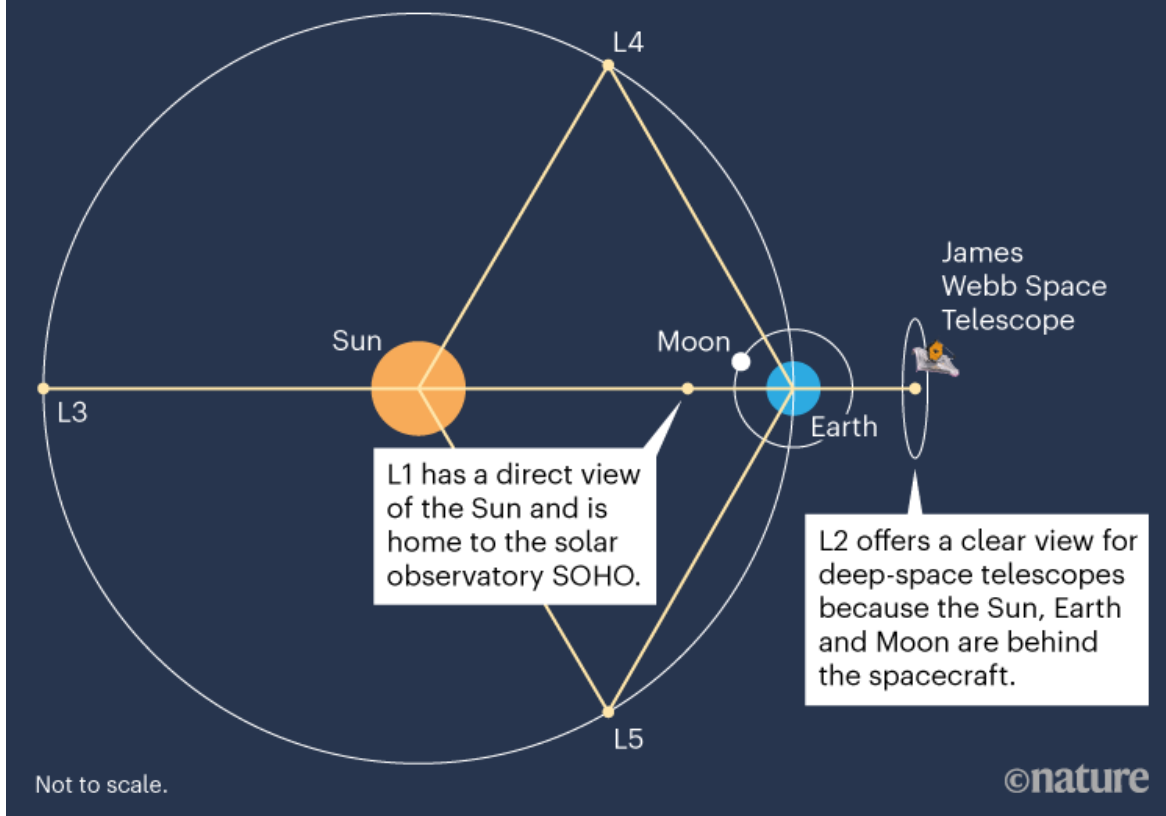
Lagrange point, or L2. The US\$10-billion observatory could spend 20 or more years there, gathering unprecedented insights about the Universe as it stares into deep space.

Webb, which is the most complex telescope ever built, has been heading towards L2 since [its Christmas Day launch](#). On 24 January, it fired a set of thrusters and nudged itself into orbit around the point, which it will circle once every six months or so. L2 is on the opposite side of Earth from the Sun, about 1.5 million kilometres away, or four times the distance to the Moon. There, the gravitational pull of the Sun and Earth equals the centripetal force required for Webb to move with them.

Only a handful of space missions have travelled to L2, which is one of five Lagrange points in the Sun–Earth system. But more missions are planned, because the location is particularly good for sensitive astronomical observatories such as Webb. “There are a couple of unique things about L2 that make it ideal for astronomy missions,” says David Milligan, a spacecraft operations manager at the European Space Agency (ESA) in Darmstadt, Germany.

VANTAGE POINTS

The James Webb Space Telescope will orbit a gravitationally special position in space known as the second Lagrange point, or L2. Of the five Lagrange points in the Sun-Earth system, two are home to spacecraft.



©nature

Source: Adapted based on materials from NASA/WMAP Science Team

Those include the ability to look at most of the sky unimpeded. Telescopes that orbit Earth, such as the Hubble Space Telescope, have a lot of their view blocked by the planet for much of the time. Facing away from the Sun, the Webb telescope can keep it, as well as Earth and the Moon, behind it. “L2 is really nice because it’s got the brightest objects — the Sun, the Earth and the Moon — on the same side as far as the spacecraft is concerned,” says Karen Richon, an engineer who heads Webb’s flight-dynamics team at the NASA Goddard Space Flight Center in Greenbelt, Maryland. “You can make a big sunshield and block all three of those all the time.”

That's exactly what Webb does. From L2, its tennis-court-sized sunshield always blocks the Sun, while its 6.5-metre-wide primary mirror gazes into the darkness of deep space. Webb will study a number of astronomical objects, including the most distant galaxies in the Universe, the atmospheres of extrasolar planets and stellar nurseries shrouded in dust.

Cold reception

L2's other big advantage is that it's cold. Earth-orbiting missions go in and out of sunlight on each orbit, experiencing huge temperature swings that cause equipment to expand and contract. Scientific instruments that have to remain cold to function do better at L2, where the temperature is much more stable. Webb's four scientific instruments operate at temperatures of about -233°C — or 40 degrees above absolute zero — to spot faint glimmers of heat coming from stars, galaxies and other cosmic objects.

The Lagrange points are named after their identifier, mathematician Joseph-Louis Lagrange, who in 1772 discovered them as locations where a small body can orbit in concert with two larger masses. That makes L1 and L2, the closest Lagrange points to Earth, obvious places to exploit for space exploration.

“There is a natural flow from Earth into these locations,” says Kathleen Howell, an aerospace engineer at Purdue University in West Lafayette, Indiana. Yet “only in the past few decades have we even known that path was there”.

This animation shows how the Webb telescope will orbit L2 from two perspectives. Credit: NASA's Goddard Space Flight Center

The first spacecraft to travel to a Lagrange point was NASA's International Sun-Earth Explorer 3 mission, which launched in 1978 and went to L1, a point on the sunward side of Earth. That mission showed it was possible to send spacecraft into orbit around a Lagrange point, Howell says. In 1995, ESA sent the Solar and Heliospheric Observatory to an orbit around L1; it and several other missions are still studying the Sun and space weather from that point.

The first mission to operate from L2 was the Wilkinson Microwave Anisotropy Probe, a NASA mission that studied the afterglow of the Big Bang between 2001 and 2010. ESA has sent several spacecraft to L2, including its now-defunct Herschel Space Observatory, which, like Webb, studied infrared astronomy. There are currently two other missions at L2: ESA's star-mapping Gaia spacecraft and the Russian–German astrophysical observatory Spektr-RG. All three are in different orbits, so there is no danger of them smashing into one another, Milligan says. Also, he notes, “space is huge”.

Thrust and burn

No spacecraft are located precisely at the L2 point, because it is gravitationally unstable. “We never actually get to L2 — we get near it,” Richon says. Webb travels along an ellipse with a semimajor axis (the maximum distance between the spacecraft and L2) that ranges between 250,000 and 832,000 kilometres. Webb does not pass into the Moon’s shadow, allowing its solar panels to remain fully charged and its antennas to communicate constantly with Earth.

To stay in this orbit, Webb needs to make small adjustments about once every three weeks, burning its thrusters to keep it looping around L2. Otherwise, the mission would drift off into interplanetary space. If nothing goes wrong, Webb’s lifetime will be dictated by when it runs out of the fuel it carries to keep it in position around L2.

But NASA has been looking into ways to keep L2 missions operating beyond their planned lifetimes. Webb could, in theory, be visited by a robotic spacecraft to rendezvous and supply more fuel. Howell has also been designing orbits for service spacecraft to travel from a planned ‘gateway’ space station near the Moon to L2 and back again. Future planned missions to L2 include NASA’s Nancy Grace Roman Space Telescope, scheduled to launch in 2027, and ESA’s planet-hunting Plato and Ariel missions, slated for launch in 2026 and 2029, respectively.

Entering orbit around L2 marks the end of Webb’s first month of complicated deployments, such as unfurling its sunshield. On 8 January, [it](#)

[passed a milestone](#) when it unfolded the final segment of its primary mirror. Since then, engineers have been adjusting the alignment of the 18 hexagonal segments that comprise the mirror. Next come four months of cooling and calibrating its four science instruments, before it begins doing science no earlier than June.

Webb is a collaboration between NASA, ESA and the Canadian Space Agency.

Nature **601**, 495 (2022)

doi: <https://doi.org/10.1038/d41586-022-00128-0>

Updates & Corrections

- **Correction 25 January 2022:** The original version of this story incorrectly said that the Solar System has five Lagrange points. In fact, there are five Lagrange points for any system with two massive bodies, such as the Sun–Earth system.

This article was downloaded by **calibre** from <https://www.nature.com/articles/d41586-022-00128-0>

| [Section menu](#) | [Main menu](#) |

- NEWS
- 21 January 2022

Why scientists are racing to develop more COVID antivirals

The first crop of antivirals against SARS-CoV-2 is promising. But new drugs will be needed to counter the looming threat of resistance.

- [Max Kozlov](#)



Pharmacy shelves worldwide are being stocked with COVID-19 antivirals Paxlovid (pictured) and molnupiravir. Credit: YONHAP/EPA-

EFE/Shutterstock

The roll-out of COVID-19 vaccines at the beginning of 2021 marked a key turning point in the fight against the global pandemic. Another major milestone arrived at the end of the year, with the approval of two oral antiviral treatments — [molnupiravir and Paxlovid](#) — that promise to reduce the number of COVID-19 hospitalizations and deaths. But as these pills slowly make their way into pharmacies worldwide, researchers are already looking ahead to the drugs that could supersede them.

“These are our first-generation antivirals against coronaviruses,” says Sara Cherry, an immunologist at the Perelman School of Medicine at the University of Pennsylvania in Philadelphia. Our experience with antivirals against other diseases, like hepatitis C and HIV, proves that “we can do better and better over time”, she adds.

Clinical-trial data showed that molnupiravir, developed by the pharmaceutical firm Merck, based in Kenilworth, New Jersey, and the biotechnology company Ridgeback Biotherapeutics in Miami, Florida, cut hospitalizations and deaths by 30%, compared with people who took placebos. Meanwhile, Paxlovid (nirmatrelvir and ritonavir), made by Pfizer, based in New York City, cut hospitalizations and deaths by 89%. UK regulators approved molnupiravir in November and Paxlovid in December, and US regulators granted emergency authorizations for both drugs in December. Other countries have followed suit with their own approvals, and many are negotiating with the drug makers to buy courses of the drugs or to manufacture their own generic versions.

For now, the pills are in short supply. Drug makers are still scaling up production of the antivirals, which are in huge demand to treat the highly transmissible [Omicron variant](#). But when they become more widely available — and if their clinical-trial data is borne out in the real world — the pills will become vital tools to prevent people from becoming seriously ill with COVID-19, says Cherry.

It’s too soon to tell whether SARS-CoV-2 is likely to develop any resistance to these first-generation antivirals, says Tim Sheahan, a coronavirologist at the University of North Carolina at Chapel Hill. Although its sky-high rate

of replication is a breeding ground for mutations, he says, the virus also causes acute infections that offer relatively little time for resistance-causing mutations to accumulate.

But the threat of resistance is particularly severe for ‘monotherapies’ such as molnupiravir and Paxlovid that each target only one part of the virus. That’s why it’s imperative to develop new antivirals aimed at different targets, or ones that can be combined into a single treatment to attack the virus on multiple fronts, says Sheahan.

A race against resistance

Successful antivirals have typically targeted two key pieces of a virus’s biological machinery, a polymerase and a protease, both of which are essential for viral replication. The current COVID pills are no exception: Paxlovid inhibits SARS-CoV-2’s main protease, whereas molnupiravir tricks its RNA polymerase into incorporating part of the drug into the virus’s RNA, creating so many errors that it cannot survive. A third drug — remdesivir, developed by Gilead, based in Foster City, California — inhibits RNA polymerase, but treatment is expensive and currently requires intravenous infusions over three consecutive days, making it inaccessible to many people.

Unfortunately, molnupiravir’s mode of attack means that it might not be wise to include it in a combination therapy, says Luis Schang, a virologist at Cornell University in Ithaca, New York. If the treatment does not completely wipe out the virus in a patient, some of the RNA errors it creates might inadvertently give the virus resistance against the other drug in the combination. That’s why it’s a key priority for researchers to find an accessible drug that effectively blocks the virus’s RNA polymerase, he says, which could be used in partnership with a protease inhibitor such as Paxlovid. One option may be an oral version of remdesivir, which Gilead is currently testing.

Other antiviral drug candidates are slowly working their way through the clinical-trial pipeline, says Carl Dieffenbach, director of the division of AIDS at the US National Institute of Allergy and Infectious Diseases

(NIAID). He says that one promising candidate is a protease inhibitor, developed by Shionogi & Company, based in Osaka, Japan, and Hokkaido University in Japan, that is currently in phase II/III clinical trials in Asia. The candidate targets the same protease as Paxlovid but would only require patients to take a single pill each day.

That simpler regimen could help to avert the rise of resistance, Cherry says. Unfinished treatments can hasten drug resistance by allowing the virus to develop defences against the drug while it continues multiplying and wreaking havoc in the body. Both molnupiravir and Paxlovid consist of several pills that must be taken twice a day for five consecutive days. “The second you have people taking something multiple times a day when they’re sick is when you have issues with compliance,” Cherry says.

Target practice

Researchers should also develop treatments that target other parts of the virus, Schang says. “This time we got lucky with a virus that encodes both a polymerase and a protease, and here we are two years later with only a suboptimal arsenal,” he says. “We really have to identify and validate new targets for antivirals so that when the next [pandemic] happens, we have a much broader pipeline to choose from.”

Other potential targets include a different protease in SARS-CoV-2 called PL_{pro}, and an enzyme called methyltransferase that stabilizes the virus’s RNA, says Matt Hall, the director of the early translation branch at the US National Center for Advancing Translational Sciences (NCATS). Clear Creek Bio, a biotechnology firm based in Cambridge, Massachusetts, announced on 6 January that it will collaborate with NCATS to develop an oral drug targeting the PL_{pro} enzyme.

Dieffenbach says that researchers would ideally like to identify targets that are common to entire families of viruses and inhibit them with a single drug. That would potentially allow public-health officials to rapidly deploy an effective antiviral the next time a novel virus with pandemic potential emerges.

Developing such broad-spectrum drugs will take significant public and private investment, and the cooperation of pharmaceutical companies, says Hall. Calls for such efforts were not heeded in the wake of the 2003 SARS-CoV outbreak, he adds, but the latest pandemic has underlined the need for action. Last year, the United States appropriated US\$1.2 billion to NIAID to launch the Antiviral Drug Discovery Centers for Pathogens of Pandemic Concern, which will fund basic research on developing antivirals for seven virus families. Hall says this gives him hope that antiviral research will continue even as the COVID-19 pandemic wanes.

But all antivirals face an inherent limitation, says Dieffenbach: they must be taken within days of infection to stop a virus from proliferating. Antivirals are only effective if people acknowledge that they might be ill, and can access tests that provide a timely diagnosis. “We can build the best drugs in the world, but if people don’t understand that they have to get on board quickly, they’re not going to do any good,” says Dieffenbach. “Pills do not take themselves.”

Nature **601**, 496 (2022)

doi: <https://doi.org/10.1038/d41586-022-00112-8>

This article was downloaded by **calibre** from <https://www.nature.com/articles/d41586-022-00112-8>

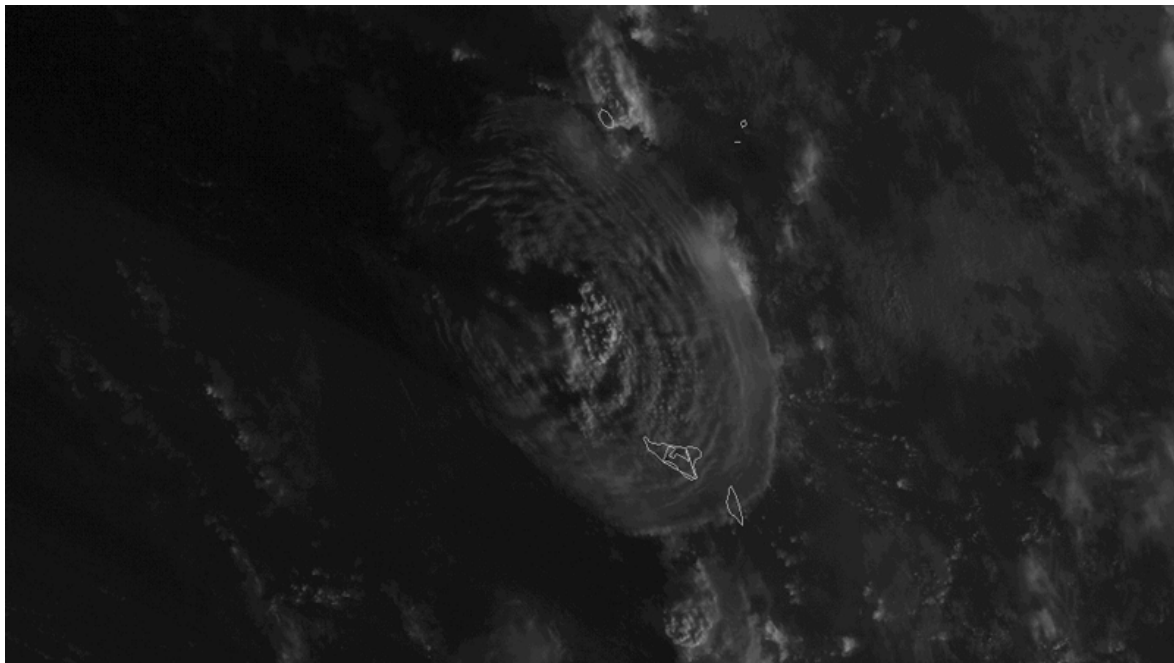
| [Section menu](#) | [Main menu](#) |

- NEWS
- 18 January 2022

Tonga volcano eruption created puzzling ripples in Earth's atmosphere

Powerful waves ringing through the atmosphere after the eruption of Hunga Tonga–Hunga Ha'apai are unlike anything seen before.

- [David Adam](#)



The US National Oceanic and Atmospheric Administration's GOES-West satellite captured the explosive eruption of Hunga Tonga–Hunga Ha'apai. Credit: NOAA

Scientists are racing to understand a puzzling series of massive ripples in Earth's atmosphere triggered by the eruption of the Tongan volcano at the weekend. Satellite data shows that the event — which some fear might have devastated the Pacific-island nation — provoked an unusual pattern of atmospheric gravity waves. Previous volcanic eruptions have not produced such a signal, leaving experts stumped.

"It's really unique. We have never seen anything like this in the data before," says Lars Hoffmann, an atmospheric scientist at the Jülich Supercomputing Centre in Germany.

The discovery was made in images collected by the Atmospheric Infrared Sounder (AIRS), mounted on NASA's Aqua satellite, in the hours after the eruption of the Hunga Tonga–Hunga Ha'apai volcano on 14 January.

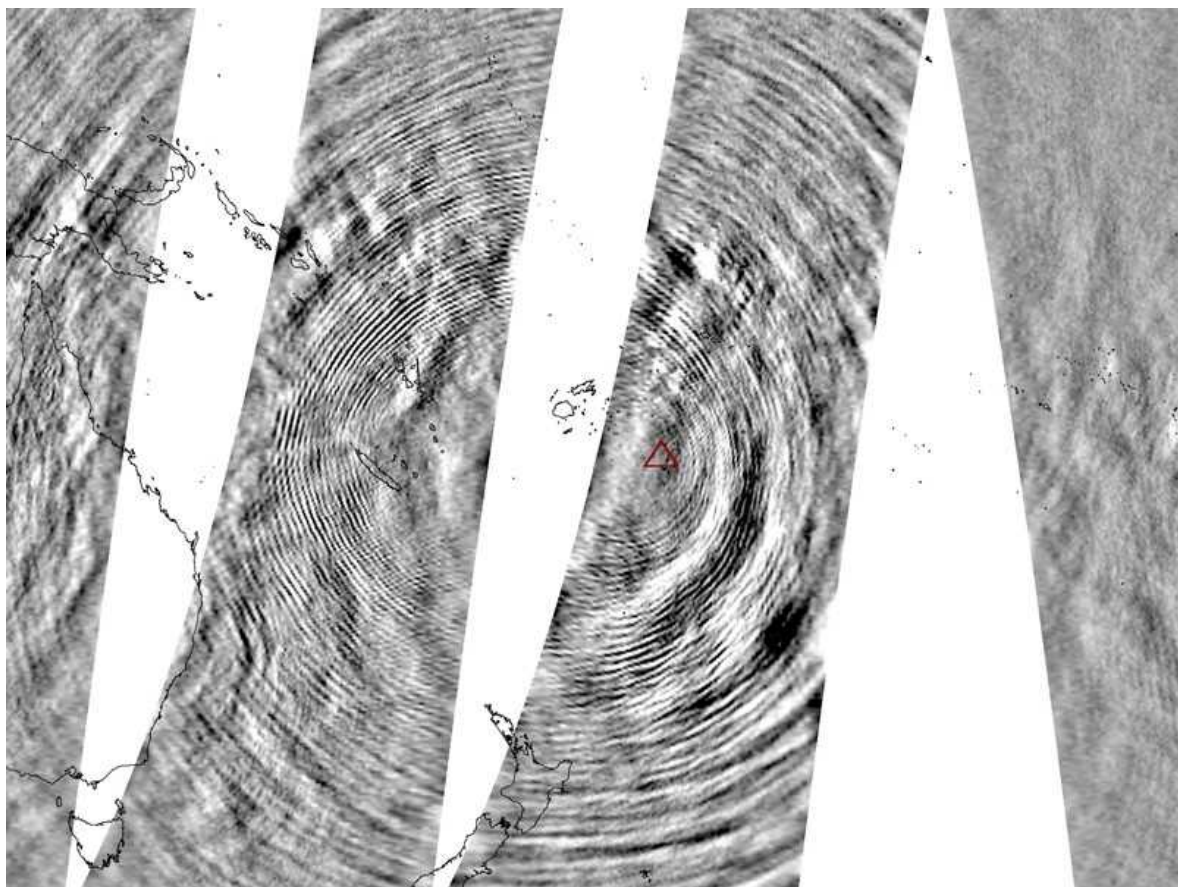
They show dozens of concentric circles, each representing a fast-moving wave in the gases of the atmosphere, stretching for more than 16,000 kilometres. The waves reached from the ocean surface to the ionosphere, and researchers think that they probably passed around the globe several times.

'Nice concentric wave patterns'

"This instrument has been operating for something like 20 years now and we have never seen such nice concentric wave patterns," Hoffmann adds.

Atmospheric gravity waves occur when air molecules in the atmosphere are vertically, rather than horizontally, disturbed in the air column. This can happen as wind picks up speed as it rises over a mountaintop, or as a result of convection in local weather systems.

The up-and-down waves transfer energy and momentum through the atmosphere, and often show their effects in the way in which they cause high clouds to form in a series of ripples.



Images from the Atmospheric Infrared Sounder on NASA's Aqua satellite show dozens of concentric circles, which are fast-moving atmospheric waves. Credit: Lars Hoffmann, Jülich Supercomputing Centre. AIRS Level-1 data by NASA DES DISC

In theory, the rapid updraft of hot air and ash from an erupting volcano into the upper atmosphere could trigger gravity waves on a much larger scale. But nothing like this has been observed with previous eruptions analysed since the AIRS instrument was launched in May 2002.

“That’s what’s really puzzling us,” says Corwin Wright, an atmospheric physicist at the University of Bath, UK. “It must have something to do with the physics of what’s going on, but we don’t know what yet.”

He and his co-workers suspect that a “great big, messy pile of hot gases” in the upper atmosphere might be what kicks the waves off. The hot gas is “going up high into the stratosphere and knocking the air around”, he says.

Eruption heard across the planet

The eruption of the Hunga Tonga-Hunga Ha'apai volcano was heard across the South Pacific, and even in parts of the United States. Ash has covered many regions of Tonga, but a loss of power, phone lines and Internet connectivity has made it difficult for aid agencies to assess the extent of injuries, fatalities and damage.

Wright, who was the first to spot the wave patterns in data supplied by Hoffmann, says that the images show what looks like a mixture of wave sizes and types.

The convection in the atmosphere seems to be “very complicated and bumpy, and it’s generating a whole family of things at the same time”, he says. “That is what we currently think is going on, but we’ve only been looking at it for a few hours.”

The discovery was prompted by a [tweet](#) sent to Wright on 15 January from Scott Osprey, a climate scientist at the University of Oxford, UK, who asked: “Wow, I wonder how big the atmospheric gravity waves are from this eruption?!”

Explosive speed

Osprey says that the eruption might have been unique in causing these waves because it happened very quickly relative to other eruptions. “This event seems to have been over in minutes, but it was explosive and it’s that impulse that is likely to kick off some strong gravity waves,” he says.

The eruption might have lasted moments, but the impacts could be long-lasting. Gravity waves can interfere with a cyclical reversal of wind direction in the tropics, Osprey says, and this could affect weather patterns as far away as Europe. “We’ll be looking very carefully at how that evolves,” he says.

The imagery and data collected from the eruption has been “spectacular” and has presented scientists with an exciting opportunity, says Vicki Ferrini,

a marine geophysicist at Columbia University in New York City. But she adds that she and others remain deeply concerned for the people of Tonga, particularly given the absence so far of detailed information on the scale of the disaster.

Researchers in New Zealand say that they are closely monitoring the volcano for further eruptions. “We are just keeping our ears to the ground,” says Shane Cronin, a volcanologist at the University of Auckland. The volcano could be resupplied with large amounts of magma from deep underground and produce more explosive eruptions, he says. But if it has exhausted its main supply, it might produce only smaller eruptions, largely hidden beneath the surface of the ocean.

Nature **601**, 497 (2022)

doi: <https://doi.org/10.1038/d41586-022-00127-1>

Additional reporting by Smriti Mallapaty.

This article was downloaded by **calibre** from <https://www.nature.com/articles/d41586-022-00127-1>

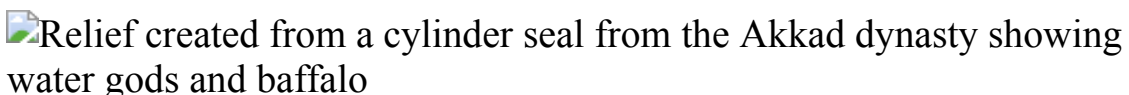
| [Section menu](#) | [Main menu](#) |

- NEWS FEATURE
- 26 January 2022

Did a mega drought topple empires 4,200 years ago?

People abandoned thriving cities in Mesopotamia, the Indus Valley and farther afield at about the same time as a decades-long drought gripped parts of the planet.

- [Michael Marshall](#) 0



Water flows from a vessel held by a god in this seal of an Akkadian king from around 2200 bc, about the time that a drought affected the empire.
Credit: The Art Archive/Shutterstock

The missing earthworms were a sign. As archaeologist Harvey Weiss and his colleagues excavated a site in northeast Syria, they found a buried layer of wind-blown silt so barren there was hardly any evidence of earthworms at work during that ancient era. Something drastic had happened thousands of years ago — something that choked the land with dust for decades, leaving a blanket of soil too inhospitable even for earthworms.

The drought hit in roughly 2200 bc, when the Akkadian Empire dominated what is now Syria and Iraq. By 2150 bc, the empire was no more. The central authority had disintegrated, and many people had voted with their feet, leaving the region.

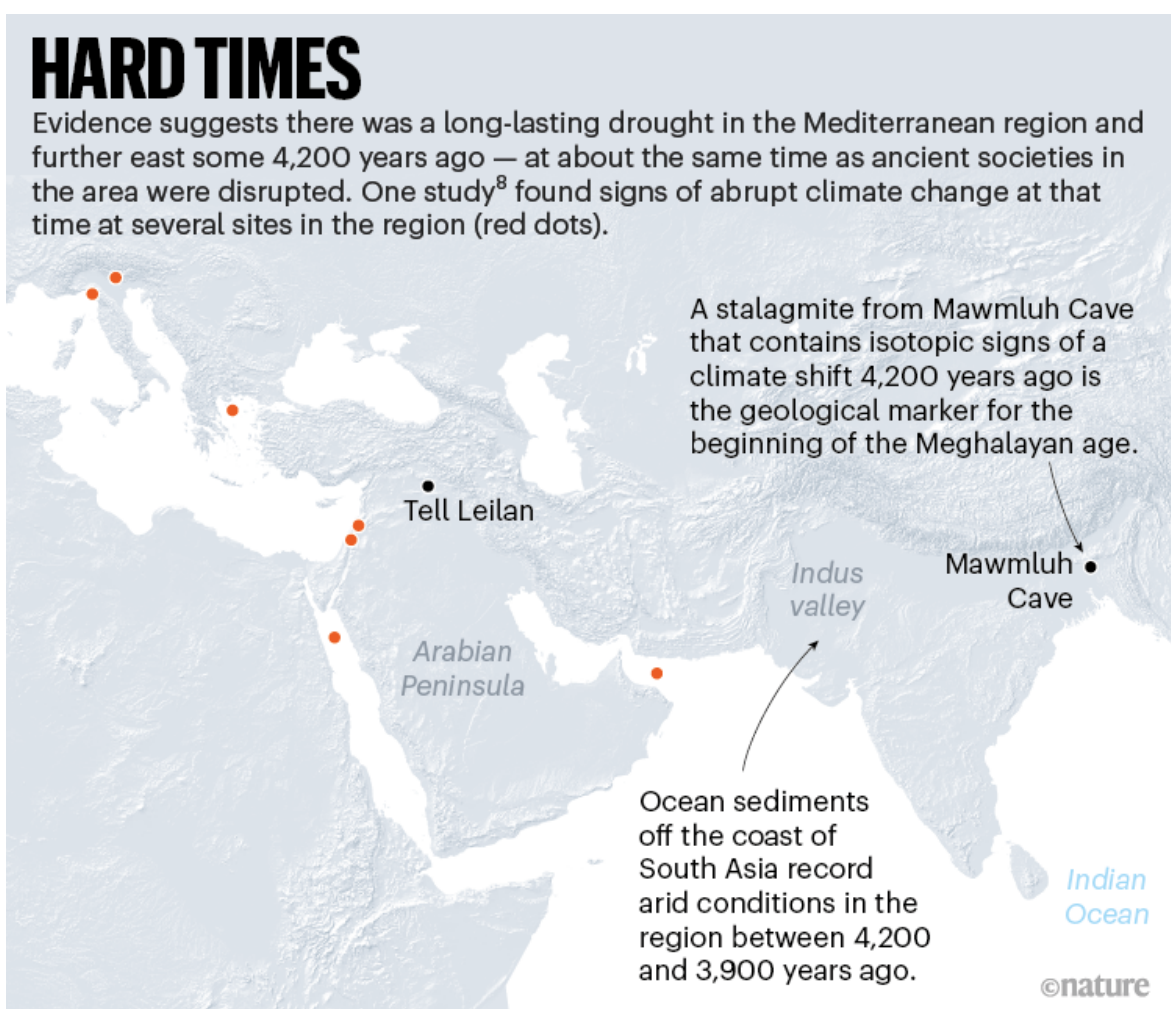
The overlap between an epic drought and the collapse of the Akkadian Empire was no mere coincidence, according to Weiss, an archaeologist at Yale University in New Haven, Connecticut. When he and his colleagues

discovered the evidence of drought in the early 1990s, they proposed that the abrupt climate disruption had brought the ancient empire down¹. This example has become a grim warning of how vulnerable complex societies can be to climate change.

For Weiss, it was the start of a research endeavour spanning decades. He has become convinced that the drought of 2200 bc was not confined to Mesopotamia, but rather that it had effects around the globe. What's more, the Akkadian Empire was not the only complex society that was disrupted or overthrown as a result. "We've got Mesopotamia, the Nile, the Aegean and the Mediterranean all the way to Spain," says Weiss. In all these places, he says, there is evidence from around 4,200 years (kyr) ago for a drying climate, for the collapse of central authorities, and for people moving to escape the newly arid zones (see 'Hard times').

HARD TIMES

Evidence suggests there was a long-lasting drought in the Mediterranean region and further east some 4,200 years ago — at about the same time as ancient societies in the area were disrupted. One study⁸ found signs of abrupt climate change at that time at several sites in the region (red dots).



Source: Ref. 8

The drying is now known by many in the field as the 4.2 ka bp event; also written as 4.2 kyr bp (bp meaning before 1950). It has become increasingly prominent in studies of Earth's recent past. Most significantly, in 2018 it became enshrined in the geological timescale as the start of the current age, the Meghalayan, named after a region in India in which a stalagmite holds a record of the climatic shift. Such geological boundaries can only be defined on the basis of global transitions — so the implication was that the 4.2 ka bp event affected the entire planet.

However, the 4.2 ka bp event has been dogged by controversy. The choice to use it to mark the start of the Meghalayan has faced constant criticism. Many researchers argue that evidence indicates the event was not a global one. Instead, it seems that there was a series of droughts around this time, rather than one long dry spell — or that the shifts were confined to certain regions.

The difference between a global drought and asynchronous dry spells matters, because it has implications for understanding the origins of the climatic changes. Furthermore, the debate touches on the long-running anthropological arguments over whether climatic shifts can be said to cause societal disruption, and what is meant when societies are said to have collapsed.

Nevertheless, a consensus is beginning to emerge that some type of drying event happened around 4,200 years ago across an extended area that had an impact on the people living there — even if it was not the global upheaval that Weiss argues for.

"It's pretty conclusive that the 4.2 ky event exists in the Mediterranean," says Nick Scroxton, a palaeoclimatologist at Maynooth University in Ireland. The drought affected parts of the Middle East, but he says that the evidence elsewhere is "inconclusive".

This isn't just a matter of ancient history. If a centuries-long drought gripped large parts of the planet thousands of years ago, it could happen again. So researchers say it is crucial to nail down exactly what happened during that drought so long ago.

Abandoned city

The story of research into the 4.2 ka bp event begins in northeast Syria, at an archaeological site called Tell Leilan. This hill holds the preserved remains of a city that thrived there for centuries before and during the time of the Akkadian Empire. Weiss and his colleagues started excavating there in the late 1970s.

In the early 1990s, Weiss realized that the city had temporarily been abandoned. People lived there from 2700 to 2200 bc and then, after a 300-year hiatus, there are signs of occupation again around 1900 bc, he says.

What's more, it seemed obvious why. The team found evidence in the soil that Tell Leilan's climate dried out around 2200 bc, and that this drought lasted for decades¹. They described a 20-centimetre-thick layer of grey sand-like pellets, mixed with other fine powders — a stark contrast to the thick loams from around 2300 bc. "We didn't have an explanation for what had caused it, but we knew from our local data that there was an aridification event," says Weiss.

The drought presumably made it harder to raise crops, meaning there would not have been enough food for the city's population. And the pattern was not unique to Tell Leilan. "There were similar abandonments extending from the Mediterranean to the Indus," says Weiss. This suggested that the drought spanned much of southwest Asia, leading to societal upheaval.

Weiss and his colleagues published their evidence for the Tell Leilan drought¹, and the idea of a wider climate event, in 1993. He describes the initial reaction from colleagues as disbelief at the idea of a "major abrupt climate event disturbing a regional empire". But he was not the first to make such a claim for that time period, and supporting evidence gradually built up. In 2006, a team that included geochemist Giovanni Zanchetta at the University of Pisa in Italy reported evidence² from an Italian cave of a drought in the region around 4,200 years ago.



Excavations at Tell Leilan in Syria revealed signs of a drought when people left the city. Credit: H. Weiss/Yale University

On the archaeological side, Weiss and others compiled evidence that societies on several continents were disrupted around 4,200 years ago. In Egypt, a time of instability known as the First Intermediate Period occurred roughly from 2181 to 2055 bc. The pharaohs of the preceding Old Kingdom lost control of the country and competing power bases emerged.

There is evidence that the flow of the Nile River decreased from 2200 bc. Weiss says the best explanation is a decrease in the monsoon rains that feed the Nile, which would have contributed to the political instability that felled the Old Kingdom. (Egyptologists are wary of this argument, however; some maintain that political upheaval at the time didn't lead to the abandonment of cities.)

The 4.2 ka bp event achieved even greater prominence in 2018, when the International Commission on Stratigraphy recognized geological evidence of the 4.2 ka bp event as the beginning of the Meghalayan. To mark the start of this age, the commission chose a record of past climate contained in a

stalagmite in Mawmluh Cave in the Meghalaya region of India³. But even as the commission’s decision meant that the 4.2 ka bp event was now official, it also brought underlying problems to the fore.

Debating dates

The main uncertainty bedevilling the detective story around the 4.2 ka bp event is that it is hard to reconstruct past climates.

There are a number of difficulties, including how to interpret the inherently indirect data from climate proxies. And it is not always possible to precisely date a climatic shift or event. One of the best methods is uranium–thorium dating, which relies on the radioactive decay of uranium to thorium, and can give dates with an uncertainty as small as 1%. But if a stalagmite never had much uranium in the first place, or has been heavily contaminated with other substances, the dates become fuzzy. “What’s happened is that a lot of the records that are used to describe a global 4.2 event were not originally intended for this type of analysis,” says Stacy Carolin, a palaeoclimatologist at the University of Cambridge, UK. Many of the records, she says, have a low resolution and there are no markers that can be dated at — or near — the time of the 4.2 ka bp event.

That was the problem with the dating of the Mawmluh Cave stalagmite, she says: “Originally, it was just done at low resolution and there weren’t very many uranium–thorium ages.” Later analyses of other stalagmites in the cave found that the drying event did not occur at 4,200 years bp, but at 4,300 years bp. “It’s 100 years off,” says Carolin.

Multiple specialists, including Scroxton and Zanchetta, agree that the Mawmluh Cave record is not reliable enough.

Weiss contests this. “The continuous and global replication of the Mawmluh Cave 4.2 ka bp event over the past 10 years, at high resolution, is one of the marvels of modern palaeoclimatology,” he says.

Many researchers say that error margins spanning centuries are commonplace in studies of geological records from this time period. As a

result, some climatic changes that happened centuries before or after 4,200 years ago have been taken as evidence for the 4.2 ka bp drought, says Bruce Railsback, a geochemist at the University of Georgia in Athens.

When the resolution is better, it often reveals a messier picture. In a 2020 preprint⁴, Scroxton and his colleagues studied a stalagmite from Madagascar and found evidence of drying for much of the period between 4,320 and 3,830 years bp. The ‘classic’ timeframe of 4,200 years bp falls in that period, but the drought seems to have been drawn out — although not entirely continuous — rather than abrupt.

These types of uncertainty regarding exactly how and when the climate changed in each region make it harder to draw links to changes in human societies. And there are other controversial aspects to the idea of climate-driven collapses. Many anthropologists argue against this kind of explanation because it neglects societies’ abilities to adapt. In a 2021 study⁵, environmental historian Dagomar Degroot, at Georgetown University in Washington DC, and his colleagues identified five pathways by which past societies survived climatic crises — for example, switching to meat-rich diets when cereal harvests became unreliable. This means that there is no simple causal relationship between climatic shifts and societal disruption.

“It’s very difficult to identify the relationship between an environmental event and a societal effect,” says Monica Bini, a geoarchaeologist at the University of Pisa.

It is also crucial to consider what aspects of a society have collapsed, says Alan Greaves, an archaeologist at the University of Liverpool, UK. “The palace system or that kind of thing, for certain, may collapse.” Societies such as the Maya stopped building monumental structures. But Greaves says we should not read too much into that. “Are you talking about the collapse of an entire society,” he asks, “or the very visible elite palace structures?” The people of the Akkadian Empire did not all die 4,200 years ago. “We haven’t got mass graves of people who all died of starvation.”

Weiss agrees that it is important not to misinterpret the word ‘collapse’. He says there is clear evidence that when the drought struck Mesopotamia, many people left. “Humans have the resilient capacity to actually move from

a place that is affected by drought to a place that is not.” The Akkadian people moved towards the Tigris and Euphrates rivers, where people had long practised irrigation agriculture.

Other societies had even more complex stories. Scroxton and his colleagues studied the Harappan society of the Indus Valley in South Asia. According to Scroxton, people abandoned the northern cities between 4,200 and 3,900 years bp, and the southern cities more gradually between 3,900 and 3,300 years bp — making the Harappan civilization a largely rural society.

It had previously been suggested that the summer monsoon rains in that region failed as a result of the 4.2 ka bp event, but Scroxton and colleagues’ analyses⁶ of palaeoclimate records suggested evidence of two successive droughts. The first was associated with the 4.2 ka bp event, but it affected winter rainfall, which was reduced between 4,260 and 3,970 years bp. This, they argue, contributed to the early exoduses from northern cities. The second drought struck between 4,000 and 3,700 years bp, and contributed to the abandonment of the southern cities. This drought did affect the summer monsoon, but came long after the 4.2 ka bp event.



This stalagmite from Mawmluh Cave in northeastern India formed in layers over the course of thousands of years. It holds evidence of a sharp drop in precipitation in the region around 4,200 years ago. Credit: Ashish Sinha

“We’re the first study to show a mechanism by which the 4.2 ka event can influence the Harappan civilization,” says Scroxton. The drought associated with the 4.2 ka bp event helped to drive the abandonment of some Harappan cities, and might have left the others vulnerable to the second drought that followed.

Studies such as this indicate that the effects of the 4.2 ka bp event extend well beyond Mesopotamia. But just how big the event was remains contested.

A global event?

Weiss has compiled records from around the world, published over the past few decades, that he argues show drying around 4,200 years ago. In his view, the event was not confined to western Asia but was truly global, reaching even the Americas. The evidence extends “from Colorado to Massachusetts and down the western spine of South America and even to Brazil”, he says.

Most other climatologists are deeply sceptical about this. “There’s really not great evidence that it had great impacts in North America,” says Kathleen Johnson, a palaeoclimatologist at the University of California, Irvine. She adds that, in general, the Southern Hemisphere is under-sampled, so researchers don’t have a clear picture of how the climate there changed.

Climatologists and archaeologists also object, saying that there is, as yet, no solid explanation for why the global climate would have changed so drastically at that time. “There’s no trigger for this type of event,” says Carolin. She uses an earlier climatic shift, the 8.2 ka bp event, when global temperatures abruptly cooled⁷, as a comparison. This change has been linked to the collapse of part of an ice sheet in North America, causing two glacial lakes to drain into the sea and disrupting the transport of heat from the Equator to the poles. “We know when water rushed into the North Atlantic,” says Carolin. Without such a mechanism, the evidence for a global 4.2 ka bp event relies solely on the disputed coincidence of the palaeoclimate records.

So, for now, most palaeoclimatologists are inclined to agree with Scroxton and say that the strong evidence for the 4.2 ka bp event is limited to the

Mediterranean and southern Asia. “It wasn’t a global event,” says Johnson.

In line with this, last year Greaves and his colleagues reanalysed 14 palaeoclimate records that claimed to find an abrupt climate shift around 4,200 years ago⁸. They found a mixed picture: some did show an abrupt drying, some showed a drying that lingered for many centuries, and some showed no significant change. The simplest explanation for the pattern, they found, was a drought in the central Mediterranean and Levant, which led to increased dust storms in Mesopotamia and the Zagros Mountains. “It’s regionalized, it’s localized,” says Greaves. The team proposes that a rainfall belt might have shifted north, causing localized droughts. “It’s a very tentative suggestion,” he says.

A further possibility is that the 4.2 ka bp event was actually several distinct droughts or changes in precipitation patterns, which have been conflated owing to the uncertainties in palaeoclimate dating. In 2018, Railsback and his colleagues published evidence⁹ from a cave in Namibia that there was not one event, but two, that, in total, lasted about a century around 4.1 ka bp. He adds that the effects were not the same everywhere. “It was a dry event in some places, most notably the mid-latitude North Hemisphere, and a wet event in others, most notably latitudinal zones in the Southern Hemisphere.”

Carolin and her colleagues identified a similar pattern in a 2019 study¹⁰ of a stalagmite from Iran. They found two periods with increased levels of magnesium and calcium, which suggest a dustier environment. The first dusty spell began abruptly 4,510 years bp and lasted 110 years; the second began about 4,260 years bp and lasted 290 years. The team interprets this as being driven by two successive droughts.

“There are a number of megadrought events around that time that have all been lumped together,” says Johnson. “They don’t all start at the same time, and there are conflicting records from some places that show wet conditions.”

Pinning this down will require more palaeoclimate data. That includes assessing under-sampled places such as Africa and the Americas. But palaeoclimatologists also need to be more picky, says Carolin. “You can’t

just use any old stalagmite, especially if it's dirty and it's going to cause inaccuracies in your ages.”

If the 4.2 ka bp event truly was localized, it could invalidate the Meghalayan boundary, because such stage divisions are supposed to be global. But, more importantly, grasping the extent and timing of the event will clarify how much and how suddenly the climate can change. If there was no external trigger such as ice release into the North Atlantic, Scroxton says, the 4.2 ka bp event is “the largest unforced event we know of, the largest example of what the climate system just does on its own”.

And that has researchers wondering whether something like the 4.2 ka bp event could happen again, somewhere in the world — adding immeasurably to the damage done by human-caused climate change. “How likely is it,” asks Carolin, “that we’re going to shift into a period of drier conditions that lasts for 100 years?”

Nature **601**, 498-501 (2022)

doi: <https://doi.org/10.1038/d41586-022-00157-9>

References

1. 1.

Weiss, H. *et al.* *Science* **261**, 995–1004 (1993).

2. 2.

Drysdale, R. *et al.* *Geology* **34**, 101–104 (2006).

3. 3.

Berkelhammer, M. *et al.* in *Climates, Landscapes, and Civilizations* (eds Giosan, L., Fuller, D. Q., Nicoll, K., Flad, R. K. & Clift, P. D.) Vol. 198 (AGU, 2012).

4. 4.

Scroxton, N. *et al.* Preprint at Climate of the Past Discussions
<https://doi.org/10.5194/cp-2020-137> (2020).

5. 5.

Degroot, D. *et al.* *Nature* **591**, 539–550 (2021).

6. 6.

Scroxton, N. *et al.* Preprint at Climate of the Past Discussions
<https://doi.org/10.5194/cp-2020-138> (2020).

7. 7.

Duan, P. *et al.* *Quat. Sci. Rev.* **268**, 107104 (2021).

8. 8.

Ön, Z. B., Greaves, A. M., Akçer-Ön, S. & Özeren, M. S. *Clim. Change* **165**, 7 (2021).

9. 9.

Railsback, L. B. *et al.* *Quat. Sci. Rev.* **186**, 78–90 (2018).

10. 10.

Carolin, S. A. *et al.* *Proc. Natl Acad. Sci USA* **116**, 67–72 (2019).

This article was downloaded by **calibre** from <https://www.nature.com/articles/d41586-022-00157-9>

Books & Arts

- **[A call for governments to save soil](#)** [24 January 2022]
Book Review • To ensure food security, the world must stop letting fertile soil wash and blow away.
- **[The future of global health, and mapping the unseen: Books in brief](#)** [22 December 2021]
Book Review • Andrew Robinson reviews five of the week's best science picks.

- BOOK REVIEW
- 24 January 2022

A call for governments to save soil

To ensure food security, the world must stop letting fertile soil wash and blow away.

- [Emma Marris](#) 0



Rock becomes visible as topsoil is eroded away.Credit: Martin Harvey/Getty

A World Without Soil: The Past, Present, and Precarious Future of the Earth Beneath Our Feet Jo Handelsman Yale Univ. Press (2021)

Soil creates life from death. The production of more than 95% of the food we eat relies on soil, a heady mix of rock particles, decaying organic matter, roots, fungi and microorganisms. Yet this precious resource is eroding at a global average of 13.5 tonnes per hectare per year. Instead of nourishing

crops, fertile topsoil is ending up in inconvenient places such as ditches, reservoirs and the ocean.

Microbiologist Jo Handelsman takes on the challenge of making readers care in *A World Without Soil*, aided by environmental researcher Kayla Cohen. Their prologue takes the form of a letter about soil erosion that Handelsman wishes she had sent to US president Barack Obama while working in the White House's Office of Science and Technology Policy in the mid-2010s. Alas, she did not understand the true gravity of the problem until the waning days of the administration. Her biggest regret? That she wasn't able to make soil management the federal priority she thinks it should be.

Soil can be created over time, as dead things break down and contribute energy and nutrients to an ecosystem based on the underlying rock. But it erodes 10–30 times faster than it is produced. Globally, erosion reduces annual crop yields by 0.3%. At that rate, 10% of production could be lost by 2050. In erosion hotspots such as Nigeria, 80% of the land has been degraded. In Iowa, up to 17% of land is almost devoid of topsoil. Almost more convincing than the many facts and figures is a colour photograph of a field in Iowa with so little topsoil that the pale, lifeless sandy rubble beneath pokes through.

Age-old solutions

A sense of dread builds in the chapters that cover the basic science of soil as well as the causes and consequences of its erosion. The last part of the book brings a burst of enthusiasm, as the authors turn to possible solutions — many of them simple, and some millennia old. These involve improving holding capacity through planting diverse crops in rotation; increasing organic content with additions such as compost and biochar; reducing the erosional effects of water and wind by reshaping the land with contouring, terraces, windbreaks and the like; and ploughing as little as possible.

In a chapter on traditional soil-management techniques around the world, Handelsman and Cohen describe deep black “plaggen” soils on Scottish islands, made rich with cattle manure; rice terraces managed for 2,000 years by the Ifugao people in the Philippines; the milpa farming system of the

Maya in Latin America, with its 25-year rotation of crops including trees; and compost made of seaweed, shells and plant material by the Māori in New Zealand. Each system yields rich agricultural productivity while maintaining deep banks of carbon-rich, fertile soil. “We know how to do this,” write Handelsman and Cohen.



Cactus farming in Mexico, where the traditional system of crop rotation helps to replenish the soil. Credit: Omar Torres/AFP/Getty

Why, then, is fertile soil being allowed to wash and blow away? The answer, not surprisingly, rests in the shackles of global capitalism. Farming's profit margins are razor-thin, forcing producers to plant the highest-yielding variety of the highest-profit crop from field edge to field edge every season. Terracing, rotating crops and forgoing tilling enrich soil in the long run, but nibble into profits this year. And farmers can't pay their mortgages or lease equipment with the aroma of deep black topsoil.

Handelsman and Cohen urge the world to demand real change in how mainstream agricultural production is managed. “The burden of protecting soil cannot be relegated to indigenous people and environmental activists,” they note. But their specific suggestions are a little underwhelming. They join the calls for international soil treaties, but given how poorly climate

treaties have worked, I am cynical about the potential of such agreements. Countries seem likely to both under-promise and under-deliver unless there are costly penalties for failure. The same goes for the consumer-facing labels that the authors propose for food produced on farms that are working to improve their soil. Similar labels have not put a meaningful dent in climate change or other environmental problems — and many customers cannot afford to spend more on “soil-friendly” food.

Top-down change

What farming needs is a top-down overhaul. Handelsman and Cohen gesture at this with proposed discounts on crop-insurance premiums for farmers who increase the carbon in their soil. More is needed. Governments must pay farmers to build soil. In the United States, farmers can apply for funding for anti-erosion improvements through the Environmental Quality Incentives Program, run by the Department of Agriculture. Funding announced this month will increase the amount of land planted with cover crops to 12 million hectares by 2030 — but even that would represent only some 7% of US cropland. It is not enough.

We need to change how we think of farming. We have already begun to move towards a model in which farmers are less independent businesspeople growing and selling food, and more government-supported land stewards managing a complex mix of food production, soil fertility, wildlife habitat and more. Around the world, many farmers depend on subsidies, drought relief and payments from piecemeal schemes to conserve soil and nature. Such programmes — currently small-scale, ad hoc fixes for a broken system — should be the core of the agricultural sector.

Our land, our fresh water, our biodiversity and our soil are too precious to be destroyed by the market price of commodity grains and other foodstuffs. We must invest deeply and thoughtfully in our farmers so that they can invest deeply and thoughtfully in the land, becoming holistic landscape-management professionals. This is the future of farming.

doi: <https://doi.org/10.1038/d41586-022-00158-8>

This article was downloaded by **calibre** from <https://www.nature.com/articles/d41586-022-00158-8>

| [Section menu](#) | [Main menu](#) |

- BOOK REVIEW
- 22 December 2021

The future of global health, and mapping the unseen: Books in brief

Andrew Robinson reviews five of the week's best science picks.

- [Andrew Robinson](#) 0

GLOBAL HEALTH SECURITY



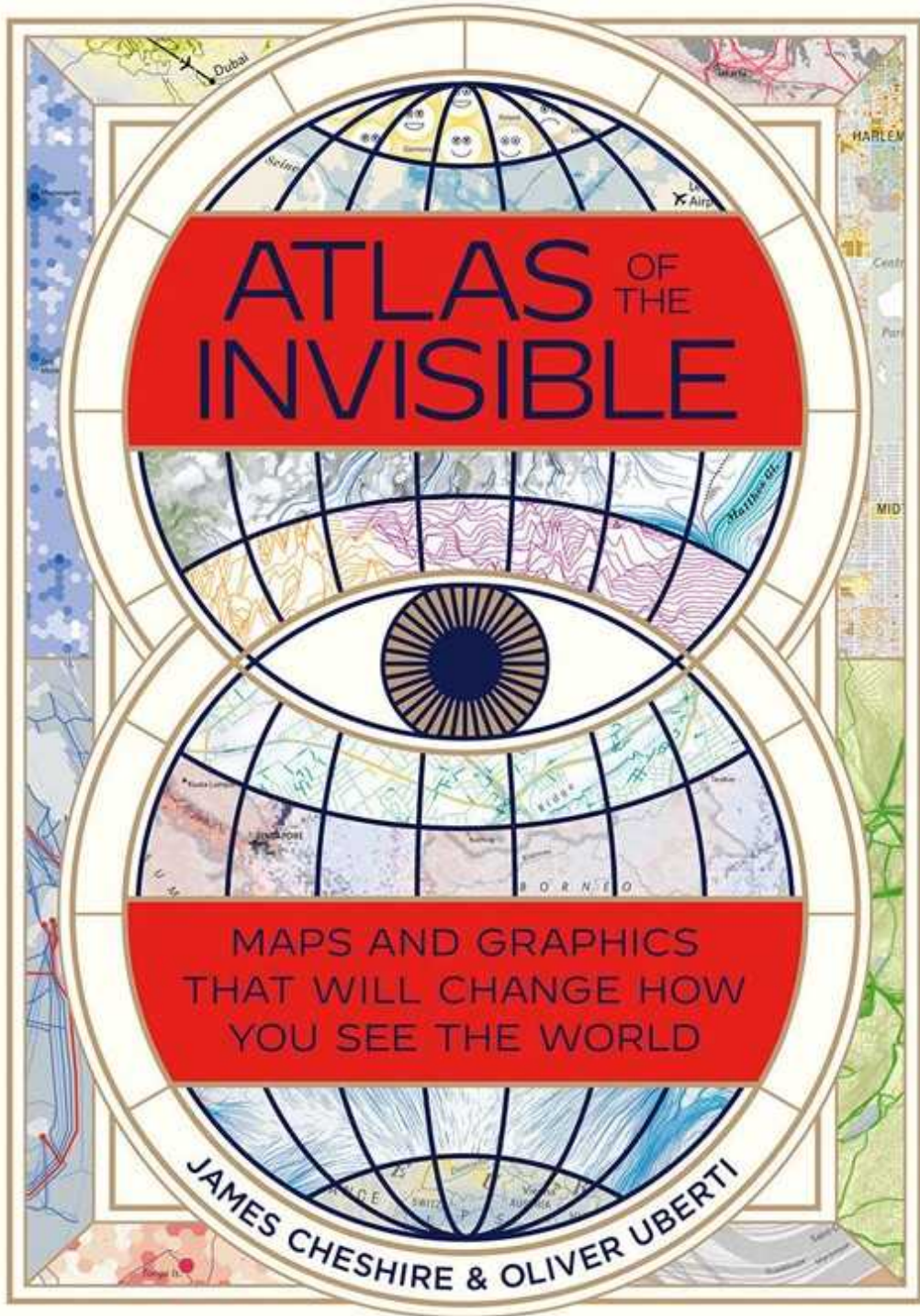
A BLUEPRINT FOR THE FUTURE

LAWRENCE O. GOSTIN

Global Health Security

Lawrence O. Gostin *Harvard Univ. Press* (2021)

“No one is safe from infectious diseases unless everyone is safe,” says World Health Organization adviser Lawrence Gostin. Discouraged but inspired by COVID-19, his wide-ranging study analyses the science and politics of past and present global disease, with hypothetical exercises about a new influenza, bioterrorism and cholera. He recommends steps to reduce pandemic risk, such as increasing surveillance of animal pathogens and their movement. Above all, he calls for a “new politics”, free from nationalistic populism.



Atlas of the Invisible

James Cheshire & Oliver Uberti *Particular* (2021)

A circular map of Earth looking down on the North Pole shows 400 fibre-optic cables laid on the ocean floor between 1989 and 2020, providing access to the Internet. It is one of many maps in this intriguing, if sometimes perplexing, book by former *National Geographic* design editor Oliver Uberti and cartographer James Cheshire. They describe the volume as an “ode to the unseen”: a world invisible through text and numbers alone, ranging from the development of genius to aircraft carbon dioxide emissions.

Geoengineering

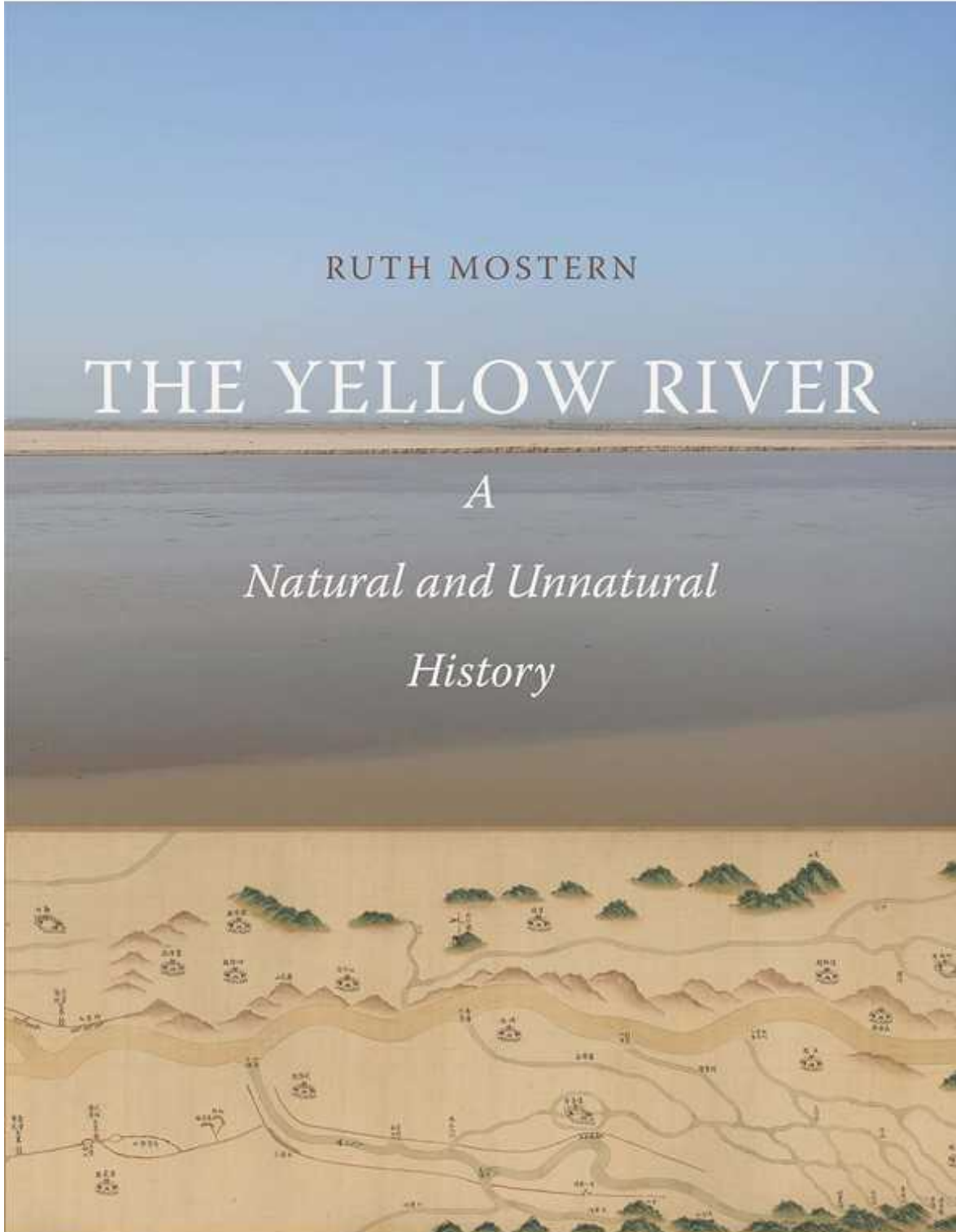
The Gamble

Gernot Wagner

Geoengineering

Gernot Wagner *Polity* (2021)

Without solar geoengineering to deal with climate change, will Earth inevitably become uninhabitable? The hugely controversial, if probably inexpensive, proposal — to cool the planet by using aerosols or other methods to reflect away some of the Sun’s radiation — defines economist Gernot Wagner’s thought-provoking study. Two decades ago, he considered the idea “nuts”. He still does, but today he advocates extensive new research and thinks we have to take the “gamble”, despite the risks. The issue is now “not if, but when”.



RUTH MOSTERN

THE YELLOW RIVER

A

Natural and Unnatural

History

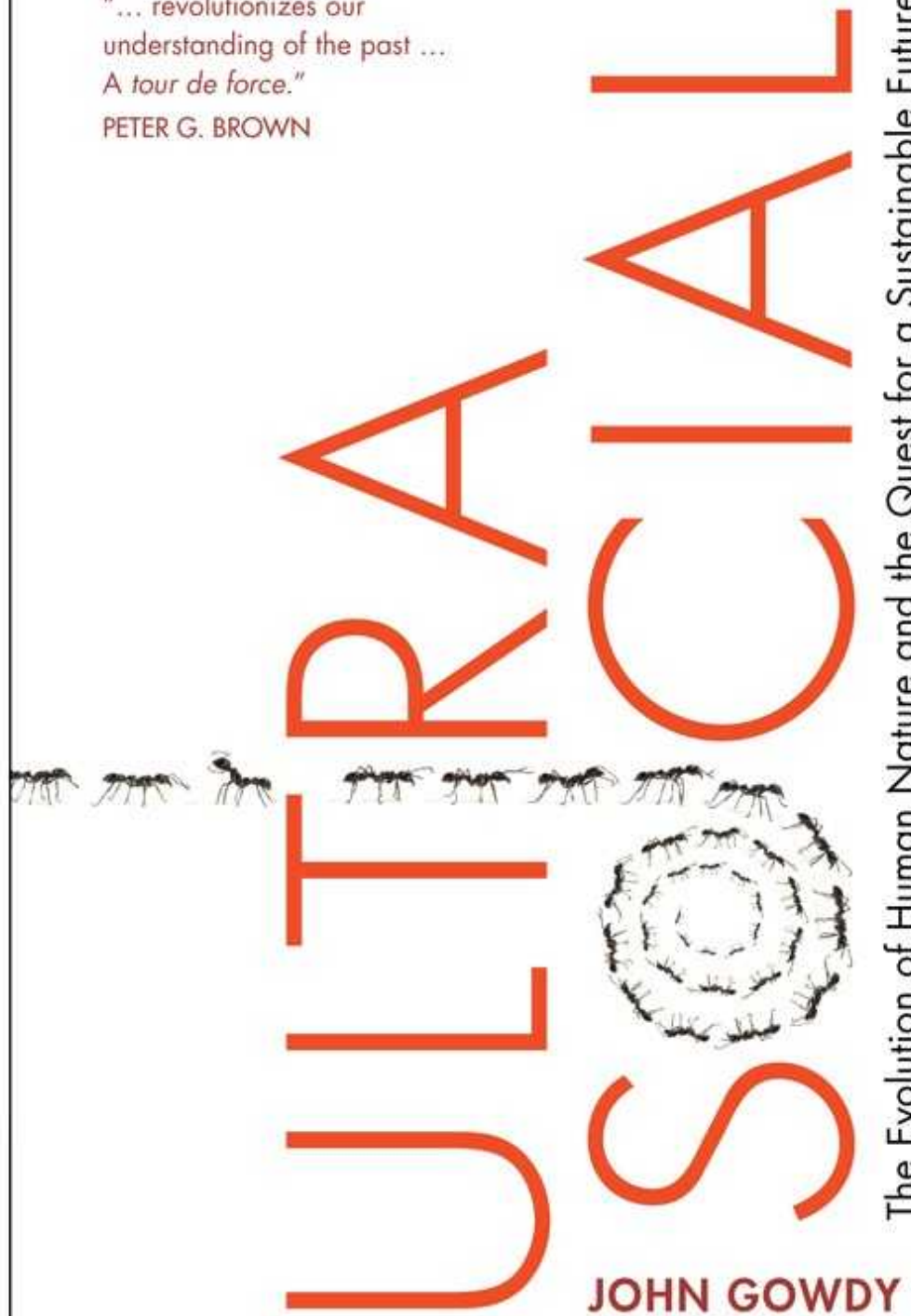
The Yellow River

Ruth Mostern *Yale Univ. Press* (2021)

China's Yellow River is "the most sediment-laden river in the world", writes environmental historian Ruth Mostern in her survey of three millennia, based on an innovative historical geographic-information system. The river's name refers to the endless yellow sediment flowing from its upper plateau; its other epithet, "China's Sorrow", evokes the frequent course changes and floods in its lower reaches. It has been subject to nearly perpetual construction and repair projects from imperial times to now, amid ongoing uncertainty.

"... revolutionizes our
understanding of the past ...
A tour de force."

PETER G. BROWN



The Evolution of Human Nature and the Quest for a Sustainable Future

Ultrasocial

John Gowdy *Cambridge Univ. Press* (2021)

Modern human society, like that of ants and termites, is dedicated to producing economic surplus. It is “ultrasocial”, says economist John Gowdy: so “complex, stratified and interconnected” that humans seem part of a “self-regulating superorganism”. To avoid climate-change catastrophe, he argues, we must live like hunter-gatherers — social in small groups, sustainable and egalitarian. But in attributing modern ills to the invention of agriculture, private property, cities and hierarchies, he oversimplifies history.

Nature **601**, 504 (2022)

doi: <https://doi.org/10.1038/d41586-021-03816-5>

This article was downloaded by **calibre** from <https://www.nature.com/articles/d41586-021-03816-5>

| [Section menu](#) | [Main menu](#) |

Opinion

- **Build up big-team science** [25 January 2022]
Comment • Researchers are creating grass-roots collaborative networks to tackle difficult questions in primate studies and more, but they need funding and other support.
- **Nobel nominators — which women will you suggest?** [18 January 2022]
Correspondence •
- **Theranos's lesson for investors: speak to lab workers** [25 January 2022]
Correspondence •
- **US visa policies trap foreign PhD graduates in academia**
[25 January 2022]
Correspondence •
- **Fund industrial fellowships for faculty to benefit graduates**
[25 January 2022]
Correspondence •

- COMMENT
- 25 January 2022

Build up big-team science

Researchers are creating grass-roots collaborative networks to tackle difficult questions in primate studies and more, but they need funding and other support.

- [Nicholas A. Coles](#) ⁰,
- [J. Kiley Hamlin](#) ¹,
- [Lauren L. Sullivan](#) ²,
- [Timothy H. Parker](#) ³ &
- [Drew Altschul](#) ⁴



Tamarins are one of more than 40 primate species that researchers can study through the ManyPrimates collaboration. Credit: Getty

Are some of science's biggest questions simply unanswerable without redefining how research is done? This is the question that motivated the researchers who would later establish the ManyBabies Consortium: a grass-roots network of some 450 collaborators from more than 200 institutions who pool resources to complete massive studies on infant development (see, for example, ref. 1). Human infants are perhaps the most powerful learning machines on the planet — and understanding how that learning occurs could inform artificial intelligence, public policy, education and more. Yet a full understanding of infant learning seemed difficult (if not impossible) under the current research model.

Consider the question of what captures infants' attention. Surely the probability that an infant will pay attention to, say, a rabbit, depends on presentation (for example, by a mother or a stranger), the child's previous experiences with mammals, what else is present alongside the rabbit, and much more. Unpacking this effectively would require dozens of experimental conditions and hundreds of infant participants. But most research projects are run by individual principal investigators and a shifting population of PhD students, meaning that data-collection efforts typically recruit fewer than 25 infants for each condition being tested².

But what if researchers worked interdependently and distributed work across many laboratories? Such consortia might be able to answer questions that no individual lab could tackle alone. In a proof-of-concept study, the ManyBabies Consortium used word of mouth, social media and e-mail lists to amass a team of 69 labs to test whether infants across several world regions prefer 'baby talk': the high-pitched, sing-song speech that adults in many cultures use with babies. Data from 2,329 infants in 16 countries provided a resounding yes, demonstrating that infants even prefer baby talk that is not in their native language³. This study, the largest of its kind, was cited more than 100 times within a year of its publication, according to Google Scholar.

The ManyBabies Consortium is not a one-off. It is part of a broader movement towards grass-roots big-team science: endeavours in which an unusually large number of researchers — often dispersed across institutions and world regions — self-organize to pool intellectual and material resources in pursuit of a

common goal⁴. In addition to the ManyBabies Consortium, the authors have collectively been involved in creating the Psychological Science Accelerator (involving some 1,200 researchers)⁵, the Disturbance and Resources Across Global Grasslands network (DRAGNet; around 100 researchers; <https://dragnetglobal.weebly.com>) and the ManyPrimates project (comprising about 150 researchers⁶; see ‘Examples of big-team science’). These self-organized consortia pool resources to conduct massive studies in psychology, ecology and primatology, respectively. They perform collaborative endeavours similar to those of the Human Genome Project and groups within CERN, Europe’s particle-physics lab near Geneva, Switzerland, but have been founded without formal funding mechanisms or well-developed infrastructure.

Examples of big-team science

Large teams of researchers have come together in various ways to tackle difficult questions in science, from soil samples to cancer biology.

Consortium or project name	How and when organized	Example of project finding or question	Data collection
Psychological Science Accelerator	Grass-roots consortium launched by a 2017 blogpost. Now involves some 1,200 researchers.	‘Cognitive reappraisal’ improves emotional reactions to the COVID-19 pandemic.	Data from more than 20,000 people in 87 countries collected by more than 450 researchers ¹² .

Consortium or project name	How and when organized	Example of project finding or question	Data collection
ManyBabies Consortium	<p>Grass-roots consortium launched by a 2015 blogpost. Now involves around 450 researchers.</p> <p>Infants prefer ‘baby talk’ even when it’s not in their native language.</p>	<p>Data from 2,329 infants collected by 150 researchers in 16 countries across the world³.</p>	
ManyPrimates project	<p>Grass-roots consortium launched through 2018 symposium, word of mouth, e-mail and social media; now involves about 150 researchers.</p> <p>Among 41 closely related primate species, phylogeny matters more for short-term memory than do ecology or social factors.</p>	<p>81 researchers studied 421 primates⁸.</p>	

Consortium or project name	How and when organized	Example of project finding or question	Data collection
Nutrient Network (NutNet)	Launched in 2006 through e-mail and Twitter requests to join the network. Data collection began in 2007.	Does herbivory and light availability resolve the loss of plant species caused by nutrient addition?	Using data from the broader Nutrient Network experiment (>130 collaborating sites), researchers documented effects of controlled combinations of nutrient addition and herbivore exclusion on plant diversity at 40 sites across the globe ¹³ .
Many Smiles Collaboration	Grass-roots effort launched in 2018. Collaborators formed adversarial teams recruited through social media and e-mail.	Does facial expression affect emotions?	Nearly 50 researchers collected data from 3,878 participants across 19 countries ¹⁴ .

Consortium or project name	How and when organized	Example of project finding or question	Data collection
Reproducibility Project: Cancer Biology	Launched in 2013 through funding provided by Arnold Ventures to the Center of Open Science and Science Exchange.	Can the results of experiments from high-impact cancer biology papers be reproduced?	200 collaborators attempted to replicate 158 effects from 50 preclinical experiments ¹⁵ .
Disturbance and Resources Across Global Grasslands network (DRAGNet)	Grass-roots consortium conceived in 2018. Data collection began in 2019; network built through e-mail and Twitter.	When grasslands are disturbed by tilling and nutrient additions, how do they respond?	Some 90 researchers monitor 70 sites in 18 countries (https://dragnetglobal.weebly.com).

We have found that grass-roots big-team science is capable of generating knowledge that is difficult to obtain — but faces several barriers to sustainability.

Barrier 1: rewarding team players

Michele Grigsby Coffey, a historian at the University of Memphis in Tennessee, has described academia as “a selfish sport” in which researchers “are rewarded for self-absorbed fixations”, and in which “prioritizing yourself at the expense of others is encouraged”⁷. Big-team science, however, is a team sport that often requires researchers to prioritize discovery over their own self-interests. For example, the first ManyPrimates study (of which D.A. is a co-author) examined the working-memory capacity of more than 40 species of primate by testing whether the animals could remember the locations of hidden food after short time delays⁸. D.A. estimates that he committed some 200 hours to the project. Yet on the resulting paper, the consortium is listed as the first author, the corresponding author e-mail is a shared mailbox and D.A. occupies one of 79 slots in the alphabetically sorted author list. Such authorship arrangements highlight the accomplishments of the team over any individual.

Pursuing relatively selfless ideals of big-team science can mean being penalized by the referees of the selfish sport of academia. For example, when one of us (N.A.C.) was nominated to direct the Psychological Science Accelerator during a postdoctoral fellowship, a well-meaning adviser told him that it was an important role and that he was a great fit, but that pursuing it would “kill chances of getting a tenure-track position”. The more senior co-authors of this manuscript (J.K.H., L.L.S. and T.H.P.) have offered junior colleagues similar warnings. For instance, they have seen members of hiring committees baulk when a job candidate’s CV contains several papers in which their name is in the middle of a long list of authors. A selfish sport rewards stars — not those who have crucial supporting roles. Indeed, when one of us in a big-team effort expressed excitement about a recent milestone to a department head, the response was: “Great. Just make sure you have work coming out of your own research group.”



Projects by the ManyBabies Consortium explore infant cognition. The pictured ongoing project involves 88 collaborators from 27 countries on 4 continents, who are collecting data from more than 1,000 infants. Caption: Centre for Infant Cognition/UBC

Academia could change the game by rewarding researchers who make large contributions to team efforts. Otherwise, teams will be forced to find other ways to increase benefits or decrease the costs of participation. For example, project leaders could fund collaborators, as is being done for a collaboration designing tools to predict the replicability of research findings in the social and behavioural sciences, supported by the US Defense Advanced Research Projects Agency (www.cos.io/score). Such solutions, however, prohibit researchers with fewer resources from leading big-team science efforts. As an alternative, some collaborations offer non-financial perks. For example, both DRAGNet and the Nutrient Network offer participating researchers exclusive access to the full project database. However, these policies conflict with goals to make science more open and inclusive. A reduction in costs could be

accomplished by recruiting even more researchers to split the bill, but this makes coordination much more difficult.

Barrier 2: diversity

One large potential benefit of this way of doing science is the opportunity to increase the diversity of participants, researchers and research questions. But we have noticed a worrisome trend: pre-existing inequality in science infrastructure seems to be perpetuated in big-team science.

A 2021 analysis noted that researchers in previously colonized countries often lack the access to lab space and funding that are necessary to participate in big-team science⁹. Not surprisingly, perhaps, these inequalities also seem to affect who leads these endeavours. Not a single behavioural-science big-team project included in this analysis was led by a researcher in a developing nation. Furthermore, the combined governing and steering boards of ManyBabies, the Psychological Science Accelerator, the Nutrient Network and DRAGNet include only 4 (of 32) members from outside North America or Western Europe (17 are from the United States, 5 from Canada, 6 from Western Europe, 1 from Kenya, 1 from Argentina, 1 from Australia and 1 from India).

Big-team science should find ways to enable change. For example, the Psychological Science Accelerator uses donations to award participation grants to researchers in under-represented regions. The ManyBabies Consortium launched an extension of its first study that provides funding, training and support for data collection in Africa — an operation that would have been impossible without support from the Jacobs Foundation in Zurich, Switzerland. DRAGNet minimizes costs at institutions that have few resources by getting them to ship seed samples for processing at better-resourced institutions. Many Primates fosters connections in the global south by participating in local meetings and reaching the community through publications in languages such as Spanish and French.

Researchers can also help to close the infrastructure gap by training and supporting researchers in under-represented areas. For example, a big-team project testing how people in various African regions evaluate moral

transgressions is led by a PhD student from Nigeria, and is supported by several members of the Psychological Science Accelerator^{[10](#)}.



Researchers who collaborate in DRAGNet investigate questions such as how disturbance and added nutrients affect plant communities across as many as 70 site locations and 18 countries. Credit: Lauren Sullivan

Barrier 3: funding and sustainability

Despite well-recognized outputs, we all scramble constantly to keep our big-team initiatives going. These grass-roots projects can be established with little funding, but they are difficult to maintain without financial support. Big-team science needs funds to retain researchers who know how to coordinate the next wave of science, to support tools for managing increasingly complex workflows, and to support participation from researchers who are not well resourced.

For example, the first Psychological Science Accelerator study examined how people around the world judge others on the basis of facial appearance¹¹. The project involved 241 collaborators and 11,570 participants spanning 41 countries. In principle, this study should have cost hundreds of thousands of dollars. If participants and research assistants were each paid just US\$5 for every 30-minute data-collection session, the cost would be more than \$115,000. The price tag gets much bigger when factoring in labour for project management, which included acquiring more than 150 ethics-approval documents, translating study materials into 23 languages and developing research tools to track progress and validate data from labs all over the world (see go.nature.com/3jcsutx). Yet the project officially operated on less than \$2,000; hundreds of collaborators donated their time and resources to make up the difference (see go.nature.com/3qstumf).

Operations that run on shoestring donations are neither sustainable nor scalable. This hard truth became apparent at the beginning of 2020, when the Psychological Science Accelerator received 66 urgent proposals for global research projects on the psychology of the COVID-19 pandemic. Financial considerations meant that the network had to reject all but three. One rejected proposal aimed to test whether reminding people to consider accuracy before sharing news could help to curb COVID-19 misinformation in different world regions and demographics. Every time we see a post promoting false claims that the antiparasitic drug ivermectin prevents COVID-19, that pregnant women should not get vaccinated or that COVID-19 vaccines contain microchips, we are painfully reminded of the work we did not have the funds to support.

Why is it so hard to get funding for grass-roots big-team science initiatives? Government and philanthropic funders have provided various reasons. For instance, they worry that big-team science will ultimately prove to be unsustainable because of academia's selfish rulebook. They say that big-team science is still not diverse enough in terms of researchers and research questions. They say that their systems are not set up to process proposals with hundreds of collaborators, or to handle funding requests that go out to dozens of research sites. Most frustratingly, they say that big-team science has managed so far without their support.

Leading the big-team-science movement can sometimes feel like climbing the world's tallest mountains without so much as a rope. We have caught glimpses

of the peaks and can imagine the views they might offer, but we lack the resources to climb higher. Every step forward will become increasingly treacherous until academic institutions and funders provide long-overdue support.

Nature **601**, 505–507 (2022)

doi: <https://doi.org/10.1038/d41586-022-00150-2>

References

1. 1.
Byers-Heinlein, K. *et al.* *Can. Psychol. Can.* **61**, 349–363 (2020).
2. 2.
Oakes, L. M. *Infancy* **22**, 436–469 (2017).
3. 3.
ManyBabies Consortium. *Adv. Methods Pract. Psychol. Sci.* **3**, 24–52 (2020).
4. 4.
Forscher, P. S. *et al.* Preprint at PsyArXiv
<https://doi.org/10.31234/osf.io/2mdxh> (2020).
5. 5.
Moshontz, H. *et al.* *Adv. Methods Pract. Psychol. Sci.* **1**, 501–515 (2018).
6. 6.
Many Primates *et al.* *PLoS ONE* **14**, e0223675 (2019).
7. 7.

Grigsby Coffey, M. ‘The Unselfish Academic’ *Auntie Bellum Magazine* (3 December 2016).

8. 8.

Many Primates *et al.* Preprint at PsyArXiv
<https://doi.org/10.31234/osf.io/5etnf> (2021).

9. 9.

Silan, M. *et al.* *Assoc. Psychol. Sci. Obs.* **34** (6), 64–69 (2021).

10. 10.

Adetula, A. *et al.* Preprint at AfricArXiv
<https://doi.org/10.31730/osf.io/hxjbu> (2021).

11. 11.

Jones, B. C. *et al.* *Nature Hum. Behav.* **5**, 159–169 (2021).

12. 12.

Wang, K. *et al.* *Nature Hum. Behav.* **5**, 1089–1110 (2021).

13. 13.

Borer, E. T. *et al.* *Nature* **508**, 517–520 (2014).

14. 14.

Coles, N. A. *et al.* Preprint at PsyArXiv
<https://doi.org/10.31234/osf.io/cvpuw> (2021).

15. 15.

Errington, T. M. *et al.* *eLife* **10**, e71601 (2021).

| [Section menu](#) | [Main menu](#) |

- CORRESPONDENCE
- 18 January 2022

Nobel nominators — which women will you suggest?

- [Alice C. McHardy](#) ✉

It is the time of the year when many researchers, me included, are invited to nominate candidates for the Nobel prize committees to consider. By the end of this month, I, for instance, must choose up to three scientists and submit a summary of the discovery that makes them most deserving of the Nobel Prize in Physiology or Medicine. So, too, must thousands of other senior researchers from whom recommendations are sought — professors, laureates and members of scholarly societies (groups stamped by historical barriers to women in science).

Access options

Subscribe to nature+

Get immediate online access to the entire Nature family of 50+ journals

\$29.99

monthly

[Subscribe](#)

Subscribe to Journal

Get full journal access for 1 year

\$199.00

only \$3.90 per issue

[Subscribe](#)

All prices are NET prices.

VAT will be added later in the checkout.

Tax calculation will be finalised during checkout.

Buy article

Get time limited or full article access on ReadCube.

\$32.00

[Buy](#)

All prices are NET prices.

Additional access options:

- [Log in](#)
- [Learn about institutional subscriptions](#)

Nature **601**, 508 (2022)

doi: <https://doi.org/10.1038/d41586-022-00133-3>

This article was downloaded by **calibre** from <https://www.nature.com/articles/d41586-022-00133-3>

- CORRESPONDENCE
- 25 January 2022

Theranos's lesson for investors: speak to lab workers

- [Richard D. Unwin](#) ORCID: <http://orcid.org/0000-0001-7955-9111>⁰,
- [Daniela S. Couto](#) ORCID: <http://orcid.org/0000-0001-5254-9044>¹ &
- [Simon J. Clark](#) ORCID: <http://orcid.org/0000-0001-8394-8355>²

The fraud conviction of Elizabeth Holmes, the chief executive of the now-defunct US biotechnology company Theranos in Palo Alto, California, highlights the need for early peer review of scientific data from start-up companies ([Nature 601, 173–174; 2022](#)). But that is unlikely to happen in the highly secretive start-up world, in which investment is based on the only real asset of value — intellectual property and know-how. So how can investors perform suitable due diligence? In our view, they must speak directly to the engineers and scientists expected to deliver on breakthrough technologies.

Access options

Subscribe to nature+

Get immediate online access to the entire Nature family of 50+ journals

\$29.99

monthly

[Subscribe](#)

Subscribe to Journal

Get full journal access for 1 year

\$199.00

only \$3.90 per issue

[Subscribe](#)

All prices are NET prices.

VAT will be added later in the checkout.

Tax calculation will be finalised during checkout.

Buy article

Get time limited or full article access on ReadCube.

\$32.00

[Buy](#)

All prices are NET prices.

Additional access options:

- [Log in](#)
- [Learn about institutional subscriptions](#)

Nature **601**, 508 (2022)

doi: <https://doi.org/10.1038/d41586-022-00167-7>

This article was downloaded by **calibre** from <https://www.nature.com/articles/d41586-022-00167-7>

- CORRESPONDENCE
- 25 January 2022

US visa policies trap foreign PhD graduates in academia

- [Jianyang Geng](#) ✉

Preparing PhD graduates for career opportunities outside academia would be impractical in the United States (see [T. van den Broek et al. *Nature* 600, 386; 2021](#)). US working-visa policies would first need to be refreshed, given that half of the country's postdocs and almost half of its full-time graduate students in natural sciences and engineering are from overseas (see [go.nature.com/3fo0](#)).

Access options

Subscribe to nature+

Get immediate online access to the entire Nature family of 50+ journals

\$29.99

monthly

[Subscribe](#)

Subscribe to Journal

Get full journal access for 1 year

\$199.00

only \$3.90 per issue

Subscribe

All prices are NET prices.

VAT will be added later in the checkout.

Tax calculation will be finalised during checkout.

Buy article

Get time limited or full article access on ReadCube.

\$32.00

Buy

All prices are NET prices.

Additional access options:

- [Log in](#)
- [Learn about institutional subscriptions](#)

Nature **601**, 508 (2022)

doi: <https://doi.org/10.1038/d41586-022-00168-6>

This article was downloaded by **calibre** from <https://www.nature.com/articles/d41586-022-00168-6>

- CORRESPONDENCE
- 25 January 2022

Fund industrial fellowships for faculty to benefit graduates

- [Yun Hang Hu](#) [ORCID: http://orcid.org/0000-0002-5358-8667](#) 0

Faculty members with industrial experience could help to meet the challenge of preparing PhD holders for career tracks outside academia (see [T. van den Broek et al. *Nature* 600, 386; 2021](#)). However, such experience is still unusual among academic staff, even in engineering.

Access options

Subscribe to nature+

Get immediate online access to the entire Nature family of 50+ journals

\$29.99

monthly

[Subscribe](#)

Subscribe to Journal

Get full journal access for 1 year

\$199.00

only \$3.90 per issue

Subscribe

All prices are NET prices.
VAT will be added later in the checkout.
Tax calculation will be finalised during checkout.

Buy article

Get time limited or full article access on ReadCube.

\$32.00

Buy

All prices are NET prices.

Additional access options:

- [Log in](#)
- [Learn about institutional subscriptions](#)

Nature **601**, 508 (2022)

doi: <https://doi.org/10.1038/d41586-022-00169-5>

This article was downloaded by **calibre** from <https://www.nature.com/articles/d41586-022-00169-5>

Work

- **[How lab leaders can support students' non-academic career plans](#)** [24 January 2022]
Career Feature • Nervous about advising junior lab colleagues who want to switch sectors? Don't be, say scientists who have made the move.
- **[Seven technologies to watch in 2022](#)** [25 January 2022]
Technology Feature • Our fifth annual round-up of the tools that look set to shake up science this year.
- **[The ancient whale from my Egyptian home town](#)** [24 January 2022]
Where I Work • Abdullah Gohar studies fossils from the Faiyum Depression, which occurred where he grew up.

- CAREER FEATURE
- 24 January 2022

How lab leaders can support students' non-academic career plans

Nervous about advising junior lab colleagues who want to switch sectors? Don't be, say scientists who have made the move.

- [Nikki Forrester](#) ✉

[Find a new job](#)



Academic positions are becoming scarcer — so mentors should support trainees who want to pursue a career in industry. Credit: Thomas Barwick/Getty

Although many PhD students are aware of the limited job prospects in academia, few have the resources or support they need to pursue non-academic careers. In 2020, only 10% of engineering PhD graduates and 16% of those in physical and earth sciences ended up in academic positions in the United States, according to the National Science Foundation Survey of Earned Doctorates.

And, according to the 2019 *Nature* survey of PhD students (see [Nature 575, 403–406; 2019](#)), only 26% of this group said their programme had prepared them ‘very well’ for a satisfying career. *Nature* will rerun the survey later this year.

Laboratory leaders are uniquely positioned to help their graduate students to learn about non-academic career opportunities and gain experiences outside of the laboratory to make them competitive for these jobs. Four scientists share advice about what principal investigators (PIs) can do to support students who are interested in non-academic careers.

ANNE KROOK: Voice your support for alternative paths

Founder and principal of Practical Workplace Advice in Seattle, Washington.

PIs need to have career-centred conversations with their students from the first minute they start in the lab and repeatedly throughout their programmes. Doing anything else is dishonest: once you look at placement numbers, it is completely clear that most graduate students and postdocs are not going to get faculty positions.

I ended up leaving academia after I didn’t get tenure. I moved to Seattle, Washington, where I bartended for a year before getting a job at Amazon. I worked there for 13 years and held many roles, most recently director of

infrastructure. It was an incredibly demanding and lively intellectual environment. Now, I give practical workplace advice to graduate students as part of my business, which I started in 2014.

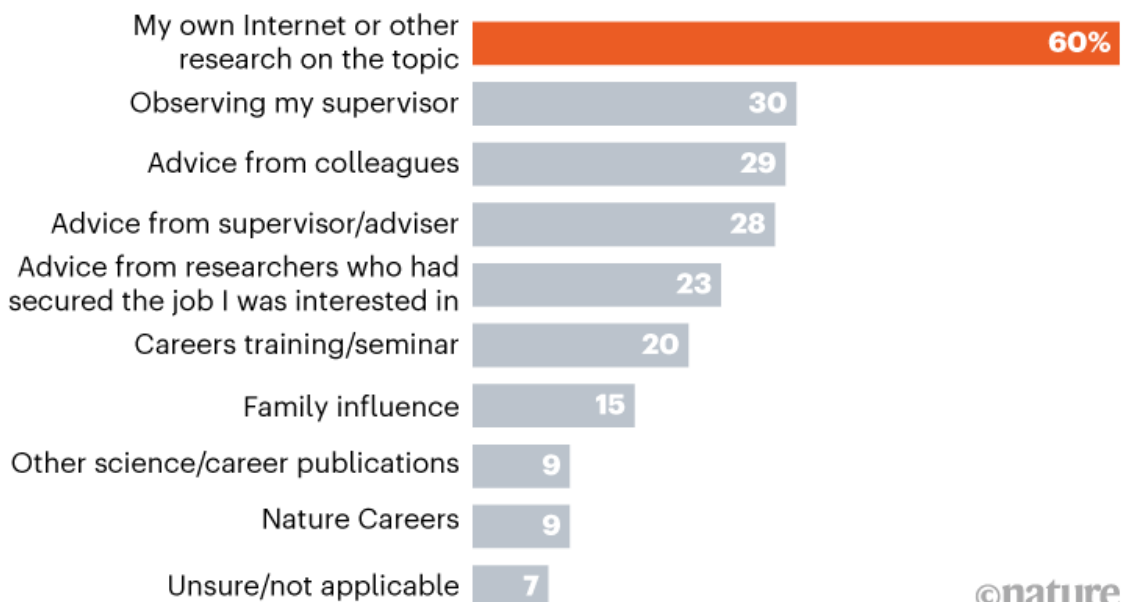
I teach graduate students and postdocs about how to enter the non-academic job market. I also give talks on negotiating compensation and how women can manage difficult workplace interactions outside academia.

Although PIs often don't have intimate knowledge of careers outside academia, they are uniquely positioned to give permission to, or even encourage, their lab members to pursue non-academic careers. Some PhD students and postdocs might think that their PIs don't know or care about non-academic careers (see 'Do-It-Yourself Careers Guidance'). But if a PI says out loud that those jobs are OK to pursue, an early-career scientist in their lab might feel that they can go forward with those searches. At least once per year, PIs can tell everyone in their lab, "I know many of you are not going to get another job in academia, and that's OK. I want you to know that I support you in your search for that job, and I will do everything I can to help you."

DO-IT-YOURSELF CAREERS GUIDANCE

When crafting a plan for their scientific futures, PhD students are more likely to rely on the Internet than advice from their peers or supervisors.

How did you arrive at your current career decision?



©nature

Source: *Nature's* 2019 PhD student survey

Instead, graduate students and postdocs continually tell me that they're afraid to say they're looking for such jobs, although everyone knows what the employment statistics are for academic positions. Lab leaders should also give their those they advise time to work with career-services teams at their institution, go to a CV-writing workshop and attend recruiting events.

Another thing PIs can do is organize a team video call every month with three people who have gone to work outside academia. Ask them to describe what they do, what the hardest problem they have to solve is, what they learnt in graduate school or as a postdoc that was helpful and what they wish they had learnt. Doing this will introduce students and postdocs to people in different fields and positions and will demystify leaving the academic world.

INGA CONTI-JERPE: Give students time to explore

Scientific development lead for isoFoodtrace in San Francisco, California.

During both my master's and PhD programmes, I was never completely committed to staying on the academic career track. I got my PhD in marine biology from the University of Hong Kong, where I used stable-isotope analysis to study coral-reef ecology. Now, I use this tool at my company isoFoodtrace, based in Hong Kong, which validates food labels and verifies, for example, whether a food item is organic or whether seafood is farmed or wild-caught.

I had never considered starting my own company before, but my business partner Colin Luk was the catalyst. We were in the same PhD programme and sat next to each other for four years. He had opened a cafe and bar in Hong Kong before pursuing his PhD, so he had a lot of experience in the food and beverage industry. Colin had the experience and mindset to look at the work I was doing from a non-academic perspective.

David Baker, a marine biologist and my PhD adviser, supported me in starting my own business. He's very aware of the academic job situation and is open about wanting to help his students to prepare for whatever careers they want to pursue. Although his attitude was great, he couldn't give me unlimited advice on leaving academia — because he'd never done it himself. However, after I left the lab at the conclusion of my postdoc contract in December 2020, he started his own business, so now he has experience that he can draw on to guide his students who are interested in starting their own businesses in the future.

It's crucial for PIs and universities to expose graduate students to people with non-academic careers so students can learn about other options, hear different perspectives and grow their networks. Building connections between early-career researchers and people outside academia is the most important thing that universities can facilitate. Graduate students already have transferable skills, but the way to get a job is often by knowing somebody who knows somebody.

PIs and universities should also let graduate students and postdocs do internships and explore different career options. One opportunity that I'm extremely grateful for was working on a consulting project for the airport

authority of Hong Kong during my PhD programme. The airport authority wanted to transplant more than 500 colonies of the soft coral *Guaiagorgia* spp. that were present on the existing airport seawall, to minimize the environmental impact of building a third runway. We tested the feasibility of transplanting these corals, which involved severing them from their attachment point and reattaching them to new substrates at a suitable site. Then, we transplanted the coral colonies at the airport.

That was the first time I worked on something where I had to care about not just the science, but also what the clients wanted. It gave me practice in thinking about project goals and outcomes, and it helped me to work out what I liked and didn't like. It's hard to find out what career you might want to pursue if you've never tried it.



Eduardo Santos conducting field work in New Zealand.Credit: Luana L. S. Santos

EDUARDO SANTOS: Ask students about their career interests and goals

Data science senior analyst at Santander Brasil in São Paulo, Brazil.

I'm an example of a scientist who moved from academia to industry: in May 2021, I left my lecturer position at the University of São Paulo, Brazil, and became a data analyst at a bank. My skills in data analysis and project management are well suited to the business world, and I still apply the scientific method in my job.

Before making this transition, I had conversations with my students about the standard academic career path, in which the goal is to obtain a faculty position and get tenure.

In my case, I got tenure at a good university, and then I voluntarily left to pursue this role. My students wanted to know what was going on and why, so we've had long chats about what drove me to change my mind and ultimately to change careers.

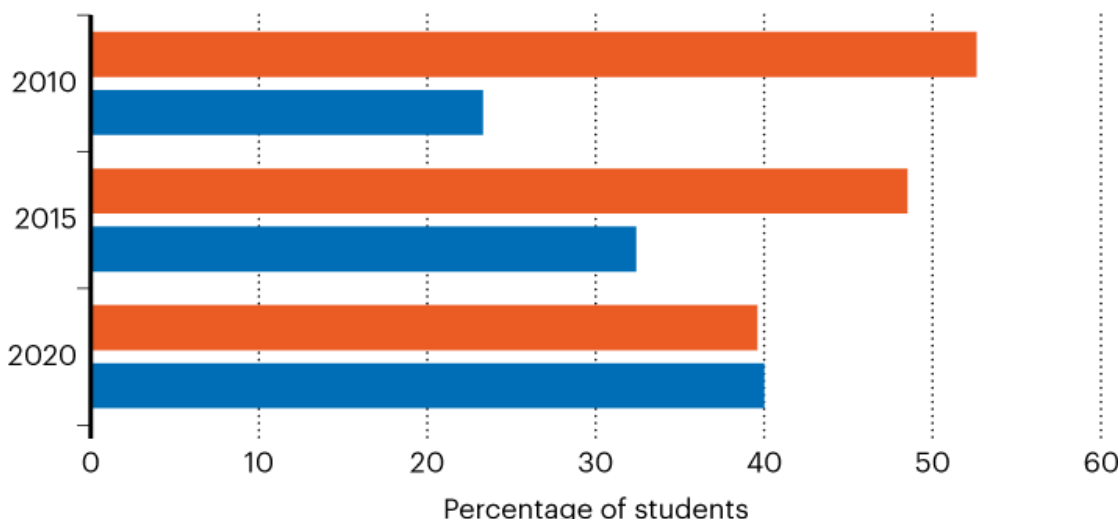
Before leaving academia, I had very sincere talks with junior members and interns in my lab about what kind of research they wanted to do, where they wanted to be in five years, what they could expect in terms of academic career prospects and why they needed to think deeply about their career paths. I tried to have those conversations periodically to find out whether their interests or career goals had changed.

Some of my students were hesitant about pursuing academic careers, so I made sure that they knew what they were getting into. I told them how few academic jobs are available, instead of just focusing on the romantic aspects of doing research. I've had several difficult conversations with students about their future prospects in academia (see 'Out of Academia'). Often, they're grateful we had those sincere talks because it helped them to pursue the right career paths.

OUT OF ACADEMIA

More US PhD graduates reported securing jobs in industry than finding positions in academia in 2020, representing a huge shift over the last decade.

■ Academia ■ Industry



©nature

Source: US National Science Foundation survey

One student, who was pursuing a master's degree, told me she wasn't planning on continuing research after finishing her programme. She told me that she loved baking. I told her that if baking makes her happy and she thinks she has a career option down that road, then go for it. She took a job at a bakery during her programme and realized she didn't like it. Now, she's finishing her dissertation and looking for jobs in data science. It's great that she took the time to explore and work out what she wants to do.

Young researchers often feel obliged to end up in academia, and can feel like a failure if they don't. It's important to change that perspective. There are many careers outside academic research where scientists can succeed. I tried to emphasize that graduate students and postdocs develop a range of skills that they will carry forwards for the rest of their lives. The most important thing that PIs can do is listen to young researchers. Ask them what they want to do, why they want to follow a certain career path, what kinds of skills they want to develop, what their strengths are and what they'd like to

improve. I always tried to understand their points of view and then gently offered advice when I could.

REGINA BAUCOM: Devise a mentoring plan to help your students

Ecology and evolutionary biologist at the University of Michigan in Ann Arbor.

If lab leaders look at the people they train as a commodity, then they can get stuck in this idea that their students can go only into academia. But if PIs look at people as individuals who are going to do wonderful things, regardless of whether they go into tenure-track positions or not, then they can divorce themselves from the other mindset. To me, the end goal is to get someone to where they want to go by training them to be an excellent scientist.

I start having conversations with students about their career paths during recruitment. I want to get a sense of what they're thinking and what they want to do, whether it's research, teaching, outreach, working at a non-governmental organization or something else. When a student joins my lab, we devise a mentoring plan and talk about it at least once per year. The plan asks each student about what they've accomplished in the past year, what they were most proud of and how they're feeling about the progress they've made. It also includes questions about what support and resources they'll need moving forwards and what they want to accomplish in the future.

I emphasize that, during a graduate programme, they will be doing science and will be trained as a scientist. Then, once their first paper is done and they're moving forwards on their second and third papers, we'll start looking for opportunities that will support their career interests. I like focusing on career opportunities during the later stages of their graduate programmes because students in early stages have to prioritize their time, so they don't burn out from taking on too much too soon.

For instance, if a student is interested in science outreach, I'll help connect them with employees at local museums. One of my students decided to take

extra statistics courses and a course in geographic information system mapping. She graduated in 2020 with a PhD in ecology and evolutionary biology and a certificate in data science. Now, she is working as a data analyst and postdoc. I feel that, in academia, we should always be supporting students in improving their knowledge base and skills. I also connect students with people in my network who have non-academic careers, such as in industry or environmental law, to expose them to different paths and help them to expand their networks.

Nature **601**, 655-657 (2022)

doi: <https://doi.org/10.1038/d41586-022-00162-y>

These interviews have been edited for length and clarity.

This article was downloaded by **calibre** from <https://www.nature.com/articles/d41586-022-00162-y>.

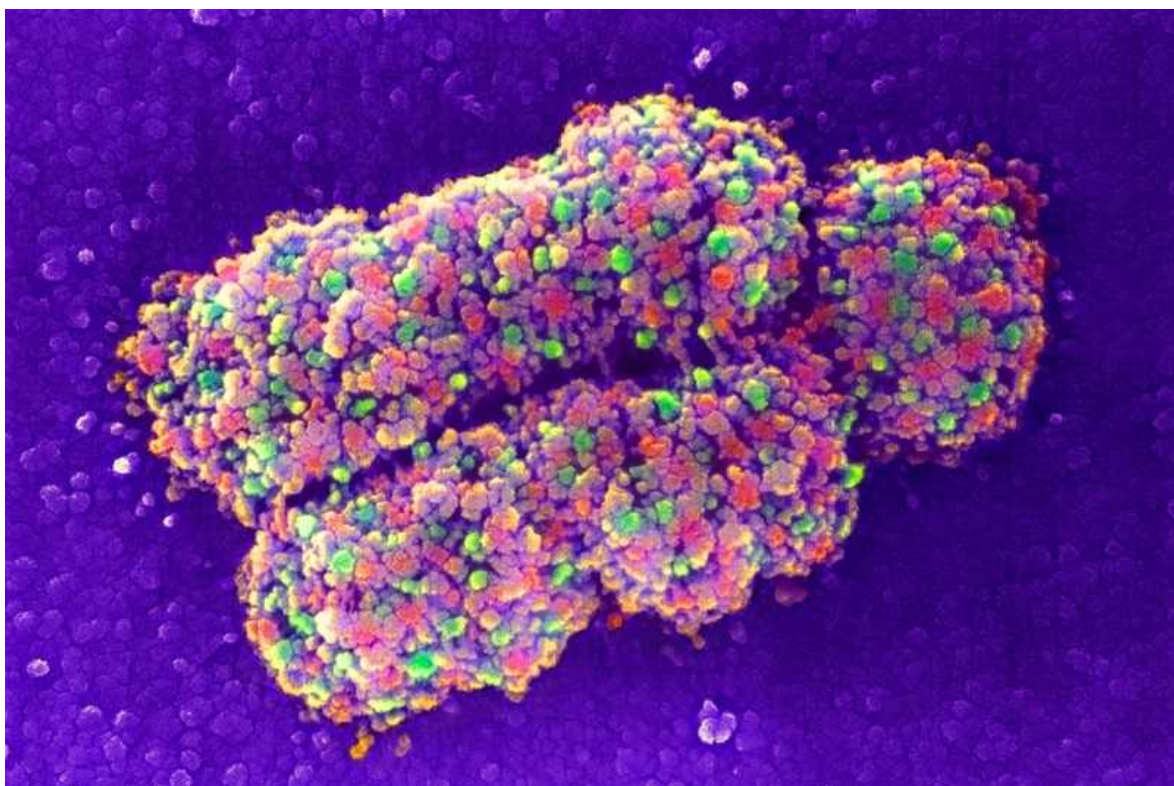
| [Section menu](#) | [Main menu](#) |

- TECHNOLOGY FEATURE
- 25 January 2022

Seven technologies to watch in 2022

Our fifth annual round-up of the tools that look set to shake up science this year.

- [Michael Eisenstein](#) ⁰



The Telomere-to-Telomere Consortium is sequencing whole chromosomes. Credit: Adrian T. Sumner/SPL

From gene editing to protein-structure determination to quantum computing, here are seven technologies that are likely to have an impact on science in the year ahead.

Fully finished genomes

Roughly one-tenth of the human genome remained uncharted when genomics researchers Karen Miga at the University of California, Santa Cruz, and Adam Phillippy at the National Human Genome Research Institute in Bethesda, Maryland, launched the Telomere-to-Telomere (T2T) consortium in 2019. Now, that number has dropped to zero. In a preprint published in May last year, the consortium reported the first end-to-end sequence of the human genome, adding nearly 200 million new base pairs to the widely used human consensus genome sequence known as GRCh38, and writing the final chapter of the Human Genome Project¹.

First released in 2013, GRCh38 has been a valuable tool — a scaffold on which to map sequencing reads. But it's riddled with holes. This is largely because the widely used sequencing technology developed by Illumina, in San Diego, California, produces reads that are accurate, but short. They are not long enough to unambiguously map highly repetitive genomic sequences, including the telomeres that cap chromosome ends and the centromeres that coordinate the partitioning of newly replicated DNA during cell division.

Long-read sequencing technologies proved to be the game-changer. Developed by Pacific Biosciences in Menlo Park, California, and Oxford Nanopore Technologies (ONT) in Oxford, UK, these technologies can sequence tens or even hundreds of thousands of bases in a single read, but — at least at the outset — not without errors. By the time the T2T team reconstructed^{2,3} their first individual chromosomes — X and 8 — in 2020, however, Pacific Biosciences' sequencing had advanced to the extent that T2T scientists could detect tiny variations in long stretches of repeated sequences. These subtle ‘fingerprints’ made long repetitive chromosome segments tractable, and the rest of the genome quickly fell into line. The ONT platform also captures many modifications to DNA that modulate gene expression, and T2T was able to map these ‘epigenetic tags’ genome-wide as well⁴.

The genome T2T solved was from a cell line that contains two identical sets of chromosomes. Normal diploid human genomes contain two versions of

each chromosome, and researchers are now working on ‘phasing’ strategies that can confidently assign each sequence to the appropriate chromosome copy. “We’re already getting some pretty phenomenal phased assemblies,” says Miga.

This diploid assembly work is being conducted in collaboration with T2T’s partner organization, the Human Pan-genome Reference Consortium, which aspires to produce a more representative genome map, based on hundreds of donors from around the world. “We’re aiming to capture an average of 97% of human allelic diversity,” says Erich Jarvis, one of the consortium’s lead investigators and a geneticist at the Rockefeller University in New York City. As chair of the Vertebrate Genomes Project, Jarvis also hopes to leverage these complete genome assembly capabilities to generate full sequences for every vertebrate species on Earth. “I think within the next 10 years, we’re going to be doing telomere-to-telomere genomes routinely,” he says.

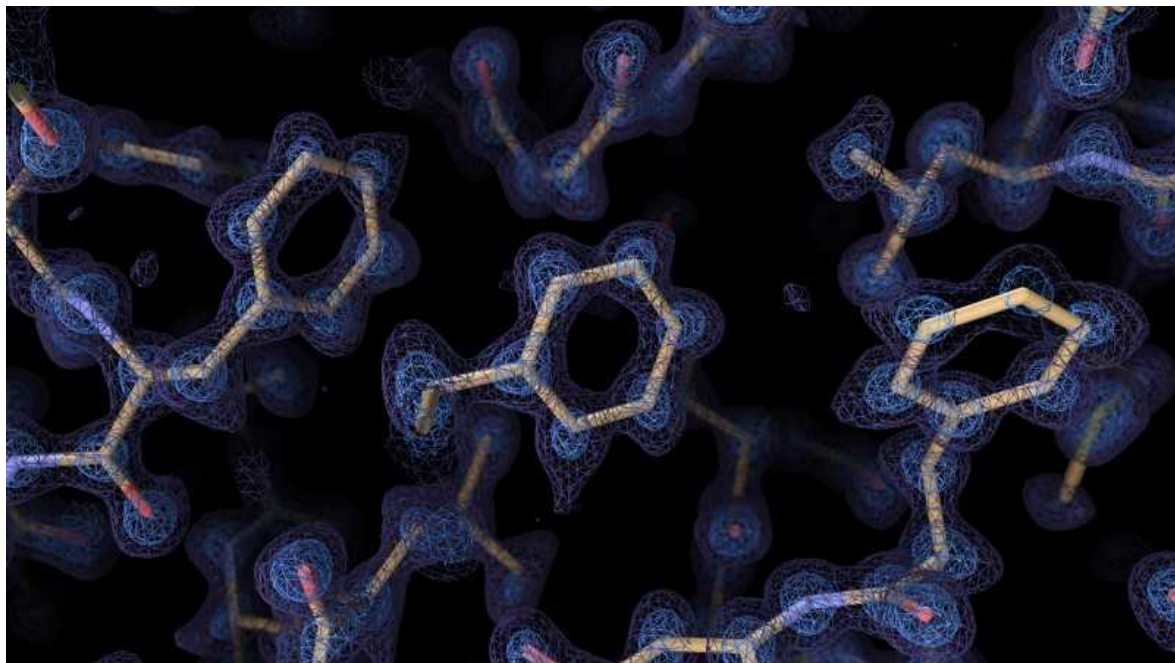
Protein structure solutions

Structure dictates function. But it can be hard to measure. Major experimental and computational advances in the past two years have given researchers complementary tools for determining protein structures with unprecedented speed and resolution.

The AlphaFold2 structure-prediction algorithm, developed by Alphabet subsidiary DeepMind in London, relies on ‘deep learning’ strategies to extrapolate the shape of a folded protein from its amino acid sequence⁵. Following a decisive victory at the 2020 Critical Assessment of protein Structure Prediction competition, in which computational biologists test their structure-prediction algorithms head-to-head, AlphaFold2’s reputation — and adoption — has soared. “For some of the structures, the predictions are almost eerily good,” says Janet Thornton, senior scientist and former director of the European Bioinformatics Institute in Hinxton, UK. Since its public release last July, AlphaFold2 has been applied to proteomes, to determine the structures of all the proteins expressed in humans⁶ and in 20 model organisms (see *Nature* **595**, 635; 2021), as well as nearly 440,000 proteins in the Swiss-Prot database, greatly increasing the number of

proteins for which high-confidence modelling data are available. The AlphaFold algorithm has also proven its ability to tackle multi-chain protein complexes⁷.

In parallel, improvements in cryogenic-electron microscopy (cryo-EM) are enabling researchers to experimentally solve even the most challenging proteins and complexes. Cryo-EM scans flash-frozen molecules with an electron beam, generating images of the proteins in multiple orientations that can then be computationally reassembled into a 3D structure. In 2020, improvements in cryo-EM hardware and software enabled two teams to generate structures with a resolution of less than 1.5 ångströms, capturing the position of individual atoms^{8,9}. “Prior to this, we bandied about the term ‘atomic resolution’ with wild abandon, but it’s only been near-atomic,” says Bridget Carragher, co-director of the New York Structural Biology Center’s Simons Electron Microscopy Center in New York City. “This truly is atomic.” And, although both teams used an especially well-studied model protein called apoferritin, Carragher says, these studies suggest that near-atomic resolution is feasible for other, more difficult targets as well.\



Images from cryo-electron microscopy are helping to solve complex structures.Credit: Paul Emsley/MRC Laboratory of Molecular Biology

Many experimentalists who were initially sceptical of AlphaFold2 now see it as a clear complement to experimental methods such as cryo-EM, where its computational models can aid in data analysis and reconstruction. And cryo-EM can generate findings currently out of reach for computational prediction. Carragher's team, for instance, is using 'time-resolved' cryo-EM to capture rapid conformational changes that occur when proteins interact with other molecules. "We can trap things and see what's happening on the order of a hundred milliseconds," she says.

There is also considerable excitement around a related method, cryo-electron tomography (cryo-ET), which captures naturalistic protein behaviour in thin sections of frozen cells. But interpretation of these crowded, complicated images is challenging, and Carragher thinks computational advances from the machine-learning world will be essential. "How else are we going to solve these almost intractable problems?" she asks.

Quantum simulation

Atoms are, well, atomic in size. But under the right conditions, they can be coaxed into a highly-excited, super-sized state with diameters on the order of one micrometre or more. By performing this excitation on carefully positioned arrays of hundreds of atoms in a controlled fashion, physicists have demonstrated that they can solve challenging physics problems that push conventional computers to their limits.

Quantum computers manage data in the form of qubits. Coupled together using the quantum physics phenomenon called entanglement, qubits can influence each other at a distance. These qubits can drastically increase the computing power that can be achieved with a given allotment of qubits relative to an equivalent number of bits in a classical computer.

Several groups have successfully used individual ions as qubits, but their electrical charges make them challenging to assemble at high density. Physicists including Antoine Browaeys at the French national research agency CNRS in Paris and Mikhail Lukin at Harvard University in Cambridge, Massachusetts, are exploring an alternative approach. The teams use optical tweezers to precisely position uncharged atoms in tightly packed

2D and 3D arrays, then apply lasers to excite these particles into large-diameter ‘Rydberg atoms’ that become entangled with their neighbours^{10,11}. “Rydberg atom systems are individually controllable, and their interactions can be turned on and off,” explains physicist Jaewook Ahn at the Korea Advanced Institute of Science and Technology in Daejeon, South Korea. This in turn confers programmability.

This approach has gained considerable momentum in the span of just a few years, with technological advances that have improved the stability and performance of Rydberg atom arrays, as well as rapid scaling from a few dozen qubits to several hundred. Early applications have focused on defined problems, such as predicting properties of materials, but the approach is versatile. “So far, any theoretical model that the theorists came up with, there was a way to implement it,” Browaeys says.

Pioneers in the field have founded companies that are developing Rydberg atom array-based systems for laboratory use, and Browaeys estimates that such quantum simulators could be commercially available in a year or two. But this work could also pave the way towards quantum computers that can be applied more generally, including in economics, logistics and encryption. Researchers are still struggling to define this still-nascent technology’s place in the computing world, but Ahn draws parallels to the Wright brothers’ early push into aviation. “That first airplane didn’t have any transportation advantages,” says Ahn, “but it eventually changed the world.”

Precise genome manipulation

For all its genome-editing prowess, CRISPR–Cas9 technology is better suited to gene inactivation than repair. That’s because although targeting the Cas9 enzyme to a genomic sequence is relatively precise, the cell’s repair of the resulting double-stranded cut is not. Mediated by a process called non-homologous end-joining, CRISPR–Cas9 repairs are often muddied by small insertions or deletions.

Most genetic diseases require gene correction rather than disruption, notes David Liu, a chemical biologist at Harvard University in Cambridge. Liu and his team have developed two promising approaches to do just that. Both

exploit CRISPR's precise targeting while also limiting Cas9's ability to cut DNA at that site. The first, called base editing, couples a catalytically impaired form of Cas9 to an enzyme that aids chemical conversion of one nucleotide to another — for example, cytosine to thymine or adenine to guanine (see *Nature* <https://doi.org/10.1038/hc2t>; 2016). But only certain base-to-base changes are currently accessible using this method. Prime editing, the team's newer development, links Cas9 to a type of enzyme known as reverse transcriptase and uses a guide RNA that is modified to include the desired edit to the genomic sequence (see *Nature* **574**, 464–465; 2019). Through a multistage biochemical process, these components copy the guide RNA into DNA that ultimately replaces the targeted genome sequence. Importantly, both base and prime editing cut only a single DNA strand, a safer and less disruptive process for cells.

First described in 2016, base editing is already en route to the clinic: Beam Therapeutics, founded by Liu and also based in Cambridge, got the nod in November from the US Food and Drug Administration to trial this approach in humans for the first time, with the goal of repairing the gene that causes sickle-cell disease.

Prime editing is not as far along, but improved iterations continue to emerge, and the method's promise is clear. Hyongbum Henry Kim, a genome-editing specialist at Yonsei University College of Medicine in Seoul, and his team have shown that they can achieve up to 16% efficiency using prime editing to correct retinal gene mutations in mice¹². “If we used recently reported, more advanced versions, the efficiencies would be improved even more,” he says. And Liu’s group has found that prime machinery can aid the insertion of gene-sized DNA sequences into the genome, potentially offering a safer, more tightly controlled strategy for gene therapy¹³. The process is relatively inefficient, but even a little repair can sometimes go a long way, Liu notes. “In some cases, it’s known that if you can replace a gene at a 10% or even a 1% level, you can rescue the disease,” he says.

Targeted genetic therapies

Nucleic acid-based medicines might be making an impact in the clinic, but they are still largely limited in terms of the tissues in which they can be

applied. Most therapies require either local administration or *ex vivo* manipulation of cells that are harvested from and then transplanted back into a patient. One prominent exception is the liver, which filters the bloodstream and is proving to be a robust target for selective drug delivery. In this instance, intravenous — or even subcutaneous — administration can get the job done.

“Just getting delivery at all to any tissue is difficult, when you really think about the challenge,” says Daniel Anderson, a chemical engineer at the Massachusetts Institute of Technology (MIT) in Cambridge. “Our bodies are designed to use the genetic information we have, not to accept newcomers.” But researchers are making steady progress in developing strategies that can help to shepherd these drugs to specific organ systems while sparing other, non-target tissues.

Adeno-associated viruses are the vehicle of choice for many gene-therapy efforts, and animal studies have shown that careful selection of the right virus combined with tissue-specific gene promoters can achieve efficient, organ-restricted delivery¹⁴. Viruses are sometimes challenging to manufacture at scale, however, and can elicit immune responses that undermine efficacy or produce adverse events.

Lipid nanoparticles provide a non-viral alternative, and several studies published over the past few years highlight the potential to tune their specificity. For example, the selective organ targeting (SORT) approach developed by biochemist Daniel Siegwart and his colleagues at the University of Texas Southwestern Medical Center in Dallas, enables the rapid generation and screening of lipid nanoparticles to identify those that can effectively target cells in tissues such as the lung or spleen¹⁵. “That was one of the first papers that showed that if you do systematic screening of these lipid nanoparticles and start changing their compositions, you can skew the biodistribution,” says Roy van der Meel, a biomedical engineer at the Eindhoven University of Technology in the Netherlands. Several groups are also exploring how protein components such as cell-specific antibodies might assist the targeting process, Anderson notes.

Anderson is particularly excited about the preclinical progress in targeting blood and immune cell precursors in bone marrow demonstrated by

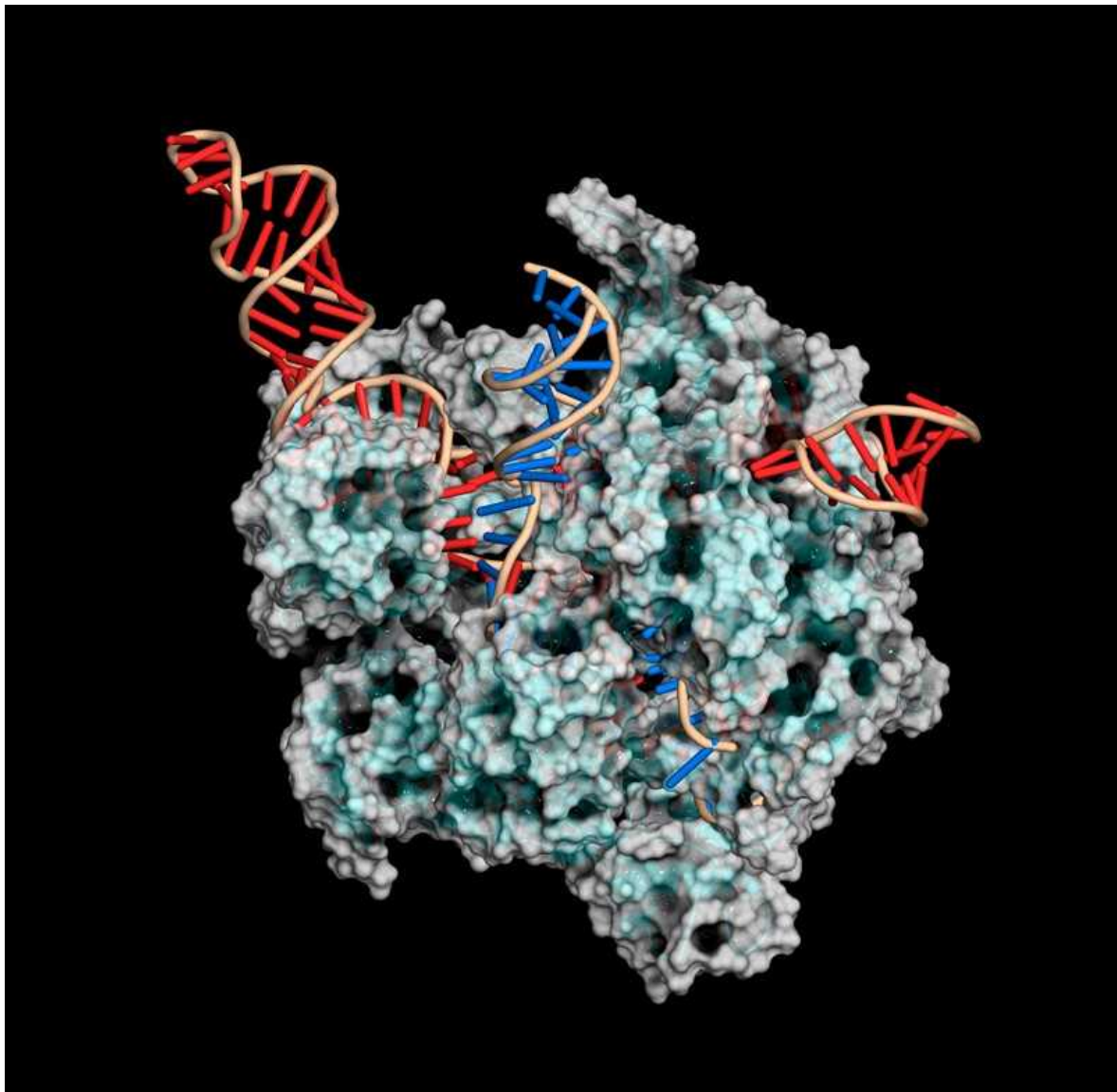
companies such as Beam Therapeutics and Intellia in Cambridge, both of which are using specially designed formulations of lipid nanoparticles. Success in targeting those tissues, he says, could spare patients from the gruelling process involved with current *ex vivo* gene therapies, which includes chemotherapy to kill existing bone marrow before transplantation. “Doing these things *in vivo* could really change treatment for patients,” says Anderson.

Spatial multi-omics

The explosion in single-cell ’omics development means researchers can now routinely derive genetic, transcriptomic, epigenetic and proteomic insights from individual cells — sometimes simultaneously (see go.nature.com/3nnhooo). But single-cell techniques also sacrifice crucial information by ripping these cells out of their native environments.

In 2016, researchers led by Joakim Lundeberg at the KTH Royal Institute of Technology in Stockholm devised a strategy to overcome this problem. The team prepared slides with barcoded oligonucleotides — short strands of RNA or DNA — that can capture messenger RNA from an intact tissue slice, such that each transcript could be assigned to a particular position in the sample according to its barcode. “No one really believed that we could pull out a transcriptome-wide analysis from a tissue section,” says Lundeberg. “But it turned out to be surprisingly easy.”

The field of spatial transcriptomics has since exploded. Multiple commercial systems are now available, including the Visium Spatial Gene Expression platform from 10x Genomics, which builds on Lundeberg’s technology. Academic groups continue to develop innovative methods that can map gene expression with ever-increasing depth and spatial resolution.



A CRISPR–Cas9 gene-editing complex uses a guide RNA (red) to cut DNA (blue). Credit: Mulekuul/SPL

Now researchers are layering further 'omic insights on top of their spatial maps. For example, biomedical engineer Rong Fan at Yale University in New Haven, Connecticut, developed a platform known as DBiT-seq¹⁶, which employs a microfluidic system that can simultaneously generate barcodes for thousands of mRNA transcripts and hundreds of proteins labelled with oligonucleotide-tagged antibodies. This can provide a much more accurate assessment of how cellular gene expression influences protein production and activity than could be obtained from transcriptomic data

alone, and Fan's team has been using it to investigate processes such as immune cell activation. "We're seeing early signs of how immune cells in the skin react to the Moderna COVID-19 vaccine," he says. Some commercial systems can also capture spatial data from multiple proteins in parallel with transcriptomic insights, including the Visium platform and Nanostring's GeoMx system.

Meanwhile, Lundeberg's group has refined its spatial transcriptomics method to simultaneously capture DNA sequence data. This has allowed his team to start mapping the spatiotemporal events underlying tumorigenesis. "We could follow these genetic changes in space, how they evolve into additional genetic variants that eventually lead to the tumour," he says.

Fan's team has demonstrated spatial mapping of chromatin modifications in tissue samples, which can reveal the cellular gene regulatory landscapes that influence processes such as development, differentiation and intercellular communication¹⁷. Fan is confident that the method can be paired with spatial analysis of RNA, and even proteins. "We have preliminary data showing that this is totally doable," he says.

CRISPR-based diagnostics

The CRISPR–Cas system's capacity for precise cleavage of specific nucleic acid sequences stems from its role as a bacterial 'immune system' against viral infection. This link inspired early adopters of the technology to contemplate the system's applicability to viral diagnostics. "It just makes a lot of sense to use what they're designed for in nature," says Pardis Sabeti, a geneticist at the Broad Institute of MIT and Harvard in Cambridge. "You have billions of years of evolution on your side."

But not all Cas enzymes are created equal. Cas9 is the go-to enzyme for CRISPR-based genome manipulation, but much of the work in CRISPR-based diagnostics has employed the family of RNA-targeting molecules known as Cas13, first identified in 2016 by molecular biologist Feng Zhang and his team at the Broad. "Cas13 uses its RNA guide to recognize an RNA target by base-pairing, and activates a ribonuclease activity that can be harnessed as a diagnostic tool by using a reporter RNA," explains Jennifer

Doudna at the University of California, Berkeley, who shared the 2020 Nobel Prize in Chemistry with Emmanuelle Charpentier, now at the Max Planck Unit for the Science of Pathogens in Berlin, for developing the genome-editing capabilities of CRISPR–Cas9. This is because Cas13 doesn't just cut the RNA targeted by the guide RNA, it also performs 'collateral cleavage' on any other nearby RNA molecules. Many Cas13-based diagnostics use a reporter RNA that tethers a fluorescent tag to a quencher molecule that inhibits that fluorescence. When Cas13 is activated after recognizing viral RNA, it cuts the reporter and releases the fluorescent tag from the quencher, generating a detectable signal. Some viruses leave a strong enough signature that detection can be achieved without amplification, simplifying point-of-care diagnostics. For example, last January, Doudna and Melanie Ott at the Gladstone Institute of Virology in San Francisco, California, demonstrated a rapid, nasal-swab-based CRISPR–Cas13 test for amplification-free detection of SARS-CoV-2 using a mobile phone camera¹⁸.

RNA-amplification procedures can boost sensitivity for trace viral sequences, and Sabeti and her colleagues have developed a microfluidic system that screens for multiple pathogens in parallel using amplified genetic material from just a few microlitres of sample¹⁹. "Right now, we have an assay to do 21 viruses simultaneously for less than US\$10 a sample," she says. Sabeti and her colleagues have developed tools for CRISPR-based detection of more than 169 human viruses at once, she adds.

Other Cas enzymes could flesh out the diagnostic toolbox, Doudna notes, including the Cas12 proteins, which exhibit similar properties to Cas13 but target DNA rather than RNA. Collectively, these could detect a broader range of pathogens, or even enable efficient diagnosis of other non-infectious diseases. "That could be very useful if you could do that relatively quickly, especially as different cancer subtypes become defined by particular types of mutations," Doudna says.

Nature **601**, 658–661 (2022)

doi: <https://doi.org/10.1038/d41586-022-00163-x>

References

1. 1.
Nurk, S. *et al.* Preprint at bioRxiv
<https://doi.org/10.1101/2021.05.26.445798> (2021).
2. 2.
Miga, K. H. *et al.* *Nature* **585**, 79–84 (2020).
3. 3.
Logsdon, G. A. *et al.* *Nature* **593**, 101–107 (2021).
4. 4.
Gershman, A. *et al.* Preprint at bioRxiv
<https://doi.org/10.1101/2021.05.26.443420> (2021).
5. 5.
Jumper, J. *et al.* *Nature* **596**, 583–589 (2021).
6. 6.
Tunyasuvunakool, K. *et al.* *Nature* **596**, 590–596 (2021).
7. 7.
Evans, R. *et al.* Preprint at bioRxiv
<https://doi.org/10.1101/2021.10.04.463034> (2021).
8. 8.
Nakane, T. *et al.* *Nature* **587**, 152–156 (2020).
9. 9.

Yip, K. M., Fischer, N., Paknia, E., Chari, A. & Stark, H. *Nature* **587**, 157–161 (2020).

10. 10.

Bernien, H. *et al.* *Nature* **551**, 579–584 (2017).

11. 11.

Barredo, D., Lienhard, V., de Léséleuc, S., Lahaye, T. & Browaeys, A. *Nature* **561**, 79–82 (2018).

12. 12.

Jang, H. *et al.* *Nature Biomed. Eng.* <https://doi.org/10.1038/s41551-021-00788-9> (2021).

13. 13.

Anzalone, A. V. *et al.* Preprint at bioRxiv
<https://doi.org/10.1101/2021.11.01.466790> (2021).

14. 14.

Levy, J. M. *et al.* *Nature Biomed. Eng.* **4**, 97–110 (2020).

15. 15.

Cheng, Q. *et al.* *Nature Nanotechnol.* **15**, 313–320 (2020).

16. 16.

Liu, Y. *et al.* *Cell* **183**, 1665–1681 (2020).

17. 17.

Deng, Y. *et al.* Preprint at bioRxiv
<https://doi.org/10.1101/2021.06.06.447244> (2021).

18. 18.

Fozouni, P. *et al.* *Cell* **184**, 323–333 (2021).

19. 19.

Ackerman, C. M. *et al.* *Nature* **582**, 277–282 (2020).

This article was downloaded by **calibre** from <https://www.nature.com/articles/d41586-022-00163-x>

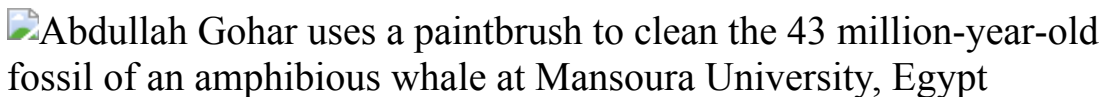
| [Section menu](#) | [Main menu](#) |

- WHERE I WORK
- 24 January 2022

The ancient whale from my Egyptian home town

Abdullah Gohar studies fossils from the Faiyum Depression, which occurred where he grew up.

- [Jack Leeming](#)



Abdullah Gohar is lab manager at Mansoura University Vertebrate Paleontology Center in Egypt. Credit: Mohamed Abd El Ghany/Reuters/Alamy

If you pick up any book about the palaeontology of whales, there's a strong chance that you'll see 'Faiyum Depression' somewhere in there. Faiyum, Egypt, is a desert now, but it was once teeming with life and has the highest concentration in the world of whale bones from before 40 million years ago. I'm a whale researcher, but that's not the only reason I'm familiar with the region: I grew up in Faiyum.

This picture shows me removing sediment from the fossilized bones of an ancient four-legged whale, as part of my job as a laboratory manager at Mansoura University Vertebrate Paleontology Center in Egypt.

We described this whale in an August 2021 article ([A. S. Gohar et al. Proc. R. Soc. B Biol. Sci. 288, 20211368; 2021](#)) and named it *Phiomicetus anubis* — the first word comes from 'Faiyum' phonetically, and the second is from the Pharaonic Egyptian god of death. The whale must have meant death to

many creatures that lived beside it 43 million years ago: it had a vast, strong jaw, weighed 600 kilograms and was about 3 metres long.

In evolutionary history, whales transformed from tiny, four-legged plant-eating creatures no bigger than house cats to the sea-faring giants we know today. Smack in the middle of this transformation is *Phiomicetus*. It was amphibious — much like a modern crocodile — and had four legs to help it move across land.

Phiomicetus is the first whale to be discovered, named and studied by an Egyptian team. That feels special to me. Hopefully, it shows the world that Egypt doesn't contain only antiquities and treasures of that kind. It has something more valuable and much older.

We don't just study huge animals. In October last year, members of my research group published a paper on *Qatranimys safroutus*, a small, ancient rodent from Faiyum, weighing only around 45 grams ([3S. F. Al-Ashqar et al. PeerJ 9, e12074; 2021](#)). You can expect more discoveries in the near future — big and small — from all of us.

Nature **601**, 664 (2022)

doi: <https://doi.org/10.1038/d41586-022-00164-w>

This article was downloaded by **calibre** from <https://www.nature.com/articles/d41586-022-00164-w>

Research

- **[Hot surfaces cooled by isolating steam from spray](#)** [26 January 2022]
News & Views • An innovative microstructure design distributes water to rapidly cool a hot surface without interference from the steam that is created in the process. This approach could enable safer and more efficient power generation.
- **[A grave matter of ancient kinship in Neolithic Britain](#)** [23 December 2021]
News & Views • An investigation into the nature of genetic connections between individuals interred in the same chambers of an ancient tomb in Britain about 5,700 years ago sheds light on kinship in an early society.
- **[Bronze Age genomes reveal migration to Britain](#)** [22 December 2021]
News & Views • The genomes of hundreds of individuals who lived in Great Britain and in continental Europe during the Bronze Age provide evidence for a migration of people from the continent to southern Britain between 1000 and 875 bc.
- **[Self-heating plasmas offer hope for energy from fusion](#)** [26 January 2022]
News & Views • Experiments have validated a way of producing nuclear energy known as laser-driven fusion, in which a plasma is heated and compressed. The milestone offers crucial evidence that the plasma can supply its own heat.
- **[Cardiovascular diseases disrupt the bone-marrow niche](#)**
[23 December 2021]
News & Views • The production of blood cells, including some immune cells, relies heavily on the bone-marrow microenvironment. Cardiovascular diseases are now found to corrupt this niche, leading to imbalances in blood-cell production.
- **[The challenges and opportunities of battery-powered flight](#)**
[26 January 2022]
Perspective • The economic, technical, environmental and safety requirements of battery-powered aircraft are considered, and promising technologies and future prospects for battery innovation are discussed.
- **[A radio transient with unusually slow periodic emission](#)**
[26 January 2022]
Article • Analysis of archival low-frequency radio data from the Murchison Widefield Array reveals a periodic transient with an unusual periodicity of 18.18 min, the source of which is localized to our Galaxy and could be an ultra-long-period magnetar.

- **Time-crystalline eigenstate order on a quantum processor** [30 November 2021]
Article • A study establishes a scalable approach to engineer and characterize a many-body-localized discrete time crystal phase on a superconducting quantum processor.
- **Quantum register of fermion pairs** [26 January 2022]
Article • Entangled pairs of fermionic atoms in an optical lattice array have long-lived motional coherence, and the motion of each pair results in a robust qubit, protected by exchange symmetry.
- **Burning plasma achieved in inertial fusion** [26 January 2022]
Article • A burning plasma, a critical step towards self-sustaining fusion, is achieved at the US National Ignition Facility, with a subset of experiments demonstrating fusion self-heating beyond radiation and conduction losses.
- **Deep physical neural networks trained with backpropagation** [26 January 2022]
Article • A hybrid algorithm that applies backpropagation is used to train layers of controllable physical systems to carry out calculations like deep neural networks, but accounting for real-world noise and imperfections.
- **Emergent interface vibrational structure of oxide superlattices** [26 January 2022]
Article • The vibrational states emerging at the interface in oxide superlattices are characterized theoretically and at atomic resolution, showing the impact of material length scales on structure and vibrational response.
- **Unconventional spectral signature of Tc in a pure d-wave superconductor** [26 January 2022]
Article • A high-precision angle-resolved photoemission spectroscopy (ARPES) study on the superconductor Bi2212 resolves the spectroscopic singularity associated with the superconducting transition temperature, and indicates that the transition is driven by phase fluctuations.
- **Inhibiting the Leidenfrost effect above 1,000 °C for sustained thermal cooling** [26 January 2022]
Article • Structured thermal armours on the surface of a solid inhibit the Leidenfrost effect, even when heated to temperatures in excess of 1,000 °C, pointing the way towards new cooling strategies for high-temperature solids.
- **Centimetre-scale perovskite solar cells with fill factors of more than 86 per cent** [26 January 2022]
Article • Perovskite solar cells including charge transport material fabricated using a reverse-doping process have the highest certified efficiency for cells of 1-cm² active area and the

highest fill factor reported so far.

- **Age of the oldest known Homo sapiens from eastern Africa**

[12 January 2022]

Article • Geochemical analyses correlating the stratum that overlies the sediments containing the Omo fossils with material from a volcanic eruption suggest that these fossils (the oldest known modern human fossils in eastern Africa) are over 200,000 years old.

- **A high-resolution picture of kinship practices in an Early Neolithic tomb** [22 December 2021]

Article • Archaeological and ancient DNA analyses of 35 individuals entombed at Hazleton North long cairn approximately 5,700 years ago are used to reconstruct kinship practices in Early Neolithic Britain.

- **Large-scale migration into Britain during the Middle to Late Bronze Age** [22 December 2021]

Article • Genome-wide ancient DNA data from individuals from the Middle Bronze Age to Iron Age documents large-scale movement of people from the European continent between 1300 and 800 bc that was probably responsible for spreading early Celtic languages to Britain.

- **Spatial maps in piriform cortex during olfactory navigation** [22 December 2021]

Article • Studies using neural ensemble recordings in rats show that cells in the piriform cortex carry a spatial representation of the environment and link locations to olfactory sensory inputs.

- **Human blastoids model blastocyst development and implantation** [02 December 2021]

Article • Blastoids derived from naive PXGL-cultured human pluripotent stem cells in which Hippo, TGF- β and ERK pathways are inhibited closely recapitulate aspects of blastocyst development, form cells resembling blastocyst-stage cells and thus provide a model system for implantation and development studies.

- **A naturally inspired antibiotic to target multidrug-resistant pathogens** [05 January 2022]

Article • The discovery and synthesis of a colistin congener provide a promising clinical lead against mcr-1-encoding colistin-resistant pathogens, which are responsible for an increasing number of deaths from antibiotic-resistant infections.

- **Long-acting capsid inhibitor protects macaques from repeat SHIV challenges** [07 December 2021]

Article • A single dose of a small-molecule HIV capsid inhibitor provides long-term protection from repeated simian–human immunodeficiency virus challenges in macaques and might serve as a novel strategy for HIV prevention in humans.

- **A COVID-19 peptide vaccine for the induction of SARS-CoV-2 T cell immunity** [23 November 2021]

Article • A phase I open-label trial evaluating the immunogenicity, reactogenicity and safety of a peptide-based SARS-CoV-2 vaccine candidate to induce SARS-CoV-2-specific T cell responses.
- **Multi-omic machine learning predictor of breast cancer therapy response** [07 December 2021]

Article • Integration of pre-treatment tumour features in predictive models using machine learning could inform on response to therapy.
- **Decoding gene regulation in the fly brain** [05 January 2022]

Article • A chromatin accessibility atlas of 240,919 cells in the adult and developing Drosophila brain reveals 95,000 enhancers, which are integrated in cell-type specific enhancer gene regulatory networks and decoded into combinations of functional transcription factor binding sites using deep learning.
- **Ageing exacerbates ribosome pausing to disrupt cotranslational proteostasis** [19 January 2022]

Article • Ageing alters the kinetics of translation elongation in both *Caenorhabditis elegans* and *Saccharomyces cerevisiae*.
- **Structural insights into inhibitor regulation of the DNA repair protein DNA-PKcs** [05 January 2022]

Article • Cryo-electron microscopy structures of DNA-dependent protein kinase catalytic subunit bound to ATPyS and four inhibitors (wortmannin, NU7441, AZD7648 and M3814) provide molecular details and insights useful for drug design.
- **Architecture of the chloroplast PSI–NDH supercomplex in *Hordeum vulgare*** [08 December 2021]

Article • Cryo-electron microscopy structures of the photosystem I–NADH dehydrogenase-like supercomplex in barley provide structural details to elucidate the functions and regulation of photosystem I-dependent cyclic electron transport in chloroplasts.
- **The Living Planet Index does not measure abundance** [26 January 2022]

Matters Arising •
- **Reply to: The Living Planet Index does not measure abundance** [26 January 2022]

Matters Arising •
- **Shifting baselines and biodiversity success stories** [26 January 2022]

Matters Arising •

- **Reply to: Shifting baselines and biodiversity success stories** [26 January 2022]
Matters Arising •
- **Emphasizing declining populations in the Living Planet Report** [26 January 2022]
Matters Arising •
- **Reply to: Emphasizing declining populations in the Living Planet Report** [26 January 2022]
Matters Arising •
- **Do not downplay biodiversity loss** [26 January 2022]
Matters Arising •
- **Reply to: Do not downplay biodiversity loss** [26 January 2022]
Matters Arising •

- NEWS AND VIEWS
- 26 January 2022

Hot surfaces cooled by isolating steam from spray

An innovative microstructure design distributes water to rapidly cool a hot surface without interference from the steam that is created in the process. This approach could enable safer and more efficient power generation.

- [James C. Bird](#) ⁰

A few droplets of water sprinkled on a hot frying pan will quickly boil away. Yet the same droplets on a much hotter pan will instead remain intact by floating on their own insulating vapour — a phenomenon referred to as the Leidenfrost effect¹. Eye-catching though it might be, this behaviour can have dire consequences in applications that require intense water cooling, including nuclear power plants, in which inefficient cooling due to the Leidenfrost effect can lead to nuclear meltdown. [Writing in Nature](#), Jiang *et al.*² report a surface design capable of inhibiting this effect, to allow spray cooling at temperatures exceeding 1,100 °C, which is 600 °C higher than alternative strategies have achieved.

Access options

Subscribe to nature+

Get immediate online access to the entire Nature family of 50+ journals

\$29.99

monthly

Subscribe

Subscribe to Journal

Get full journal access for 1 year

\$199.00

only \$3.90 per issue

Subscribe

All prices are NET prices.

VAT will be added later in the checkout.

Tax calculation will be finalised during checkout.

Buy article

Get time limited or full article access on ReadCube.

\$32.00

Buy

All prices are NET prices.

Additional access options:

- [Log in](#)
- [Learn about institutional subscriptions](#)

Nature **601**, 509-510 (2022)

doi: <https://doi.org/10.1038/d41586-022-00123-5>

References

1. 1.

Leidenfrost, J. G. *De aquae communis nonnullis qualitatibus tractatus* (Ovenius, 1756).

2. 2.

Jiang, M. *et al. Nature* **601**, 568–572 (2022).

3. 3.

Bergman, T. L., Incropera, F. P., DeWitt, D. P. & Lavine, A. S. *Fundamentals of Heat and Mass Transfer* 8th edn, 598–602 (Wiley, 2017) .

4. 4.

Kwon, H., Bird, J. C. & Varanasi, K. K. *Appl. Phys. Lett.* **103**, 201601 (2013).

5. 5.

Farokhnia, N., Sajadi, S. M., Irajizad, P. & Ghasemi, H. *Langmuir* **33**, 2541–2550 (2017).

This article was downloaded by **calibre** from <https://www.nature.com/articles/d41586-022-00123-5>

| [Section menu](#) | [Main menu](#) |

- NEWS AND VIEWS
- 23 December 2021

A grave matter of ancient kinship in Neolithic Britain

An investigation into the nature of genetic connections between individuals interred in the same chambers of an ancient tomb in Britain about 5,700 years ago sheds light on kinship in an early society.

- [Neil Carlin](#) 0

Archaeologists have long suggested that the placement of human remains in tombs during the Stone Age of northwestern Europe reflects one of the ways in which kinship was created and negotiated. Biological descent is presumed to have played a part, but relatively few cases of close genetic relationships have previously been uncovered from these tombs. This is partly because only a couple of studies have investigated the genetic lineage of multiple burials from the same site. Now, an innovative study of a chambered tomb at Hazleton North in southwestern Britain has analysed the genomes of 35 out of at least 41 people, including 22 adults, buried there over the course of a century. [Writing in Nature](#), Fowler *et al.*¹ reveal notable information about the social relationships between these individuals, who lived around 5,700 years ago. The authors' findings provide a uniquely high-resolution, multigenerational and spatio-temporal analysis of the connections between the people who were interred together in the monument.

Access options

Subscribe to nature+

Get immediate online access to the entire Nature family of 50+ journals

\$29.99

monthly

[Subscribe](#)

Subscribe to Journal

Get full journal access for 1 year

\$199.00

only \$3.90 per issue

[Subscribe](#)

All prices are NET prices.

VAT will be added later in the checkout.

Tax calculation will be finalised during checkout.

Buy article

Get time limited or full article access on ReadCube.

\$32.00

[Buy](#)

All prices are NET prices.

Additional access options:

- [Log in](#)
- [Learn about institutional subscriptions](#)

Nature **601**, 510-512 (2022)

doi: <https://doi.org/10.1038/d41586-021-03799-3>

References

1. 1.
Fowler, C. *et al.* *Nature* **601**, 584–587 (2022).
2. 2.
Meadows, J., Barclay, A. & Bayliss, A. *Camb. Archaeol. J.* **17**, 45–64 (2007).
3. 3.
Rowley-Conwy, P. A. & Legge, A. J. in *The Oxford Handbook of Neolithic Europe* (eds Fowler, C., Harding, J. & Hofmann, D.) 429–446 (Oxford Univ. Press, 2015).
4. 4.
Olalde, I. *et al.* *Nature* **555**, 190–196 (2018).
5. 5.
Bentley, R. A. *et al.* *Proc. Natl Acad. Sci. USA* **109**, 9326–9330 (2012).
6. 6.
Sánchez-Quinto, F. *et al.* *Proc. Natl Acad. Sci. USA* **116**, 9469–9474 (2019).
7. 7.
Cassidy, L. M. *et al.* *Nature* **582**, 384–388 (2020).
8. 8.

Carsten, J. *After Kinship* (Cambridge Univ. Press, 2003).

9. 9.

Brück, J. *Antiquity* **95**, 228–237 (2021).

10. 10.

Bickle, P. *Camb. Archaeol. J.* **30**, 201–218 (2020).

11. 11.

Robb, J. & Harris, O. J. T. *Am. Antiq.* **83**, 128–147 (2018).

This article was downloaded by **calibre** from <https://www.nature.com/articles/d41586-021-03799-3>

| [Section menu](#) | [Main menu](#) |

- NEWS AND VIEWS
- 22 December 2021

Bronze Age genomes reveal migration to Britain

The genomes of hundreds of individuals who lived in Great Britain and in continental Europe during the Bronze Age provide evidence for a migration of people from the continent to southern Britain between 1000 and 875 bc.

- [Daniel G. Bradley](#) 0

Around the year 2300 bc, a man now nicknamed the Amesbury Archer was buried with exceptional riches near the ancient stone monument Stonehenge in southern England. The Amesbury Archer and the items buried with him provide a snapshot of a culture in the south of Britain that used metal and created distinctive ceramics, known as Bell Beaker pottery. This man was also an immigrant: analysis of oxygen isotopes in the enamel layers of his teeth that had formed in childhood suggested he originated from the Alps in central Europe¹. [Writing in Nature](#), Patterson *et al.*² analyse his genome and those of hundreds of other ancient individuals buried across Britain, as well as in continental Europe, to unravel Britain's migratory past with unprecedented granularity.

Access options

Subscribe to nature+

Get immediate online access to the entire Nature family of 50+ journals

\$29.99

monthly

Subscribe

Subscribe to Journal

Get full journal access for 1 year

\$199.00

only \$3.90 per issue

Subscribe

All prices are NET prices.

VAT will be added later in the checkout.

Tax calculation will be finalised during checkout.

Buy article

Get time limited or full article access on ReadCube.

\$32.00

Buy

All prices are NET prices.

Additional access options:

- [Log in](#)
- [Learn about institutional subscriptions](#)

Nature **601**, 512-513 (2022)

doi: <https://doi.org/10.1038/d41586-021-03770-2>

References

1. 1.

Fitzpatrick, A. P. *The Amesbury Archer and the Boscombe Bowmen* (Wessex Archaeology, 2013).

2. 2.

Patterson, N. *et al. Nature* **601**, 588–594 (2022).

3. 3.

Anthony, D. W. *Am. Anthropol.* **92**, 895–914 (1990).

4. 4.

Booth, T. J. *World Archaeol.* **51**, 586–601 (2019).

5. 5.

Lazaridis, I. *et al. Nature* **536**, 419–424 (2016).

6. 6.

Hofmanová, Z. *et al. Proc. Natl Acad. Sci. USA* **113**, 6886–6891 (2016).

7. 7.

Allentoft, M. E. *et al. Nature* **522**, 167–172 (2015).

8. 8.

Haak, W. *et al. Nature* **522**, 207–211 (2015).

9. 9.

Cassidy, L. M. *et al. Proc. Natl Acad. Sci. USA* **113**, 368–373 (2016).

10. 10.

Olalde, I. *et al. Nature* **555**, 190–196 (2018).

11. 11.

Cunliffe, B. W. *Europe Between the Oceans: 9000 BC–AD 1000* (Yale Univ. Press, 2008).

12. 12.

Brace, S. *et al.* *Nature Ecol. Evol.* **3**, 765–771 (2019).

13. 13.

Leslie, S. *et al.* *Nature* **519**, 309–314 (2015).

14. 14.

Kershaw, J. & Røyrvik, E. C. *Antiquity* **90**, 1670–1680 (2016).

15. 15.

Booth, T. J., Brück, J., Brace, S. & Barnes, I. *Camb. Archaeol. J.* **31**, 379–400 (2021).

This article was downloaded by **calibre** from <https://www.nature.com/articles/d41586-021-03770-2>

| [Section menu](#) | [Main menu](#) |

- NEWS AND VIEWS
- 26 January 2022

Self-heating plasmas offer hope for energy from fusion

Experiments have validated a way of producing nuclear energy known as laser-driven fusion, in which a plasma is heated and compressed. The milestone offers crucial evidence that the plasma can supply its own heat.

- [Nigel Woolsey](#) ⁰

Many of the world's current energy sources are both unsustainable and harmful to the environment, so the idea that a relatively safe fuel is abundant in seawater will come as welcome news to many. But the energy is released in the process of nuclear fusion, in which two atomic nuclei combine to form a heavier nucleus — a difficult scientific and engineering feat to achieve, with many unanswered questions. [Writing in Nature](#), Zylstra *et al.*¹ answer one such question by showing that, in the laser-driven approach to fusion, in which a plasma is compressed and heated, the plasma can be further heated by the fusion reactions themselves — a key requirement for self-sustaining fusion energy. Companion papers from the same group of researchers, by Kritchler *et al.*² in [Nature Physics](#) and Ross *et al.*³ on the [arXiv preprint server](#), detail the process of optimizing the experiment design.

Access options

Subscribe to nature+

Get immediate online access to the entire Nature family of 50+ journals

\$29.99

monthly

[Subscribe](#)

Subscribe to Journal

Get full journal access for 1 year

\$199.00

only \$3.90 per issue

[Subscribe](#)

All prices are NET prices.

VAT will be added later in the checkout.

Tax calculation will be finalised during checkout.

Buy article

Get time limited or full article access on ReadCube.

\$32.00

[Buy](#)

All prices are NET prices.

Additional access options:

- [Log in](#)
- [Learn about institutional subscriptions](#)

Nature **601**, 514-515 (2022)

doi: <https://doi.org/10.1038/d41586-022-00124-4>

References

1. 1.

Zylstra, A. B. *et al. Nature* **601**, 542–548 (2022).

2. 2.

Kritchler, A. L. *et al. Nature Phys.* <https://doi.org/10.1038/s41567-021-01485-9> (2022).

3. 3.

Ross, J. S. *et al.* Preprint at <https://arxiv.org/abs/2111.04640> (2021).

4. 4.

Ross, J. S. *et al. Phys. Rev. E* **91**, 021101 (2015).

5. 5.

Glenzer, S. H. *et al. Science* **327**, 1228–1231 (2010).

6. 6.

Robey, H. F., Berzak Hopkins, L., Milovich, J. L. & Meezan, N. B. *Phys. Plasmas* **25**, 012711 (2018).

This article was downloaded by **calibre** from <https://www.nature.com/articles/d41586-022-00124-4>

- NEWS AND VIEWS
- 23 December 2021

Cardiovascular diseases disrupt the bone-marrow niche

The production of blood cells, including some immune cells, relies heavily on the bone-marrow microenvironment. Cardiovascular diseases are now found to corrupt this niche, leading to imbalances in blood-cell production.

- [Tomer Itkin](#) ⁰ &
- [Shahin Rafii](#) ¹

According to the World Health Organization, cardiovascular diseases are the world's leading cause of death (go.nature.com/3dvysp6). The development and progression of cardio-vascular disease (CVD) could be influenced by a perturbation in the balance of haematopoiesis, the process by which blood cells (including immune cells) are generated from haematopoietic stem and progenitor cells (HSPCs). Indeed, inflammatory blood cells that are derived from haematopoietic progenitor cells in the bone marrow have been implicated in cardiovascular disorders such as athero-sclerosis, a condition in which cholesterol builds up in the arteries; myo-cardial infarction (heart attack); and ischaemia, a form of heart failure that results from a lack of oxygen supply (reviewed in ref. 1). This relationship between the cardiac and haemato-poietic systems was thought to be unidirectional. However, [writing in *Nature Cardiovascular Research*](#), Rohde *et al.*² provide evidence from individuals with CVD, as well as from mouse models of such disease, suggesting that the crosstalk between the cardio-vascular system and the bone marrow is bidirectional.

Access options

Subscribe to nature+

Get immediate online access to the entire Nature family of 50+ journals

\$29.99

monthly

[Subscribe](#)

Subscribe to Journal

Get full journal access for 1 year

\$199.00

only \$3.90 per issue

[Subscribe](#)

All prices are NET prices.

VAT will be added later in the checkout.

Tax calculation will be finalised during checkout.

Buy article

Get time limited or full article access on ReadCube.

\$32.00

[Buy](#)

All prices are NET prices.

Additional access options:

- [Log in](#)
- [Learn about institutional subscriptions](#)

Nature **601**, 515–517 (2022)

doi: <https://doi.org/10.1038/d41586-021-03550-y>

References

1. 1.

Poller, W. C., Nahrendorf, M. & Swirski, F. K. *Circ. Res.* **126**, 1061–1085 (2020).

2. 2.

Rohde, D. *et al.* *Nature Cardiovasc. Res.* **1**, 28–44 (2022).

3. 3.

Morrison, S. J. & Scadden, D. T. *Nature* **505**, 327–334 (2014).

4. 4.

Rafii, S., Butler, J. M. & Ding, B.-S. *Nature* **529**, 316–325 (2016).

5. 5.

Agarwala, S. & Tamplin, O. J. *Trends Cell Biol.* **28**, 987–998 (2018).

6. 6.

Yan, H., Baldridge, M. T. & King, K. Y. *Blood* **132**, 559–564 (2018).

7. 7.

Ferraro, F. *et al.* *Sci. Transl. Med.* **3**, 104ra101 (2011).

8. 8.

Hoffmann, J. *et al.* *Nature Commun.* **12**, 3964 (2021).

9. 9.

Kusumbe, A. P., Ramasamy, S. K. & Adams, R. H. *Nature* **507**, 323–328 (2014).

10. 10.

Baudino, T. A. *et al.* *Genes Dev.* **16**, 2530–2543 (2002).

11. 11.

Itkin, T. *et al.* *Nature* **532**, 323–328 (2016).

12. 12.

Lévesque, J.-P. *et al.* *Stem Cells* **25**, 1954–1965 (2007).

13. 13.

Hooper, A. T. *et al.* *Cell Stem Cell* **4**, 263–274 (2009).

14. 14.

Nolan, D. J. *et al.* *Dev. Cell* **26**, 204–219 (2013).

15. 15.

Dolgalev, I. & Tikhonova, A. N. *Front. Cell Dev. Biol.* **9**, 622519 (2021).

16. 16.

Han, X. *et al.* *Cell Stem Cell* **28**, 1160–1176 (2021).

17. 17.

Palikuqi, B. *et al.* *Nature* **585**, 426–432 (2020).

| [Section menu](#) | [Main menu](#) |

- Perspective
- [Published: 26 January 2022](#)

The challenges and opportunities of battery-powered flight

- [Venkatasubramanian Viswanathan](#) ORCID: [orcid.org/0000-0003-1060-5495](#)¹,
- [Alan H. Epstein](#) ORCID: [orcid.org/0000-0002-2850-5831](#)²,
- [Yet-Ming Chiang](#) ORCID: [orcid.org/0000-0002-0833-7674](#)³,
- [Esther Takeuchi](#)^{4,5},
- [Marty Bradley](#)⁶,
- [John Langford](#)⁷ &
- [Michael Winter](#)⁸

[Nature](#) volume **601**, pages 519–525 (2022)

- 2400 Accesses
- 47 Altmetric
- [Metrics details](#)

Subjects

- [Aerospace engineering](#)
- [Batteries](#)

Abstract

Aircraft, and the aviation ecosystem in which they operate, are shaped by complex trades among technical requirements, economics and

environmental concerns, all built on a foundation of safety. This Perspective explores the requirements of battery-powered aircraft and the chemistries that hold promise to enable them. The difference between flight and terrestrial needs and chemistries are highlighted. Safe, usable specific energy rather than cost is the major constraint for aviation. We conclude that battery packs suitable for flight with specific energy approaching 600 kilowatt hours per kilogram may be achievable in the next decade given sufficient investment targeted at aeronautical applications.

This is a preview of subscription content

Access options

Subscribe to nature+

Get immediate online access to the entire Nature family of 50+ journals

\$29.99

monthly

[Subscribe](#)

Subscribe to Journal

Get full journal access for 1 year

\$199.00

only \$3.90 per issue

[Subscribe](#)

All prices are NET prices.

VAT will be added later in the checkout.

Tax calculation will be finalised during checkout.

Buy article

Get time limited or full article access on ReadCube.

\$32.00

[Buy](#)

All prices are NET prices.

Additional access options:

- [Log in](#)
- [Learn about institutional subscriptions](#)

Fig. 1: Energy and power used for flight.

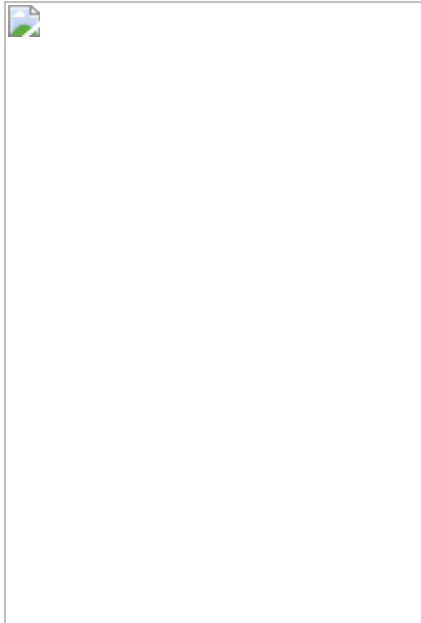


Fig. 2: History of usable energy density in aviation.

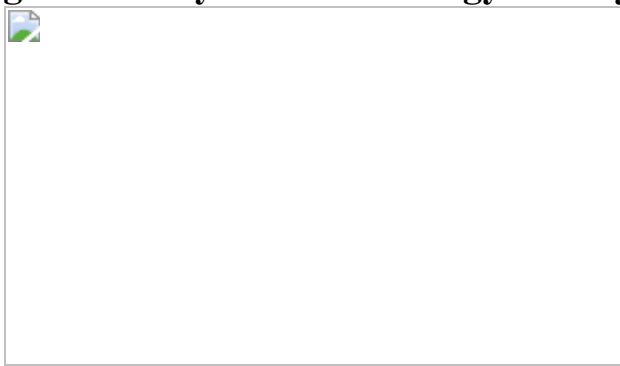


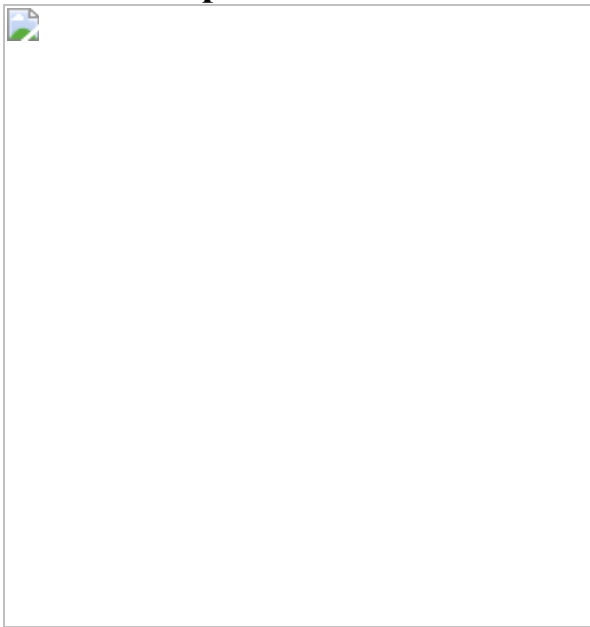
Fig. 3: Translating battery cell performance to aircraft range.



Fig. 4: Illustration of various losses in practically achieved specific energy at the cell level.



Fig. 5: Differences in mechanism of current Li-ion batteries based on insertion and possible future batteries based on conversion.



References

1. 1.

Soreau, R. in *The Practical Engineer* vol. 9 (6 April 1894) 266–267
(Technical Publishing Co., 1894).

2. 2.

Fleming, G. G. & deLépinay, I. Environmental trends in aviation to 2050. In *ICAO Environmental Report 2019* Ch. 1 (International Civil Aviation Organization, 2019).

3. 3.

Sindreu, J. Next stop for electric-vehicle SPAC mania: the Jetsons. *Wall Street Journal* (11 February 2021).

4. 4.

National Academies of Sciences, Engineering, and Medicine. *Commercial Aircraft Propulsion and Energy Systems Research: Reducing Global Carbon Emissions*, <https://doi.org/10.17226/23490> (National Academies Press, 2016). **A review of the state of the art and prospects for low-carbon propulsion for commercial aircraft including electric drive technologies.**

5. 5.

Epstein, A. H. & O'Flarity, S. M. Considerations for reducing aviation's CO₂ with aircraft electric propulsion. *J. Propul. Power* 35, 572–582 (2019). **An analysis of the potential and requirements for electric propulsion to substantially reduce aviation's CO₂, concluding that very considerable investment and advancement is required.**

6. 6.

Hepperle, M. Electric flight—potential and limitations. In *AVT-209 Workshop on Energy Efficient Technologies and Concepts of Operation 9-1–9-30* (NATO, 2012).

7. 7.

Schneider, D. C. Jr *An Exploratory Analysis Of Commercial Airline Contingency Fuel Calculations: With Forecasting And Optimization*. PhD thesis, The George Washington Univ. (2009).

8. 8.

Kondo, T. Fuel conservation—reserve fuel optimization. In *Proc. 2005 Boeing Performance and Flight Operations Engineering Conf.* 3 (2005).

9. 9.

Pratt & Whitney Canada. *PT6 Flat Rate Overhaul Program* <https://www.pwc.ca/en/products-and-services/services/maintenance-programs-and-solutions/pwcmart-maintenance-solutions/pwcmart-pt6a/flat-rate-overhaul-program> (2021).

10. 10.

737NG maintenance analysis & budget. *Aircraft Commerce* **70**, 12–30 (2010).

11. 11.

Langford, J. S. & Hall, D. K. Electrified aircraft propulsion. *Bridge* **50**, 21–27 (2020). **A presentation connecting fundamental aircraft design parameters and battery performance to aircraft capability.**

12. 12.

Kadhiresan, A. R. & Duffy, M. J. Conceptual design and mission analysis for eVTOL urban air mobility flight vehicle configurations. In *AIAA Aviation 2019 Forum* 2873 (AIAA, 2019).

13. 13.

Silva, C., Johnson, W. R., Solis, E., Patterson, M. D. & Antcliff, K. R. VTOL urban air mobility concept vehicles for technology

development. In *2018 Aviation Technology, Integration and Operations Conf.* 3847 (AIAA, 2018).

14. 14.

Duffy, M. J., Wakayama, S. R., Hupp, R., Lacy, R. & Stauffer, M. A study in reducing the cost of vertical flight with electric propulsion. In *17th AIAA Aviation Technology, Integration and Operations Conf.* (AIAA, 2017).

15. 15.

Antcliff, K. R. et al. Mission analysis and aircraft sizing of a hybrid-electric regional aircraft. In *54th AIAA Aerospace Sciences Meeting* 1028 (AIAA, 2016).

16. 16.

Lents, C. E. & Hardin, L. W. Fuel burn and energy consumption reductions of a single-aisle class parallel hybrid propulsion system. In *AIAA Propulsion and Energy 2019 Forum* 4396 (AIAA, 2019).

17. 17.

Voskuijl, M., van Bogaert, J. & Rao, A. G. Analysis and design of hybrid electric regional turboprop aircraft. *CEAS Aeronaut. J.* **9**, 15–25 (2017); correction **11**, 303 (2020).

18. 18.

US Federal Aviation Authority. *Events with Smoke, Fire, Extreme Heat or Explosion Involving Lithium Batteries*, https://www.faa.gov/hazmat/resources/lithium_batteries/media/Battery_incident_chart.pdf (FAA, accessed 28 August 2021).

19. 19.

European Aviation Safety Agency. *Special Condition LSA Propulsion Lithium Batteries*. Doc. No. SC-LSA-F2480-01 (EASA, 2017).

20. 20.

Society of Automotive Engineers. *Design and Development of Rechargeable Lithium Battery Systems for Aerospace Applications*. Standard AIR6343 (SEA, 2020).

21. 21.

Office of Energy Efficiency & Renewable Energy. *Battery500: Progress Update*, <https://www.energy.gov/eere/articles/battery500-progress-update> (DOE, 19 May 2020).

22. 22.

Soloveichik, G. ARPA-E IONICS program update. In *2020 IONICS Annual Review Meeting* <https://www.arpa-e.energy.gov/2020-ionics-annual-review-meeting> (ARPA-E, 2020).

23. 23.

Cuberg. Cuberg next-gen electric aviation battery technology receives U.S. Department of energy validation of industry-leading performance. *PR Newswire*, <https://www.prnewswire.com/news-releases/cuberg-next-gen-electric-aviation-battery-technology-receives-us-department-of-energy-validation-of-industry-leading-performance-301078332.html> (17 June 2020).

24. 24.

Singh, J. & Holme, T. QuantumScape next-generation solid-state battery presentation. *Zenodo* <https://doi.org/10.5281/zenodo.4609278> (2020).

25. 25.

24M Technologies. ARPA-E IONICS. In *2020 IONICS Annual Review Meeting* <https://www.arpa-e.energy.gov/2020-ionics-annual-review-meeting> (ARPA-E, 2020).

26. 26.

Davis, S. J. et al. Net-zero emissions energy systems. *Science* <https://doi.org/10.1126/science.aas9793> (2018).

27. 27.

Zhu, Y. et al. Design principles for self-forming interfaces enabling stable lithium-metal anodes. *Proc. Natl Acad. Sci.* **117**, 27195–27203 (2020).

28. 28.

Lain, M. J., Brandon, J. & Kendrick, E. Design strategies for high power vs. high energy lithium ion cells. *Batteries* **5**, 64 (2019).

29. 29.

Yang, Y. et al. Liquefied gas electrolytes for wide-temperature lithium metal batteries. *Energy Environ. Sci.* **13**, 2209–2219 (2020).

30. 30.

Albertus, P., Babinec, S., Litzelman, S. & Newman, A. Status and challenges in enabling the lithium metal electrode for high-energy and low-cost rechargeable batteries. *Nat. Energy* **3**, 16–21 (2017).

31. 31.

Hatzell, K. B. et al. Challenges in lithium metal anodes for solid-state batteries. *ACS Energy Lett.* **5**, 922–934 (2020).

32. 32.

Solid Power: Battery Data.
https://s28.q4cdn.com/717221730/files/doc_presentations/Solid-Power-Investor-Presentation-June-2021-Final.pdf (accessed 28 August 2021).

33. 33.

Famprikis, T., Canepa, P., Dawson, J. A., Islam, M. S. & Masquelier, C. Fundamentals of inorganic solid-state electrolytes for batteries. *Nat. Mater.* **18**, 1278–1291 (2019).

34. 34.

Smith, P. F., Takeuchi, K. J., Marschilok, A. C. & Takeuchi, E. S. Holy grails in chemistry: investigating and understanding fast electron/cation coupled transport within inorganic ionic matrices. *Acc. Chem. Res.* **50**, 544–548 (2017). **A perspective highlighting the challenges in meeting diverse application needs within a battery chemistry, pointing out the need for new chemistry breakthroughs to address these needs.**

35. 35.

Gallagher, K. G. et al. Quantifying the promise of lithium–air batteries for electric vehicles. *Energy Environ. Sci.* **7**, 1555–1563 (2014).

36. 36.

Crittenden, M. Ultralight batteries for electric airplanes. *IEEE Spectr.* **57**, 44–49 (2020).

37. 37.

Zhang, H., Li, X. & Zhang, H. *Li–S and Li–O₂ Batteries with High Specific Energy* (Springer, 2017).

38. 38.

Zu, C.-X. & Li, H. Thermodynamic analysis on energy densities of batteries. *Energy Environ. Sci.* **4**, 2614 (2011).

39. 39.

Krause, F. C. et al. High specific energy lithium primary batteries as power sources for deep space exploration. *J. Electrochem. Soc.* **165**, A2312–A2320 (2018).

40. 40.

Liu, W., Li, H., Xie, J.-Y. & Fu, Z.-W. Rechargeable room-temperature CF_x -sodium battery. *ACS Appl. Mater. Interfaces* **6**, 2209–2212 (2014).

41. 41.

Krishnamurthy, V. & Viswanathan, V. Beyond transition metal oxide cathodes for electric aviation: The case of rechargeable CF_x . *ACS Energy Lett.* **5**, 3330–3335 (2020). **An analysis pointing out the opportunities around conversion cathodes and challenges associated with making CF_x battery chemistry rechargeable.**

42. 42.

Hua, X. et al. Revisiting metal fluorides as lithium-ion battery cathodes. *Nat. Mater.* **20**, 841–850 (2021).

43. 43.

Neubauer, J., Pesaran, A., Bae, C., Elder, R. & Cunningham, B. Updating United States Advanced Battery Consortium and Department of Energy battery technology targets for battery electric vehicles. *J. Power Sources* **271**, 614–621 (2014).

44. 44.

National Academies of Sciences, Engineering, and Medicine. *Advances, Challenges, and Long-Term Opportunities in Electrochemistry: Addressing Societal Needs: Proceedings of a Workshop—in Brief*, <https://doi.org/10.17226/25760> (National Academies Press, 2020). **A review of the opportunities enabled by new tools, computational simulations and experimental characterization for discovering new electrochemical devices.**

45. 45.

Grey, C. P. & Tarascon, J. M. Sustainability and in situ monitoring in battery development. *Nat. Mater.* **16**, 45–56 (2016).

46. 46.

Liu, D. et al. Review of recent development of in situ/operando characterization techniques for lithium battery research. *Adv. Mater.* **31**, 1806620 (2019).

47. 47.

Meng, Y. S. & Arroyo-de Dompablo, M. E. Recent advances in first principles computational research of cathode materials for lithium-ion batteries. *Acc. Chem. Res.* **46**, 1171–1180 (2012).

48. 48.

Severson, K. A. et al. Data-driven prediction of battery cycle life before capacity degradation. *Nat. Energy* **4**, 383–391 (2019).

49. 49.

Dave, A. et al. Autonomous discovery of battery electrolytes with robotic experimentation and machine learning. *Cell Rep. Phys. Sci.* **1**, 100264 (2020).

50. 50.

Sripad, S. & Viswanathan, V. Performance metrics required of next-generation batteries to make a practical electric semi truck. *ACS Energy Lett.* **2**, 1669–1673 (2017).

51. 51.

Fang, C., Wang, X. & Meng, Y. S. Key issues hindering a practical lithium-metal anode. *Trends Chem.* **1**, 152–158 (2019).

52. 52.

Reddy, M. A., Breitung, B. & Fichtner, M. Improving the energy density and power density of CF_x by mechanical milling: a primary lithium battery electrode. *ACS Appl. Mater. Interfaces* **5**, 11207–11211 (2013).

53. 53.

Li, Y., Khurram, A. & Gallant, B. M. A high-capacity lithium-gas battery based on sulfur fluoride conversion. *J. Phys. Chem. C* **122**, 7128 (2018).

Author information

Affiliations

1. Department of Mechanical Engineering, Carnegie Mellon University, Pittsburgh, PA, USA

Venkatasubramanian Viswanathan

2. Department of Aeronautics and Astronautics, Massachusetts Institute of Technology, Cambridge, MA, USA

Alan H. Epstein

3. Department of Materials Science and Engineering, Massachusetts Institute of Technology, Cambridge, MA, USA

Yet-Ming Chiang

4. Department of Materials Science and Chemical Engineering, Stony Brook University, Stony Brook, NY, USA

Esther Takeuchi

5. Interdisciplinary Science Department, Brookhaven National Laboratory, Upton, NY, USA

Esther Takeuchi

6. Department of Aerospace and Mechanical Engineering, University of Southern California, Los Angeles, CA, USA

Marty Bradley

7. Electra.aero, Falls Church, VA, USA

John Langford

8. Pratt & Whitney, Hartford, CT, USA

Michael Winter

Contributions

input from M.W., M.B. and J.L. V.V. coordinated the battery portion with input from Y.-M.C. and E.T. All authors reviewed and edited the entire manuscript.

Corresponding authors

Correspondence to [Venkatasubramanian Viswanathan](#) or [Alan H. Epstein](#).

Ethics declarations

Competing interests

V.V. is a technical consultant at QuantumScape Corporation and Chief Scientist at Aionics Inc. Y.-M.C. is co-founder and Chief Scientist at 24M Technologies Inc. M.B. is a technical consultant to Electra.aero and Ampaire.

Peer review information

Nature thanks Marca Doeuff and the other, anonymous, reviewer(s) for their contribution to the peer review of this work.

Additional information

Publisher's note Springer Nature remains neutral with regard to jurisdictional claims in published maps and institutional affiliations.

Rights and permissions

[Reprints and Permissions](#)

About this article

Cite this article

Viswanathan, V., Epstein, A.H., Chiang, YM. *et al.* The challenges and opportunities of battery-powered flight. *Nature* **601**, 519–525 (2022). <https://doi.org/10.1038/s41586-021-04139-1>

- Received: 06 November 2020
- Accepted: 14 October 2021
- Published: 26 January 2022
- Issue Date: 27 January 2022
- DOI: <https://doi.org/10.1038/s41586-021-04139-1>

Share this article

Anyone you share the following link with will be able to read this content:

[Get shareable link](#)

Sorry, a shareable link is not currently available for this article.

[Copy to clipboard](#)

Provided by the Springer Nature SharedIt content-sharing initiative

How can battery-powered aircraft get off the ground?

- Benjamin Thompson
- Nick Petrić Howe

Nature Podcast 26 Jan 2022

This article was downloaded by **calibre** from <https://www.nature.com/articles/s41586-021-04139-1>

| [Section menu](#) | [Main menu](#) |

- Article
- [Published: 26 January 2022](#)

A radio transient with unusually slow periodic emission

- [N. Hurley-Walker](#) ORCID: [orcid.org/0000-0002-5119-4808¹](https://orcid.org/0000-0002-5119-4808),
- [X. Zhang](#) ORCID: [orcid.org/0000-0002-2218-5638^{2,3}](https://orcid.org/0000-0002-2218-5638),
- [A. Bahramian](#) ORCID: [orcid.org/0000-0003-2506-6041¹](https://orcid.org/0000-0003-2506-6041),
- [S. J. McSweeney](#) ORCID: [orcid.org/0000-0001-6114-7469¹](https://orcid.org/0000-0001-6114-7469),
- [T. N. O'Doherty](#) ORCID: [orcid.org/0000-0001-9258-1508¹](https://orcid.org/0000-0001-9258-1508),
- [P. J. Hancock](#) ORCID: [orcid.org/0000-0002-4203-2946¹](https://orcid.org/0000-0002-4203-2946),
- [J. S. Morgan](#) ORCID: [orcid.org/0000-0001-9224-5483¹](https://orcid.org/0000-0001-9224-5483),
- [G. E. Anderson](#) ORCID: [orcid.org/0000-0001-6544-8007¹](https://orcid.org/0000-0001-6544-8007),
- [G. H. Heald](#) ORCID: [orcid.org/0000-0002-2155-6054²](https://orcid.org/0000-0002-2155-6054) &
- [T. J. Galvin](#) ORCID: [orcid.org/0000-0002-2801-766X¹](https://orcid.org/0000-0002-2801-766X)

[Nature](#) volume **601**, pages 526–530 (2022)

- 3882 Accesses
- 2089 Altmetric
- [Metrics details](#)

Subjects

- [Astrophysical magnetic fields](#)
- [Compact astrophysical objects](#)
- [High-energy astrophysics](#)
- [Time-domain astronomy](#)
- [Transient astrophysical phenomena](#)

Abstract

The high-frequency radio sky is bursting with synchrotron transients from massive stellar explosions and accretion events, but the low-frequency radio sky has, so far, been quiet beyond the Galactic pulsar population and the long-term scintillation of active galactic nuclei. The low-frequency band, however, is sensitive to exotic coherent and polarized radio-emission processes, such as electron-cyclotron maser emission from flaring M dwarfs¹, stellar magnetospheric plasma interactions with exoplanets² and a population of steep-spectrum pulsars³, making Galactic-plane searches a prospect for blind-transient discovery. Here we report an analysis of archival low-frequency radio data that reveals a periodic, low-frequency radio transient. We find that the source pulses every 18.18 min, an unusual periodicity that has, to our knowledge, not been observed previously. The emission is highly linearly polarized, bright, persists for 30–60 s on each occurrence and is visible across a broad frequency range. At times, the pulses comprise short-duration (<0.5 s) bursts; at others, a smoother profile is observed. These profiles evolve on timescales of hours. By measuring the dispersion of the radio pulses with respect to frequency, we have localized the source to within our own Galaxy and suggest that it could be an ultra-long-period magnetar.

This is a preview of subscription content

Access options

Subscribe to nature+

Get immediate online access to the entire Nature family of 50+ journals

\$29.99

monthly

[Subscribe](#)

Subscribe to Journal

Get full journal access for 1 year

\$199.00

only \$3.90 per issue

[Subscribe](#)

All prices are NET prices.

VAT will be added later in the checkout.

Tax calculation will be finalised during checkout.

Buy article

Get time limited or full article access on ReadCube.

\$32.00

[Buy](#)

All prices are NET prices.

Additional access options:

- [Log in](#)
- [Learn about institutional subscriptions](#)

Fig. 1: Sixty-four of the 71 detected pulses of GLEAM-X J162759.5-523504.3 aligned to its measured period P and period derivative \dot{P} .

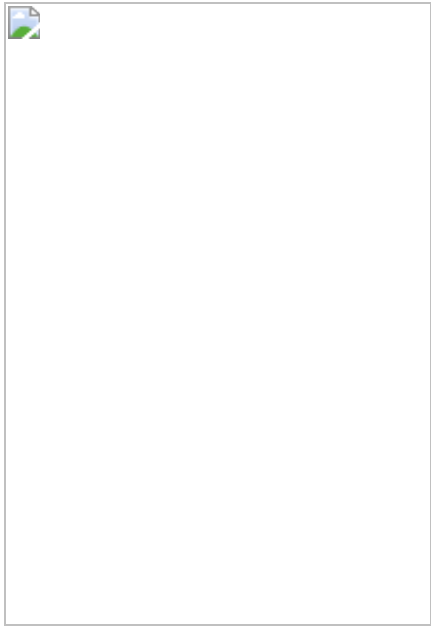


Fig. 2: Maximum brightness of each pulse and total pulse fluence as a function of time across the two observed intervals of activity.



Fig. 3: Dynamic spectrum of the observation recorded at 03:59 on 10 January 2018.

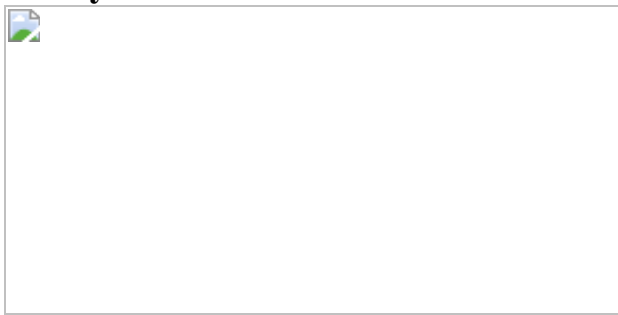
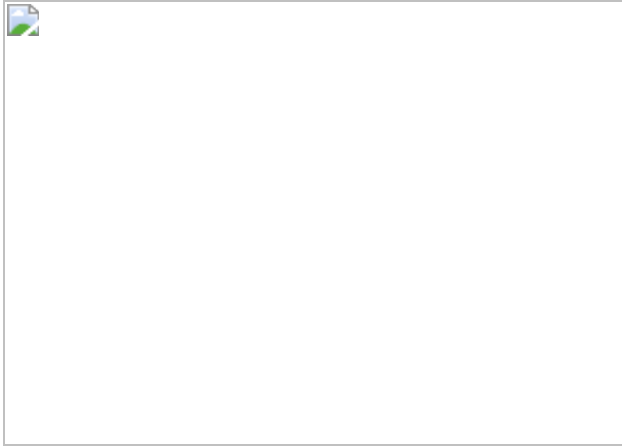


Fig. 4: Transient parameter space populated with common known radio transients.



Data availability

Data that support this paper are available at the following public repository: https://github.com/nhurleywalker/GLEAM-X_Periodic_Transient. Further data products can be supplied by the authors on reasonable request.

Code availability

Code that supports this paper is available at the following public repository: https://github.com/nhurleywalker/GLEAM-X_Periodic_Transient. Figure 3 was generated using https://github.com/nhurleywalker/Transient_Phase_Space. Further code can be supplied by the authors on reasonable request.

References

1. 1.

Lynch, C. R., Lenc, E., Kaplan, D. L., Murphy, T. & Anderson, G. E. 154 MHz detection of faint, polarized flares from UV Ceti. *Astrophys. J. Lett.* **836**, L30 (2017).

2. 2.

Vedantham, H. K. et al. Coherent radio emission from a quiescent red dwarf indicative of star–planet interaction. *Nat. Astron.* **4**, 577–583 (2020).

3. 3.

Swainston, N. A. et al. Discovery of a steep-spectrum low-luminosity pulsar with the Murchison Widefield Array. *Astrophys. J. Lett.* **911**, L26 (2021).

4. 4.

Yao, J. M., Manchester, R. N. & Wang, N. A new electron-density model for estimation of pulsar and FRB distances. *Astrophys. J.* **835**, 29 (2017).

5. 5.

Hutschenreuter, S. & Enßlin, T. A. The Galactic Faraday depth sky revisited. *Astron. Astrophys.* **633**, A150 (2020).

6. 6.

Vedantham, H. K. et al. Symmetric achromatic variability in active galaxies: a powerful new gravitational lensing probe? *Astrophys. J.* **845**, 89 (2017).

7. 7.

Bannister, K. W. et al. Real-time detection of an extreme scattering event: constraints on Galactic plasma lenses. *Science* **351**, 354–356 (2016).

8. 8.

Benz, A. O. & Güdel, M. Physical processes in magnetically driven flares on the Sun, stars, and young stellar objects. *Annu. Rev. Astron. Astrophys.* **48**, 241–287 (2010).

9. 9.

Zarka, P., Treumann, R. A., Ryabov, B. P. & Ryabov, V. B. Magnetically-driven planetary radio emissions and application to extrasolar planets. *Astrophys. Space Sci.* **277**, 293–300 (2001).

10. 10.

Marsh, T. R. et al. A radio-pulsing white dwarf binary star. *Nature* **537**, 374–377 (2016).

11. 11.

Hyman, S. D. et al. A powerful bursting radio source towards the Galactic Centre. *Nature* **434**, 50–52 (2005).

12. 12.

Szary, A., Zhang, B., Melikidze, G. I., Gil, J. & Xu, R.-X. Radio efficiency of pulsars. *Astrophys. J.* **784**, 59 (2014).

13. 13.

Levin, L. et al. Radio emission evolution, polarimetry and multifrequency single pulse analysis of the radio magnetar PSR J1622–4950. *Mon. Not. R. Astron. Soc.* **422**, 2489–2500 (2012).

14. 14.

Rea, N., Pons, J. A., Torres, D. F. & Turolla, R. The fundamental plane for radio magnetars. *Astrophys. J. Lett.* **748**, L12 (2012).

15. 15.

Olausen, S. A. & Kaspi, V. M. The McGill magnetar catalog. *Astrophys. J. Suppl.* **212**, 6 (2014).

16. 16.

Carbone, D. et al. New methods to constrain the radio transient rate: results from a survey of four fields with LOFAR. *Mon. Not. R. Astron. Soc.* **459**, 3161–3174 (2016).

17. 17.

Polisensky, E. et al. Exploring the transient radio sky with VLITE: early results. *Astrophys. J.* **832**, 60 (2016).

18. 18.

Stewart, A. J. et al. LOFAR MSSS: detection of a low-frequency radio transient in 400 h of monitoring of the North Celestial Pole. *Mon. Not. R. Astron. Soc.* **456**, 2321–2342 (2016).

19. 19.

Bell, M. E. et al. The Murchison Widefield Array Transients Survey (MWATS). A search for low-frequency variability in a bright Southern Hemisphere sample. *Mon. Not. R. Astron. Soc.* **482**, 2484–2501 (2019).

20. 20.

Hajela, A., Mooley, K. P., Intema, H. T. & Frail, D. A. A GMRT 150 MHz search for variables and transients in Stripe 82. *Mon. Not. R. Astron. Soc.* **490**, 4898–4906 (2019).

21. 21.

Keith, M. J. et al. The High Time Resolution Universe Pulsar Survey – I. System configuration and initial discoveries. *Mon. Not. R. Astron. Soc.* **409**, 619–627 (2010).

22. 22.

Cameron, A. D., Barr, E. D., Champion, D. J., Kramer, M. & Zhu, W. W. An investigation of pulsar searching techniques with the fast folding algorithm. *Mon. Not. R. Astron. Soc.* **468**, 1994–2010 (2017).

23. 23.

Hurley-Walker, N. et al. Galactic and Extragalactic All-sky Murchison Widefield Array (GLEAM) survey – I. A low-frequency extragalactic catalogue. *Mon. Not. R. Astron. Soc.* **464**, 1146–1167 (2017).

24. 24.

Pietka, M., Fender, R. P. & Keane, E. F. The variability time-scales and brightness temperatures of radio flares from stars to supermassive black holes. *Mon. Not. R. Astron. Soc.* **446**, 3687–3696 (2015).

25. 25.

Tingay, S. J. et al. The Murchison Widefield Array: the square kilometre array precursor at low radio frequencies. *Publ. Astron. Soc. Aust.* **30**, e007 (2013).

26. 26.

Wayth, R. B. et al. The Phase II Murchison Widefield Array: design overview. *Publ. Astron. Soc. Aust.* **35**, e033 (2018).

27. 27.

Wayth, R. B. et al. GLEAM: the Galactic and Extragalactic All-Sky MWA survey. *Publ. Astron. Soc. Aust.* **32**, e025 (2015).

28. 28.

Offringa, A. R. et al. Parametrizing Epoch of Reionization foregrounds: a deep survey of low-frequency point-source spectra with the Murchison Widefield Array. *Mon. Not. R. Astron. Soc.* **458**, 1057–1070 (2016).

29. 29.

Hurley-Walker, N. et al. Galactic and Extragalactic All-sky Murchison Widefield Array (GLEAM) survey II: galactic plane $345^\circ < l < 67^\circ$,

$180^\circ < l < 240^\circ$. *Publ. Astron. Soc. Aust.* **36**, e047 (2019).

30. 30.

Offringa, A. R. et al. WSCLEAN: an implementation of a fast, generic wide-field imager for radio astronomy. *Mon. Not. R. Astron. Soc.* **444**, 606–619 (2014).

31. 31.

Sutinjo, A. et al. Understanding instrumental Stokes leakage in Murchison Widefield Array polarimetry. *Radio Sci.* **50**, 52–65 (2015).

32. 32.

Lenc, E. et al. The challenges of low-frequency radio polarimetry: lessons from the Murchison Widefield Array. *Publ. Astron. Soc. Aust.* **34**, e040 (2017).

33. 33.

Riseley, C. J. et al. The Polarised GLEAM Survey (POGS) I: first results from a low-frequency radio linear polarisation survey of the southern sky. *Publ. Astron. Soc. Aust.* **35**, e043 (2018).

34. 34.

Riseley, C. J. et al. The Polarised GLEAM Survey (POGS) II: results from an all-sky rotation measure synthesis survey at long wavelengths. *Publ. Astron. Soc. Aust.* **37**, e029 (2020).

35. 35.

Brentjens, M. A. & De Bruyn, A. Faraday rotation measure synthesis. *Astron. Astrophys.* **441**, 1217–1228 (2005).

36. 36.

Lafler, J. & Kinman, T. D. An RR Lyrae star survey with Ihe Lick 20-INCH Astrograph II. The calculation of RR Lyrae periods by electronic computer. *Astrophys. J. Suppl.* **11**, 216 (1965).

37. 37.

Stellingwerf, R. F. Period determination using phase dispersion minimization. *Astrophys. J.* **224**, 953–960 (1978).

38. 38.

Schwarzenberg-Czerny, A. Fast and statistically optimal period search in uneven sampled observations. *Astrophys. J. Lett.* **460**, L107 (1996).

39. 39.

Clarke, D. String/Rope length methods using the Lafler-Kinman statistic. *Astron. Astrophys.* **386**, 763–774 (2002).

40. 40.

Manchester, R. N., Hobbs, G. B., Teoh, A. & Hobbs, M. The Australia Telescope National Facility Pulsar Catalogue. *Astron. J* **129**, 1993–2006 (2005).

41. 41.

Hurley-Walker, N. & Hancock, P. J. De-distorting ionospheric effects in the image plane. *Astron. Comput.* **25**, 94–102 (2018).

42. 42.

Gehrels, N. et al. The Swift gamma-ray burst mission. *Astrophys. J.* **611**, 1005–1020 (2004).

43. 43.

Burrows, D. N. et al. The Swift X-ray telescope. *Space Sci. Rev.* **120**, 165–195 (2005).

44. 44.

NASA High Energy Astrophysics Science Archive Research Center (HEASARC). HEAsoft: Unified Release of FTOOLS and XANADU (2014).

45. 45.

Champion, D. et al. High-cadence observations and variable spin behaviour of magnetar Swift J1818.0–1607 after its outburst. *Mon. Not. R. Astron. Soc.* **498**, 6044–6056 (2020).

46. 46.

Lorimer, D. R. & Kramer, M. *Handbook of Pulsar Astronomy* (Cambridge Univ. Press, 2012).

47. 47.

Zhang, B., Harding, A. K. & Muslimov, A. G. Radio pulsar death line revisited: is PSR J2144–3933 anomalous? *Astrophys. J. Lett.* **531**, L135–L138 (2000).

Acknowledgements

N.H.-W. is the recipient of an Australian Research Council Future Fellowship (project number FT190100231) and G.E.A. is the recipient of an Australian Research Council Discovery Early Career Researcher Award (project number DE180100346) funded by the Australian Government. This scientific work makes use of the Murchison Radio-astronomy Observatory, operated by CSIRO. We acknowledge the Wajarri Yamatji people as the traditional owners of the observatory site. Support for the operation of the Murchison Widefield Array is provided by the Australian Government (NCRIS), under a contract to Curtin University administered by Astronomy Australia Limited. We acknowledge the Pawsey Supercomputing Centre, which is supported by the Western Australian Government and the Australian Government. The National Radio Astronomy Observatory is a

facility of the National Science Foundation operated under cooperative agreement by Associated Universities, Inc. This project was supported by resources and expertise provided by CSIRO IMT Scientific Computing. This work used resources of China SKA Regional Centre prototype funded by the National Key R&D Programme of China (2018YFA0404603) and Chinese Academy of Sciences (114231KYSB20170003).

Author information

Affiliations

1. International Centre for Radio Astronomy Research (ICRAR), Curtin University, Bentley, Western Australia, Australia
N. Hurley-Walker, A. Bahramian, S. J. McSweeney, T. N. O'Doherty, P. J. Hancock, J. S. Morgan, G. E. Anderson & T. J. Galvin
2. CSIRO, Space and Astronomy, Bentley, Western Australia, Australia
X. Zhang & G. H. Heald
3. Shanghai Astronomical Observatory, Chinese Academy of Sciences, Shanghai, China
X. Zhang

Contributions

N.H.-W. calibrated and processed the data for the observations described herein, determined the position and flux density of the source and prepared the manuscript, with contributions from all co-authors. X.Z. processed all polarization data, including performing polarization calibration and analysis. A.B. and S.J.M. performed the analysis to derive the period and period derivative. A.B. performed the X-ray observations and analysis. S.J.M. calculated and applied the dispersion measure and barycentric corrections. T.N.O. developed the original detection methodology, performed the original archive search and made the initial discovery. P.J.H.

helped to develop the detection methodology and provided supercomputing support. G.E.A. contributed to astrophysical calculations and interpretation of the data. T.J.G., G.H.H., J.S.M. and X.Z. determined polarization calibration methods. T.J.G. performed early refinement of the period estimate.

Corresponding author

Correspondence to [N. Hurley-Walker](#).

Ethics declarations

Competing interests

The authors declare no competing interests.

Peer review information

Nature thanks the anonymous reviewers for their contribution to the peer review of this work. Peer reviewer reports are available.

Additional information

Publisher's note Springer Nature remains neutral with regard to jurisdictional claims in published maps and institutional affiliations.

Extended data figures and tables

[Extended Data Fig. 1 Dynamic spectra of the observations used to calculate the dispersion measure.](#)

From top to bottom, separated by horizontal black lines, we show the observations 1205008192 (72–103 MHz), 1205007112 (103–134 MHz), 1205011432 (139–170 MHz), 1205010352 (170–200 MHz) and 1205009272 (200–231 MHz). These observations were taken on 13 March

2018 between 20:12 and 21:24 (see Fig. 1). The left panel shows the data aligned using a period of 1091.1690 s, whereas the right panel shows the same, including a dispersion correction of 57 pc cm^{-3} . Strong ionospheric scintillation is visible in the 72–103-MHz data, causing ripples in the brightness of the source over time.

Extended Data Fig. 2 The explored search space in P and \dot{P} for the pulses recorded from GLEAM-X J162759.5-523504.3.

The contours show the peak flux density of the mean profile at 154 MHz recovered at each combination of P (y axis) and \dot{P} (x axis), in levels of 15, 14, 13, 12 and 11 Jy. The best-fit values of $P = 1,091.1690 \text{ s}$ and $\dot{P} = 6 \times 10^{-10} \text{ s}^{-1}$ are marked with a dark red ‘+’.

Extended Data Fig. 3 The flux density of GLEAM-X J162759.5-523504.3 as a function of frequency.

This is derived from the same observations shown in Extended Data Fig. 1. Points are determined via an average of the source profile in each frequency bin, weighting by the signal-to-noise ratio of the frequency-averaged profile. A power-law fit using the data spanning 95–195 MHz is shown in blue, with $\alpha = -1.16 \pm 0.04$.

Extended Data Fig. 4 X-ray luminosity and spectral properties of magnetars compared with the X-ray luminosity limits of GLEAM-X J162759.5-523504.3.

The two faintest known magnetars are labelled. The coloured contours represent expected Swift XRT count rates for putative X-ray luminosities and blackbody temperatures for a source at 1.3 kpc, assuming a hydrogen column density of $N_{\text{H}} \approx 2 \times 10^{21} \text{ cm}^{-2}$. The grey dashed line represents the implied luminosity upper limit for GLEAM-X J162759.5-523504.3 based on the $3 - \sigma$ upper limit obtained from the Swift XRT observation. From the

magnetar fundamental plane, we predict GLEAM-X J162759.5-523504.3 to have a quiescent luminosity 4.5 orders of magnitude lower than our limit from the Swift XRT.

Extended Data Fig. 5 Pulse profiles for the three detections on 3 January 2018 compared with a wide pulse detected on 14 March 2018.

Barycentric corrections and dedispersion have been applied. The data are all taken at the same frequency, 170–200 MHz. Vertical dashed lines encapsulating the profile found on 13 March 2018 are overplotted to guide the eye.

Extended Data Fig. 6 Images in full Stokes and polarized intensity (in Jy beam^{-1}), and RM (in rad m^{-2}), of the region $5^\circ \times 5^\circ$ around GLEAM-X J162759.5-523504.3.

The images were made using observation 1200354592 on 18 January 2018 at 23:49, using only the interval where the source was producing emission. Faraday rotation over the imaged bandwidth of 30 MHz causes the Stokes Q, U and V emission to average to zero. The polarized intensity shows the maximum value of the RM spectrum. Where the polarized intensity is less than seven times the local noise, the corresponding RM value has been masked.

Extended Data Fig. 7 A scatter plot of period derivative \dot{P} against period P .

GLEAM-X J162759.5-523504.3 is shown as a blue arrow with an upper limit on \dot{P} (see [Methods](#)) in context with the known pulsars⁴⁰ (black dots), X-ray-detected magnetars¹⁵ (red dots and arrows) and magnetars known to emit in both X-ray and radio frequencies (red circles around black dots). The slowest (and radio-quiet) X-ray magnetar 1E 161348–5055 is also shown with an upper limit on \dot{P} . The green

dashed and dot-dashed lines correspond to the theoretical ‘death lines’ for pulsar radio emission for cases I and III calculated by Zhang et al.^{[47](#)}.

Rights and permissions

[Reprints and Permissions](#)

About this article

Cite this article

Hurley-Walker, N., Zhang, X., Bahramian, A. *et al.* A radio transient with unusually slow periodic emission. *Nature* **601**, 526–530 (2022).
<https://doi.org/10.1038/s41586-021-04272-x>

- Received: 30 July 2021
- Accepted: 19 November 2021
- Published: 26 January 2022
- Issue Date: 27 January 2022
- DOI: <https://doi.org/10.1038/s41586-021-04272-x>

Share this article

Anyone you share the following link with will be able to read this content:

[Get shareable link](#)

Sorry, a shareable link is not currently available for this article.

[Copy to clipboard](#)

Provided by the Springer Nature SharedIt content-sharing initiative

This article was downloaded by **calibre** from <https://www.nature.com/articles/s41586-021-04272-x>

| [Section menu](#) | [Main menu](#) |

- Article
- Open Access
- [Published: 30 November 2021](#)

Time-crystalline eigenstate order on a quantum processor

- [Xiao Mi](#) [ORCID: orcid.org/0000-0003-0507-0211¹](#),
¹[na1](#),
- [Matteo Ippoliti²](#),
²[na1](#),
- [Chris Quintana¹](#),
- [Ami Greene¹](#),
- [Zijun Chen¹](#),
- [Jonathan Gross¹](#),
- [Frank Arute¹](#),
- [Kunal Arya¹](#),
- [Juan Atalaya¹](#),
- [Ryan Babbush¹](#),
- [Joseph C. Bardin](#) [ORCID: orcid.org/0000-0002-6523-6730^{1,3}](#),
- [Joao Basso](#) [ORCID: orcid.org/0000-0001-5547-691X¹](#),
- [Andreas Bengtsson¹](#),
- [Alexander Bilmes¹](#),
- [Alexandre Bourassa^{1,4}](#),
- [Leon Brill¹](#),
- [Michael Broughton¹](#),
- [Bob B. Buckley¹](#),
- [David A. Buell¹](#),
- [Brian Burkett](#) [ORCID: orcid.org/0000-0001-8474-6317¹](#),
- [Nicholas Bushnell¹](#),
- [Benjamin Chiaro¹](#),
- [Roberto Collins¹](#),
- [William Courtney¹](#),
- [Dripto Debroy¹](#),
- [Sean Demura](#) [ORCID: orcid.org/0000-0003-3727-7380¹](#),
- [Alan R. Derk¹](#),
- [Andrew Dunsworth¹](#),

- [Daniel Eppens](#) [ORCID: orcid.org/0000-0001-7134-5733¹](#),
- [Catherine Erickson¹](#),
- [Edward Farhi¹](#),
- [Austin G. Fowler¹](#),
- [Brooks Foxen¹](#),
- [Craig Gidney¹](#),
- [Marissa Giustina¹](#),
- [Matthew P. Harrigan](#) [ORCID: orcid.org/0000-0001-9412-0553¹](#),
- [Sean D. Harrington](#) [ORCID: orcid.org/0000-0003-0521-8378¹](#),
- [Jeremy Hilton¹](#),
- [Alan Ho¹](#),
- [Sabrina Hong¹](#),
- [Trent Huang¹](#),
- [Ashley Huff¹](#),
- [William J. Huggins](#) [ORCID: orcid.org/0000-0003-2735-1380¹](#),
- [L. B. Ioffe¹](#),
- [Sergei V. Isakov¹](#),
- [Justin Iveland¹](#),
- [Evan Jeffrey¹](#),
- [Zhang Jiang¹](#),
- [Cody Jones¹](#),
- [Dvir Kafri¹](#),
- [Tanuj Khattar¹](#),
- [Seon Kim¹](#),
- [Alexei Kitaev¹](#),
- [Paul V. Klimov¹](#),
- [Alexander N. Korotkov^{1,5}](#),
- [Fedor Kostritsa¹](#),
- [David Landhuis](#) [ORCID: orcid.org/0000-0001-9804-2185¹](#),
- [Pavel Laptev¹](#),
- [Joonho Lee^{1,6}](#),
- [Kenny Lee¹](#),
- [Aditya Locharla¹](#),
- [Erik Lucero¹](#),
- [Orion Martin¹](#),
- [Jarrod R. McClean](#) [ORCID: orcid.org/0000-0002-2809-0509¹](#),
- [Trevor McCourt¹](#),
- [Matt McEwen](#) [ORCID: orcid.org/0000-0002-9544-141X^{1,7}](#),
- [Kevin C. Miao¹](#),

- [Masoud Mohseni](#)¹,
- [Shirin Montazeri](#) [ORCID: orcid.org/0000-0002-7124-4585](#)¹,
- [Wojciech Mruczkiewicz](#) [ORCID: orcid.org/0000-0002-8497-6363](#)¹,
- [Ofer Naaman](#) [ORCID: orcid.org/0000-0002-7760-9186](#)¹,
- [Matthew Neeley](#) [ORCID: orcid.org/0000-0002-5548-0051](#)¹,
- [Charles Neill](#) [ORCID: orcid.org/0000-0001-8509-9836](#)¹,
- [Michael Newman](#)¹,
- [Murphy Yuezhen Niu](#)¹,
- [Thomas E. O'Brien](#)¹,
- [Alex Opremcak](#)¹,
- [Eric Ostby](#)¹,
- [Balint Pato](#)¹,
- [Andre Petukhov](#)¹,
- [Nicholas C. Rubin](#)¹,
- [Daniel Sank](#)¹,
- [Kevin J. Satzinger](#) [ORCID: orcid.org/0000-0001-5865-0813](#)¹,
- [Vladimir Shvarts](#)¹,
- [Yuan Su](#)¹,
- [Doug Strain](#)¹,
- [Marco Szalay](#)¹,
- [Matthew D. Trevithick](#)¹,
- [Benjamin Villalonga](#)¹,
- [Theodore White](#)¹,
- [Z. Jamie Yao](#)¹,
- [Ping Yeh](#) [ORCID: orcid.org/0000-0003-0837-1028](#)¹,
- [Juhwan Yoo](#)¹,
- [Adam Zalcman](#) [ORCID: orcid.org/0000-0002-2585-2424](#)¹,
- [Hartmut Neven](#)¹,
- [Sergio Boixo](#) [ORCID: orcid.org/0000-0002-1090-7584](#)¹,
- [Vadim Smelyanskiy](#)¹,
- [Anthony Megrant](#) [ORCID: orcid.org/0000-0002-6371-6140](#)¹,
- [Julian Kelly](#) [ORCID: orcid.org/0000-0002-2596-2121](#)¹,
- [Yu Chen](#)¹,
- [S. L. Sondhi](#)^{8,9},
- [Roderich Moessner](#)¹⁰,
- [Kostyantyn Kechedzhi](#)¹,
- [Vedika Khemani](#) [ORCID: orcid.org/0000-0003-2653-0555](#)² &
- [Pedram Roushan](#) ¹

Nature volume 601, pages 531–536 (2022)

- 50k Accesses
- 2 Citations
- 637 Altmetric
- [Metrics details](#)

Subjects

- [Phase transitions and critical phenomena](#)
- [Quantum information](#)
- [Quantum simulation](#)
- [Statistical physics](#)

Abstract

Quantum many-body systems display rich phase structure in their low-temperature equilibrium states¹. However, much of nature is not in thermal equilibrium. Remarkably, it was recently predicted that out-of-equilibrium systems can exhibit novel dynamical phases^{2,3,4,5,6,7,8} that may otherwise be forbidden by equilibrium thermodynamics, a paradigmatic example being the discrete time crystal (DTC)^{7,9,10,11,12,13,14,15}. Concretely, dynamical phases can be defined in periodically driven many-body-localized (MBL) systems via the concept of eigenstate order^{7,16,17}. In eigenstate-ordered MBL phases, the entire many-body spectrum exhibits quantum correlations and long-range order, with characteristic signatures in late-time dynamics from all initial states. It is, however, challenging to experimentally distinguish such stable phases from transient phenomena, or from regimes in which the dynamics of a few select states can mask typical behaviour. Here we implement tunable controlled-phase (CPHASE) gates on an array of superconducting qubits to experimentally observe an MBL-DTC and demonstrate its characteristic spatiotemporal response for generic initial states^{7,9,10}. Our work employs a time-reversal protocol to quantify the impact of external decoherence, and leverages quantum typicality to circumvent the exponential cost of densely sampling the eigenspectrum. Furthermore, we locate the phase transition out of the DTC with an experimental finite-size analysis. These results establish a scalable approach to studying non-equilibrium phases of matter on quantum processors.

[Download PDF](#)

Main

In an equilibrium setting, quantum phases of matter are classified by long-range order or broken symmetries in low-temperature states (Fig. 1a). The existence of ordered phases in periodically driven (Floquet) systems, on the other hand, is counterintuitive: as energy is not conserved, one expects thermalization to a featureless maximum-entropy state that is incompatible with quantum order. However, this heat death is averted in the presence of many-body localization, where strong disorder causes the emergence of an extensive number of local conservation laws that prevent thermalization^{18,19,20,21,22,23}, making it possible to stabilize intrinsically dynamical phases⁷.

Fig. 1: Order in eigenstates.

 figure 1

a, Equilibrium phases are characterized by long-range order in low-energy eigenstates of time-independent Hamiltonians (for example, an Ising ferromagnet with a pair of degenerate ground states that resemble ‘Schrödinger cats’ of polarized states). **b**, Thermalizing Floquet systems typically have no ordered states in the spectrum. **c**, In MBL Floquet systems, every eigenstate can show order. In MBL-DTC, every eigenstate resembles a long-range ordered ‘Schrödinger cat’ of a random configuration of spins and its inversion, with even/odd superpositions split by π .

Dynamics in a Floquet system is governed by a unitary time evolution operator, whose eigenvalues lie on the unit circle. While the entire Floquet spectrum is featureless in a thermalizing phase (Fig. 1b), an MBL Floquet phase can have an order parameter associated with each eigenstate. As an example, in the spatiotemporally ordered MBL-DTC, the spectrum has a distinctive pattern of pairing between long-range ordered ‘Schrödinger cat’ eigenstates whose eigenvalues are separated by an angle π (refs. 7,9,10; Fig. 1c). This pairing manifests as a stable subharmonic response, wherein local observables show period-doubled oscillations that spontaneously break the discrete time translation symmetry of the drive for infinitely long times. The unique

combination of spatial long-range order and time translation symmetry breaking in an isolated dissipation-free quantum many-body system is the hallmark of the MBL-DTC.

Experimentally observing a non-equilibrium phase such as the MBL-DTC is a challenge owing to limited programmability, coherence and size of noisy intermediate-scale quantum hardware. Subharmonic response, by itself, is not a unique attribute of the MBL-DTC; rather, it is a feature of many dynamical phenomena whose study has a rich history²⁴ (also Ch. 8 in ref. 12). Most recently, interesting DTC-like dynamical signatures have been observed in a range of quantum platforms from trapped ions²⁵ to nitrogen vacancy centres²⁶ to NMR spins^{27,28}. However, each of these platforms lacks one or more necessary conditions for stabilizing an MBL-DTC^{12,29}, either owing to an absence of the requisite type of disorder^{25,27} or owing to the interactions being too long ranged^{26,27,28}. The observed signatures, instead, have been shown to arise from slow thermalization^{26,30}, effectively mean-field dynamics²⁸, or prethermal dynamics from special initial states^{12,29,31,32}, and are separated from the MBL-DTC by a spectral phase transition where eigenstate order disappears. Thus, despite the recent progress, observing an MBL-DTC remains an outstanding challenge^{12,29}.

Here we perform the following necessary benchmarks for experimentally establishing an eigenstate-ordered non-equilibrium phase of matter: drive parameters are varied to demonstrate stability of the phase in an extended parameter region and across disorder realizations; the limitations of finite size and finite coherence time are addressed, respectively, by varying system size and verifying that any decay of the subharmonic response is consistent with purely extrinsic decoherence assessed in an independent experiment; the existence of spatiotemporal order across the entire spectrum is established. The flexibility of our quantum processor, combined with the scalable experimental protocols devised in the following, allows us to fulfil these criteria and observe an MBL-DTC.

The experiment is conducted on an open-ended, linear chain of $\langle L=20 \rangle$ superconducting transmon qubits ($\langle \{Q\}_1 \rangle$ to $\langle \{Q\}_{20} \rangle$) that are isolated from a two-dimensional grid. We drive the qubits via a time-periodic (Floquet) circuit $\langle \{\hat{U}\}_\text{rm{F}} \rangle$ with $\langle t \rangle$ identical cycles (Fig. 2a) of $\langle \{\hat{U}\}_\text{rm{F}} \rangle$:

$$\begin{aligned} \$\$ \langle \hat{U} \rangle_\text{rm{F}} = & \mathop{\text{underbrace}}\nolimits\{\langle \text{rm{e}} \rangle\}^{\langle -\frac{i}{2} \sum_i \langle h_i \rangle \langle \hat{Z}_i \rangle \rangle} \limits_{\langle \text{rm{longitudinal}} \rangle}, \\ & \langle \text{rm{fields}} \rangle, \mathop{\text{underbrace}}\nolimits\{\langle \text{rm{e}} \rangle\}^{\langle -\frac{i}{4} \sum_i \langle \varphi_i \rangle \langle \hat{Z}_i \rangle \langle \hat{Z}_{i+1} \rangle \rangle} \limits_{\langle \text{rm{Ising}} \rangle}, \\ & \langle \text{rm{interaction}} \rangle, \mathop{\text{underbrace}}\nolimits\{\langle \text{rm{e}} \rangle\}^{\langle -\frac{i}{2} \langle \pi \rangle \rangle} \end{aligned}$$

```

}}\g\sum _{i}\{\hat{X}\}_{i}\}}}\limits_{x,\{\rm rotation\},\{\rm by\},\{\rm pi\}}\}g}$$
(1)

```

where $\{\hat{X}\}_i$ and $\{\hat{Z}\}_i$ are Pauli operators. Each angle $\{\varphi_i\}$ is sampled randomly from $[-1.5\pi, -0.5\pi]$ for every realization of the circuit. Overall, $\{\hat{U}\}_{\rm F}$ implements an interacting Ising model that is periodically ‘kicked’ by a transverse pulse that rotates all qubits by $\{g\}$ about the x axis. In this work, $\{g\}$ is tuned within the range $[0.5, 1.0]$ to explore the DTC phase and its transition into a thermal phase. At $\{g=1\}$, the model implements a $\{\pi\}$ pulse that exactly flips all qubits (in the z basis) and returns them to the initial state over two periods. A key signature of the DTC is the presence of robust period doubling, (that is, extending over a finite extent in parameter space, even as $\{g\}$ is tuned away from $\{1\}$, and for all initial states). Strong Ising interactions, which produce long-range spatial order, are essential for this robustness^{7,10}. This is in contrast to a system of decoupled qubits ($\{\varphi=0\}$) that rotate by a continuously varying angle $\{\pi g\}$ every period instead of being locked at period doubling. Prior theoretical work²⁹ has shown that model (1) is expected to exhibit a transition to a thermal phase at a critical value $\{g_c\} \approx 0.84$.

Fig. 2: Observing an MBL-DTC.



a, The experimental circuit composed of $\backslash(t\backslash)$ identical cycles of the unitary $\langle\langle\langle\hat{U}\rangle\rangle\rangle_{\langle\langle\langle F\rangle\rangle\rangle}$. The local polarization of each qubit, $\langle\langle\langle\hat{Z}(t)\rangle\rangle\rangle$, is measured at the end. In the following panels, we investigate a number of disorder instances each with a different random bit-string initial state. **b**, Experimental values

of $\langle \hat{Z}(t) \rangle$ measured at Q_{11} . Data are shown for five representative circuit instances deep in the thermal ($g = 0.60$; left) and MBL-DTC ($g = 0.97$; right) phases. **c**, Autocorrelator $\langle \bar{A} \rangle = \overline{\langle \hat{Z}(0) \hat{Z}(t) \rangle}$ at Q_{11} , obtained from averaging the results of 36 circuit instances. For the same circuit instances, the average autocorrelator at the output of $\langle \langle \hat{U} \rangle \rangle \langle \langle \text{rm}\{\text{ECHO}\} \rangle \rangle = \langle \langle \hat{U} \rangle \rangle \langle \langle \text{rm}\{F\} \rangle \rangle^{\dagger} \langle \langle t \rangle \rangle \langle \langle \hat{U} \rangle \rangle \langle \langle \text{rm}\{F\} \rangle \rangle^{\dagger} \langle \langle t \rangle \rangle$ is also measured and its square root, $\langle \langle \bar{A} \rangle \rangle_0$, is shown alongside $\langle \langle \bar{A} \rangle \rangle$ for comparison. The left (right) panels correspond to $g = 0.60$ (0.97). **d**, Top panels: the ratio $\langle \langle \bar{A} / \langle \langle \bar{A} \rangle \rangle_0 \rangle \rangle$ obtained from **c**. Bottom panels: $\langle \langle \bar{A} / \langle \langle \bar{A} \rangle \rangle_0 \rangle \rangle$ as a function of t and qubit location. The left (right) panels correspond to $g = 0.60$ (0.97).

Achieving MBL in this model for $(g \sim 1)$ requires disorder in the two-qubit interaction, $\langle \langle \varphi_i \rangle \rangle$, which is even under Ising symmetry^{12,29}, $\langle \langle \langle \langle \text{rm}\{\pi\} \rangle \rangle \rangle \langle \langle \varphi_i \rangle \rangle \langle \langle X_i \rangle \rangle$, a condition that was not met by some past DTC experiments^{25,27}. Ising-odd terms (that is, $\langle h_i \rangle$) are approximately dynamically decoupled by the x pulses over two periods, thereby lowering their effective disorder strength and hindering localization (in the absence of independent disorder in the $\langle \langle \varphi_i \rangle \rangle$); see Appendix A in ref. 29. Utilizing continuously tunable CPHASE gates, described further in the [Supplementary Information](#), allows us to engineer strong disorder in $\langle \langle \varphi_i \rangle \rangle$ to fulfil this key requirement. Recently, a complementary approach to MBL-DTC using nuclear spins in diamond has also come into fruition³³.

We first measure the hallmark of an MBL-DTC: the persistent oscillation of local qubit polarizations $\langle \langle \hat{Z}(t) \rangle \rangle$ at a period twice that of $\langle \langle \langle \langle \hat{U} \rangle \rangle \rangle \langle \langle \text{rm}\{F\} \rangle \rangle$, irrespective of the initial state^{7,9,12,29}. This subharmonic response is probed using a collection of random bit-string states (for example, $\langle \langle \text{mathrm}\{01011...\} \rangle \rangle$), where $|0\rangle$ ($|1\rangle$) denotes a single-qubit ground (excited) state in the $|z\rangle$ basis. For each bit-string state, we generate a random instance of $\langle \langle \langle \langle \hat{U} \rangle \rangle \rangle \langle \langle \text{rm}\{F\} \rangle \rangle$, and then measure $\langle \langle \hat{Z}(t) \rangle \rangle$ every cycle. Figure 2b shows $\langle \langle \hat{Z}(t) \rangle \rangle$ in a few different instances for a qubit near the centre of the chain, $|Q_{11}\rangle$, measured with $(g=0.60)$ and $(g=0.97)$. The former is deep in the thermal phase, and indeed we observe rapid decay of $\langle \langle \hat{Z}(t) \rangle \rangle$ towards 0 within 10 cycles for each instance. In contrast, for $(g=0.97)$, $\langle \langle \hat{Z}(t) \rangle \rangle$ shows large period-doubled oscillations persisting to over 100 cycles, suggestive of an MBL-DTC phase. The disorder-averaged autocorrelator, $\langle \langle \bar{A} \rangle \rangle = \overline{\langle \langle \hat{Z}(0) \hat{Z}(t) \rangle \rangle}$, shows similar features (Fig. 2c).

We note that the data for $(g=0.97)$ are modulated by a gradually decaying envelope, which may arise from either external decoherence or slow internal thermalization^{26,30}. To establish DTC, additional measurements are needed to quantify the impact of

decoherence. This is achieved via an ‘echo’ circuit $\langle \{\hat{U}\}_{\{\rm{rm}{ECHO}\}} \rangle = \langle \{\hat{U}\}_{\{\rm{rm}{F}\}}^{\dagger} \rangle^t \langle \hat{U} \rangle_{\{\rm{rm}{F}\}}^t \rangle$ that reverses the time evolution after t steps (see Supplementary Information). Deviations of $\langle \{\hat{U}\}_{\{\rm{rm}{ECHO}\}} \rangle$ from the identity operation are purely due to decoherence, and can be quantified via decay of the autocorrelator $\langle \{A\}_0 \rangle_{\text{equiv}} \langle \langle \hat{Z} \rangle \langle \hat{U} \rangle_{\{\rm{rm}{ECHO}\}}^{\dagger} \rangle^t \langle \hat{Z} \rangle \rangle^{1/2}$ (the square root accounts for the fact that $\langle \{\hat{U}\}_{\{\rm{rm}{ECHO}\}} \rangle$ acts twice as long as $\langle \{\hat{U}\}_{\{\rm{rm}{F}\}}^{\dagger} \rangle$). Time-reversal techniques were also recently used in an investigation of DTC in NMR systems²⁷ and the study of out-of-time-ordered commutators³⁴.

Comparison between the disorder-averaged $\langle \langle \bar{A} \rangle_0 \rangle$ and $\langle \langle \bar{A} \rangle \rangle$ reveals qualitatively different behaviours in the two phases (Fig. 2c). In the thermal phase ($g=0.60$), $\langle \langle \bar{A} \rangle \rangle$ approaches 0 much more quickly than $\langle \langle \bar{A} \rangle_0 \rangle$ does, indicating that the observed decay of $\langle \langle \bar{A} \rangle \rangle$ is mostly induced by intrinsic thermalization. In the MBL-DTC phase ($g=0.97$), $\langle \langle \bar{A} \rangle_0 \rangle$ nearly coincides with the envelope of $\langle \langle \bar{A} \rangle \rangle$, suggesting that decay of the latter is primarily induced by decoherence. We also find, consistent with theoretical models (see Supplementary Section IV), that the reference signal $\langle \langle \bar{A} \rangle_0 \rangle$ may be used to normalize $\langle \langle \bar{A} \rangle \rangle$ and reveal its ideal behaviour: $\langle \langle \bar{A} / \langle \langle \bar{A} \rangle_0 \rangle \rangle$, shown in the upper panels of Fig. 2d, decays rapidly for ($g=0.60$) but retains near-maximal amplitudes for ($g=0.97$). Similar contrast between the two phases is seen in the error-mitigated autocorrelators $\langle \langle \bar{A} / \langle \langle \bar{A} \rangle_0 \rangle \rangle$ for all qubits (bottom panels of Fig. 2d). The observation of a stable noise-corrected subharmonic response is suggestive of an MBL-DTC phase.

We now demonstrate the insensitivity of the subharmonic response to the choice of initial states, a necessary consequence of eigenstate order. In contrast, various prethermal mechanisms in driven systems predict strong dependence of the thermalization rate on the initial state (for example, through its quantum numbers^{27,32} or its energy under an effective time-independent Hamiltonian $\langle \{\hat{H}\}_{\{\rm{rm}{eff}\}} \rangle$) (refs. 31,35,36) that approximately governs the dynamics for small system sizes and/or finite times). To elucidate this aspect of the MBL-DTC phase, we measure in detail the distribution of autocorrelator values over initial bit-string states.

We begin by examining the position- and disorder-averaged autocorrelator $\langle [\bar{A}] \rangle$ over three representative bit-string initial states, shown in the left panel of Fig. 3a. The square brackets indicate averaging over qubits in the chain. The three time traces are nearly indistinguishable. This behaviour is in clear contrast with a model without eigenstate order, implemented by a family of drives \langle

($\{\hat{U}\}_{\{\rm{rm}{F}\}}^{\{\text{'}\}}$) where the $\{\varphi_i\}$ angles are set to a uniform value, $\{\varphi_i\} = -0.4$). Note that this value of $\{\varphi_i\} = -0.4$ is chosen to be small enough that a leading-order high-frequency Floquet–Magnus expansion to obtain $\{\hat{H}\}_{\{\rm{rm}{eff}\}}$ is a reasonable approximation (see Supplementary Information). Without disorder in the $\{\varphi_i\}$, the drive $\{\hat{U}\}_{\{\rm{rm}{F}\}}^{\{\text{'}\}}$ is not asymptotically localized but exhibits prethermal DTC-like behaviour (see [Methods](#)). Here, $\{|\bar{A}|^l\}$ for $\{\hat{U}\}_{\{\rm{rm}{F}\}}^{\{\text{'}\}}$ (disorder averaged over random $\{h_i\}$ alone), shown in the right panel of Fig. [3a](#), reveals markedly different decay rates for the three states. The random bit-string state, in particular, decays faster than the polarized or Néel states.

Fig. 3: Distinguishing MBL-DTC from prethermal phenomena.



a, Site- and disorder-averaged autocorrelators $\{|\bar{A}|^l\}$ measured with $(g=0.94)$. In the left panel (MBL-DTC), each dataset is averaged over 24 disorder instances of $\{\varphi_i\}$ and $\{h_i\}$, with the initial state fixed at one of the following: Néel, $(|01\rangle^{\otimes 10})$; polarized, $(|0\rangle^{\otimes 20})$; random, $(|00111000010011001111\rangle)$. In the right panel (prethermal), the same values of $\{h_i\}$ and initial states are used but $\{\varphi_i\} = -0.4$. **b**, Histograms of $\{|\bar{A}|^l\}$, from 500 random bit-string initial states, averaged over cycles 30 and 31 and the same disorder instances as in **a**. The standard deviation (mean) of $\{|\bar{A}|^l\}$, $\{\sigma\}$ (μ), is also listed. Location of the polarized (Néel) state is indicated by a purple (red) arrow. Inset: same collection of $\{|\bar{A}|^l\}$ plotted over the energies of the bit-string states, calculated from the effective Hamiltonian $\{\hat{H}\}_{\{\rm{rm}{eff}\}}$ approximating the drive (see text). Dashed lines show averaged values within energy windows separated by 0.2. **c**, $\{\langle \hat{Z}(t) \rangle\}$ for two bit-string initial states that differ only at $\{Q_{11}\}$. Top panel shows a single circuit instance with disordered $\{\varphi_i\}$ and bottom panel shows an instance with uniform $\{\varphi_i\} = -0.4$. **d**, Left and middle panels: relative difference

between the two signals $\langle \langle \bar{\zeta} \rangle \rangle_{\{r\}}$ as a function of t and qubit location, averaged over time windows of 10 cycles and over 64 disorder instances for $\langle \langle \hat{U} \rangle \rangle_{\{F\}}$ and 81 instances for $\langle \langle \hat{U} \rangle \rangle_{\{F\}} \text{text}'$. Right panel: qubit dependence of $\langle \langle \bar{\zeta} \rangle \rangle_{\{r\}}$, averaged from $t=51$ to $t=60$.

A more comprehensive analysis is based on sampling the absolute values of $|\langle \bar{A} \rangle|$ for 500 random initial bit-string states (Fig. 3b). For the MBL-DTC $\langle \langle \hat{U} \rangle \rangle_{\{F\}}$, the histogram is symmetrical with a mean $\langle \mu = 0.391 \rangle$. Here the non-zero standard deviation $\langle \sigma \rangle$ probably arises from finite experimental accuracy and number of disorder instances, as analysis in the Supplementary Information shows that $|\langle \bar{A} \rangle|$ is independent of the initial state. In contrast, the $\langle \langle \hat{U} \rangle \rangle_{\{F\}}^{\text{text}'}$ model has a significantly lower mean $\langle \mu = 0.140 \rangle$. Moreover, the histogram is asymmetrical, with outliers at high $|\langle \bar{A} \rangle|$ including the polarized and Néel states (51% and 88% higher than the mean, respectively). These two states are special because they are low-temperature states that sit near the edge of the spectrum of $\langle \langle \hat{H} \rangle \rangle_{\{eff\}}$ (see Supplementary Information). Plotting the autocorrelator $\langle \langle \bar{A} \rangle \rangle$ against the energy of each bit string under $\langle \langle \hat{H} \rangle \rangle_{\{eff\}}$, in the inset of Fig. 3b, reveals a clear correlation. No such correlation is present in the MBL model.

Independent confirmation of MBL as the mechanism underlying the stability of DTC is achieved by characterizing the propagation of correlations. In MBL dynamics, local perturbations spread at most logarithmically in time²⁰, as opposed to algebraic $\langle \langle \sim t^{\alpha} \rangle \rangle$ spreading in thermalizing dynamics. We prepare two initial bit-string states differing by only a single bit flip at $\langle \langle Q_{11} \rangle \rangle$ and measure $\langle \langle \hat{Z}(t) \rangle \rangle$ for each site in both states (Fig. 3c). It can be seen that the difference in the two signals, $\langle \langle \zeta_1 \rangle \rangle$ and $\langle \langle \zeta_2 \rangle \rangle$, decays rapidly with the distance from $\langle \langle Q_{11} \rangle \rangle$ for disordered $\langle \langle \varphi_i \rangle \rangle$ and becomes undetectable at $\langle \langle Q_{14} \rangle \rangle$. On the other hand, for uniform $\langle \langle \varphi_i = -0.4 \rangle \rangle$, $\langle \langle \zeta_1 \rangle \rangle$ and $\langle \langle \zeta_2 \rangle \rangle$ have a much more pronounced difference that remains significant at $\langle \langle Q_{14} \rangle \rangle$. This difference is further elucidated by the ratio $\langle \langle \zeta_{\{r\}} \rangle \rangle = |\langle \langle \zeta_1 \rangle \rangle - \langle \langle \zeta_2 \rangle \rangle| / (\langle \langle \zeta_1 \rangle \rangle + \langle \langle \zeta_2 \rangle \rangle)$, shown in Fig. 3d. Physically, $\langle \langle \zeta_{\{r\}} \rangle \rangle$ corresponds to the relative change in local polarization as a result of the bit flip, and is inherently robust against qubit decoherence (see Supplementary Information). We observe that up to $t=100$, $\langle \langle \zeta_{\{r\}} \rangle \rangle$ remains sharply peaked around the initial perturbation $\langle \langle Q_{11} \rangle \rangle$ for disordered $\langle \langle \varphi_i \rangle \rangle$. In contrast, a propagating light cone is visible for $\langle \langle \varphi_i = -0.4 \rangle \rangle$, with the perturbation reaching all qubits across the chain as t increases. The spatial profiles of $\langle \langle \zeta_{\{r\}} \rangle \rangle$ at $t=51$ to $t=60$ (right panel of Fig. 3d) show that $\langle \langle \zeta_{\{r\}} \rangle \rangle$ is much sharper for

disordered $\langle \varphi_i \rangle$). This slow propagation provides another experimental diagnostic in support of MBL.

Our measurement of $\langle |\bar{A}| \rangle$ for 500 initial states in Fig. 3d provides clear evidence of initial-state independence. Still, a direct sampling of states is practically limited to small fractions of the computational basis (0.05% in this case) and would suffer from the exponential growth of the Hilbert space on larger systems. A more scalable alternative is to use random, highly entangled states to directly measure spectrally averaged quantities (quantum typicality^{37,38,39}; see Supplementary Information). The autocorrelator $\langle A \rangle$ averaged over all $\langle 2^L \rangle$ bit strings agrees, up to an error exponentially small in L , with $\langle A \rangle_{\psi} = \langle \psi | \hat{Z}(0) \hat{Z}(t) | \psi \rangle$, where $\langle | \psi \rangle$ is a typical Haar-random many-body state in the Hilbert space of L qubits. We prepare such a state by evolving a bit string with a random circuit $\langle \hat{U} \rangle_{\rm rm{S}}$ of variable depth K (Fig. 4b), and couple an ancilla qubit to the system to measure the two-time operator $\langle \hat{Z}(0) \hat{Z}(t) \rangle$ (Fig. 4a). Experimental results for the error-mitigated, spectrally averaged signal $\langle A \rangle_{\psi}/\langle A \rangle_{\psi,0}$ on qubit $\langle Q \rangle_{11}$ (Fig. 4c) show behaviour consistent with a stable MBL-DTC. The effect of the state-preparation circuit $\langle \hat{U} \rangle_{\rm rm{S}}$ is illustrated by the dependence of $\langle \sigma \rangle$ for $\langle A \rangle_{\psi}$ on K . As shown in Fig. 4d, $\langle \sigma \rangle$ steadily decreases as K increases, reducing from a value of 0.025 at $K=0$ to a value of 0.006 at $K=20$, while $\langle \mu \rangle$ remains largely unchanged. This is consistent with the fact that $\langle | \psi \rangle$ becomes closer to a Haar-random state as K increases. We use a single disorder instance to study the convergence of the quantum typicality protocol because disorder averaging independently leads to narrow distributions even for $K=0$ (Fig. 3b). Results for prethermal and thermalizing dynamics are shown in Supplementary Fig. 10.

Fig. 4: Probing average spectral response via quantum typicality.

 **figure 4**

a, Scheme for measuring the autocorrelator, $\langle \{A\}_{\{\psi\}} \rangle = \langle \hat{Z}(0) \hat{Z}(t) \rangle$, on $\langle \{Q\}_{\{11\}} \rangle$, of a scrambled quantum state $\langle |\psi\rangle \rangle$. $\langle |\psi\rangle \rangle$ is created by scrambling a bit-string state with a circuit $\langle \{\hat{U}\}_{\{\rm{rm}\{S\}\}} \rangle$. The x -axis projection of an ancilla qubit $\langle \{Q\}_{\{\rm{rm}\{a\}\}} \rangle$, $\langle \{\langle \hat{X} \rangle\}_{\{\rm{rm}\{a\}\}} \rangle$, is measured at the end.

b, $\langle \{\hat{U}\}_{\{\rm{rm}\{S\}\}} \rangle$ contains K layers of controlled-Z (CZ) gates interleaved with random single-qubit rotations, $\langle R_{i,k} \rangle$, around a random axis along the equatorial plane of the Bloch sphere by an angle $\langle \text{in } [0.4\pi, 0.6\pi] \rangle$.

c, Upper panel: $\langle \{A\}_{\{\psi\}} \rangle$ for a single disorder instance with $K=20$ cycles in $\langle \{\hat{U}\}_{\{\rm{rm}\{S\}\}} \rangle$. The square root of the autocorrelator, obtained by replacing $\langle \{\hat{U}\}_{\{\rm{rm}\{F\}\}}^t \rangle$ with $\langle \{\hat{U}\}_{\{\rm{rm}\{ECHO\}\}} \rangle$, $\langle \{A\}_{\{\psi, 0\}} \rangle$, is also shown. Bottom panel: normalized autocorrelator, $\langle \{A\}_{\{\psi\}} \rangle / \langle \{A\}_{\{\psi, 0\}} \rangle$, as a function of t .

d, Histograms of $\langle \{A\}_{\{\psi\}} \rangle$ from a single disorder instance, averaged over cycles 30 and 31. Each histogram corresponds to a different

number of scrambling cycles, $\langle K \rangle$, and includes data from 500 random initial bit-string states before $\langle \hat{U} \hat{S} \rangle$.

The scaling with $\langle L \rangle$ of the spectrally averaged autocorrelator, at a time $\langle t \rangle$ $\sim \langle \text{poly}(L) \rangle$, provides a sharp diagnostic: this saturates to a finite value in the MBL-DTC, while it scales to zero with increasing $\langle L \rangle$ in the thermal phase and in prethermal cases where, for instance, a vanishing fraction of the spectrum of an appropriate $\langle \hat{H} \hat{\text{rm}}\{\text{eff}\} \rangle$ shows order (see Supplementary Information). While the averaged autocorrelator may be unduly affected by outlier states and/or long (but $\langle O(1) \rangle$) thermalization times at small system sizes and times (thereby making the complementary bit-string analysis of Fig. 3 essential), the polynomial scaling of this protocol establishes a proof of principle for efficiently verifying the presence or absence of an MBL-DTC in a range of models as quantum processors scale up in size to surpass the limits of classical simulation⁴⁰.

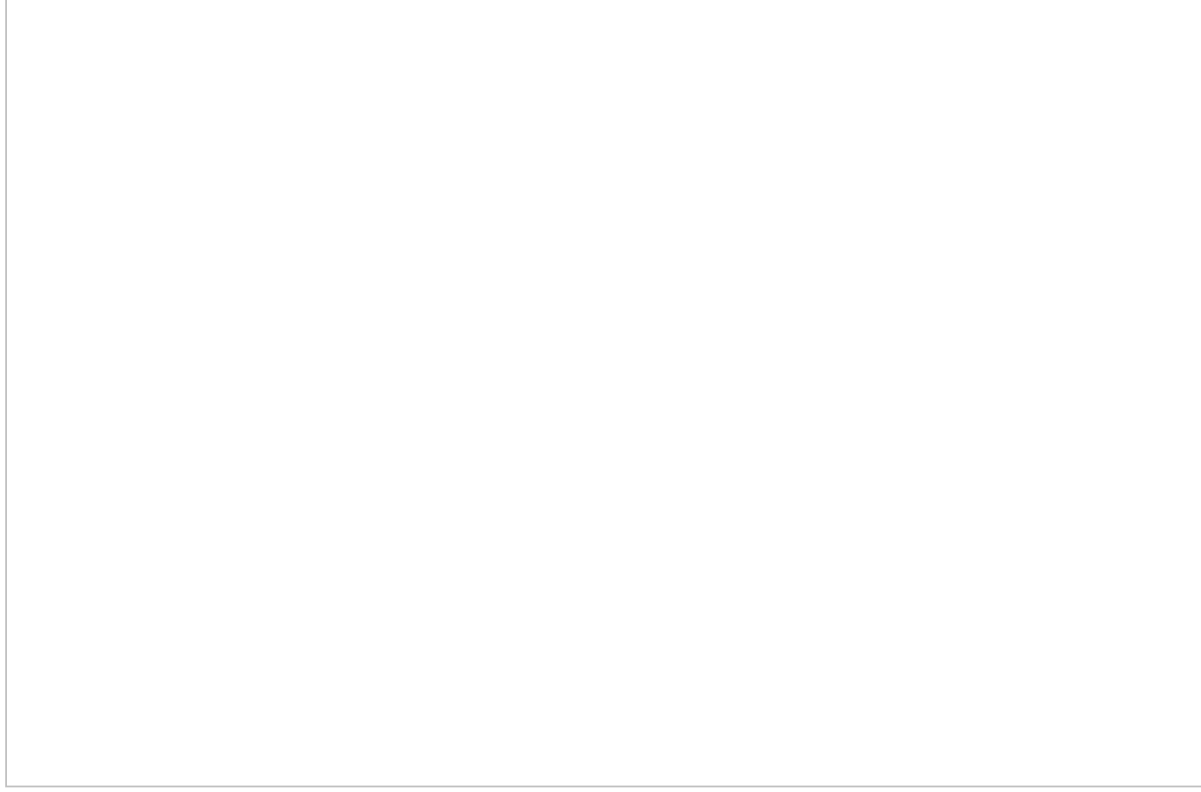
Finally, we systematically vary $\langle g \rangle$ in small increments and obtain an experimental finite-size analysis to establish the extent of the MBL phase and the transition out of it. Defining phases of matter, whether in or out of equilibrium, requires a limit of large system size. Thus, it is important to examine the stability of the MBL-DTC and thermalizing regimes observed in our finite-size quantum processor as the size of the system is increased. To address this, we measure an Edwards–Anderson spin-glass order parameter^{41,42}

$$\langle \hat{Z}_i \hat{Z}_j \rangle = \frac{1}{L-2} \sum_{i \neq j} \langle \chi^{\text{SG}} \rangle = \frac{1}{L-2} \sum_{i \neq j} \langle \hat{Z}_i \hat{Z}_j \rangle - \langle \hat{Z}_i \rangle^2 \quad (2)$$

(the primed sum excludes edge qubits $\langle Q_1 \rangle$, $\langle Q_L \rangle$), as a function of time. This quantity measures the persistence of random ('glassy') spatial patterns in the initial bit-string state: at late times, χ^{SG} vanishes with increasing $\langle L \rangle$ in the thermalizing phase $\langle g < g_c \rangle$, while it is extensive in the MBL-DTC $\langle g > g_c \rangle$. As a result, it is expected to show a finite-size crossing at $\langle g \rangle \approx g_c$ (although the precise location is subject to strong finite-size and finite-time drifts^{43,44}). Experimentally, $\langle \chi^{\text{SG}} \rangle$ is constructed from bit-string samples obtained by jointly reading out all qubits and then averaged over cycles and disorder instances (Fig. 5). The size of the qubit chain is varied by restricting the drive $\langle \hat{U} \hat{F} \rangle$ to contiguous subsets of 8, 12 and 16 qubits (as well as the entire 20-qubit chain). We observe increasing (decreasing) trends in $\langle \chi^{\text{SG}} \rangle$ versus $\langle L \rangle$ when $\langle g \rangle$ is above (below) a critical value $\langle g_c \rangle$, consistent with numerical simulations (see Supplementary Information).

Fig. 5: Estimating phase transition by varying system size.

 figure 5



Disorder-averaged spin-glass order parameter $\langle \langle \chi \rangle \rangle_{\rm SG}$ as a function of g for different chain lengths L , measured between $t=51$ and $t=60$. Error bars correspond to statistical errors alone and do not include hardware (for example, gate) errors. Inset shows the size dependence of $\langle \langle \chi \rangle \rangle_{\rm SG}$ for two different values of g . See [Methods](#) for measurement details.

In conclusion, we have demonstrated the possibility of engineering and characterizing non-equilibrium phases of matter on a quantum processor, providing the experimental observation of an MBL-DTC. The scalability of our protocols sets a blueprint for future studies of non-equilibrium phases and phase transitions on complex quantum systems beyond classical simulability. The efficient verification of eigenstate order can inspire a general strategy for establishing whether a desired property, such as a particular phase, is in fact present in a quantum processor.

Methods

Edge qubits

In computing various site-averaged quantities such as $\langle [\bar{A}] \rangle$ or $\langle \chi^{\{\rm SG\}} \rangle$, we have excluded contributions from the edge qubits $\langle Q_1 \rangle$ and $\langle Q_{20} \rangle$. This is because they may be affected by the presence of edge modes independent of the bulk DTC response⁴⁵.

Estimating distribution of autocorrelation functions

The measurements in Fig. 3a, b are conducted without error mitigation (that is, normalization via the echo circuits $\langle \hat{U}_{\rm ECHO} \rangle$). This is primarily due to the already high number of experimental circuits that need to be measured given the large collection of initial states and disorder instances. Adding echo circuits to each of these instances would make the data acquisition time unfeasibly long. We note that the experimental conclusions for Fig. 3a, b are in agreement with noiseless simulation of the same circuit instances, which reveals the same features as experimental data. See Supplementary Fig. 9 for details.

‘Prethermalization’ in $\langle \hat{U}_{\rm F}^{\prime} \rangle$ model

We refer to the circuit $\langle \hat{U}_{\rm F}^{\prime} \rangle$ (with uniform angles $\varphi_i = -0.4$) used in Fig. 3 as prethermal. The choice of value for φ_i is such that the dynamics is governed by an effective Hamiltonian $\langle \hat{H}_{\rm eff} \rangle$ for long times (see Supplementary Information for a derivation). Strictly speaking, a prethermal DTC requires $\langle \hat{H}_{\rm eff} \rangle$ to have a symmetry-breaking phase transition at a finite temperature T_c —in that case, ordered initial states at temperatures $T < T_c$ show long-lived oscillations (with an amplitude that depends on the equilibrium value of the symmetry-breaking order parameter at temperature T (ref. 31)). While short-ranged models in one dimension (such as the one under consideration) cannot have order at any finite temperature, thermal correlation lengths at low temperatures may still exceed the system size. This allows low-temperature states to show long-lived oscillations with a finite amplitude, even if the equilibrium order parameter is asymptotically zero for such states.

Measurement of the spin-glass order parameter

In Fig. 5, every data point is averaged over 40 disorder instances and 10 cycles ($t=51$ to $t=60$). To construct $\langle \chi^{\{\rm SG\}} \rangle$, we sample 40,000 bit strings at the output of $\langle \hat{U}_{\rm F}^{\prime} \rangle^t$ for each cycle and disorder instance. To address the inhomogeneity of qubit coherence, smaller qubit chains are also averaged over different possible combinations of qubits. For example, $\langle L=12 \rangle$ is averaged over 12-qubit chains made from $\langle Q_1 \rangle$ to $\langle Q_{12} \rangle$, $\langle Q_3 \rangle$ to $\langle Q_{15} \rangle$ and so on. The $|0\rangle^{\otimes L}$ state is used as the initial

state for all disorder instances. Error bars are estimated by resampling data from the 40 disorder instances via the jackknife method.

Comparison between many-body echo and single-qubit errors

The many-body echo circuits $\langle \{\hat{U}\}_{\{\rm ECHO\}} \rangle = \langle \{\hat{U}\}_{\{\rm rm\{F\}\}} \rangle^{\{\rm dagger\}} \rangle^{\{t\}} \langle \hat{U} \rangle_{\{\{\rm rm\{F\}\}\}}^{\{t\}}$ are chosen for characterizing decoherence effects since they capture the complex interplay between Floquet dynamics and single-qubit errors. More specifically, the decay of a particular observable (for example, $\langle \hat{Z}(t) \rangle$) depends not only on single-qubit error rates, but also on how much the quantum operator $\langle \hat{Z} \rangle$ is ‘spread’ to different qubits over time. This effect is visible in the different decay rates for the echo data with $(g=0.60)$ and $(g=0.97)$ in Fig. 2. Nevertheless, for values of (g) close to 1, the decay rate of local observables $\langle \bar{A}_0 \rangle$ should be close to single-qubit error rates²⁹ and at least some basic comparison may be made.

A description of gate errors, characterized through cross-entropy benchmarking⁴⁰, can be found in Supplementary Fig. 1. The single-qubit errors are also characterized through standard metrics of $\langle T_1 \rangle$, $\langle T_2^{\{\rm ast\}} \rangle$ and $\langle T_2^{\{\rm CPMG\}} \rangle$. We find $T_1 = 16.1$ (5.3) μs across the 20-qubit chain, where the value in parenthesis represents the standard deviation. $\langle T_2^{\{\rm ast\}} \rangle$, which is characterized through Ramsey measurements, is found to be $\langle T_2^{\{\rm ast\}} \rangle = 5.8$ (2.8) μs . $\langle T_2^{\{\rm CPMG\}} \rangle$, characterized through CPMG measurements, is found to be $\langle T_2^{\{\rm CPMG\}} \rangle = 16.6$ (3.7) μs .

These values may be compared to the characteristic decay rates of the echo experiment (that is, $\langle \bar{A}_0 \rangle$ in Fig. 2c) at $(g=0.97)$, which are found to be 6.4 (1.1) μs across the qubit chain. Here the quantum system is strongly localized, and the decay of the echo experiment is dominated by single-qubit decoherence²⁹. Given that this decay rate is closest to the value of $\langle T_2^{\{\rm ast\}} \rangle$, the extrinsic decoherence in our experiments is probably limited by low-frequency noise (the main contributor to $\langle T_2^{\{\rm ast\}} \rangle$) and, to some extent, energy relaxation and high-frequency noise as well. A more detailed characterization of decoherence mechanisms is left as the subject of future research.

Classical computational complexity of DTC circuits

The computational complexity of DTC circuits in the thermal and critical regimes asymptotically scales as an exponent of depth and number of qubits. Even though our 20-qubit experiment can be simulated on classical computers, it demonstrates a scalable protocol that could be applied to larger systems with higher connectivity geometries beyond the capacity of classical algorithms. We expect the circuit- and

geometry-dependent scaling exponent to be smaller than that for the two-dimensional random circuits implemented in refs. ^{40,34}. Therefore, to challenge classical supercomputers, we would need DTC circuits larger than those in refs. ^{40,34}. Calculation of this threshold is beyond the scope of this paper.

Data availability

The experimental data contained in the main text and Supplementary Information are available for download at <https://doi.org/10.5281/zenodo.5570676>.

Code availability

The Python simulation code used in theoretical analysis is available for download at <https://doi.org/10.5281/zenodo.5570676>.

References

1. 1. Wen, X.-G. *Quantum Field Theory of Many-Body Systems: From the Origin of Sound to an Origin of Light and Electrons* (Oxford Univ. Press, 2007).
2. 2. Bukov, M., D’Alessio, L. & Polkovnikov, A. Universal high-frequency behavior of periodically driven systems: from dynamical stabilization to Floquet engineering. *Adv. Phys.* **64**, 139–226 (2015).
3. 3. Harper, F., Roy, R., Rudner, M. S. & Sondhi, S. Topology and broken symmetry in Floquet systems. *Annu. Rev. Condens. Matter Phys.* **11**, 345–368 (2020).
4. 4. Oka, T. & Aoki, H. Photovoltaic Hall effect in graphene. *Phys. Rev. B* **79**, 081406 (2009).
5. 5. Rudner, M. S., Lindner, N. H., Berg, E. & Levin, M. Anomalous edge states and the bulk-edge correspondence for periodically driven two-dimensional systems.

Phys. Rev. X **3**, 031005 (2013).

6. 6.

Titum, P., Berg, E., Rudner, M. S., Refael, G. & Lindner, N. H. Anomalous Floquet–Anderson insulator as a nonadiabatic quantized charge pump. *Phys. Rev. X* **6**, 021013 (2016).

7. 7.

Khemani, V., Lazarides, A., Moessner, R. & Sondhi, S. Phase structure of driven quantum systems. *Phys. Rev. Lett.* **116**, 250401 (2016).

8. 8.

Po, H. C., Fidkowski, L., Morimoto, T., Potter, A. C. & Vishwanath, A. Chiral Floquet phases of many-body localized bosons. *Phys. Rev. X* **6**, 041070 (2016).

9. 9.

Else, D. V., Bauer, B. & Nayak, C. Floquet time crystals. *Phys. Rev. Lett.* **117**, 090402 (2016).

10. 10.

von Keyserlingk, C. W., Khemani, V. & Sondhi, S. L. Absolute stability and spatiotemporal long-range order in Floquet systems. *Phys. Rev. B* **94**, 085112 (2016).

11. 11.

Sacha, K. & Zakrzewski, J. Time crystals: a review. *Rep. Prog. Phys.* **81**, 016401 (2017).

12. 12.

Khemani, V., Moessner, R. & Sondhi, S. A brief history of time crystals. Preprint at <https://arxiv.org/abs/1910.10745> (2019).

13. 13.

Wilczek, F. Quantum time crystals. *Phys. Rev. Lett.* **109**, 160401 (2012).

14. 14.

Bruno, P. Impossibility of spontaneously rotating time crystals: a no-go theorem. *Phys. Rev. Lett.* **111**, 070402 (2013).

15. 15.

Watanabe, H. & Oshikawa, M. Absence of quantum time crystals. *Phys. Rev. Lett.* **114**, 251603 (2015).

16. 16.

Huse, D. A., Nandkishore, R., Oganesyan, V., Pal, A. & Sondhi, S. L. Localization-protected quantum order. *Phys. Rev. B* **88**, 014206 (2013).

17. 17.

Pekker, D., Refael, G., Altman, E., Demler, E. & Oganesyan, V. Hilbert-glass transition: new universality of temperature-tuned many-body dynamical quantum criticality. *Phys. Rev. X* **4**, 011052 (2014).

18. 18.

Basko, D., Aleiner, I. & Altshuler, B. Metal-insulator transition in a weakly interacting many-electron system with localized single-particle states. *Ann. Phys.* **321**, 1126–1205 (2006).

19. 19.

Nandkishore, R. & Huse, D. A. Many-body localization and thermalization in quantum statistical mechanics. *Annu. Rev. Condens. Matter Phys.* **6**, 15–38 (2015).

20. 20.

Abanin, D. A., Altman, E., Bloch, I. & Serbyn, M. Colloquium: Many-body localization, thermalization, and entanglement. *Rev. Mod. Phys.* **91**, 021001 (2019).

21. 21.

Ponte, P., Papić, Z., Huvaneers, F. M. C. & Abanin, D. A. Many-body localization in periodically driven systems. *Phys. Rev. Lett.* **114**, 140401 (2015).

22. 22.

Lazarides, A., Das, A. & Moessner, R. Fate of many-body localization under periodic driving. *Phys. Rev. Lett.* **115**, 030402 (2015).

23. 23.

Bordia, P., Luschen, H., Schneider, U., Knap, M. & Bloch, I. Periodically driving a many-body localized quantum system. *Nat. Phys.* **13**, 460–464 (2017).

24. 24.

Faraday, M. On a peculiar class of acoustical figures; and on certain forms assumed by groups of particles upon vibrating elastic surfaces. *Phil. Trans. R. Soc.* **121**, 299–340 (1831).

25. 25.

Zhang, J. et al. Observation of a discrete time crystal. *Nature* **543**, 217–220 (2017).

26. 26.

Choi, S. et al. Observation of discrete time-crystalline order in a disordered dipolar many-body system. *Nature* **543**, 221–225 (2017).

27. 27.

Rovny, J., Blum, R. L. & Barrett, S. E. Observation of discrete-time-crystal signatures in an ordered dipolar many-body system. *Phys. Rev. Lett.* **120**, 180603 (2018).

28. 28.

Pal, S., Nishad, N., Mahesh, T. S. & Sreejith, G. J. Temporal order in periodically driven spins in star-shaped clusters. *Phys. Rev. Lett.* **120**, 180602 (2018).

29. 29.

Ippoliti, M., Kechedzhi, K., Moessner, R., Sondhi, S. & Khemani, V. Many-body physics in the NISQ era: quantum programming a discrete time crystal. *PRX Quantum* **2**, 030346 (2021).

30. 30.

Ho, W. W., Choi, S., Lukin, M. D. & Abanin, D. A. Critical time crystals in dipolar systems. *Phys. Rev. Lett.* **119**, 010602 (2017).

31. 31.

Else, D., Bauer, B. & Nayak, C. Prethermal phases of matter protected by time-translation symmetry. *Phys. Rev. X* **7**, 011026 (2017).

32. 32.

Luitz, D. J., Moessner, R., Sondhi, S. L. & Khemani, V. Prethermalization without temperature. *Phys. Rev. X* **10**, 021046 (2020).

33. 33.

Randall, J. et al. Many-body-localized discrete time crystal with a programmable spin-based quantum simulator. *Science* **374**, 1474–1478 (2021).

34. 34.

Mi, X. et al. Information scrambling in quantum circuits. *Science* **374**, 1479–1483 (2021).

35. 35.

Abanin, D. A., De Roeck, W., Ho, W. W. & Huvaneers, F. Effective Hamiltonians, prethermalization, and slow energy absorption in periodically driven many-body systems. *Phys. Rev. B* **95**, 014112 (2017).

36. 36.

Mori, T., Ikeda, T. N., Kaminishi, E. & Ueda, M. Thermalization and prethermalization in isolated quantum systems: a theoretical overview. *J. Phys. B* **51**, 112001 (2018).

37. 37.

Popescu, S., Short, A. J. & Winter, A. Entanglement and the foundations of statistical mechanics. *Nat. Phys.* **2**, 754–758 (2006).

38. 38.

Goldstein, S., Lebowitz, J. L., Tumulka, R. & Zanghì, N. Canonical typicality. *Phys. Rev. Lett.* **96**, 050403 (2006).

39. 39.

Richter, J. & Pal, A. Simulating hydrodynamics on noisy intermediate-scale quantum devices with random circuits. *Phys. Rev. Lett.* **126**, 230501 (2021).

40. 40.

Arute, F. et al. Quantum supremacy using a programmable superconducting processor. *Nature* **574**, 505–510 (2019).

41. 41.

Edwards, S. F. & Anderson, P. W. Theory of spin glasses. *J. Phys. F* **5**, 965–974 (1975).

42. 42.

Kjäll, J. A., Bardarson, J. H. & Pollmann, F. Many-body localization in a disordered quantum Ising chain. *Phys. Rev. Lett.* **113**, 107204 (2014).

43. 43.

Pal, A. & Huse, D. A. Many-body localization phase transition. *Phys. Rev. B* **82**, 174411 (2010).

44. 44.

Abanin, D. et al. Distinguishing localization from chaos: challenges in finite-size systems. *Ann. Phys.* **427**, 168415 (2021).

45. 45.

Yates, D. J., Abanov, A. G. & Mitra, A. Long-lived π edge modes of interacting and disorder-free Floquet spin chains. Preprint at <https://arxiv.org/abs/2105.13766> (2021).

Acknowledgements

This work was supported in part by the Defense Advanced Research Projects Agency via the DRINQS programme (M.I., V.K., R.M. and S.L.S.), by a Google Research Award: Quantum Hardware For Scientific Research In Physics (V.K. and M.I.), and by the Sloan Foundation through a Sloan Research Fellowship (V.K.) The views, opinions and/or findings expressed are those of the authors and should not be interpreted as

representing the official views or policies of the Department of Defense or the US Government. M.I. was funded in part by the Gordon and Betty Moore Foundation's EPiQS Initiative through grant GBMF8686. This work was partly supported by the Deutsche Forschungsgemeinschaft under grant SFB 1143 (project-id 247310070), the cluster of excellence ct.qmat (EXC 2147, project-id 390858490) and a Leverhulme International Professorship (S.L.S.).

Author information

Author notes

1. These authors contributed equally: Xiao Mi, Matteo Ippoliti

Affiliations

1. Google Research, Mountain View, CA, USA

Xiao Mi, Chris Quintana, Ami Greene, Zijun Chen, Jonathan Gross, Frank Arute, Kunal Arya, Juan Atalaya, Ryan Babbush, Joseph C. Bardin, Joao Basso, Andreas Bengtsson, Alexander Bilmes, Alexandre Bourassa, Leon Brill, Michael Broughton, Bob B. Buckley, David A. Buell, Brian Burkett, Nicholas Bushnell, Benjamin Chiaro, Roberto Collins, William Courtney, Dripto Debroy, Sean Demura, Alan R. Derk, Andrew Dunsworth, Daniel Eppens, Catherine Erickson, Edward Farhi, Austin G. Fowler, Brooks Foxen, Craig Gidney, Marissa Giustina, Matthew P. Harrigan, Sean D. Harrington, Jeremy Hilton, Alan Ho, Sabrina Hong, Trent Huang, Ashley Huff, William J. Huggins, L. B. Ioffe, Sergei V. Isakov, Justin Iveland, Evan Jeffrey, Zhang Jiang, Cody Jones, Dvir Kafri, Tanuj Khattar, Seon Kim, Alexei Kitaev, Paul V. Klimov, Alexander N. Korotkov, Fedor Kostritsa, David Landhuis, Pavel Laptev, Joonho Lee, Kenny Lee, Aditya Locharla, Erik Lucero, Orion Martin, Jarrod R. McClean, Trevor McCourt, Matt McEwen, Kevin C. Miao, Masoud Mohseni, Shirin Montazeri, Wojciech Mruczkiewicz, Ofer Naaman, Matthew Neeley, Charles Neill, Michael Newman, Murphy Yuezhen Niu, Thomas E. O'Brien, Alex Opremcak, Eric Ostby, Balint Pato, Andre Petukhov, Nicholas C. Rubin, Daniel Sank, Kevin J. Satzinger, Vladimir Shvarts, Yuan Su, Doug Strain, Marco Szalay, Matthew D. Trevithick, Benjamin Villalonga, Theodore White, Z. Jamie Yao, Ping Yeh, Juhwan Yoo, Adam Zalcman, Hartmut Neven, Sergio Boixo, Vadim Smelyanskiy, Anthony Megrant, Julian Kelly, Yu Chen, Kostyantyn Kechedzhi & Pedram Roushan

2. Department of Physics, Stanford University, Stanford, CA, USA

Matteo Ippoliti & Vedika Khemani

3. Department of Electrical and Computer Engineering, University of Massachusetts, Amherst, MA, USA

Joseph C. Bardin

4. Pritzker School of Molecular Engineering, University of Chicago, Chicago, IL, USA

Alexandre Bourassa

5. Department of Electrical and Computer Engineering, University of California, Riverside, CA, USA

Alexander N. Korotkov

6. Department of Chemistry, Columbia University, New York, NY, USA

Joonho Lee

7. Department of Physics, University of California, Santa Barbara, CA, USA

Matt McEwen

8. Department of Physics, Princeton University, Princeton, NJ, USA

S. L. Sondhi

9. Rudolf Peierls Centre for Theoretical Physics, University of Oxford, Oxford, UK

S. L. Sondhi

10. Max-Planck-Institut für Physik komplexer Systeme, Dresden, Germany

Roderich Moessner

Contributions

M.I., K.K., V.K., R.M. and S.L.S. conceived the project. X.M., C.Q. and P.R. executed the experiment. All the aforementioned discussed the project in progress and interpreted the results. M.I., K.K., V.K. and X.M. designed measurement protocols. Z.C., A.G., J.G. and X.M. implemented and calibrated the CPHASE gates. M.I. and V.K. performed theoretical and numerical analyses. M.I., K.K., V.K., R.M., X.M. and

P.R. wrote the manuscript. M.I. and X.M. wrote the Supplementary Information. Y.C., K.K., V.K., H.N., P.R. and V. Smelyanskiy led and coordinated the project. Infrastructure support was provided by Google Quantum AI. All authors contributed to revising the manuscript and the Supplementary Information.

Corresponding authors

Correspondence to [Vedika Khemani](#) or [Pedram Roushan](#).

Ethics declarations

Competing interests

The authors declare no competing interests.

Peer review information

Nature thanks Mohammad Hafezi and the other, anonymous, reviewer(s) for their contribution to the peer review of this work.

Additional information

Publisher's note Springer Nature remains neutral with regard to jurisdictional claims in published maps and institutional affiliations.

Supplementary information

[Supplementary Information](#)

This file contains Sections I–VIII, including Figs. 1–10 and additional references.

Rights and permissions

Open Access This article is licensed under a Creative Commons Attribution 4.0 International License, which permits use, sharing, adaptation, distribution and reproduction in any medium or format, as long as you give appropriate credit to the original author(s) and the source, provide a link to the Creative Commons license, and indicate if changes were made. The images or other third party material in this article are included in the article's Creative Commons license, unless indicated otherwise in a

credit line to the material. If material is not included in the article's Creative Commons license and your intended use is not permitted by statutory regulation or exceeds the permitted use, you will need to obtain permission directly from the copyright holder. To view a copy of this license, visit <http://creativecommons.org/licenses/by/4.0/>.

[Reprints and Permissions](#)

About this article

Cite this article

Mi, X., Ippoliti, M., Quintana, C. *et al.* Time-crystalline eigenstate order on a quantum processor. *Nature* **601**, 531–536 (2022). <https://doi.org/10.1038/s41586-021-04257-w>

- Received: 30 July 2021
- Accepted: 17 November 2021
- Published: 30 November 2021
- Issue Date: 27 January 2022
- DOI: <https://doi.org/10.1038/s41586-021-04257-w>

Share this article

Anyone you share the following link with will be able to read this content:

[Get shareable link](#)

Sorry, a shareable link is not currently available for this article.

[Copy to clipboard](#)

Provided by the Springer Nature SharedIt content-sharing initiative

This article was downloaded by **calibre** from <https://www.nature.com/articles/s41586-021-04257-w>

- Article
- [Published: 26 January 2022](#)

Quantum register of fermion pairs

- [Thomas Hartke](#) [ORCID: orcid.org/0000-0001-7978-0473¹](#),
- [Botond Oreg](#) [ORCID: orcid.org/0000-0002-0998-1824¹](#),
- [Ningyuan Jia¹](#) &
- [Martin Zwierlein](#) ¹

[Nature](#) volume **601**, pages 537–541 (2022)

- 1300 Accesses
- 74 Altmetric
- [Metrics details](#)

Subjects

- [Qubits](#)
- [Ultracold gases](#)

Abstract

Quantum control of motion is central for modern atomic clocks¹ and interferometers². It enables protocols to process and distribute quantum information^{3,4}, and allows the probing of entanglement in correlated states of matter⁵. However, the motional coherence of individual particles can be fragile to maintain, as external degrees of freedom couple strongly to the environment. Systems in nature with robust motional coherence instead often involve pairs of particles, from the electrons in helium, to atom pairs⁶, molecules⁷ and Cooper pairs. Here we demonstrate long-lived motional

coherence and entanglement of pairs of fermionic atoms in an optical lattice array. The common and relative motion of each pair realize a robust qubit, protected by exchange symmetry. The energy difference between the two motional states is set by the atomic recoil energy, is dependent on only the mass and the lattice wavelength, and is insensitive to the noise of the confining potential. We observe quantum coherence beyond ten seconds. Modulation of the interactions between the atoms provides universal control of the motional qubit. The methods presented here will enable coherently programmable quantum simulators of many-fermion systems⁸, precision metrology based on atom pairs and molecules^{9,10} and, by implementing further advances^{11,12,13}, digital quantum computation using fermion pairs¹⁴.

This is a preview of subscription content

Access options

Subscribe to nature+

Get immediate online access to the entire Nature family of 50+ journals

\$29.99

monthly

[Subscribe](#)

Subscribe to Journal

Get full journal access for 1 year

\$199.00

only \$3.90 per issue

[Subscribe](#)

All prices are NET prices.
VAT will be added later in the checkout.
Tax calculation will be finalised during checkout.

Buy article

Get time limited or full article access on ReadCube.

\$32.00

[Buy](#)

All prices are NET prices.

Additional access options:

- [Log in](#)
- [Learn about institutional subscriptions](#)

Fig. 1: Spatial qubit encoding in a pair of entangled fermions.

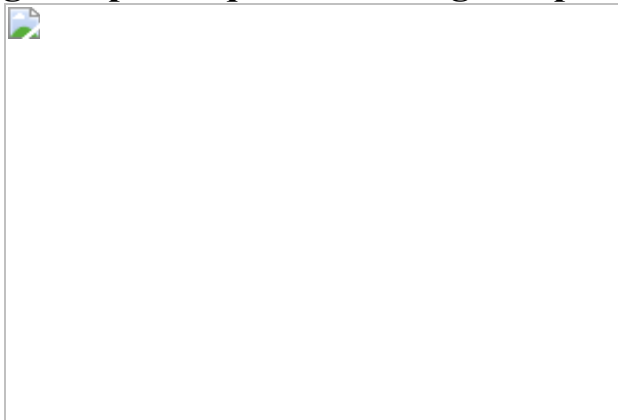


Fig. 2: Simultaneous coherent manipulation and parallel readout of hundreds of motional fermion pair qubits.

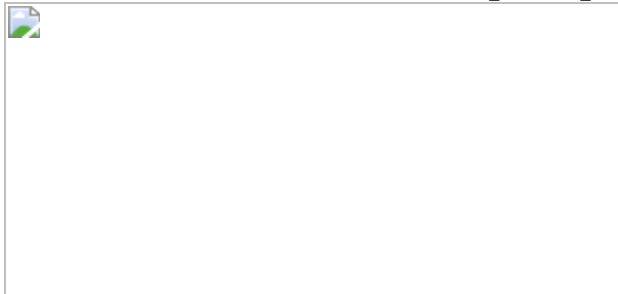


Fig. 3: Crossover from fermion pair to molecule qubit.

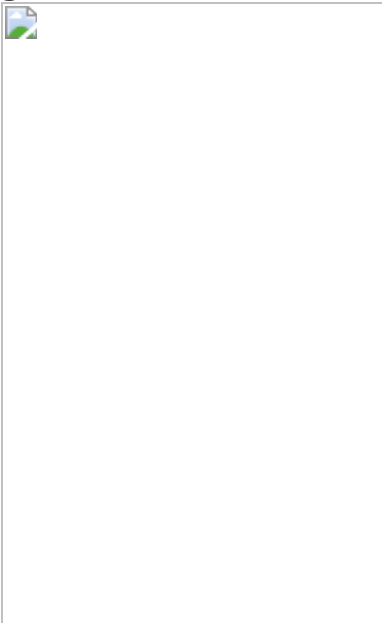
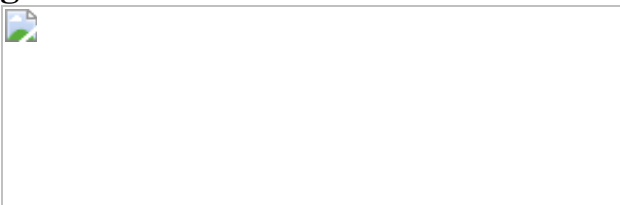


Fig. 4: Second-scale coherence of the fermion pair qubit.



Data availability

The data that support the findings of this study are available from the corresponding authors upon reasonable request. [Source data](#) are provided with this paper.

References

1. 1.

Ludlow, A. D., Boyd, M. M., Ye, J., Peik, E. & Schmidt, P. O. Optical atomic clocks. *Rev. Mod. Phys.* **87**, 637–701 (2015).

2. 2.

Xu, V. et al. Probing gravity by holding atoms for 20 seconds. *Science* **366**, 745–749 (2019).

3. 3.

Jaksch, D., Briegel, H.-J., Cirac, J. I., Gardiner, C. W. & Zoller, P. Entanglement of atoms via cold controlled collisions. *Phys. Rev. Lett.* **82**, 1975–1978 (1999).

4. 4.

Duan, L.-M., Lukin, M. D., Cirac, J. I. & Zoller, P. Long-distance quantum communication with atomic ensembles and linear optics. *Nature* **414**, 413–418 (2001).

5. 5.

Islam, R. et al. Measuring entanglement entropy in a quantum many-body system. *Nature* **528**, 77–83 (2015).

6. 6.

Bergschneider, A. et al. Experimental characterization of two-particle entanglement through position and momentum correlations. *Nat. Phys.* **15**, 640–644 (2019).

7. 7.

Greiner, M., Regal, C. A., Stewart, J. T. & Jin, D. S. Probing pair-correlated fermionic atoms through correlations in atom shot noise. *Phys. Rev. Lett.* **94**, 110401 (2005).

8. 8.

Gross, C. & Bakr, W. S. Quantum gas microscopy for single atom and spin detection. *Nat. Phys.* **17**, 1316–1323 (2021).

9. 9.

Schiller, S., Bakalov, D. & Korobov, V. I. Simplest molecules as candidates for precise optical clocks. *Phys. Rev. Lett.* **113**, 023004 (2014).

10. 10.

Kondov, S. S. et al. Molecular lattice clock with long vibrational coherence. *Nat. Phys.* **15**, 1118–1122 (2019).

11. 11.

Weitenberg, C. et al. Single-spin addressing in an atomic Mott insulator. *Nature* **471**, 319–324 (2011).

12. 12.

Hollerith, S. et al. Quantum gas microscopy of Rydberg macrodimers. *Science* **364**, 664–667 (2019).

13. 13.

Browaeys, A. & Lahaye, T. Many-body physics with individually controlled Rydberg atoms. *Nat. Phys.* **16**, 132–142 (2020).

14. 14.

Mamaev, M., Thywissen, J. H. & Rey, A. M. Quantum computation toolbox for decoherence-free qubits using multi-band alkali atoms. *Adv. Quantum Technol.* **3**, 1900132 (2020).

15. 15.

Bauer, B., Bravyi, S., Motta, M. & Kin-Lic Chan, G. Quantum algorithms for quantum chemistry and quantum materials science. *Chem. Rev.* **120**, 12685–12717 (2020).

16. 16.

Viverit, L., Menotti, C., Calarco, T. & Smerzi, A. Efficient and robust initialization of a qubit register with fermionic atoms. *Phys. Rev. Lett.* **93**, 110401 (2004).

17. 17.

Serwane, F. et al. Deterministic preparation of a tunable few-fermion system. *Science* **332**, 336–338 (2011).

18. 18.

Chiu, C. S., Ji, G., Mazurenko, A., Greif, D. & Greiner, M. Quantum state engineering of a Hubbard system with ultracold fermions. *Phys. Rev. Lett.* **120**, 243201 (2018).

19. 19.

Myrskog, S. H., Fox, J. K., Mitchell, M. W. & Steinberg, A. M. Quantum process tomography on vibrational states of atoms in an optical lattice. *Phys. Rev. A* **72**, 013615 (2005).

20. 20.

Müller, T., Fölling, S., Widera, A. & Bloch, I. State preparation and dynamics of ultracold atoms in higher lattice orbitals. *Phys. Rev. Lett.* **99**, 200405 (2007).

21. 21.

Förster, L. et al. Microwave control of atomic motion in optical lattices. *Phys. Rev. Lett.* **103**, 233001 (2009).

22. 22.

Bakr, W. S. et al. Orbital excitation blockade and algorithmic cooling in quantum gases. *Nature* **480**, 500–503 (2011).

23. 23.

van Frank, S. et al. Interferometry with non-classical motional states of a Bose–Einstein condensate. *Nat. Commun.* **5**, 4009 (2014).

24. 24.

Kwiat, P. G., Berglund, A. J., Altepeter, J. B. & White, A. G. Experimental verification of decoherence-free subspaces. *Science* **290**, 498–501 (2000).

25. 25.

Kielpinski, D. et al. A decoherence-free quantum memory using trapped ions. *Science* **291**, 1013–1015 (2001).

26. 26.

Chin, C., Grimm, R., Julienne, P. & Tiesinga, E. Feshbach resonances in ultracold gases. *Rev. Mod. Phys.* **82**, 1225–1286 (2010).

27. 27.

Köhl, M., Moritz, H., Stöferle, T., Günter, K. & Esslinger, T. Fermionic atoms in a three dimensional optical lattice: observing Fermi surfaces, dynamics, and interactions. *Phys. Rev. Lett.* **94**, 080403 (2005).

28. 28.

Diener, R. B. & Ho, T.-L. Fermions in optical lattices swept across Feshbach resonances. *Phys. Rev. Lett.* **96**, 010402 (2006).

29. 29.

Zürn, G. et al. Fermionization of two distinguishable fermions. *Phys. Rev. Lett.* **108**, 075303 (2012).

30. 30.

Busch, T., Englert, B.-G., Rzażewski, K. & Wilkens, M. Two cold atoms in a harmonic trap. *Found. Phys.* **28**, 549–559 (1998).

31. 31.

Idziaszek, Z. & Calarco, T. Two atoms in an anisotropic harmonic trap. *Phys. Rev. A* **71**, 050701 (2005).

32. 32.

Bolda, E., Tiesinga, E. & Julienne, P. Ultracold dimer association induced by a far-off-resonance optical lattice. *Phys. Rev. A* **71**, 033404 (2005).

33. 33.

Sala, S. et al. Coherent molecule formation in anharmonic potentials near confinement-induced resonances. *Phys. Rev. Lett.* **110**, 203202 (2013).

34. 34.

Sala, S. & Saenz, A. Theory of inelastic confinement-induced resonances due to the coupling of center-of-mass and relative motion. *Phys. Rev. A* **94**, 022713 (2016).

35. 35.

Ishmukhamedov, I. S. & Melezlik, V. S. Tunneling of two bosonic atoms from a one-dimensional anharmonic trap. *Phys. Rev. A* **95**, 062701 (2017).

36. 36.

Thompson, S. T., Hodby, E. & Wieman, C. E. Ultracold molecule production via a resonant oscillating magnetic field. *Phys. Rev. Lett.* **95**, 190404 (2005).

37. 37.

Hartke, T., Oreg, B., Jia, N. & Zwierlein, M. Doublon–hole correlations and fluctuation thermometry in a Fermi–Hubbard gas. *Phys. Rev. Lett.* **125**, 113601 (2020).

38. 38.

Fuchs, G. D., Dobrovitski, V. V., Toyli, D. M., Heremans, F. J. & Awschalom, D. D. Gigahertz dynamics of a strongly driven single quantum spin. *Science* **326**, 1520–1522 (2009).

39. 39.

Haller, E. et al. Confinement-induced resonances in low-dimensional quantum systems. *Phys. Rev. Lett.* **104**, 153203 (2010).

40. 40.

Donley, E. A., Claussen, N. R., Thompson, S. T. & Wieman, C. E. Atom–molecule coherence in a Bose–Einstein condensate. *Nature* **417**, 529–533 (2002).

41. 41.

Syassen, N. et al. Atom–molecule Rabi oscillations in a Mott insulator. *Phys. Rev. Lett.* **99**, 033201 (2007).

42. 42.

Hartmann, S. R. & Hahn, E. L. Nuclear double resonance in the rotating frame. *Phys. Rev.* **128**, 2042–2053 (1962).

43. 43.

Liu, L. R. et al. Molecular assembly of ground-state cooled single atoms. *Phys. Rev. X* **9**, 021039 (2019).

44. 44.

Levine, H. et al. Parallel implementation of high-fidelity multiqubit gates with neutral atoms. *Phys. Rev. Lett.* **123**, 170503 (2019).

45. 45.

Mandel, O. et al. Controlled collisions for multi-particle entanglement of optically trapped atoms. *Nature* **425**, 937–940 (2003).

46. 46.

Anderlini, M. et al. Controlled exchange interaction between pairs of neutral atoms in an optical lattice. *Nature* **448**, 452–456 (2007).

47. 47.

Trotzky, S. et al. Time-resolved observation and control of superexchange interactions with ultracold atoms in optical lattices. *Science* **319**, 295–299 (2008).

48. 48.

Greif, D., Uehlinger, T., Jotzu, G., Tarruell, L. & Esslinger, T. Short-range quantum magnetism of ultracold fermions in an optical lattice. *Science* **340**, 1307–1310 (2013).

49. 49.

Kaufman, A. M. et al. Entangling two transportable neutral atoms via local spin exchange. *Nature* **527**, 208–211 (2015).

50. 50.

Rom, T. et al. State selective production of molecules in optical lattices. *Phys. Rev. Lett.* **93**, 073002 (2004).

51. 51.

Greene, C. H., Dickinson, A. S. & Sadeghpour, H. R. Creation of polar and nonpolar ultra-long-range Rydberg molecules. *Phys. Rev. Lett.* **85**,

2458–2461 (2000).

52. 52.

Guardado-Sánchez, E. et al. Quench dynamics of a Fermi gas with strong nonlocal interactions. *Phys. Rev. X* **11**, 021036 (2021).

53. 53.

Ho, A. F. Fermions in optical lattices near a Feshbach resonance: from band insulator to Mott insulator. *Phys. Rev. A* **73**, 061601 (2006).

54. 54.

Koga, A., Kawakami, N., Rice, T. M. & Sigrist, M. Orbital-selective Mott transitions in the degenerate Hubbard model. *Phys. Rev. Lett.* **92**, 216402 (2004).

55. 55.

Kubo, K. Pairing symmetry in a two-orbital Hubbard model on a square lattice. *Phys. Rev. B* **75**, 224509 (2007).

56. 56.

Yan, B. et al. Observation of dipolar spin-exchange interactions with lattice-confined polar molecules. *Nature* **501**, 521–525 (2013).

57. 57.

Baron, J. et al. Order of magnitude smaller limit on the electric dipole moment of the electron. *Science* **343**, 269–272 (2014).

58. 58.

Cairncross, W. B. et al. Precision measurement of the electron's electric dipole moment using trapped molecular ions. *Phys. Rev. Lett.* **119**, 153001 (2017).

59. 59.

Cheuk, L. W. et al. Quantum-gas microscope for fermionic atoms. *Phys. Rev. Lett.* **114**, 193001 (2015).

60. 60.

Murmann, S. et al. Two fermions in a double well: exploring a fundamental building block of the Hubbard model. *Phys. Rev. Lett.* **114**, 080402 (2015).

61. 61.

Mitra, D. et al. Quantum gas microscopy of an attractive Fermi–Hubbard system. *Nat. Phys.* **14**, 173–177 (2018).

62. 62.

Chen, Y., Xiao, D.-W., Zhang, R. & Zhang, P. Analytical solution for the spectrum of two ultracold atoms in a completely anisotropic confinement. *Phys. Rev. A* **101**, 053624 (2020).

63. 63.

D’Errico, C. et al. Feshbach resonances in ultracold 39K. *New J. Phys.* **9**, 223–223 (2007).

64. 64.

Daniel, D. J. Exact solutions of Mathieu’s equation. *Prog. Theor. Exp. Phys.* **2020**, 043A01 (2020).

65. 65.

Laucht, A. et al. Breaking the rotating wave approximation for a strongly driven dressed single-electron spin. *Phys. Rev. B* **94**, 161302 (2016).

66. 66.

Wang, G., Liu, Y.-X. & Cappellaro, P. Observation of the high-order Mollow triplet by quantum mode control with concatenated continuous driving. *Phys. Rev. A* **103**, 022415 (2021).

Acknowledgements

We thank C. Robens for discussions. This work was supported by the NSF through the Center for Ultracold Atoms and Grant PHY-2012110, ONR (grant number N00014-17-1-2257), AFOSR (grant number FA9550-16-1-0324), AFOSR-MURIs on Quantum Phases of Matter (grant number FA9550-14-1-0035) and on Full Quantum State Control at Single Molecule Levels (grant number FA9550-21-1-0069), the Gordon and Betty Moore Foundation through grant GBMF5279, and the Vannevar Bush Faculty Fellowship. M.Z. acknowledges support from the Alexander von Humboldt Foundation.

Author information

Affiliations

1. Department of Physics, MIT-Harvard Center for Ultracold Atoms, Research Laboratory of Electronics, MIT, Cambridge, MA, USA

Thomas Hartke, Botond Oreg, Ningyuan Jia & Martin Zwierlein

Contributions

The experiment was designed by all authors. T.H., B.O. and N.J. collected and analysed the data. All authors contributed to the manuscript.

Corresponding authors

Correspondence to [Thomas Hartke](#) or [Martin Zwierlein](#).

Ethics declarations

Competing interests

The authors declare no competing interests.

Peer review information

Nature thanks the anonymous reviewers for their contribution to the peer review of this work.

Additional information

Publisher's note Springer Nature remains neutral with regard to jurisdictional claims in published maps and institutional affiliations.

Extended data figures and tables

Extended Data Fig. 1 Qubit control protocols.

a, Protocol to transfer population between the fermion pair qubit eigenstates at the recoil gap via a Rabi drive of interactions using the magnetic field (Fig. 2 data). **b**, Protocols for Ramsey measurements of the qubit energy splitting $|\Delta E|$ (Fig. 3 data). **c**, Protocols for measuring coherence at the recoil gap (Fig. 4 data).

Extended Data Fig. 2 Strong driving.

A strongly driven Rabi oscillation at the avoided crossing of Fig. 1c exhibits non-sinusoidal response. The predicted Rabi coupling $\Delta U/4 = h \times 151.98$ Hz (see Fig. 2d), which is driven at a modulation frequency of 140.65 Hz, is comparable to the recoil energy gap $E_R = h \times 140.76(3)$ Hz. The solid line shows a phenomenological guide to the eye composed of three sinusoids with frequencies near E_R/h , $2E_R/h$ and $3E_R/h$.

Source data

Extended Data Fig. 3 Coherence at strong interactions.

The standard deviation of the fermion pair qubit state in an echo sequence with randomized extra phase (standard deviation of $\langle\langle n \rangle\rangle_{|1,1\rangle}$) quantifies the coherence of the register array at strong interactions. A fitted exponential without offset has $1/e$ time constant $\tau = 2.3(1)$ s at $|\Delta E| = h \times 1.594(7)$ kHz (orange), $\tau = 0.84(5)$ s at $|\Delta E| = h \times 8.98(7)$ kHz (red) and $\tau = 0.49(2)$ s at $|\Delta E| = h \times 50.7(4)$ kHz (purple), corresponding to magnetic fields $B = 206.976(8)$ G, $B = 204.235(8)$ G and $B = 202.091(8)$ G, respectively. Error bars of τ represent fit error. These data are used in Fig. 4b.

[Source data](#)

Source data

[Source Data Fig. 2](#)

[Source Data Fig. 3](#)

[Source Data Fig. 4](#)

[Source Data Extended Data Fig. 2](#)

[Source Data Extended Data Fig. 3](#)

Rights and permissions

[Reprints and Permissions](#)

About this article

[Cite this article](#)

Hartke, T., Oreg, B., Jia, N. *et al.* Quantum register of fermion pairs. *Nature* **601**, 537–541 (2022). <https://doi.org/10.1038/s41586-021-04205-8>

- Received: 23 March 2021
- Accepted: 03 November 2021
- Published: 26 January 2022
- Issue Date: 27 January 2022
- DOI: <https://doi.org/10.1038/s41586-021-04205-8>

Share this article

Anyone you share the following link with will be able to read this content:

[Get shareable link](#)

Sorry, a shareable link is not currently available for this article.

[Copy to clipboard](#)

Provided by the Springer Nature SharedIt content-sharing initiative

This article was downloaded by **calibre** from <https://www.nature.com/articles/s41586-021-04205-8>

- Article
- Open Access
- [Published: 26 January 2022](#)

Burning plasma achieved in inertial fusion

- [A. B. Zylstra](#) [ORCID: orcid.org/0000-0003-0489-7479](#)¹_{nal},
- [O. A. Hurricane](#) [ORCID: orcid.org/0000-0002-8600-5448](#)¹_{nal},
- [D. A. Callahan](#)¹,
- [A. L. Kritchler](#) [ORCID: orcid.org/0000-0002-9694-1088](#)¹,
- [J. E. Ralph](#)¹,
- [H. F. Robey](#)²,
- [J. S. Ross](#)¹,
- [C. V. Young](#) [ORCID: orcid.org/0000-0002-8075-7550](#)¹,
- [K. L. Baker](#)¹,
- [D. T. Casey](#) [ORCID: orcid.org/0000-0003-2125-677X](#)¹,
- [T. Döppner](#) [ORCID: orcid.org/0000-0002-5703-7125](#)¹,
- [L. Divol](#)¹,
- [M. Hohenberger](#) [ORCID: orcid.org/0000-0002-5887-9711](#)¹,
- [S. Le Pape](#)³,
- [A. Pak](#)¹,
- [P. K. Patel](#)¹,
- [R. Tommasini](#) [ORCID: orcid.org/0000-0002-1070-3565](#)¹,
- [S. J. Ali](#) [ORCID: orcid.org/0000-0003-1823-3788](#)¹,
- [P. A. Amendt](#)¹,
- [L. J. Atherton](#)¹,
- [B. Bachmann](#) [ORCID: orcid.org/0000-0001-7992-0018](#)¹,
- [D. Bailey](#)¹,
- [L. R. Benedetti](#)¹,
- [L. Berzak Hopkins](#)¹,
- [R. Betti](#)⁴,
- [S. D. Bhandarkar](#)¹,
- [J. Biener](#) [ORCID: orcid.org/0000-0002-3722-3924](#)¹,
- [R. M. Bionta](#)¹,

- [N. W. Birge²](#),
- [E. J. Bond¹](#),
- [D. K. Bradley¹](#),
- [T. Braun ORCID: orcid.org/0000-0002-4633-5311¹](#),
- [T. M. Briggs¹](#),
- [M. W. Bruhn¹](#),
- [P. M. Celliers¹](#),
- [B. Chang¹](#),
- [T. Chapman¹](#),
- [H. Chen ORCID: orcid.org/0000-0002-0181-1695¹](#),
- [C. Choate¹](#),
- [A. R. Christopherson¹](#),
- [D. S. Clark¹](#),
- [J. W. Crippen⁵](#),
- [E. L. Dewald¹](#),
- [T. R. Dittrich¹](#),
- [M. J. Edwards¹](#),
- [W. A. Farmer ORCID: orcid.org/0000-0001-6758-220X¹](#),
- [J. E. Field¹](#),
- [D. Fittinghoff ORCID: orcid.org/0000-0002-6089-8911¹](#),
- [J. Frenje⁶](#),
- [J. Gaffney ORCID: orcid.org/0000-0002-2408-0047¹](#),
- [M. Gatun Johnson ORCID: orcid.org/0000-0002-2383-1275⁶](#),
- [S. H. Glenzer ORCID: orcid.org/0000-0001-9112-0558⁷](#),
- [G. P. Grim ORCID: orcid.org/0000-0002-9648-3427¹](#),
- [S. Haan¹](#),
- [K. D. Hahn¹](#),
- [G. N. Hall¹](#),
- [B. A. Hammel¹](#),
- [J. Harte¹](#),
- [E. Hartouni¹](#),
- [J. E. Heebner¹](#),
- [V. J. Hernandez¹](#),
- [H. Herrmann ORCID: orcid.org/0000-0002-5092-5373²](#),
- [M. C. Herrmann¹](#),
- [D. E. Hinkel¹](#),
- [D. D. Ho¹](#),
- [J. P. Holder ORCID: orcid.org/0000-0003-1833-4001¹](#),
- [W. W. Hsing¹](#),

- [H. Huang⁵](#),
- [K. D. Humbird¹](#),
- [N. Izumi ORCID: orcid.org/0000-0003-1114-597X¹](#),
- [L. C. Jarrott¹](#),
- [J. Jeet ORCID: orcid.org/0000-0002-9109-1563¹](#),
- [O. Jones¹](#),
- [G. D. Kerbel¹](#),
- [S. M. Kerr ORCID: orcid.org/0000-0003-4822-564X¹](#),
- [S. F. Khan¹](#),
- [J. Kilkenny⁵](#),
- [Y. Kim²](#),
- [H. Geppert Kleinrath²](#),
- [V. Geppert Kleinrath ORCID: orcid.org/0000-0002-6869-5772²](#),
- [C. Kong⁵](#),
- [J. M. Koning ORCID: orcid.org/0000-0002-8713-7741¹](#),
- [J. J. Kroll¹](#),
- [M. K. G. Kruse¹](#),
- [B. Kustowski ORCID: orcid.org/0000-0003-2085-3206¹](#),
- [O. L. Landen ORCID: orcid.org/0000-0002-1499-8217¹](#),
- [S. Langer¹](#),
- [D. Larson¹](#),
- [N. C. Lemos¹](#),
- [J. D. Lindl¹](#),
- [T. Ma ORCID: orcid.org/0000-0002-6657-9604¹](#),
- [M. J. MacDonald ORCID: orcid.org/0000-0002-6295-6978¹](#),
- [B. J. MacGowan ORCID: orcid.org/0000-0003-1040-1900¹](#),
- [A. J. Mackinnon¹](#),
- [S. A. MacLaren¹](#),
- [A. G. MacPhee¹](#),
- [M. M. Marinak¹](#),
- [D. A. Mariscal¹](#),
- [E. V. Marley¹](#),
- [L. Masse¹](#),
- [K. Meaney²](#),
- [N. B. Meezan ORCID: orcid.org/0000-0002-7671-2886¹](#),
- [P. A. Michel¹](#),
- [M. Millot ORCID: orcid.org/0000-0003-4414-3532¹](#),
- [J. L. Milovich ORCID: orcid.org/0000-0002-9762-3591¹](#),
- [J. D. Moody¹](#),

- [A. S. Moore¹](#),
- [J. W. Morton⁸](#),
- [T. Murphy](#) [ORCID: orcid.org/0000-0002-6137-9873²](#),
- [K. Newman¹](#),
- [J.-M. G. Di Nicola¹](#),
- [A. Nikroo¹](#),
- [R. Nora¹](#),
- [M. V. Patel¹](#),
- [L. J. Pelz¹](#),
- [J. L. Peterson](#) [ORCID: orcid.org/0000-0002-5167-5708¹](#),
- [Y. Ping](#) [ORCID: orcid.org/0000-0002-4879-9072¹](#),
- [B. B. Pollock¹](#),
- [M. Ratledge⁵](#),
- [N. G. Rice⁵](#),
- [H. Rinderknecht](#) [ORCID: orcid.org/0000-0003-4969-5571⁴](#),
- [M. Rosen¹](#),
- [M. S. Rubery⁸](#),
- [J. D. Salmonson¹](#),
- [J. Sater¹](#),
- [S. Schiaffino¹](#),
- [D. J. Schlossberg](#) [ORCID: orcid.org/0000-0002-8713-9448¹](#),
- [M. B. Schneider¹](#),
- [C. R. Schroeder¹](#),
- [H. A. Scott¹](#),
- [S. M. Sepke¹](#),
- [K. Sequoia⁵](#),
- [M. W. Sherlock¹](#),
- [S. Shin¹](#),
- [V. A. Smalyuk¹](#),
- [B. K. Spears](#) [ORCID: orcid.org/0000-0001-6946-8996¹](#),
- [P. T. Springer¹](#),
- [M. Stadermann¹](#),
- [S. Stoupin¹](#),
- [D. J. Strozzi](#) [ORCID: orcid.org/0000-0001-8814-3791¹](#),
- [L. J. Suter¹](#),
- [C. A. Thomas⁴](#),
- [R. P. J. Town¹](#),
- [E. R. Tubman¹](#),
- [P. L. Volegov](#) [ORCID: orcid.org/0000-0003-0361-7500²](#),

- [C. R. Weber¹](#),
- [K. Widmann](#) ORCID: [orcid.org/0000-0001-5623-6619¹](https://orcid.org/0000-0001-5623-6619),
- [C. Wild²](#),
- [C. H. Wilde²](#),
- [B. M. Van Wonterghem¹](#),
- [D. T. Woods¹](#),
- [B. N. Woodworth¹](#),
- [M. Yamaguchi⁵](#),
- [S. T. Yang¹](#) &
- [G. B. Zimmerman¹](#)

Nature volume 601, pages 542–548 (2022)

- 17k Accesses
- 840 Altmetric
- [Metrics details](#)

Subjects

- [Laser-produced plasmas](#)
- [Nuclear fusion and fission](#)

Abstract

Obtaining a burning plasma is a critical step towards self-sustaining fusion energy¹. A burning plasma is one in which the fusion reactions themselves are the primary source of heating in the plasma, which is necessary to sustain and propagate the burn, enabling high energy gain. After decades of fusion research, here we achieve a burning-plasma state in the laboratory. These experiments were conducted at the US National Ignition Facility, a laser facility delivering up to 1.9 megajoules of energy in pulses with peak powers up to 500 terawatts. We use the lasers to generate X-rays in a radiation cavity to indirectly drive a fuel-containing capsule via the X-ray ablation pressure, which results in the implosion process compressing and heating the fuel via mechanical work. The burning-plasma state was created using a strategy to increase the spatial scale of the capsule^{2,3} through two different implosion concepts^{4,5,6,7}. These experiments show fusion self-heating in excess of the mechanical work injected into the implosions, satisfying several burning-plasma metrics^{3,8}. Additionally, we describe a subset of experiments that appear to have crossed the static self-heating boundary, where fusion heating surpasses the energy losses from radiation and conduction. These

results provide an opportunity to study α -particle-dominated plasmas and burning-plasma physics in the laboratory.

[Download PDF](#)

Main

Fusion research fundamentally aims to create a system that produces more energy than was required to create it, a necessary condition for energy applications; in practice, the fusion reaction must be self-sustaining, with self-heating overtaking loss mechanisms, termed ‘ignited’⁹. Such conditions are reached in astrophysical objects including the cores of stars, novae and type 1a supernovae, and in thermonuclear weapons. Ignition in the laboratory requires heating the fuel to incredibly high temperatures, where it becomes a ‘plasma’ and fusion reactions readily occur, while also controlling energy losses. Several approaches have been developed to heat and confine plasma over the past several decades, with most pursuing deuterium–tritium (DT) fuel, which most easily achieves ignition. The dominant approaches to plasma confinement are ‘inertial’, an impulsive burn while the fuel is confined by its own inertia, and ‘magnetic’, in which specialized configurations of magnetic fields provide confinement to the charged particles in the plasma. In order for a DT fusion ($D + T \rightarrow \alpha$ (3.5 MeV) + n (14 MeV)) plasma to become thermally unstable and ignite, it must first obtain a ‘burning’ state. In this regime, self-heating from α -particle deposition exceeds the external heating input into the DT⁸; this ratio is denoted Q_α , where the self-heating is taken relative to the heating power to the plasma—for inertial fusion this is the PdV compressional work on the fuel and not the total laser energy (P , pressure, dV , volume change). $Q_\alpha > 1$ is a burning plasma.

A burning-plasma state signifies a transformational change to the energy and power balance in the DT plasma, opening up the potential for rapidly increasing performance. In the impulsive case of inertial confinement fusion (ICF)¹⁰, Q_α can be stated either as a power during burn, or as an energy integrated over the burn duration, whereas for the near-steady-state operation of magnetic fusion energy (MFE), Q_α is a statement of power. As α -particles carry 1/5 of the total fusion energy per D + T reaction, $Q_\alpha = Q/5$, where Q is the total fusion energy compared to the heating energy supplied. (Or in the MFE case, stated in terms of total fusion power over heating power; for example, the goal of ITER¹¹ is to reach $Q_\alpha \approx 2$ ($Q \approx 10$), whereas the record from the JET tokamak¹² is $Q_\alpha \approx 0.13$ ($Q \approx 0.67$).)

A burning plasma is distinct from other scientific milestones in inertial fusion. In 2014, the first milestone of ‘fuel gain’¹³ ($G_{\text{fuel}} > 1$) was achieved¹⁴, in which the fusion

yield exceeds the energy delivered to the fuel; this corresponds to approximately 12–14 kJ of yield at the National Ignition Facility (NIF). At 20–22 kJ, the yield was approximately doubled by self-heating feedback, termed ‘ α -heating’¹⁵. The next scientific milestone is a burning plasma, as described previously; this is the scientific milestone achieved in this work. No net energy gain, G , relative to the laser energy is expected for a burning plasma. Because of energy losses incurred in achieving the required compressed state, ICF implosions must achieve ignition before a net energy gain is possible. A net energy gain would require fusion yields greater than the laser energy, 1.9 MJ. Although short of ignition or energy gain, a burning plasma ($Q_\alpha > 1$) is a new physics regime for laboratory fusion^{1,11,16}. Studying burning plasmas will elucidate other new physics in this regime, such as self-heating-driven instabilities or kinetic effects in the plasma, which probably depend on the confinement approach.

In a tokamak, the predominant approach to magnetic confinement, once the plasma discharge is generated by resistive heating, external power sources, such as radio-frequency antenna, provide additional plasma heating as the plasma is brought to fusion conditions. In indirect-drive ICF, the way energy is delivered to the fusion fuel is different and much less direct. At NIF¹⁷, 192 lasers deliver up to 1.9 MJ of frequency-tripled light into a high atomic number (Z) ‘hohlraum’ (Fig. 1) that serves the purpose of an X-ray converter generating a nearly Planckian X-ray bath, an approach known as ‘indirect drive’¹⁸. The incident beam-by-beam laser pointing and power in time are designed⁶ to generate a specific radiation temperature (T_{rad}) history (Fig. 1, bottom left) inside the hohlraum, with sufficient uniformity in a way that is matched to specifics of the target geometry and the desired final plasma state. The exposed surface of a capsule at the centre of the hohlraum absorbs approximately 10–15% of the X-rays, causing the outer edge of the capsule (the ablator) to ionize, generate high pressures of the order of hundreds of Mbar (1 Mbar = 10^{11} Pa), and expand away from the capsule—a process termed ablation. A shell of cryogenic DT fuel is layered against the inside surface of the ablator, which is in partial-pressure equilibrium with DT vapour in the centre of the capsule (Fig. 1, top left). The inwardly directed acceleration caused by the ablation drives the capsule and DT fuel inwards upon itself (an implosion, shown schematically at the right of Fig. 1) with enormous acceleration (about 10^{14} m s^{-2}) obtaining velocities of approximately $350\text{--}400 \text{ km s}^{-1}$ in a matter of nanoseconds. Most of the X-ray energy (about 92–95%) absorbed by the capsule is consumed by the ablation process, but as a result the DT fuel obtains considerable (about 10–20 kJ) kinetic energy inside a very small volume.

Fig. 1: Schematic of the indirect-drive inertial confinement approach to fusion.

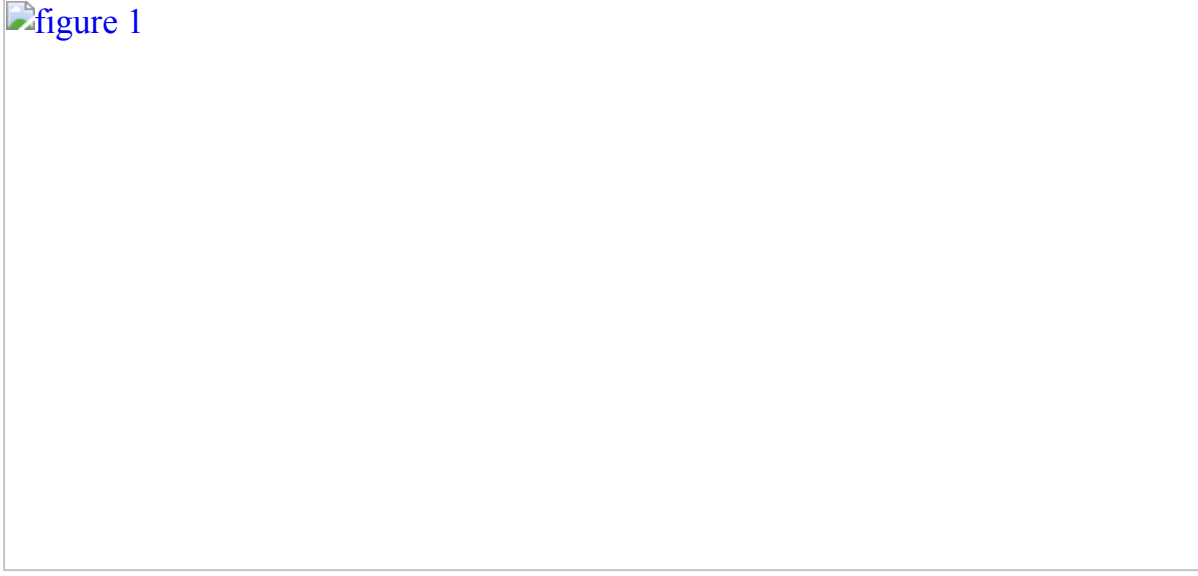


figure 1

Centre, A typical indirect-drive target configuration with key engineering elements labelled. Laser beams (blue) enter the hohlraum through laser entrance holes at various angles. Top left, A schematic pie diagram showing the radial distribution and dimensions of materials in diamond (high-density carbon, HDC) ablator implosions. Bottom left, The temporal laser power pulse-shape (blue) and associated hohlraum radiation temperature (green). Right, At the centre of the hohlraum, the capsule is bathed in X-rays, which ablate the outer surface of the capsule. The pressure generated drives the capsule inward upon itself (an implosion) which compresses and heats the fusion fuel during the implosion process.

Shortly after the DT fuel acquires peak kinetic energy, the pressure (P) inside the implosion rises markedly, to levels of many hundreds of Gbar (1 Gbar = 10^{14} Pa), as kinetic energy is converted into internal energy in the DT (a process termed stagnation). An ICF implosion is a pressure amplifier, sacrificing absorbed energy to achieve high energy density and central pressures that are factors of thousands higher than the pressure at the ablation front. The high central pressure is necessary because only a small fraction of the energy at NIF can ever be coupled into the DT fuel, and heating a large mass of DT fuel is energetically costly, as reflected in the heat capacity of DT, $c_{\text{DT}} = 115 \text{ kJ mg}^{-1} \text{ keV}^{-1}$ ($9.9 \times 10^3 \text{ J kg}^{-1} \text{ K}^{-1}$). In these experiments the total fuel mass is approximately 200 μg and the hot-spot mass is approximately 20–30 μg . As a high ion temperature (T_i) is also needed for fusion, while the fuel stagnates at the centre of the implosion, the DT forms a hot spot from the fuel's inner surface and PdV work is done on the hot spot, generating very high ion and electron temperatures in near thermal equilibrium ($T_i \approx T_e \approx 4\text{--}5 \text{ keV}$, $1 \text{ keV} = 1.16 \times 10^7 \text{ K}$, where T_i and T_e are the ion and electron temperatures). If the conditions of high temperature and pressure

are achieved, the hot spot initiates copious DT fusion reactions and self-heating further increases T_i .

ICF experiments have already demonstrated considerable fusion performance enhancement from self-heating^{14,15}, and more recent advances^{19,20,21} have generated experiments with approximately 50 kJ fusion yields that were close to the burning-plasma threshold³. These experiments used capsules with similar inner radii, between 0.91 and 0.95 mm. Within the maximum laser energy NIF can deliver, these previous designs were limited in the energy coupled to the capsule, and thus in the fuel kinetic energy, by the ability to control the symmetry of the radiation environment within the hohlraum, primarily because an ablated plasma bubble expands from where the outer beams hit the wall (Fig. 1), intercepting the inner beams and thereby suppressing drive at the hohlraum waist^{22,23}. Two tactics have been used to enable symmetry control with more efficient hohlraums driving larger capsules: adjusting cross-beam energy transfer between the outer to inner beams^{4,24,25} by changing the laser wavelength separation ($\Delta\lambda$); and incorporating a pocket in the hohlraum wall at the outer beam location to delay the bubble propagation⁵. These tactics have been used to design higher-efficiency hohlraums that control symmetry; we use these hohlraums to drive capsules that are about 10% larger than prior experiments to realize the strategy for achieving a burning plasma laid out in a previous work². These experimental campaigns are known as ‘Hybrid E’ and ‘I-Raum’; the Hybrid-E campaign uses $\Delta\lambda$ exclusively, whereas I-Raum uses a combination of the pocket and $\Delta\lambda$. Key data and analysis supporting this burning-plasma analysis are given in complementary papers: Ross et al.⁷ (experiments) and Kritch et al.⁶.

Four experiments with these new designs have been conducted that have generated record performance at NIF, with triple the fusion yield compared to past experiments^{4,19,21}, to a maximum of approximately 170 kJ reported here. The experiments are referred to by an experiment number denoting the date of the experiment (for example, in the format YYMMDD, where YY = year, MM = month and DD = day). N201101 and N210207 were experiments using the Hybrid-E platform, and N201122 and N210220 were experiments using the I-Raum platform. The experiments in November (N201101 and N201122) achieved much higher performance relative to past work owing to their increased scale and favourable implosion design parameters, yet each suffered from low-mode degradations; these low-mode asymmetries were mitigated on the subsequent experiments (N210207 and N210220), resulting in higher performance^{6,7}.

On each NIF experiment a comprehensive suite of optical, X-ray and nuclear diagnostics measure key aspects of the implosion performance. Key data are shown in Extended Data Table 1: the total fusion yield in kJ, ion temperature (T_i , measured from

DD reactions)⁷, hot-spot volume and burn width in ps. For a full description of the experimental data and changes between the experiments, see ref. ⁷. Analytic models using these data are used to infer characteristics of the implosion process and hot spot including the pressure, hot-spot internal energy, implosion velocity and peak kinetic energy in the fuel during implosion, PdV work done on the hot spot, and areal density of the hot spot in g cm⁻². These quantities are required to evaluate the burning-plasma criteria. Most of these inferences are described in a previous work²⁶ and Methods; the implosion velocity (v_{imp}) can be inferred from the time of maximum neutron output ('bang time') and an implosion dynamics 'rocket model' that is calibrated to near-neighbour surrogate experiments in which the implosion trajectory is tracked radiographically^{27,28}.

Although it would be desirable to have a direct measure that indicates a burning plasma, such a measurement is not yet known to exist, so inferences from data must be used instead. G_{fuel} has a direct connection to ignited fusion requirements and suggests a simple metric for assessing a burning plasma from $G_{\text{fuel}} = Y/E_{PdV,\text{tot}}$, where Y is the fusion yield and $E_{PdV,\text{tot}}$ is the total PdV work on the fuel (see Methods for how this quantity is evaluated). Figure 2a (also Extended Data Table 1) shows a plot of G_{fuel} data from many DT implosions at NIF versus the product $PT^{1.6}\tau$, where τ is a confinement time; this is a Lawson-like criterion applicable for G_{fuel} (Methods).

Fig. 2: Simple metrics for assessing a burning plasma.

 **figure 2**

a, Total fuel gain versus Lawson-like parameter; $G_{\text{fuel}} > 5$ corresponds to the burning-plasma regime. **b**, Probability distributions for G_{fuel} for high-performing experiments. In these plots the width of the shaded region is proportional to the probability distribution and the solid lines mark the 16th, 50th and 84th percentiles of the distribution **c**, Total α -heating energy versus fuel kinetic energy, $E_{\alpha}/\text{KE}_{\text{fuel}} > 1$ corresponds to $Q_{\alpha} > 1$. **d**, Probability distributions in $E_{\alpha}/\text{KE}_{\text{fuel}}$ criteria for high-performing experiments. Error bars in **a**, **c** are 1 standard deviation (s.d.) and are shown only for the I-Raum and Hybrid-E points. Historical data are from refs. [4](#),[14](#),[15](#),[19](#),[20](#),[21](#),[29](#),[30](#),[31](#).

As can be seen in Fig. 2a, most experimental series show a linear trend between G_{fuel} and $(P\{T\}_{\{\rm{rm}\{i\}}})^{1.6}\tau$ and have $G_{\text{fuel}} \leq 5$; however, the Hybrid-E and I-Raum implosion series show a transition to a super-linear trend between G_{fuel} and $(P\{T\}_{\{\rm{rm}\{i\}}})^{1.6}\tau$ (as expected when self-heating exceeds the hot-spot internal energy) and have $G_{\text{fuel}} > 5$. The non-burning-plasma regime is denoted by the grey shaded region ($G_{\text{fuel}} < 5$). In this and the following figures, historical data from NIF are shown from refs. 4,14,15,19,20,21,29,30,31, labelled by the names of those predecessor campaigns.

Figure 2b shows the probable distribution of the G_{fuel} values plotted in Fig. 2a, with the probability distribution in the inferred data quantities included to evaluate the uncertainty (Methods). For comparison, we include a set of previous high-performing NIF experiments from refs. 4,19,21. The abscissa of Fig. 2b are NIF experiment numbers; although several experiments in years prior to November 2020 came very close to the threshold of $G_{\text{fuel}} = 5$, only the experiments reported here have so far clearly surpassed it (see Extended Data Table 1 for values, where the quoted likelihood is the fraction of the distribution above the threshold).

Alternatively, comparing the total energy produced in α -particles, $E_{\alpha} = Y/5$, to the peak kinetic energy of the DT fuel, KE_{fuel} (Fig. 2c), is another simple metric. Similar to Fig. 2b, Fig. 2d shows the probable range of $E_{\alpha}/KE_{\text{fuel}}$, with normally distributed uncertainties in the input data versus experiment number for the eight highest performing DT experiments at NIF, where again only these four experiments clearly exceed $E_{\alpha}/KE_{\text{fuel}} > 1$ (see Extended Data Table 1 for values). Because indirect-drive implosions have a small fraction of ablator mass remaining at peak velocity it is important to point out that KE_{fuel} is not the total implosion kinetic energy at peak velocity; instead, because the stagnating shell is compressible and extended radially, only a fraction of the kinetic energy of the ablator can be converted to internal energy before peak burn and disassembly.

Although G_{fuel} and $E_{\alpha}/KE_{\text{fuel}}$ are suggestive metrics for an ICF burning plasma, two more rigorous and more stringent metrics already exist in the literature^{3,8}. The burning-plasma statement that ‘ α -deposition is the dominant source of plasma heating’ is complicated by the temporal nature of an implosion, where the PdV work on the hot spot that does the heating comes before the time of peak fusion rate, a consideration that is not analogous to MFE. Prior works by Hurricane et al. gave a condition on velocity (v_{cond})^{2,3} relative to the plasma conditions, which we slightly modify (Methods) to:

$$\$ \$ \{v\}_{\{\{\rm c\}\}\{\rm o\}\{\rm n\}\{\rm d\}}\}(\rho R_{\{\{\rm h\}\}\{\rm s\}}\}, \\ \{T\}_{\{\{\rm i\}\}}\})=5.3\times 10^{25} \rho R_{\{\{\rm h\}\}\{\rm s\}}\}\frac{\langle\sigma v\rangle}{\langle T\rangle_{\{\{\rm i\}\}}}>\{v\}_{\{\{\rm i\}\}\{\rm m\}\{\rm p\}}\} \$ \$$$

(1)

in units of keV, g, cm and s. Here, ρR_{hs} is the hot-spot areal density and $\langle\sigma v\rangle$ is the fusion reactivity.

To evaluate the Hurricane metric, the temperature and areal density of the hot spot, and the implosion velocity, are needed (Methods). The thermonuclear reactivity $\langle\sigma v\rangle$ is a function of the hot-spot conditions, specifically the temperature; we use the $\langle\sigma v\rangle$ evaluation of Bosch and Hale³². Figure 3a shows the experiments in hot-spot temperature and areal density parameter space. Previous experiments are shown as points, and the present four experiments are shown as full probability distributions (red, N201101; blue, N201122; purple, N210207; grey, N210220), with contours enclosing 80% of the distribution. In Fig. 3a a single contour of equation (1) for $v_{imp}=385 \text{ km s}^{-1}$, representative of these experiments, is shown. When evaluating the criteria for the actual inferred velocity of each experiment, with uncertainty, is used. These are the first experiments to exceed the Hurricane criterion, as clearly shown by the probability distributions in Fig. 3b. The likelihood of these four experiments exceeding the criteria is 89% (N201101), 79% (N201122), and 100% for both N210207 and N210220.

Fig. 3: ICF-specific burning-plasma metrics.

 **figure 3**

a, Criteria on temperature and hot-spot ρR established by Hurricane et al.³. Previous experiments are shown as points, and the present four experiments are shown as full probability distributions (red, N201101; blue, N201122; purple, N210207; grey, N210220), with contours enclosing 80% of the distribution. A single contour of equation (1) for $v_{\text{imp}} = 385 \text{ km s}^{-1}$ is given by the solid black line. **b**, Probability distribution for experiments exceeding the Hurricane criterion, >1 is a burning plasma. **c**, Criteria on α -heating and PdV work from a previous work⁸, including estimates from data inferences (solid symbols) and from 2D simulations (open symbols). **d**, Probability distribution for experiments exceeding the Betti criteria. For these

experiments distributions are shown for data-inferred $E_{PdV,hs}$ (blue) and using 2D simulations (orange). Error bars in **a**, **c** are 1 s.d. and are shown only for the I-Raum and Hybrid-E points. Historical data are from refs. [4,14,15,19,20,21,29,30,31](#).

Equation (1) should be roughly equivalent to the burning-plasma criteria found by Betti et al. ($3.5\times$ yield amplification and $0.5E_\alpha/E_{PdV,hs} > 1$)⁸, but for completeness we use both. The first criterion by Betti et al., $Y_{amp} \geq 3.5$, is satisfied by our inferred yield amplifications given in Extended Data Table 1, inferred with the prescription in ref. [26](#) and from two-dimensional (2D) simulations⁶ using HYDRA³³. Two quantities are required to evaluate the second Betti et al. burning-plasma metric. The α -deposited energy (E_α) is straightforward as it is simply 20% of the measured total fusion yield (given in Extended Data Table 1), which is approximately 20 kJ for the first two experiments, about 33 kJ for N210207, and about 31 kJ for N210220. The second input for these criteria is the PdV work done upon the hot spot, which must be inferred; however, such inferences are prone to large uncertainties in the presence of considerable α -heating and bremsstrahlung X-ray losses. We perform this inference in two ways (Methods), first using an analytic hydrodynamic piston model³⁴ of an implosion, and second by extracting PdV work from the 2D radiation–hydrodynamics simulations that best match the experimental observables described in ref⁶. These two estimates are used to estimate a range in hot-spot PdV work, and are both plotted in Fig. 3c compared to previous experiments at NIF, with a 1–1 line to denote the burning-plasma regime (above the line). Probability distributions for the metric quantity itself are shown in Fig. 3d. From Betti’s criteria, with the experimental (simulated) $E_{PdV,hs}$, we assess that 74% (0%) and 97% (2%) probability for experiments N201101 and N201122, respectively, are in the burning-plasma regime. The difference in probability reflects the fact that the simulated PdV work is higher and thus is more pessimistic for satisfying the criteria, with the simulated values for these experiments being below the burning-plasma threshold. With improved performance, experiments N210207 and N210220 are assessed to be in the burning-plasma regime with 100% confidence by both experimental and simulated methodologies. These correspond to an inferred $Q_\alpha \approx 1.4\text{--}1.6$ for experiment N210207, and $Q_\alpha \approx 1.3\text{--}2.0$ for experiment N210220.

Several metrics for assessing whether these implosions created a burning-plasma state have been discussed and presented in Extended Data Table 1 and Figs. 2, 3. In each case, burning-plasma likelihoods are calculated by propagating uncertainties in each quantity through the metric (Methods), shown in the figures with likelihood values discussed and summarized in Extended Data Table 1. Quantitatively, we see that the first two (N201101 and N201122) are probably in the burning-plasma regime by all metrics, except Betti’s, when evaluated with the simulated $E_{PdV,hs}$; the most recent experiments (N210207 and N210220) are overwhelmingly likely to have passed this

threshold. Qualitatively, our confidence in this conclusion is further increased by the use of multiple independent metrics.

The achievement of a burning-plasma state is key progress towards the larger goal of ‘ignition’ and overall energy gain in inertial fusion. The fusion yields reported here (approximately 0.17 MJ) are lower than the input laser energy (approximately 1.9 MJ), but are nearly equal to the capsule absorbed energy (giving capsule gain of about 0.7–0.8) and are an order of magnitude greater than the input energy transferred to the fusion fuel. Moreover, the total fusion power ($5mP_a$ where P_a is the power per unit mass) generated in the two highest performing experiments are at petawatt levels (for example, approximately 1.6 ± 0.2 PW for N210207).

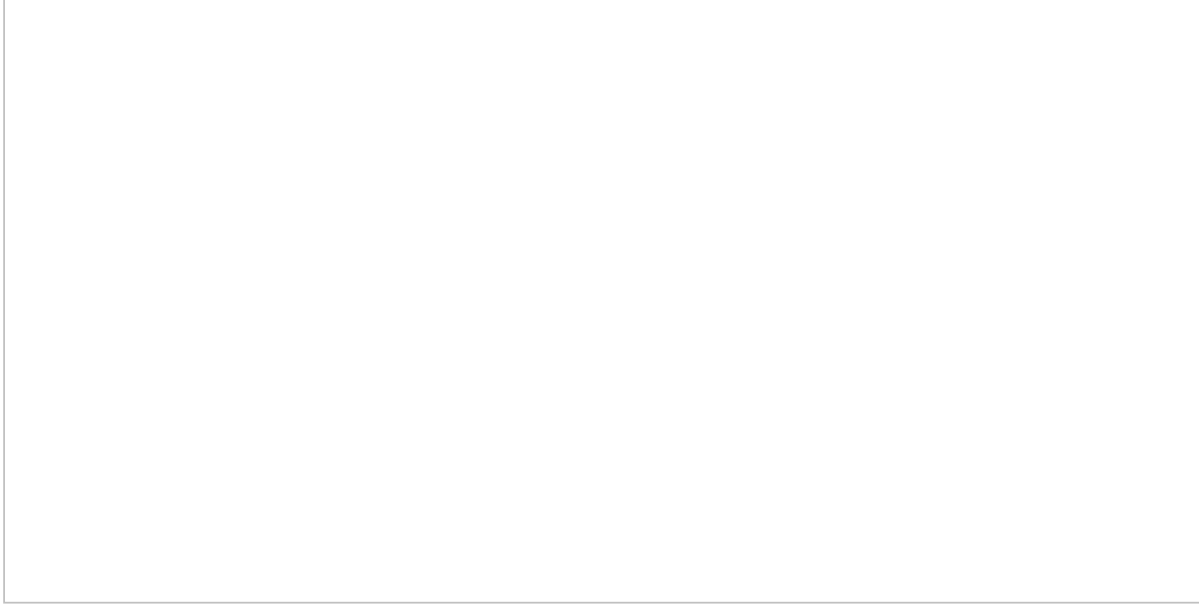
In the burning-plasma regime, self-heating can overtake loss mechanisms, which include bremsstrahlung losses, thermal conductivity and negative PdV work upon expansion. Simple expressions for the power-balance terms are given in the Methods and values for the four experiments are given in Extended Data Table 1. Here, we use a bremsstrahlung enhancement factor $f_b \approx 1.15$ that is inferred from the data³⁵. The first two experiments have self-heating comparable to the radiation losses. An important new regime is when self-heating power (P_a) is greater than both the radiation (P_b) and conduction losses (P_e)—that is, $f_a P_a > P_b + P_e$, where f_a is the fraction of α -particles stopping in the hot spot³⁶. A contour for this regime is shown in Fig. 3a by the black dashed line. Experiment N210220 is close to entering this regime, and we infer that experiment N210207 has entered this regime with 82% likelihood. The level of α -heating in this work is still short of that required for ignition.

To achieve ignition—defined as a yield amplification ($Y_{\text{amp}} \approx 20\text{--}30$) consistent with about 1 MJ fusion yield³⁷, and then high gain—further progress is needed. Figure 4 shows these experiments in the larger context of ignition, in the parameter space of hot-spot pressure and energy (Fig. 4, left) and in yield amplification versus a Lawson-like parameter called the ‘ignition threshold factor’ experimentally inferred (ITFX)^{8,26,38} for conditions without α -heating (n_α) (Fig. 4, right). Figure 4, right, plots this quantity as $\sqrt{\left(\frac{P^2 E_{\text{hs}}}{\text{ITFX}_{n_\alpha}}\right)^2 - \left(\frac{n_\alpha}{\alpha}\right)^2}$, which is approximately equivalent to χ_{n_α} as defined previously⁸. Proximity to ignition can be gauged qualitatively in terms of the product $P^2 E_{\text{hs}}$ (equivalent to $(\rho R_{\text{hs}} T_i)^3$), or in terms of ITFX _{n_α} or $\chi_{n_\alpha} \approx 1$, representing ignition. Figure 4, left, shows contours of $P^2 E_{\text{hs}}$ relative to N210207, showing that this metric has been improved by a factor of several from previous results. From Fig. 4 we clearly see that these four experiments are the closest to ignition, but a further increase in ITFX _{n_α} from approximately 0.6 → 1 is required. As this Article was being finalized, a new experiment in this series on 8 August 2021 produced approximately 1.35 MJ of fusion yield and capsule gain of

approximately 5, breaking all previous records. This was announced by our institution in a press release³⁹; this experiment will be described in a future publication.

Fig. 4: Parameter space relevant for proximity to ignition.

 figure 4



Left, hot-spot pressure and energy. The product $P^2 E_{hs}$ is representative of proximity to ignition; contours of this metric relative to N210207 are shown by the dashed grey curves. Right, yield amplification (Y_{amp}) versus $ITFX_{na}$. These are the highest performing ICF experiments so far and the closest to ignition. The inset shows these experiments in detail with both inferred (solid) and simulated (open) Y_{amp} . Error bars are 1 s.d. and are shown only for the I-Raum and Hybrid-E points, plus shot N180128. Historical data are from refs. [4](#),[14](#),[15](#),[19](#),[20](#),[21](#),[29](#),[30](#),[31](#).

As discussed in the complementary papers^{6,7}, these experiments have clear and specific degradation mechanisms, which can be mitigated for further improvement in performance. More generally, the ICF programme at NIF is pursuing several approaches that can enable additional progress: reducing degradation mechanisms including low-mode asymmetry^{40,41,42} and radiative losses from mix³⁵, further increasing energy coupled to the capsule^{4,43}, and improving compression of the fuel⁴⁴.

In conclusion, we have generated in the laboratory a burning- plasma state in which the plasma is predominantly self-heated. This was accomplished using inertial fusion implosions at the US NIF; previous experiments here were just below the threshold for a burning plasma. We increased the capsule scale relative to previous work, increased the coupling efficiency from laser energy to the capsule, and controlled implosion symmetry using new tactics. Four experiments have been conducted that have passed

the threshold for a burning plasma by several metrics, with especially high confidence on the most recent two experiments. Additionally, the highest performing experiment (N210207) is in a more stringent regime where the self-heating surpasses energy losses from radiation and conduction. Although these results are short of total energy gain from the system owing to the inherent inefficiencies of ICF, these experiments represent a substantial step towards this goal with record values of parameters that assess our proximity to ignition at NIF. Several promising avenues for further increases in performance are identified and will be pursued by the US inertial fusion programme, in addition to novel physics in the burning-plasma regime such as α -particle-driven processes.

Methods

Terminology

Definitions of commonly used mathematical symbols are summarized in Extended Data Table 2.

Reproducibility

Experiments subsequent to those described in this Article have demonstrated the reproducibility of a burning-plasma state at NIF, with two additional experiments that have performance comparable to the highest-performing experiments in this Article. These newer experiments, N210307 and N210605, were conducted in the Hybrid E platform. N210307 repeated N210207, albeit using a capsule from a different fabrication batch and produced a yield of approximately 145 kJ with an experimentally inferred $Q_\alpha = 1.34 \pm 0.07$ from the Hurricane criterion. Experiment N210605 reduced the thickness of the ice layer relative to N210207 and resulted in a lower yield (135 kJ) but high ion temperature, with $Q_\alpha = 1.40 \pm 0.10$, again from the Hurricane criterion. These additional experiments confirm that the burning-plasma state is reproducible at NIF, and full details and analysis on them will be presented in future publications.

Inferred hot-spot conditions

Hot-spot conditions must be inferred from measured quantities using a model. The simplest hot-spot model is to assume an isobaric volume of uniform conditions, as used in a previous work¹⁴ between equations 2 and 3, in which case the hot-spot number density is given by

$$\text{\$}\$n=1.2\times 10^6\sqrt{\frac{Y}{\langle\sigma v\rangle V_{hs}}}\tau,\$\$$$

(2)

where Y is the fusion yield in J, $\langle\sigma v\rangle$ is the fusion reactivity, which depends on the ion temperature (T_i), V_{hs} is the hot-spot volume in cm^3 , and τ is the burn duration in s, for equimolar DT mixtures. The remaining hot-spot quantities follow from the inferred density, including the pressure ($P = (1 + Z)n k_B T_i$, with k_B Boltzmann's constant), hot-spot energy ($E_{hs} = 1.5PV_{hs}$), and areal density $\rho R \sqrt{3V}/(2.5\pi a^3)$.

A more detailed inference is to use a one-dimensional (1D) profile in radius for temperature and density, maintaining the isobaric assumption. A conduction-limited profile follows the expression⁴⁵:

$$\$T(r) = \{T\}_{\min} + (\{T\}_0 - \{T\}_{\min}) \left[1 - \frac{r - \{R\}_0}{1 + \beta} \right]^2, \quad (3)$$

where T_{\min} is the temperature at the boundary, T_0 is the central temperature and R_0 is the hot-spot boundary. β is the thermal conductivity power law, 2.5 from classical Spitzer conductivity. Following a previous work²⁶ we use a lower value, $\beta=2/3$, which accounts for additional physics, dynamical processes and reproduces radiation-hydrodynamics simulations. The density profile is then determined by the isobaric assumption through $P \propto nT$ being constant. T_{\min} is taken as 1 keV leaving T_0 , R_0 and P as free parameters in the model; the data are compared to synthetic data calculated from this 1D profile with the model parameters adjusted to minimize residuals. As in the zero-dimensional (0D) model, the hot-spot energy simply follows from pressure and volume, and the areal density is the mass density integrated over the inferred radial profile.

In either dimensionality the model's radius is matched to the experimental measurements, which take a contour of emission level, by calculating synthetic emission images to calculate an equivalent contour radius. The measurements include 2D and three-dimensional (3D) asymmetries, so an equivalent spherical volume, and radius, are calculated using the modal decompositions, where the emission contour measured from the equator (R_{eq}) and pole (R_{po}) are

$\$ \$ \{R\}_{{\ell}} = \{P\}_0 + \sum_{{\ell}'} \delta_{\ell\ell'} P_{{\ell}'} \cos \theta, \$$

$$(4) \quad \$\$ R_{\rm m} = M_0 \left(1 + \sum_m (\delta_m M_m) \right) \times \cos [m(\varphi - \varphi_i)] \\ (5)$$

$$\$ \$ \{R\}_{\{\rm hs\}} = \frac{\{R\}_{\{\rm eq\}} \{R\}_{\{\rm po\}}}{\{M\}_0}, \$ \$ (6)$$

where P_0 and M_0 are the average measured sizes from each view, δP_ℓ (δM_m) is the relative modal amplitude, often referred to as P_ℓ/P_0 with the nomenclature above chosen for clarity. P_ℓ are the Legendre polynomials, and ϕ_m are the orientation of the azimuthal modes. R_{hs} is the hot-spot radius as a function of both θ and ϕ , which is integrated to obtain the volume. Here, the dominant parameters are P_0 , M_0 and δP_2 , which are given in ref. [7](#).

Implosion velocity (v_{imp}) is inferred using a rocket model of the implosion^{[46](#)} constrained by both supporting experiments, especially in-flight radiography, and the measured time of peak nuclear production on each experiment. The inferred yield amplification given in Extended Data Table [1](#) is a function of the measured yield, shell compression and fuel mass (m_{fuel}); both the velocity and Y_{amp} inferences use the prescription given in a previous work^{[26](#)}. The fuel kinetic energy then follows from $\frac{1}{2} m_{\text{fuel}} v_{\text{imp}}^2$. Our techniques for inferring the PdV work done on the fuel are discussed in the following section.

A comparison of inferred values using 0D and 1D models are shown in Extended Data Table [3](#). Inferred pressures are highly consistent between these calculations, whereas hot-spot energies and areal densities are higher in the 1D model owing to substantial mass near the 1 keV temperature cut-off.

Inferring G fuel

The total fusion yield produced by a mass (m) of DT, over a characteristic confinement time, τ , is $Y \approx 5mP_\alpha\tau$ —with $P_\alpha = 8.2 \times 10^{24} \rho \langle \sigma v \rangle$ in $\text{GJ g}^{-1} \text{s}^{-1}$ the specific DT fusion power for a given mass density, ρ , of DT with reaction rate $\langle \sigma v \rangle$ —and the internal energy in that DT is $E_{\text{hs}} = c_{\text{DT}} m T_i$. Therefore, one can write (O.A.H. et al., manuscript in preparation)

$$\begin{aligned} \$\$ \{G\}_{\{\rm fuel\}} = & \frac{Y}{E_{\rm dV,tot}} \approx \\ & \frac{\frac{Y}{E_{\rm hs}}}{1 + \frac{E_{\rm fuel}}{E_{\rm hs}}} - \frac{q}{10} \frac{Y}{E_{\rm hs}}, \\ (7) \end{aligned}$$

with

$$\$\$ \frac{Y}{E_{\rm hs}} \approx 4.6 \times 10^{26} P \langle \sigma v \rangle \langle T \rangle^2 \tau, \\ (8)$$

where P is in Gbar, T_i in keV, and τ in s. In equation (7), the total energy delivered by PdV work, $E_{PdV,\text{tot}}$, is determined from the hot spot and compressed, but cold, DT fuel energy at stagnation, E_{hs} and E_{fuel} , respectively, at peak compression. The last term in the denominator represents a correction for additional energy retained by self-heating of the fuel from α -particle deposition but not then lost as bremsstrahlung. So, $E_{PdV,\text{tot}} \approx E_{\text{hs}} + E_{\text{fuel}} - qY/10$, where q is a ‘quality’ factor, $0 \leq q \leq 1$, measuring the ability of the implosion to retain self-heating energy (O.A.H. et al., manuscript in preparation). Here we use $q \approx 0.7$, inferred from simulations, and the factor of 10 results from one-fifth of the fusion energy released as α -particles and half of those produced up until the time of peak fusion burn. Albeit generally arrived at in a different fashion than above, the product $P(\langle \sigma v \rangle / T^2)\tau$ is Lawson’s⁹ parameter for ignition. Figure 2a uses the useful reaction-rate approximation $\langle \langle \sigma v \rangle \rangle \approx 4.2 \times 10^{-20} \langle T \rangle^{\langle \langle i \rangle \rangle^3.6}$ (in units of $\text{cm}^3 \text{s}^{-1}$ for ion temperature range $3.5 < T_i < 6.5 \text{ keV}$) to simplify the abscissa.

An expression for the fuel gain is given in equation (7). The yield is measured and the hot-spot energy is inferred as described in the previous section. Precisely determining the cold-fuel energy from data is not straightforward. For the purposes of this analysis we actually require the total PdV work done on all the DT. This is at a minimum the fuel kinetic energy and internal energy at peak velocity, which are both inferred. This neglects any work done by the inflowing remaining ablator material on the fuel, which can occur in these implosions. In this case the hot-spot energy is more than half the previous estimate; in this scenario we assume equipartition between the hot spot and cold fuel to evaluate equation (7).

Inferred PdV work

The primary uncertainty in the Betti metric⁸ is in the inference of PdV work on the hot spot. Here we use three methodologies: two inferences using an analytic model, and a direct extraction of PdV work from simulations that match the experimental observables.

We use the hydrodynamic piston model of an implosion described previously³⁴. This analytic model abstracts the implosion process using opposed pistons to represent the imploding shell. In spherical geometry, the stagnation pressure from this mechanical work on the hot spot is given by (equation 24 in ref. ³⁴):

$$\text{Equation 9: } \frac{\rho \delta R_{\text{ave}}}{v_{\text{imp}}^2 R_{\text{hs}}} = \frac{(1-f)^2}{(1+f)^2},$$

where $\rho \delta R_{\text{ave}}$ is the average shell areal density, calculated from the measured neutron ‘down-scattered ratio’ (DSR) using the relation $\rho \delta R_{\text{ave}} \approx 19.3 \text{DSR}$, v_{imp} is the implosion velocity and R_{hs} is the average hot-spot radius (which can be obtained from the volume, V_{hs} , given in Extended Data Table 1). The factor f^2 represents the effect of mode-1 asymmetry and is a measure of the residual kinetic energy (kinetic energy that is never converted into internal energy) in the implosion.

From the piston pressure we obtain the hot-spot internal energy (E_{hs}) from

$$\frac{E_{hs}}{V} = \frac{3}{2} P_{piston} \quad (10)$$

In the absence of α -heating (which adds energy to the hot-spot) and radiative X-ray losses, or when α -heating exactly balances X-ray losses, then $E_{hs} = E_{PdV,hs}$. For low yield amplification implosions ($Y_{amp} < 1.5$), X-ray losses dominate over α -heating energy gains, so $E_{hs} < E_{PdV,hs}$. For higher yield amplification implosions ($Y_{amp} > 2$), α -heating energy gains start to dominate over X-ray losses, so $E_{hs} > E_{PdV,hs}$. The estimated values for these four experiments are given in Extended Data Table 4 as the piston methodology.

We can also estimate the stagnated fuel mass in a similar fashion, using

$$m_{shell} = 4\pi R_{ave}^2 \rho \Delta R \quad (11)$$

which allows us to then estimate the total mass that stagnates from $m_{shell} + m_{hs}$, with m_{hs} from the hot-spot inferences described earlier. We then estimate the PdV work from

$$E_{PdV} = P_{hs} V_{hs} = 0.73 \frac{m_{shell} + m_{fuel}}{m_{hs}} \frac{m_{fuel}}{m_{hs}} \quad (12)$$

where m_{fuel} is the initial fuel mass. The factor of 0.73 is derived from 1D simulations in which the imploding mass stagnates efficiently, and we drop the residual kinetic energy factor f^2 because the inferred shell mass does not include non-stagnated material. This estimate leads to smaller estimates of $E_{PdV,hs}$ than the first empirical estimate, and are given in Extended Data Table 4 as the stagnated mass estimate.

For analysis of previously published campaigns we use the simple relation $E_{PdV,hs} \approx (0.5\text{--}0.7)\text{KE}_{\text{fuel}}(1 - f^2)$, this is easy to evaluate with the available data and the factor 0.5–0.7 accounts for a wide range of 1D to 2D/3D behaviour observed on past experiments. For comparison, the proportionality constant inferred from the first methodology (equation (10)) is between 0.60 and 0.73 for our four experiments.

We also use radiation–hydrodynamics simulations to estimate the PdV work done on these implosions. The first simulation-based methodology is to use 2D simulations with degradation mechanisms that match the observed performance, and interrogate the work done upon the mass elements that form the hot spot to infer $E_{PdV,hs}$. The simulation methodology is described in ref. [6](#), and the values of $E_{PdV,hs}$ for this method are given in Extended Data Table [4](#). The same fusion performance can be generated with varying application of degradation mechanisms that either degrade $E_{PdV,hs}$ or do not; an estimate of the 2D simulation uncertainty of ± 0.5 kJ is estimated by studying multiple simulations.

A similar energy-balance analysis can be done with 1D simulations, in which the work done upon the hot spot is well defined with a Lagrangian mesh. The 1D simulations are tuned to match the measured yields, but are expected to underestimate $E_{PdV,hs}$ since they cannot properly incorporate residual kinetic energy. This estimate is given in Extended Data Table [4](#) as an upper bound.

We have thus developed four methodologies for estimating $E_{PdV,hs}$. In the main analysis we use a combination of the empirical piston model estimate as the more pessimistic data-based inference, and use the 2D simulated $E_{PdV,hs}$ as the most robust computational description of the experiments.

Modified Hurricane metric

At peak burn, the time rate of change of hot-spot volume, dV/dt , is nearly zero, and therefore so is the heating rate, so time integration is needed. Mathematically, a statement of a burning plasma appropriate for ICF is

$$\begin{aligned} & \text{\$\$}\{\int\}_{0}^{\{t\}_{\{\rm pf\}}}\{P\}_{\{\alpha\}}\{\rm d\}t>-\int\}_{0}^{\{t\}_{\min V}}\frac{P}{m}\{\rm d\}V,\text{\$\$} \\ (13) \end{aligned}$$

where t_{pf} is the time of peak fusion rate, and $t_{\min V}$ is the time of minimum hot-spot volume.

The integrals in equation (13) are easily approximated² without knowing the details of the actual implosion using the mathematical method of steepest descent; assuming that the thermodynamic quantities of interest, such as T , P , ρ , and so on, are impulsive, being highly peaked around the time of stagnation. Ultimately, the solution to equation (13), in terms of only burn-average hot-spot areal density, ρR_{hs} , T_i and v_{imp} is equation (1) after a correction to the original derivation.

A recent note from our colleagues at Los Alamos⁴⁷ discovered an arithmetic error in the derivation of the criteria as published in ref. ³. The error is in going from equation 8 to equation 9 in ref. ³, in which the conversion to peak temperature (T_0) to burn-averaged temperature (T_{hs}) should be, for $n \approx 4$,

$$\begin{aligned} & \text{\$\$}\backslash\begin{array}{c}\backslash\frac{\backslash\langle\sigma v\rangle}{\{T\}_0}\backslash\approx\{\left(\backslash\frac{n+1}{n}\right)^{\backslash\frac{n-1}{2}}\}\backslash\frac{\backslash\langle\sigma v\rangle\{T\}_0}{\{\rm hs\}}\backslash\approx\\& \backslash 1.40\backslash\frac{\backslash\langle\sigma v\rangle}{\{T\}_0}\backslash\end{array}\text{\$\$} \\ (14) \end{aligned}$$

Additionally, we now believe that the inclusion of the fraction of α -particles stopping in the hot spot (f_α) in ref. ³ was inappropriate. When considering the temperature evolution of a defined mass—for example, the self-heating criterion in [equation \(17\)](#)—this is necessary because f_α is fundamentally the fraction of α -particle energy deposited into that mass. On the other hand, the burning-plasma criteria is one on the energy of the hot spot,

$$\begin{aligned} & \text{\$\$}\{E\}_{\{\rm hs\}}=\{c\}_{\{\rm DT\}}\{m\}_{\{\rm hs\}} \\ & \{T\}_{\{\rm hs\}},\text{\$\$} \end{aligned}$$

(15)

and α -particles that escape the hot spot still contribute to its energy via generation of additional hot-spot mass, as seen by examining the time derivative of the above:

Therefore, the inclusion of f_α in a burning-plasma criterion is inappropriate. We note that not including an f_α factor is consistent with other criteria, for example, ref. ⁸. With these two modifications to the criterion published in ref. ³ we use a new criterion (equation (1)). This modified criterion is slightly more restrictive for the burning-plasma threshold in the regime relevant to these experiments.

Model uncertainties for Hurricane's metric

The Hurricane metric³ depends on more quantities than the Betti metric, although these quantities are more straightforward to infer than $E_{PdV,hs}$. The metric reduces to equation (1) where ρR_{hs} and v_{imp} are inferred as described previously, and T_i is measured. $\langle \sigma v \rangle$ contains some systematic uncertainty from the evaluation used. Data uncertainties are well defined for T_i and in the inference of ρR_{hs} and v_{imp} , and are propagated as described in the next section; the inferred ρR_{hs} can also vary between models, which will be discussed.

Equation (1) depends on the fusion reactivity; in this work we use the evaluation from Bosch and Hale³². Recent publications have presented alternative evaluations⁴⁸ which differ by about 2%. We note that the

inferred $\langle \rho R \rangle \propto 1/\sqrt{\langle \sigma v \rangle}$ from equation (2), so the condition in equation (1) depends on the reactivity as $1/\sqrt{\langle \sigma v \rangle}$. f_α is also weakly increasing with ρR , leading to the condition being slightly less than square-root dependent on $\langle \sigma v \rangle$, so this criterion has <1% uncertainty from the choice of $\langle \sigma v \rangle$ evaluation.

The Hurricane criterion is sensitive to the inferred hot-spot ρR , which can vary between models depending on the spatial dependence of ρ . As shown in Extended Data Table 3, the 0D and 1D hot-spot models agree quite well. We also check these values using a 3D reconstruction of the hot-spot density and temperature profiles (a yet unpublished method of L. Divol, but briefly described in ref. 35): for N201101 this gives a value of $\rho R_{hs} \approx 0.36 - 0.38 \text{ g cm}^{-2}$ to the 1-keV contour for N201101 and $\rho R_{hs} \approx 0.35 - 0.36 \text{ g cm}^{-2}$ for N201122. These values are consistent with the simple models described earlier.

Self-heating regime

The hot-spot per unit mass power balance is:

$$\frac{c_{DT}}{\rho \alpha} = \frac{P_\alpha}{\rho \alpha} - \frac{f_b P_b}{\rho \alpha} - \frac{P_e}{\rho \alpha} - \frac{P_m}{\rho \alpha} \frac{dV}{dt}, \quad (17)$$

which describes the temporal evolution of the temperature (T) in terms of the balance of self heating (P_α) versus bremsstrahlung (P_b) and electron conduction (P_e) losses plus PdV work. Here electron conduction losses are calculated relative to a hot-spot boundary that is defined relative to a fraction of the peak burn rate or a specified ion temperature. Thermal conduction cools the hot spot while increasing the mass of the hot spot. Because the fusion burn rate is more strongly dependent on the temperature of the spot than its mass in the temperature range achieved by compression alone, α -heating must provide sufficient heating for the hot-spot temperature to increase in the presence of this conduction into an increasing

mass. Hot-spot volume change, dV/dt , is negative on implosion, increasing T . During expansion the PdV term becomes an energy loss term. The bremsstrahlung loss can be enhanced beyond the emission of clean DT by the presence of high-Z contamination of the DT (that is, mix), by a fraction f_b . In equation (17), f_a is the fraction of α -particles stopped in the hot spot, evaluated using fits with modern stopping-power theory³⁶.

Uncertainty analysis

We perform uncertainty analysis for all hot-spot quantities by propagating the normally distributed uncertainties in measured quantities through the 0D and 1D models described earlier. The model input parameters are those that fully describe the system, and are constrained by the measured yield, ion temperature, burn widths (from both X-rays and γ -rays), and volume from the 17% contour of neutron emissivity. Distributions of model parameters are generated using Markov chain Monte Carlo (MCMC), calculated with the tensorflow⁴⁹ probability package. The log-likelihood function for MCMC is defined by the measurements and calculated with the log-likelihood function

$$-\frac{1}{2} \sum_i \left(\frac{m_i - y_i}{\delta y_i} \right)^2 \quad (18)$$

which is summed over all observables (i) where m_i is the model value, y_i is the measured value and δy_i is the uncertainty in the measurement. This methodology produces full distributions of the model parameters including any correlations, from the model parameter distributions we generate full distributions of all hot-spot parameters, some of which exhibit correlation, such as in the temperature and areal density required to evaluate the Hurricane metric, which are partially anti-correlated (evident in Fig. 3a). Other inferences, such as the implosion velocity or kinetic energy, are treated with normally distributed uncertainties that are uncorrelated with the hot-spot inferences.

Power-balance relations

In evaluating the power-balance relations relevant to [equation \(17\)](#), we use the following expressions for the individual terms:

$$\text{P}_\alpha = 8.2 \times 10^{24} \rho \langle \sigma v \rangle \quad , \quad (19)$$

$$\text{P}_b = 3.1 \times 10^7 \rho \sqrt{T}, \quad (20)$$

$$\text{P}_e = 5.9 \times 10^3 \frac{\rho}{R^2}. \quad (21)$$

In these expressions the specific powers are given in units of $\text{GJ g}^{-1} \text{s}^{-1}$ and thus are multiplied by the inferred hot-spot mass to obtain power. ρ is the hot-spot mass in g cm^{-3} , $\langle \sigma v \rangle$ is the fusion reactivity evaluated as a function of temperature in $\text{cm}^3 \text{s}^{-1}$, T is the temperature in keV, and ρR is the hot-spot areal density in g cm^{-2} . The self-heating power P_α is multiplied by the fraction of α -particle energy deposited in the hot spot (f_α) using the evaluation published in ref. [36](#); for all four experiments, $f_\alpha \approx 0.77\text{--}0.80$.

Data availability

Raw data were generated at the National Ignition Facility. Derived data supporting the findings of this study are available from the corresponding authors upon request.

References

1. 1.

National Academies of Sciences, Engineering, and Medicine. *Final Report of the Committee on a Strategic Plan for U.S. Burning Plasma Research* (National Academies Press, 2019).

2. 2.

Hurricane, O. A. et al. Beyond alpha-heating: driving inertially confined fusion implosions toward a burning-plasma state on the National Ignition Facility. *Plasma Phys. Control. Fusion* **61**, 014033 (2019).

3. 3.

Hurricane, O. A. et al. Approaching a burning plasma on the NIF. *Phys. Plasmas* **26**, 052704 (2019).

4. 4.

Zylstra, A. B. et al. Record energetics for an inertial fusion implosion at NIF. *Phys. Rev. Lett.* **126**, 025001 (2021).

5. 5.

Robey, H. F., Berzak Hopkins, L., Milovich, J. L. & Meezan, N. B. The I-Raum: a new shaped hohlraum for improved inner beam propagation in indirectly-driven ICF implosions on the National Ignition Facility. *Phys. Plasmas* **25**, 012711 (2018).

6. 6.

Kritch, A. et al. Design of inertial fusion implosions reaching the burning plasma regime. *Nat. Phys.* (in the press).

7. 7.

Ross, J. S. et al. Experiments conducted in the burning plasma regime with inertial fusion implosions. Preprint at <https://arxiv.org/abs/2111.04640> (2021).

8. 8.

Betti, R. et al. Alpha heating and burning plasmas in inertial confinement fusion. *Phys. Rev. Lett.* **114**, 255003 (2015).

9. 9.

Lawson, J. D. Some criteria for a power producing thermonuclear reactor. *Proc. Phys. Soc. B* **70**, 6 (1957).

10. 10.

Nuckolls, J., Wood, L., Thiessen, A. & Zimmerman, G. Laser compression of matter to super-high densities: thermonuclear (CTR) applications. *Nature* **239**, 139–142 (1972).

11. 11.

Green, B. & ITER International Team and Participant Teams ITER: burning plasma physics experiment. *Plasma Phys. Control. Fusion* **45**, 687–706 (2003).

12. 12.

Keilhacker, M. et al. High fusion performance from deuterium–tritium plasmas in JET. *Nucl. Fusion* **39**, 209–234 (1999).

13. 13.

Atzeni, S. & Meyer-ter-Vehn, J. *The Physics of Inertial Fusion* (Oxford Univ. Press, 2004).

14. 14.

Hurricane, O. et al. Fuel gain exceeding unity in an inertially confined fusion implosion. *Nature* **506**, 343–348 (2014).

15. 15.

Hurricane, O. A. et al. Inertially confined fusion plasmas dominated by alpha-particle self-heating. *Nat. Phys.* **12**, 800–806 (2016).

16. 16.

Coppi, B. In *Academician A. D. Sakharov. Scientific Works. To His Centenary* (eds B. L. Altshuler, et al.) (Fizmatlit, 2021).

17. 17.

Moses, E. I. et al. The National Ignition Facility: transition to a user facility. In *8th Intl Conf. Inertial Fusion Sciences and Applications (IFSA 2013)* Vol. 688 012073 (2016).

18. 18.

Lindl, J. Development of the indirect-drive approach to inertial confinement fusion and the target physics basis for ignition and gain. *Phys. Plasmas* **2**, 3933–4024 (1995).

19. 19.

Le Pape, S. et al. Fusion energy output greater than the kinetic energy of an imploding shell at the National Ignition Facility. *Phys. Rev. Lett.* **120**, 245003 (2018).

20. 20.

Casey, D. T. et al. The high velocity, high adiabat, “Bigfoot” campaign and tests of indirect-drive implosion scaling. *Phys. Plasmas* **25**, 056308 (2018).

21. 21.

Baker, K. L. et al. Hotspot parameter scaling with velocity and yield for high-adiabat layered implosions at the National Ignition Facility. *Phys. Rev. E* **102**, 023210 (2020).

22. 22.

Callahan, D. A. et al. Exploring the limits of case-to-capsule ratio, pulse length, and picket energy for symmetric hohlraum drive on the National Ignition Facility Laser. *Phys. Plasmas* **25**, 056305 (2018).

23. 23.

Hopkins, L. B. et al. Toward a burning plasma state using diamond ablator inertially confined fusion (ICF) implosions on the National Ignition Facility (NIF). *Plasma Phys. Control. Fusion* **61**, 014023 (2018).

24. 24.

Michel, P. et al. Symmetry tuning via controlled crossed-beam energy transfer on the National Ignition Facility. *Phys. Plasmas* **17**, 056305 (2010).

25. 25.

Glenzer, S. H. et al. Symmetric inertial confinement fusion implosions at ultra-high laser energies. *Science* **327**, 1228–1231 (2010).

26. 26.

Patel, P. K. et al. Hotspot conditions achieved in inertial confinement fusion experiments on the National Ignition Facility. *Phys. Plasmas* **27**, 050901 (2020).

27. 27.

Landen, O. L. et al. Capsule implosion optimization during the indirect-drive National Ignition Campaign. *Phys. Plasmas* **18**, 051002 (2011).

28. 28.

Meezan, N. B. et al. X-ray driven implosions at ignition relevant velocities on the National Ignition Facility. *Phys. Plasmas* **20**, 056311 (2013).

29. 29.

Baker, K. L. et al. High-performance indirect-drive cryogenic implosions at high adiabat on the National Ignition Facility. *Phys. Rev. Lett.* **121**, 135001 (2018).

30. 30.

Döppner, T. et al. Achieving 280 Gbar hot spot pressure in DT-layered CH capsule implosions at the national ignition facility. *Phys. Plasmas* **27**, 042701 (2020).

31. 31.

Hohenberger, M. et al. Integrated performance of large HDC-capsule implosions on the National Ignition Facility. *Phys. Plasmas* **27**, 112704 (2020).

32. 32.

Bosch, H.-S. & Hale, G. Improved formulas for fusion cross-sections and thermal reactivities. *Nucl. Fusion* **32**, 611–631 (1992).

33. 33.

Marinak, M. M. et al. Three-dimensional HYDRA simulations of National Ignition Facility targets. *Phys. Plasmas* **8**, 2275–2280 (2001).

34. 34.

Hurricane, O. A. et al. An analytic asymmetric-piston model for the impact of mode-1 shell asymmetry on ICF implosions. *Phys. Plasmas* **27**, 062704 (2020).

35. 35.

Pak, A. et al. Impact of localized radiative loss on inertial confinement fusion implosions. *Phys. Rev. Lett.* **124**, 145001 (2020).

36. 36.

Zylstra, A. B. & Hurricane, O. A. On alpha-particle transport in inertial fusion. *Phys. Plasmas* **26**, 062701 (2019).

37. 37.

Christopherson, A. R., Betti, R. & Lindl, J. D. Thermonuclear ignition and the onset of propagating burn in inertial fusion implosions. *Phys. Rev. E* **99**, 021201 (2019).

38. 38.

Spears, B. K. et al. Performance metrics for inertial confinement fusion implosions: Aspects of the technical framework for measuring progress in the National Ignition Campaign. *Phys. Plasmas* **19**, 056316 (2012).

39. 39.

LLNL. National Ignition Facility experiment puts researchers at threshold of fusion ignition. *Lawrence Livermore National Laboratory – News* <https://www.llnl.gov/news/national-ignition-facility-experiment-puts-researchers-threshold-fusion-ignition> (18 August 2021).

40. 40.

Rinderknecht, H. G. et al. Azimuthal drive asymmetry in inertial confinement fusion implosions on the National Ignition Facility. *Phys. Rev. Lett.* **124**, 145002 (2020).

41. 41.

Tommasini, R. et al. Time-resolved fuel density profiles of the stagnation phase of indirect-drive inertial confinement implosions. *Phys. Rev. Lett.* **125**, 155003 (2020).

42. 42.

Casey, D. T. et al. Evidence of three-dimensional asymmetries seeded by high-density carbon-ablator nonuniformity in experiments at the National Ignition Facility. *Phys. Rev. Lett.* **126**, 025002 (2021).

43. 43.

Amendt, P. et al. Ultra-high (>30%) coupling efficiency designs for demonstrating central hot-spot ignition on the National Ignition Facility using a Frustraum. *Phys. Plasmas* **26**, 082707 (2019).

44. 44.

Landen, O. L. et al. Yield and compression trends and reproducibility at NIF. *High Energy Density Phys.* **36**, 100755 (2020).

45. 45.

Cerjan, C., Springer, P. T. & Sepke, S. M. Integrated diagnostic analysis of inertial confinement fusion capsule performance. *Phys. Plasmas* **20**, 056319 (2013).

46. 46.

Hurricane, O. A. et al. On the importance of minimizing “coast-time” in X-ray driven inertially confined fusion implosions. *Phys. Plasmas* **24**, 092706 (2017).

47. 47.

Albright, B. et al. Comment on the burning plasma condition of Hurricane et. al [*Phys. Plasmas* 26, 052704, 2019] and implications for the experimental achievement of a burning plasma state on the NIF. Report No. LA-UR-21-25149 (Los Alamos National Laboratory, 2021).

48. 48.

de Souza, R. S., Boston, S. R., Coc, A. & Iliadis, C. Thermonuclear fusion rates for tritium + deuterium using Bayesian methods. *Phys. Rev. C* **99**, 014619 (2019).

49. 49.

Abadi, M. et al. Tensorflow: a system for large-scale machine learning. In *Proc. 12th USENIX Symp. Operating Systems Design and*

Implementation (OSDI'16) (eds Keeton, K. & Roscoe, T.) 265–283
(USENIX Association, 2016).

Acknowledgements

We thank B. Coppi (MIT), S. C. Cowley (PPPL), D. Whyte (MIT), J. Hammer (LLNL), M. Farrell (GA) and J. Kline (LANL) for discussions. The contributions of NIF operations and target fabrication teams to the success of these experiments are acknowledged. This work was performed under the auspices of the US Department of Energy by Lawrence Livermore National Laboratory under contract DE-AC52-07NA27344. This document was prepared as an account of work sponsored by an agency of the US government. Neither the US government nor Lawrence Livermore National Security, LLC, nor any of their employees makes any warranty, expressed or implied, or assumes any legal liability or responsibility for the accuracy, completeness, or usefulness of any information, apparatus, product, or process disclosed, or represents that its use would not infringe privately owned rights. Reference herein to any specific commercial product, process, or service by trade name, trademark, manufacturer, or otherwise does not necessarily constitute or imply its endorsement, recommendation, or favouring by the US government or Lawrence Livermore National Security, LLC. The views and opinions of authors expressed herein do not necessarily state or reflect those of the US government or Lawrence Livermore National Security, LLC, and shall not be used for advertising or product endorsement purposes. Document release number: LLNL-JRNL-819741-DRAFT.

Author information

Author notes

1. These authors contributed equally: A. B. Zylstra, O. A. Hurricane

Affiliations

1. Lawrence Livermore National Laboratory, Livermore, CA, USA

A. B. Zylstra, O. A. Hurricane, D. A. Callahan, A. L. Kritcher, J. E. Ralph, J. S. Ross, C. V. Young, K. L. Baker, D. T. Casey, T. Döppner, L. Divol, M. Hohenberger, A. Pak, P. K. Patel, R. Tommasini, S. J. Ali, P. A. Amendt, L. J. Atherton, B. Bachmann, D. Bailey, L. R. Benedetti, L. Berzak Hopkins, S. D. Bhandarkar, J. Biener, R. M. Bionta, E. J. Bond, D. K. Bradley, T. Braun, T. M. Briggs, M. W. Bruhn, P. M. Celliers, B. Chang, T. Chapman, H. Chen, C. Choate, A. R. Christopherson, D. S. Clark, E. L. Dewald, T. R. Dittrich, M. J. Edwards, W. A. Farmer, J. E. Field, D. Fittinghoff, J. Gaffney, G. P. Grim, S. Haan, K. D. Hahn, G. N. Hall, B. A. Hammel, J. Harte, E. Hartouni, J. E. Heebner, V. J. Hernandez, M. C. Herrmann, D. E. Hinkel, D. D. Ho, J. P. Holder, W. W. Hsing, K. D. Humbird, N. Izumi, L. C. Jarrott, J. Jeet, O. Jones, G. D. Kerbel, S. M. Kerr, S. F. Khan, J. M. Koning, J. J. Kroll, M. K. G. Kruse, B. Kustowski, O. L. Landen, S. Langer, D. Larson, N. C. Lemos, J. D. Lindl, T. Ma, M. J. MacDonald, B. J. MacGowan, A. J. Mackinnon, S. A. McLaren, A. G. MacPhee, M. M. Marinak, D. A. Mariscal, E. V. Marley, L. Masse, N. B. Meezan, P. A. Michel, M. Millot, J. L. Milovich, J. D. Moody, A. S. Moore, K. Newman, J.-M. G. Di Nicola, A. Nikroo, R. Nora, M. V. Patel, L. J. Pelz, J. L. Peterson, Y. Ping, B. B. Pollock, M. Rosen, J. D. Salmonson, J. Sater, S. Schiaffino, D. J. Schlossberg, M. B. Schneider, C. R. Schroeder, H. A. Scott, S. M. Sepke, M. W. Sherlock, S. Shin, V. A. Smalyuk, B. K. Spears, P. T. Springer, M. Stadermann, S. Stoupin, D. J. Strozzi, L. J. Suter, R. P. J. Town, E. R. Tubman, C. R. Weber, K. Widmann, B. M. Van Wonterghem, D. T. Woods, B. N. Woodworth, S. T. Yang & G. B. Zimmerman

2. Los Alamos National Laboratory, Los Alamos, NM, USA

H. F. Robey, N. W. Birge, H. Herrmann, Y. Kim, H. Geppert Kleinrath, V. Geppert Kleinrath, K. Meaney, T. Murphy, P. L. Volegov & C. H. Wilde

3. Laboratoire pour l'utilisation des Lasers Intenses chez École Polytechnique, Palaiseau, France

S. Le Pape

4. Laboratory for Laser Energetics, University of Rochester, Rochester, NY, USA

R. Betti, H. Rinderknecht & C. A. Thomas

5. General Atomics, San Diego, CA, USA

J. W. Crippen, H. Huang, J. Kilkenny, C. Kong, M. Ratledge, N. G. Rice, K. Sequoia & M. Yamaguchi

6. Massachusetts Institute of Technology, Cambridge, MA, USA

J. Frenje & M. Gatu Johnson

7. SLAC National Accelerator Laboratory, Menlo Park, CA, USA

S. H. Glenzer

8. Atomic Weapons Establishment, Aldermaston, UK

J. W. Morton & M. S. Rubery

9. Diamond Materials, Freiburg, Germany

C. Wild

Contributions

A.B.Z. hot-spot analysis lead, Hybrid-E experimental lead, wrote sections of the paper; O.A.H. capsule scale/burning-plasma strategy, theory, 0D hot-spot models, and wrote sections of paper; D.A.C. empirical hohlraum P_2 model and hohlraum strategy; A.L.K. Hybrid-E design lead, integrated hohlraum group lead, wrote sections of paper; J.E.R. N201101 and N210207 experimentalist and shot-responsible individual (shot RI); H.F.R. original I-Raum design lead; J.S.R. I-Raum experimental lead and N201122 shot RI; C.V.Y. present I-Raum design lead, wrote sections of paper; K.L.B. Hybrid shot RI; D.T.C. Hybrid shot RI; T.D. Hybrid shot RI; L.D. 3D hot-spot analysis; M.H. Hybrid shot RI; S.L.P. Hybrid shot RI; A.P. Hybrid and

I-Raum shot RI, physics of capsule engineering defects; P.K.P. 1D hot-spot analysis, Y_{amp} and GLC inference; R.T. Hybrid shot RI; S.J.A. capsule microstructure physics; P.A.A. hohlraum physics; L.J.A. engineering and targets; B.B. penumbral X-ray diagnostic; D.B. computational physics; L.R.B. X-ray framing camera; L.B.H. HDC design and campaign lead; R.B. ICF physics/ignition theory; S.D.B. cryo-layering; J.B. capsule fabrication; R.M.B. RTNAD nuclear diagnostic; N.W.B. neutron diagnostics; E.J.B. project engineering; D.K.B. diagnostics; T.B. capsule fab and metrology; T.M.B. cryo-layering; M.W.B. project engineering; P.M.C. DT EOS measurements; B.C. HYDRA code development; T.C. LPI physics; H.C. GLEH X-ray diagnostic; C.C. target fab planning; A.R.C. ignition theory; D.S.C. capsule/instability physics; J.W.C. capsule fabrication; E.L.D. experiments; T.R.D. capsule physics; M.J.E. programme management; W.A.F. hohlraum physics; J.E.F. 2DConA image analysis; D.F. nuclear diagnostics; J.F. magnetic recoil spectrometer nuclear diagnostic; J.G. ensemble simulations; M.G.J. magnetic recoil spectrometer diagnostic; S.H.G. ICF physics; G.P.G. nuclear diagnostics; S.H. capsule physics, iPOM analysis; K. D. Hahn neutron diagnostics; G.N.H. experiments; B.A.H. capsule physics; J.H. computational physics; E.H. nuclear time-of-flight diagnostics; J.E.H. MOR and PAM stability, SSD improvements, and FC control; V.J.H. MOR and PAM stability, SSD improvements, and FC control; H. Herrman gamma diagnostics; M.C.H. programme management; D.E.H. hohlraum physics, CBET studies in Hybrid-C; D.D.H. capsule physics; J.P.H. X-ray diagnostics; W.W.H. management; H. Huang capsule fabrication; K. D. Humbird ensemble simulations; N.I. X-ray diagnostics; L.C.J. X-ray diagnostics; J.J. neutron diagnostics; O.J. hohlraum physics; G.D.K. HYDRA code development; S.M.K. neutron diagnostics; S.F.K. X-ray diagnostics and analysis; J.K. diagnostic management; Y.K. gamma diagnostics; H.G.K. gamma diagnostics; V.G.K. neutron diagnostics; C.K. capsules; J.M.K. HYDRA code development; J.J.K. targets; M.K.G.K. ICF physics; B.K. ensemble simulations; O.L.L. velocity analysis; S.L. laser plasma instability (PF3D) code development; D.L. NIF facility management; N.C.L. optical diagnostics; J.D.L. ICF physics; T. Ma ICF physics; M.J.M. X-ray diagnostics; B.J.M. mode-1 analysis, backscatter; A.J.M. diagnostic management; S.A.M. integrated design physics; A.G.M. X-ray diagnostics; M.M.M. HYDRA code development lead; D.A.M. X-ray diagnostics; E.V.M. X-ray diagnostics; L.M. capsule physics; K.M. gamma

diagnostics; N.B.M. advanced hohlraum lead; P.A.M. LPI physics; M.M. optical diagnostics; J.L.M. hohlraum physics; J.D.M. hohlraum physics; A.S.M. neutron diagnostics; J.W.M. hohlraum physics; T. Murphy neutron and gamma diagnostics; K.N. project engineering; J.G.D.N. MOR and PAM stability, SSD improvements and FC control; A.N. target fab engineering, capsule and fab planning; R.N. ensembles simulations; M.V.P. HYDRA code development; L.J.P. MOR and PAM stability, SSD improvement and FC control; J.L.P. ensembles simulations; Y.P. hohlraum physics; B.B.P. hohlraum physics; M. Ratledge capsule fabrication; N.G.R. capsule fabrication; H.R. RTNAD mode-1 analysis; M. Rosen hohlraum physics; M.S.R. X-ray diagnostics; J.D.S. hohlraum physics; J.S. mode-1 analysis; S. Schiaffino capsules; D. J. Schlossberg neutron diagnostics; M.B.S. hohlraum diagnostics; C.R.S. HYDRA code development; H.A.S. NLTE opacities (Cretin) code development; S.M.S. HYDRA code development; K.S. mode-1 metrology; M.W.S. kinetic physics; S. Shin sagometer data and particle analysis; V.A.S. capsule physics; B.K.S. ensemble simulations; P.T.S. dynamic model, ignition theory; M.S. capsules; S. Stoupin X-ray diagnostics; D. J. Strozzi hohlraum/LPI physics; L.J.S. hohlraum physics; C.A.T. Bigfoot design physics; R.P.J.T. programme management; E.R.T. optical diagnostics; P.L.V. neutron imaging diagnostics; C.R.W. capsule/instability physics; K.W. X-ray diagnostics; C.W. capsule fabrication; C.H.W. neutron diagnostics; B.M.V.W. NIF operations lead; D.T.W. hohlraum physics; B.N.W. project engineering; M.Y. capsule fabrication; S.T.Y. MOR and PAM stability, SSD improvements and FC control; G.B.Z. computational physics lead.

Corresponding authors

Correspondence to [A. B. Zylstra](#) or [O. A. Hurricane](#).

Ethics declarations

Competing interests

The authors declare no competing interests.

Peer review information

Nature thanks Shinsuke Fujioka, Erik Lefebvre and Nigel Woolsey for their contribution to the peer review of this work.

Additional information

Extended data

is available for this paper at <https://doi.org/10.1038/s41586-021-04281-w>.

Publisher's note Springer Nature remains neutral with regard to jurisdictional claims in published maps and institutional affiliations.

Extended data figures and tables

Extended Data Table 1 Scalar metrics for these experiments

Extended Data Table 2 Symbols

Extended Data Table 3 Hot-spot models

Extended Data Table 4 *PdV* work methodologies

Rights and permissions

Open Access This article is licensed under a Creative Commons Attribution 4.0 International License, which permits use, sharing, adaptation, distribution and reproduction in any medium or format, as long as you give appropriate credit to the original author(s) and the source, provide a link to the Creative Commons license, and indicate if changes were made. The images or other third party material in this article are included in the article's Creative Commons license, unless indicated otherwise in a credit line to the material. If material is not included in the article's Creative Commons license and your intended use is not permitted by statutory regulation or exceeds the permitted use, you will need to obtain permission directly from the copyright holder. To view a copy of this license, visit <http://creativecommons.org/licenses/by/4.0/>.

[Reprints and Permissions](#)

About this article

Cite this article

Zylstra, A.B., Hurricane, O.A., Callahan, D.A. *et al.* Burning plasma achieved in inertial fusion. *Nature* **601**, 542–548 (2022).
<https://doi.org/10.1038/s41586-021-04281-w>

- Received: 24 May 2021
- Accepted: 25 November 2021
- Published: 26 January 2022
- Issue Date: 27 January 2022
- DOI: <https://doi.org/10.1038/s41586-021-04281-w>

Share this article

Anyone you share the following link with will be able to read this content:

[Get shareable link](#)

Sorry, a shareable link is not currently available for this article.

[Copy to clipboard](#)

Provided by the Springer Nature SharedIt content-sharing initiative

[Design of inertial fusion implosions reaching the burning plasma regime](#)

- A. L. Kritcher
- C. V. Young

- G. B. Zimmerman

Letter Open Access 26 Jan 2022

Self-heating plasmas offer hope for energy from fusion

- Nigel Woolsey

News & Views 26 Jan 2022

This article was downloaded by **calibre** from <https://www.nature.com/articles/s41586-021-04281-w>

| [Section menu](#) | [Main menu](#) |

- Article
- Open Access
- [Published: 26 January 2022](#)

Deep physical neural networks trained with backpropagation

- [Logan G. Wright](#) [ORCID: orcid.org/0000-0001-7696-1260](#)^{1,2} natl,
- [Tatsuhiro Onodera](#) [ORCID: orcid.org/0000-0002-6912-6504](#)^{1,2} natl,
- [Martin M. Stein](#)¹,
- [Tianyu Wang](#) [ORCID: orcid.org/0000-0002-6087-6376](#)¹,
- [Darren T. Schachter](#)³,
- [Zoey Hu](#)¹ &
- [Peter L. McMahon](#) [ORCID: orcid.org/0000-0002-1177-9887](#)¹

Nature volume **601**, pages 549–555 (2022)

- 15k Accesses
- 186 Altmetric
- [Metrics details](#)

Subjects

- [Computational science](#)
- [Nonlinear optics](#)

Abstract

Deep-learning models have become pervasive tools in science and engineering. However, their energy requirements now increasingly limit their scalability¹. Deep-learning accelerators^{2,3,4,5,6,7,8,9} aim to perform deep learning energy-efficiently, usually targeting the inference phase and often by exploiting physical substrates beyond conventional electronics. Approaches so far^{10,11,12,13,14,15,16,17,18,19,20,21,22} have been unable to apply the backpropagation algorithm to train unconventional novel hardware *in situ*. The advantages of backpropagation have made it the de facto training

method for large-scale neural networks, so this deficiency constitutes a major impediment. Here we introduce a hybrid *in situ*–*in silico* algorithm, called physics-aware training, that applies backpropagation to train controllable physical systems. Just as deep learning realizes computations with deep neural networks made from layers of mathematical functions, our approach allows us to train deep physical neural networks made from layers of controllable physical systems, even when the physical layers lack any mathematical isomorphism to conventional artificial neural network layers. To demonstrate the universality of our approach, we train diverse physical neural networks based on optics, mechanics and electronics to experimentally perform audio and image classification tasks. Physics-aware training combines the scalability of backpropagation with the automatic mitigation of imperfections and noise achievable with *in situ* algorithms. Physical neural networks have the potential to perform machine learning faster and more energy-efficiently than conventional electronic processors and, more broadly, can endow physical systems with automatically designed physical functionalities, for example, for robotics^{23,24,25,26}, materials^{27,28,29} and smart sensors^{30,31,32}.

[Download PDF](#)

Main

Like many historical developments in artificial intelligence^{33,34}, the widespread adoption of deep neural networks (DNNs) was enabled in part by synergistic hardware. In 2012, building on earlier works, Krizhevsky et al. showed that the backpropagation algorithm could be efficiently executed with graphics-processing units to train large DNNs³⁵ for image classification. Since 2012, the computational requirements of DNN models have grown rapidly, outpacing Moore’s law¹. Now, DNNs are increasingly limited by hardware energy efficiency.

The emerging DNN energy problem has inspired special-purpose hardware: DNN ‘accelerators’^{2,3,4,5,6,7,8}, most of which are based on direct mathematical isomorphism between the hardware physics and the mathematical operations in DNNs (Fig. 1a, b). Several accelerator proposals use physical systems beyond conventional electronics⁸, such as optics⁹ and analogue electronic crossbar arrays^{3,4,12}. Most devices target the inference phase of deep learning, which accounts for up to 90% of the energy costs of deep learning in commercial deployments¹, although, increasingly, devices are also addressing the training phase (for example, ref. 7).

Fig. 1: Introduction to PNNs.

 **figure 1**

a, Artificial neural networks contain operational units (layers): typically, trainable matrix-vector multiplications followed by element-wise nonlinear activation functions. **b**, DNNs use a sequence of layers and can be trained to implement multi-step (hierarchical) transformations on input data. **c**, When physical systems evolve, they perform, in effect, computations. We partition their controllable properties into input data and control parameters. Changing parameters alters the transformation performed on data. We consider three examples. In a mechanical (electronic) system, input data and parameters are encoded into time-dependent forces (voltages) applied to a metal plate (nonlinear circuit). The controlled multimode oscillations (transient voltages) are then measured by a microphone (oscilloscope). In a nonlinear optical system, pulses pass through a $\chi^{(2)}$ crystal, producing nonlinearly mixed outputs. Input data and parameters are encoded in the input pulses' spectra, and outputs are obtained from the frequency-doubled pulses' spectra. **d**, Like DNNs constructed from sequences of trainable nonlinear mathematical functions, we construct deep PNNs with sequences of trainable physical transformations. In PNNs, each physical layer implements a controllable physical function, which does need to be mathematically isomorphic to a conventional DNN layer.

However, implementing trained mathematical transformations by designing hardware for strict, operation-by-operation mathematical isomorphism is not the only way to perform efficient machine learning. Instead, we can train the hardware’s physical transformations directly to perform desired computations. Here we call this approach physical neural networks (PNNs) to emphasize that physical processes, rather than mathematical operations, are trained. This distinction is not merely semantic: by breaking the traditional software–hardware division, PNNs provide the possibility to opportunistically construct neural network hardware from virtually any controllable physical system(s). As anyone who has simulated the evolution of complex physical systems appreciates, physical transformations are often faster and consume less energy than their digital emulations. This suggests that PNNs, which can harness these physical transformations most directly, may be able to perform certain computations far more efficiently than conventional paradigms, and thus provide a route to more scalable, energy-efficient and faster machine learning.

PNNs are particularly well motivated for DNN-like calculations, much more so than for digital logic or even other forms of analogue computation. As expected from their robust processing of natural data, DNNs and physical processes share numerous structural similarities, such as hierarchy, approximate symmetries, noise, redundancy and nonlinearity³⁶. As physical systems evolve, they perform transformations that are effectively equivalent to approximations, variants and/or combinations of the mathematical operations commonly used in DNNs, such as convolutions, nonlinearities and matrix–vector multiplications. Thus, using sequences of controlled physical transformations (Fig. 1c), we can realize trainable, hierarchical physical computations, that is, deep PNNs (Fig. 1d).

Although the paradigm of constructing computers by directly training physical transformations has ancestry in evolved computing materials¹⁸, it is today emerging in various fields, including optics^{14,15,17,20}, spintronic nano-oscillators^{10,37}, nanoelectronic devices^{13,19} and small-scale quantum computers³⁸. A closely related trend is physical reservoir computing (PRC)^{21,22}, in which the transformations of an untrained physical ‘reservoir’ are linearly combined by a trainable output layer. Although PRC harnesses generic physical processes for computation, it is unable to realize DNN-like hierarchical computations. In contrast, approaches that train the physical transformations^{13,14,15,16,17,18,19} themselves can, in principle, overcome this limitation. To train physical transformations experimentally, researchers have frequently relied on gradient-free learning algorithms^{10,18,19,20}. Gradient-based learning algorithms, such as the backpropagation algorithm, are considered essential for the efficient training and good generalization of large-scale DNNs³⁹. Thus, proposals to realize gradient-based training in physical hardware have appeared^{40,41,42,43,44,45,46,47}. These inspiring proposals nonetheless make assumptions that exclude many physical systems, such as linearity, dissipation-free evolution or

that the system be well described by gradient dynamics. The most general proposals^{13,14,15,16} overcome such constraints by performing training in silico, that is, learning wholly within numerical simulations. Although the universality of in silico training is empowering, simulations of nonlinear physical systems are rarely accurate enough for models trained in silico to transfer accurately to real devices.

Here we demonstrate a universal framework using backpropagation to directly train arbitrary physical systems to execute DNNs, that is, PNNs. Our approach is enabled by a hybrid in situ–in silico algorithm, called physics-aware training (PAT). PAT allows us to execute the backpropagation algorithm efficiently and accurately on any sequence of physical input–output transformations. We demonstrate the universality of this approach by experimentally performing image classification using three distinct systems: the multimode mechanical oscillations of a driven metal plate, the analogue dynamics of a nonlinear electronic oscillator and ultrafast optical second-harmonic generation (SHG). We obtain accurate hierarchical classifiers that utilize each system’s unique physical transformations, and that inherently mitigate each system’s unique noise processes and imperfections. Although PNNs are a radical departure from traditional hardware, it is easy to integrate them into modern machine learning. We show that PNNs can be seamlessly combined with conventional hardware and neural network methods via physical–digital hybrid architectures, in which conventional hardware learns to opportunistically cooperate with unconventional physical resources using PAT. Ultimately, PNNs provide routes to improving the energy efficiency and speed of machine learning by many orders of magnitude, and pathways to automatically designing complex functional devices, such as functional nanoparticles²⁸, robots^{25,26} and smart sensors^{30,31,32}.

An example PNN based on nonlinear optics

Figure 2 shows an example PNN based on broadband optical pulse propagation in quadratic nonlinear media (ultrafast SHG). Ultrafast SHG realizes a physical computation roughly analogous to a nonlinear convolution, transforming the input pulse’s near-infrared spectrum (about 800-nm centre wavelength) into the blue (about 400 nm) through a multitude of nonlinear frequency-mixing processes ([Methods](#)). To control this computation, input data and parameters are encoded into sections of the spectrum of the near-infrared pulse by modulating its frequency components using a pulse shaper (Fig. 2a). This pulse then propagates through a nonlinear crystal, producing a blue pulse whose spectrum is measured to read out the result of the physical computation.

Fig. 2: An example PNN, implemented experimentally using broadband optical SHG.

 **figure 2**

a, Input data are encoded into the spectrum of a laser pulse ([Methods](#), Supplementary Section 2). To control transformations implemented by the broadband SHG process, a portion of the pulse's spectrum is used as trainable parameters (orange). The physical computation result is obtained from the spectrum of a blue (about 390 nm) pulse generated within a $\chi^{(2)}$ medium. **b**, To construct a deep PNN, the outputs of the SHG transformations are used as inputs to subsequent SHG transformations, with independent trainable parameters. **c, d**, After training the SHG-PNN (see main text, Fig. 3), it classifies test vowels with 93% accuracy. **c**, The confusion matrix for the PNN on the test set. **d**, Representative examples of final-layer output spectra, which show the SHG-PNN's prediction.

To realize vowel classification with SHG, we construct a multilayer SHG-PNN (Fig. 2b) where the input data for the first physical layer consist of a vowel-formant frequency vector. After the final physical layer, the blue output spectrum is summed using a digital computer into seven spectral bins (Fig. 2b, d, Supplementary Figs. 21, 22). The predicted vowel is identified by the bin with the maximum energy (Fig. 2c). In each layer, the output spectrum is digitally renormalized before being passed to the next layer (via the pulse shaper), along with a trainable digital rescaling.

Mathematically, this transformation is given by

$$(\{\{\bf{x}\}\})^{[l+1]} = \frac{a\{\bf{y}\}}{\max(\{\{\bf{y}\}\})^{[l]} + b},$$

where $\mathbf{x}^{[l]}$ and $\mathbf{y}^{[l]}$ are the inputs and outputs of the $[l]$ th layer, respectively, and a and b are scalar parameters of the transformation. Thus, the SHG-PNN's computations are carried out almost entirely by the trained optical transformations, without digital activation functions or output layers.

Deep PNNs essentially combine the computational philosophy of techniques such as PRC^{21,22} with the trained hierarchical computations and gradient-based training of deep learning. In PRC, a physical system, often with recurrent dynamics, is used as an untrained feature map and a trained linear output layer (typically on a digital computer) combines these features to approximate desired functions. In PNNs, the backpropagation algorithm is used to adjust physical parameters so that a sequence of physical systems performs desired computations physically, without needing an output layer. For additional details, see Supplementary Section 3.

Physics-aware training

To train the PNNs' parameters using backpropagation, we use PAT (Fig. 3). In the backpropagation algorithm, automatic differentiation determines the gradient of a loss function with respect to trainable parameters. This makes the algorithm N -times more efficient than finite-difference methods for gradient estimation (where N is the number of parameters). The key component of PAT is the use of mismatched forward and backward passes in executing the backpropagation algorithm. This technique is well known in neuromorphic computing^{48,49,50,51,52,53}, appearing recently in direct feedback alignment⁵² and quantization-aware training⁴⁸, which inspired PAT. PAT generalizes these strategies to encompass arbitrary physical layers, arbitrary physical network architectures and, more broadly, to differentially programmable physical devices.

Fig. 3: Physics-aware training.

 **figure 3**

a, PAT is a hybrid *in situ*–*in silico* algorithm to apply backpropagation to train controllable physical parameters so that physical systems perform machine-learning tasks accurately even in the presence of modelling errors and physical noise. Instead of performing the training solely within a digital model (*in silico*), PAT uses the physical systems to compute forward passes. Although only one layer is depicted in **a**, PAT generalizes naturally to multiple layers ([Methods](#)). **b**, Comparison of the validation accuracy versus training epoch with PAT and *in silico* training, for the experimental SHG-PNN depicted in Fig. [2b](#). **c**, Final experimental test accuracy for PAT and *in silico* training for SHG-PNNs with increasing numbers of physical layers. The length of error bars represent two standard errors.

PAT proceeds as follows (Fig. [3](#)). First, training input data (for example, an image) are input to the physical system, along with trainable parameters. Second, in the forward pass, the physical system applies its transformation to produce an output. Third, the physical output is compared with the intended output to compute the error. Fourth, using a differentiable digital model, the gradient of the loss is estimated with respect to the controllable parameters. Finally, the parameters are updated according to the inferred gradient. This process is repeated, iterating over training examples, to reduce the error. See [Methods](#) for the intuition behind why PAT works and the general multilayer algorithm.

The essential advantages of PAT stem from the forward pass being executed by the actual physical hardware, rather than by a simulation. Our digital model for SHG is very accurate (Supplementary Fig. 20) and includes an accurate noise model (Supplementary Figs. 18, 19). However, as evidenced by Fig. 3b, in silico training with this model still fails, reaching a maximum vowel-classification accuracy of about 40%. In contrast, PAT succeeds, accurately training the SHG-PNN, even when additional layers are added (Fig. 3b, c).

Diverse PNNs for image classification

PNNs can learn to accurately perform more complex tasks, can be realized with virtually any physical system and can be designed with a variety of physical network architectures. In Fig. 4, we present three PNN classifiers for the MNIST (Modified National Institute of Standards and Technology database) handwritten digit classification task, based on three distinct physical systems. For each physical system, we also demonstrate a different PNN architecture, illustrating the variety of physical networks possible. In all cases, models were constructed and trained using PyTorch⁵⁴.

Fig. 4: Image classification with diverse physical systems.

 **figure 4**

We trained PNNs based on three physical systems (mechanics, electronics and optics) to classify images of handwritten digits. **a**, The mechanical PNN: the multimode oscillations of a metal plate are driven by time-dependent forces that encode the input image data and parameters. **b**, The mechanical PNN multilayer architecture. **c**, The validation classification accuracy versus training epoch for the mechanical PNN trained using PAT. The same curves are shown also for a reference model where the physical transformations implemented by the speaker are replaced by identity operations. **d**, Confusion matrix for the mechanical PNN after training. **e–h**, The same as **a–d**, respectively, but for a nonlinear analogue-electronic PNN. **i–l**, The same as **a–d**, respectively, for a hybrid physical-digital PNN based on broadband optical SHG. The final test accuracy is 87%, 93% and 97% for the mechanical, electronic and optics-based PNNs, respectively.

In the mechanical PNN (Fig. 4a–d), a metal plate is driven by time-varying forces, which encode both input data and trainable parameters. The plate’s multimode oscillations enact controllable convolutions on the input data (Supplementary Figs. 16, 17). Using the plate’s trainable transformation sequentially three times, we classify 28-by-28 (784 pixel) images that are input as an unrolled time series. To control the transformations of each physical layer, we train element-wise rescaling of the forces applied to the plate (Fig. 4b, [Methods](#)). PAT trains the three-layer mechanical PNN to 87% accuracy, close to a digital linear classifier⁵⁵. When the mechanical computations are replaced by identity operations, and only the digital rescaling operations are trained, the performance of the model is equivalent to random guessing (10%). This shows that most of the PNN’s functionality comes from the controlled physical transformations.

An analogue-electronic PNN is implemented with a circuit featuring a transistor (Fig. 4e–h), which results in a noisy, nonlinear transient response (Supplementary Figs. 12, 13). The usage and architecture of the electronic PNN are mostly similar to that of the mechanical PNN, with several minor differences ([Methods](#)). When trained using PAT, the analogue-electronic PNN performs the classification task with 93% test accuracy.

Using broadband SHG, we demonstrate a physical–digital hybrid PNN (Fig. 4i–l). This hybrid PNN involves trainable digital linear input layers followed by trainable ultrafast SHG transformations. The trainable SHG transformations boost the performance of the digital baseline from roughly 90% accuracy to 97%. The classification task’s difficulty is nonlinear with respect to accuracy, so this improvement typically requires increasing the number of digital operations by around one order of magnitude⁵⁵. This illustrates how a hybrid physical–digital PNN can automatically learn to offload portions of a computation from an expensive digital processor to a fast, energy-efficient physical co-processor.

To show the potential for PNNs to perform more challenging tasks, we simulated a multilayer PNN based on a nonlinear oscillator network. This PNN is trained with PAT to perform the MNIST task with 99.1% accuracy, and the Fashion-MNIST task, which is considered significantly harder⁵⁶, with 90% accuracy, in both cases with simulated physical noise, and with mismatch between model and simulated experiment of over 20% (Supplementary Section 4).

Discussion

Our results show that controllable physical systems can be trained to execute DNN calculations. Many systems that are not conventionally used for computation appear to offer, in principle, the capacity to perform parts of machine-learning-inference calculations orders of magnitude faster and more energy-efficiently than conventional

hardware (Supplementary Section 5). However, there are two caveats to note. First, owing to underlying symmetries and other constraints, some systems may be well suited for accelerating a restricted class of computations that share the same constraints. Second, PNNs trained using PAT can only provide significant benefits during inference, as PAT uses a digital model. Thus, as in the hybrid network presented in Fig. 4*i–l*, we expect such PNNs to serve as a resource, rather than as a complete replacement, for conventional general-purpose hardware (Supplementary Section 5).

Techniques for training hardware *in situ*^{7,40,41,42,43,44,45,46,47} and methods for reliable *in silico* training (for example, refs. ^{57,58,59,60}) complement these weaknesses. Devices trained using *in situ* learning algorithms will perform learning entirely in hardware, potentially realizing learning faster and more energy-efficiently than current approaches. Such devices are suited to settings in which frequent retraining is required. However, to perform both learning and inference, these devices have more specific hardware requirements than inference-only hardware, which may limit their achievable inference performance. *In silico* training can train many physical parameters of a device, including ones set permanently during fabrication^{12,13,14,15,16}. As the resulting hardware will not perform learning, it can be optimized for inference. Although accurate, large-scale *in silico* training has been implemented^{4,5,6,57,58,59,60}, this has been achieved with only analogue electronics, for which accurate simulations and controlled fabrication processes are available. PAT may be used in settings where a simulation–reality gap cannot be avoided, such as if hardware is designed at the limit of fabrication tolerances, operated outside usual regimes or based on platforms other than conventional electronics.

Improvements to PAT could extend the utility of PNNs. For example, PAT’s backward pass could be replaced by a neural network that directly estimates parameter updates for the physical system. Implementing this ‘teacher’ neural network with a PNN would allow subsequent training to be performed without digital assistance.

This work has focused so far on the potential application of PNNs as accelerators for machine learning, but PNNs are promising for other applications as well, particularly those in which physical, rather than digital, data are processed or produced. PNNs can perform computations on data within its physical domain, allowing for smart sensors^{30,31,32} that pre-process information before conversion to the electronic domain (for example, a low-power, microphone-coupled circuit tuned to recognize specific hotwords). As the achievable sensitivity, resolution and energy efficiency of many sensors is limited by conversion of information to the digital electronic domain, and by processing of that data in digital electronics, PNN sensors should have advantages. More broadly, with PAT, one is simply training the complex functionality of physical systems. Although machine learning and sensing are important functionalities, they are

but two of many^{23,24,25,26,27,28,29,30,31,32} that PAT, and the concept of PNNs, could be applied to.

Methods

Physics-aware training

To train the PNNs presented in Figs. 2–4, we used PAT to enable us to perform backpropagation on the physical apparatuses as automatic differentiation (autodiff) functions within PyTorch⁵⁴ (v1.6). We used PyTorch Lightning⁶¹ (v0.9) and Weights and Biases⁶² (v0.10) during development as well. PAT is explained in detail in Supplementary Section 1, where it is compared with standard backpropagation, and training physical devices in silico. Here we provide only an overview of PAT in the context of a generic multilayer PNN (Supplementary Figs. 2, 3).

PAT can be formalized by the use of custom constituent autodiff functions for the physically executed submodules in an overall network architecture (Supplementary Fig. 1). In PAT, each physical system’s forward functionality is provided by the system’s own controllable physical transformation, which can be thought of as a parameterized function $\langle\{f\}_\{\{\rm rm\{p\}\}\}\rangle$ that relates the input x , parameters θ , and outputs y of the transformation via $y = f_p(x, \theta)$. As a physical system cannot be auto-differentiated, we use a differentiable digital model $\langle\{f\}_\{\{\rm rm\{m\}\}\}\rangle$ to approximate each backward pass through a given physical module. This structure is essentially a generalization of quantization-aware training⁴⁸, in which low-precision neural network hardware is approximated by quantizing weights and activation values on the forward pass, but storing weights and activations, and performing the backward pass with full precision.

To see how this works, we consider here the specific case of a multilayer feedforward PNN with standard stochastic gradient descent. In this case, the PAT algorithm with the above-defined custom autodiff functions results in the following training loop:

Perform forward pass:

$$\$ \$ \{ \{ \bf{x} \} \}^{\{[l+1]\}} = \{ \{ \boldsymbol{y} \} \}^{\{[l]\}} = \{ f \}_\{\{\rm rm\{p\}\}\} (\{ \{ \bf{x} \} \}^{\{[l]\}}, \{ \{ \boldsymbol{\theta} \} \}^{\{[l]\}}) \$ \$ \\ (1)$$

Compute (exact) error vector:

$$\$ \$ \{ g \}_\{\{ \bf{y} \} \}^{\{[N]\}} = \frac{\partial L}{\partial \{ \bf{y} \}^{\{[N]\}}} = \frac{\partial \{ \mathcal{L} \}}{\partial \{ \bf{y} \}^{\{[N]\}}} \\$$

$$\begin{aligned} & \{\{\bf y\}\}^{\wedge \{\leftarrow[N]\right\}}(\{\{\bf y\}\}^{\wedge \{\leftarrow[N]\}}, \\ & \{\{\bf y\}\}_{\wedge \{\rm target\}}) \$\$ \\ (2) \end{aligned}$$

Perform backward pass

$$\begin{aligned} & \{\{\bf g\}_{\wedge \{\{\bf y\}\}^{\wedge \{l-1\}}} = \{\leftarrow[\frac{\partial \{\rm m\}}{\partial \{\bf x\}} \{\bf f\}_{\wedge \{\rm m\}}] \\ & \{\{\rm \partial\} \{\bf x\}\} (\{\{\bf x\}\}^{\wedge \{l\}}, \{\boldsymbol{\theta}\}^{\wedge \{l\}}) \right\}^{\wedge \{\leftarrow[T]\}} \{\bf g\}_{\wedge \{\{\bf y\}\}^{\wedge \{l\}}} \$\$ \\ (3a) \quad & \{\{\bf g\}_{\wedge \{\boldsymbol{\theta}\}^{\wedge \{\leftarrow[l-1]\}}} = \{\leftarrow[\frac{\partial \{\boldsymbol{\theta}\}}{\partial \{\boldsymbol{\theta}\}} (\{\{\bf x\}\}^{\wedge \{\leftarrow[l]\}}, \\ & \{\{\boldsymbol{\theta}\}\}^{\wedge \{\leftarrow[l]\}}) \right\}^{\wedge \{\leftarrow[T]\}} \{\bf g\}_{\wedge \{\{\bf y\}\}^{\wedge \{\leftarrow[l]\}}} \$\$ \\ (3b) \quad & \end{aligned}$$

Update parameters:

$$\begin{aligned} & \{\{\boldsymbol{\theta}\}^{\wedge \{\leftarrow[l]\}}\} \rightarrow \{\{\boldsymbol{\theta}\}^{\wedge \{\leftarrow[l]\}} - \eta \frac{1}{N} \sum_k \{\{\bf g\}_{\wedge \{\{\boldsymbol{\theta}\}\}^{\wedge \{\leftarrow[l]\}}}^{\wedge \{k\}}\} \$\$ \\ (4) \end{aligned}$$

where $\{\{\bf g\}_{\wedge \{\{\boldsymbol{\theta}\}\}^{\wedge \{\leftarrow[l]\}}}\}$ and $\{\{\bf g\}_{\wedge \{\{\bf y\}\}^{\wedge \{\leftarrow[l]\}}}\}$ are estimators of the physical systems' exact gradients, $\{\frac{\partial L}{\partial \{\boldsymbol{\theta}\}}\}^{\wedge \{l\}}$ and $\{\frac{\partial L}{\partial \{\bf y\}}\}^{\wedge \{l\}}$, respectively for the $\{l\}$ th layer, obtained by auto-differentiation of the model, L is the loss, $\{\mathcal{l}\}$ is the loss function (for example, cross-entropy or mean-squared error), $\{\{\bf y\}\}_{\wedge \{\rm target\}}$ is the desired (target) output, N is the size of the batch and η is the learning rate. $\{\{\bf x\}\}^{\wedge \{l+1\}}$ is the input vector to the $\{l+1\}$ th layer, which for the hidden layers of the feedforward architecture is equal to the output vector of the previous layer, $\{\{\bf x\}\}^{\wedge \{l+1\}} = \{\{\bf y\}\}^{\wedge \{l\}} = \{\bf f\}_{\wedge \{\rm p\}} \left(\{\{\bf x\}\}^{\wedge \{\leftarrow[l]\}} \right)$, where $\{\{\boldsymbol{\theta}\}\}^{\wedge \{l\}}$ is the controllable (trainable) parameter vector for the $\{l\}$ th layer. For the first layer, the input data vector $\{\{\bf x\}\}^{\wedge \{\leftarrow[1]\}}$ is the data to be operated on. In PAT, the error vector is exactly estimated ($\{\{\bf g\}_{\wedge \{\{\bf y\}\}^{\wedge \{\leftarrow[N]\}}} = \frac{\partial L}{\partial \{\bf y\}} \{\{\bf y\}\}^{\wedge \{N\}}$) as the forward pass is performed by the physical system. This error vector is then backpropagated via equation (3), which involves Jacobian matrices of the differential digital model evaluated at the correct inputs at each layer (that is, the actual physical inputs) $\{\{\leftarrow[\frac{\partial \{\rm m\}}{\partial \{\bf x\}} \{\bf f\}_{\wedge \{\rm m\}}]\}\} \{\{\rm \partial\} \{\bf x\}\}$

$(\{\{\bf{x}\}\}^{\wedge}[l], \{\boldsymbol{\theta}\}^{\wedge}[l])^{\text{right}}]^{\wedge}\{\rm{T}\})$), where T represents the transpose operation. Thus, in addition to utilizing the output of the PNN ($(\{\bf{y}\}\}^{\wedge}[N])$) via physical computations in the forward pass, intermediate outputs ($(\{\bf{y}\}\}^{\wedge}[l])$) are also utilized to facilitate the computation of accurate gradients in PAT.

As it is implemented just by defining a custom autodiff function, generalizing PAT for more complex architectures, such as multichannel or hybrid physical–digital models, with different loss functions and so on is straightforward. See Supplementary Section 1 for details.

An intuitive motivation for why PAT works is that the training’s optimization of parameters is always grounded in the true optimization landscape by the physical forward pass. With PAT, even if gradients are estimated only approximately, the true loss function is always precisely known. As long as the gradients estimated by the backward pass are reasonably accurate, optimization will proceed correctly. Although the required training time is expected to increase as the error in gradient estimation increases, in principle it is sufficient for the estimated gradient to be pointing closer to the direction of the true gradient than its opposite (that is, that the dot product of the estimated and true gradients is positive). Moreover, by using the physical system in the forward pass, the true output from each intermediate layer is also known, so gradients of intermediate physical layers are always computed with respect to correct inputs. In any form of in silico training, compounding errors build up through the imperfect simulation of each physical layer, leading to a rapidly diverging simulation–reality gap as training proceeds (see Supplementary Section 1 for details). As a secondary benefit, PAT ensures that learned models are inherently resilient to noise and other imperfections beyond a digital model, as the change of loss along noisy directions in parameter space will tend to average to zero. This makes training robust to, for example, device–device variations, and facilitates the learning of noise-resilient (and, more speculatively, noise-enhanced) models⁸.

Differentiable digital models

To perform PAT, a differentiable digital model of the physical system’s input–output transformation is required. Any model, $\langle f \rangle_{\langle m \rangle}$, of the physical system’s true forward function, $\langle f \rangle_{\langle p \rangle}$, can be used to perform PAT, so long as it can be auto-differentiated. Viable approaches include traditional physics models, black-box machine-learning models^{13,63,64} and physics-informed machine-learning⁶⁵ models.

In this work, we used the black-box strategy for our differentiable digital models, namely DNNs trained on input–output vector pairs from the physical systems as \

($\{f\}_{\{\rm rm\{m\}\}}\}$) (except for the mechanical system). Two advantages of this approach are that it is fully general (it can be applied even to systems in which one has no underlying knowledge-based model of the system) and that the accuracy can be extremely high, at least for physical inputs, $\langle(\{\bf x\}, \{\boldsymbol{\theta}\})\rangle$, within the distribution of the training data (for out-of-distribution generalization, we expect physics-based approaches to offer advantages). In addition, the fact that each physical system has a precise corresponding DNN means that the resulting PNN can be analysed as a network of DNNs, which may be useful for explaining the PNN's learned physical algorithm.

For our DNN differentiable digital models, we used a neural architecture search⁶⁶ to optimize hyperparameters, including the learning rate, number of layers and number of hidden units in each layer. Typical optimal architectures involved 3–5 layers with 200–1,000 hidden units in each, trained using the Adam optimizer, mean-squared loss function and learning rates of around 10^{-4} . For more details, see Supplementary Section [2D.1](#).

For the nonlinear optical system, the test accuracy of the trained digital model (Supplementary Fig. [20](#)) shows that the model is remarkably accurate compared with typical simulation–experiment agreement in broadband nonlinear optics, especially considering that the pulses used exhibit a complex spatiotemporal structure owing to the pulse shaper. The model is not, however, an exact description of the physical system: the typical error for each element of the output vector is about 1–2%. For the analogue electronic circuit, agreement is also good, although worse than the other systems (Supplementary Fig. [23](#)), corresponding to around 5–10% prediction error for each component of the output vector. For the mechanical system, we found that a linear model was sufficient to obtain excellent agreement, which resulted in a typical error of about 1% for each component of the output vector (Supplementary Fig. [26](#)).

In silico training

To train PNNs in silico, we applied a training loop similar to the one described above for PAT except that both the forward and backward passes are performed using the model (Supplementary Figs. [1](#), [3](#)), with one exception noted below.

To improve the performance of in silico training as much as possible and permit the fairest comparison with PAT, we also modelled the input-dependent noise of the physical system and used this within the forward pass of in silico training. To do this, we trained, for each physical system, an additional DNN to predict the eigenvectors of the output vector's noise covariance matrix, as a function of the physical system's input vector and parameter vector. These noise models thus provided an input- and parameter-dependent estimate of the distribution of noise in the output vector

produced by the physical system. We were able to achieve excellent agreement between the noise models' predicted noise distributions and experimental measurements (Supplementary Figs. 18, 19). We found that including this noise model improved the performance of experiments performed using parameters derived from in silico training. Consequently, all in silico training results presented in this paper make use of such a model, except for the mechanical system, where a simpler, uniform noise model was found to be sufficient. For additional details, see Supplementary Section 2D.2.

Although including complex, accurate noise models does not allow in silico training to perform as well as PAT, we recommend that such models be used whenever in silico training is performed, such as for physical architecture search and design and possibly pre-training (Supplementary Section 5), as the correspondence with experiment (and, in particular, the predicted peak accuracy achievable there) is significantly improved over simpler noise models, or when ignoring physical noise.

Ultrafast nonlinear optical pulse propagation experiments

For experiments with ultrafast nonlinear pulse propagation in quadratic nonlinear media (Supplementary Figs. 8–10), we shaped pulses from a mode-locked titanium:sapphire laser (Spectra Physics Tsunami, centred around 780 nm and pulse duration around 100 fs) using a custom pulse shaper. Our optical pulse shaper used a digital micromirror device (DMD, Vialux V-650L) and was inspired by the design in ref. 67. Despite the binary modulations of the individual mirrors, we were able to achieve multilevel spectral amplitude modulation by varying the duty cycle of gratings written to the DMD along the dimension orthogonal to the diffraction of the pulse frequencies. To control the DMD, we adapted code developed for ref. 68, which is available at ref. 69.

After being shaped by the pulse shaper, the femtosecond pulses were focused into a 0.5-mm-long beta-barium borate crystal. The multitude of frequencies within the broadband pulses then undergo various nonlinear optical processes, including sum-frequency generation and SHG. The pulse shaper imparts a complex phase and spatiotemporal structure on the pulse, which depend on the input and parameters applied through the spectral modulations. These features would make it impossible to accurately model the experiment using a one-dimensional pulse propagation model. For simplicity, we refer to this complex, spatiotemporal quadratic nonlinear pulse propagation as ultrafast SHG.

Although the functionality of the SHG-PNN does not rely on a closed-form mathematical description or indeed on any form of mathematical isomorphism, some readers may find it helpful to understand the approximate form of the input–output

transformation realized in this experimental apparatus. We emphasize that the following model is idealistic and meant to convey key intuitions about the physical transformation: the model does not describe the experimental transformation in a quantitative manner, owing to the numerous experimental complexities described above.

The physical transformation of the ultrafast SHG setup is seeded by the infrared light from the titanium:sapphire laser. This ultrashort pulse can be described by the Fourier transform of the electric field envelope of the pulse, $\langle\{A\}_0(\omega)\rangle$, where ω is the frequency of the field detuned relative to the carrier frequency. For simplicity, consider a pulse consisting of a set of discrete frequencies or frequency bins, whose spectral amplitudes are described by the discrete vector $\langle\{\{\bf A\}\}_0\{\{\bf 0\}\}\rangle = \{[A]_0(\omega_1), [A]_0(\omega_2), \dots, [A]_0(\omega_N)\} \rangle^{\{\rm rm{T}\}}$. After passing through the pulseshaper, the spectral amplitudes of the pulse are then given by

$$\$ \$ \langle\{\bf A\}\rangle = \{[\sqrt{x_1} A_0(\omega_1), \sqrt{x_2} A_0(\omega_2), \dots, \sqrt{x_{N_x}} A_0(\omega_{N_x+1}), \sqrt{x_{N_x+2}} A_0(\omega_{N_x+2}), \dots, \sqrt{x_{N_x+N}} A_0(\omega_{N_x+N})]\}^{\{\rm rm{T}\}}, \$ \$ (5)$$

where $\langle\{N\}_x\rangle$ is the dimensionality of the data vector, $\langle\{\theta_i\}\rangle$ are the trainable pulse-shaper amplitudes and $\langle\{x_i\}\rangle$ are the elements of the input data vector. Thus, the output from the pulse shaper encodes both the machine-learning data as well as the trainable parameters. Square roots are present in equation (5) because the pulse shaper was deliberately calibrated to perform an intensity modulation.

The output from the pulse shaper (equation (5)) is then input to the ultrafast SHG process. The propagation of an ultrashort pulse through a quadratic nonlinear medium results in an input–output transformation that roughly approximates an autocorrelation, or nonlinear convolution, assuming that the dispersion during propagation is small and the input pulse is well described by a single spatial mode. In this limit, the output blue spectrum $\langle B(\omega_i) \rangle$ is mathematically given by

$$\$ \$ B(\omega_i) = k \sum_j A(\omega_i + \omega_j) A(\omega_i - \omega_j), \$ \$ (6)$$

where the sum is over all frequency bins j of the pulsed field. The output of the trainable physical transformation $\langle\{\bf y\}\rangle = \{f\}_{\{\rm rm{p}\}}\langle\{\bf x\}\rangle$, $\langle\{\theta\}\rangle$ is given by the blue pulse's spectral power, $\langle\{\bf y\}\rangle = [\{B\}_{\{\omega_1\}}]^2, [\{B\}_{\{\omega_2\}}]^2, \dots, [\{B\}_{\{\omega_{N_x}\}}]^2]$

$\{B\}_\{\{\omega_N\}\}|\}^2]\}^{\{\rm{T}\}}\},)$ where $\{N\}$ is the length of the output vector.

From this description, it is clear that the physical transformation realized by the ultrafast SHG process is not isomorphic to any conventional neural network layer, even in this idealized limit. Nonetheless, the physical transformation retains some key features of typical neural network layers. First, the physical transformation is nonlinear as the SHG process involves the squaring of the input field. Second, as the terms within the summation in equation (6) involve both parameters and input data, the transformation also mixes the different elements of the input data and parameters to produce an output. This mixing of input elements is similar, but not necessarily directly mathematically equivalent to, the mixing of input vector elements that occur in the matrix-vector multiplications or convolutions that appear in conventional neural networks.

Vowel classification with ultrafast SHG

A task often used to demonstrate novel machine-learning hardware is the classification of spoken vowels according to formant frequencies^{10,11}. The task involves predicting the spoken vowels given a 12-dimensional input data vector of formant frequencies extracted from audio recordings¹⁰. Here we use the vowel dataset from ref. 10, which is based on data originally from ref. 70; data available at <https://homepages.wmich.edu/~hillenbr/voweldata.html>. This dataset consists of 273 data input–output pairs. We used 175 data pairs as the training set—49 for the validation and 49 for the test set. For the results in Figs. 2, 3, we optimized for the hyperparameters of the PNN architecture using the validation error and only evaluated the test error after all optimization was conducted. In Fig. 3c, for each PNN with a given number of layers, the experiment was conducted with two different training, validation and test splits of the vowel data. In Fig. 3c, the line plots the mean over the two splits, and the error bars are the standard error of the mean.

For the vowel-classification PNN presented in Figs. 2, 3, the input vector to each SHG physical layer is encoded in a contiguous short-wavelength section of the spectral modulation vector sent to the pulse shaper, and the trainable parameters are encoded in the spectral modulations applied to the rest of the spectrum. For the physical layers after the first layer, the input vector to the physical system is the measured spectrum obtained from the previous layer. For convenience, we performed digital renormalization of these output vectors to maximize the dynamic range of the input and ensure that inputs were within the allowed range of 0 to 1 accepted by the pulse shaper. Relatedly, we found that training stability was improved by including additional trainable digital re-scaling parameters to the forward-fed vector, allowing the overall bias and amplitude scale of the physical inputs to each layer to be adjusted

during training. These digital parameters appear to have a negligible role in the final trained PNN (when the physical transformations are replaced by identity operations, the network can be trained to perform no better than chance, and the final trained values of the scale and bias parameters are all very close to 1 and 0, respectively). We hypothesize that these trainable rescaling parameters are helpful during training to allow the network to escape noise-affected subspaces of parameter space. See Supplementary Section 2E.1 for details.

The vowel-classification SHG-PNN architecture (Supplementary Fig. 21) was designed to be as simple as possible while still demonstrating the use of a multilayer architecture with a physical transformation that is not isomorphic to a conventional DNN layer, and so that the computations involved in performing the classification were essentially all performed by the physical system itself. Many aspects of the design are not optimal with respect to performance, so design choices, such as our specific choice to partition input data and parameter vectors into the controllable parameters of the experiment, should not be interpreted as representing any systematic optimization. Similarly, the vowel-classification task was chosen as a simple example of multidimensional machine-learning classification. As this task can be solved almost perfectly by a linear model, it is in fact poorly suited to the nonlinear optical transformations of our SHG-PNN, which are fully nonlinear (Supplementary Figs. 9, 10). Overall, readers should not interpret this PNN’s design as suggestive of optimal design strategies for PNNs. For initial guidelines on optimal design strategies, we instead refer readers to Supplementary Section 5.

MNIST handwritten digit image classification with a hybrid physical–digital SHG-PNN

The design of the hybrid physical–digital MNIST PNN based on ultrafast SHG for handwritten digit classification (Fig. 4i–l) was chosen to demonstrate a proof-of-concept PNN in which substantial digital operations were co-trained with substantial physical transformations, and in which no digital output layer was used (although a digital output layer can be used with PNNs, and we expect such a layer will usually improve performance, we wanted to avoid confusing readers familiar with reservoir computing, and so avoided using digital output layers in this work).

The network (Supplementary Fig. 29) involves four trainable linear input layers that operate on MNIST digit images, whose outputs are fed into four separate channels in which the SHG physical transformation is used twice in succession (that is, it is two physical layers deep). The output of the final layers of each channel (the final SHG spectra) are concatenated, then summed into ten bins to perform a classification. The structure of the input layer was chosen to minimize the complexity of inputs to the pulse shaper. We found that the output second-harmonic spectra produced by the

nonlinear optical process tended towards featureless triangular spectra if inputs were close to a random uniform distribution. Thus, to ensure that output spectra varied significantly with respect to changes in the input spectral modulations, we made sure that inputs to the pulse shaper would exhibit a smoother structure in the following way. For each of 4 independent channels, 196-dimensional input images (downsampled from 784-dimensional 28×28 images) are first operated on by a 196 by 50 trainable linear matrix, and then (without any nonlinear digital operations), a second 50 by 196 trainable linear matrix. The second 50 by 196 matrix is identical for all channels, the intent being that this matrix identifies optimal ‘input modes’ to the SHG process. By varying the middle dimension of this two-step linear input layer, one may control the amount of structure (number of ‘spectral modes’) allowed in inputs to the pulse shaper, as the middle dimension effectively controls the rank of the total linear matrix. We found that a middle dimension below 30 resulted in the most visually varied SHG output spectra, but that 50 was sufficient for good performance on the MNIST task. In this network, we also utilized skip connections between layers in each channel. This was done so that the network would be able to ‘choose’ to use the linear digital operations to perform the linear part of the classification task (for which nearly 90% accuracy can be obtained⁵⁵) and to thus rely on the SHG co-processor primarily for the harder, nonlinear part of the classification task. Between the physical layers in each channel, a trainable, element-wise rescaling was used to allow us to train the second physical layer transformations efficiently. That is, $\langle\{x\}_i\rangle = \langle a \rangle_i \langle y \rangle_i + \langle b \rangle_i$, where $\langle\{b\}_i\rangle$ and $\langle\{a\}_i\rangle$ are trainable parameters, and $\langle\{x\}_i\rangle$ and $\langle\{y\}_i\rangle$ are the input to the pulse shaper and the measured output spectrum from the previous physical layer, respectively.

For further details on the nonlinear optical experimental setup and its characterization, we refer readers to Supplementary Section 2A. For further details on the vowel-classification SHG-PNN, we refer readers to Supplementary Section 2E.1, and for the hybrid physical–digital MNIST handwritten digit-classification SHG-PNN, we refer readers to Supplementary Section 2E.4.

Analogue electronic circuit experiments

The electronic circuit used for our experiments (Supplementary Fig. 11) was a resistor-inductor-capacitor oscillator (RLC oscillator) with a transistor embedded within it. It was designed to produce as nonlinear and complex a response as possible, while still containing only a few simple components (Supplementary Figs. 12, 13). The experiments were carried out with standard bulk electronic components, a hobbyist circuit breadboard and a USB data acquisition (DAQ) device (Measurement Computing USB-1208-HS-4AO), which allowed for one analogue input and one analogue output channel, with a sampling rate of 1 MS s^{-1} .

The electronic circuit provides only a one-dimensional time-series input and one-dimensional time-series output. As a result, to partition the inputs to the system into trainable parameters and input data so that we could control the circuit's transformation of input data, we found it was most convenient to apply parameters to the one-dimensional input time-series vector by performing trainable, element-wise rescaling on the input time-series vector. That is, $\{\{x\}_i\} = \{a\}_i \{y\}_i + \{b\}_i$, where $\{\{b\}_i\}$ and $\{\{a\}_i\}$ are trainable parameters, $\{\{y\}_i\}$ are the components of the input data vector and $\{\{x\}_i\}$ are the re-scaled components of the voltage time series that is then sent to the analogue circuit. For the first layer, $\{\{y\}_i\}$ are the unrolled pixels of the input MNIST image. For hidden layers, $\{\{y\}_i\}$ are the components of the output voltage time-series vector from the previous layer.

We found that the electronic circuit's output was noisy, primarily owing to the timing jitter noise that resulted from operating the DAQ at its maximum sampling rate (Supplementary Fig. 23). Rather than reducing this noise by operating the device more slowly, we were motivated to design the PNN architecture presented in Fig. 4 in a way that allowed it to automatically learn to function robustly and accurately, even in the presence of up to 20% noise per output vector element (See Supplementary Fig. 24 for an expanded depiction of the architecture). First, seven, three-layer feedforward PNNs were trained together, with the final prediction provided by averaging the output of all seven, three-layer PNNs. Second, skip connections similar to those used in residual neural networks were employed⁷¹. These measures make the output of the network effectively an ensemble average over many different subnetworks⁷¹, which allows it to perform accurately and train smoothly despite the very high physical noise and multilayer design.

For further details on the analogue electronic experimental setup and its characterization, we refer readers to Supplementary Section 2B. For further details on the MNIST handwritten digit-classification analogue electronic PNN, we refer readers to Supplementary Section 2E.2.

Oscillating mechanical plate experiments

The mechanical plate oscillator was constructed by attaching a 3.2 cm by 3.2 cm by 1 mm titanium plate to a long, centre-mounted screw, which was fixed to the voice coil of a commercial full-range speaker (Supplementary Figs. 14, 15). The speaker was driven by an audio amplifier (Kinter K2020A+) and the oscillations of the plate were recorded using a microphone (Audio-Technica ATR2100x-USB Cardioid Dynamic Microphone). The diaphragm of the speaker was completely removed so that the sound recorded by the microphone is produced only by the oscillating metal plate.

As the physical input (output) to (from) the mechanical oscillator is a one-dimensional time series, similar to the electronic circuit, we made use of element-wise trainable rescaling to conveniently allow us to train the oscillating plate's physical transformations.

The mechanical PNN architecture for the MNIST handwritten digit classification task was chosen to be the simplest multilayer PNN architecture possible with such a one-dimensional dynamical system (Supplementary Fig. 27). As the mechanical plate's input–output responses are primarily linear convolutions (Supplementary Figs. 16, 17), it is well suited to the MNIST handwritten digit classification task, achieving nearly the same performance as a digital linear model⁵⁵.

For further details on the oscillating mechanical plate experimental setup and its characterization, we refer readers to Supplementary Section 2C. For further details on the MNIST handwritten digit-classification oscillating mechanical plate PNN, we refer readers to Supplementary Section 2E.3.

Data availability

All data generated during and code used for this work are available at <https://doi.org/10.5281/zenodo.4719150>.

Code availability

An expandable demonstration code for applying PAT to train PNNs is available at <https://github.com/mcmahon-lab/Physics-Aware-Training>. All code used for this work is available at <https://doi.org/10.5281/zenodo.4719150>.

References

1. 1.
Patterson, D. et al. Carbon emissions and large neural network training. Preprint at <https://arxiv.org/abs/2104.10350> (2021).
2. 2.
Reuther, A. et al. Survey of machine learning accelerators. In *2020 IEEE High Performance Extreme Computing Conference (HPEC)* 1–12 (IEEE, 2020).
3. 3.

Xia, Q., & Yang, J. J. Memristive crossbar arrays for brain-inspired computing. *Nat. Mater.* **18**, 309–323 (2019).

4. 4.

Burr, G. W. et al. Neuromorphic computing using non-volatile memory. *Adv. Phys. X* **2**, 89–124 (2017).

5. 5.

Khaddam-Aljameh, R. et al. HERMES core—a 14nm CMOS and PCM-based in-memory compute core using an array of 300ps/LSB linearized CCO-based ADCs and local digital processing. In *2021 Symposium on VLSI Circuits* (IEEE, 2021).

6. 6.

Narayanan, P. et al. Fully on-chip MAC at 14nm enabled by accurate row-wise programming of PCM-based weights and parallel vector-transport in duration-format. In *2021 Symposium on VLSI Technology* (IEEE, 2021).

7. 7.

Kohda, Y. et al. Unassisted true analog neural network training chip. In *2020 IEEE International Electron Devices Meeting (IEDM)* (IEEE, 2020).

8. 8.

Marković, D., Mizrahi, A., Querlioz, D. & Grollier, J. Physics for neuromorphic computing. *Nat. Rev. Phys.* **2**, 499–510 (2020).

9. 9.

Wetzstein, G. et al. Inference in artificial intelligence with deep optics and photonics. *Nature* **588**, 39–47 (2020).

10. 10.

Romera, M. et al. Vowel recognition with four coupled spin-torque nano-oscillators. *Nature* **563**, 230–234 (2018).

11. 11.

Shen, Y. et al. Deep learning with coherent nanophotonic circuits. *Nat. Photon.* **11**, 441–446 (2017).

12. 12.

Prezioso, M. et al. Training and operation of an integrated neuromorphic network based on metal-oxide memristors. *Nature* **521**, 61–64 (2015).

13. 13.

Euler, H.-C. R. et al. A deep-learning approach to realizing functionality in nanoelectronic devices. *Nat. Nanotechnol.* **15**, 992–998 (2020).

14. 14.

Hughes, T. W., Williamson, I. A., Minkov, M. & Fan, S. Wave physics as an analog recurrent neural network. *Sci. Adv.* **5**, eaay6946 (2019).

15. 15.

Wu, Z., Zhou, M., Khoram, E., Liu, B. & Yu, Z. Neuromorphic metasurface. *Photon. Res.* **8**, 46–50 (2020).

16. 16.

Furuhasha, G., Niiyama, T. & Sunada, S. Physical deep learning based on optimal control of dynamical systems. *Phys. Rev. Appl.* **15**, 034092 (2021).

17. 17.

Lin, X. et al. All-optical machine learning using diffractive deep neural networks. *Science* **361**, 1004–1008 (2018).

18. 18.

Miller, J. F., Harding, S. L. & Tufte, G. Evolution-in-materio: evolving computation in materials. *Evol. Intell.* **7**, 49–67 (2014).

19. 19.

Chen, T. et al. Classification with a disordered dopant-atom network in silicon. *Nature* **577**, 341–345 (2020).

20. 20.

Bueno, J. et al. Reinforcement learning in a large-scale photonic recurrent neural network. *Optica* **5**, 756–760 (2018).

21. 21.

Tanaka, G. et al. Recent advances in physical reservoir computing: a review. *Neural Netw.* **115**, 100–123 (2019).

22. 22.

Appeltant, L. et al. Information processing using a single dynamical node as complex system. *Nat. Commun.* **2**, 468 (2011).

23. 23.

Mouret, J.-B. & Chatzilygeroudis, K. 20 years of reality gap: a few thoughts about simulators in evolutionary robotics. In *Proc. Genetic and Evolutionary Computation Conference Companion* 1121–1124 (2017).

24. 24.

Howison, T., Hauser, S., Hughes, J. & Iida, F. Reality-assisted evolution of soft robots through large-scale physical experimentation: a review. *Artif. Life* **26**, 484–506 (2021).

25. 25.

de Avila Belbute-Peres, F., Smith, K., Allen, K., Tenenbaum, J. & Kolter, J. Z. End-to-end differentiable physics for learning and control. *Adv. Neural Inf. Process. Syst.* **31**, 7178–7189 (2018).

26. 26.

Degrave, J., Hermans, M., Dambre, J. & Wyffels, F. A differentiable physics engine for deep learning in robotics. *Front. Neurorobot.* **13**, 6 (2019).

27. 27.

Molesky, S. et al. Inverse design in nanophotonics. *Nat. Photon.* **12**, 659–670 (2018).

28. 28.

Peurifoy, J. et al. Nanophotonic particle simulation and inverse design using artificial neural networks. *Sci. Adv.* **4**, eaar4206 (2018).

29. 29.

Stern, M., Arinze, C., Perez, L., Palmer, S. E. & Murugan, A. Supervised learning through physical changes in a mechanical system. *Proc. Natl Acad. Sci. USA* **117**, 14843–14850 (2020).

30. 30.

Zhou, F. & Chai, Y. Near-sensor and in-sensor computing. *Nat. Electron.* **3**, 664–671 (2020).

31. 31.

Martel, J. N., Mueller, L. K., Carey, S. J., Dudek, P. & Wetzstein, G. Neural sensors: learning pixel exposures for HDR imaging and video compressive sensing with programmable sensors. *IEEE Trans. Pattern Anal. Mach. Intell.* **42**, 1642–1653 (2020).

32. 32.

Mennel, L. et al. Ultrafast machine vision with 2D material neural network image sensors. *Nature* **579**, 62–66 (2020).

33. 33.

Brooks, R. A. Intelligence without reason. In *Proc. 12th International Joint Conference on Artificial Intelligence* Vol. 1, 569–595 (Morgan Kaufmann, 1991).

34. 34.

Hooker, S. The hardware lottery. Preprint at <https://arxiv.org/abs/2009.06489> (2020).

35. 35.

Krizhevsky, A., Sutskever, I. & Hinton, G. E. Imagenet classification with deep convolutional neural networks. *Adv. Neural Inf. Process. Syst.* **25**, 1097–1105 (2012).

36. 36.

Lin, H. W., Tegmark, M. & Rolnick, D. Why does deep and cheap learning work so well? *J. Stat. Phys.* **168**, 1223–1247 (2017).

37. 37.

Grollier, J. et al. Neuromorphic spintronics. *Nat. Electron.* **3**, 360–370 (2020).

38. 38.

Mitarai, K., Negoro, M., Kitagawa, M. & Fujii, K. Quantum circuit learning. *Phys. Rev. A* **98**, 032309 (2018).

39. 39.

Poggio, T., Banburski, A. & Liao, Q. Theoretical issues in deep networks. *Proc. Natl Acad. Sci. USA* **117**, 30039–30045 (2020).

40. 40.

Scellier, B. & Bengio, Y. Equilibrium propagation: bridging the gap between energy-based models and backpropagation. *Front. Comput. Neurosci.* **11** (2017).

41. 41.

Ernoult, M., Grollier, J., Querlioz, D., Bengio, Y. & Scellier, B. Equilibrium propagation with continual weight updates Preprint at <https://arxiv.org/abs/2005.04168> (2020).

42. 42.

Laborieux, A. et al. Scaling equilibrium propagation to deep convnets by drastically reducing its gradient estimator bias. *Front. Neurosci.* **15** (2021).

43. 43.

Martin, E. et al. Eqspike: spike-driven equilibrium propagation for neuromorphic implementations. *iScience* **24**, 102222 (2021).

44. 44.

Dillavou, S., Stern, M., Liu, A. J., & Durian, D. J. Demonstration of decentralized, physics-driven learning. Preprint at <https://arxiv.org/abs/2108.00275> (2021).

45. 45.

Hermans, M., Burm, M., Van Vaerenbergh, T., Dambre, J. & Bienstman, P. Trainable hardware for dynamical computing using error backpropagation through physical media. *Nat. Commun.* **6**, 6729 (2015).

46. 46.

Hughes, T. W., Minkov, M., Shi, Y. & Fan, S. Training of photonic neural networks through in situ backpropagation and gradient measurement. *Optica* **5**, 864–871 (2018).

47. 47.

Lopez-Pastor, V. & Marquardt, F. Self-learning machines based on Hamiltonian echo backpropagation. Preprint at <https://arxiv.org/abs/2103.04992> (2021).

48. 48.

Hubara, I., Courbariaux, M., Soudry, D., El-Yaniv, R. & Bengio, Y. Quantized neural networks: training neural networks with low precision weights and activations. *J. Mach. Learn. Res.* **18**, 6869–6898 (2017).

49. 49.

Frye, R. C., Rietman, E. A. & Wong, C. C. Back-propagation learning and nonidealities in analog neural network hardware. *IEEE Trans. Neural Netw.* **2**, 110–117 (1991).

50. 50.

Cramer, B. et al. Surrogate gradients for analog neuromorphic computing. Preprint at <https://arxiv.org/abs/2006.07239> (2020).

51. 51.

Adhikari, S. P. et al. Memristor bridge synapse-based neural network and its learning. *IEEE Trans Neural Netw. Learn. Syst.* **23**, 1426–1435 (2012).

52. 52.

Lillicrap, T. P., Cownden, D., Tweed, D. B. & Akerman, C. J. Random synaptic feedback weights support error backpropagation for deep learning. *Nat. Commun.* **7**, 13276 (2016).

53. 53.

Launay, J., Poli, I., Boniface, F., & Krzakala, F. Direct feedback alignment scales to modern deep learning tasks and architectures. Preprint at <https://arxiv.org/abs/2006.12878> (2020).

54. 54.

Paszke, A. et al. PyTorch: an imperative style, high-performance deep learning library. *Adv. Neural Inf. Process. Syst.* **32**, 8024–8035 (2019).

55. 55.

LeCun, Y., Bottou, L., Bengio, Y. & Haffner, P. Gradient-based learning applied to document recognition. *Proc. IEEE* **86**, 2278–2324 (1998).

56. 56.

Xiao, H., Rasul, K., & Vollgraf, R. Fashion-MNIST: a novel image dataset for benchmarking machine learning algorithms. Preprint at <https://arxiv.org/abs/1708.07747> (2017).

57. 57.

Spoon, K. et al. Toward software-equivalent accuracy on transformer-based deep neural networks with analog memory devices. *Front. Comput. Neurosci.* **53**, (2021).

58. 58.

Kariyappa, S. et al. Noise-resilient DNN: tolerating noise in PCM-based AI accelerators via noise-aware training. *IEEE Trans. Electron Devices* **68**, 4356–4362 (2021).

59. 59.

Gokmen, T., Rasch, M. J. & Haensch, W. The marriage of training and inference for scaled deep learning analog hardware. In *2019 IEEE International Electron Devices Meeting (IEDM)* (IEEE, 2019).

60. 60.

Rasch, M. J. et al. A flexible and fast PyTorch toolkit for simulating training and inference on analog crossbar arrays. In *2021 IEEE 3rd International Conference on Artificial Intelligence Circuits and Systems (AICAS)* (IEEE, 2021).

61. 61.

Falcon, W. et al. PyTorch Lightning (2019);
<https://github.com/PyTorchLightning/pytorch-lightning>

62. 62.

Biewald, L. Experiment Tracking with Weights and Biases (2020);
<https://www.wandb.com/>

63. 63.

Kasim, M. F. et al. Building high accuracy emulators for scientific simulations with deep neural architecture search. Preprint at <https://arxiv.org/abs/2001.08055> (2020).

64. 64.

Rahmani, B. et al. Actor neural networks for the robust control of partially measured nonlinear systems showcased for image propagation through diffuse media. *Nat. Mach. Intell.* **2**, 403–410 (2020).

65. 65.

Karniadakis, G. E. et al. Physics-informed machine learning. *Nat. Rev. Phys.* **3**, 422–440 (2021).

66. 66.

Akiba, T., Sano, S., Yanase, T., Ohta, T. & Koyama, M. Optuna: a next-generation hyperparameter optimization framework. In *Proc. 25th ACM SIGKDD International Conference on Knowledge Discovery & Data Mining* 2623–2631 (2019).

67. 67.

Liu, W. et al. Programmable controlled mode-locked fiber laser using a digital micromirror device. *Opt. Lett.* **42**, 1923–1926 (2017).

68. 68.

Matthès, M. W., del Hougne, P., de Rosny, J., Lerosey, G. & Popoff, S. M. Optical complex media as universal reconfigurable linear operators. *Optica* **6**, 465–472 (2019).

69. 69.

Popoff, S. M. & Matthès, M. W. ALP4lib: q Python wrapper for the Vialux ALP-4 controller suite to control DMDs. *Zenodo*

<https://doi.org/10.5281/zenodo.4076193> (2020).

70. 70.

Hillenbrand, J., Getty, L. A., Wheeler, K. & Clark, M. J. Acoustic characteristics of American English vowels. *J. Acoust. Soc. Am.* **97**, 3099–3111 (1995).

71. 71.

Veit, A., Wilber, M. & Belongie, S. Residual networks behave like ensembles of relatively shallow networks Preprint at <https://arxiv.org/abs/1605.06431> (2016).

Acknowledgements

We thank NTT Research for their financial and technical support. Portions of this work were supported by the National Science Foundation (award CCF-1918549). L.G.W. and T.W. acknowledge support from Mong Fellowships from Cornell Neurotech during early parts of this work. P.L.M. acknowledges membership of the CIFAR Quantum Information Science Program as an Azrieli Global Scholar. We acknowledge discussions with D. Ahsanullah, M. Anderson, V. Kremenetski, E. Ng, S. Popoff, S. Prabhu, M. Saebo, H. Tanaka, R. Yanagimoto, H. Zhen and members of the NTT PHI Lab/NSF Expeditions research collaboration, and thank P. Jordan for discussions and illustrations.

Author information

Author notes

1. These authors contributed equally: Logan G. Wright, Tatsuhiro Onodera

Affiliations

1. School of Applied and Engineering Physics, Cornell University, Ithaca, NY, USA

Logan G. Wright, Tatsuhiro Onodera, Martin M. Stein, Tianyu Wang, Zoey Hu & Peter L. McMahon

2. NTT Physics and Informatics Laboratories, NTT Research, Inc., Sunnyvale, CA, USA

Logan G. Wright & Tatsuhiro Onodera

3. School of Electrical and Computer Engineering, Cornell University, Ithaca, NY, USA

Darren T. Schachter

Contributions

L.G.W., T.O. and P.L.M. conceived the project and methods. T.O. and L.G.W. performed the SHG-PNN experiments. L.G.W. performed the electronic-PNN experiments. M.M.S. performed the oscillating-plate-PNN experiments. T.W., D.T.S. and Z.H. contributed to initial parts of the work. L.G.W., T.O., M.M.S. and P.L.M. wrote the manuscript. P.L.M. supervised the project.

Corresponding authors

Correspondence to [Logan G. Wright](#), [Tatsuhiro Onodera](#) or [Peter L. McMahon](#).

Ethics declarations

Competing interests

L.G.W., T.O., M.M.S. and P.L.M. are listed as inventors on a US provisional patent application (number 63/178,318) on physical neural networks and physics-aware training. The other authors declare no competing interests.

Peer review information

Nature thanks Tayfun Gokmen and Damien Querlioz for their contribution to the peer review of this work. Peer reviewer reports are available.

Additional information

Publisher's note Springer Nature remains neutral with regard to jurisdictional claims in published maps and institutional affiliations.

Supplementary information

[Supplementary Information](#)

This file contains Supplementary Sections 1–5, including Supplementary Figs. 1–37 and References—see the contents page for details.

[Peer Review File](#)

Rights and permissions

Open Access This article is licensed under a Creative Commons Attribution 4.0 International License, which permits use, sharing, adaptation, distribution and reproduction in any medium or format, as long as you give appropriate credit to the original author(s) and the source, provide a link to the Creative Commons license, and indicate if changes were made. The images or other third party material in this article are included in the article's Creative Commons license, unless indicated otherwise in a credit line to the material. If material is not included in the article's Creative Commons license and your intended use is not permitted by statutory regulation or exceeds the permitted use, you will need to obtain permission directly from the copyright holder. To view a copy of this license, visit <http://creativecommons.org/licenses/by/4.0/>.

[Reprints and Permissions](#)

About this article

Cite this article

Wright, L.G., Onodera, T., Stein, M.M. *et al.* Deep physical neural networks trained with backpropagation. *Nature* **601**, 549–555 (2022). <https://doi.org/10.1038/s41586-021-04223-6>

- Received: 19 May 2021
- Accepted: 09 November 2021
- Published: 26 January 2022
- Issue Date: 27 January 2022
- DOI: <https://doi.org/10.1038/s41586-021-04223-6>

Share this article

Anyone you share the following link with will be able to read this content:

[Get shareable link](#)

Sorry, a shareable link is not currently available for this article.

[Copy to clipboard](#)

Provided by the Springer Nature SharedIt content-sharing initiative

This article was downloaded by **calibre** from <https://www.nature.com/articles/s41586-021-04223-6>

| [Section menu](#) | [Main menu](#) |

- Article
- Open Access
- [Published: 26 January 2022](#)

Emergent interface vibrational structure of oxide superlattices

- [Eric R. Hoglund](#) ORCID: [orcid.org/0000-0002-3409-4960¹](https://orcid.org/0000-0002-3409-4960),
- [De-Liang Bao](#) ORCID: [orcid.org/0000-0002-5070-4765²](https://orcid.org/0000-0002-5070-4765),
- [Andrew O'Hara](#) ORCID: [orcid.org/0000-0002-0323-9039²](https://orcid.org/0000-0002-0323-9039),
- [Sara Makarem](#) ORCID: [orcid.org/0000-0002-6254-5036¹](https://orcid.org/0000-0002-6254-5036),
- [Zachary T. Piontkowski](#) ORCID: [orcid.org/0000-0002-6282-0106³](https://orcid.org/0000-0002-6282-0106),
- [Joseph R. Matson⁴](#),
- [Ajay K. Yadav⁵](#),
- [Ryan C. Haislmaier⁶](#),
- [Roman Engel-Herbert^{7,8}](#),
- [Jon F. Ihlefeld¹](#),
- [Jayakanth Ravichandran⁹](#),
- [Ramamoorthy Ramesh](#) ORCID: [orcid.org/0000-0003-0524-1332⁵](https://orcid.org/0000-0003-0524-1332),
- [Joshua D. Caldwell](#) ORCID: [orcid.org/0000-0003-0374-2168⁴](https://orcid.org/0000-0003-0374-2168),
- [Thomas E. Beechem^{3,10,11}](#),
- [John A. Tomko¹²](#),
- [Jordan A. Hachtel](#) ORCID: [orcid.org/0000-0002-9728-0920¹³](https://orcid.org/0000-0002-9728-0920),
- [Sokrates T. Pantelides](#) ORCID: [orcid.org/0000-0002-2963-7545^{2,14}](https://orcid.org/0000-0002-2963-7545),
- [Patrick E. Hopkins](#) ORCID: [orcid.org/0000-0002-3403-743X^{1,12,15}](https://orcid.org/0000-0002-3403-743X) &
- [James M. Howe¹](#)

[Nature](#) volume 601, pages 556–561 (2022)

- 2017 Accesses
- 36 Altmetric
- [Metrics details](#)

Subjects

- [Atomistic models](#)
- [Surfaces, interfaces and thin films](#)
- [Transmission electron microscopy](#)

Abstract

As the length scales of materials decrease, the heterogeneities associated with interfaces become almost as important as the surrounding materials. This has led to extensive studies of emergent electronic and magnetic interface properties in superlattices^{[1,2,3,4,5,6,7,8,9](#)}. However, the interfacial vibrations that affect the phonon-mediated properties, such as thermal conductivity^{[10,11](#)}, are measured using macroscopic techniques that lack spatial resolution. Although it is accepted that intrinsic phonons change near boundaries^{[12,13](#)}, the physical mechanisms and length scales through which interfacial effects influence materials remain unclear. Here we demonstrate the localized vibrational response of interfaces in strontium titanate–calcium titanate superlattices by combining advanced scanning transmission electron microscopy imaging and spectroscopy, density functional theory calculations and ultrafast optical spectroscopy. Structurally diffuse interfaces that bridge the bounding materials are observed and this local structure creates phonon modes that determine the global response of the superlattice once the spacing of the interfaces approaches the phonon spatial extent. Our results provide direct visualization of the progression of the local atomic structure and interface vibrations as they come to determine the vibrational response of an entire superlattice. Direct observation of such local atomic and vibrational phenomena demonstrates that their spatial extent needs to be quantified to understand macroscopic behaviour. Tailoring interfaces, and knowing their local vibrational response, provides a means of pursuing designer solids with emergent infrared and thermal responses.

[Download PDF](#)

Main

The hierarchy of lattices in superlattices presents a tunable phonon–material interaction where, at small-to-moderate-period thicknesses, coherent and localized interface phonons have a major role in controlling properties. The vibrations and coupling present at interfaces in superlattices, in a broader context, occur at other interphase and intergranular boundaries and can result in remarkable properties^{[3,14,15,16,17,18,19,20,21,22,23,24](#)}. Probing vibrations with the lateral spatial resolution required to provide knowledge that can be used for interface engineering and customization of thermal and infrared properties has remained prohibitively difficult^{[10,12,15,25,26,27](#)}. The spectral and spatial resolution of monochromated electron

energy loss spectroscopy (EELS) in a scanning transmission electron microscope (STEM) provides a unique opportunity to probe the spatial extent of vibrational excitations that are conventionally assessed by infrared light or neutrons. Such resolving capabilities have so far been demonstrated in resolving phonons associated with chemical changes at point defects and stacking faults in crystals^{[28,29,30,31](#)}.

Segmented STEM detectors used for integrated differential phase contrast (iDPC) can image both light and heavy elements, providing knowledge of local symmetry, which dictates vibrational properties^{[32,33,34](#)}. Hence, STEM imaging and EELS provides a toolset to understand the intertwined local symmetry and vibrational properties at material interfaces.

Here we combine advanced STEM-iDPC and monochromated EELS experiments with density functional theory (DFT) calculations to quantify the local symmetry and vibrational states in strontium titanate (SrTiO_3 , STO)–calcium titanate (CaTiO_3 , CTO) superlattices. We measure the spatial extent of TiO_6 octahedral rotation across the STO–CTO interfaces (that is, octahedral coupling) and relate this information to the local titanium (Ti) and oxygen (O) vibrational response measured with high-spatial-resolution EELS. Second-harmonic-generation (SHG) measurements are performed to measure the macroscopic opto-electronic properties and interface density. DFT calculations are used to model the structural evolution of the superlattices and provide insights into the origins of their differing vibrational states. Finally, through ultrafast optical spectroscopy measurements, we assess the lifetime of the zone-centre phonon modes, providing insight into the macroscopic property progression observed in these oxide heterostructures. We show that as the superlattice layer thickness approaches the width of the structurally diffuse interfaces, where octahedral coupling occurs, the layers lose uniqueness and adopt the structure and vibrational response of the interface. Thus, the vibrational response of the interface becomes characteristic of the entire material.

To evaluate the influence of interfaces, we synthesized five STO–CTO superlattices with layer thicknesses of 27, 6, 4, 3 and 2 pseudo-cubic unit cells (SL27, SL6, SL4, SL3 and SL2, respectively). For (S)TEM and experiments we focus on SL27, SL4 and SL2, which are shown schematically in Fig. [1a](#). Large-period SL27 and short-period SL2 were chosen to represent superlattices with well separated and closely spaced interfaces, respectively. SL4 was chosen as an intermediate. SL6 and SL3 were included for the optics-based experiments to provide additional data points.

Fig. 1: Period-dependent changes in the symmetry of STO–CTO superlattices.

 **figure 1**

a, Superlattice structures calculated from DFT with coloured-bar schematics denoting the chemically (left) and structurally (right) defined interfaces. Here green, blue and cyan rectangles correspond to STO, CTO and interface layers, respectively; the same colours are used in **e**, **f**, **h**, **i**, **k**, **l**. Green, blue, grey and red circles in **a**, **e**, **f**, **h**, **i**, **k** correspond to Sr, Ca, Ti and O atoms, respectively. **b–d**, The [100] zone-axis SADP for SL27 (**b**), SL4 (**c**) and SL2 (**d**) grown on NGO. The coloured arrows correspond to ordered reflections from the three possible domains. The solid arrows indicate ordered reflections that exist and the hollow arrows indicate absences. Insets: ball-and-stick models of the orientations present with border colours matching the arrows. The red and blue arrows and insets are viewed along an out-of-phase tilt axis and the yellow are viewed along an in-phase tilt axis. In **c**, **d**, superlattice reflections are seen in the 001 direction. In **b**, closely spaced superlattice reflections appear as streaking of the fundamental reflections. **e–m**, ADF images (**e**, **h**, **k**), iDPC images (**f**, **i**, **l**) and octahedral tilt angles (**g**, **j**, **m**) of SL27 (**e–g**), SL4 (**h–j**) and SL2 (**k–m**). The legend in **g** illustrates the in-plane (green) and out-of-plane (black) tilt angles (θ), which are defined as half of the projected O–Ti–O bond angle. The tilt angles for a one unit-cell column are overlayed in each iDPC image to demonstrate the changing in-plane (green triangles) and out-of-plane (grey triangles) tilt angles. In **g**, **j**, **m**, solid and dashed curves are from experimental measurements and calculations, respectively. The error bars represent one standard deviation. Chemically abrupt interfaces are illustrated to

the left of the ADF images (**e**, **h**, **k**) and model structures (**a**), illustrating the abrupt change between STO (green) and CTO (blue) layers. Chemically diffuse interfaces are illustrated to the right of the iDPC images (**f**, **i**, **l**) and model structures (**a**), illustrating the non-abrupt symmetry changes that are occurring as a result of octahedral coupling.

To quantify the structure, we acquired selected-area electron diffraction patterns (SADPs). The SADPs reveal that the orientation of octahedral tilts are different in the SL27 structure compared with the SL4 and SL2 structures. The large-period SL27 structure shows ordered reflections from two of three possible *Pbnm*-CTO domains (Fig. [1b](#)), each with an in-plane *c* axis as illustrated by the ball-and-stick insets. Ordered reflections observed from the SL4 and SL2 samples indicate a single out-of-plane *c* axis, as shown in Fig. [1c,d](#) and simulated in [Supplementary Figs. 1, 2](#). This microstructural transition is accompanied by a relaxation of the lattice parameters to a single intermediate value ([Supplementary Fig. 3](#), [Supplementary Tables 1, 2](#)). Thus, as the layer thickness decreases, the underlying crystal structure adapts, which could be enabled by octahedral tilt^{[3,4,19,21,22](#)}.

To investigate the potential of octahedral tilting in the superlattices further, we use annular dark-field (ADF) and iDPC imaging to quantify the octahedral tilting (Fig. [1e–m](#)). The atomic-number (*Z*) contrast of the ADF images (Fig. [1e,h,k](#)) allows for discrimination between the brighter strontium (Sr) and darker calcium (Ca) atoms and shows chemically abrupt transitions between the two. In-plane (green triangles) and out-of-plane (grey triangles) tilt angles are overlaid on each iDPC image (Fig. [1f,i,l](#)) to demonstrate the changing octahedral tilt angles from layer to layer and from structure to structure. For example, the iDPC image of SL27 (Fig. [1f](#)) has three regions defined by observing the splitting of oxygen columns: single columns in STO, split columns in CTO and an intermediate splitting at the interface. The tilts are consistent with simple cubic $Pm\bar{3}m$ -STO containing no tilt, orthorhombic *Pbnm*-CTO along an out-of-phase tilt axis and a region where tilts transition from finite angles in CTO to none in STO. Scanning convergent-beam electron diffraction corroborates these observations ([Supplementary Fig. 4](#)).

To quantify the changes in crystal structure with reduced interface separation, the in-plane and out-of-plane octahedral angles are measured (see the legend in Fig. [1g](#)). The plane averaged tilt angle is shown in Fig. [1g,j,m](#). A coupling region is present at the STO–CTO interface of SL27 (Fig. [1g](#)). Similar coupling regions observed in other perovskite heterostructures result in extraordinary electrical and magnetic properties^{[3,7,8,9,19,20,21,22](#)}. We define the structurally diffuse interface width as one unit cell centred at the chemically abrupt TiO_2 interface as schematically shown in Fig. [1a](#).

We then turn to SL4 and SL2 to understand how the octahedra couple across the interfaces when the interface spacing is comparable to the diffuse interface width. The

CTO oxygen column splitting in SL4 is less pronounced than in SL27. Some oxygen columns within the STO layers are distinctly split whereas most appear elliptical from the partial overlap of the splitting column. The octahedra in STO and CTO are coupled, as seen in the sinusoidal profile of the tilt angles (Fig. 1j). Coupling is even more apparent in SL2 (Fig. 1m), where a nearly constant tilt angle of 7° extends throughout the entire structure. Similar titling of STO octahedra has also been observed in short-period barium titanium oxide (BaTiO_3)–STO superlattices¹⁵. Here we show that incorporation of the atomic displacements in STO is an interface-mediated process.

Using the STEM results, we define three types of superlattice: long-period superlattices, such as SL27, which exhibit monolithic phases with structurally diffuse interfaces; moderate-period superlattices (SL4) with modified monolithic phases and structurally diffuse interfaces taking up a sizable fraction of the superlattice; and short-period superlattices (SL2) comprising entirely interface regions that are better described as an ordered structure, with a global symmetry characteristic of that seen at the interfaces of all superlattices. In SL2, the material is more accurately described as having chemically ordered unit cells with a single tilt angle and a $\text{Sr}_2\text{Ca}_2\text{Ti}_4\text{O}_{12}$ basis^{5,35,36}. More simply, the short-period superlattice has become a crystal of interfaces.

We perform SHG measurements to provide further evidence of the structural regimes, which also lends insight into the electronic properties of the superlattices, as shown in Fig. 2. Both STO and CTO have inversion symmetry, so the SHG intensity of STO–CTO superlattices is directly related to the polarizability of the interface where inversion symmetry is broken. An increase in SHG intensity is observed from SL27 to SL6 as the density of interfaces increases and layers remain independent with respect to each other. However, a marked decrease in the nonlinear optical response is observed in SL4 and rapidly vanishes in superlattices with short periodicities; as the heterostructure transitions from independent monolithic layers, to coupled layers, to a single centrosymmetric structure, the second-order optical response approaches zero. In other words, the structural transitions are directly reflected in the polarizability of the superlattices.

Fig. 2: Second-harmonic intensity indicates short-period superlattices lack interfaces.

 **figure 2**

Second-harmonic intensity of STO–CTO superlattices with varying periodicity, demonstrating various regimes of structural transitions and their role in the electronic/optical properties of heterostructures. The error bars are calculated from the mean square deviation of a parabolic fit to the measured second-harmonic intensity versus incident electric field. Ball-and-stick models are included to pictorially show the connection between octahedral tilt and the presence structurally diffuse interfaces, or lack thereof.

To support the observed crystallographic structure of the superlattices and predict the effect of the observed local symmetries on vibrations, we performed DFT calculations on several prototypical superlattice models (Fig. 1a) and further consider metastable phases and layer intermixing in [Supplementary Fig. 5](#). Octahedral tilt angles for both

the experimental and theoretical results are in good agreement in both amplitude and periodicity, as indicated by the dashed curves shown in Fig. 1g,j,m. From both the structural calculations and experimental measurements, we can conclude that as the period thickness decreases, the system converges toward a single, emergent structure.

As phonon frequencies are affected by changes of bond lengths and bond angles, we expect the evolution of the octahedral tilts in our superlattices (Fig. 1) to affect the phonon density of states (PDOS), which drives the inherent thermal and infrared optical properties. To evaluate this possibility, we employed DFT to calculate the PDOS projected on the O and Ti atoms for each of the three superlattices characterized by STEM (Fig. 3a, Methods). The PDOS show three peaks at about 37 meV, about 60 meV and about 97 meV, which are further discussed in the Supplementary Information. From SL27 to SL4 and SL2, the 37-meV and 60-meV peaks redshift, whereas the 97-meV peak blueshifts, indicating an evolution of the superlattice phonon modes as the layer thickness decreases. Thus, vibrational modes assigned to the octahedra change energy as the octahedra they derive from change tilt angle with decreasing superlattice period thickness.

Fig. 3: Localized vibrational response of superlattices indicates the emergent role of the interfacial symmetry.

 figure 3

a, DFT-calculated PDOS projected on the octahedron O and Ti atoms of the SL27, SL4 and SL2 models. The arrows indicate the dominant phonon peaks. **b**, Cascade of DFT-calculated PDOS projected on STO (green), CTO (purple) and interface (orange) layers and the total DOS (black) for each superlattice model. **c–k**, Monochromated

STEM-EELS line profile analyses of the three SL structures SL27 (**c–e**), SL4 (**f–h**) and SL2 (**i–k**) with the ADF intensity (I) profile (**c, f, i**), EELS profile (**d, g, j**) and integrated spectra from each layer (**e, h, k**) (as indicated by coloured regions in the ADF profile). Energy-loss spectra are normalized by multiplying intensity by the energy squared (IE^2). The colour bars in **d, g, j** share the same labels and scales as **e, h, k**.

The attribution of peak shifts to changes in octahedral tilts is further supported by comparing the PDOS for each constituent layer and for the interface in the three superlattices (Fig. 3b). We see that in the SL27, the total DOS for the system deviates from the STO, CTO and interface spectra. However, in SL4 and SL2 the total DOS tracks the interface spectrum almost perfectly, illustrating how the interface dominates these shorter-period structures. [Supplementary Figs. 6, 8b, c](#) show examples of layer and interface modes. In other words, as the layer thickness decreases, both the structural and vibrational state converge towards the respective state of the interfaces.

The evolution in vibrational response of the superlattice is observed experimentally via spatially resolved off-axis vibrational EELS^{29,31}. With this approach, the difference in vibrational response within the diffuse interface region can be directly compared with that within the constituent layers themselves. The ADF line profiles of SL27, SL4 and SL2 are shown in Fig. 3c,f,i, and distinguish between the heavy STO and light CTO layers. The simultaneously acquired EELS are shown in Fig. 3d,g,j. Changes in the layer-to-layer response are clearly observed in the superlattices, with specific energies listed in Supplementary Table 3. For example, in SL27, the 37-meV peak is at a lower energy in the STO compared with the CTO, but the 60-meV and 97-meV peaks are at higher energies, with the interfaces exhibiting intermediate values, demonstrating the capacity to measure changes induced by local atomic displacements. Furthermore, we note that, although the interface and total-structure spectra bear some similarities, there are features in the interface spectra that cannot be reproduced by a mixture of the bulk-like neighbouring phases ([Supplementary Fig. 11a, b](#)). Unique vibrations emerging from the octahedral coupling at the interface must be present to account for the discrepancy between the total and interface spectra, as calculated via DFT. Thus, we demonstrate that variations in the localized vibrational spectra are ascribed to the regions of differing symmetry, namely, the STO, CTO and structurally diffuse interfaces.

Like the octahedral-tilt variation, spatial variations in the EELS response reduce with decreasing period. The spectral similarity from layer to layer in SL4 relative to SL27 and the exact match between the total and interface spectra indicate that the vibrational state of the superlattice is approaching that of the interfaces, demonstrating the importance of local vibrational structure as length scales decrease. The global response

of the interface vibrations further demonstrates the importance of local vibrational structure as length scales decrease.

The predominance of these interface vibrations and their global response has been shown to affect the thermal characteristics of STO–CTO superlattices, where a crossover from incoherent to coherent phonon transport is observed as the heterostructure periodicity decreases¹⁰. Previous reports have suggested that reduced zone folding of phonon dispersion leads to an increased group velocity, but direct evidence connecting underlying phononic processes, new modes and structure to the macroscopic transport mechanisms remains lacking^{10,37}. To connect the localized interface modes and structural transitions observed above to a macroscopic response, we perform Fourier transform infrared spectroscopy (FTIR) (Fig. 4a)^{10,15,16,17,18}. The residuals from a linear combination of STO and CTO films are quantified to accentuate changes unique to the superlattice. Owing to selection rules, the spectra of STO contains fewer reflectivity minima relative to CTO. As the STO and interface incorporate CTO tilt patterns, further loss of reflectivity should occur³⁸. Residuals are observed near 500 cm^{-1} and 560 cm^{-1} that decrease with decreasing period thickness (Fig. 4a). FTIR spectra from a sample on $(\text{LaAlO}_3)_{0.3}(\text{Sr}_2\text{TaAlO}_6)_{0.35}$ substrates and ultraviolet-Raman experiments show similar trends, as shown in [Supplementary Figs. 14–16](#). DFT informs that infrared-active phonons emerge in the superlattices and are associated with layer-localized, layer-delocalized and interface-localized Ti–O vibrational modes that are not infrared-active in bulk STO or CTO ([Supplementary Fig. 8](#)). The residual responses are similar in energy to those observed locally with both EELS and DFT. In addition, the sum of residuals ([Supplementary Fig. 17](#)) scales with interface density. We conclude the residuals are a consequence of the local displacements existing at the interfaces of the superlattice.

Fig. 4: FTIR and TDBS response of the STO–CTO superlattices.

 [figure 4](#)

a, Raw (solid), fitted (dashed) and residual (dot-dashed) data for FTIR from the superlattices on an NGO substrate. The 200-nm STO and CTO thin films on NGO substrates used to fit the superlattice spectra are shown in [Supplementary Figs. 13b, 15e,f](#). The difference curves are scaled by a factor of two for clarity. **b**, Phonon lifetimes (black squares) as measured via TDBS compared with the thermal conductivity (red triangles, from ref. [10](#)) of STO–CTO superlattices with varying periodicities. The strong correlation between the two techniques conclusively demonstrates a transition in phonon scattering rates across the structural transitions elucidated with STEM/EELS. The error bars represent the standard deviation.

To directly investigate the emergent phonon dynamics, we perform time-domain Brillouin scattering (TDBS) measurements, which detect the propagation of the zone-centre longitudinal modes as a function of time, thus providing a measure of their lifetime^{[39,40](#)}. For short-period superlattices (SL2), an increase in both the phonon scattering time and the thermal conductivity is observed; this is no longer described by a superlattice with interfaces, but rather has a single structure with uniform octahedral tilts. We find the previously reported thermal conductivity to be correlated with the phonon scattering times (Fig. [4](#)), with both having a minimum at SL4^{[10](#)}. Thus, in strong agreement with our STEM, EELS and SHG results, the phonon lifetime is found to increase as material interfaces vanish. This combination of structural, electronic/optical and vibrational characterization techniques unambiguously demonstrates the underlying coupling of heterostructures and emergent global properties that are driven by interfaces.

Conclusions

From a broader perspective, these results provide an alternative pathway by which nanostructuring can influence material properties. Typically, a superlattice response is thought to arise through either localized or coherent effects. The latter concerns the coherence length of the states with respect to interface periodicity, whereas for localization, discrete confined quantum states exist that are different to those in the bulk. Neither of these views explain the changes in the vibrational response observed here, because they neglect underlying symmetry changes that can propagate into the constituent materials. When scaling the phases that constitute the material to unit-cell dimensions, the solid takes on a new symmetry that cannot be explained by a combination of the constituent materials. In these STO–CTO superlattices, this new structure results from octahedral coupling between the layers. Here we have directly imaged these localized changes in symmetry and their impact on vibrations using a combination of STEM iDPC and monochromated EELS, with the conclusions drawn supported by DFT. We have further demonstrated how the observed localized phenomena evolve from locally affecting the superlattice at larger periods to dictating the global response of the superlattice as the period decreases via nonlinear optical and

phonon lifetime measurements. It is important to note that the reported changes in symmetry are not from the global periodicity of the superlattice. Rather, it is the local symmetry changes at the interfaces, and their spatial distribution, that ultimately dictate the entire macroscopic response of the solid as the period thickness decreases. Therefore, tailoring interfaces, and knowing their local response, provides a means of pursuing ‘designer’ solids with emergent infrared and thermal responses not inherent within either of the constituent bulk materials.

Methods

Thin-film growth

Superlattices grown on NdGaO_3 (NGO) substrates were synthesized using reflection high-energy electron diffraction assisted pulsed laser deposition. Further discussion of the growth is found in ref. [10](#) and its supplementary information. Superlattices grown on $(\text{LaAlO}_3)_{0.3}(\text{Sr}_2\text{TaAlO}_6)_{0.35}$ (LSAT) substrates were realized via hybrid molecular beam epitaxy as outlined in ref. [41](#).

Electron microscopy

Selected-area diffraction patterns are from a Thermo Fisher 80–300 kV Titan operating at 300 kV and equipped with a Gatan OneView camera.

Scanning convergent-beam electron diffraction, ADF and iDPC images were acquired on a Thermo Fisher Themis Z-STEM operating at 300 kV. ADF and iDPC images were acquired with a convergence angle of 30 mrad, a probe current of 200 pA and a dwell time of 625 nm px^{-1} . A 145-mm camera length projected onto the ADF detector with a 200-mrad outer radius and 40-mrad inner radius. The segmented ADF detector used for iDPC had a 38-mrad outer radius and a 10-mrad inner radius. The iDPC images (Fig. [1f, i, l](#)) allow the measurement of the positions of the O and Ti columns, enabling quantification of the octahedral tilt angles^{[42,43](#)}. The position of the metal sites was refined by thresholding, finding the centre of mass, then fitting with two-dimensional Gaussians. The spacing of the O columns necessitated locating the atomic columns manually.

Vibrational EELS spectra were acquired at an operating voltage of 60 kV using a Nion HERMES monochromated aberration-corrected dedicated STEM with a convergence angle of 32 mrad, an entrance aperture collection angle of 25 mrad and an energy dispersion of 0.413 meV per channel for the SL2 and SL4 acquisitions and 0.826 meV per channel for the SL27 acquisition, and the achieved energy resolution varied between 12 meV and 17 meV ([Supplementary Fig. 12](#)). In this study, all EELS spectra

were acquired in an off-axis mode, obtained by shifting the electron diffraction pattern with respect to EELS entrance aperture. In EELS, delocalized dipole scattering can dominate signals and mask local variations in phonon populations, which can be detected by impact scattering. However, by acquiring EELS from only electrons scattered out to high angles, the dipole scattering is reduced more than the impact scattering and the localized signals can be retrieved^{29,31}. Here we displace the optic axis from the EELS entrance aperture by about 50 mrad in the non-dispersive axis of the spectrometer, and only integrate pixels in the top half of the acquired signal. Thus, the off-axis EELS shown in this study has an effective collection semi-angle of about 12.5 mrad that is scattered about 55.5 mrad from the central optic axis. By integrating the signal at higher angles, we preferentially select vibrations that have undergone impact scattering, which is a more spatially localized signal, and exclude the electrons that have undergone dipole scattering to low angles, which is spatially delocalized.

Vibrational EELS background removal with fitted functions can introduce error because the realistic background does not have a functional shape, owing to overlapping of the zero-loss peak and real spectral features such as non-resolvable acoustic or low-energy optic phonons. Therefore, we choose to take an alternative approach, normalizing the intensity of the spectra by multiplying by the energy squared (E^2), thus uniformly normalizing the spectra to a quadratic background. To increase the signal-to-noise ratio and for comparison with theoretical predictions, we take the average of all spectra in STO, CTO and the interface layers, akin to layer DOS in DFT. The interface signal is defined as one unit cell in length for consistency with structural characterization. Interfaces are assigned using the second derivative of the off-axis high-angle annular dark-field signal. An example of interface assignment for SL4 is shown in [Supplementary Fig. 9](#). The layer-averaged signals from each layer can then be easily compared with one another and the average superlattice signal. An initial concern of qualitatively comparing the vibrational response of the layers and interfaces was possible thickness-dependent trends in scattering probability relative to other excitations. To eliminate these effects, we compare the thickness dependent trends ([Supplementary Fig. 10](#)) and find that the layer-averaged signals converge after a few layers. We use the layers after signal convergence for comparing superlattices. In SL2, structural characterization showed that we cannot define a structural interface or structurally unique layers. We therefore had three choices: (1) define the entire period as a layer, which is the same as the average superlattice signal and provides no comparable spectra; (2) revert to the definition for chemically defined interfaces, which provides STO and CTO layer-average spectra for comparison with each other and the average superlattice signal; or (3) use the structurally diffuse interface width of one unit cell, which provides the interface, STO and CTO layers. The third definition does not leave an actual STO or CTO layer, because only a single atomic plane of TiO₂ remains between the interfaces. The lack of a complete STO and CTO layer was part of the rational for a single phase

in the iDPC analysis, making the third choice inconsistent with the structural analysis. The second choice would be inconsistent with the EELS analysis of SL27 and SL2. We chose the third choice so that the EELS analysis between the three superlattices was consistent, and because atomic-resolution conditions were not used in all EELS experiments, making the one-atomic-plane delineation of layers infeasible. The lack of spectral change from the STO layer to the interface layer to the CTO layer observed in the EELS analysis of SL2 then shows that the layers behave similarly, which is consistent with each having a similar symmetry.

Calculations

The DFT calculations used the Vienna Ab initio Simulation Package (VASP)⁴⁴ with the projected-augmented wave (PAW)^{45,46} method and the local-density approximation (LDA)⁴⁷. Phonon calculations were performed using the LDA for exchange correlation because it has been found to perform better for phonons at the Γ point, which is of interest here, in bulk CTO and STO^{48,49,50}. The plane-wave basis energy cut-off is 600 eV. The superlattice structural models were constructed by alternatively combining *Pbnm*-phase STO and CTO in the *c* direction with specific thicknesses. An SL8 model was chosen to obtain tilt angles for a large-period superlattice, knowing that the interface coupling is limited to a few atomic planes and the prohibitive computational requirements for simulating SL27. For structural relaxation, the structures were relaxed until the atomic forces were less than 0.01 eV \AA^{-1} . The lattice parameters were also optimized for each superlattice model. Phonon calculations were performed using the finite-difference method. For structural relaxation and phonon calculations, the *k*-samplings are $6 \times 6 \times 6$ for bulk STO and CTO, $4 \times 4 \times 2$ for SL2 and SL4, and $2 \times 2 \times 2$ for SL8. A full-width at half-maximum of 16 cm^{-1} was used to plot the projected PDOS.

The PDOS of each model was obtained by performing a weighted average over the respective constituent layers. The projected PDOS of the respective constituent layers was normalized by the number of atoms per layer to provide a consistent comparison between the three superlattices. The total PDOS of each model was then obtained by $n_{\text{total}} = (x \times n_{\text{STO}} + y \times n_{\text{CTO}} + z \times n_{\text{int}}) / (x + y + z)$, where *x*, *y* and *z* are the numbers of atoms considered in each layer. In particular, the PDOS of SL27 was obtained by averaging the phonon modes of the intrinsic bulk STO, the intrinsic bulk CTO and the SL8 interface. The interface in all models is defined as one unit cell on either side of the chemically defined interface, which is consistent with experimental and calculated structures. As the primary structural changes are associated with TiO_6 octahedra, we can assume that the distinct vibrational state of different superlattices are primarily contributed by Ti/O-related vibrational modes. Therefore, we project the PDOS on Ti and O atoms, emphasizing the symmetry–phonon relation. As only the phonon modes

parallel to fields are activated, the PDOS is also projected in the (110) plane that is perpendicular to the electron beam. For completeness, we have also projected the PDOS on the A-site atoms, which can be found in [Supplementary Fig. 7](#).

Optical spectroscopies

Raman spectroscopy was performed on samples synthesized atop NGO with a Horiba LabRam Raman instrument employing a 325-nm laser focused using a $\times 40/0.5$ numerical aperture objective. Laser powers were verified to be inconsequential to the results. At this wavelength, the skin depth for the exciting ultraviolet light is 26 nm within STO whereas it is more than 1 μm for CTO. Despite the transparency of CTO, all Raman-examined films were 200 nm in thickness and thus contain at least 100 nm of STO. This is more than three times the skin depth and thus the underlying NGO does not affect the Raman experiment. The monolithic samples show a response expected from their bulk form^{48,51,52,53,54,55,56,57}. Raman and FTIR spectra were fitted using a least-squares minimized linear combination of acquired monolithic spectra. This extenuated the differences between the superlattice and the constituent materials and helped remove the substrate response in the FTIR.

Second-harmonic generation

SHG measurements were performed on SL27, SL6, SL4, SL3, SL2 and SL1 with nominal thicknesses of 200 nm atop NGO substrates. In contrast to linear optical measurements, which are dictated by the average of the linear response of the materials comprising the superlattice⁵⁸, the higher-rank dielectric tensor associated with SHG vanishes if the constituent materials have inversion symmetry. The home-built SHG microscope is centred on a 1,040-nm neodymium-doped yttrium orthovanadate, roughly 100-fs Gaussian laser source that is focused to the sample surface at an incident angle of 45° relative to the surface normal using a $\times 10$ microscope objective (numerical aperture 0.28). The incident beam polarization is rotated using a half-wave plate. The forward-scattered beam, containing both the fundamental and second-harmonic frequencies, is collected with a lens. Through a series of band-pass filters, non-second-harmonic components are filtered out, whereas the second-harmonic component is focused to an amplified avalanche photodiode. The generated voltage is further amplified via lock-in detection demodulated at the laser repetition rate. The reported second-harmonic values are the parabolic coefficient determined by fitting the measured SHG intensity (for example, lock-in photodiode response) as a function of incident laser power for each sample. The square dependence of measured intensity versus incident field indicates that no higher harmonics are measured or that no optical leakage of the fundamental frequency is reaching the detector.

Time-domain Brillouin scattering

The TDBS measurements were performed using an 80-MHz, 800-nm titanium:sapphire oscillator (about 100-fs pulses) that is split into two optical paths before reaching the sample. The first beam is used as a high-energy pump pulse, that, when focused to the sample surface, stimulates coherent acoustic phonon modes via rapid thermal expansion of the material. This pump pulse is frequency doubled (400 nm) for these measurements to increase optical absorption in the STO–CTO layers. The second beam is sent down a mechanical delay stage to vary the time at which the pulse reaches the sample surface; this low-energy ‘probe’ pulse monitors changes in the optical properties of the sample following excitation as a function of time delay between the two pulses. As the coherent longitudinal phonon mode propagates through the superlattice, the probe beam partially reflects off the sample surface and partially off the coherent wave. The distance between these partial reflections evolves in time owing to propagation of the phonon mode, and thus operates as a Fabry–Perot interferometer, where for distances that are integer multiples of the probe wavelength, constructive interference is observed in the signal, and for half-integer wavelength distances, the two reflections destructively interfere and reduce the signal. The temporal decay of these sinusoidally varying oscillations is a direct monitor of the lifetime of the pump-generated longitudinal vibrational mode within the superlattice structure.

Data availability

The datasets generated during and/or analysed during the current study are available from the corresponding authors on reasonable request. Please contact E.R.H. regarding STEM imagining data. Please contact E.R.H. or J.A.H. regarding EELS data. Please contact S.T.P. regarding DFT data. Please contact P.E.H. regarding SHG and Brillouin zone scattering data. Please contact E.R.H. regarding Raman or FTIR data.

References

1. 1.

Zhao, W. et al. Direct imaging of electron transfer and its influence on superconducting pairing at FeSe/SrTiO₃ interface. *Sci. Adv.* **4**, 1–7 (2018).

2. 2.

Chen, Y. Z. et al. Extreme mobility enhancement of two-dimensional electron gases at oxide interfaces by charge-transfer-induced modulation doping. *Nat.*

Mater. **14**, 801–806 (2015).

3. 3.

Domínguez, C. et al. Length scales of interfacial coupling between metal and insulator phases in oxides. *Nat. Mater.* **19**, 1182–1187 (2020).

4. 4.

Moon, E. J. et al. Effect of interfacial octahedral behavior in ultrathin manganite films. *Nano Lett.* **14**, 2509–2514 (2014).

5. 5.

Balachandran, P. V. Massive band gap variation in layered oxides through cation ordering. *Nat. Commun.* **6**, 6191 (2015).

6. 6.

Aguado-Puente, P. & Junquera, J. Structural and energetic properties of domains in $\text{PbTiO}_3/\text{SrTiO}_3$ superlattices from first principles. *Phys. Rev. B* **85**, 184105 (2012).

7. 7.

Chen, B. et al. Spatially controlled octahedral rotations and metal–insulator transitions in nickelate superlattices. *Nano Lett.* **21**, 1295–1302 (2021).

8. 8.

Hwang, J. et al. Structural origins of the properties of rare earth nickelate superlattices. *Phys. Rev. B* **87**, 060101 (2013).

9. 9.

Zhai, X. et al. Correlating interfacial octahedral rotations with magnetism in $(\text{LaMnO}_{3+\delta})\text{N}/(\text{SrTiO}_3)\text{N}$ superlattices. *Nat. Commun.* **5**, 4283 (2014).

10. 10.

Ravichandran, J. et al. Crossover from incoherent to coherent phonon scattering in epitaxial oxide superlattices. *Nat. Mater.* **13**, 168–172 (2014).

11. 11.

Luckyanova, M. N. et al. Coherent phonon heat conduction in superlattices. *Science* **338**, 936–939 (2012).

12. 12.

Ratchford, D. C. et al. Controlling the infrared dielectric function through atomic-scale heterostructures. *ACS Nano* **13**, 6730–6741 (2019).

13. 13.

Paudel, T. R. & Lambrecht, W. R. L. Computational study of phonon modes in short-period AlN/GaN superlattices. *Phys. Rev. B* **80**, 7 (2009).

14. 14.

Nataf, G. F. et al. Domain wall engineering: mastering topological defects in ferroelectric and ferroelastic materials. *Nature* **2**, 634–648 (2020).

15. 15.

Tenne, D. A. et al. Probing nanoscale ferroelectricity by ultraviolet Raman spectroscopy. *Science* **313**, 1614–1616 (2006).

16. 16.

Vattuone, L., Savio, L. & Rocca, M. in *Oxide Materials at the Two-Dimensional Limit* Vol. 234 (eds Netzer, F. P. & Fortunelli, A.) 169–199 (Springer, 2016).

17. 17.

Premper, J. et al. Surface stress and lattice dynamics in oxide ultrathin films. *Phys. Status Solidi B* **257**, 1900650 (2020).

18. 18.

Schober, A. et al. Vibrational properties of LaNiO₃ films in the ultrathin regime. *APL Mater.* **8**, 061102 (2020).

19. 19.

Rondinelli, J. M. & Spaldin, N. A. Substrate coherency driven octahedral rotations in perovskite oxide films. *Phys. Rev. B* **82**, 113402 (2010).

20. 20.

He, J., Borisevich, A., Kalinin, S. V., Pennycook, S. J. & Pantelides, S. T. Control of octahedral tilts and magnetic properties of perovskite oxide heterostructures by substrate symmetry. *Phys. Rev. Lett.* **105**, 227203 (2010).

21. 21.

Biegalski, M. D. et al. Impact of symmetry on the ferroelectric properties of CaTiO_3 thin films. *Appl. Phys. Lett.* **106**, 162904–162915 (2015).

22. 22.

Middey, S. et al. Epitaxial strain modulated electronic properties of interface controlled nickelate superlattices. *Phys. Rev. B* **98**, 045115–045118 (2018).

23. 23.

Petzelt, J. et al. Grain boundary effects on dielectric, infrared and Raman response of SrTiO_3 nanograins ceramics. *J. Eur. Ceram. Soc.* **26**, 2855–2859 (2006).

24. 24.

Tai, K., Lawrence, A., Harmer, M. P. & Dillon, S. J. Misorientation dependence of Al_2O_3 grain boundary thermal resistance. *Appl. Phys. Lett.* **102**, 034101–034104 (2013).

25. 25.

Koh, Y. K., Cao, Y., Cahill, D. G. & Jena, D. Heat-transport mechanisms in superlattices. *Adv. Funct. Mater.* **19**, 610–615 (2009).

26. 26.

Simkin, M. V. & Mahan, G. D. Minimum thermal conductivity of superlattices. *Phys. Rev. Lett.* **84**, 927–930 (2000).

27. 27.

Li, Y.-H. et al. Probing lattice vibrations at SiO_2/Si surface and interface with nanometer resolution. *Chin. Phys. Lett.* **36**, 026801 (2019).

28. 28.

Yan, X. et al. Single-defect phonons imaged by electron microscopy. *Nature* **589**, 65–69 (2021).

29. 29.

Hage, F. S., Radtke, G., Kepaptsoglou, D. M., Lazzeri, M. & Ramasse, Q. M. Single-atom vibrational spectroscopy in the scanning transmission electron microscope. *Science* **367**, 1124–1127 (2020).

30. 30.

Venkatraman, K., Levin, B. D. A., March, K., Rez, P. & Crozier, P. A. Vibrational spectroscopy at atomic resolution with electron impact scattering. *Nat. Phys.* **15**, 1237–1241 (2019).

31. 31.

Hage, F. S., Kepaptsoglou, D. M., Ramasse, Q. M. & Allen, L. J. Phonon spectroscopy at atomic resolution. *Phys. Rev. Lett.* **122**, 016103–016105 (2019).

32. 32.

Lazić, I., Bosch, E. G. T. & Lazar, S. Phase contrast STEM for thin samples: integrated differential phase contrast. *Ultramicroscopy* **160**, 265–280 (2016).

33. 33.

de Graaf, S., Momand, J., Mitterbauer, C., Lazar, S. & Kooi, B. J. Resolving hydrogen atoms at metal–metal hydride interfaces. *Sci. Adv.* **6**, eaay4312 (2020).

34. 34.

Zheng, Q. et al. Direct visualization of anionic electrons in an electride reveals inhomogeneities. *Sci. Adv.* **7**, eabe6819 (2021).

35. 35.

King, G. & Woodward, P. M. Cation ordering in perovskites. *J. Mater. Chem.* **20**, 5785–5796 (2010).

36. 36.

Rondinelli, J. M. & Fennie, C. J. Octahedral rotation-induced ferroelectricity in cation ordered perovskites. *Adv. Mater.* **24**, 1961–1968 (2012).

37. 37.

Wang, Y., Huang, H. & Ruan, X. Decomposition of coherent and incoherent phonon conduction in superlattices and random multilayers. *Phys. Rev. B* **90**, 165406 (2014).

38. 38.

Shi, F., Fu, G., Xiao, E.-C. & Li, J. Lattice vibrational characteristics and dielectric properties of pure phase CaTiO₃ ceramic. *J. Mater. Sci. Mater. Electron.* **31**, 18070–18076 (2020).

39. 39.

Tomko, J. A. et al. Tunable thermal transport and reversible thermal conductivity switching in topologically networked bio-inspired materials. *Nat. Nanotechnol.* **13**, 959–964 (2018).

40. 40.

Giri, A. et al. Experimental evidence of suppression of subterahertz phonons and thermal conductivity in GaAs/AlAs superlattices due to extrinsic scattering processes. *J. Phys. Chem. C* **122**, 29577–29585 (2018).

41. 41.

Haislmaier, R. C. et al. Overlapping growth windows to build complex oxide superlattices. *APL Mater.* **6**, 111104 (2018).

42. 42.

He, Q. et al. Towards 3D mapping of BO₆ octahedron rotations at perovskite heterointerfaces, unit cell by unit cell. *ACS Nano* **9**, 8412–8419 (2015).

43. 43.

Aso, R., Kan, D., Shimakawa, Y. & Kurata, H. Atomic level observation of octahedral distortions at the perovskite oxide heterointerface. *Sci. Rep.* **3**, 2214 (2013).

44. 44.

Kresse, G. & Furthmüller, J. Efficient iterative schemes for ab initio total-energy calculations using a plane-wave basis set. *Phys. Rev. B* **54**, 11169–11186 (1996).

45. 45.

Blöchl, P. E. Projector augmented-wave method. *Phys. Rev. B* **50**, 17953–17979 (1994).

46. 46.

Kresse, G. & Joubert, D. From ultrasoft pseudopotentials to the projector augmented-wave method. *Phys. Rev. B* **59**, 1758–1775 (1999).

47. 47.

Perdew, J. P. & Zunger, A. Self-interaction correction to density-functional approximations for many-electron systems. *Phys. Rev. B* **23**, 5048–5079 (1981).

48. 48.

Železný, V. et al. Temperature dependence of infrared-active phonons in CaTiO₃: a combined spectroscopic and first-principles study. *Phys. Rev. B* **66**, 224303 (2002).

49. 49.

Himmetoglu, B., Janotti, A., Peelaers, H., Alkauskas, A. & Van de Walle, C. G. First-principles study of the mobility of SrTiO₃. *Phys. Rev. B* **90**, 241204 (2014).

50. 50.

Zhang, Y., Sun, J., Perdew, J. P. & Wu, X. Comparative first-principles studies of prototypical ferroelectric materials by LDA, GGA, and SCAN meta-GGA. *Phys. Rev. B* **96**, 035143 (2017).

51. 51.

McMillan, P. & Ross, N. The Raman spectra of several orthorhombic calcium oxide perovskites. *Phys. Chem. Miner.* **16**, 21–28 (1988).

52. 52.

Schaufele, R. F. & Weber, M. J. First- and second-order Raman scattering of SrTiO₃. *J. Chem. Phys.* **46**, 2859–2861 (1967).

53. 53.

Hirata, T., Ishioka, K. & Kitajima, M. Vibrational spectroscopy and X-ray diffraction of perovskite compounds $\text{Sr}_{1-x}\text{M}_x\text{TiO}_3$ ($\text{M} = \text{Ca}, \text{Mg}$; $0 \leq x \leq 1$). *J. Solid State Chem.* **124**, 353–359 (1996).

54. 54.

Balachandran, U. & Eror, N. G. Laser-induced Raman scattering in calcium titanate. *Solid State Commun.* **44**, 815–818 (1982).

55. 55.

Zheng, H. et al. Raman spectroscopy of CaTiO_3 -based perovskite solid solutions. *J. Mater. Res.* **19**, 488–495 (2004).

56. 56.

Petzelt, J. et al. Dielectric, infrared, and Raman response of undoped SrTiO_3 ceramics: evidence of polar grain boundaries. *Phys. Rev. B* **64**, 184111 (2001).

57. 57.

Gillet, P., Guyot, F., Price, G. D., Tournerie, B. & Cleach, A. L. Phase changes and thermodynamic properties of CaTiO_3 . Spectroscopic data, vibrational modelling and some insights on the properties of MgSiO_3 perovskite. *Phys. Chem. Miner.* **20**, 159–170 (1993).

58. 58.

Ghahramani, E., Moss, D. J. & Sipe, J. E. Linear optical properties of strained $(\text{Si})_n/(\text{Ge})_n$ superlattices on (001) Si substrates. *Phys. Rev. B* **41**, 5112–5125 (1990).

Acknowledgements

E.R.H., J.A.T., S.M. and P.E.H. appreciate support from the Office of Naval Research through a MURI Program, grant number N00014-18-1-2429. J.A.T., S.M. and P.E.H. acknowledge support from Army Research Office, grant number W911NF-21-1-0119. Use of the Thermo Fisher Scientific Z-STEM and Titan instruments within UVa's Nanoscale Materials Characterization Facility (NMCF) was fundamental to this work. Theory at Vanderbilt University was supported by the US Department of Energy, Office of Science, Basic Energy Sciences, Materials Science and Engineering Directorate grant number DE-FG02-09ER46554 and by the McMinn Endowment.

Calculations were performed at the National Energy Research Scientific Computing Center (NERSC), a US Department of Energy Office of Science User Facility located at Lawrence Berkeley National Laboratory, operated under contract number DE-AC02-05CH11231. The oxide heteroepitaxy synthesis work at Berkeley and Penn State is supported by the Quantum Materials program from the DOE Office of Science, Basic Energy Sciences, under contract number DE-AC02-05CH11231, and by the MRSEC for Nanoscale Science at Penn State through grant DMR1420620. EELS experiments conducted as part of a user proposal at the Center for Nanophase Materials Sciences, which is a DOE Office of Science User Facility using instrumentation within ORNL's Materials Characterization Core provided by UT-Battelle, LLC, under contract number DE-AC05- 00OR22725 with the DOE and sponsored by the Laboratory Directed Research and Development Program of Oak Ridge National Laboratory, managed by UT-Battelle, LLC, for the US Department of Energy. R.R. also acknowledges the ARO MURI under agreement W911NF-21-2-0162. J.R. acknowledges support from the Army Research Office with award numbers W911NF-19-1-0137 and W911NF-21-1-0327. J.D.C. and J.R.M. acknowledge funding under NSF, Division of Materials Research award number 1904793. S.M. acknowledges support from the NIH Biotechnology Training Program.

Author information

Affiliations

1. Department of Materials Science and Engineering, University of Virginia, Charlottesville, VA, USA
Eric R. Hoglund, Sara Makarem, Jon F. Ihlefeld, Patrick E. Hopkins & James M. Howe
2. Department of Physics and Astronomy, Vanderbilt University, Nashville, TN, USA
De-Liang Bao, Andrew O'Hara & Sokrates T. Pantelides
3. Sandia National Laboratories, Albuquerque, NM, USA
Zachary T. Piontkowski & Thomas E. Beechem
4. Department of Mechanical Engineering and Electrical Engineering, Vanderbilt University, Nashville, TN, USA
Joseph R. Matson & Joshua D. Caldwell

5. Department of Materials Science and Engineering, University of California Berkley, Berkley, CA, USA

Ajay K. Yadav & Ramamoorthy Ramesh

6. Department of Materials Science and Engineering, Pennsylvania State University, University Park, PA, USA

Ryan C. Haislmaier

7. Paul-Drude-Institut für Festkörperelektronik, Berlin, Germany

Roman Engel-Herbert

8. Institut für Physik, Humboldt-Universität zu Berlin, Berlin, Germany

Roman Engel-Herbert

9. Department of Chemical Engineering and Materials Science, University of Southern California, Los Angeles, CA, USA

Jayakanth Ravichandran

10. Center for Integrated Nanotechnologies, Sandia National Laboratories, Albuquerque, NM, USA

Thomas E. Beechem

11. School of Mechanical Engineering and the Birck Nanotechnology Center, Purdue University, West Lafayette, IN, USA

Thomas E. Beechem

12. Department of Mechanical and Aerospace Engineering, University of Virginia, Charlottesville, VA, USA

John A. Tomko & Patrick E. Hopkins

13. Center for Nanophase Materials Sciences, Oak Ridge National Laboratory, Oak Ridge, TN, USA

Jordan A. Hachtel

14. Department of Electrical and Computer Engineering, Vanderbilt University, Nashville, TN, USA

Sokrates T. Pantelides

15. Department of Physics, University of Virginia, Charlottesville, VA, USA

Patrick E. Hopkins

Contributions

E.R.H., J.A.H. and J.M.H. contributed to the acquisition, analysis and understanding of all scanning electron microscopy data. D.-L.B., A.O. and S.T.P. contributed all density functional theory calculations and corresponding analysis. S.M. and J.A.T. contributed acquisition, analysis and understanding of the SHG and TDBS spectroscopy data. Z.T.P. and T.E.B. contributed acquisition analysis, and understanding of ultraviolet-Raman data. J.R.M., T.E.B. and J.D.C. contributed acquisition, analysis and understanding of Fourier-transform infrared spectroscopy data. A.K.Y., R.C.H., R.E.H., J.R. and R.R. contributed growth expertise and samples used in the analysis. J.F.I. and P.E.H. contributed an understanding of how the crystal and vibrational structure impacted broader material properties.

Corresponding authors

Correspondence to [Eric R. Hoglund](#), [Jordan A. Hachtel](#), [Sokrates T. Pantelides](#), [Patrick E. Hopkins](#) or [James M. Howe](#).

Ethics declarations

Competing interests

The authors declare no competing interests.

Peer review information

Nature thanks Jens Kreisel and the other, anonymous, reviewer(s) for their contribution to the peer review of this work. Peer reviewer reports are available.

Additional information

Publisher's note Springer Nature remains neutral with regard to jurisdictional claims in published maps and institutional affiliations.

Supplementary information

Supplementary Information

This file contains Supplementary Sections 1–6, including Supplementary Tables 1–3, Figs. 1–17 and References.

Peer Review File

Rights and permissions

Open Access This article is licensed under a Creative Commons Attribution 4.0 International License, which permits use, sharing, adaptation, distribution and reproduction in any medium or format, as long as you give appropriate credit to the original author(s) and the source, provide a link to the Creative Commons license, and indicate if changes were made. The images or other third party material in this article are included in the article's Creative Commons license, unless indicated otherwise in a credit line to the material. If material is not included in the article's Creative Commons license and your intended use is not permitted by statutory regulation or exceeds the permitted use, you will need to obtain permission directly from the copyright holder. To view a copy of this license, visit <http://creativecommons.org/licenses/by/4.0/>.

Reprints and Permissions

About this article

Cite this article

Hoglund, E.R., Bao, DL., O’Hara, A. *et al.* Emergent interface vibrational structure of oxide superlattices. *Nature* **601**, 556–561 (2022). <https://doi.org/10.1038/s41586-021-04238-z>

- Received: 19 May 2021
- Accepted: 09 November 2021
- Published: 26 January 2022
- Issue Date: 27 January 2022
- DOI: <https://doi.org/10.1038/s41586-021-04238-z>

Share this article

Anyone you share the following link with will be able to read this content:

[Get shareable link](#)

Sorry, a shareable link is not currently available for this article.

[Copy to clipboard](#)

Provided by the Springer Nature SharedIt content-sharing initiative

This article was downloaded by **calibre** from <https://www.nature.com/articles/s41586-021-04238-z>

| [Section menu](#) | [Main menu](#) |

- Article
- [Published: 26 January 2022](#)

Unconventional spectral signature of T_c in a pure d -wave superconductor

- [Su-Di Chen](#)^{1,2,3} na1 nAff10,
- [Makoto Hashimoto](#) ORCID: orcid.org/0000-0003-1689-8997⁴ na1,
- [Yu He](#) ORCID: orcid.org/0000-0003-0425-4529^{1,2,3} nAff11,
- [Dongjoon Song](#) ORCID: orcid.org/0000-0003-3759-9646⁵ nAff12,
- [Jun-Feng He](#) ORCID: orcid.org/0000-0001-5584-9827^{1,2,3} nAff13,
- [Ying-Fei Li](#)^{1,2,3},
- [Shigeyuki Ishida](#) ORCID: orcid.org/0000-0001-9445-8079⁵,
- [Hiroshi Eisaki](#)⁵,
- [Jan Zaanen](#)⁶,
- [Thomas P. Devereaux](#) ORCID: orcid.org/0000-0001-8072-9237^{3,7},
- [Dung-Hai Lee](#) ORCID: orcid.org/0000-0002-4793-5829^{8,9},
- [Dong-Hui Lu](#) ORCID: orcid.org/0000-0002-9708-0443⁴ &
- [Zhi-Xun Shen](#) ORCID: orcid.org/0000-0002-1454-0281^{1,2,3}

[Nature](#) volume 601, pages 562–567 (2022)

- 1794 Accesses
- 72 Altmetric
- [Metrics details](#)

Subjects

- [Phase transitions and critical phenomena](#)
- [Superconducting properties and materials](#)

Abstract

In conventional superconductors, the phase transition into a zero-resistance and perfectly diamagnetic state is accompanied by a jump in the specific heat and the opening of a spectral gap¹. In the high-transition-temperature (high- T_c) cuprates, although the transport, magnetic and thermodynamic signatures of T_c have been known since the 1980s², the spectroscopic singularity associated with the transition remains unknown. Here we resolve this long-standing puzzle with a high-precision angle-resolved photoemission spectroscopy (ARPES) study on overdoped $(\text{Bi},\text{Pb})_2\text{Sr}_2\text{CaCu}_2\text{O}_{8+\delta}$ (Bi2212). We first probe the momentum-resolved electronic specific heat via spectroscopy and reproduce the specific heat peak at T_c , completing the missing link for a holistic description of superconductivity. Then, by studying the full momentum, energy and temperature evolution of the spectra, we reveal that this thermodynamic anomaly arises from the singular growth of in-gap spectral intensity across T_c . Furthermore, we observe that the temperature evolution of in-gap intensity is highly anisotropic in the momentum space, and the gap itself obeys both the d -wave functional form and particle–hole symmetry. These findings support the scenario that the superconducting transition is driven by phase fluctuations. They also serve as an anchor point for understanding the Fermi arc and pseudogap phenomena in underdoped cuprates.

This is a preview of subscription content

Access options

Subscribe to nature+

Get immediate online access to the entire Nature family of 50+ journals

\$29.99

monthly

[Subscribe](#)

Subscribe to Journal

Get full journal access for 1 year

\$199.00

only \$3.90 per issue

[Subscribe](#)

All prices are NET prices.

VAT will be added later in the checkout.

Tax calculation will be finalised during checkout.

Buy article

Get time limited or full article access on ReadCube.

\$32.00

[Buy](#)

All prices are NET prices.

Additional access options:

- [Log in](#)
- [Learn about institutional subscriptions](#)

Fig. 1: Momentum-resolved specific heat from ARPES.

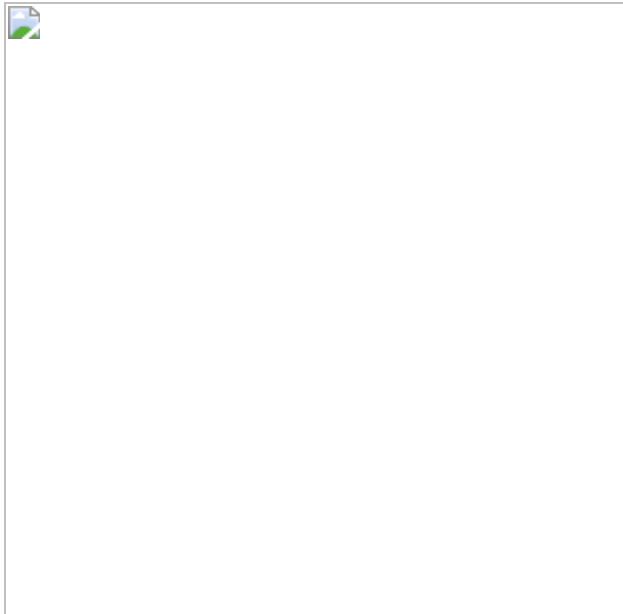


Fig. 2: Spectroscopic signature of T_c .

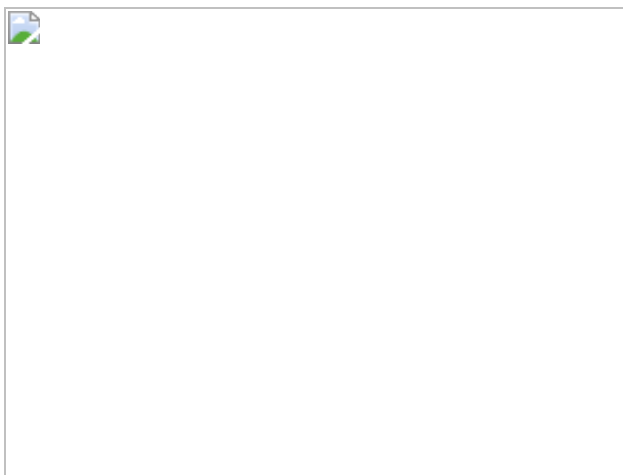


Fig. 3: Momentum dependence of gap and in-gap intensity.

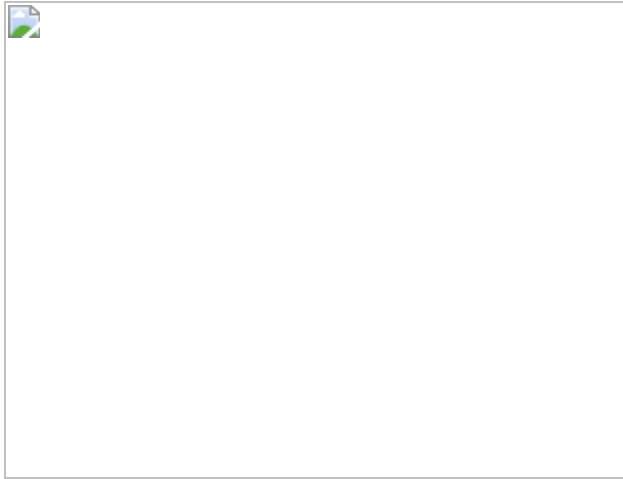
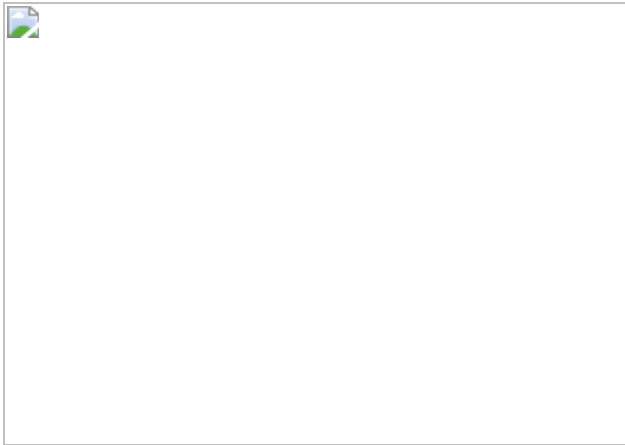


Fig. 4: Particle–hole symmetry of the gap.



Data availability

The raw data were generated at beamline 5-4 of the Stanford Synchrotron Radiation Lightsource and the Shen laboratory at Stanford University. The derived data supporting the findings of this study are available within the article and the Extended Data. [Source data](#) are provided with this paper.

References

1. 1.
Tinkham, M. *Introduction to Superconductivity* (Dover, 2004).
2. 2.
Schrieffer, J. R. & Brooks, J. S. *Handbook of High-Temperature Superconductivity: Theory and Experiment* (Springer, 2007).
3. 3.
Damascelli, A., Hussain, Z. & Shen, Z.-X. Angle-resolved photoemission studies of the cuprate superconductors. *Rev. Mod. Phys.* **75**, 473–541 (2003).
4. 4.

Kondo, T. et al. Disentangling Cooper-pair formation above the transition temperature from the pseudogap state in the cuprates. *Nat. Phys.* **7**, 21–25 (2011).

5. 5.

Reber, T. J. et al. The origin and non-quasiparticle nature of Fermi arcs in $\text{Bi}_2\text{Sr}_2\text{CaCu}_2\text{O}_{8+\delta}$. *Nat. Phys.* **8**, 606–610 (2012).

6. 6.

Kondo, T. et al. Point nodes persisting far beyond T_c in Bi2212. *Nat. Commun.* **6**, 7699 (2015).

7. 7.

Zaki, N. et al. Cuprate phase diagram and the influence of nanoscale inhomogeneities. *Phys. Rev. B* **96**, 195163 (2017).

8. 8.

Chen, S.-D. et al. Incoherent strange metal sharply bounded by a critical doping in Bi2212. *Science* **366**, 1099–1102 (2019).

9. 9.

He, Y. et al. Superconducting fluctuations in overdoped $\text{Bi}_2\text{Sr}_2\text{CaCu}_2\text{O}_{8+\delta}$. *Phys. Rev. X* **11**, 031068 (2021).

10. 10.

Hashimoto, M. et al. Direct spectroscopic evidence for phase competition between the pseudogap and superconductivity in $\text{Bi}_2\text{Sr}_2\text{CaCu}_2\text{O}_{8+\delta}$. *Nat. Mater.* **14**, 37–42 (2014).

11. 11.

Reber, T. J. et al. Pairing, pair-breaking, and their roles in setting the T_c of cuprate high temperature superconductors. Preprint at <https://arxiv.org/abs/1508.06252> (2015).

12. 12.

Gomes, K. K. et al. Visualizing pair formation on the atomic scale in the high- T_c superconductor $\text{Bi}_2\text{Sr}_2\text{CaCu}_2\text{O}_{8+\delta}$. *Nature* **447**, 569–572 (2007).

13. 13.

Timusk, T. & Statt, B. The pseudogap in high-temperature superconductors: an experimental survey. *Reports Prog. Phys.* **62**, 61–122 (1999).

14. 14.

Loram, J. W., Luo, J., Cooper, J. R., Liang, W. Y. & Tallon, J. L. Evidence on the pseudogap and condensate from the electronic specific heat. *J. Phys. Chem. Solids* **62**, 59–64 (2001).

15. 15.

Tallon, J. L., Storey, J. G., Cooper, J. R. & Loram, J. W. Locating the pseudogap closing point in cuprate superconductors: absence of entrant or reentrant behavior. *Phys. Rev. B* **101**, 174512 (2020).

16. 16.

Keimer, B., Kivelson, S. A., Norman, M. R., Uchida, S. & Zaanen, J. From quantum matter to high-temperature superconductivity in copper oxides. *Nature* **518**, 179–186 (2015).

17. 17.

Mannella, N. et al. Correction of non-linearity effects in detectors for electron spectroscopy. *J. Electron Spectros.* **141**, 45–59 (2004).

18. 18.

Reber, T. J., Plumb, N. C., Waugh, J. A. & Dessau, D. S. Effects, determination, and correction of count rate nonlinearity in multi-channel analog electron detectors. *Rev. Sci. Instrum.* **85**, 043907 (2014).

19. 19.

Kondo, T. et al. Formation of gapless Fermi arcs and fingerprints of order in the pseudogap state of cuprate superconductors. *Phys. Rev. Lett.* **111**, 157003 (2013).

20. 20.

Norman, M. R., Randeria, M., Jankó, B. & Campuzano, J. C. Condensation energy and spectral functions in high-temperature superconductors. *Phys. Rev. B* **61**, 14742 (2000).

21. 21.

Cuk, T. et al. Coupling of the B_{1g} phonon to the antinodal electronic states of $\text{Bi}_2\text{Sr}_2\text{Ca}_{0.92}\text{Y}_{0.08}\text{Cu}_2\text{O}_{8+\delta}$. *Phys. Rev. Lett.* **93**, 117003 (2004).

22. 22.

Sobota, J. A., He, Y. & Shen, Z.-X. Angle-resolved photoemission studies of quantum materials. *Rev. Mod. Phys.* **93**, 025006 (2021).

23. 23.

Emery, V. J. & Kivelson, S. A. Importance of phase fluctuations in superconductors with small superfluid density. *Nature* **374**, 434–437 (1995).

24. 24.

Wang, Y. et al. Field-enhanced diamagnetism in the pseudogap state of the cuprate $\text{Bi}_2\text{Sr}_2\text{CaCu}_2\text{O}_{8+\delta}$ superconductor in an intense magnetic field. *Phys. Rev. Lett.* **95**, 247002 (2005).

25. 25.

Li, L. et al. Diamagnetism and Cooper pairing above T_c in cuprates. *Phys. Rev. B* **81**, 054510 (2010).

26. 26.

Uemura, Y. J. et al. Magnetic-field penetration depth in $\text{TI}_2\text{Ba}_2\text{CuO}_{6+\delta}$ in the overdoped regime. *Nature* **364**, 605–607 (1993).

27. 27.

Božović, I., He, X., Wu, J. & Bollinger, A. T. Dependence of the critical temperature in overdoped copper oxides on superfluid density. *Nature* **536**, 309–311 (2016).

28. 28.

Eckl, T., Scalapino, D. J., Arrigoni, E. & Hanke, W. Pair phase fluctuations and the pseudogap. *Phys. Rev. B* **66**, 140510 (2002).

29. 29.

Franz, M. & Millis, A. J. Phase fluctuations and spectral properties of underdoped cuprates. *Phys. Rev. B* **58**, 14572–14580 (1998).

30. 30.

Berg, E. & Altman, E. Evolution of the Fermi surface of d -wave superconductors in the presence of thermal phase fluctuations. *Phys. Rev. Lett.* **99**, 247001 (2007).

31. 31.

Lee-Hone, N. R., Dodge, J. S. & Broun, D. M. Disorder and superfluid density in overdoped cuprate superconductors. *Phys. Rev. B* **96**, 024501 (2017).

32. 32.

Li, Z.-X., Kivelson, S. A. & Lee, D.-H. Superconductor-to-metal transition in overdoped cuprates. *npj Quantum Mater.* **6**, 36 (2021).

33. 33.

Kosterlitz, J. M. & Thouless, D. J. Ordering, metastability and phase transitions in two-dimensional systems. *J. Phys. C* **6**, 1181–1203 (1973).

34. 34.

Janke, W. & Matsui, T. Crossover in the XY model from three to two dimensions. *Phys. Rev. B* **42**, 10673–10681 (1990).

35. 35.

Presland, M. R., Tallon, J. L., Buckley, R. G., Liu, R. S. & Flower, N. E. General trends in oxygen stoichiometry effects on T_c in Bi and Tl superconductors. *Physica C* **176**, 95–105 (1991).

36. 36.

Chen, S.-D. *High-Precision Photoemission Study of Overdoped Bi2212 Superconductors*. PhD thesis, Stanford Univ. (2021).

Acknowledgements

We thank S. A. Kivelson, M. Sulangi, J. L. Tallon, and F. Wang for discussions, and J. L. Tallon for sharing the specific heat data. We thank J.-J. Wen, W. He, and Y. S. Lee for help with magnetic susceptibility measurements. Synchrotron ARPES measurements were performed at Beamline 5-4, Stanford Synchrotron Radiation Lightsource, SLAC National

Accelerator Laboratory. The works at Stanford University and SLAC are supported by the US Department of Energy, Office of Science, Office of Basic Energy Sciences, Division of Materials Sciences and Engineering, under contract no. DE-AC02-76SF00515. The works at UC Berkeley and LBNL are supported by the US Department of Energy, Office of Science, Office of Basic Energy Sciences, Materials Sciences and Engineering Division under contract no. DE-AC02-05-CH11231 within the Quantum Materials Program (KC2202).

Author information

Author notes

1. Su-Di Chen

Present address: Kavli Energy NanoScience Institute, University of California, Berkeley, Berkeley, CA, USA

2. Yu He

Present address: Department of Applied Physics, Yale University, New Haven, CT, USA

3. Dongjoon Song

Present address: Center for Correlated Electron Systems, Institute for Basic Science, Seoul, Republic of Korea

4. Jun-Feng He

Present address: Department of Physics, University of Science and Technology of China, Hefei, China

5. These authors contributed equally: Su-Di Chen, Makoto Hashimoto

Affiliations

1. Department of Applied Physics, Stanford University, Stanford, CA,
USA

Su-Di Chen, Yu He, Jun-Feng He, Ying-Fei Li & Zhi-Xun Shen

2. Department of Physics, Stanford University, Stanford, CA, USA

Su-Di Chen, Yu He, Jun-Feng He, Ying-Fei Li & Zhi-Xun Shen

3. Stanford Institute for Materials and Energy Sciences, SLAC National Accelerator Laboratory and Stanford University, Menlo Park, CA,
USA

Su-Di Chen, Yu He, Jun-Feng He, Ying-Fei Li, Thomas P.
Devereaux & Zhi-Xun Shen

4. Stanford Synchrotron Radiation Lightsource, SLAC National Accelerator Laboratory, Menlo Park, CA, USA

Makoto Hashimoto & Dong-Hui Lu

5. National Institute of Advanced Industrial Science and Technology,
Tsukuba, Japan

Dongjoon Song, Shigeyuki Ishida & Hiroshi Eisaki

6. Institute Lorentz for Theoretical Physics, Leiden University, Leiden,
The Netherlands

Jan Zaanen

7. Department of Materials Science and Engineering, Stanford
University, Stanford, CA, USA

Thomas P. Devereaux

8. Department of Physics, University of California, Berkeley, Berkeley,
CA, USA

Dung-Hai Lee

9. Materials Sciences Division, Lawrence Berkeley National Laboratory,
Berkeley, CA, USA

Dung-Hai Lee

Contributions

S.-D.C., M.H. and Y.-F.L. performed the ARPES experiments. M.H., D.-H. Lu, S.-D.C., Y.H., J.-F.H. and Y.-F.L. contributed to instrument development. D.S., S.I., H.E. and S.-D.C. prepared and characterized the samples. S.-D.C. analysed the data with input from T.P.D., J.Z., D.-H. Lee, and Z.-X.S. S.-D.C., M.H., D.-H. Lee and Z.-X.S. wrote the manuscript with input from all authors. Z.-X.S. supervised the project.

Corresponding author

Correspondence to [Zhi-Xun Shen](#).

Ethics declarations

Competing interests

The authors declare no competing interests.

Peer review information

Nature thanks the anonymous reviewers for their contribution to the peer review of this work.

Additional information

Publisher's note Springer Nature remains neutral with regard to jurisdictional claims in published maps and institutional affiliations.

Extended data figures and tables

Extended Data Fig. 1 Bulk characterization of T_c .

a–e, Real part of the a.c. magnetic susceptibility (χ') for thin crystals exfoliated from the cleaved surfaces. The sample name and excitation field amplitude are marked in each panel. The field frequency is 4 kHz. **f**, As in **a**, for a thick crystal. The grey lines in **a–f** mark $T_c \approx 77$ K.

[Source data](#)

Extended Data Fig. 2 Consistency of temperature scans.

a–f, Momentum-integrated EDCs from temperature scans. The sample and cut location are marked on top of each panel (see also Extended Data Table 1). The y-axis tick increment is 0.5 for all panels. The curves are offset in steps of 0.5 (**a–d**) and 1 (**e, f**) for clarity, and the number beneath each set of curves represents the temperature in K. Each EDC is normalized such that its average intensity equals 1 in the energy window given at the bottom of the corresponding panel. The consistency between curves measured during warming and cooling showcases the stability of the set-up and the absence of sample ageing effects.

[Source data](#)

Extended Data Fig. 3 Momentum summation.

a, $S^\theta(T)/S^\theta(140\text{ K})$ plotted as a function of Fermi surface angle θ . We assume that $S^{\theta=0}(T) \propto T$. All the other data points are interpolated from the temperature evolutions shown in Fig. 1b. **b**, Spectral function of the antibonding band integrated along the Brillouin zone boundary. **c**, $S^\theta(140\text{ K})$ as a function of θ . Inset shows the tight-binding Fermi surface in the first quadrant of Brillouin zone. Curves in **b** and **c** are calculated using an ARPES-determined tight-binding dispersion with different constant scattering rates. The antinodal scattering rate at 140 K is around 35 meV in our ARPES data. **d**, Temperature evolution of S calculated using data in **a**

and **c**. **e**, Temperature dependence of γ obtained as the derivative of data in **d**. In **d** and **e**, the bulk results are plotted in black for comparison.

[Source data](#)

Extended Data Fig. 4 Determination of the tight-binding parameters.

a, The dispersion of the antibonding band near the chemical potential (coloured circles) is extracted from ARPES data taken at 250 K on an overdoped Bi2212 sample with a slightly different doping ($p \approx 0.196$ from ref. 8). The temperature is chosen such that there are no gaps and more dispersion above the chemical potential can be identified. Data from different momentum cuts (as marked in **b**) are offset in steps of 0.1 eV for clarity. All data points are fitted at once to the tight-binding expression and the results are plotted as grey crosses. **b**, Momentum locations of data in **a** (coloured dots) plotted together with the antibonding Fermi surface (black curves) calculated from the fitting results. The black lines mark the first Brillouin zone. **c**, As in Fig. 2a, with the tight-binding dispersion plotted in grey. To compensate for the doping difference, we fix t_0 , t_1 , and reduce μ by 2.5 meV such that the Van Hove energy from the tight-binding model matches that of the OD77 ($p \approx 0.210$) sample studied in the text.

[Source data](#)

Extended Data Fig. 5 Gap determination.

a–f, k_F EDCs divided by the resolution-convolved Fermi function. The corresponding Fermi surface angle is labelled on top of each panel. The EDCs are offset for clarity and the number above each EDC marks the temperature in K. With minimal assumptions, we take the binding energy of the EDC maximum below the chemical potential (vertical blue bars) as the gap size. For the procedure to be robust against noise, we first perform a polynomial fit to each EDC near its maximum (red curves) and then extract the energy position of the maximum from the fitted curve. With increasing temperature, we stop the analysis once the maximum shifts to zero energy.

[Source data](#)

Extended Data Fig. 6 Anisotropic gap filling and finite energy resolution.

a, b, As in Fig. 3c, d. The Fermi surface angle and the ratio between gap size at 30 K (Δ_{30K}) and energy resolution (Reso) are labelled beneath each curve in **a**. **c, d**, As in **a, b**, but obtained from data intentionally broadened in energy such that all curves have the same Δ_{30K}/Reso of 2.1. The broadening is directly performed on data without Fermi-function division, such as those in Extended Data Fig. 2. The close resemblance between the top and bottom panels indicate that the anisotropic gap filling is not an artefact from finite resolution.

[Source data](#)

Extended Data Fig. 7 EDC fitting for examining particle-hole symmetry.

a–d, Fermi-function-divided EDCs along the blue curves in Fig. 4c. The cut number is labelled on top of each panel. Curves are offset according to their k_y values for clarity. Each EDC is fitted using two Lorentzian peaks with identical width plus a constant background. The results are plotted in red, and the extracted peak positions are marked by the vertical blue bars.

[Source data](#)

Extended Data Fig. 8 Spectral properties without phase fluctuations.

a, Expected temperature evolution of the superconducting gap for a pure d -wave superconductor in the mean-field theory, where T_c is set by gap opening. **b, c**, Simulated temperature evolutions of A_0 with different scattering rates Γ . The spectral function is calculated as $A(k, E) = (1 - \alpha)\Gamma/\{\pi[(E - E_k)^2 + \Gamma^2]\} + \alpha\Gamma/\{\pi[(E + E_k)^2 + \Gamma^2]\}$, where \

$\langle E \rangle_k = \sqrt{\langle \varepsilon \rangle_k^2 + \langle \Delta \rangle_k^2}$, $\alpha = (1 - \varepsilon_k/E_k)/2$, and ε_k is the tight-binding bandstructure. **d**, As in **a**, with the gap sizes divided by their corresponding *d*-wave form factors. **e, f**, Numerical derivatives of data in **b** and **c**, respectively. The vertical grey line in each panel marks T_c . Regardless of the choice of Γ , A_0 always stays constant for $T > T_c$ and shows a sharp drop across T_c with decreasing temperature. This singularity also shows up as a jump at T_c in the temperature derivative of A_0 . As such, the temperature evolutions of Δ_k , A_0 and dA_0/dT shown here are qualitatively different from those in Fig. 3.

[Source data](#)

Extended Data Table 1 Details of each ARPES experiment

Source data

[Source Data Fig. 1](#)

[Source Data Fig. 2](#)

[Source Data Fig. 3](#)

[Source Data Fig. 4](#)

[Source Data Extended Data Fig. 1](#)

[Source Data Extended Data Fig. 2](#)

[Source Data Extended Data Fig. 3](#)

[Source Data Extended Data Fig. 4](#)

[Source Data Extended Data Fig. 5](#)

[**Source Data Extended Data Fig. 6**](#)

[**Source Data Extended Data Fig. 7**](#)

[**Source Data Extended Data Fig. 8**](#)

Rights and permissions

[Reprints and Permissions](#)

About this article

Cite this article

Chen, SD., Hashimoto, M., He, Y. *et al.* Unconventional spectral signature of T_c in a pure d -wave superconductor. *Nature* **601**, 562–567 (2022).

<https://doi.org/10.1038/s41586-021-04251-2>

- Received: 02 August 2021
- Accepted: 13 November 2021
- Published: 26 January 2022
- Issue Date: 27 January 2022
- DOI: <https://doi.org/10.1038/s41586-021-04251-2>

Share this article

Anyone you share the following link with will be able to read this content:

[Get shareable link](#)

Sorry, a shareable link is not currently available for this article.

[Copy to clipboard](#)

Provided by the Springer Nature SharedIt content-sharing initiative

This article was downloaded by **calibre** from <https://www.nature.com/articles/s41586-021-04251-2>

| [Section menu](#) | [Main menu](#) |

- Article
- [Published: 26 January 2022](#)

Inhibiting the Leidenfrost effect above 1,000 °C for sustained thermal cooling

- [Mengnan Jiang^{1,2} na1](#),
- [Yang Wang](#) ORCID: orcid.org/0000-0002-7464-9916^{1,2,3} na1,
- [Fayu Liu¹](#),
- [Hanheng Du⁴](#),
- [Yuchao Li¹](#),
- [Huanhuan Zhang¹](#),
- [Suet To⁴](#),
- [Steven Wang¹](#),
- [Chin Pan¹](#),
- [Jihong Yu](#) ORCID: orcid.org/0000-0003-1615-5034³,
- [David Quéré](#) ORCID: orcid.org/0000-0003-2117-4651⁵ &
- [Zuankai Wang](#) ORCID: orcid.org/0000-0002-3510-1122^{1,2,6}

[Nature](#) volume 601, pages 568–572 (2022)

- 2408 Accesses
- 83 Altmetric
- [Metrics details](#)

Subjects

- [Fluid dynamics](#)

- [Mechanical engineering](#)
- [Wetting](#)

Abstract

The Leidenfrost effect, namely the levitation of drops on hot solids¹, is known to deteriorate heat transfer at high temperature². The Leidenfrost point can be elevated by texturing materials to favour the solid–liquid contact^{2,3,4,5,6,7,8,9,10} and by arranging channels at the surface to decouple the wetting phenomena from the vapour dynamics³. However, maximizing both the Leidenfrost point and thermal cooling across a wide range of temperatures can be mutually exclusive^{3,7,8}. Here we report a rational design of structured thermal armours that inhibit the Leidenfrost effect up to 1,150 °C, that is, 600 °C more than previously attained, yet preserving heat transfer. Our design consists of steel pillars serving as thermal bridges, an embedded insulating membrane that wicks and spreads the liquid and U-shaped channels for vapour evacuation. The coexistence of materials with contrasting thermal and geometrical properties cooperatively transforms normally uniform temperatures into non-uniform ones, generates lateral wicking at all temperatures and enhances thermal cooling. Structured thermal armours are limited only by their melting point, rather than by a failure in the design. The material can be made flexible, and thus attached to substrates otherwise challenging to structure. Our strategy holds the potential to enable the implementation of efficient water cooling at ultra-high solid temperatures, which is, to date, an uncharted property.

This is a preview of subscription content

Access options

Subscribe to nature+

Get immediate online access to the entire Nature family of 50+ journals

\$29.99

monthly

[Subscribe](#)

Subscribe to Journal

Get full journal access for 1 year

\$199.00

only \$3.90 per issue

[Subscribe](#)

All prices are NET prices.

VAT will be added later in the checkout.

Tax calculation will be finalised during checkout.

Buy article

Get time limited or full article access on ReadCube.

\$32.00

[Buy](#)

All prices are NET prices.

Additional access options:

- [Log in](#)
- [Learn about institutional subscriptions](#)

Fig. 1: The STA design.

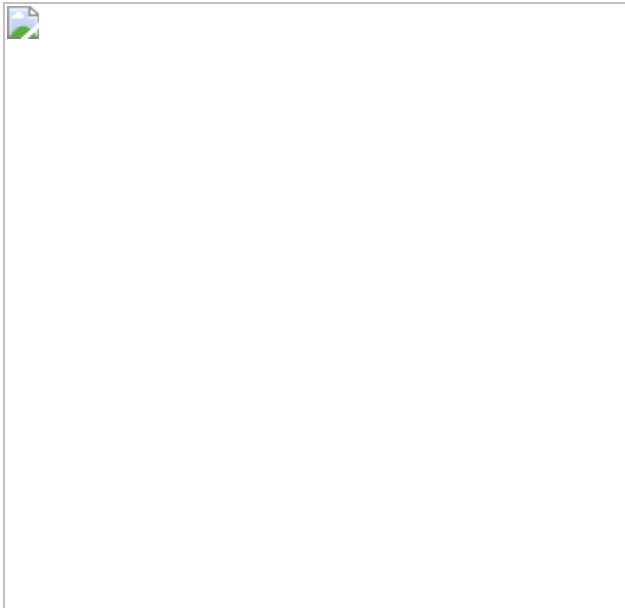


Fig. 2: Performances of the STA material.

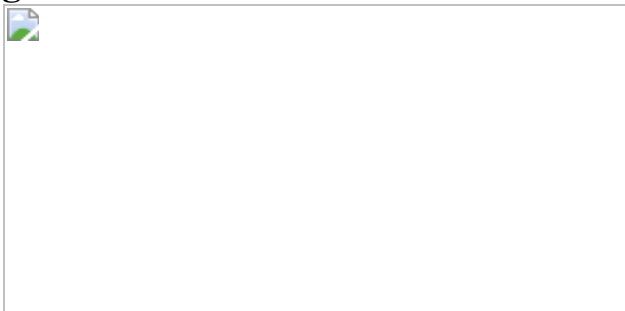


Fig. 3: Testing the limits of STAs.

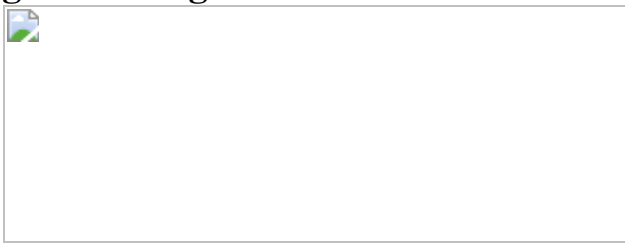


Fig. 4: Curved and flexible STA.



Data availability

The data that support the findings of this study are available from the corresponding authors.

References

1. 1.

Leidenfrost, J. G. *De aquae communis nonnullis qualitatibus tractatus* (Ovenius, 1756).

2. 2.

Talari, V., Behar, P., Lu, Y., Haryadi, E. & Liu, D. Leidenfrost drops on micro/nanostructured surfaces. *Front. Energy* **12**, 22–42 (2018).

3. 3.

Farokhnia, N., Sajadi, S. M., Irajizad, P. & Ghasemi, H. Decoupled hierarchical structures for suppression of Leidenfrost phenomenon. *Langmuir* **33**, 2541–2550 (2017).

4. 4.

Weickgenannt, C. M. et al. Inverse-Leidenfrost phenomenon on nanofiber mats on hot surfaces. *Phys. Rev. E* **84**, 036310 (2011).

5. 5.

Kim, H. et al. On the effect of surface roughness height, wettability, and nanoporosity on Leidenfrost phenomena. *Appl. Phys. Lett.* **98**, 083121 (2011).

6. 6.

Kruse, C. et al. Extraordinary shifts of the Leidenfrost temperature from multiscale micro/nanostructured surfaces. *Langmuir* **29**, 9798–

9806 (2013).

7. 7.

Kwon, H. M., Bird, J. C. & Varanasi, K. K. Increasing Leidenfrost point using micro-nano hierarchical surface structures. *Appl. Phys. Lett.* **103**, 201601 (2013).

8. 8.

Nair, H. et al. The Leidenfrost temperature increase for impacting droplets on carbon-nanofiber surfaces. *Soft Matter* **10**, 2102–2109 (2014).

9. 9.

Geraldi, N. R. et al. Leidenfrost transition temperature for stainless steel meshes. *Mater. Lett.* **176**, 205–208 (2016).

10. 10.

Sajadi, S. M., Irajizad, P., Kashyap, V., Farokhnia, N. & Ghasemi, H. Surfaces for high heat dissipation with no Leidenfrost limit. *Appl. Phys. Lett.* **111**, 021605 (2017).

11. 11.

Li, J. et al. Directional transport of high-temperature Janus droplets mediated by structural topography. *Nat. Phys.* **12**, 606–612 (2016).

12. 12.

van Erp, R., Soleimanzadeh, R., Nela, L., Kampitsis, G. & Matioli, E. Co-designing electronics with microfluidics for more sustainable cooling. *Nature* **585**, 211–216 (2020).

13. 13.

Dhillon, N. S., Buongiorno, J. & Varanasi, K. K. Critical heat flux maxima during boiling crisis on textured surfaces. *Nat. Commun.* **6**, 8247 (2015).

14. 14.

Gao, X. & Li, R. in *Advanced Cooling Technologies and Applications* (ed. Sohel Murshed, S. M.) Ch. 3 (IntechOpen, 2019).

15. 15.

Tiwei, T. et al. High efficiency direct liquid jet impingement cooling of high power devices using a 3D-shaped polymer cooler. In *Proc. 2017 IEEE International Electron Devices Meeting (IEDM)* 32.5.1–32.5.4 (IEEE, 2017).

16. 16.

Vakarelski, I. U., Patankar, N. A., Marston, J. O., Chan, D. Y. & Thoroddsen, S. T. Stabilization of Leidenfrost vapour layer by textured superhydrophobic surfaces. *Nature* **489**, 274–277 (2012).

17. 17.

Saranadhi, D. et al. Sustained drag reduction in a turbulent flow using a low-temperature Leidenfrost surface. *Sci. Adv.* **2**, e1600686 (2016).

18. 18.

Burton, J. C., Sharpe, A. L., van der Veen, R. C., Franco, A. & Nagel, S. R. Geometry of the vapor layer under a Leidenfrost drop. *Phys. Rev. Lett.* **109**, 074301 (2012).

19. 19.

Adera, S., Raj, R., Enright, R. & Wang, E. N. Non-wetting droplets on hot superhydrophilic surfaces. *Nat. Commun.* **4**, 2518 (2013).

20. 20.

Hsu, S. H., Ho, Y. H., Ho, M. X., Wang, J. C. & Pan, C. On the formation of vapor film during quenching in de-ionized water and elimination of film boiling during quenching in natural sea water. *Int. J. Heat Mass Transfer* **86**, 65–71 (2015).

21. 21.

Rahman, M. M., Pollack, J. & McCarthy, M. Increasing boiling heat transfer using low conductivity materials. *Sci. Rep.* **5**, 13145 (2015).

22. 22.

Wei, M. et al. Heat transfer suppression by suspended droplets on microstructured surfaces. *Appl. Phys. Lett.* **116**, 233703 (2020).

23. 23.

Deng, T. et al. Nonwetting of impinging droplets on textured surfaces. *Appl. Phys. Lett.* **94**, 133109 (2009).

24. 24.

Bernardin, J. D., Stebbins, C. J. & Mudawar, I. Effects of surface roughness on water droplet impact history and heat transfer regimes. *Int. J. Heat Mass Transfer* **40**, 73–88 (1996).

25. 25.

Tran, T. et al. Droplet impact on superheated micro-structured surfaces. *Soft Matter* **9**, 3272–3282 (2013).

26. 26.

Mao, X. et al. Silica nanofibrous membranes with robust flexibility and thermal stability for high-efficiency fine particulate filtration. *RSC Adv.* **2**, 12216–12223 (2012).

27. 27.

Kim, S. H., Ahn, H. S., Kim, J., Kaviany, M. & Kim, M. H. Dynamics of water droplet on a heated nanotubes surface. *Appl. Phys. Lett.* **102**, 233901 (2013).

28. 28.

Lee, G. C. et al. Induced liquid-solid contact via micro/nano multiscale texture on a surface and its effect on the Leidenfrost temperature. *Exp. Therm Fluid Sci.* **84**, 156–164 (2017).

29. 29.

Kim, S. H., Lee, G., Kim, H. & Kim, M. H. Leidenfrost point and droplet dynamics on heated micropillar array surface. *Int. J. Heat Mass Transfer* **139**, 1–9 (2019).

30. 30.

Hasimoto, H. On the periodic fundamental solutions of the Stokes equations and their application to viscous flow past a cubic array of spheres. *J. Fluid Mech.* **5**, 317–328 (1959).

Acknowledgements

We acknowledge financial support from the Research Grants Council of Hong Kong (no. 11218321, no. C1006-20WF and no. 11213320), the Tencent Foundation through the XPLORER PRIZE, the Innovation and Technology Council (no. 9440248), the National Natural Science Foundation of China (grant nos. 51975502 and 21621001) and the 111 Project (no. B17020).

Author information

Author notes

1. These authors contributed equally: Mengnan Jiang, Yang Wang

Affiliations

1. Department of Mechanical Engineering, City University of Hong Kong, Hong Kong, China

Mengnan Jiang, Yang Wang, Fayu Liu, Yuchao Li, Huanhuan Zhang, Steven Wang, Chin Pan & Zuankai Wang

2. Research Center for Nature-inspired Engineering, City University of Hong Kong, Hong Kong, China

Mengnan Jiang, Yang Wang & Zuankai Wang

3. State Key Laboratory of Inorganic Synthesis and Preparative Chemistry, College of Chemistry, International Center of Future Science, Jilin University, Changchun, China

Yang Wang & Jihong Yu

4. State Key Laboratory of Ultra-precision Machining Technology, Department of Industrial and Systems Engineering, The Hong Kong Polytechnic University, Hong Kong, China

Hanheng Du & Suet To

5. Physique & Mécanique des Milieux Hétérogènes, UMR 7636 du CNRS, ESPCI, PSL Research University, Paris, France

David Quéré

6. Shenzhen Research Institute, City University of Hong Kong, Shenzhen, China

Zuankai Wang

Contributions

Z.W. conceived the research. Z.W., D.Q. and J.Y. supervised the research. M.J. and Y.W. designed the experiments. Y.L., S.W. and C.P. participated in the discussion of the experimental design. H.Z. set up the electrospinning equipment. Y.W. prepared and characterized the membranes. H.D. and S.T. conducted the fabrication of the steel pillar arrays. M.J., Y.W. and F.L. assembled, characterized the samples and carried out the experiments. D.Q. and M.J. built the models with input from Y.W. and Z.W. All authors analysed the data. Z.W., D.Q., J.Y. and M.J. wrote the manuscript with input from the other authors.

Corresponding authors

Correspondence to [Jihong Yu](#), [David Quéré](#) or [Zuankai Wang](#).

Ethics declarations

Competing interests

Z.W., M.J. and Y.W. are co-authors on a filed US patent no. 63/072,995, which describes the methods used herein.

Additional information

Publisher's note Springer Nature remains neutral with regard to jurisdictional claims in published maps and institutional affiliations.

Extended data figures and tables

[Extended Data Fig. 1 Preparation of the samples.](#)

a. Fabrication process of steel pillar arrays with U-shaped grooves. The arrays are fabricated using a precision milling process. The tip of the milling cutter is a ball nose with a diameter of 300 µm. The spindle rotational and translational speeds, and depth-of-cut are 60,000 r/min, 150 mm/min and 40 µm, respectively. The desired depth of 400 µm is reached

after ten successive cuts (step 1) after which the sample is rotated by 90°, and ten new cuts are performed. The SEM image is a side-view of the pillars with their U-shaped grooves. **b.** SEM images of the fibrous membranes treated at various temperatures. Images are obtained with a FEI Quanta 450 FEG microscope after membranes were inserted into a tube furnace (GSL-1500X) at the target temperature and calcinated for 1 h in air. **c.** Fibrous membranes are embedded into pillar arrays at the desired depth using a pre-designed 3D mold. After removing the mold, the obtained STA is consolidated by a sintering step performed at 800 °C for typically 5 min. **d.** SEM image of the pillars without U-shaped grooves. This material is made for achieving the sample B. It is fabricated using 2-flute end mill with a diameter of 300 µm. During micro-milling, the spindle rotational and translational speeds are 60,000 r/min and 150 mm/min, and the depth-of-cut is 30 µm.

Extended Data Fig. 2 Water drops contacting STA brought to high temperatures.

a. Side view of water contacting STA at $T = 500$ °C. As water (dyed in red) contacts a STA, it immediately impregnates the membrane, without penetrating the U-shaped channels. The liquid is kept within the membrane by capillarity and by the vapour pressure inside the channels. The scale bar is 0.5 mm. **b.** Top views of water drops (approximately 17 µL) on STA at $T = 800$ °C and $T = 1150$ °C (around 1200 °C, the membrane starts to melt). Drops behave as reported in Fig. 1c ($T = 1000$ °C). Images framed in red show the formation of non-uniform and isolated bubbles, that break within several milliseconds owing to an intense boiling. The lifetimes of the drop are 0.35 s and 0.28 s, respectively, showing the persistence of wicking even at ultra-high temperature. Scale bars show 2 mm.

Extended Data Fig. 3 Evaporation time τ of a water drop with volume Ω as a function of the temperature T of its substrate.

The respective values of Ω are (from top to bottom) 13, 6, 4, 6, 30 and 17 µL, which affects the absolute value of the time but not its trend. For many data (those of refs. [5](#), [27,28](#) and [29](#)), we observe a classical Leidenfrost

behaviour, with a strong decrease of τ around the boiling point (BP), followed by a sharp rise of this time at the Leidenfrost transition. Short evaporation times correspond to τ of order 1 s, and they are observed in this case between the BP and the LFP. For the data of Ref. ³, the behaviour is different, with a slow decrease of the time τ as a function of temperature. Its values remain above the regime of quick disappearance, except for AAO+nanoparticles where the regime of interest is achieved between 500 °C and 570 °C. By contrast, the STA sample achieves a low τ in a range of 1000 °C, between 200 °C and 1200 °C. Data in our work are mean ± s.d. from at least five independent measurements.

Extended Data Fig. 4 Percentage of the drop volume that heterogeneously boils on the different samples at T = 1000 °C.

Values are obtained from image analysis after at least 30 drops contacted the samples. Data are mean ± s.d. from at least thirty independent measurements.

Extended Data Fig. 5 Schematic showing the temperature measurement.

The thermocouple is inserted in the steel block at a distance $\delta_s \approx 1$ mm below the pillar tops. The ratio between the conduction thermal resistance and the convective thermal resistance of steel, defined as the Biot number $Bi = \delta_s h_s / k_s$ (where $h_s \approx 2 * 10^3$ W/m²K is the convection heat transfer coefficient and $k_s \approx 25$ W/mK is the thermal conductivity of steel), is 0.07 << 1. This suggests that the temperature at the top surface is comparable to that measured with the thermocouple.

Extended Data Fig. 6 Control experiment based on pillar arrays covered by a conductive copper membrane.

High-speed views of the evaporation dynamics of a water drop deposited on pillar arrays covered by a conductive Cu membrane ($T = 500$ °C). The whole surface has a uniform temperature and the water drop remains in the

Leidenfrost state all along its lifetime. The lifetime (in red) is two orders of magnitude larger than on STA, demonstrating that insulating membranes are essential for inhibiting the Leidenfrost effect.

Extended Data Fig. 7 Thermal characteristics of STA surfaces.

a. Temperature map of a STA surface brought to 1000 °C. Temperature is measured with an infrared camera (FLIR T1050sc) operating at 30 Hz, with an emissivity setting at 0.95. At $t = 0$ ms, temperature is nearly uniform. The tops of the steel pillars are slightly cooler (by 15 °C) than the membrane, which might be due to the embedded position of the membrane. 198 ms after a drop impact, we observe a strong temperature difference (about 290 °C) between pillars and membrane. **b.** Evaporation time τ of a water drop of 17 µL deposited on STA at $T = 1000$ °C, as a function of the pillar density $\phi = a^2/(a+b)^2$. **c.** Mean heat flux q as a function of ϕ . q is deduced from the time τ and from the measured evaporating solid/liquid area. An optimum of performance is found around $\phi = 0.25$. Data are mean \pm s.d. from at least five independent measurements.

Extended Data Fig. 8 Upper limit of the pore diameter for the insulating membrane embedded in a STA and dimensionless phase plots.

a. Ratio P_L/P_v (Laplace pressure in a pore relative to vapor pressure) as a function of the pore diameter d . Between $d = 2$ µm and $d = 21$ µm, the STA operates in the wicking regime. However, the ratio P_L/P_v becomes smaller than unity at high d . As a result, vapor can penetrate the wicked membrane and a mixed state is observed. For all tests, the STA temperature is 1000 °C and the U-shaped channel height ε is 150 µm. **b.** Dimensionless phase plots showing τ/τ_o (evaporation time relative to the wicking time) as a function of P_L/P_v , at fixed $\varepsilon = 150$ µm, and for a STA temperature of 1000 °C. The data show that STA operates in the domains expected from our models ($P_L/P_v > 1$, $\tau/\tau_o > 1$). As a complement, we can estimate the numbers τ/τ_o and P_L/P_v for liquid nitrogen on STA at 30 °C or at 1000 °C (Supplementary Video 2). For the parameters of liquid nitrogen ($R \approx 1.2$ mm, $L \approx 2 \cdot 10^5$ J/kg, $\eta \approx 0.17$

mPa s , $\gamma \approx 9 \text{ mN/m}$, $d \approx 3 \mu\text{m}$), we find at 30°C ($k_v \approx 17 \text{ mW/m/K}$, $\eta_v \approx 12 \mu\text{Pa s}$, $\rho_v \approx 1.8 \text{ kg/m}^3$) $\tau/\tau_o \approx 1.3$ and $P_L/P_v \approx 600$ – all quantities larger than unity; at 1000°C ($k_v \approx 57 \text{ mW/m/K}$, $\eta_v \approx 37 \mu\text{Pa s}$, $\rho_v \approx 0.4 \text{ kg/m}^3$), the latter values become $\tau/\tau_o \approx 2.3$ and $P_L/P_v \approx 3$ – still larger than unity.

Extended Data Fig. 9 Schematic showing the fabrication of U-shaped channels.

a. Fabrication of U-shaped channels with different heights ($50 \mu\text{m}$, $100 \mu\text{m}$, $120 \mu\text{m}$). Arc-shaped grooves with a height of $50 \mu\text{m}$, $100 \mu\text{m}$ and $120 \mu\text{m}$ are obtained with a flat milling cutter with a tip diameter of $300 \mu\text{m}$ that provides grooves with a depth of $340 \mu\text{m}$, $290 \mu\text{m}$ and $270 \mu\text{m}$, respectively, as shown in Steps 1–3. Then, the flat bottom cutter is replaced with a ball nose cutter with a diameter of $200 \mu\text{m}$ to further fit the profile of the arcs, as shown in Steps 4–5. **b.** Making pillars with a wire electrical discharge machine (WEDM). In Step 1, the steel workpiece moves under the molybdenum wire with a diameter of $180 \mu\text{m}$, which results in U-shaped grooves. Then, the workpiece is rotated by 90° and Step 1 is repeated. The current, voltage and machining compensation are 2 A , 80 V and $80 \mu\text{m}$, respectively.

Extended Data Fig. 10 Cooling performances of large-scale and curved STA.

a. Optical image of STA fabricated on a steel block of $40 \times 40 \times 10 \text{ mm}$. **b.** Comparison of time-dependent heat dissipating abilities of STA and sample A at 1000°C . Samples are cooled by a water flow (rate of approximately 150 mL/min) released from 4 nozzles placed 5 cm above the surface. Within about 20 s , the temperature on STA drops by 850°C , whereas temperature hardly changes on A. **c.** Corresponding heat flux as a function of time on both samples. **d.** Optical image of a curved STA sample, with width 2 cm , height 1 cm , and radius of curvature of the top surface 2.5 cm . **e.** Heat dissipating abilities between the curved STA and bare sample. Under a water flow of 20 mL/min , there is a 900°C drop on the STA sample within 1 minute , whereas there is no appreciable cooling on the bare sample. **f.** Corresponding heat fluxes as a function of time for both samples.

Supplementary information

Supplementary Video 1

Behaviours and lifetimes of water drops deposited on samples A, B and STA brought to $T = 1,000\text{ }^\circ\text{C}$. The volume of the water drops is approximately 17 μl . On pillar arrays (sample A), drops exhibit a typical Leidenfrost state, with a long evaporation lifetime. On the pillar/membrane without channels (sample B), drops are in a mixed wicking/Leidenfrost state. By contrast, drops on STA persistently wick the membrane, which generates constant boiling and a 50-fold reduction in their lifetime.

Supplementary Video 2

Behaviours and lifetimes of liquid nitrogen drops on sample A at room temperature, STA at room temperature and STA at $T = 1,000\text{ }^\circ\text{C}$. The impact velocity and diameter of the drops are approximately 45 cm s^{-1} and 2.4 mm, respectively. Liquid nitrogen adopts a Leidenfrost state on A at room temperature. By contrast, a complete wicking with intense boiling is observed on STA, both at room temperature and at $1,000\text{ }^\circ\text{C}$, with respective lifetimes of approximately 130 ms and 240 ms.

Supplementary Video 3

Cooling performances of large-scale samples A and STA at $T = 1,000\text{ }^\circ\text{C}$, due to continuous water drops. Both samples are fabricated on steel, and have dimensions of $40 \times 40 \times 10\text{ mm}^3$. Water is released from four nozzles placed 5 cm above the surface, with a flow rate of approximately 150 ml min^{-1} .

Rights and permissions

Reprints and Permissions

About this article

Cite this article

Jiang, M., Wang, Y., Liu, F. *et al.* Inhibiting the Leidenfrost effect above 1,000 °C for sustained thermal cooling. *Nature* **601**, 568–572 (2022). <https://doi.org/10.1038/s41586-021-04307-3>

- Received: 13 April 2021
- Accepted: 03 December 2021
- Published: 26 January 2022
- Issue Date: 27 January 2022
- DOI: <https://doi.org/10.1038/s41586-021-04307-3>

Share this article

Anyone you share the following link with will be able to read this content:

[Get shareable link](#)

Sorry, a shareable link is not currently available for this article.

[Copy to clipboard](#)

Provided by the Springer Nature SharedIt content-sharing initiative

[Hot surfaces cooled by isolating steam from spray](#)

- James C. Bird

News & Views 26 Jan 2022

[Why water skitters off sizzling surfaces — and how to stop it](#)

- Shamini Bundell

Nature Video 27 Jan 2022

This article was downloaded by **calibre** from <https://www.nature.com/articles/s41586-021-04307-3>

| [Section menu](#) | [Main menu](#) |

- Article
- [Published: 26 January 2022](#)

Centimetre-scale perovskite solar cells with fill factors of more than 86 per cent

- [Jun Peng](#) [ORCID: orcid.org/0000-0002-1044-8744¹](#),
- [Felipe Kremer²](#),
- [Daniel Walter](#) [ORCID: orcid.org/0000-0002-4622-1912¹](#),
- [Yiliang Wu¹](#),
- [Yi Ji](#) [ORCID: orcid.org/0000-0001-8462-6438³](#),
- [Jin Xiang³](#),
- [Wenzhu Liu](#) [ORCID: orcid.org/0000-0003-0239-9089⁴](#),
- [The Duong¹](#),
- [Heping Shen¹](#),
- [Teng Lu⁵](#),
- [Frank Brink²](#),
- [Dingyong Zhong³](#),
- [Li Li](#) [ORCID: orcid.org/0000-0003-4066-2298⁶](#),
- [Olivier Lee Cheong Lem⁶](#),
- [Yun Liu](#) [ORCID: orcid.org/0000-0002-5404-3909⁵](#),
- [Klaus J. Weber](#) [ORCID: orcid.org/0000-0002-2421-6178¹](#),
- [Thomas P. White](#) [ORCID: orcid.org/0000-0001-8493-9450¹](#) &
- [Kylie R. Catchpole](#) [ORCID: orcid.org/0000-0003-4858-1820¹](#)

Nature volume **601**, pages 573–578 (2022)

- 1854 Accesses

- 18 Altmetric
- [Metrics details](#)

Subjects

- [Solar cells](#)

Abstract

Owing to rapid development in their efficiency¹ and stability², perovskite solar cells are at the forefront of emerging photovoltaic technologies. State-of-the-art cells exhibit voltage losses^{3,4,5,6,7,8} approaching the theoretical minimum and near-unity internal quantum efficiency^{9,10,11,12,13}, but conversion efficiencies are limited by the fill factor (<83%, below the Shockley–Queisser limit of approximately 90%). This limitation results from non-ideal charge transport between the perovskite absorber and the cell’s electrodes^{5,8,13,14,15,16}. Reducing the electrical series resistance of charge transport layers is therefore crucial for improving efficiency. Here we introduce a reverse-doping process to fabricate nitrogen-doped titanium oxide electron transport layers with outstanding charge transport performance. By incorporating this charge transport material into perovskite solar cells, we demonstrate 1-cm² cells with fill factors of >86%, and an average fill factor of 85.3%. We also report a certified steady-state efficiency of 22.6% for a 1-cm² cell (23.33% ± 0.58% from a reverse current–voltage scan).

This is a preview of subscription content

Access options

Subscribe to nature+

Get immediate online access to the entire Nature family of 50+ journals

\$29.99

monthly

[Subscribe](#)

Subscribe to Journal

Get full journal access for 1 year

\$199.00

only \$3.90 per issue

[Subscribe](#)

All prices are NET prices.

VAT will be added later in the checkout.

Tax calculation will be finalised during checkout.

Buy article

Get time limited or full article access on ReadCube.

\$32.00

[Buy](#)

All prices are NET prices.

Additional access options:

- [Log in](#)
- [Learn about institutional subscriptions](#)

Fig. 1: XPS characterization of TiO_xN_y films annealed at different temperatures.

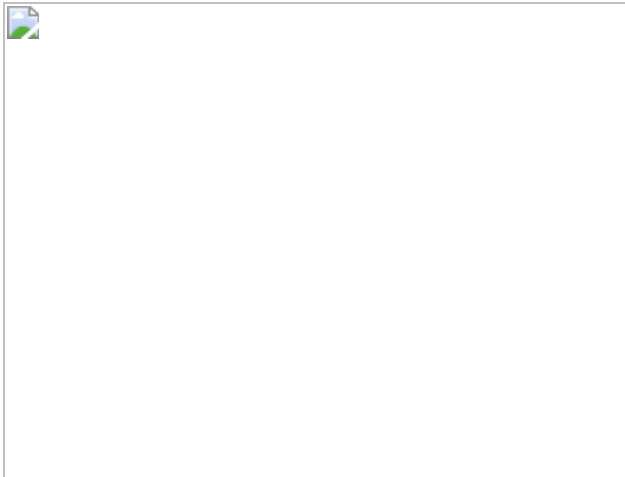


Fig. 2: TEM characterization and simulation of the diffraction pattern.

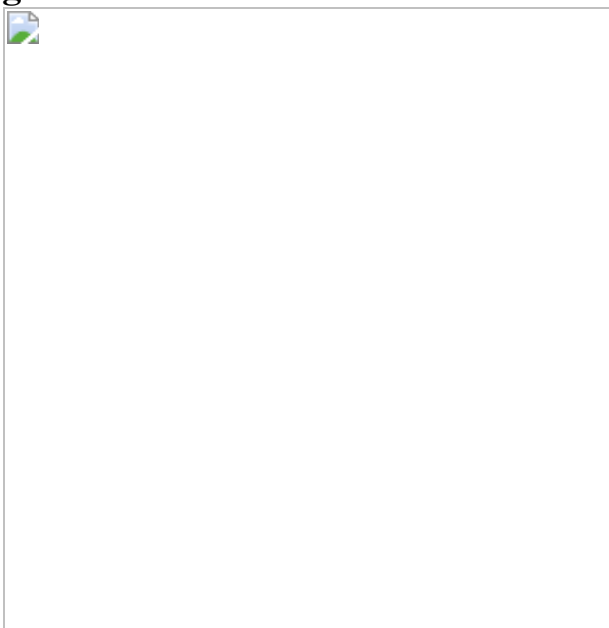


Fig. 3: Optoelectronic properties of TiO_xN_y films annealed at different temperatures.

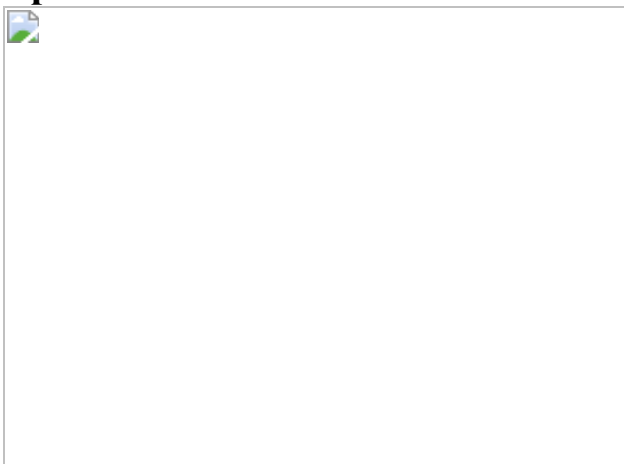
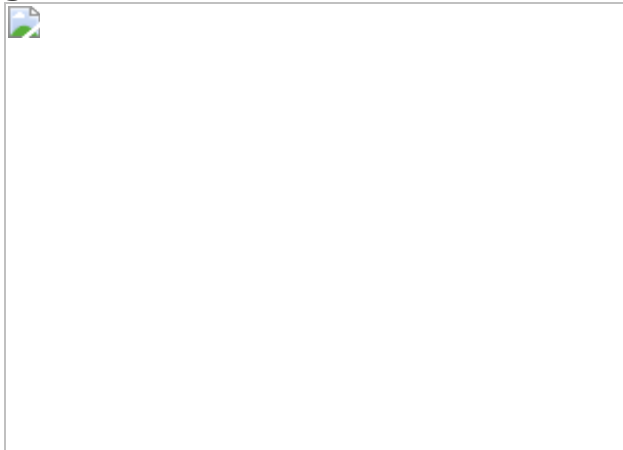


Fig. 4: Device characterization and simulation.



Data availability

The data that support the findings of this study are available from the corresponding authors on reasonable request.

References

1. 1. Green, A. M. et al. Solar cell efficiency tables (version 57). *Prog. Photovolt.* **29**, 3–15 (2021).
2. 2. Bai, S. et al. Planar perovskite solar cells with long-term stability using ionic liquid additives. *Nature* **571**, 245–250 (2019).
3. 3. Saliba, M. et al. Incorporation of rubidium cations into perovskite solar cells improves photovoltaic performance. *Science* **354**, 206–209 (2016).
4. 4.

Correa-Baena, J.-P. et al. Identifying and suppressing interfacial recombination to achieve high open-circuit voltage in perovskite solar cells. *Energy Environ. Sci.* **10**, 1207–1212 (2017).

5. 5.

Peng, J. et al. A universal double-side passivation for high open-circuit voltage in perovskite solar cells: role of carbonyl groups in poly(methyl methacrylate). *Adv. Energy Mater.* **8**, 1801208 (2018).

6. 6.

Luo, D. et al. Enhanced photovoltage for inverted planar heterojunction perovskite solar cells. *Science* **360**, 1442–1446 (2018).

7. 7.

Yang, S. et al. Tailoring passivation molecular structure for extremely small open-circuit voltage loss in perovskite solar cells. *J. Am. Chem. Soc.* **141**, 5781–5787 (2019).

8. 8.

Peng, J. et al. Nanoscale localized contacts for high fill factors in polymer-passivated perovskite solar cells. *Science* **371**, 390–395 (2021).

9. 9.

Kim, M. et al. Methylammonium chloride induces intermediate phase stabilization for efficient perovskite solar cells. *Joule* **3**, 2179–2192 (2019).

10. 10.

Min, H. et al. Efficient, stable solar cells by using inherent bandgap of α -phase formamidinium lead iodide. *Science* **366**, 749–752 (2019).

11. 11.

Zhu, H. et al. Tailored amphiphilic molecular mitigators for perovskite solar cells with 23.5% efficiency. *Adv. Mater.* **32**, 1907757 (2020).

12. 12.

Jiang, Q. et al. Surface passivation of perovskite film for efficient solar cells. *Nat. Photon.* **13**, 460–466 (2019).

13. 13.

Jung, E. H. et al. Efficient, stable and scalable perovskite solar cells using poly(3-hexylthiophene). *Nature* **567**, 511–515 (2019).

14. 14.

Giordano, F. et al. Enhanced electronic properties in mesoporous TiO₂ via lithium doping for high-efficiency perovskite solar cells. *Nat. Commun.* **7**, 10379 (2016).

15. 15.

Peng, J. et al. Efficient indium-doped TiO_x electron transport layers for high-performance perovskite solar cells and perovskite-silicon tandems. *Adv. Energy Mater.* **7**, 1601768 (2017).

16. 16.

Zhou, H. et al. Interface engineering of highly efficient perovskite solar cells. *Science* **345**, 542–546 (2014).

17. 17.

Asahi, R., Morikawa, T., Ohwaki, T., Aoki, K. & Taga, Y. Visible-light photocatalysis in nitrogen-doped titanium oxides. *Science* **293**, 269–271 (2001).

18. 18.

Asahi, R., Morikawa, T., Irie, H. & Morikawa, T. Nitrogen-doped titanium dioxides as visible-light-sensitive photocatalyst: design, development, and prospects. *Chem. Rev.* **114**, 9824–9852 (2014).

19. 19.

Shasti, M. & Mortezaali, A. The effect of nitrogen doping of TiO₂ compact blocking layers on perovskite solar cell performance. *Solid State Sci.* **92**, 68–75 (2019).

20. 20.

Zhang, Z. et al. Enhancement of perovskite solar cells efficiency using N-doped TiO₂ nanorod arrays as electron transfer layer. *Nanoscale Res. Lett.* **12**, 43 (2017).

21. 21.

NIST X-ray Photoelectron Spectroscopy Database NIST Standard Reference Database 20 (National Institute of Standards and Technology, 2000); <https://doi.org/10.18434/T4T88K>

22. 22.

Shahiduzzaman, M. D. et al. Low-temperature processed TiO_x electron transport layer for efficient planar perovskite solar cells. *Nanomaterials* **10**, 1676 (2020).

23. 23.

Zhang, L. et al. N-TiO₂-coated polyester filters for visible light—photocatalytic removal of gaseous toluene under static and dynamic flow conditions. *J. Environ. Chem. Eng.* **4**, 357–364 (2016).

24. 24.

Batzill, M., Morales, E. H. & Diebold, U. Influence of nitrogen doping on the defect formation and surface properties of TiO₂ rutile and

anatase. *Phys. Rev. Lett.* **96**, 026103 (2006).

25. 25.

Napoli, F. et al. The nitrogen photoactive centre in N-doped titanium dioxide formed via interaction of N atoms with the solid. Nature and energy level of the species. *Chem. Phys. Lett.* **477**, 135–138 (2009).

26. 26.

Milošv, I., Strehblow, H.-H., Navinšek, B. & Metikoš-Huković, M. Electrochemical and thermal oxidation of TiN coatings studied by XPS. *Surf. Interface Anal.* **23**, 529–539 (1995).

27. 27.

Wyckoff, R. W. G. *Crystal Structures 1*, 85–237 (Interscience, 1963).

28. 28.

Howard, C. J., Sabine, T. M. & Dickson, F. Structural and thermal parameters for rutile and anatase. *Acta Cryst. B* **47**, 462–468 (1991).

29. 29.

Yang, X. et al. Dual-function electron-conductive, hole-blocking titanium nitride contacts for efficient silicon solar cells. *Joule* **3**, 1314–1327 (2019).

30. 30.

Peelaers, H., Kioupakis, E. & Van de Walle, C. G. Free-carrier absorption in transparent conducting oxides: phonon and impurity scattering in SnO₂. *Phys. Rev. B* **92**, 235201 (2015).

31. 31.

Khenkin, M. V. et al. Consensus statement for stability assessment and reporting for perovskite photovoltaics based on ISOS procedures. *Nat.*

Energy **5**, 35–49 (2020).

32. 32.

Lin, Y.-H. et al. A piperidinium salt stabilizes efficient metal-halide perovskite solar cells. *Science* **369**, 96–102 (2020).

33. 33.

Hanaor, D. A. & Sorrell, C. C. Review of the anatase to rutile phase transformation. *J. Mater. Sci.* **46**, 855–874 (2011).

34. 34.

Brudnik, A., Bucko, M., Radecka, M., Trenczek-Zajac, A. & Zakrzewska, K. Microstructure and optical properties of photoactive TiO₂:N thin films. *Vacuum* **82**, 936–941 (2008).

35. 35.

Morikawa, T., Asahi, R., Ohwaki, T., Aoki, K. & Taga, Y. Band-gap narrowing of titanium dioxide by nitrogen doping. *Jpn. J. Appl. Phys.* **40**, L561–L563 (2001).

36. 36.

Ding, B. et al. Facile and scalable fabrication of highly efficient lead iodide perovskite thin-film solar cells in air using gas pump method. *ACS Appl. Mater. Interfaces* **8**, 20067–20073 (2016).

37. 37.

Shi, L. et al. Accelerated lifetime testing of organic–inorganic perovskite solar cells encapsulated by polyisobutylene. *ACS Appl. Mater. Interfaces* **9**, 25073–25081 (2017).

38. 38.

Stadelmann, P. A. EMS - a software package for electron diffraction analysis and HREM image simulation in materials science.
Ultramicroscopy **21**, 131–145 (1987).

Acknowledgements

This work was supported by the Australian Government through the Australian Renewable Energy Agency and the Australian Research Council. Responsibility for the views, information or advice expressed herein is not accepted by the Australian Government. J.P. acknowledges the financial support of a Postdoc Fellowship from the Australian Centre for Advanced Photovoltaics. T.P.W. is the recipient of an Australian Research Council Future Fellowship (project number FT180100302) funded by the Australian Government. T.P.W. also acknowledges the support of the Open Fund of the State Key Laboratory of Optoelectronic Materials and Technologies (Sun Yat-sen University). D.Z. acknowledges funding from the National Natural Science Foundation of China (grant numbers 11574403 and 11974431). The work was partly conducted at the ACT node of the Australian National Fabrication Facility, and the ANU node of the Australian Microscopy and Microanalysis Facility. We thank S. Surve and S. Zhao for experimental assistance.

Author information

Affiliations

1. School of Engineering, The Australian National University, Canberra, Australian Capital Territory, Australia

Jun Peng, Daniel Walter, Yiliang Wu, The Duong, Heping Shen, Klaus J. Weber, Thomas P. White & Kylie R. Catchpole

2. Centre for Advanced Microscopy, The Australian National University, Canberra, Australian Capital Territory, Australia

Felipe Kremer & Frank Brink

3. School of Physics & State Key Laboratory of Optoelectronic Materials and Technologies, Sun Yat-sen University, Guangzhou, China

Yi Ji, Jin Xiang & Dingyong Zhong

4. Research Center for New Energy Technology, Shanghai Institute of Microsystem and Information Technology, Chinese Academy of Sciences, Shanghai, China

Wenzhu Liu

5. Research School of Chemistry, The Australian National University, Canberra, Australian Capital Territory, Australia

Teng Lu & Yun Liu

6. Australian National Fabrication Facility, Research School of Physics, The Australian National University, Canberra, Australian Capital Territory, Australia

Li Li & Olivier Lee Cheong Lem

Contributions

J.P. conceived the idea, designed the overall experiments and led the project. J.P. optimized the sputtered TiO_xN_y thin films. J.P. and Y.W. prepared and characterized the perovskite cell devices. F.K. and F.B. performed the TEM measurements and analysis. D.W., T.P.W. and K.J.W. conducted the device numerical simulation. Y.J. and J.X. performed the XPS/UPS measurements and analysis. D.Z. supervised the XPS/UPS measurements and analysis. Y.W. performed the Hall effect measurements and analysis. W.L. performed the EQE measurements. T.L. and Y.L. performed the atomic force microscopy measurements. T.D. and H.S. performed the steady-state and time-resolved photoluminescence, UV–Vis transmittance and absorption measurements. L.L. and O.L.C.L. conducted the SEM measurements. K.R.C. and T.P.W. supervised the project. J.P. wrote the manuscript. All authors contributed to the discussion of the results and revision of the manuscript.

Corresponding authors

Correspondence to [Jun Peng](#), [Thomas P. White](#) or [Kylie R. Catchpole](#).

Ethics declarations

Competing interests

The Australian National University has filed a PCT patent (PCT/AU2021/051266) related to the subject matter of this manuscript.

Peer review information

Nature thanks Michael McGehee, Md. Shahiduzzaman and the other, anonymous, reviewer(s) for their contribution to the peer review of this work.

Additional information

Publisher's note Springer Nature remains neutral with regard to jurisdictional claims in published maps and institutional affiliations.

Extended data figures and tables

[Extended Data Fig. 1 Surface morphology characterisation by AFM.](#)

a, Bare FTO substrate. **b**, FTO/TiN substrate without post-annealing treatment (labeled as ‘As-deposited’). **c**, FTO/TiO_xN_y substrate annealed at 300°C (labeled as ‘300 C’). **d**, FTO/TiO_xN_y substrate annealed at 350°C (labeled as ‘350 C’). **e**, FTO/TiO_xN_y substrate annealed at 400°C (labeled as ‘400 C’). **f**, FTO/TiO_xN_y substrate annealed at 450°C (labeled as ‘450

C'). **g**, FTO/TiO_xN_y substrate annealed at 500°C (labeled as ‘500 C’). **h**, FTO/TiO_xN_y substrate annealed at 550°C (labeled as ‘550 C’). Note that the legend of ‘RMS’ represents root mean square of the surface roughness.

Extended Data Fig. 2 XPS element analysis.

The atomic ratio of O to Ti and N to Ti for TiO_xN_y thin films annealed at different temperatures.

Extended Data Fig. 3 TEM characterisation.

a, TiO_xN_y without annealing (‘As-deposited’). **b**, TiO_xN_y annealed at 300°C. **c**, TiO_xN_y annealed at 400°C. **d**, TiO_xN_y annealed at 500°C.

Extended Data Fig. 4 TEM characterisation and simulation of the diffraction pattern.

a and **b**, TiO_xN_y annealed at 350°C. **c** and **d**, TiO_xN_y annealed at 450°C. **e** and **f**, TiO_xN_y annealed at 550°C. Note that the non-continuous diffraction ring visible in Fig. 4f diffraction pattern is caused by the low crystal density within the specimen.

Extended Data Fig. 5 Optical bandgap characterisation.

Tauc plots for the as-deposited TiN film and TiO_xN_y films annealed at different temperatures. Note that all films (~50 nm) were deposited on quartz substrates.

Extended Data Fig. 6 Device structure.

a, The cross-sectional SEM image of the TiO_xN_y-based cell with a structure of glass/FTO/TiO_xN_y (~40 nm)/meso-TiO₂ (~50 nm)/ultrathin PMMA:PCBM (<3nm)/Perovskite (~500 nm)/ultrathin PMMA (<3 nm)/P3HT:CuPc (~65 nm)/Gold. **b**, The cross-sectional SEM image of the

TiO_x -based cell with a structure of glass/FTO/ TiO_x (~ 50 nm)/meso- TiO_2 (~ 50 nm)/ultrathin PMMA:PCBM (< 3 nm)/Perovskite (~ 500 nm)/ultrathin PMMA (< 3 nm)/P3HT:CuPc (~ 65 nm)/Gold. Note that the meso- TiO_2 and perovskite represent mesoporous TiO_2 and $\text{Cs}_{0.05}\text{FA}_{0.9}\text{MA}_{0.05}\text{PbI}_{2.74}\text{Br}_{0.26}$, respectively.

Extended Data Fig. 7 Device characterisation.

a, V_{OC} and J_{SC} distribution for the TiO_x -based cells (12 cells) and the TiO_xN_y -based cells (14 cells). **b**, The $J-V$ curve of the perovskite cells based on the TiO_xN_y ETLs, which were annealed at 550°C . **c**, The $J-V$ parameters distribution of the TiO_xN_y (annealed at 550°C) based cells (15 cells).

Extended Data Fig. 8 Effects of electron transport layers with different carrier densities on the performance of perovskite solar cells.

a, Simulated $J-V$ curves where only ETL doping is varied using dopant densities taken from Hall effect measurements. **b**, Experimental $J-V$ curves for the reference TiO_x and TiO_xN_y PSCs. Reduction in FF and increase in Ohmic series resistance is predominantly due to electron depletion in the ETL layer. **c**, Energy level diagram of electron quasi-Fermi levels and conduction band, illustrating the resistive voltage loss in the ETL for the lowly-doped cases. Note that Energy levels and electron concentrations are calculated at 22.5 mA/cm^2 for ETLs with doping densities equivalent to TiO_x ($5 \times 10^{14} \text{ cm}^{-3}$) and TiO_xN_y ($3 \times 10^{17} \text{ cm}^{-3}$). **d**, Electron concentration in the ETL for doping levels from $5 \times 10^{14} - 10^{18} \text{ cm}^{-3}$. Note that the dash-dot horizontal lines mark the dopant defect concentration, indicating the magnitude of electron depletion. With the exception of extremely high doping at 10^{18} cm^{-3} , in no case does the free electron concentration reach even the same order of magnitude as the fixed dopant concentration. **e-f**, Contour plots of perovskite solar cell fill factor (**e**) and open-circuit voltage (**f**) across a range of ETL doping levels and electron affinity. Note that the

stars mark the conditions simulated in Fig. 9a. The vertical dashed lines mark the doping levels of the TiO_x and optimized TiO_xN_y films fabricated in this work. Electron depletion from the ETL suggests that high doping is in general necessary to achieve fill factors on the order of 85% or above.

Extended Data Fig. 9 Device stability characterisation.

a, Light-soaking stability tests. **b**, Damp-heat stability tests. Note that SPO represents steady-state power output measured by maximum power point voltage (V_{MPP}) tracking under continuous 1 sun illumination intensity. The device structure of the encapsulated cells is glass/FTO/ TiO_xN_y (or TiO_x)/m- TiO_2 /PMMA:PCBM/Perovskite/PMMA/P3HT:CuPc/MoO_x (~10 nm)/IZO (~40 nm)/Au, where the perovskite is $\text{Cs}_{0.05}\text{FA}_{0.9}\text{MA}_{0.05}\text{PbI}_{2.74}\text{Br}_{0.26}$. Details of encapsulation are provided in the experimental section.

Extended Data Table 1 Summarised parameters for the Hall-effect measurements

Supplementary information

Supplementary Information

This file contains model details, Figs. 1–6, Tables 1–5 and additional references.

Rights and permissions

Reprints and Permissions

About this article

Cite this article

Peng, J., Kremer, F., Walter, D. *et al.* Centimetre-scale perovskite solar cells with fill factors of more than 86 per cent. *Nature* **601**, 573–578 (2022). <https://doi.org/10.1038/s41586-021-04216-5>

- Received: 28 January 2021
- Accepted: 09 November 2021
- Published: 26 January 2022
- Issue Date: 27 January 2022
- DOI: <https://doi.org/10.1038/s41586-021-04216-5>

Share this article

Anyone you share the following link with will be able to read this content:

[Get shareable link](#)

Sorry, a shareable link is not currently available for this article.

[Copy to clipboard](#)

Provided by the Springer Nature SharedIt content-sharing initiative

This article was downloaded by **calibre** from <https://www.nature.com/articles/s41586-021-04216-5>

- Article
- Open Access
- [Published: 12 January 2022](#)

Age of the oldest known *Homo sapiens* from eastern Africa

- [Céline M. Vidal](#) [ORCID: orcid.org/0000-0002-9606-4513](#)^{1,2},
- [Christine S. Lane](#) [ORCID: orcid.org/0000-0001-9206-3903](#)¹,
- [Asfawossen Asrat](#) [ORCID: orcid.org/0000-0002-6312-8082](#)^{3,4},
- [Dan N. Barfod](#)⁵,
- [Darren F. Mark](#)⁵,
- [Emma L. Tomlinson](#)⁶,
- [Amdemichael Zafu Tadesse](#)⁷,
- [Gezahegn Yirgu](#)³,
- [Alan Deino](#)⁸,
- [William Hutchison](#) [ORCID: orcid.org/0000-0002-5456-3277](#)⁹,
- [Aurélien Mounier](#)^{10,11} &
- [Clive Oppenheimer](#) [ORCID: orcid.org/0000-0003-4506-7260](#)^{1,12}

[Nature](#) volume 601, pages 579–583 (2022)

- 48k Accesses
- 1356 Altmetric
- [Metrics details](#)

Subjects

- [Archaeology](#)
- [Geochemistry](#)
- [Volcanology](#)

Abstract

Efforts to date the oldest modern human fossils in eastern Africa, from Omo-Kibish^{1,2,3} and Herto^{4,5} in Ethiopia, have drawn on a variety of chronometric evidence, including $^{40}\text{Ar}/^{39}\text{Ar}$ ages of stratigraphically associated tuffs. The ages that are generally reported for these fossils are around 197 thousand years (kyr) for the Kibish Omo I^{3,6,7}, and around 160–155 kyr for the Herto hominins^{5,8}. However, the stratigraphic relationships and tephra correlations that underpin these estimates have been challenged^{6,8}. Here we report geochemical analyses that link the Kamoya's Hominid Site (KHS) Tuff⁹, which conclusively overlies the member of the Omo-Kibish Formation that contains Omo I, with a major explosive eruption of Shala volcano in the Main Ethiopian Rift. By dating the proximal deposits of this eruption, we obtain a new minimum age for the Omo fossils of 233 ± 22 kyr. Contrary to previous arguments^{6,8}, we also show that the KHS Tuff does not correlate with another widespread tephra layer, the Waideido Vitric Tuff, and therefore cannot anchor a minimum age for the Herto fossils. Shifting the age of the oldest known *Homo sapiens* fossils in eastern Africa to before around 200 thousand years ago is consistent with independent evidence for greater antiquity of the modern human lineage¹⁰.

[Download PDF](#)

Main

Only eight sites in Africa have yielded possible early anatomically modern *Homo sapiens* fossils from the late Middle Pleistocene (approximately 350–130 thousand years ago (ka))¹¹. Most of these have considerable age uncertainty or debatable *H. sapiens* apomorphy¹¹. A principal method for constraining the fossil ages is the use of single-crystal $^{40}\text{Ar}/^{39}\text{Ar}$ isotope dating applied to stratigraphically associated volcanic ash (tephra) beds^{12,13,14}. However, many distal tephra deposits consist largely of glass and lack suitable crystals for dating. In this case, geochemical fingerprinting can be used to match a tephra layer to more readily dated proximal deposits with larger, more abundant phenocrysts. The most widely accepted fossils that are interpreted as possessing unequivocal modern cranial apomorphies (that is, a tall cranial vault and a chin) and classified as *H. sapiens* are two Ethiopian finds^{11,15,16}, namely the Omo I¹ and Herto specimens⁴. Accordingly, the evidence that constrains their ages assumes particular importance but is a topic of considerable geochronological controversy^{3,6,8}.

The Omo I remains were discovered in the late 1960s in the lower Omo valley of southern Ethiopia^{1,14}, at the surface of a siltstone near the top of Member I of the Omo-Kibish Formation (Fig. [1a, b](#)). The maximum age of Omo I was derived from the $^{40}\text{Ar}/^{39}\text{Ar}$ age of 196 ± 4 kyr (2σ)^{3,6,17} obtained for alkali feldspar phenocrysts from the three youngest pumice clasts that were sampled from a heterogeneous tuffaceous deposit correlated with the Nakaa'kire Tuff³, which is reported to lie “near, but

probably slightly below” the fossils³ (Fig. 1b). Recalculated using a more widely adopted age of 28.201 million years (Myr) for the irradiation monitor (sanidine from the Fish Canyon Tuff of Colorado)¹⁸, the Nakaa’kire Tuff age shifts marginally to 197 ± 4 kyr. Owing to the uncertain stratigraphic relationship between this tuff and the hominin fossils¹⁹, much attention has been focused on dating the KHS Tuff—a widespread, more-than-2-m-thick deposit of fine ash fallout at the base of Member II of the Omo-Kibish Formation (Fig. 1b). The KHS Tuff overlies Member I, where Omo I was retrieved around 1.4 m lower down section, and is demonstrably younger than the fossils^{3,9}. Although the Nakaa’kire Tuff was identified in several sections below the KHS Tuff, the latter was not found in the same section from which the dated pumice clasts correlated with the Nakaa’kire Tuff (on the basis of major element composition) were sampled³. The fine grain size of the KHS Tuff has precluded direct $^{40}\text{Ar}/^{39}\text{Ar}$ dating, and no correlation to a source volcano or proximal pyroclastic unit has to our knowledge been made previously. However, drawing on published major element glass compositions, it has been correlated with both tephra TA-55^{20,21} from the Konso Formation and the directly $^{40}\text{Ar}/^{39}\text{Ar}$ -dated 184 ± 10 kyr unit D²² (recalculated age) of the Gademotta Formation⁶ (Fig. 1b). Relating the sediment flux in the Omo-Kibish basin with high lake levels that correspond to Mediterranean sapropel deposition^{9,23}, a slightly younger age for the KHS Tuff of around 172 kyr has also been proposed⁶. Either of these ages (184 or 172 kyr) would be consistent with the proposed age of 197 ± 4 kyr for Omo I.

Fig. 1: Late Middle Pleistocene tephrostratigraphy of the Main Ethiopian Rift.

 **figure 1**

a, Map of the MER showing silicic volcanoes and the late Middle Pleistocene sedimentary formations and relevant tephra units. White boxes with blue edges depict former correlatives of the KHS Tuff^{6,8} **b**, Synthetic stratigraphic logs of the late Middle Pleistocene formations showing former correlations for the Alyio Tuff⁶ (green), Konso SVT (pink, also identified in the Chew Bahir sediment core³³), new correlations for Konso unit TA-56 (yellow), and source eruptions (stars). LHM, lower Herto Member; UHM, upper Herto Member. **c**, Tephra ETH18-8 above the KHS Tuff at the KS locality in the Omo-Kibish Formation⁹.

The Herto *H. sapiens* fossils were recovered in the late 1990s in the Middle Awash^{4,5} (Afar rift; Fig. 1a). They were preserved in a sandstone within the upper Herto Member of the Bouri Formation (Fig. 1b). This sandstone is capped by the Waideido Vitric Tuff (WAVT) (Fig. 1b), which is widespread across western Afar and is also present at Gona²⁴, 50 km north of Herto. Direct dating of the WAVT has remained inconclusive owing to crystal contamination, but dating of pumice and obsidian clasts

in the fossiliferous sandstone yielded a maximum age of around 160 kyr (ref. 5). The WAVT was identified as a distal correlative of tephra TA-55 (Fig. 1b), on the basis of major element analysis of individual grains and major and trace element analysis of purified bulk separates^{5,25}. In Konso, unit TA-55 lies below the 155 ± 14 kyr Silver Tuff⁵ (SVT) (recalculated age) (Fig. 1b), suggesting an age for the Herto fossils of around 160–155 kyr (ref. 4). This finding was challenged, however, in a study⁶ that correlated the Kibish KHS with Konso TA-55, and therefore with the Herto WAVT (Fig. 1b). This argument suggested an age of around 172 kyr for the WAVT, contradicting the established Herto stratigraphy. The Herto research group⁸ responded by corroborating their original stratigraphy, with the WAVT above the Herto fossils, thus challenging an age of about 172 kyr for the KHS. They concluded that the KHS, Konso unit TA-55⁵, Gademotta unit D (around 184 kyr)²² and WAVT⁵ could all represent a single tephostratigraphic marker lying above the Omo-Kibish and Herto *H. sapiens* fossils, but that multiple eruptive sources would also be plausible⁸ (Fig. 1b). Given the lingering uncertainties of the stratigraphic relationship of the Nakaa'kire Tuff to Omo I, the age of the KHS Tuff becomes critical to the chronostratigraphy of these sites.

We have re-sampled the KHS Tuff and other pertinent ash deposits at Omo-Kibish, Konso and Gademotta to assess the geochemical correlations from which the ages of the oldest modern human fossils are inferred. While revisiting the sampling locality of the KHS Tuff (KS type section)⁹ at Omo-Kibish, we sampled another tephra layer in Member II (Fig. 1c) in an outcrop about 100 m from the KS type section. Unit ETH18-8 is an approximately 15-cm-thick, very well-sorted crystal-rich fine sand grey tephra layer situated 40 cm above the KHS Tuff (Fig. 1c). It is ubiquitous between the KHS section (KS) and the Chibele section (CB), and might stratigraphically correspond to unit CRF-23 previously identified above the KHS Tuff at the CB section⁹, although this cannot be confirmed through geochemical analysis because of the different microprobe conditions used.

In an attempt to identify and date the eruption that generated the KHS tuff, we included samples of ignimbrites from the caldera-forming eruptions of Shala and Corbetti volcanoes. Shala and Corbetti are the only Main Ethiopian Rift (MER) systems known to have produced major eruptions between around 170 ka and 250 ka²⁶. At Shala, the largest caldera in the central MER (Fig. 2a), we sampled at a more-than-20-m-thick exposure of the unwelded Qi2 ignimbrite²⁷ (Fig. 2b,c), southwest of Lake Shala and 350 km northeast of Omo-Kibish (Fig. 2a). We also analysed glass from a welded ignimbrite (COI2E) attributed to the formation of Corbetti caldera, dated at 177 ± 8 kyr (ref. 26). A challenge of geochemical correlations between proximal and distal tephra deposits in the region is similarity in major and trace element compositions between pyroclastic products, not only of the same volcano but

of different volcanoes in the MER²⁸. Accordingly, correlations are ideally based on a detailed suite of major, minor and trace element single-grain glass shard or pumice glass analyses.

Fig. 2: Stratigraphy and age of the Shala Qi2 ignimbrite.

 figure 2

a, Location of site ETH17-14 near Lake Shala in the MER. **b**, Synthetic stratigraphy of the Qi2 ignimbrite of Shala at location ETH17-14. **c**, Photographs of units 14A, 14B and 14C of the Qi2 ignimbrite at site ETH17-14. Field observations indicate that deposits 14A and 14B are subunits of the same phase of the Qi2 eruption. **d**, $^{40}\text{Ar}/^{39}\text{Ar}$ age pooled data plotted on ideograms for samples 14A and 14C of the Qi2 ignimbrite (bottom) yielding a preferred composite eruption age of 233 ± 22 kyr (top). Data are weighted means. Error bars show data and results at 2σ . $^{40}\text{Ar}^*$, radiogenic ^{40}Ar ; MSWD, mean square of weighted deviates; P , probability that residuals are explained by measurement errors exclusively; n , number of accepted grains.

The KHS glass shards are homogeneous pantelleritic rhyolite in composition (77.0 ± 0.3 wt% SiO_2 , 9.7 ± 0.1 wt% Al_2O_3 , 5.0 ± 0.1 wt% FeO^* (FeO^* refers to the total Fe as FeO) and 7.1 ± 0.4 wt% $\text{Na}_2\text{O} + \text{K}_2\text{O}$; Supplementary Table 1). Immobile oxide abundances, including FeO^* , CaO , Al_2O_3 and TiO_2 (Fig. 3, Supplementary Table 1), correspond with those of glasses from the proximal products of the Qi2 eruption of Shala volcano (samples ETH17-14A1, B1, B5 and C) (Figs. 2b, c, 3, Supplementary Fig. 4, Supplementary Table 1, [Supplementary Information](#)). These correlations are corroborated by comparing immobile trace element ratios for Qi2 and KHS glasses and principal component analysis (Fig. 3, Supplementary Figs. 4, 5, Supplementary Table 2, [Supplementary Information](#)).

Fig. 3: Geochemical fingerprints of MER tephra and their sources.

 figure 3

Major element abundances and trace element ratios of glasses from the Shala Qi2 ignimbrite (around 233 kyr), the Corbetti ignimbrite (around 177 kyr), the Gademotta unit D (around 184 kyr), the Kibish KHS and ETH18-8 tuffs, and the Konso TA-56 tuffs (all data from this study). Major element data are normalized to 100% anhydrous. Error bars shown are relative standard deviations derived from repeat measurements of matrix match glass secondary standards STH-S6 (for FeO*, $n = 91$; Supplementary Table 6) and ATHO-G (for Al₂O₃, CaO and TiO₂, $n = 70$; Supplementary Table 6). They are plotted in the top right corner of each plot for clarity and rescaled to the value of the centre point. In the case of element ratios, error propagation has been applied using analyses of standard ATHO-G ($n = 15$; Supplementary Table 7). Additional compositional observations and biplots are presented in Supplementary Fig. 5.

In addition, we find that the COI2E pantelleritic rhyolite glass from the 177 ± 8 kyr (ref. 26) Corbetti ignimbrite (74.3 ± 0.2 wt% SiO₂, 9.1 ± 0.1 wt% Al₂O₃, 5.6 ± 0.2 wt% FeO* and 10.1 ± 0.2 wt% Na₂O+K₂O) (Fig. 3, Supplementary Fig. 4, Supplementary Table 1, [Supplementary Information](#)) has immobile oxides and trace element abundances that match those for Kibish unit ETH18-8 and Konso TA-56 (Fig. 3, Supplementary Figs. 4, 5, Supplementary Table 2, [Supplementary Information](#)).

We used the $^{40}\text{Ar}/^{39}\text{Ar}$ dating method to analyse 113 individual sanidine crystals extracted from pumice samples ETH17-14A1 (base, 68 crystals) and ETH17-14C (top, 45 crystals) collected from the Shala Qi2 deposits (Fig. 2). The resulting data were filtered to exclude grains with low gas yields, at or below blank level, and xenocrysts with ages significantly older than the mean of the dataset (six grains with ages exceeding 1 Myr). The distributions of ages from each sample were indistinguishable at 2σ uncertainty (Fig. 2d). Combining analyses from both pumice samples yielded a weighted mean of 233 ± 22 kyr at 2σ (Fig. 2d, Supplementary Table 3), thereby dating the Qi2 eruption and the KHS tuff.

An age of 233 ± 22 kyr for KHS is consistent with the 177 ± 8 kyr age that we associate with the overlying ETH18-8 tephra (Fig. 1b). However, it casts doubt on the suggested correlation between high deposition fluxes in the Omo basin with large inflows of fresh water from the Nile River system into the Mediterranean sea^{6,7,9}, at least during the formation of Member II. Our KHS age is incongruent with the formation of Mediterranean Sapropel S6 at 172 ka⁶, and instead overlaps the timing of the formation of sapropel S8 (217 ka)^{9,29}. Although the 177 ± 8 kyr age of ETH18-8 is consistent with the formation of sapropel S6 (172 ka)²⁹, only a mudstone unit of around 40 cm thickness separates KHS from ETH18-8, which cannot account for the suggested rapid deposition in the basin concomitant with sapropel S7 (192–199 ka)³.

The revised Omo-Kibish stratigraphy is also incompatible with the 197 ± 4 kyr age reported for the Nakaa'kire Tuff^{3,7,9}, which is found in Member I of the formation^{3,7,9} and which must therefore be older than 233 ± 22 kyr. The age of 197 ± 4 kyr was inferred from three out of five dated pumice clasts from lenses found in ‘a sandy tuffaceous matrix’⁷. Although these samples had similar major element compositions to the Nakaa'kire Tuff, they were collected from a lateral outcrop and not in section^{3,7,9}. Given the uncertainty in the age and stratigraphic placement of the Nakaa'kire Tuff, as well as its heterogeneous lithology and geochemistry, the identification of the 233 ± 22 ka Qi2 eruption of Shala as the source of the KHS Tuff provides a more robust minimum age for Omo I *H. sapiens*.

Furthermore, our glass compositional data, source correlation and age estimate for KHS allow us to re-assess its identification at other archaeological sites in Ethiopia. New lithological examination of the pedogenically altered unit TA-55 at Konso (Supplementary Fig. 1) in grain size fractions of greater than 125 μm , greater than 80 μm and greater than 25 μm , after density separation, failed to identify glass shards in this deposit, which was previously correlated with the WAVT at Herto. This precluded evaluation of the reported correlation with the KHS Tuff⁶. However, with the underlying unit TA-56 now correlated with Kibish unit ETH18-8 and the 177 ± 8 kyr Corbetti ignimbrite (Fig. 3, Supplementary Figs. 4, 5), it is clear that TA-55 is younger than 177 ± 8 kyr and so cannot correlate with Qi2 or the KHS Tuff.

Although the 184 ± 10 kyr unit D of Gademotta appears close to KHS in major element contents, neither major nor trace element abundances clearly overlap (Fig. 3, Supplementary Figs. 4, 5, [Supplementary Information](#)), precluding a match. Immobile trace element ratios and principal component analysis show that unit D also differs from TA-56 (Fig. 3, Supplementary Figs. 4, 5, [Supplementary Information](#)).

The correlation of the Herto WAVT with Konso unit TA-55⁵, around 800 km south of Herto, led earlier investigators to accept the 155 ± 14 kyr age of the SVT at Konso as the *terminus ante quem* of the Herto fossils. This correlation has been debated³⁰ but reinforced by additional geochemical data²⁵. We were unable to find preserved glass in our TA-55 sample but our results undermine the tephrostratigraphic correlations proposed between the Omo-Kibish, Gademotta and Konso formations⁶ and bracket the age of the Konso TA-55 tuff between 177 ± 8 kyr (TA-56) and 155 ± 14 kyr (SVT). Although its correlation with the WAVT at Herto should be confirmed in the future using grain-discrete single-point glass analyses, this age bracket is consistent with the underlying Herto fossiliferous sandstone (approximately 160 kyr)⁵, and confirms that the Herto *H. sapiens* fossils are considerably younger than Omo I at Omo-Kibish.

Our new age constraints are congruent with most models for the evolution of modern humans, which estimate the origin of *H. sapiens* and its divergence from archaic humans at around 350–200 ka (refs. [16,31,32](#)). The challenge remains to obtain a robust maximum age for Omo I. Our revised tephrostratigraphy demonstrates that the Herto specimens postdate the Omo I remains from Omo-Kibish, and that they do not lie beneath the same tephra horizon as the Kibish fossils, as previously inferred⁸. Further geochemical data are needed to clarify the relationship between the WAVT and other MER tephra, and may ultimately identify the WAVT source, promising a more reliable minimum age for the Herto fossils. More generally, continued efforts to develop the tephrochronological framework for eastern Africa will help in addressing a range of interrelated volcanological, palaeoenvironmental and palaeoanthropological questions.

Methods

Sampling

Stratigraphic descriptions and sampling were carried out during two field seasons in 2017 and 2018. We sampled the previously described²⁷ Qi2 eruption of Shala volcano, and we revisited the Konso^{20,21}, Omo-Kibish^{3,6,9} and Gademotta^{22,34} formations (Fig. 1). At each site we described extensively the stratigraphy of the outcrops, measured the thickness of units and sampled deposits where best exposed and least altered.

$^{40}\text{Ar}/^{39}\text{Ar}$ dating

Feldspars were extracted from pumice samples at the Departments of Geography and Earth Sciences, University of Cambridge. Rocks were crushed in a jaw crusher and sieved to obtain a 250–500- μm size fraction, cleaned under water and passed through a Frantz magnetic barrier laboratory separator to isolate sanidine phenocrysts from the groundmass. Because separates would still contain other phases (primarily glass and quartz), 100–200 sanidine grains were further handpicked and then leached in 5% HF to remove any glass attached to the crystals.

Samples and neutron flux monitors were packaged in copper foil and stacked in quartz tubes with the relative positions of packets precisely measured for later reconstruction of neutron flux gradients. The sample package was irradiated for 2 h in the Oregon State University reactor, Cd-shielded facility (CLICIT). Fish Canyon sanidine (28.294 ± 0.036 (1σ) million years ago; Ma) (ref. [35](#)) was used to monitor ^{39}Ar production and establish neutron flux values (J) for the samples (Supplementary Table [4](#)). Gas was extracted from samples via step-heating using a mid-infrared (10.6 μm) CO_2 laser with a non-gaussian, uniform energy profile and a 1.5-mm beam diameter. The samples were housed in a doubly pumped ZnS-window laser cell and loaded into a stainless steel planchette containing 208 2.0-mm-diameter round wells. Liberated argon was purified of active gases—for example, CO_2 , H_2O , H_2 , N_2 and CH_4 —using three Zr-Al getters; one at 16 °C and two at 400 °C. Data were collected on a Mass Analyser Products MAP-215-50 single-collector mass spectrometer using an electron multiplier collector in dynamic collection (peak hopping) mode. Time-intensity data were regressed to inlet time with second-order polynomial or linear fits to the data. Sample runs were corrected using the standard deviation of blanks throughout the runs. Mass discrimination was monitored on a daily basis, between and within sample runs by analysis of an air standard aliquot delivered by an automated pipette system (see Supplementary Table [4](#) for D values). All blank, interference and mass discrimination calculations were performed with the MassSpec software package (MassSpec, v.8.058, A. Deino, Berkeley Geochronology Center). Decay constants and corrections (Supplementary Table [5](#)) were made using the approach of Renne et al. 2010^{[36](#)} with the parameters of Renne et al. 2011^{[35](#)}.

Following the approach of Kuiper et al. [18](#), samples with low radiogenic yields ($^{40}\text{Ar}^* < 10\%$, 23 grains), and obvious outliers (age > 1 Myr, 6 grains) were rejected. After this initial filtering, peak age distributions were defined by determining the youngest population of individual grain analyses ($n \geq 10$) that conforms to a Gaussian distribution with the expected scatter as indicated by the value of the mean square of weighted deviates (MSWD)); this second stage of filtering resulted in the rejection of an additional ten older grains, leaving 71 accepted grains.

Ages for unit samples ETH17-14A1 and ETH17-14C are reported with two sigma errors in Supplementary Table [3](#) with the raw data in Supplementary Table [4](#). These

two sub-samples from the top and bottom of the same stratigraphic unit are indistinguishable in age at 2σ uncertainty, which permits them to be combined into a single composite sample. The accepted age for this population is 234 ± 22 kyr (relative to ref. 36) or 233 ± 22 kyr (relative to ref. 18). An inverse isochron plotted through the data (Supplementary Fig. 2) yields an age of 219 ± 27 kyr (${}^{40}\text{Ar}/{}^{36}\text{Ar}_{(\text{i})} = 314 \pm 24$, MSWD = 1.1, $P = 0.19$, $n = 71$), which is indistinguishable from the accepted age.

Although we are using the Kuiper et al. (ref. 18) calibration, the Renne et al. 2011 (ref. 36) calibration has quantifiable uncertainties and is our preferred age for the sample. Nevertheless, for consistency with previous work, the latter age (233 ± 22 kyr) is used throughout the manuscript.

Sample preparation for geochemical analyses

Sample preparation was carried out in the Cambridge Tephra Laboratory in line with the protocols of the International Focus Group on Tephrochronology (INTAV)^{12,37} for geochemical characterization of volcanic glass. Pumice samples of the Qi2 Shala eruption were crushed, sieved at 500, 250, and 125 μm , and washed in purified water and hydrochloric acid (1%) in an ultrasonic bath. Glass grains from the 125–250- μm fraction were handpicked under microscope, mounted in epoxy resin stubs, then sectioned and polished. Distal tephra samples from Gademotta (unit D), Konso (TA-55/ETH18-14B and TA-56/ETH18-14A) and Omo-Kibish formations (KHS, ETH18-08) were washed through a sieve in purified water at 80 or 25 μm , then dried, described under microscope and mounted in epoxy resin stubs, then sectioned and polished. Strongly altered samples of TA-56 (ETH18-14A) and TA-55 (ETH18-14B) units from the Konso formation were density extracted to facilitate the search for volcanic glass^{38,39}. Sample ETH18-14B from TA-55 was sieved at 125, 80 and 25 μm and residues inspected under the microscope, yet no glass was found.

Major element analysis

Mounted samples were analysed for major element compositions with a SX100 CAMECA electron microprobe at the Department of Earth Sciences, University of Cambridge. Major elements were measured with an accelerating voltage of 10 kV and a 10-nA defocused beam. Elements were counted on-peak for 10 s (Na, Si), 20 s (Al, Fe and K), 60 s (Ti, Mg, Ca, and Cl), 90 s (P) and 120 s (Mn). Sodium was measured first to minimize alkali loss. The analytical accuracy was checked against international standards ATHO-G, STH-S6 and internal peralkaline obsidian from Lipari (74 wt% SiO_2 , 3.8 wt% Na_2O and 5.3 wt% K_2O). Replicate standard analyses and standard deviations are reported in Supplementary Table 6. The latter are used for error bars on biplots instead of the standard deviation of each sample, which is affected by their

natural variability. Where possible, we analysed 40–50 points per sample. All analyses are reported in Supplementary Table 1.

Trace element analysis

Trace element compositions of individual tephra shards were analysed by laser ablation inductively coupled plasma mass spectrometry (LA-ICP-MS) at the iCRAG laboratory at Trinity College Dublin. The instrument used was a Thermo iCAPQ coupled to a Photon Machines 193-nm G2 laser and a Helex two-volume cell. We used a spot size of 40 µm, depending on the area available for analysis, a repetition rate of 6 Hz and a count time of 33 s (200 pulses) on the sample and 30 s on the gas blank (background). We analysed large-enough glass shards analysed by electron microprobe analysis (EMPA) for major elements; however, spots are not tied through codes as we used the average Ca concentration of each sample as Ca correction factor.

Concentrations were calibrated using NIST612 with ^{29}Si as the internal standard. Data reduction was undertaken in Iolite v.3.4 and a secondary Ca correction factor was applied⁴⁰. Accuracies of ATHO-G and StHs6/80-G MPI-DING glass analyses are typically better than 6% for most elements. The precision is reflected by the standard deviations of replicate standard analyses (Supplementary Table 7), used for error bars on Fig. 3, Supplementary Fig. 4. Standard deviations of trace element ratios (Fig. 3) take into account error propagation. Detailed compositions of samples are reported in Supplementary Table 2.

Reporting summary

Further information on research design is available in the [Nature Research Reporting Summary](#) linked to this paper.

Data availability

All data supporting the findings of this study are available within the paper and its Supplementary Information files. Background maps for Fig. 1 are Shuttle Radar Topography Mission Digital Elevation Model data at one arcsecond resolution from the NASA Land Processes Distributed Active Archive Center (<https://earthexplorer.usgs.gov/>); settlements, lakes and other features are from (<https://www.naturalearthdata.com/>). Background image for the top left corner inset of Fig. 1 from Google Earth and plate boundaries data courtesy of the US Geological Survey.

References

1. 1.

Day, M. H. Early *Homo sapiens* remains from the Omo River region of Southwest Ethiopia: Omo human skeletal remains. *Nature* **222**, 1135–1138 (1969).

2. 2.

Fleagle, J. G., Assefa, Z., Brown, F. H. & Shea, J. J. Paleoanthropology of the Kibish Formation, southern Ethiopia: introduction. *J. Hum. Evol.* **55**, 360–365 (2008).

3. 3.

McDougall, I., Brown, F. H. & Fleagle, J. G. Stratigraphic placement and age of modern humans from Kibish, Ethiopia. *Nature* **433**, 733–736 (2005).

4. 4.

White, T. D. et al. Pleistocene *Homo sapiens* from Middle Awash, Ethiopia. *Nature* **423**, 742–747 (2003).

5. 5.

Clark, J. D. et al. Stratigraphic, chronological and behavioural contexts of Pleistocene *Homo sapiens* from Middle Awash, Ethiopia. *Nature* **423**, 747–752 (2003).

6. 6.

Brown, F. H., McDougall, I. & Fleagle, J. G. Correlation of the KHS Tuff of the Kibish Formation to volcanic ash layers at other sites, and the age of early *Homo sapiens* (Omo I and Omo II). *J. Hum. Evol.* **63**, 577–585 (2012).

7. 7.

McDougall, I., Brown, F. H. & Fleagle, J. G. Sapropels and the age of hominins Omo I and II, Kibish, Ethiopia. *J. Hum. Evol.* **55**, 409–420 (2008).

8. 8.

Sahle, Y. et al. in *Modern Human Origins and Dispersal* (eds Sahle, Y. et al.) 73–104 (2019).

9. 9.

Brown, F. H. & Fuller, C. R. Stratigraphy and tephra of the Kibish Formation, southwestern Ethiopia. *J. Hum. Evol.* **55**, 366–403 (2008).

10. 10.

Richter, D. et al. The age of the hominin fossils from Jebel Irhoud, Morocco, and the origins of the Middle Stone Age. *Nature* **546**, 293–296 (2017).

11. 11.

Mounier, A. & Mirazón Lahr, M. Deciphering African late middle Pleistocene hominin diversity and the origin of our species. *Nat. Commun.* **10**, 3406 (2019).

12. 12.

Lane, C. S., Lowe, D. J., Blockley, S. P. E., Suzuki, T. & Smith, V. C. Advancing tephrochronology as a global dating tool: applications in volcanology, archaeology, and palaeoclimatic research. *Quat. Geochronol.* **40**, 1–7 (2017).

13. 13.

Abbott, P., Jensen, B. J. L. & Lowe, D. J. Crossing new frontiers: extending tephrochronology as a global geoscientific research tool. *J. Quat. Sci.* **35**, 1–8 (2020).

14. 14.

Lowe, D. J. Tephrochronology and its application: a review. *Quat. Geochronol.* **6**, 107–153 (2011).

15. 15.

Mirazón Lahr, M. The shaping of human diversity: filters, boundaries and transitions. *Phil. Trans. R. Soc. B* **371**, 20150241 (2016).

16. 16.

Stringer, C. The origin and evolution of *Homo sapiens*. *Phil. Trans. R. Soc. B* **371**, 20150237 (2016).

17. 17.

Butzer, K. W. & Thurber, D. L. Some Late Cenozoic sedimentary formations of the lower Omo Basin. *Nature* **222**, 1138–1143 (1969).

18. 18.
Kuiper, K. F. et al. Synchronizing rock clocks of earth history. *Science* **320**, 500–504 (2008).
19. 19.
Fleagle, J., Assefa, Z., Brown, F. & Shea, J. J. Paleoanthropology of the Kibish Formation, southern Ethiopia: introduction. *J. Hum. Evol.* **55**, 360–365 (2008).
20. 20.
Nagaoka, S. et al. Lithostratigraphy and sedimentary environments of the hominid-bearing Pliocene–Pleistocene Konso Formation in the southern Main Ethiopian Rift, Ethiopia. *Palaeogeogr. Palaeoclimatol. Palaeoecol.* **216**, 333–357 (2005).
21. 21.
Katoh, S. et al. Chronostratigraphy and correlation of the Plio–Pleistocene tephra layers of the Konso Formation, southern Main Ethiopian Rift, Ethiopia. *Quat. Sci. Rev.* **19**, 1305–1317 (2000).
22. 22.
Morgan, L. & Renne, P. Diachronous dawn of Africa’s Middle Stone Age: new $^{40}\text{Ar}/^{39}\text{Ar}$ ages from the Ethiopian Rift. *Geology* **36**, 967–970 (2008).
23. 23.
Rossignol-Strick, M. Mediterranean Quaternary sapropels, an immediate response of the African monsoon to variation of insolation. *Palaeogeogr. Palaeoclimatol. Palaeoecol.* **49**, 237–263 (1985).
24. 24.
Quade, J. et al. The geology of Gona. *Geol. Soc. Am. Bull.* **446**, 1–31 (2008).
25. 25.
Hart, W. K. et al. Dating of the Herto hominin fossils. *Nature* **426**, 622–622 (2003).
26. 26.

Hutchison, W. et al. A pulse of mid-Pleistocene rift volcanism in Ethiopia at the dawn of modern humans. *Nat. Commun.* **7**, 13192 (2016).

27. 27.

Mohr, P., Mitchell, J. G. & Raynolds, R. G. H. Quaternary volcanism and faulting at O’A caldera, central Ethiopian rift. *Bull. Volcanol.* **43**, 173–189 (1980).

28. 28.

Fontijn, K. et al. Contrasting styles of post-caldera volcanism along the Main Ethiopian Rift: implications for contemporary volcanic hazards. *J. Volcanol. Geotherm. Res.* **356**, 90–113 (2018).

29. 29.

Kroon, D. et al. Oxygen isotope and sapropel stratigraphy in the Eastern Mediterranean during the last 3.2 million years. *Proc. Ocean Drill. Prog. Sci. Results* **160**, 181–189 (1998).

30. 30.

Faupl, P., Richter, W. & Urbanek, C. Geochronology: dating of the Herto hominin fossils. *Nature* **426**, 621–622 (2003).

31. 31.

Bergström, A., Stringer, C., Hajdinjak, M., Scerri, E. M. L. & Skoglund, P. Origins of modern human ancestry. *Nature* **590**, 229–237 (2021).

32. 32.

Schlebusch, C. M. et al. Southern African ancient genomes estimate modern human divergence to 350,000 to 260,000 years ago. *Science* **358**, 652–655 (2017).

33. 33.

Roberts, H. M. et al. Using multiple chronometers to establish a long, directly-dated lacustrine record: constraining more than 600,000 years of environmental change at Chew Bahir, Ethiopia. *Quat. Sci. Rev.* **266**, 107025 (2021).

34. 34.

Laury, R. L. & Albritton, C. C. Geology of Middle Stone Age archaeological sites in the main Ethiopian Rift Valley. *Geol. Soc. Am. Bull.* **86**, 999–1011 (1975).

35. 35.

Renne, P. R., Balco, G., Ludwig, K. R., Mundil, R. & Min, K. Response to the comment by W.H. Schwarz et al. on “Joint determination of ^{40}K decay constants and $^{40}\text{Ar}^*/^{40}\text{K}$ for the Fish Canyon sanidine standard, and improved accuracy for $^{40}\text{Ar}/^{39}\text{Ar}$ geochronology” by P.R. Renne et al. (2010). *Geochim. Cosmochim. Acta* **75**, 5097–5100 (2011).

36. 36.

Renne, P. R., Mundil, R., Balco, G., Min, K. & Ludwig, K. R. Joint determination of ^{40}K decay constants and $^{40}\text{Ar}^*/^{40}\text{K}$ for the Fish Canyon sanidine standard, and improved accuracy for $^{40}\text{Ar}/^{39}\text{Ar}$ geochronology. *Geochim. Cosmochim. Acta* **74**, 5349–5367 (2010).

37. 37.

Lowe, D. J. et al. Correlating tephras and cryptotephras using glass compositional analyses and numerical and statistical methods: review and evaluation. *Quat. Sci. Rev.* **175**, 1–44 (2017).

38. 38.

Blockley, S. P. E. et al. A new and less destructive laboratory procedure for the physical separation of distal glass tephra shards from sediments. *Quat. Sci. Rev.* **24**, 1952–1960 (2005).

39. 39.

Lane, C. S., Cullen, V. L., White, D., Bramham-Law, C. W. F. & Smith, V. C. Cryptotephra as a dating and correlation tool in archaeology. *J. Archaeolog. Sci.* **42**, 42–50 (2014).

40. 40.

Tomlinson, E. L., Thordarson, T., Müller, W., Thirlwall, M. & Menzies, M. A. Microanalysis of tephra by LA-ICP-MS—strategies, advantages and limitations assessed using the Thorsmörk ignimbrite (Southern Iceland). *Chem. Geol.* **279**, 73–89 (2010).

Acknowledgements

This study was supported by the Leverhulme Trust ('Nature and impacts of Middle Pleistocene volcanism in the Ethiopian Rift', 2016–21) and the Cambridge-Africa ALBORADA Research Fund ('Volcanic tie-lines between records of past climates and early modern humans in Ethiopia, 2019–21'). Ar-Ar dating was supported by grant NIGFSC IP-1683-1116 through the UK Natural Environment Research Council. The iCRAG LA-ICP-MS facility at Trinity College Dublin is supported by SFI award 13/RC/2092. We acknowledge the local and regional authorities in Ethiopia for facilitating fieldwork and sample export, including the School of Earth Sciences Addis Ababa University, the Oromiya Regional State, the Ngangatom Woreda Local Administration and the FDRE Ministry of Mines, Petroleum and Natural Gas. We are grateful to Y. Beyene for assistance in accessing the Konso tephra localities; Ethioder and their drivers for logistical support; and field assistants Alex in Omo-Kibish and Demelash in Konso. We thank D. Colby for facilitating access to the Corbetti sample and A. Piermattei, I. Buisman and J. Day for assistance with sample preparation and microprobe analyses in Cambridge. The manuscript has benefited from comments by W. Hart and C. Feibel, and we are grateful to them for their input.

Author information

Affiliations

1. Department of Geography, University of Cambridge, Cambridge, UK

Céline M. Vidal, Christine S. Lane & Clive Oppenheimer

2. Fitzwilliam College, University of Cambridge, Cambridge, UK

Céline M. Vidal

3. School of Earth Sciences, Addis Ababa University, Addis Ababa, Ethiopia

Asfawossen Asrat & Gezahegn Yirgu

4. Department of Mining and Geological Engineering, Botswana International University of Science and Technology, Palapye, Botswana

Asfawossen Asrat

5. NEIF Argon Isotopes, University of Glasgow, SUERC, Glasgow, UK

Dan N. Barfod & Darren F. Mark

6. Trinity College Dublin, University of Dublin, Dublin, Ireland

Emma L. Tomlinson

7. Department of Geosciences, Environment and Society, Université Libre de Bruxelles, Brussels, Belgium

Amdemichael Zafu Tadesse

8. Berkeley Geochronology Center, Berkeley, CA, USA

Alan Deino

9. School of Earth and Environmental Sciences, University of St Andrews, St Andrews, UK

William Hutchison

10. Histoire Naturelle de l'Homme Préhistorique (HNHP, UMR 7194), MNHN/CNRS/UPVD, Musée de l'Homme, Paris, France

Aurélien Mounier

11. Leverhulme Centre for Human Evolutionary Studies, Department of Archaeology, University of Cambridge, Cambridge, UK

Aurélien Mounier

12. McDonald Institute for Archaeological Research, Cambridge, UK

Clive Oppenheimer

Contributions

C.M.V., C.O., C.S.L., A.A. and W.H. designed the study. C.M.V. and C.S.L. designed and conducted field and laboratory work and acquired, analysed and interpreted stratigraphic and geochemical data. A.A., G.Y., A.Z.T. and A.D. designed fieldwork and acquired and interpreted stratigraphic data in the field. D.N.B. and D.F.M. analysed and interpreted radiometric data. E.L.T. analysed samples for trace elements. A.M. contributed to palaeoanthropological discussion of the manuscript. All authors contributed to preparation and revision of the manuscript and approved the submitted version.

Corresponding author

Correspondence to [Céline M. Vidal](#).

Ethics declarations

Competing interests

The authors declare no competing or financial interests.

Peer review information

Nature thanks Craig Feibel, William Hart and the other, anonymous, reviewer(s) for their contribution to the peer review of this work.

Additional information

Publisher's note Springer Nature remains neutral with regard to jurisdictional claims in published maps and institutional affiliations.

Supplementary information

[Supplementary Information](#)

This file contains information on tephra geochemistry, Supplementary Figs. 1–5, and additional references.

[Reporting Summary](#)

[Supplementary Table 1](#)

Major element normalized composition of tephra samples.

[Supplementary Table 2](#)

Trace element abundances (ppm) of tephra samples.

[Supplementary Table 3](#)

Single-crystal $^{40}\text{Ar}/^{39}\text{Ar}$ ages for unit A and unit C of the Qi2 ignimbrite of Shala.

Supplementary Table 4

Argon isotopic data for the Qi2 samples.

Supplementary Table 5

Decay constants and correction factors.

Supplementary Table 6

Average compositions of EPMA secondary standards for years 2018–2019.

Supplementary Table 7

Standard compositions for LA-ICP-MS analyses.

Rights and permissions

Open Access This article is licensed under a Creative Commons Attribution 4.0 International License, which permits use, sharing, adaptation, distribution and reproduction in any medium or format, as long as you give appropriate credit to the original author(s) and the source, provide a link to the Creative Commons license, and indicate if changes were made. The images or other third party material in this article are included in the article's Creative Commons license, unless indicated otherwise in a credit line to the material. If material is not included in the article's Creative Commons license and your intended use is not permitted by statutory regulation or exceeds the permitted use, you will need to obtain permission directly from the copyright holder. To view a copy of this license, visit <http://creativecommons.org/licenses/by/4.0/>.

Reprints and Permissions

About this article

Cite this article

Vidal, C.M., Lane, C.S., Asrat, A. *et al.* Age of the oldest known *Homo sapiens* from eastern Africa. *Nature* **601**, 579–583 (2022). <https://doi.org/10.1038/s41586-021-04275-8>

- Received: 29 March 2021
- Accepted: 23 November 2021
- Published: 12 January 2022
- Issue Date: 27 January 2022
- DOI: <https://doi.org/10.1038/s41586-021-04275-8>

Share this article

Anyone you share the following link with will be able to read this content:

[Get shareable link](#)

Sorry, a shareable link is not currently available for this article.

[Copy to clipboard](#)

Provided by the Springer Nature SharedIt content-sharing initiative

This article was downloaded by **calibre** from <https://www.nature.com/articles/s41586-021-04275-8>

| [Section menu](#) | [Main menu](#) |

- Article
- [Published: 22 December 2021](#)

A high-resolution picture of kinship practices in an Early Neolithic tomb

- [Chris Fowler](#) ORCID: orcid.org/0000-0003-3794-9298^{1 na1},
- [Iñigo Olalde](#) ORCID: orcid.org/0000-0002-2660-6807^{2,3,4 na1},
- [Vicki Cummings](#) ORCID: orcid.org/0000-0001-9460-1517⁵,
- [Ian Armit](#)⁶,
- [Lindsey Büster](#) ORCID: orcid.org/0000-0003-4121-9431⁶,
- [Sarah Cuthbert](#)⁷,
- [Nadin Rohland](#)^{3,8},
- [Olivia Cheronet](#)⁹,
- [Ron Pinhasi](#) ORCID: orcid.org/0000-0003-1629-8131⁹ &
- [David Reich](#) ORCID: orcid.org/0000-0002-7037-5292^{3,8,10,11}

Nature volume 601, pages 584–587 (2022)

- 5690 Accesses
- 2 Citations
- 848 Altmetric
- [Metrics details](#)

Subjects

- [Archaeology](#)

- [Genetic variation](#)
- [Population genetics](#)
- [Social anthropology](#)

Abstract

To explore kinship practices at chambered tombs in Early Neolithic Britain, here we combined archaeological and genetic analyses of 35 individuals who lived about 5,700 years ago and were entombed at Hazleton North long cairn¹. Twenty-seven individuals are part of the first extended pedigree reconstructed from ancient DNA, a five-generation family whose many interrelationships provide statistical power to document kinship practices that were invisible without direct genetic data. Patrilineal descent was key in determining who was buried in the tomb, as all 15 intergenerational transmissions were through men. The presence of women who had reproduced with lineage men and the absence of adult lineage daughters suggest virilocal burial and female exogamy. We demonstrate that one male progenitor reproduced with four women: the descendants of two of those women were buried in the same half of the tomb over all generations. This suggests that maternal sub-lineages were grouped into branches whose distinctiveness was recognized during the construction of the tomb. Four men descended from non-lineage fathers and mothers who also reproduced with lineage male individuals, suggesting that some men adopted the children of their reproductive partners by other men into their patriline. Eight individuals were not close biological relatives of the main lineage, raising the possibility that kinship also encompassed social bonds independent of biological relatedness.

This is a preview of subscription content

Access options

Subscribe to nature+

Get immediate online access to the entire Nature family of 50+ journals

\$29.99

monthly

[Subscribe](#)

Subscribe to Journal

Get full journal access for 1 year

\$199.00

only \$3.90 per issue

[Subscribe](#)

All prices are NET prices.

VAT will be added later in the checkout.

Tax calculation will be finalised during checkout.

Buy article

Get time limited or full article access on ReadCube.

\$32.00

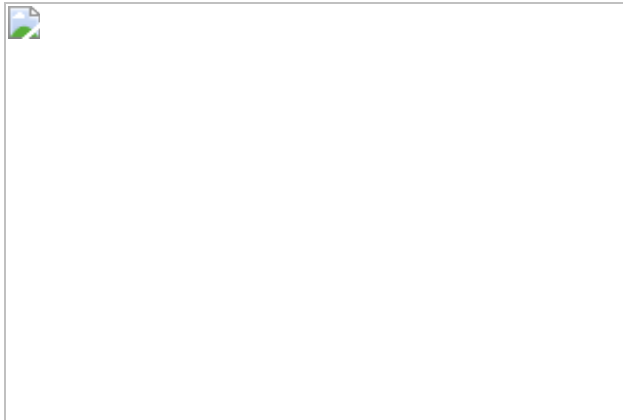
[Buy](#)

All prices are NET prices.

Additional access options:

- [Log in](#)
- [Learn about institutional subscriptions](#)

Fig. 1: The Hazleton North pedigree in the context of the physical structure of the tomb.



Data availability

The aligned sequences are available through the European Nucleotide Archive, accession [PRJEB46958](#); the genotype dataset is available as a [Supplementary Data file](#).

References

1. 1.

Saville, A. *Hazleton North, Gloucestershire, 1979–82: the Excavation of a Neolithic Long Cairn of the Cotswold-Severn Group* (Historic Buildings & Monuments Commission for England, 1990).

2. 2.

Brace, S. et al. Ancient genomes indicate population replacement in Early Neolithic Britain. *Nat. Ecol. Evol.* **3**, 765–771 (2019).

3. 3.

Olalde, I. et al. The Beaker phenomenon and the genomic transformation of northwest Europe. *Nature* **555**, 190–196 (2018).

4. 4.

Cassidy, L. M. et al. A dynastic elite in monumental Neolithic society. *Nature* **582**, 384–388 (2020).

5. 5.

Mitnik, A. et al. Kinship-based social inequality in Bronze Age Europe. *Science* **366**, 731–734 (2019).

6. 6.

Yaka, R. et al. Variable kinship patterns in Neolithic Anatolia revealed by ancient genomes. *Curr. Biol.* **31**, 2455–2468.e18 (2021).

7. 7.

Amorim, C. E. G. et al. Understanding 6th-century barbarian social organization and migration through paleogenomics. *Nat. Commun.* **9**, 3547 (2018).

8. 8.

Sánchez-Qinto, F. et al. Megalithic tombs in western and northern Neolithic Europe were linked to a kindred society. *Proc. Natl Acad. Sci. USA* **116**, 9469–9474 (2019).

9. 9.

Scheib, C. L. et al. East Anglian early Neolithic monument burial linked to contemporary Megaliths. *Ann. Hum. Biol.* **46**, 145–149 (2019).

10. 10.

Schneider, D. M. *A Critique of the Study of Kinship* (Univ. Michigan Press, 1984).

11. 11.

Carsten, J. *After Kinship* (Cambridge Univ. Press, 2003).

12. 12.

Brück, J. Ancient DNA, kinship and relational identities in Bronze Age Britain. *Antiquity* **95**, 228–237 (2021).

13. 13.

Meadows, J., Barclay, A. & Bayliss, A. A short passage of time: the dating of the hazleton long cairn revisited. *Cambridge Archaeol. J.* **17**, 45–64 (2007).

14. 14.

Rowley-Conwy, P. & Legge, T. in *The Oxford Handbook of Neolithic Europe* (eds. Fowler, C., Hofmann, D. & Harding, J.) 429–446 (Oxford Univ. Press, 2015).

15. 15.

Cuthbert, G. S. *Enriching the Neolithic: the Forgotten People of the Barrows*. PhD thesis, Univ. Exeter (2019).

16. 16.

Rogers, J. et al. in *Hazleton North, Gloucestershire, 1979-82: The Excavation of a Neolithic Long Cairn of the Cotswold-Severn Group* (ed. A. Saville) 182–198 (Historic Buildings & Monuments Commission for England, 1990).

17. 17.

Hedges, R., Saville, A. & O'Connell, T. Characterizing the diet of individuals at the Neolithic chambered tomb of Hazleton North, Gloucestershire, England, using stable isotopic analysis. *Archaeometry* **50**, 114–128 (2008).

18. 18.

Charlton, S. et al. New insights into Neolithic milk consumption through proteomic analysis of dental calculus. *Archaeol. Anthropol. Sci.* **11**, 6183–6196 (2019).

19. 19.

Neil, S., Evans, J., Montgomery, J. & Scarre, C. Isotopic evidence for residential mobility of farming communities during the transition to agriculture in Britain. *R. Soc. Open Sci.* **3**, 150522 (2016).

20. 20.

Smith, M. & Brickley, M. *People of the Long Barrows: Life, Death and Burial in Earlier Neolithic Britain* (The History Press, 2009).

21. 21.

Surowiec, A., Snyder, K. T. & Creanza, N. A worldwide view of matriliney: using cross-cultural analyses to shed light on human kinship systems. *Philos. Trans. R. Soc. B Biol. Sci.* **374**, 20180077 (2019).

22. 22.

Fowler, C. Social arrangements: kinship, descent and affinity in the mortuary architecture of Early Neolithic Britain and Ireland. *Archaeol. Dialogues* (in the press).

23. 23.

Robb, J. & Harris, O. J. T. Becoming gendered in European prehistory: was Neolithic gender fundamentally different? *Am. Antiq.* **83**, 128–147 (2018).

24. 24.

Stone, L. & King, D. E. *Kinship and Gender: An Introduction* (Routledge, 2018).

25. 25.

Robb, J. What can we really say about skeletal part representation, MNI and funerary ritual? A simulation approach. *J. Archaeol. Sci. Reports* **10**, 684–692 (2016).

26. 26.

Rohland, N., Glocke, I., Aximu-Petri, A. & Meyer, M. Extraction of highly degraded DNA from ancient bones, teeth and sediments for high-throughput sequencing. *Nat. Protoc.* **13**, 2447–2461 (2018).

27. 27.

Gansauge, M. T., Aximu-Petri, A., Nagel, S. & Meyer, M. Manual and automated preparation of single-stranded DNA libraries for the sequencing of DNA from ancient biological remains and other sources of highly degraded DNA. *Nat. Protoc.* **15**, 2279–2300 (2020).

28. 28.

Rohland, N., Harney, E., Mallick, S., Nordenfelt, S. & Reich, D. Partial uracil–DNA–glycosylase treatment for screening of ancient DNA. *Philos. Trans. R. Soc. Lond. B* **370**, 20130624 (2015).

29. 29.

Fu, Q. et al. An early modern human from Romania with a recent Neanderthal ancestor. *Nature* **524**, 216–219 (2015).

30. 30.

Fu, Q. et al. DNA analysis of an early modern human from Tianyuan Cave, China. *Proc. Natl Acad. Sci. USA* **110**, 2223–2227 (2013).

31. 31.

Olalde, I. et al. The genomic history of the Iberian Peninsula over the past 8000 years. *Science* **363**, 1230–1234 (2019).

32. 32.

Li, H. & Durbin, R. Fast and accurate short read alignment with Burrows–Wheeler transform. *Bioinformatics* **25**, 1754–1760 (2009).

33. 33.

Korneliussen, T. S., Albrechtsen, A. & Nielsen, R. ANGSD: analysis of next generation sequencing data. *BMC Bioinformatics* **15**, 356 (2014).

34. 34.

Fu, Q. et al. A revised timescale for human evolution based on ancient mitochondrial genomes. *Curr. Biol.* **23**, 553–559 (2013).

35. 35.

Weissensteiner, H. et al. HaploGrep 2: mitochondrial haplogroup classification in the era of high-throughput sequencing. *Nucleic Acids Res.* **44**, W58-W63 (2016).

36. 36.

Kennett, D. J. et al. Archaeogenomic evidence reveals prehistoric matrilineal dynasty. *Nat. Commun.* **8**, 14115 (2017).

37. 37.

van de Loosdrecht, M. et al. Pleistocene North African genomes link Near Eastern and sub-Saharan African human populations. *Science* **360**, 548–552 (2018).

38. 38.

Busing, F. M. T. A., Meijer, E. & Van Der Leeden, R. Delete- m Jackknife for Unequal m. *Stat. Comput.* **9**, 3–8 (1999).

39. 39.

Monroy Kuhn, J. M., Jakobsson, M. & Günther, T. Estimating genetic kin relationships in prehistoric populations. *PLoS ONE* **13**, e0195491 (2018).

40. 40.

Williams, C. et al. A rapid, accurate approach to inferring pedigrees in endogamous populations. Preprint at <https://doi.org/10.1101/2020.02.25.965376> (2020).

41. 41.

Kong, A. et al. Fine-scale recombination rate differences between sexes, populations and individuals. *Nature* **467**, 1099–1103 (2010).

42. 42.

Hanghøj, K., Moltke, I., Andersen, P. A., Manica, A. & Korneliussen, T. S. Fast and accurate relatedness estimation from high-throughput sequencing data in the presence of inbreeding. *Gigascience* **8**, giz034 (2019).

43. 43.

Patterson, N. et al. Ancient admixture in human history. *Genetics* **192**, 1065–1093 (2012).

44. 44.

Cassidy, L. M. et al. Neolithic and Bronze Age migration to Ireland and establishment of the insular Atlantic genome. *Proc. Natl Acad. Sci. USA* **113**, 368–373 (2016).

45. 45.

Lazaridis, I. et al. Ancient human genomes suggest three ancestral populations for present-day Europeans. *Nature* **513**, 409–413 (2014).

46. 46.

Biagini, S. A. et al. People from Ibiza: an unexpected isolate in the Western Mediterranean. *Eur. J. Hum. Genet.* **27**, 941–951 (2019).

47. 47.

Ringbauer, H., Novembre, J. & Steinrücken, M. Parental relatedness through time revealed by runs of homozygosity in ancient DNA. *Nat. Commun.* **12**, 5425 (2021).

Acknowledgements

This work was supported by US National Institutes of Health grant GM100233, by the Allen Discovery Center programme, a Paul G. Allen Frontiers Group advised programme of the Paul G. Allen Family Foundation, by John Templeton Foundation grant 61220, by a gift from J.-F. Clin, and by the Howard Hughes Medical Institute. I.O. is supported by a Ramón y Cajal grant from Ministerio de Ciencia e Innovación, Spanish Government (RYC2019-027909-I/AEI/10.13039/501100011033). We thank J. Harris and A. Brookes at the Corinium Museum for providing permission to sample skeletal material from Hazleton North; T. Booth, A. Mittnik, H. Ringbauer and A. Whittle for valuable discussions; and N. Adamski, R. Bernardos, G. Bravo, K. Callan, E. Curtis, A. M. Lawson, M. Mah, S. Mallick, A. Micco, L. Qiu, K. Stewardson, A. Wagner, J. N. Workman and F. Zalzala for contributions to laboratory and bioinformatic work.

Author information

Author notes

1. These authors contributed equally: Chris Fowler, Iñigo Olalde

Affiliations

1. School of History, Classics and Archaeology, Newcastle University, Newcastle upon Tyne, UK

Chris Fowler

2. BIOMICs Research Group, University of the Basque Country UPV/EHU, Vitoria-Gasteiz, Spain

Iñigo Olalde

3. Department of Genetics, Harvard Medical School, Boston, MA, USA

Iñigo Olalde, Nadin Rohland & David Reich

4. Ikerbasque—Basque Foundation of Science, Bilbao, Spain

Iñigo Olalde

5. School of Natural Sciences, University of Central Lancashire, Preston, Lancashire, UK

Vicki Cummings

6. Department of Archaeology, University of York, York, UK

Ian Armit & Lindsey Büster

7. Department of Archaeology, University of Exeter, Exeter, UK

Sarah Cuthbert

8. Broad Institute of MIT and Harvard, Cambridge, MA, USA

Nadin Rohland & David Reich

9. Department of Evolutionary Anthropology, University of Vienna, Vienna, Austria

Olivia Cheronet & Ron Pinhasi

10. Department of Human Evolutionary Biology, Harvard University, Cambridge, MA, USA

David Reich

11. Howard Hughes Medical Institute, Boston, MA, USA

David Reich

Contributions

N.R., O.C., S.C., R.P. and D.R. performed or supervised laboratory work. C.F., V.C., I.A., L.B. and S.C. assembled or contextualized archaeological material. C.F. and I.O. analysed data. C.F., I.O. and D.R. wrote the manuscript. C.F., I.O. and S.C. wrote the supplement.

Corresponding authors

Correspondence to [Chris Fowler](#), [Iñigo Olalde](#), [Ron Pinhasi](#) or [David Reich](#).

Ethics declarations

Competing interests

The authors declare no competing interests.

Additional information

Peer review information *Nature* thanks Neil Carlin, Mehmet Somel and the other, anonymous, reviewer(s) for their contribution to the peer review of this work. Peer reviewer reports are available.

Publisher's note Springer Nature remains neutral with regard to jurisdictional claims in published maps and institutional affiliations.

Extended data figures and tables

[**Extended Data Fig. 1 The Hazleton North chambered tomb.**](#)

a, Distribution of human remains in both chambers. The schematics in **a** are adapted from ref. ¹, original figures © Historic England. **b**, Right humerus from Individual C showing helical fracture (red arrow), tooth marks (yellow arrow) and gnawed proximal and distal ends (white arrows).

Extended Data Fig. 2 Degrees of biological relatedness among individuals at Hazleton North.

([Supplementary Information Section 2.2](#)). Pairs with fewer than 15,000 overlapping SNPs are indicated with an asterisk.

Extended Data Fig. 3 Using allelic mismatch rate patterns along the chromosomes to differentiate types of relationships for individuals sharing the same amount of DNA.

a, Differentiating between parent-offspring and sibling relationships. Allelic mismatch rate values across sliding windows of 20 Mb, moving by 1 Mb each step. As an example, we show values at chromosome 17 and include for reference a comparison between two unrelated Neolithic individuals from Britain (in brown), and a comparison between one individual and himself (in purple) to show how mismatch rates behave when two chromosomes are shared. The mismatch rate pattern for SP1m-SC1f is compatible with one chromosome shared along the entire chromosome 14 (in fact, along all autosomal chromosomes ([Supplementary Table 6](#))), indicating a parent-offspring relationship. In contrast, the NC7f-SP3m comparison shows regions on chromosome 17 where no chromosome is shared (~65–70 Mb), other regions where two chromosomes are shared (~0–25 Mb) and other regions where one chromosome is shared (~25–60 Mb), compatible with a sibling relationship. **b**, Comparing DNA sharing patterns between SC9f and her paternal grandparents. We show mismatch rate values at chromosome 2 and include for reference a parent-offspring comparison (SE1m-SP2m; in blue) to show how mismatch rates behave when one chromosome is shared. Two recombination events (one at ~145 Mb and other at ~220 Mb) in SC9f's father's gamete result in SC9f sharing one chromosome with SC3m from the start of the chromosome to ~145 Mb, one chromosome with SC4f from 145 to 220 Mb and one chromosome with

SC3m from 220 Mb to the end of the chromosome. This pattern of sharing one chromosome with either SC3m or SC4f (but never both) at every location of the genome is characteristic of comparisons between a grandchild and his/her two grandparents and is also observed in the other autosomal chromosomes.

Extended Data Fig. 4 Alternative family tree fitting all the genetic evidence except the IBD breakpoints co-localization analysis.

([Supplementary Section 2.4](#), Extended Data Figure 5). Individuals are coloured according to the female sub-lineage they belong to (NC1m and NC5m do not belong to any of the four major sub-lineages and are thus given a different color).

Extended Data Fig. 5 Using co-localization of IBD breakpoints to disambiguate between family tree in Fig. 1c and family tree in Extended Data Fig. 4.

a, We show mismatch rate values across sliding windows of 20 Mb on chromosome 3, moving by 1 Mb each step, for comparisons between SC3m and his four second-degree relatives. **b**, **c**, Recombination events on chromosome 3 needed to explain the observed mismatch rate patterns under **b**, the scenario of tree in Fig. 1c where 4 recombination events are required, or **c**, the scenario of the tree in Extended Data Fig. 4 where 10 recombination events are required including the extremely implausible occurrence of two recombination events at the same genomic locations in four different gametes.

Extended Data Fig. 6 Testing the validity of the family pedigree in Fig. 1c using X-chromosome relatedness and number of shared IBD segments.

a, Relatedness coefficients in the X-chromosome for first- and second-degree relationships with more than 300 overlapping SNPs. For each comparison, expected values according to the type of relationship in the

family tree in Fig. 1c are shown in grey boxes. Bars represent 95% confidence intervals. **b**, Number of shared IBD segments on chromosomes 1-22 for first- and second-degree relationships. Pairs are grouped according to their type of relationship in the family tree in Fig. 1c.

Extended Data Fig. 7 Testing the consistency of the kinship results using NgsRelate42.

a, Correlation between the relatedness coefficient r and the Theta coefficient computed with *NgsRelate*, restricting to comparisons with more than 15,000 overlapping SNPs. **b**, Cotterman coefficients k_0 and k_2 for first- and second-degree relationships, as computed with *NgsRelate*.

Extended Data Fig. 8 Comparing autosomal relatedness between reproductive partners, different male reproductive partners of a female and different female reproductive partners of a male.

To estimate relatedness coefficients between unsampled and sampled male reproductive partners of a female, we doubled the relatedness coefficient obtained between the son of the unsampled male and the sampled male, to account for the fact that a son is one degree of relationship further away from their father's relatives as compared to his father. Bars represent 95% confidence intervals.

Extended Data Fig. 9 Principal Component Analysis and inbreeding analysis.

a, Principal component analysis of Hazleton North individuals and other ancient individuals from Britain and Ireland. Ancient individuals were projected onto the principal components computed on a set of present-day West Eurasians genotyped on the Human Origins Array (not shown in the figure). Individuals with fewer than 15,000 SNPs on the Human Origins dataset were excluded for this analysis. **b**, Runs of homozygosity (ROH) in different length categories for the Hazleton North individuals with more than 400,000 SNPs covered. ROH were computed using *hapROH*⁴⁷. Below,

we plot the expected ROH length distribution for the offspring of closely related parents in outbred populations and for individuals from populations with small effective population size⁴⁷.

Extended Data Table 1 Key details for sampled individuals

Extended Data Table 2 Statistically significant patterns in genetic data

Supplementary information

Supplementary Information

This Supplementary Information file contains four sections and additional references. Section 1: Osteological summary of human remains from Hazleton North. Section 2: Genetic analysis of biological relatedness and family tree reconstruction. Section 3: Statistical testing of kinship patterns. Section 4: Comparison of generational reconstruction with Bayesian model of radiocarbon dates from Hazleton North.

Reporting Summary

Peer Review File

Supplementary Tables

This file contains Supplementary Tables 1–7.

Supplementary Data

Genotype dataset.

Rights and permissions

Reprints and Permissions

About this article

Cite this article

Fowler, C., Olalde, I., Cummings, V. *et al.* A high-resolution picture of kinship practices in an Early Neolithic tomb. *Nature* **601**, 584–587 (2022). <https://doi.org/10.1038/s41586-021-04241-4>

- Received: 22 June 2021
- Accepted: 15 November 2021
- Published: 22 December 2021
- Issue Date: 27 January 2022
- DOI: <https://doi.org/10.1038/s41586-021-04241-4>

Share this article

Anyone you share the following link with will be able to read this content:

[Get shareable link](#)

Sorry, a shareable link is not currently available for this article.

[Copy to clipboard](#)

Provided by the Springer Nature SharedIt content-sharing initiative

Further reading

- [A grave matter of ancient kinship in Neolithic Britain](#)

- Neil Carlin

Nature (2022)

[A grave matter of ancient kinship in Neolithic Britain](#)

- Neil Carlin

News & Views 23 Dec 2021

This article was downloaded by **calibre** from <https://www.nature.com/articles/s41586-021-04241-4>

| [Section menu](#) | [Main menu](#) |

- Article
- [Published: 22 December 2021](#)

Large-scale migration into Britain during the Middle to Late Bronze Age

- [Nick Patterson](#)^{1,2} na1,
- [Michael Isakov](#) [ORCID: orcid.org/0000-0001-6468-5908](#)³ na1,
- [Thomas Booth](#)⁴ na1,
- [Lindsey Büster](#) [ORCID: orcid.org/0000-0003-4121-9431](#)⁵ na1,
- [Claire-Elise Fischer](#)⁵ na1,
- [Iñigo Olalde](#) [ORCID: orcid.org/0000-0002-2660-6807](#)^{6,7,8},
- [Harald Ringbauer](#)^{1,2},
- [Ali Akbari](#)^{1,6},
- [Olivia Cheronet](#) [ORCID: orcid.org/0000-0001-6760-1204](#)⁹,
- [Madeleine Bleasdale](#)⁵,
- [Nicole Adamski](#)^{6,10},
- [Eveline Altena](#) [ORCID: orcid.org/0000-0001-8911-7771](#)¹¹,
- [Rebecca Bernardos](#) [ORCID: orcid.org/0000-0003-4625-3727](#)⁶,
- [Selina Brace](#) [ORCID: orcid.org/0000-0003-2126-6732](#)⁴,
- [Nasreen Broomandkhoshbacht](#) [ORCID: orcid.org/0000-0001-5350-1608](#)^{6,10},
- [Kimberly Callan](#) [ORCID: orcid.org/0000-0003-3170-8514](#)^{6,10},
- [Francesca Candilio](#)¹²,
- [Brendan Culleton](#)¹³,
- [Elizabeth Curtis](#)^{6,10},
- [Lea Demetz](#)⁹,
- [Kellie Sara Duffett Carlson](#)⁹,
- [Ceiridwen J. Edwards](#)¹⁴,

- [Daniel M. Fernandes](#) ORCID: orcid.org/0000-0002-7434-6552^{9,15},
- [M. George B. Foody](#) ORCID: orcid.org/0000-0002-5482-7332¹⁵,
- [Suzanne Freilich](#) ORCID: orcid.org/0000-0003-0472-6311⁹,
- [Helen Goodchild](#) ORCID: orcid.org/0000-0003-4788-5945⁵,
- [Aisling Kearns](#)⁶,
- [Ann Marie Lawson](#) ORCID: orcid.org/0000-0003-0990-2329^{6,10},
- [Iosif Lazaridis](#) ORCID: orcid.org/0000-0002-4094-9347^{1,6},
- [Matthew Mah](#) ORCID: orcid.org/0000-0001-8987-6436^{2,6,10},
- [Swapan Mallick](#)^{2,6,10},
- [Kirsten Mandl](#)⁹,
- [Adam Micco](#)^{2,6},
- [Megan Michel](#)^{6,10},
- [Guillermo Bravo Morante](#)⁹,
- [Jonas Oppenheimer](#)^{6,10},
- [Kadir Toykan Özdogan](#)⁹,
- [Lijun Qiu](#)⁶,
- [Constanze Schattke](#)⁹,
- [Kristin Stewardson](#)^{6,10},
- [J. Noah Workman](#)⁶,
- [Fatma Zalzala](#)^{6,10},
- [Zhao Zhang](#)⁶,
- [Bibiana Agustí](#)¹⁶,
- [Tim Allen](#)¹⁷,
- [Katalin Almássy](#)¹⁸,
- [Luc Amkreutz](#) ORCID: orcid.org/0000-0003-4664-5552^{19,20},
- [Abigail Ash](#)²¹,
- [Christèle Baillif-Ducros](#) ORCID: orcid.org/0000-0003-3050-3082²²,
- [Alistair Barclay](#)²³,
- [László Bartosiewicz](#)²⁴,
- [Katherine Baxter](#)²⁵,
- [Zsolt Bernert](#)²⁶,
- [Jan Blažek](#)²⁷,
- [Mario Bodružić](#) ORCID: orcid.org/0000-0002-8112-5918²⁸,
- [Philippe Boissinot](#)²⁹,

- [Clive Bonsall³⁰](#),
- [Pippa Bradley²³](#),
- [Marcus Brittain³¹](#),
- [Alison Brookes³²](#),
- [Fraser Brown¹⁷](#),
- [Lisa Brown³³](#),
- [Richard Brunning](#) [ORCID: orcid.org/0000-0002-9415-550X³⁴](#),
- [Chelsea Budd³⁵](#),
- [Josip Burmaz³⁶](#),
- [Sylvain Canet²²](#),
- [Silvia Carnicero-Cáceres³⁷](#),
- [Morana Čaušević-Bully³⁸](#),
- [Andrew Chamberlain](#) [ORCID: orcid.org/0000-0003-1517-6538³⁹](#),
- [Sébastien Chauvin²²](#),
- [Sharon Clough](#) [ORCID: orcid.org/0000-0002-0851-7157²³](#),
- [Natalija Čondić⁴⁰](#),
- [Alfredo Coppa](#) [ORCID: orcid.org/0000-0002-7708-2484^{6,9,41}](#),
- [Oliver Craig](#) [ORCID: orcid.org/0000-0002-4296-8402⁵](#),
- [Matija Črešnar^{42,43}](#),
- [Vicki Cummings](#) [ORCID: orcid.org/0000-0001-9460-1517⁴⁴](#),
- [Szabolcs Czifra](#) [ORCID: orcid.org/0000-0001-9009-5792⁴⁵](#),
- [Alžběta Danielisová⁴⁶](#),
- [Robin Daniels⁴⁷](#),
- [Alex Davies¹⁷](#),
- [Philip de Jersey⁴⁸](#),
- [Jody Deacon⁴⁹](#),
- [Csilla Deminger⁵⁰](#),
- [Peter W. Ditchfield⁵¹](#),
- [Marko Dizdar⁵²](#),
- [Miroslav Dobeš⁴⁶](#),
- [Miluše Dobisíková⁵³](#),
- [László Domboróczki⁵⁴](#),
- [Gail Drinkall⁵⁵](#),
- [Ana Đukić⁵⁶](#),

- [Michal Ernée](#) ORCID: orcid.org/0000-0003-4847-8532⁴⁶,
- [Christopher Evans](#)³¹,
- [Jane Evans](#)⁵⁷,
- [Manuel Fernández-Götz](#)³⁰,
- [Slavica Filipović](#)⁵⁸,
- [Andrew Fitzpatrick](#)⁵⁹,
- [Harry Fokkens](#) ORCID: orcid.org/0000-0002-0006-7518²⁰,
- [Chris Fowler](#) ORCID: orcid.org/0000-0003-3794-9298⁶⁰,
- [Allison Fox](#)⁶¹,
- [Zsolt Gallina](#)⁶²,
- [Michelle Gamble](#)⁶³,
- [Manuel R. González Morales](#)⁶⁴,
- [Borja González-Rabanal](#) ORCID: orcid.org/0000-0002-1802-994X⁶⁵,
- [Adrian Green](#)⁶⁶,
- [Katalin Gyenessei](#) ORCID: orcid.org/0000-0002-3670-6975⁶⁷,
- [Diederick Habermehl](#)⁶⁸,
- [Tamás Hajdu](#)^{26,69},
- [Derek Hamilton](#)⁷⁰,
- [James Harris](#)³²,
- [Chris Hayden](#)¹⁷,
- [Joep Hendriks](#)⁷¹,
- [Bénédicte Hernu](#)⁷²,
- [Gill Hey](#)¹⁷,
- [Milan Hornák](#)⁴²,
- [Gábor Ilon](#)⁷³,
- [Eszter Istvánovits](#)⁷⁴,
- [Andy M. Jones](#) ORCID: orcid.org/0000-0001-9349-7818⁷⁵,
- [Martina Blečić Kavur](#)⁷⁶,
- [Kevin Kazek](#)⁷⁷,
- [Robert A. Kenyon](#)⁷⁸,
- [Amal Khreisheh](#)³⁴,
- [Viktória Kiss](#)⁹⁴,
- [Jos Kleijne](#) ORCID: orcid.org/0000-0002-5854-7055⁸⁰,
- [Mark Knight](#)³¹,

- [Lisette M. Kootker](#) ORCID: [orcid.org/0000-0002-3551-2730⁸¹](http://orcid.org/0000-0002-3551-2730),
- [Péter F. Kovács⁸²](#),
- [Anita Kozubová⁸³](#),
- [Gabriella Kulcsár⁷⁹](#),
- [Valéria Kulcsár⁸⁴](#),
- [Christophe Le Pennec⁸⁵](#),
- [Michael Legge⁸⁶](#),
- [Matt Leivers⁸⁷](#),
- [Louise Loe¹⁷](#),
- [Olalla López-Costas⁸⁸](#),
- [Tom Lord⁸⁹](#),
- [Dženi Los³⁶](#),
- [James Lyall⁹⁰](#),
- [Ana B. Marín-Arroyo⁶⁵](#),
- [Philip Mason⁴³](#),
- [Damir Matošević⁹¹](#),
- [Andy Maxted⁹²](#),
- [Lauren McIntyre¹⁷](#),
- [Jacqueline McKinley⁸⁸](#),
- [Kathleen McSweeney³⁰](#),
- [Bernard Meijlink⁹³](#),
- [Balázs G. Mende⁷⁹](#),
- [Marko Mendušić⁹⁵](#),
- [Milan Metlička⁹⁶](#),
- [Sophie Meyer⁹⁷](#),
- [Kristina Mihovilić⁹⁸](#),
- [Lidija Milasinovic⁹⁹](#),
- [Steve Minnitt³⁴](#),
- [Joanna Moore](#) ORCID: [orcid.org/0000-0003-3918-4583¹⁰⁰](http://orcid.org/0000-0003-3918-4583),
- [Geoff Morley¹⁰¹](#),
- [Graham Mullan¹⁰²](#),
- [Margaréta Musilová¹⁰³](#),
- [Benjamin Neil³¹](#),
- [Rebecca Nicholls¹⁰⁴](#),

- [Mario Novak](#) ORCID: orcid.org/0000-0002-4567-8742¹⁰⁵,
- [Maria Pala](#)¹⁵,
- [Martin Papworth](#)¹⁰⁶,
- [Cécile Paresys](#)²²,
- [Ricky Patten](#)³¹,
- [Domagoj Perkić](#)¹⁰⁷,
- [Krisztina Pesti](#)¹⁰⁸,
- [Alba Petit](#)¹⁰⁹,
- [Katarína Petriščáková](#) ORCID: orcid.org/0000-0003-0356-4023¹¹⁰,
- [Coline Pichon](#)¹¹¹,
- [Catriona Pickard](#)³⁰,
- [Zoltán Pilling](#)¹¹²,
- [T. Douglas Price](#) ORCID: orcid.org/0000-0001-5951-5621¹¹³,
- [Siniša Radović](#) ORCID: orcid.org/0000-0001-7838-7952¹¹⁴,
- [Rebecca Redfern](#)¹¹⁵,
- [Branislav Resutík](#)¹⁰³,
- [Daniel T. Rhodes](#)¹¹⁶,
- [Martin B. Richards](#) ORCID: orcid.org/0000-0003-3118-0967¹⁵,
- [Amy Roberts](#)¹¹⁷,
- [Jean Roefstra](#)¹¹⁸,
- [Pavel Sankot](#)¹¹⁹,
- [Alena Šefčáková](#)¹²⁰,
- [Alison Sheridan](#) ORCID: orcid.org/0000-0001-6204-3776¹²¹,
- [Sabine Skae](#)¹²²,
- [Miroslava Šmolíková](#)¹¹⁰,
- [Krisztina Somogyi](#)¹²³,
- [Ágnes Somogyvári](#)¹²⁴,
- [Mark Stephens](#)¹²⁵,
- [Géza Szabó](#)¹²⁶,
- [Anna Szécsényi-Nagy](#)⁷⁹,
- [Tamás Szeniczey](#)^{26,69},
- [Jonathan Tabor](#)³¹,
- [Károly Tankó](#)¹²⁷,
- [Clenis Tavarez Maria](#)¹²⁸,

- [Rachel Terry](#)¹²⁹,
- [Biba Teržan](#)⁴²,
- [Maria Teschler-Nicola](#)^{9,130},
- [Jesús F. Torres-Martínez](#)¹³¹,
- [Julien Trapp](#)⁷⁷,
- [Ross Turle](#)¹³²,
- [Ferenc Ujvári](#)¹⁰⁸,
- [Menno van der Heiden](#)¹³³,
- [Petr Veleminsky](#) ORCID: orcid.org/0000-0003-3691-7817⁵³,
- [Barbara Veselka](#)^{134,135},
- [Zdeněk Vytláčil](#)⁵³,
- [Clive Waddington](#)¹³⁶,
- [Paula Ware](#)¹²⁵,
- [Paul Wilkinson](#)¹³⁷,
- [Linda Wilson](#)¹⁰²,
- [Rob Wiseman](#)³¹,
- [Eilidh Young](#)¹³⁸,
- [Joško Zaninović](#)¹³⁹,
- [Andrej Žitňan](#)¹⁴⁰,
- [Carles Lalueza-Fox](#) ORCID: orcid.org/0000-0002-1730-5914¹⁴¹,
- [Peter de Knijff](#) ORCID: orcid.org/0000-0002-0899-771X¹¹,
- [Ian Barnes](#) ORCID: orcid.org/0000-0001-8322-6918⁴,
- [Peter Halkon](#)¹⁴²,
- [Mark G. Thomas](#) ORCID: orcid.org/0000-0002-2452-981X¹⁴³,
- [Douglas J. Kennett](#) ORCID: orcid.org/0000-0001-6144-7365¹⁴⁴,
- [Barry Cunliffe](#)¹⁴⁵,
- [Malcolm Lillie](#) ORCID: orcid.org/0000-0002-6054-3651^{35,146},
- [Nadin Rohland](#)^{2,6},
- [Ron Pinhasi](#) ORCID: orcid.org/0000-0003-1629-8131^{9,147},
- [Ian Armit](#) ⁵ &
- [David Reich](#) ORCID: orcid.org/0000-0002-7037-5292^{1,2,6,10}

Nature volume **601**, pages 588–594 (2022)

- 8239 Accesses

- 1 Citations
- 664 Altmetric
- [Metrics details](#)

Subjects

- [Archaeology](#)
- [Genetic variation](#)

Abstract

Present-day people from England and Wales have more ancestry derived from early European farmers (EEF) than did people of the Early Bronze Age¹. To understand this, here we generated genome-wide data from 793 individuals, increasing data from the Middle to the Late Bronze Age and Iron Age in Britain by 12-fold, and western and central Europe by 3.5-fold. Between 1000 and 875 bc, EEF ancestry increased in southern Britain (England and Wales) but not northern Britain (Scotland) due to incorporation of migrants who arrived at this time and over previous centuries, and who were genetically most similar to ancient individuals from France. These migrants contributed about half the ancestry of people of England and Wales from the Iron Age, thereby creating a plausible vector for the spread of early Celtic languages into Britain. These patterns are part of a broader trend of EEF ancestry becoming more similar across central and western Europe in the Middle to the Late Bronze Age, coincident with archaeological evidence of intensified cultural exchange^{2,3,4,5,6}. There was comparatively less gene flow from continental Europe during the Iron Age, and the independent genetic trajectory in Britain is also reflected in the rise of the allele conferring lactase persistence to approximately 50% by this time compared to approximately 7% in central Europe where it rose rapidly in frequency only a millennium later. This suggests that dairy products were used in qualitatively different ways in Britain and in central Europe over this period.

This is a preview of subscription content

Access options

Subscribe to nature+

Get immediate online access to the entire Nature family of 50+ journals

\$29.99

monthly

[Subscribe](#)

Subscribe to Journal

Get full journal access for 1 year

\$199.00

only \$3.90 per issue

[Subscribe](#)

All prices are NET prices.

VAT will be added later in the checkout.

Tax calculation will be finalised during checkout.

Buy article

Get time limited or full article access on ReadCube.

\$32.00

[Buy](#)

All prices are NET prices.

Additional access options:

- [Log in](#)
- [Learn about institutional subscriptions](#)

Fig. 1: Ancient DNA dataset.



Fig. 2: Increase in EEF ancestry during the MBA to LBA.



Fig. 3: By-individual analysis of the southern Britain time transect.

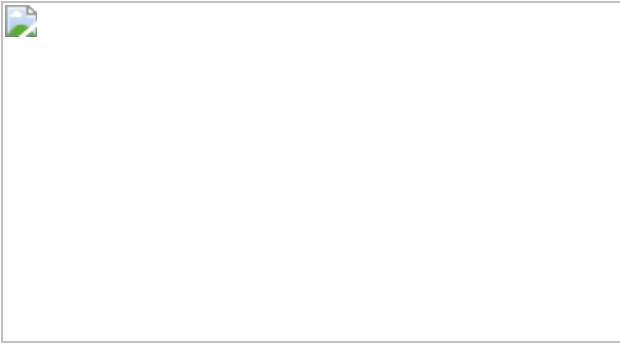
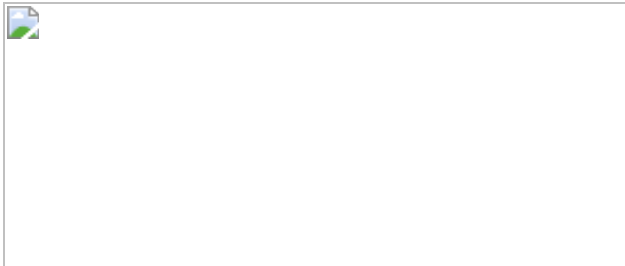


Fig. 4: Genetic change in Britain in the context of Europe-wide trends.



Data availability

The raw data are available as aligned sequences (.bam files) through the European Nucleotide Archive under accession number [PRJEB47891](#). The newly generated genotype data are available as a Supplementary Data file. The previously published data co-analysed with our newly reported data can be obtained as described in the original publications, which are all referenced in Supplementary Table 3; a compiled dataset that includes the merged genotypes used in this paper is available as the Allen Ancient DNA Resource at <https://reich.hms.harvard.edu/allen-ancient-dna-resource#downloadable-genotypes-present-day-and-ancient-dna-data>. Any other relevant data are available from the corresponding authors on reasonable request.

Code availability

This study uses publicly available software, which we fully reference.

References

1. 1.

Galinsky, K. J., Loh, P. R., Mallick, S., Patterson, N. J. & Price, A. L. Population structure of UK Biobank and ancient Eurasians reveals adaptation at genes influencing blood pressure. *Am. J. Hum. Genet.* **99**, 1130–1139 (2016).

2. 2.

Cunliffe, B. *Britain Begins* (Oxford Univ. Press, 2013).

3. 3.

Koch, J. T. & Cunliffe, B. W. (eds) *Celtic from the West 2: Rethinking the Bronze Age and the Arrival of Indo-European in Atlantic Europe* (Oxbow Books, 2013).

4. 4.

Needham, S. & Bowman, S. Flesh-hooks, technological complexity and the Atlantic Bronze Age feasting complex. *Eur. J. Archaeol.* **8**, 93–136 (2005).

5. 5.

Marcigny, C., Bourgeois, J. & Talon, M. in *Rythmes et Contours de la Géographie Culturelle sur le Littoral de la Manche Entre le IIIe et le Début du Ier Millénaire* (eds Lehoerff, A. & Talon, M.) 63–78 (Oxbow Books, 2017).

6. 6.

Marcigny, C. in *Les Anglais in Normandie* 47–54 (2011).

7. 7.

Cassidy, L. M. et al. Neolithic and Bronze Age migration to Ireland and establishment of the insular Atlantic genome. *Proc. Natl Acad. Sci. USA* **113**, 368–373 (2016).

8. 8.

Olalde, I. et al. The Beaker phenomenon and the genomic transformation of northwest Europe. *Nature* **555**, 190–196 (2018).

9. 9.

Brace, S. et al. Ancient genomes indicate population replacement in Early Neolithic Britain. *Nat. Ecol. Evol.* **3**, 765–771 (2019).

10. 10.

Schiffels, S. et al. Iron Age and Anglo-Saxon genomes from East England reveal British migration history. *Nat. Commun.* **7**, 10408 (2016).

11. 11.

Reich, D., Thangaraj, K., Patterson, N., Price, A. L. & Singh, L. Reconstructing Indian population history. *Nature* **461**, 489–494 (2009).

12. 12.

Lazaridis, I. et al. Ancient human genomes suggest three ancestral populations for present-day Europeans. *Nature* **513**, 409–413 (2014).

13. 13.

Evans, J. A., Chenery, C. A. & Montgomery, J. A summary of strontium and oxygen isotope variation in archaeological human tooth enamel excavated from Britain. *J. Anal. At. Spectrom.* **27**, 754–764 (2012).

14. 14.

Fitzpatrick, A. P. *The Amesbury Archer and the Boscombe Bowmen: Early Bell Beaker Burials at Boscombe Down, Amesbury, Wiltshire, Great Britain: Excavations at Boscombe Down Vol. 1* (Wessex Archaeology, 2011).

15. 15.

Millard, A. R. in *Cliffs End Farm, Isle of Thanet, Kent: A Mortuary and Ritual Site of the Bronze Age, Iron Age and Anglo-Saxon Period With Evidence for Long-Distance Maritime Mobility* (eds McKinley, J. I. et al.) 135–146 (Wessex Archaeology, 2014).

16. 16.

Champion, T. C., Haselgrove, C., Armit, I., Creighton, J. & Gwilt, A. *Understanding the British Iron Age: An Agenda for Action. A Report for the Iron Age Research Seminar and the Council of the Prehistoric Society* (Trust for Wessex Archaeology, 2001).

17. 17.

Ringbauer, H., Novembre, J. & Steinrücken, M. Parental relatedness through time revealed by runs of homozygosity in ancient DNA. *Nat. Commun.* **12**, 5425 (2021).

18. 18.

Olalde, I. et al. The genomic history of the Iberian Peninsula over the past 8000 years. *Science* **363**, 1230–1234 (2019).

19. 19.

Busby, G. B. J. et al. The peopling of Europe and the cautionary tale of Y chromosome lineage R-M269. *Proc. Biol. Sci.* **279**, 884–892 (2012).

20. 20.

Halkon, P. *The Arras Culture of Eastern Yorkshire: Celebrating the Iron Age* (Oxbow Books, 2020).

21. 21.

Bellwood, P. S. & Renfrew, C. *Examining the Farming/Language Dispersal Hypothesis* (McDonald Institute for Archaeological Research, 2002).

22. 22.

Sims-Williams, P. An alternative to ‘Celtic from the East’ and ‘Celtic from the West’. *Cambridge Archaeol. J.* **30**, 511–529 (2020).

23. 23.

Mallory, J. P. *The Origins of the Irish* (Thames & Hudson, 2013).

24. 24.

Rodway, S. The Ogham inscriptions of Scotland and Brittonic Pictish. *J. Celt. Linguist.* **21**, 173–234 (2020).

25. 25.

Herm, G. *The Celts: The People Who Came Out of the Darkness* (Weidenfeld and Nicolson, 1976).

26. 26.

Guggisberg, M. in *Oxford Handbook of the European Iron Age* (eds Rebay-Silsbury, K., Haselgrove, C. & Wells, P.) (Oxford Univ. Press, 2018).

27. 27.

Booth, T. J. A stranger in a strange land: a perspective on archaeological responses to the palaeogenetic revolution from an archaeologist working amongst palaeogeneticists. *World Archaeol.* **51**, 586–601 (2019).

28. 28.

Anthony, D. W. Migration in archeology: the baby and the bathwater. *Am. Anthropol.* **92**, 895 – 914 (1990).

29. 29.

Vander Linden, M. Population history in third-millennium-bc Europe: assessing the contribution of genetics. *World Archaeol.* **48**, 714–728 (2016).

30. 30.

Haak, W. et al. Massive migration from the steppe was a source for Indo-European languages in Europe. *Nature* **522**, 207–211 (2015).

31. 31.

Pinhasi, R., Fernandes, D. M., Sirak, K. & Cheronet, O. Isolating the human cochlea to generate bone powder for ancient DNA analysis. *Nat. Protoc.* **14**, 1194–1205 (2019).

32. 32.

the cranial base for ancient DNA analysis. *Biotechniques* **62**, 283–289 (2017).

33. 33.

Dabney, J. et al. Complete mitochondrial genome sequence of a Middle Pleistocene cave bear reconstructed from ultrashort DNA fragments. *Proc. Natl Acad. Sci. USA* **110**, 15758–15763 (2013).

34. 34.

Korlevic, P. et al. Reducing microbial and human contamination in DNA extractions from ancient bones and teeth. *Biotechniques* **59**, 87–93 (2015).

35. 35.

Rohland, N., Glocke, I., Aximu-Petri, A. & Meyer, M. Extraction of highly degraded DNA from ancient bones, teeth and sediments for high-throughput sequencing. *Nat. Protoc.* **13**, 2447–2461 (2018).

36. 36.

Gansauge, M. T. et al. Single-stranded DNA library preparation from highly degraded DNA using T4 DNA ligase. *Nucleic Acids Res.* **45**, e79 (2017).

37. 37.

Gansauge, M.-T., Aximu-Petri, A., Nagel, S. & Meyer, M. Manual and automated preparation of single-stranded DNA libraries for the sequencing of DNA from ancient biological remains and other sources of highly degraded DNA. *Nat. Protoc.* **15**, 2279–2300 (2020).

38. 38.

Briggs, A. & Heyn, P. in *Methods in Molecular Biology* Vol. 840 143–154 (Springer, 2012).

39. 39.

Rohland, N., Harney, E., Mallick, S., Nordenfelt, S. & Reich, D. Partial uracil-DNA-glycosylase treatment for screening of ancient DNA. *Phil. Trans. R. Soc. B* **370**, 20130624 (2015).

40. 40.

Fu, Q. et al. DNA analysis of an early modern human from Tianyuan Cave, China. *Proc. Natl Acad. Sci. USA* **110**, 2223–2227 (2013).

41. 41.

Maricic, T., Whitten, M. & Paabo, S. Multiplexed DNA sequence capture of mitochondrial genomes using PCR products. *PLoS ONE* **5**, e14004 (2010).

42. 42.

Fu, Q. et al. An early modern human from Romania with a recent Neanderthal ancestor. *Nature* **524**, 216–219 (2015).

43. 43.

Behar, D. M. et al. A "Copernican" reassessment of the human mitochondrial DNA tree from its root. *Am. J. Hum. Genet.* **90**, 675–684 (2012).

44. 44.

Li, H. & Durbin, R. Fast and accurate short read alignment with Burrows-Wheeler transform. *Bioinformatics* **25**, 1754–1760 (2009).

45. 45.

Weissensteiner, H. et al. HaploGrep 2: mitochondrial haplogroup classification in the era of high-throughput sequencing. *Nucleic Acids Res.* **44**, W58–W63 (2016).

46. 46.

Fu, Q. et al. A revised timescale for human evolution based on ancient mitochondrial genomes. *Curr. Biol.* **23**, 553–559 (2013).

47. 47.

Korneliussen, T. S., Albrechtsen, A. & Nielsen, R. ANGSD: analysis of next generation sequencing data. *BMC Bioinformatics* **15**, 356 (2014).

48. 48.

Sawyer, S., Krause, J., Guschanski, K., Savolainen, V. & Paabo, S. Temporal patterns of nucleotide misincorporations and DNA fragmentation in ancient DNA. *PLoS ONE* **7**, e34131 (2012).

49. 49.

Skoglund, P. et al. Separating endogenous ancient DNA from modern day contamination in a Siberian Neandertal. *Proc. Natl Acad. Sci. USA* **111**, 2229–2234 (2014).

50. 50.

Patterson, N. et al. Ancient admixture in human history. *Genetics* **192**, 1065–1093 (2012).

51. 51.

Kennett, D. J. et al. Archaeogenomic evidence reveals prehistoric matrilineal dynasty. *Nat. Commun.* **8**, 14115 (2017).

52. 52.

Mathieson, I. et al. Genome-wide patterns of selection in 230 ancient Eurasians. *Nature* **528**, 499–503 (2015).

53. 53.

Bronk Ramsey, C. Bayesian analysis of radiocarbon dates. *Radiocarbon* **51**, 337–360 (2009).

54. 54.

Reimer, P. J. et al. The IntCal20 northern hemisphere radiocarbon age calibration curve (0–55 cal kBP). *Radiocarbon* **62**, 725–757 (2020).

Acknowledgements

We thank P. Csengeri, T. de Rider, M. Giesen, E. Melis, A. Parkin and A. Schmitt for their contribution to sample selection and collection of archaeological data; R. Crellin, J. Koch, K. Kristiansen and G. Kroonen for comments on the manuscript; A. Williamson for manually revising Y chromosome haplogroup determinations and making corrections to nine; and M. Lee for assistance with data entry. This work was funded in part by the European Research Council (ERC) under the European Union’s Horizon 2020 research and innovation programme (grant agreement no. 834087; the COMMOS Project to I.A.). M.N. was supported by the Croatian Science Fund grant (HRZZ IP-2016-06-1450). P.V., M.Dobeš and Z.V. were supported by the Ministry of Culture of the Czech Republic (DKRVO 2019-2023/7.I.c, 00023272). M.E. was supported by Czech Academy of Sciences award Praemium Academiae. M.Dobisíková and A.Danielisová were supported by the grant RVO 67985912 of the Institute of Archaeology of the Czech Academy of Sciences. M.G.B.F. was funded by The Leverhulme Trust via a Doctoral Scholarship scheme awarded to M.Pala and M.B.R. Support to M.Legge came from the South, West & Wales Doctoral Training

Partnership. M.G.'s osteological analyses were funded by Culture Vannin. A.S.-N. was supported by the János Bolyai Research Scholarship of the Hungarian Academy of Sciences. T.H., T.S. and K.K.'s work was supported by a grant from the Hungarian Research, Development and Innovation Office (project number: FK128013). We acknowledge support for radiocarbon dating and stable isotope analyses as well as access to skeletal material from Manx National Heritage and A. Fox. Dating analysis was funded by Leverhulme Trust grant RPG-388. M.G.T. and I.B. were supported by a Wellcome Trust Investigator Award (project 100713/Z/12/Z). I.O. was supported by a Ramón y Cajal grant from Ministerio de Ciencia e Innovación, Spanish Government (RYC2019-027909-I). The research directed at Harvard was funded by NIH grants GM100233 and HG012287, by John Templeton Foundation grant 61220, by a gift from Jean-François Clin, and by the Allen Discovery Center program, a Paul G. Allen Frontiers Group advised program of the Paul G. Allen Family Foundation. D.R. is also an Investigator of the Howard Hughes Medical Institute.

Author information

Author notes

1. These authors contributed equally: Nick Patterson, Michael Isakov, Thomas Booth, Lindsey Büster, Claire-Elise Fischer

Affiliations

1. Department of Human Evolutionary Biology, Harvard University, Cambridge, MA, USA

Nick Patterson, Harald Ringbauer, Ali Akbari, Iosif Lazaridis & David Reich

2. Broad Institute of MIT and Harvard, Cambridge, MA, USA

Nick Patterson, Harald Ringbauer, Matthew Mah, Swapan Mallick, Adam Micco, Nadin Rohland & David Reich

3. Harvard College, Cambridge, MA, USA

Michael Isakov

4. Department of Earth Sciences, Natural History Museum, London, UK

Thomas Booth, Selina Brace & Ian Barnes

5. Department of Archaeology, University of York, York, UK

Lindsey Büster, Claire-Elise Fischer, Madeleine Bleasdale, Helen Goodchild, Oliver Craig & Ian Armit

6. Department of Genetics, Harvard Medical School, Boston, MA, USA

Iñigo Olalde, Ali Akbari, Nicole Adamski, Rebecca Bernardos, Nasreen Broomandkhoshbacht, Kimberly Callan, Elizabeth Curtis, Aisling Kearns, Ann Marie Lawson, Iosif Lazaridis, Matthew Mah, Swapna Mallick, Adam Micco, Megan Michel, Jonas Oppenheimer, Lijun Qiu, Kristin Stewardson, J. Noah Workman, Fatma Zalzala, Zhao Zhang, Alfredo Coppa, Nadin Rohland & David Reich

7. BIOMICS Research Group, University of the Basque Country UPV/EHU, Vitoria-Gasteiz, Spain

Iñigo Olalde

8. Ikerbasque—Basque Foundation of Science, Bilbao, Spain

Iñigo Olalde

9. Department of Evolutionary Anthropology, University of Vienna, Vienna, Austria

Olivia Cheronet, Lea Demetz, Kellie Sara Duffett Carlson, Daniel M. Fernandes, Suzanne Freilich, Kirsten Mandl, Guillermo Bravo Morante, Kadir Toykan Özdoğan, Constanze Schattke, Alfredo Coppa, Maria Teschler-Nicola & Ron Pinhasi

10. Howard Hughes Medical Institute, Boston, MA, USA
Nicole Adamski, Nasreen Broomandkhoshbacht, Kimberly Callan, Elizabeth Curtis, Ann Marie Lawson, Matthew Mah, Swapna Mallick, Megan Michel, Jonas Oppenheimer, Kristin Stewardson, Fatma Zalzala & David Reich
11. Department of Human Genetics, Leiden University Medical Center, Leiden, Netherlands
Eveline Altena & Peter de Knijff
12. Servizio di Bioarcheologia, Museo delle Civiltà, Rome, Italy
Francesca Candilio
13. Institutes of Energy and the Environment, Pennsylvania State University, University Park, PA, USA
Brendan Culleton
14. Department of Biological and Geographical Sciences, School of Applied Sciences, University of Huddersfield, Huddersfield, UK
Ceiridwen J. Edwards
15. CIAS, Department of Life Sciences, University of Coimbra, Coimbra, Portugal
Daniel M. Fernandes, M. George B. Foody, Maria Pala & Martin B. Richards
16. INSITU S.C.P. Centelles, Barcelona, Spain
Bibiana Agustí
17. Oxford Archaeology, Oxford, UK

Tim Allen, Fraser Brown, Alex Davies, Chris Hayden, Gill Hey, Louise Loe & Lauren McIntyre

18. Městské Muzeum v Čelákovicích, Čelákovice, Czech Republic

Katalin Almássy

19. National Museum of Antiquities, Leiden, Netherlands

Luc Amkreutz

20. Faculty of Archaeology, Leiden University, Leiden, Netherlands

Luc Amkreutz & Harry Fokkens

21. Independent Researcher, Soham, Ely, UK

Abigail Ash

22. Institut National de Recherches Archéologiques Préventives (INRAP),
Paris, France

Christèle Baillif-Ducros, Sylvain Canet, Sébastien Chauvin & Cécile
Paresys

23. Cotswold Archaeology, Cirencester, UK

Alistair Barclay, Pippa Bradley & Sharon Clough

24. Department of Archaeology and Classical Studies, Stockholm
University, Stockholm, Sweden

László Bartosiewicz

25. Leeds Museums and Galleries, Leeds Discovery Centre, Leeds, UK

Katherine Baxter

26. Department of Anthropology, Hungarian Natural History Museum,
Budapest, Hungary

Zsolt Bernert, Tamás Hajdu & Tamás Szeniczey

27. Institute of Preservation of Archaeological Heritage of Northwest
Bohemia, Most, Czech Republic

Jan Blažek

28. Stratum Ltd, Seget Donji, Croatia

Mario Bodružić

29. TRACES, Ecole des Hautes Etudes en Sciences Sociales, Toulouse,
France

Philippe Boissinot

30. School of History, Classics and Archaeology, University of Edinburgh,
Edinburgh, UK

Clive Bonsall, Manuel Fernández-Götz, Kathleen
McSweeney & Catriona Pickard

31. Cambridge Archaeological Unit, Department of Archaeology,
University of Cambridge, Cambridge, UK

Marcus Britann, Christopher Evans, Mark Knight, Benjamin
Neil, Ricky Patten, Jonathan Tabor & Rob Wiseman

32. Corinium Museum, Cirencester, UK

Alison Brookes & James Harris

33. Wiltshire Museum, Devizes, UK

Lisa Brown

34. South West Heritage Trust, Somerset Heritage Centre, Taunton, UK
Richard Brunning, Amal Khreisheh & Steve Minnitt
35. Department of Historical, Philosophical and Religious Studies, Umeå University, Umeå, Sweden
Chelsea Budd & Malcolm Lillie
36. Kaducej Ltd, Split, Croatia
Josip Burmaz & Dženi Los
37. Instituto de Medicina Legal y Ciencias Forenses de Cantabria, Santander, Spain
Silvia Carnicero-Cáceres
38. Université de Franche Comté/UMR Chrono-Environnement, Besançon, France
Morana Čaušević-Bully
39. School of Earth and Environmental Sciences, University of Manchester, Manchester, UK
Andrew Chamberlain
40. Archaeological Museum Zadar, Zadar, Croatia
Natalija Čondić
41. Department of Environmental Biology, University of Rome, La Sapienza, Rome, Italy
Alfredo Coppa
42. Department of Archaeology, Centre for Interdisciplinary Research in Archaeology, Faculty of Arts, Ljubljana, Slovenia

Matija Črešnar, Milan Horňák & Biba Teržan

43. Institute for the Protection of Cultural Heritage of Slovenia,
Conservation Centre, Centre for Preventive Archaeology, Ljubljana,
Slovenia

Matija Črešnar & Philip Mason

44. School of Natural Sciences, University of Central Lancashire, Preston,
UK

Vicki Cummings

45. Hungarian National Museum, Budapest, Hungary

Szabolcs Czifra

46. Institute of Archaeology of the Czech Academy of Sciences, Prague,
Prague, Czech Republic

Alžběta Danielisová, Miroslav Dobeš & Michal Ernée

47. Tees Archaeology, Hartlepool, UK

Robin Daniels

48. Guernsey Museums & Galleries, St Peter Port, UK

Philip de Jersey

49. Amgueddfa Cymru—National Museum Wales, Cardiff, UK

Jody Deacon

50. Kuny Domokos Museum, Tata, Hungary

Csilla Deminger

51. Research Laboratory for Archaeology, School of Archaeology,
University of Oxford, Oxford, UK

Peter W. Ditchfield

52. Institute of Archaeology, Zagreb, Croatia

Marko Dizdar

53. Department of Anthropology, The National Museum, Prague, Prague,
Czech Republic

Miluše Dobisíková, Petr Velemínský & Zdeněk Vytlačil

54. Department of Archaeology, Dobó István Castle Museum, Eger,
Hungary

László Domboróczki

55. The Orkney Museum, Kirkwall, UK

Gail Drinkall

56. Archaeological Museum in Zagreb, Zagreb, Croatia

Ana Đukić

57. British Geological Survey, Keyworth Nottingham, Nottinghamshire,
UK

Jane Evans

58. Archaeological Museum Osijek, Osijek, Croatia

Slavica Filipović

59. Archaeology and Ancient History, University of Leicester, Leicester,
UK

Andrew Fitzpatrick

60. School of History, Classics and Archaeology, Newcastle University,
Newcastle upon Tyne, UK

Chris Fowler

61. Manx National Heritage, Eiraght Ashoonagh Vannin, Manx Museum,
Douglas, UK

Allison Fox

62. Ásatárs Ltd, Kecskemét, Hungary

Zsolt Gallina

63. Heritage and Archaeological Research Practice (HARP), Edinburgh,
UK

Michelle Gamble

64. Instituto Internacional de Investigaciones Prehistóricas de Cantabria,
Universidad de Cantabria, Santander, Spain

Manuel R. González Morales

65. Grupo EvoAdapta, Departamento de Ciencias Históricas, Universidad
de Cantabria, Santander, Spain

Borja González-Rabanal & Ana B. Marín-Arroyo

66. The Salisbury Museum, Salisbury, UK

Adrian Green

67. Department of Biological Anthropology, Institute of Biology, Faculty
of Science, Eötvös Loránd University, Budapest, Hungary

Katalin Gyenessei

68. VUhbs Archaeology, VU University, Amsterdam, Netherlands
Diederick Habermehl
69. Department of Biological Anthropology, Eötvös Loránd University, Budapest, Hungary
Tamás Hajdu & Tamás Szeniczey
70. Scottish Universities Environmental Research Centre (SUERC), East Kilbride, UK
Derek Hamilton
71. Bureau Archeologie en Bodemkwaliteit, Gemeente Nijmegen, Nijmegen, Netherlands
Joep Hendriks
72. Musée Saint-Remi, Ville de Reims, Reims, France
Bénédicte Hernu
73. Independent Researcher, Mesterháza, Hungary
Gábor Ilon
74. Jósa András Museum, Nyíregyháza, Hungary
Eszter Istvánovits
75. Cornwall Archaeology Unit, Truro, UK
Andy M. Jones
76. Faculty of Humanities, University of Primorska, Koper, Slovenia
Martina Blečić Kavur

77. Musée de La Cour d'Or, Metz, France

Kevin Kazek & Julien Trapp

78. East Dorset Antiquarian Society (EDAS), Dorset, UK

Robert A. Kenyon

79. Institute of Archaeology, Research Centre for the Humanities, Eötvös Loránd Research Network, Budapest, Hungary

Gabriella Kulcsár, Balázs G. Mende & Anna Szécsényi-Nagy

80. Groningen Institute of Archaeology, Groningen University, Groningen, Netherlands

Jos Kleijne

81. Geology and Geochemistry Cluster, Vrije Universiteit Amsterdam, Amsterdam, Netherlands

Lisette M. Kootker

82. Damjanich János Museum, Szolnok, Hungary

Péter F. Kovács

83. Archaeological Institute of the Slovak Academy of Sciences, Nitra, Slovakia

Anita Kozubová

84. University of Szeged, Faculty of Arts, Department of Archaeology, Szeged, Hungary

Valéria Kulcsár

85. Musée d'Histoire et d'Archéologie, Vannes, France

Christophe Le Pennec

86. School of History, Archaeology and Religion, Cardiff University,
Cardiff, UK

Michael Legge

87. Wessex Archaeology, Salisbury, UK

Matt Leivers

88. Group EcoPast. CRETUS. Area of Archaeology, Department of
History, Universidade de Santiago de Compostela, Santiago de
Compostela, Spain

Olalla López-Costas & Jacqueline McKinley

89. Lower Winskill Farm, Langcliffe, UK

Tom Lord

90. Geophiz.biz, West Heslerton, UK

James Lyall

91. Zavičajni Muzej Grada Rovinja, Rovinj, Croatia

Damir Matošević

92. Royal Pavilion and Museums Trust, Brighton, UK

Andy Maxted

93. Walcherse Archeologische Dienst, Middelburg, Netherlands

Bernard Meijlink

94. Institute of Archaeogenomics, Research Centre for the Humanities,
Eötvös Loránd Research Network, Budapest, Hungary

Viktória Kiss

95. Conservation Department in Šibenik, Ministry of Culture of the Republic of Croatia, Šibenik, Croatia

Marko Mendušić

96. Museum of West Bohemia, Department of Prehistory, Pilsen, Czech Republic

Milan Metlička

97. Royal Cornwall Museum, Truro, Cornwall, UK

Sophie Meyer

98. Archaeological Museum of Istria, Pula, Croatia

Kristina Mihovilić

99. National Museum of Kikinda, Kikinda, Serbia

Lidija Milasinovic

100. Department of Archaeology, Durham University, Durham, UK

Joanna Moore

101. MOLES Archaeology, Courtwood House, Sheffield, UK

Geoff Morley

102. University of Bristol Spelaeological Society, Bristol, UK

Graham Mullan & Linda Wilson

103. Municipal Monument Preservation Institute Bratislava, Bratislava, Slovakia

Margaréta Musilová & Branislav Resutík

104. Archaeological and Forensic Sciences, University of Bradford,
Bradford, UK

Rebecca Nicholls

105. Centre for Applied Bioanthropology, Institute for Anthropological
Research, Zagreb, Croatia

Mario Novak

106. National Trust, Dorset & Wiltshire, Tisbury, UK

Martin Papworth

107. Archaeological Museum, Dubrovnik Museums, Dubrovnik, Croatia

Domagoj Perkić

108. Rómer Flóris Museum of Art and History, Győr, Hungary

Krisztina Pesti & Ferenc Ujvári

109. Departament de Biologia Animal, de Biologia Vegetal i d'Ecologia,
Universitat Autònoma de Barcelona, Bellaterra, Cerdanyola del Vallés,
Spain

Alba Petit

110. The City of Prague Museum, Prague, Czech Republic

Katarína Petriščáková & Miroslava Šmolíková

111. Musée Le Vergeur, Reims, France

Coline Pichon

112. Independent researcher, Budapest, Hungary

Zoltán Pilling

113. Department of Anthropology, University of Wisconsin-Madison,
Madison, WI, USA

T. Douglas Price

114. Institute for Quaternary Palaeontology and Geology, Croatian
Academy of Sciences and Arts, Zagreb, Croatia

Siniša Radović

115. Centre for Human Bioarchaeology, Museum of London, London, UK

Rebecca Redfern

116. National Trust For Scotland, Hermiston Quay, Edinburgh, UK

Daniel T. Rhodes

117. The Novium Museum, Chichester, UK

Amy Roberts

118. Provinciaal Archeologisch Depot Noord-Holland, Castricum,
Netherlands

Jean Roefstra

119. Department of Prehistory and Classical Antiquity, The National
Museum, Prague, Prague, Czech Republic

Pavel Sankot

120. Slovak National Museum—Natural History Museum, Bratislava,
Slovakia

Alena Šefčáková

121. National Museums Scotland, Edinburgh, UK

Alison Sheridan

122. The Dock Museum, Barrow-in-Furness, UK

Sabine Skae

123. Rippl-Rónai Museum, Kaposvár, Hungary

Krisztina Somogyi

124. Katona József Museum Hungary, Kecskemét, Hungary

Ágnes Somogyvári

125. MAP Archaeological Practice, Malton, UK

Mark Stephens & Paula Ware

126. Wosinsky Mór Museum, Szekszárd, Hungary

Géza Szabó

127. MTA—ELTE Research Group for Interdisciplinary Archaeology,
Eötvös Loránd University, Budapest, Hungary

Károly Tankó

128. Museo del Hombre Dominicano, Santo Domingo, Dominican Republic

Clenis Tavarez Maria

129. Craven Museum and Gallery, Skipton, UK

Rachel Terry

130. Department of Anthropology, Natural History Museum Vienna,
Vienna, Austria

Maria Teschler-Nicola

131. Instituto Monte Bernorio de Estudios de la Antigüedad del Cantábrico (IMBEAC), Universidad Complutense de Madrid, Facultad de Geografía e Historia, Departamento de Prehistoria, Historia Antigua y Arqueología, Madrid, Spain

Jesús F. Torres-Martínez

132. Hampshire Cultural Trust, Winchester, UK

Ross Turle

133. Rijksdienst voor het Cultureel Erfgoed, Amersfoort, Netherlands

Menno van der Heiden

134. Maritime Cultures Research Institute, Department of Art, Sciences, and Archaeology, Vrije Universiteit Brussel, Brussels, Belgium

Barbara Veselka

135. Research Unit: Analytical, Environmental & Geo-Chemistry, Department of Chemistry, Vrije Universiteit Brussel, Brussels, Belgium

Barbara Veselka

136. Archaeological Research Services, Bakewell, UK

Clive Waddington

137. Swale and Thames Archaeological Survey Company, Faversham, UK

Paul Wilkinson

138. Keswick Museum, Keswick, UK

Eilidh Young

139. Krka National Park, Šibenik, Croatia

Joško Zaninović

140. AA AVALA s.r.o., Bratislava, Slovakia

Andrej Žitňan

141. Institute of Evolutionary Biology, CSIC-Universitat Pompeu Fabra,
Barcelona, Spain

Carles Lalueza-Fox

142. Department of History, University of Hull, Hull, UK

Peter Halkon

143. Research Department of Genetics, Evolution and Environment,
University College London, London, UK

Mark G. Thomas

144. Department of Anthropology, University of California, Santa Barbara,
CA, USA

Douglas J. Kennett

145. Institute of Archaeology, University of Oxford, Oxford, UK

Barry Cunliffe

146. Department of Geography, Geology and Environment, University of
Hull, Hull, UK

Malcolm Lillie

147. Human Evolution and Archaeological Sciences, University of Vienna,
Vienna, Austria

Ron Pinhasi

Contributions

D.J.K., B.Cunliffe, N.R., R.Pinhasi, I.A. and D.R. supervised the study. T.B., L.Büster, C.-E.F., O.Cheronet, S.B., B.A., T.A., K.A., L.A., A.Ash, C.B.-D., A.Barclay, L.Bartosiewicz, K.B., Z.B., J.Blažek, M.Bodružić, P.Boissinot, C.Bonsall, P.Bradley, M.Brittain, A.Brookes, F.B., L.Brown, R.Brunning, C.Budd, J.Burmaz, S.Canet, S.C.-C., M.Č.-B., A.Chamberlain, S.Chauvin, S.Clough, N.Č., A.Coppa, O.Craig, M.Č., V.C., S.Czifra, A.Danielisová, R.D., A.Davis, P.d.J., J.D., C.D., P.W.D., M.Dizdar, M.Dobeš, M.Dobisíková, L.Domboróczki, G.D., A.Đukić, C.J.E., M.E., C.E., J.E., M.F.-G., S.Filipović, A.Fitzpatrick, H.F., C.F., A.Fox, Z.G., M.G., M.R.G.M., B.G.-R., A.G., K.G., D.Habermehl, T.H., D.Hamilton, J.Harris, C.H., J.Hendriks, B.H., G.H., M.H., G.I., E.I., A.M.J., M.B.K., K.K., R.A.K., A.Khreisheh, V.Kiss, J.K., M.K., L.M.K., P.F.K., A.Kozubová, G.K., V.Kulcsár, C.L.P., M.Legge, M.Leivers, L.L., O.L.-C., T.L., D.L., J.L., A.B.M.-A., P.M., D.M., A.Maxted, L.McIntyre, J.McKinley, K.McSweeney, B.M., B.G.M., M.Mendušić, M.Metlička, S.Meyer, K.Mihovilić, L.Milasinovic, S.Minnitt, J.Moore, G.Morley, G.Mullan, M.Musilová, B.N., R.N., M.N., M.Pala, M.Papworth, C.Paresys, R.Patten, D.P., K.Pesti, A.P., K.Petriščáková, C.Pichon, C.Pickard, Z.P., T.D.P., S.R., R.R., B.R., D.T.R., M.B.R., A.R., J.R., P.S., A.Šefčáková, A.Sheridan, S.S., K.Somogyi M.Šmolíková, Á.Somogyvári, M.Stephens, G.S., A.S.-N., T.S., J.Tabor, C.T.M., R.Terry, B.T., M.T.-N., J.F.T.-M., J.Trapp, R.Turle, F.U., M.v.d.H., P.V., B.V., Z.V., C.W., P.Ware, P.Wilkinson, L.W., R.W., E.Y., J.Z., A.Ž., C.L.-F., P.H., B.Cunliffe, M.Lillie, R.Pinhasi and I.A. excavated or curated samples and provided archaeological contextualization. T.B., O.Cheronet, M.Bleasdale, N.A., E.A., S.B., N.B., K.C., F.C., B.Culleton, E.C., L.Demetz, K.S.D.C., D.M.F., M.G.B.F., S.Freilich, A.Kearns, A.M.L., K.Mandl, M.Michel, G.B.M., J.O., K.T.Ö., L.Q., C.S., K.Stewardson, J.N.W., F.Z., C.J.E., D.J.K. and N.R. generated the data through sample preparation or laboratory work. N.P., M.I., L.Büster, C.-E.F., I.O., H.R., A.Akbari, O.Cheronet, M.Bleasdale, R.Bernardos, H.G., I.L., M.Mah, S.Mallick, A.Micco, Z.Z. and D.R. curated and analysed the data. N.P., M.I., T.B., L.Büster, C.-E.F., I.O., M.Bleasdale, I.A. and D.R. wrote substantial sections of the paper.

Corresponding authors

Correspondence to [Ron Pinhasi](#), [Ian Armit](#) or [David Reich](#).

Ethics declarations

Competing interests

The authors declare no competing interests.

Peer review information

Nature thanks Daniel Bradley, Daniel Lawson, Patrick Sims-Williams, and the other, anonymous, reviewer(s) for their contribution to the peer review of this work. Peer review reports are available.

Additional information

Publisher's note Springer Nature remains neutral with regard to jurisdictional claims in published maps and institutional affiliations.

Extended data figures and tables

[Extended Data Fig. 1 Post-MBA Britain was not a mix of earlier British populations.](#)

a, *qpAdm* p-values for modelling British groups as a mix of Neolithic and Chalcolithic/EBA populations from England and Wales or Scotland (outgroups OldAfrica, OldSteppe, Turkey_N, CzechRepublic.Slovakia.Germany_3800.to.2700BP, Netherlands_C.EBA, Poland_Globular_Amphora, Spain.Portugal_4425.to.3800BP, CzechRepublic.Slovakia.Germany_4465.to.3800.BP, Sardinia_4100.to.2700BP, Sardinia_8100.to.4100BP, Spain.Portugal_6500.to.4425BP). We highlight p<0.05 (yellow) or p<0.005 (red). Both sources and target populations in this analysis remove outlier

individuals (“Filter 2” in Supplementary Table 5); we obtain qualitatively similar results when outlier individuals are not removed (not shown). **b**, To obtain insight into the source of the new ancestry in Britain in the IA, we computed $f_4(\text{England.and.Wales_IA}, \alpha(\text{England.and.Wales_N}) + (1-\alpha)(\text{England.Wales_C.EBA}); R1, R2)$ for different (R1, R2) population pairs. If England.and.Wales_IA is a simple mixture of England.and.Wales_N and England.and.Wales_C.EBA without additional ancestry, then for some mixture proportion the statistic will be consistent with zero for all (R1, R2 pairs). When (R1, R2) = (OldAfrica, OldSteppe) feasible Z-scores (Z1 in the plot) are observed when $\alpha \sim 0.85$, showing that ~85% ancestry from England.and.Wales_C.EBA ancestry is needed to contribute the observed proportion of Steppe ancestry in England.and.Wales_IA. However, when (R1, R2) is (Balkan_N, Sardinian_8100.to.4100BP), we get infeasible Z-scores (Z2) of <-6 across the range where Z1 is remotely feasible. Thus, Iron Age people from England and Wales must have ancestry from an additional population deeply related to Sardinian Early Neolithic groups.

Extended Data Fig. 2 By-individual analysis of the British time transect.

Version of Fig. 3 with the time transect extended into the Neolithic, and adding in individuals from Scotland. We plot mean estimates of EEF ancestry and one standard error bars from a Block Jackknife for all individuals in the time transect that pass basic quality control, that fit to a three-way admixture model (EEF + WHG + Yamnaya) at $p>0.01$ using *qpAdm*, and for the Neolithic period that fit a two-way admixture model (EEF + WHG) at $p>0.01$. Individuals that fit the main cluster of their time are shown in blue (southern Britain) and green (Scotland), while red and orange respectively show outliers at the ancestry tails (identified either as $p<0.005$ based on a *qpWave* test from the main cluster of individuals from their period and $|Z|>3$ for a difference in their EEF ancestry proportion from the period, or alternatively $p<0.1$ and $|Z|>3.5$). The averages for the main clusters in both southern Britain and Scotland in each archaeological period (Neolithic, C/EBA, MBA, LBA and IA) are shown in dashed lines.

Extended Data Fig. 3 Changes in the size of the mate pool over time.

Close kin unions were rare at all periods as reflected in the paucity of individuals harbouring >50 centimorgans (cM) of their genome in runs of homozygosity (ROH) of >12 cM (red dots in top panel). The number of ROH of size 4–8 cM per individual (bottom panel) reflects the rate at which distant relatives have children, providing information about the sizes of mate pools (N_e) averaged over the hundreds of years prior to when individuals lived; thus, the broad trend of an approximately fourfold drop in N_e from the Neolithic to the IA is robust, but we may miss fluctuations on a time scale of centuries. The thick black lines represent the mean N_e obtained by fitting a mathematical model of a Gaussian process with a 600-year smoothing kernel (gray area 95% confidence interval). The horizontal grey lines show period averages from maximum likelihood which can differ from the mean obtained through the mathematical modelling if the counts do not conform well to a Gaussian process. We interrupt the fitted line for periods with too little data for accurate inference (<10 individuals in a 400-year interval centered on the point).

Extended Data Fig. 4 Frequency change over time at two phenotypically important alleles.

Present-day frequencies are shown by the red dashed lines; sample sizes for each period are labelled at the bottom of each plot; and we show means along with 95% confidence intervals (Supplementary Table 8). (a–d/Top) Lactase persistence allele at rs4988235. (e–h/Bottom) Light skin pigmentation allele at rs16891982. In Britain the rise in frequency of the lactase persistence allele occurred earlier than in central Europe. This analysis is based on direct observation of alleles; imputation results are qualitatively consistent (Fig. 4b).

Extended Data Fig. 5 Y chromosome haplogroup frequency changes over time.

Estimated frequency of the characteristically British Y chromosome haplogroup R1b-P312/L21/M529 in all individuals for which we are able to make a determination and which are not first-degree relatives of a higher coverage individual in the dataset. Sample sizes for each period are labelled at the bottom, and we show means and one standard error bars from a binomial distribution. The frequency increases significantly from ~0% in the whole island Neolithic, to $89\pm4\%$ in the whole island C/EBA. It declines non-significantly to $79\pm9\%$ in the MBA and LBA (from this time onward restricting to England and Wales because of the autosomal evidence of a change in EEF ancestry in the south but not the north). It further declines to $68\pm4\%$ in the IA, a significant reduction relative to the C/EBA ($P=0.014$ by a two-sided chi-square contingency test). There is additional reduction from this time to the present, when the proportion is $43\pm3\%$ in Wales and the west of England ($P=5\times10^{-6}$ for a reduction relative to the IA), and $14\pm2\%$ in the center and east of England ($P=3\times10^{-32}$ for a reduction relative to the IA).

Extended Data Fig. 6 Version of Fig. 3a contrasting Kent to the rest of southern Britain.

We show the period 2450-1 BCE. Each point corresponds to a single individual and we show means and one standard error bars from a Block Jackknife. All the high EEF outliers during the M-LBA are from Kent—the part of the island closest to France—and in addition all the individuals from 1000-875 BCE from the group of samples showing the ramp-up from MBA to IA levels of EEF ancestry are from Kent (5 from Cliffs End Farm and 3 from East Kent Access Road). This suggests the possibility that this small region was the gateway for migration to Britain during the M-LBA. Further sampling from the rest of Britain during the M-LBA is critical in order to understand the dynamics of how this ancestry spread more broadly. However, the fact that the only sample from the second half of the LBA that is not from Kent—I12624 from Blackberry Field in Potterne in Wiltshire at 950-750 BCE—already has a proportion of EEF ancestry typical of the IA in southern Britain—suggests that this ancestry began spreading more broadly by the second half of the LBA.

Extended Data Table 1 Ancestry change over time in Britain

Extended Data Table 2 Fine genetic structure in Iron Age Britain

Supplementary information

Supplementary Information

This file contains supplementary sections 1–8 (see SI guide on page 1 for TOC).

Reporting Summary

Peer Review File

Supplementary Tables (S1–S9)

Genotype Dataset

Rights and permissions

Reprints and Permissions

About this article

Cite this article

Patterson, N., Isakov, M., Booth, T. *et al.* Large-scale migration into Britain during the Middle to Late Bronze Age. *Nature* **601**, 588–594 (2022).
<https://doi.org/10.1038/s41586-021-04287-4>

- Received: 31 December 2020
- Accepted: 29 November 2021
- Published: 22 December 2021

- Issue Date: 27 January 2022
- DOI: <https://doi.org/10.1038/s41586-021-04287-4>

Share this article

Anyone you share the following link with will be able to read this content:

[Get shareable link](#)

Sorry, a shareable link is not currently available for this article.

[Copy to clipboard](#)

Provided by the Springer Nature SharedIt content-sharing initiative

Further reading

- [**Bronze Age genomes reveal migration to Britain**](#)
 - Daniel G. Bradley

Nature (2022)

[**Bronze Age genomes reveal migration to Britain**](#)

- Daniel G. Bradley

News & Views 22 Dec 2021

This article was downloaded by **calibre** from <https://www.nature.com/articles/s41586-021-04287-4>

- Article
- [Published: 22 December 2021](#)

Spatial maps in piriform cortex during olfactory navigation

- [Cindy Poo](#) ORCID: [orcid.org/0000-0003-1698-8394¹](https://orcid.org/0000-0003-1698-8394),
- [Gautam Agarwal²](#),
- [Niccolò Bonacchi¹](#) &
- [Zachary F. Mainen](#) ORCID: [orcid.org/0000-0001-7913-9109¹](https://orcid.org/0000-0001-7913-9109)

[Nature](#) volume **601**, pages 595–599 (2022)

- 6488 Accesses
- 255 Altmetric
- [Metrics details](#)

Subjects

- [Olfactory cortex](#)
- [Sensory processing](#)

Abstract

Odours are a fundamental part of the sensory environment used by animals to guide behaviours such as foraging and navigation^{1,2}. Primary olfactory (piriform) cortex is thought to be the main cortical region for encoding odour identity^{3,4,5,6,7,8}. Here, using neural ensemble recordings in freely moving rats performing an odour-cued spatial choice task, we show that posterior piriform cortex neurons carry a robust spatial representation of the

environment. Piriform spatial representations have features of a learned cognitive map, being most prominent near odour ports, stable across behavioural contexts and independent of olfactory drive or reward availability. The accuracy of spatial information carried by individual piriform neurons was predicted by the strength of their functional coupling to the hippocampal theta rhythm. Ensembles of piriform neurons concurrently represented odour identity as well as spatial locations of animals, forming an odour–place map. Our results reveal a function for piriform cortex in spatial cognition and suggest that it is well-suited to form odour–place associations and guide olfactory-cued spatial navigation.

This is a preview of subscription content

Access options

Subscribe to nature+

Get immediate online access to the entire Nature family of 50+ journals

\$29.99

monthly

[Subscribe](#)

Subscribe to Journal

Get full journal access for 1 year

\$199.00

only \$3.90 per issue

[Subscribe](#)

All prices are NET prices.

VAT will be added later in the checkout.

Tax calculation will be finalised during checkout.

Buy article

Get time limited or full article access on ReadCube.

\$32.00

[Buy](#)

All prices are NET prices.

Additional access options:

- [Log in](#)
- [Learn about institutional subscriptions](#)

Fig. 1: Odour-cued allocentric spatial choice task.

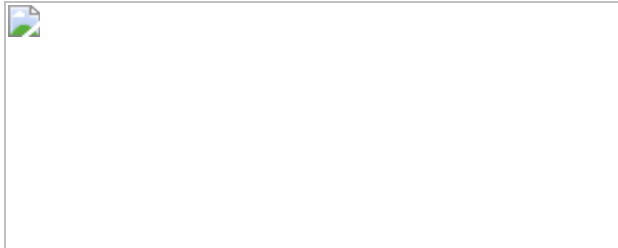


Fig. 2: Spatial representations in the piriform cortex.



Fig. 3: Spatial representations are robust and stable across task events.

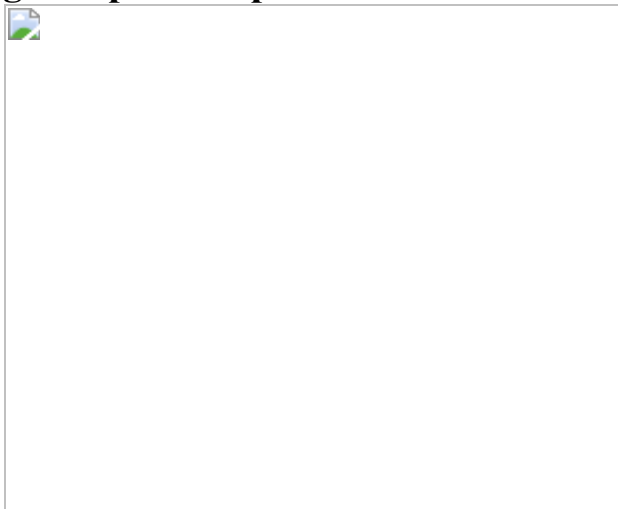
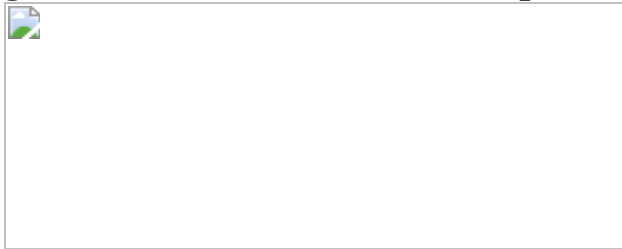


Fig. 4: Location neurons are coupled to hippocampal theta rhythms.



Data availability

Data will be made available upon reasonable request to the corresponding authors.

References

1. 1.

Baker, K. L. et al. Algorithms for olfactory search across species. *J. Neurosci.* **38**, 9383–9389 (2018).

2. 2.

Jacobs, L. F. From chemotaxis to the cognitive map: the function of olfaction. *Proc. Natl Acad. Sci. USA* **109**, 10693–10700 (2012).

3. 3.

Miura, K., Mainen, Z. F. & Uchida, N. Odor representations in olfactory cortex: distributed rate coding and decorrelated population activity. *Neuron* **74**, 1087–1098 (2012).

4. 4.

Poo, C. & Isaacson, J. S. Odor representations in olfactory cortex: ‘sparse’ coding, global inhibition, and oscillations. *Neuron* **62**, 850–861 (2009).

5. 5.

Illig, K. R. & Haberly, L. B. Odor-evoked activity is spatially distributed in piriform cortex. *J. Comp. Neurol.* **457**, 361–373 (2003).

6. 6.

Haberly, L. B. Single unit responses to odor in the prepyriform cortex of the rat. *Brain Res.* **12**, 481–484 (1969).

7. 7.

Rennaker, R. L., Chen, C.-F. F., Ruyle, A. M., Sloan, A. M. & Wilson, D. A. Spatial and temporal distribution of odorant-evoked activity in the piriform cortex. *J. Neurosci.* **27**, 1534–1542 (2007).

8. 8.

Stettler, D. D. & Axel, R. Representations of odor in the piriform cortex. *Neuron* **63**, 854–864 (2009).

9. 9.

Gire, D. H., Kapoor, V., Arrighi-Allisan, A., Seminara, A. & Murthy, V. N. Mice develop efficient strategies for foraging and navigation using complex natural stimuli. *Curr. Biol.* **26**, 1261–1273 (2016).

10. 10.

Eichenbaum, H. Using olfaction to study memory. *Ann. NY Acad. Sci.* **855**, 657–669 (1998).

11. 11.

Johnson, D. M. G., Illig, K. R., Behan, M. & Haberly, L. B. New features of connectivity in piriform cortex visualized by intracellular injection of pyramidal cells suggest that ‘primary’ olfactory cortex functions like ‘association’ cortex in other sensory systems. *J. Neurosci.* **20**, 6974–6982 (2000).

12. 12.

Franks, K. M. et al. Recurrent circuitry dynamically shapes the activation of piriform cortex. *Neuron* **72**, 49–56 (2011).

13. 13.

Hagiwara, A., Pal, S. K., Sato, T. F., Wienisch, M. & Murthy, V. N. Optophysiological analysis of associational circuits in the olfactory cortex. *Front. Neural Circuits* **6**, 18 (2012).

14. 14.

Hasselmo, M. E. & Bower, J. M. Afferent and association fiber differences in short-term potentiation in piriform (olfactory) cortex of the rat. *J. Neurophysiol.* **64**, 179–190 (1990).

15. 15.

Poo, C. & Isaacson, J. S. A major role for intracortical circuits in the strength and tuning of odor-evoked excitation in olfactory cortex. *Neuron* **72**, 41–48 (2011).

16. 16.

Haberly, L. B. & Price, J. L. Association and commissural fiber systems of the olfactory cortex of the rat. I. Systems originating in the piriform cortex and adjacent areas. *J. Comp. Neurol.* **178**, 711–740 (1978).

17. 17.

Haberly, L. B. & Bower, J. M. Olfactory cortex: model circuit for study of associative memory? *Trends Neurosci.* **12**, 258–264 (1989).

18. 18.

Hasselmo, M. E. & Linster, C. in *Models of Cortical Circuits* (eds Ulinski, P. S. et al.) 525–560 (Springer, 1999).

19. 19.

Barkai, E., Bergman, R. E., Horwitz, G. & Hasselmo, M. E. Modulation of associative memory function in a biophysical simulation of rat piriform cortex. *J. Neurophysiol.* **72**, 659–677 (1994).

20. 20.

Haberly, L. B. Parallel-distributed processing in olfactory cortex: new insights from morphological and physiological analysis of neuronal circuitry. *Chem. Senses* **26**, 551–576 (2001).

21. 21.

Wang, L. et al. Cell-type-specific whole-brain direct inputs to the anterior and posterior piriform cortex. *Front. Neural Circuits* <https://doi.org/10.3389/fncir.2020.00004> (2020).

22. 22.

Bolding, K. A. & Franks, K. M. Complementary codes for odor identity and intensity in olfactory cortex. *eLife* **6**, e22630 (2017).

23. 23.

Roland, B., Deneux, T., Franks, K. M., Bathellier, B. & Fleischmann, A. Odor identity coding by distributed ensembles of neurons in the mouse olfactory cortex. *eLife* **6**, e26337 (2017).

24. 24.

Iurilli, G. & Datta, S. R. Population coding in an innately relevant olfactory area. *Neuron* **93**, 1180–1197.e7 (2017).

25. 25.

Calu, D. J., Roesch, M. R., Stalnaker, T. A. & Schoenbaum, G. Associative encoding in posterior piriform cortex during odor discrimination and reversal learning. *Cereb. Cortex* **17**, 1342–1349 (2007).

26. 26.

Haddad, R. et al. Olfactory cortical neurons read out a relative time code in the olfactory bulb. *Nat. Neurosci.* **16**, 949–957 (2013).

27. 27.

Zelano, C., Mohanty, A. & Gottfried, J. A. Olfactory predictive codes and stimulus templates in piriform cortex. *Neuron* **72**, 178–187 (2011).

28. 28.

Howard, J. D., Plailly, J., Grueschow, M., Haynes, J.-D. & Gottfried, J. A. Odor quality coding and categorization in human posterior piriform cortex. *Nat. Neurosci.* **12**, 932–938 (2009).

29. 29.

Wang, D. et al. Task–demand-dependent neural representation of odor information in the olfactory bulb and posterior piriform cortex. *J. Neurosci.* **39**, 10002–10018 (2019).

30. 30.

Lak, A. et al. Reinforcement biases subsequent perceptual decisions when confidence is low, a widespread behavioral phenomenon. *eLife* **9**, e49834 (2020).

31. 31.

Wallace, D. G., Gorny, B. & Whishaw, I. Q. Rats can track odors, other rats, and themselves: implications for the study of spatial behavior. *Behav. Brain Res.* **131**, 185–192 (2002).

32. 32.

Millman, D. J. & Murthy, V. N. Rapid learning of odor-value association in the olfactory striatum. *J. Neurosci.* **40**, 4335–4347 (2020).

33. 33.

Tolman, E. C. Cognitive maps in rats and men. *Psychol. Rev.* **55**, 189 (1948).

34. 34.

O'Keefe, J. & Nadel, L. *The Hippocampus as a Cognitive Map* (Clarendon Press, 1978).

35. 35.

O'Keefe, J. & Recce, M. L. Phase relationship between hippocampal place units and the EEG theta rhythm. *Hippocampus* **3**, 317–330 (1993).

36. 36.

Kepcs, A., Uchida, N. & Mainen, Z. F. Rapid and precise control of sniffing during olfactory discrimination in rats. *J. Neurophysiol.* **98**, 205–213 (2007).

37. 37.

Martin, C., Beshel, J. & Kay, L. M. An olfacto-hippocampal network is dynamically involved in odor-discrimination learning. *J. Neurophysiol.* **98**, 2196–2205 (2007).

38. 38.

Schoonover, C. E., Ohashi, S. N., Axel, R. & Fink, A. J. P. Representational drift in primary olfactory cortex. *Nature* **594**, 541–546 (2021).

39. 39.

Aqrabawi, A. J. & Kim, J. C. Hippocampal projections to the anterior olfactory nucleus differentially convey spatiotemporal information during episodic odour memory. *Nat. Commun.* **9**, 2735 (2018).

40. 40.

Igarashi, K. M., Lu, L., Colgin, L. L., Moser, M.-B. & Moser, E. I. Coordination of entorhinal–hippocampal ensemble activity during associative learning. *Nature* **510**, 143–147 (2014).

41. 41.

Agster, K. L. & Burwell, R. D. Cortical efferents of the perirhinal, postrhinal, and entorhinal cortices of the rat. *Hippocampus* **19**, 1159–1186 (2009).

42. 42.

Chapuis, J. et al. Lateral entorhinal modulation of piriform cortical activity and fine odor discrimination. *J. Neurosci.* **33**, 13449–13459 (2013).

43. 43.

Allen Institute for Brain Science. *Allen Mouse Brain Connectivity Atlas* <https://connectivity.brain-map.org/> (2011).

44. 44.

Insausti, R., Herrero, M. T. & Witter, M. P. Entorhinal cortex of the rat: cytoarchitectonic subdivisions and the origin and distribution of cortical efferents. *Hippocampus* **7**, 146–183 (1997).

45. 45.

Stachenfeld, K. L., Botvinick, M. M. & Gershman, S. J. The hippocampus as a predictive map. *Nat. Neurosci.* **20**, 1643–1653 (2017).

46. 46.

Anderson, M. I. & Jeffery, K. J. Heterogeneous modulation of place cell firing by changes in context. *J. Neurosci.* **23**, 8827 (2003).

47. 47.

Moita, M. A. P., Rosis, S., Zhou, Y., LeDoux, J. E. & Blair, H. T. Hippocampal place cells acquire location-specific responses to the conditioned stimulus during auditory fear conditioning. *Neuron* **37**, 485–497 (2003).

48. 48.

Knierim, J. J. Dynamic interactions between local surface cues, distal landmarks, and intrinsic circuitry in hippocampal place cells. *J. Neurosci.* **22**, 6254–6264 (2002).

49. 49.

Radvansky, B. A. & Dombeck, D. A. An olfactory virtual reality system for mice. *Nat. Commun.* **9**, 839 (2018).

50. 50.

Fischler-Ruiz, W. et al. Olfactory landmarks and path integration converge to form a cognitive spatial map. *Neuron* 10.1016/j.neuron.2021.09.055 (2021).

51. 51.

Muller, R. U. & Kubie, J. L. The effects of changes in the environment on the spatial firing of hippocampal complex-spike cells. *J. Neurosci.* **7**, 1951–1968 (1987).

52. 52.

Moita, M. A. P., Rosis, S., Zhou, Y., LeDoux, J. E. & Blair, H. T. Putting fear in its place: remapping of hippocampal place cells during fear conditioning. *J. Neurosci.* **24**, 7015–7023 (2004).

53. 53.

Saleem, A. B., Diamanti, E. M., Fournier, J., Harris, K. D. & Carandini, M. Coherent encoding of subjective spatial position in visual cortex and hippocampus. *Nature* **562**, 124–127 (2018).

54. 54.

Town, S. M., Brimijoin, W. O. & Bizley, J. K. Egocentric and allocentric representations in auditory cortex. *PLoS Biol.* **15**, e2001878 (2017).

55. 55.

Fiser, A. et al. Experience-dependent spatial expectations in mouse visual cortex. *Nat. Neurosci.* **19**, 1658–1664 (2016).

56. 56.

Choi, G. B. et al. Driving opposing behaviors with ensembles of piriform neurons. *Cell* **146**, 1004–1015 (2011).

57. 57.

Uchida, N. & Mainen, Z. F. Speed and accuracy of olfactory discrimination in the rat. *Nat. Neurosci.* **6**, 1224–1229 (2003).

58. 58.

Felsen, G. & Mainen, Z. F. Neural substrates of sensory-guided locomotor decisions in the rat superior colliculus. *Neuron* **60**, 137–148 (2008).

59. 59.

Restle, F. Discrimination of cues in mazes: a resolution of the ‘place-vs.-response’ question. *Psychol. Rev.* **64**, 217 (1957).

60. 60.

Lopes, G. et al. Bonsai: an event-based framework for processing and controlling data streams. *Front. Neuroinform.* **9**, 7 (2015).

61. 61.

Hill, D. N., Mehta, S. B. & Kleinfeld, D. Quality metrics to accompany spike sorting of extracellular signals. *J. Neurosci.* **31**, 8699–8705 (2011).

62. 62.

Dayan, P. & Abbott, L. F. *Theoretical Neuroscience: Computational and Mathematical Modeling of Neural Systems* (MIT Press, 2001).

63. 63.

Green, D. M., Swets, J. A. et al. *Signal Detection Theory and Psychophysics* Vol. 1 (Wiley, 1966).

64. 64.

Rolls, E. T. & Tovee, M. J. Sparseness of the neuronal representation of stimuli in the primate temporal visual cortex. *J. Neurophysiol.* **73**, 713–726 (1995).

65. 65.

Willmore, B. & Tolhurst, D. J. Characterizing the sparseness of neural codes. *Network* **12**, 255–270 (2001).

66. 66.

Fan, R.-E., Chang, K.-W., Hsieh, C.-J., Wang, X.-R. & Lin, C.-J. LIBLINEAR: a library for large linear classification. *J. Mach. Learn. Res.* **9**, 1871–1874 (2008).

67. 67.

Richard, G. R. et al. Speed modulation of hippocampal theta frequency correlates with spatial memory performance. *Hippocampus* **23**, 1269–1279 (2013).

68. 68.

Kay, L. M., Beshel, J., Brea, J. & Martin, C. Olfactory oscillations: the what, how and what for. *Trends Neurosci.* **32**, 207–214 (2009).

69. 69.

Litaudon, P., Amat, C., Bertrand, B., Vigouroux, M. & Buonviso, N. Piriform cortex functional heterogeneity revealed by cellular responses to odours. *Eur. J. Neurosci.* **17**, 2457–2461 (2003).

70. 70.

Mitra, P. & Bokil, H. *Observed Brain Dynamics* (Oxford Univ. Press, 2007).

Acknowledgements

We thank J. J. Paton, B. A. Atallah, L. L. Glickfeld and J. B. Hales for comments on the manuscript; members of the Mainen laboratory, E. Lottem, M. Murakami, M. G. Bergomi, C. Linster, M. Moita, A. Fleischmann, K. M. Franks, S. R. Datta, C. E. Schoonover, A. J. P. Fink, and R. Axel for helpful discussions; A. S. Cruz and A. C. Rato for assistance with animal training; L. M. Frank and members of the Frank laboratory for experimental advice and assistance; G. Costa for scientific illustrations; Champalimaud Research Hardware Platform for custom components used in the behavioural task and recordings; and Champalimaud Vivarium Platform for animal care. We acknowledge Champalimaud Foundation (Z.F.M.), European Research Council (Advanced Investigator Grant 671251, Z.F.M.), Human Frontier Science Program (LT000402/2012, C.P.), Fundação para a Ciência e a Tecnologia (FCT-PTDC/MED-NEU/28509/2017, C.P.), and Helen Hay Whitney Foundation (C.P.) for financial support. This work was supported by

Portuguese national funds, through Fundação para a Ciência e a Tecnologia (FCT)—UIDB/04443/2020, CONGENTO, co-financed by Lisboa Regional Operational Programme (Lisboa2020), and FCT LISBOA-01-0145-FEDER-022170.

Author information

Affiliations

1. Champalimaud Foundation, Lisbon, Portugal

Cindy Poo, Niccolò Bonacchi & Zachary F. Mainen

2. W. M. Keck Science Center, The Claremont Colleges, Claremont, CA, USA

Gautam Agarwal

Contributions

The project was originally conceptualized by C.P. and Z.F.M. and further developed in collaboration with N.B. The behavioural paradigm was developed and designed by C.P., N.B. and Z.F.M. Task-related hardware was developed and constructed by N.B. and C.P. Task-related software was developed and implemented by N.B. Animal training, behaviour data collection and behavioural data analysis was performed by C.P. Neural recordings were performed by C.P. Neural data analysis was performed by C.P. and G.A. The manuscript was written by C.P., G.A. and Z.F.M. and edited and reviewed by all authors.

Corresponding authors

Correspondence to [Cindy Poo](#) or [Zachary F. Mainen](#).

Ethics declarations

Competing interests

The authors declare no competing interests.

Peer review information

Nature thanks the anonymous reviewer(s) for their contribution to the peer review of this work.

Additional information

Publisher's note Springer Nature remains neutral with regard to jurisdictional claims in published maps and institutional affiliations.

Extended data figures and tables

[Extended Data Fig. 1 Tetrode lesion sites and population summary of pPCx and CA1 neurons.](#)

(a) Tetrode lesion sites for 3 recorded rats in pPCx. See full methods for targeting and verification of tetrode recording sites. Due to the wide range of tetrode lesion sites (from -1.5 mm to -2.5 mm bregma), lesion sites from multiple histological sections were summarized onto 3 representative atlas sections. **(b)** Summary PETH for all pPCx ($n = 995$) neurons recorded. Spike timing was aligned to odour onset (left) and goal poke-in (right). Neurons were sorted based on their activity during 1 s time window after odour onset in both left and right panels. For each neuron, the mean z-scored rate during a 2 s time window prior to alignment time point was subtracted from the entire PETH. **(c)** Tetrode lesion sites for 3 recorded rats in dorsal CA1. See Full Methods for targeting and verification of tetrode recording sites. **(d)** Summary PETH for all CA1 ($n = 154$) neurons recorded.

[Extended Data Fig. 2 Correct and error trial behavior in odour-cued spatial choice task.](#)

(a) Odour sampling duration in 3 recorded rats. A minimum of 150 ms of odour sampling was enforced. Black: correct trials, 0.519 ± 0.02 s. Red: error trials, 0.448 ± 0.04 s. **(b)** Navigation duration in 3 recorded rats, as defined by time between initiation (odour) port poke-out and goal port poke-in. Goal ports were only active (reward available) after a 1.5 s delay after rats poke out of initiation ports. Black: correct trials, 3.67 ± 0.15 s. Red: error trials, 5.35 ± 0.8 s. **(c)** Rats performed better for trials in which goal location indicated by the odour cue was congruent with odour sampling location (stay trials). $n = 3$ rats, ANOVA, $p = 0.01$, Mean \pm S.D. **(d)** Actions performed for error trials. ANOVA, $p = 0.07$. Mean \pm S.D.

Extended Data Fig. 3 pPCx location selectivity remains stable across recording blocks.

(a) Rat position on the maze during two blocks within the same recording session. **(b-d)**. Occupancy normalized firing rate heat map, PETH, and raster plots associated with example cells 1-3 in Fig 2a–c. PETH and raster plots were aligned to initiation port poke-in and sorted by location. **(e)**. Z-scored mean firing rate of neurons for different port locations across blocks. **(f)** Stability of port location representation between the two blocks was calculated the pairwise Pearson's correlation coefficient for population activity across different locations in these two blocks. Values along the diagonal band in the correlation coefficient matrix represent the similarity of the pPCx population response to the same location in two recording blocks. **(f, top)** Similarity matrix obtained by computing the pairwise Pearson's correlation coefficients between locations population response vectors for blocks 1 and 2 of example session shown in (a-e). Coefficients along the diagonal band are significantly higher than off-diagonal ($r_{\text{diag}} = 0.80 \pm 0.05$, $r_{\text{offdiag}} = 0.54 \pm 0.09$, Wilcoxon rank-sum test, $p < 0.01$), indicating that location representations were stable between blocks. **(f, bottom)**. Same analysis as in the top panel but for all pPCx neurons recorded ($r_{\text{diag}} = 0.81 \pm 0.02$, $r_{\text{offdiag}} = 0.47 \pm 0.02$, Wilcoxon rank sum test, $p < 0.001$, $n = 44$ sessions, 995 neurons). We conclude from these data that uncontrolled odours were unlikely to account for the pPCx location representations observed.

Extended Data Fig. 4 Summary of pPCx and CA1 response properties for odours and port locations in task.

(a, top) Firing rate for individual pPCx neurons throughout recording sessions. Non-selective neurons: median = 0.94, range = 0.03 – 21.48 Hz, n = 531 neurons; selective neurons (for either odour or location): median = 1.95, range = 0.04 – 27.49 Hz, n = 464 neurons. **(a, bottom)** Firing rate of neurons grouped by selectivity properties. Odour-selective only neurons (Odour), n = 120 neurons, median = 1.93, range = 0.05 – 17.84 Hz. Location-selective only neurons (Loc.), n = 238, median = 2.06, range = 0.04 – 27.49 Hz. Odour and location selective neurons (Both): n = 106, median = 1.88, range = 0.14 – 17.41 Hz. **(b, top)** Firing rates for individual neurons across 4 odour identities during 0 – 1.0 s post odour onset. Neurons are grouped by selectivity properties. Red tick: median; edges of the bar indicate the 25th and 75th percentiles; circles: outliers. **(b, bottom)** Same as (b, top) but across port locations. **(c, left)** Fraction of recorded pPCx neurons in a session that was activated by different odours. Activation was measured by comparing mean firing rate for 1 s after odour onset time compared to a 1 s baseline immediately preceding odour onset (n = 33 sessions). Wilcoxon rank-sum test, $p < 0.05$, corrected for multiple comparisons (see Full Methods). **(c, right)** Histogram of number of odours that activate pPCx cells in a session. **(d)** Similar to (c) but for port locations. Location selectivity of individual neurons was obtained from comparing firing rates in 20 x 20 cm position bins centered around individual port locations on maze using ANOVA-test, $p < 0.01$. **(e)** Sparseness across odour identity for simultaneously recorded populations. Population sparseness = 0.36 ± 0.09 ; lifetime sparseness = 0.21 ± 0.05 , Mean \pm S.D. (n = 33 sessions). **(f)** Similar to (e) but for port locations. Population sparseness = 0.40 ± 0.12 ; lifetime sparseness = 0.29 ± 0.06 . **(g)** Coefficient of variation for odours aligned to odour onset. Trial-to-trial coefficient of variation for each neuron was calculated for different odour trials and averaged. **(h)** Similar to (g) but calculated for different port locations. **(i-o)** Same analysis as **(a-h)** for CA1 population. **(i, top)** Non-selective neurons: median = 1.22, range = 0.12 – 38.15 Hz, n = 88 neurons; selective neurons (for either odour or location): median = 2.35, range = 0.11 – 36.11 Hz, n = 67 neurons. **(i, bottom)** Location-selective only neurons (Loc.), n = 44, median = 1.84, range = 0.11 – 36.11 Hz. Odour and location selective neurons (Both): n =

23, median = 3.20, range = 0.26 – 20.23 Hz. (m) Population sparseness = 0.11 ± 0.05 ; lifetime sparseness = 0.16 ± 0.10 , Mean \pm S.D. (n = 15 sessions). (n) Population sparseness = 0.13 ± 0.08 ; lifetime sparseness = 0.20 ± 0.10 .

Extended Data Fig. 5 Population correlations matrices and single cell decoding accuracies.

(a) Full similarity matrix of correlation coefficients of all odour and location population vector pairs for all recorded pPCx (n = 995) and CA1 (n = 154) neurons. Off-diagonal correlation coefficients on the lower right quadrants of each matrix show that CA1 location representations are more dissimilar from each other than pPCx location representations. Off-diagonal correlation coefficients on the top right and lower left quadrants show that there were no systematic relationship population responses for individual odours and locations. (b) Population correlation coefficients for odour and locations were shown in similarity matrices. Odour: top left quadrant; location: bottom right quadrant, excluding autocorrelation coefficients (diagonal band). Wilcoxon rank-sum test, ** p < 0.01, *** p < 0.001. (c) L1 regularization pseudo-population decoding curves in Fig. 2g (black lines) were overlaid on the same x-axis for comparison. (d) Cumulative distribution function of single cell decoding accuracies for all recorded pPCx (left) and CA1 (right) neurons show that individual pPCx neurons location is significantly better coding than odour. Kolmogorov–Smirnov test, *** p < 0.001.

Extended Data Fig. 6 Pseudo-population decoding.

(a) Odour decoding accuracy for a simultaneously recorded pPCx population (example session from Fig. 2a–d) using a wide range of time windows aligned to odour onset time (left), or first respiration after odour onset (right). The black and red dots indicate time windows used for black and red lines in (c), respectively. (b) Location decoding accuracy aligned to initiation port poke-in time across a wide range of time windows. (c) Pseudo-population decoding of odour identity with different time windows and regularization. Red and purple lines use L2 regularization, while black and grey use L1 regularization (shown as black and grey lines in Fig. 2g).

By increasing the sparsity of the L1-decoder (scanning the ‘cost’ parameter over the range $2^{-7:8}$) and plotting decoding accuracy as a function of the number of contributing neurons (# of neurons with non-zero weights in the decoder), we can minimize the contribution of uninformative neurons. Here, the x-axis indicates the number of neurons being used by the decoder (i.e. neurons with non-zero kernel weights), which was controlled by changing the L1 penalty. When this penalty is large, the decoder selectively uses only the most informative neurons, leading to a much steeper rise than seen for the L2 regularization pseudo-population curves, which sample neurons randomly. Using this sparse L1-decoding approach, it is clear that odour identity can accurately be decoded from a small population of pPCx neurons (90% decoding accuracy for ~ 150 neurons). Dotted line indicates 90% accuracy. Chance level is 25%. **(d)** Same analysis as in (c) but for port locations. Note that while it conveys that relatively few neurons are needed to encode odour information, the steepness of the grey curve is sensitive to the number of recorded neurons (since a larger pool is more likely to contain an informative neuron). **(e, f)** Yellow lines show pseudo-population decoding using neurons identified by auROC (see Methods) as responsive to either odour or location. Black and grey lines are the same as those plotted in **(c, d)**, and Fig. 2g, reproduced here for ease of comparison.

Extended Data Fig. 7 Location decoding accuracy is independent of olfactory drive.

(a) Distance from port locations aligned to odour onset. **(b)** Population decoding accuracy for odour and port locations across time for simultaneously recorded pPCx ($n = 33$ sessions; 8–53 cells/session) . Pre-odour decoding used population activity from 1.5 s before odour onset; post-odour decoding used population activity 1.5 s after odour onset. Cross-validated, chance is 25%. The filled-in data points indicate the example session shown in Fig. 2. **(c)** Same analysis as in (b) for simultaneously recorded CA1 population ($n=12$ sessions, 3–14 neurons/session).

Extended Data Fig. 8 Example cells and location decoding for correct and error trials.

(a) PETH and rasters for 4 example neurons aligned to initiation port poke-in (left) and goal poke-in time (right). Black: correct trials; red: error trials. **(b)** Firing rate heat maps for example cells. Heat maps were normalized to occupancy and generated by concatenating all trials from -1 to 2 s window around initiation and goal port entry. Peak firing rates noted to the right of heat maps. **(c)** Location decoding accuracy of a classifier trained on neural activity $-0.5 - 0.5$ s around initiation port poke-in for correct trials. The classifier was tested on neural activity $-0.5 - 0.5$ s around initiation and goal port poke-ins for correct (black) and error (red) trials (cross-validated, mean \pm S.E.M., $n = 33$ sessions; 30 ± 13 neurons/session).

Extended Data Fig. 9 Sniffing and hippocampal theta-band activity in task.

(a) Sniffing behavior on maze in one example session. Heat map of basal sniffing behavior (2 Hz power) and high frequency active sniffing behavior (7-10 Hz power) on maze. Colorbar is power. **(b)** Sniffing behavior for one example session. Sniff phase was time-locked to odour port poke-in. Gray color is inhalation, white is exhalation. **(c)** Coherence between CA1-LFP and sniffing. Time is aligned to odour onset. Colorbar is coherence. **(d, top)** Average coherence of spike of all pPCx neurons to sniff (left) and CA1-LFP (right). Time is aligned to odour onset time. **(d, bottom)** Average coherence of spike of all recorded CA1 neurons to sniffing (left) and CA1-LFP (right).

Extended Data Fig. 10 Preferential coupling of odour cells to sniffing and location cells to hippocampal theta.

(a) Odour and location decoding accuracy of individual neurons. Neurons decoded odour only (red), location only (cyan), both (magenta), or neither (open circles). Decoding significance was defined as accuracy greater than the 95th percentile of classifiers trained on shuffled labels. **(b)** Mean difference in coherence between the ‘top n’ best odour decoding neuron vs ‘top n’ best location decoding neuron. Top panels of each ‘top n’ analysis show differences in spike-sniff coherence, while bottom panels show differences in spikes-to-CA1-LFP coherence. Red pixels indicate frequency-time bins in which spikes from odour decoding cells are

significantly more coherent than spikes from location decoding neurons, while blue pixels indicate the bins in which location cells are more significantly coherent than odour cells. Gray scale is coherence. (see Full Methods).

Extended Data Fig. 11 Noise correlations between pPCx neurons are consistent with distinct functional subgroups.

Noise correlations between 3 groups of neurons (6 group pairings): odour-selective (O), location-selective (L), non-selective (N) neurons. Overall noise correlation between groups increased with longer time windows. O-O and L-L correlations are higher than for N-N. Mean \pm S.E.M., ** $p < 0.01$, *** $p < 0.001$.

Supplementary information

Supplementary Information

This file contains Supplementary Discussion.

Reporting Summary

Supplementary Video 1

Supplementary Video. Three example trials of a rat behaving on odour-cued spatial navigation task.

Rights and permissions

Reprints and Permissions

About this article

Cite this article

Poo, C., Agarwal, G., Bonacchi, N. *et al.* Spatial maps in piriform cortex during olfactory navigation. *Nature* **601**, 595–599 (2022).
<https://doi.org/10.1038/s41586-021-04242-3>

- Received: 16 October 2020
- Accepted: 12 November 2021
- Published: 22 December 2021
- Issue Date: 27 January 2022
- DOI: <https://doi.org/10.1038/s41586-021-04242-3>

Share this article

Anyone you share the following link with will be able to read this content:

[Get shareable link](#)

Sorry, a shareable link is not currently available for this article.

[Copy to clipboard](#)

Provided by the Springer Nature SharedIt content-sharing initiative

This article was downloaded by **calibre** from <https://www.nature.com/articles/s41586-021-04242-3>

- Article
- Open Access
- [Published: 02 December 2021](#)

Human blastoids model blastocyst development and implantation

- [Harunobu Kagawa](#) [ORCID: orcid.org/0000-0003-0436-3805¹](#)^{nal},
- [Alok Javali](#)¹^{nal},
- [Heidar Heidari Khoei](#)¹^{nal},
- [Theresa Maria Sommer](#)¹,
- [Giovanni Sestini](#) [ORCID: orcid.org/0000-0002-6643-7585¹](#),
- [Maria Novatchkova](#)^{1,2},
- [Yvonne Scholte op Reimer](#) [ORCID: orcid.org/0000-0002-1656-9221¹](#),
- [Gaël Castel](#) [ORCID: orcid.org/0000-0002-7563-1179³](#),
- [Alexandre Bruneau](#)³,
- [Nina Maenhoudt](#) [ORCID: orcid.org/0000-0002-5523-3819⁴](#),
- [Jenna Lammers](#)^{3,5},
- [Sophie Loubersac](#)^{3,5},
- [Thomas Freour](#) [ORCID: orcid.org/0000-0002-7243-7709^{3,5}](#),
- [Hugo Vankelecom](#) [ORCID: orcid.org/0000-0002-2251-7284⁴](#),
- [Laurent David](#) [ORCID: orcid.org/0000-0003-3594-0353^{3,6}](#) &
- [Nicolas Rivron](#) [ORCID: orcid.org/0000-0003-1590-5964¹](#)

[Nature](#) volume 601, pages 600–605 (2022)

- 17k Accesses
- 5 Citations
- 1201 Altmetric
- [Metrics details](#)

Subjects

- [Embryonic induction](#)

- [Embryonic stem cells](#)

Abstract

One week after fertilization, human embryos implant into the uterus. This event requires the embryo to form a blastocyst consisting of a sphere encircling a cavity lodging the embryo proper. Stem cells can form a blastocyst model that we called a blastoid¹. Here we show that naive human pluripotent stem cells cultured in PXGL medium² and triply inhibited for the Hippo, TGF- β and ERK pathways efficiently (with more than 70% efficiency) form blastoids generating blastocyst-stage analogues of the three founding lineages (more than 97% trophectoderm, epiblast and primitive endoderm) according to the sequence and timing of blastocyst development. Blastoids spontaneously form the first axis, and we observe that the epiblast induces the local maturation of the polar trophectoderm, thereby endowing blastoids with the capacity to directionally attach to hormonally stimulated endometrial cells, as during implantation. Thus, we propose that such a human blastoid is a faithful, scalable and ethical model for investigating human implantation and development^{3,4}.

[Download PDF](#)

Main

A model of the human blastocyst would support scientific and medical progress. Its ability to predict human development will, however, depend on its ability to reproduce the sequences of blastocyst cellular determination and morphogenesis effectively, faithfully, and according to the developmental sequence and pace. Such modelling would ensure the formation of cells that reflect the blastocyst stage as a starting point to recapitulate aspects of subsequent developmental steps, including implantation. During this year, diverse ways of forming models of the human blastocyst have been proposed^{5,6,7,8,9}. However, the cells generated often do not match those of the blastocyst^{5,7,8,9} (at 5–7 days post fertilization (dpf)) and have been proposed to rather reflect later developmental stages, including gastrulation (E14) and germ layers (mesoderm and endoderm) stages¹⁰. Here we form a model of the human blastocyst that specifically generates and spatially patterns cellular analogues of the blastocyst stage with similar developmental sequence and pace, which enables the model to mimic aspects of implantation.

Inhibition of Hippo, ERK and TGF β pathways

At 4 dpf, the conceptus forms a morula that initiates cavitation to make a blastocyst. Blastocyst development (at 5–7 dpf) supports the generation of the three founding lineages¹¹: the epiblast (EPI), which is embryonic; trophectoderm (TE), which is extraembryonic; and primitive endoderm (PrE), which is extraembryonic (Fig. 1a). Peripheral cells become TE through inhibition of the Hippo pathway^{12,13}. Naive human pluripotent stem cells (PSCs) cultured in PXGL² efficiently form TE analogues upon inhibition of TGFβ and ERK pathways^{14,15,16}. We aggregated naive PSCs in non-adherent hydrogel microwells and inhibited these three pathways (Fig. 1b, Extended Data Fig. 1ac). Upon exposure to lysophosphatidic acid (LPA) (a Hippo pathway inhibitor), A83-01 (an inhibitor of TGFβ family receptors) and PD0325901 (an ERK inhibitor) in a chemically defined medium containing the STAT activator leukaemia inhibitory factor (LIF) and Y-27632 (a ROCK inhibitor), blastocyst-like structures formed efficiently (Fig. 1c–e, Supplementary Videos 1, 2; more than 70% efficiency, diameters 150–250 μm; full morphometric criteria are presented in Methods) and consistently (Extended Data Fig. 1d, more than 20 passages). LPA was essential for this high efficiency (Extended Data Fig. 1b–d). Within 4 days, the cell number (47 ± 9 to 129 ± 27) and overall size (65–200 μm) had increased (Extended Data Fig. 1e, f) to ranges similar to those for 5–7 dpf blastocysts¹⁷ (stages B3 to B6). TE cell analogues¹¹ (identified as GATA2⁺GATA3⁺CDX2⁺TROP2⁺) formed, proliferated (Fig. 1f–h, Extended Data Fig. 1g–l), and established adherens junctions (marked by epithelial cadherin (CDH1)), apical–basal polarity (indicated by atypical PKC (aPKC) localization) and tight junctions (marked by ZO-1; Fig. 1i, Extended Data Fig. 1m) while undergoing cycles of inflations and deflations¹⁸ (Extended Data Fig. 1n, Supplementary Video 2). Of note, all blastocyst-like structures set apart a unique inner cell cluster reflecting the EPI (OCT4⁺; 27 ± 13 cells; 26% of total cells) and PrE (GATA4⁺SOX17⁺PDGFRα⁺; 7 ± 5 cells; 7% of total cells) (Fig. 1f–h, Extended Data Fig. 1i, j, l). Multiple lines of naive human embryonic stem (ES) cells (Shef6, H9 and HNES1) and human naive induced PSCs (niPSC 16.2.b and cR-NCRM2) formed similar structures with comparably high efficiency (Fig. 1e, Extended Data Fig. 1o), whereas primed PSCs that reflect the post-implantation EPI did not (Extended Data Fig. 1p).

Fig. 1: Triply inhibited naive PSCs efficiently form human blastocyst-like structures comprising analogues of the three founding lineages.

 **figure 1**

a, A schematic of the time window of human peri-implantation development modelled by blastoids (days 5–7). M/MC, morula/morula compacted; B, blastocyst. **b**, One-step protocol of human blastocyst-like structure formation. N2B27, serum-free medium; PALLY, PD0325901 + A83-01 + LPA + hLIF + Y-27632. **c**, Phase-contrast image of

human blastocyst-like structures formed on a non-adherent hydrogel microwell array after 96 h. Each microwell is 200 μm in diameter. Scale bars, 400 μm . **d**, Phase-contrast images of representative human blastocyst-like structures harvested from microwells. Scale bars, 200 μm (top) and 100 μm (bottom). **e**, Percentages of microwells including a human blastocyst-like structure for different naive PSC lines cultured in the PALLY condition with optimized LPA concentration compared with a H9 control (Ctrl) deprived of the three inhibitors. The morphometric definition of blastocyst-like structures is provided in Methods. $n = 3$ microwell arrays; mean \pm s.d. **f, g**, Immunofluorescence of the epiblast (EPI) markers NANOG (yellow) (**f**) and OCT4 (yellow) (**g**), the TE markers CDX2 (cyan) (**f**) and GATA3 (cyan) (**g**), and the PrE markers SOX17 (magenta) (**f**) and GATA4 (magenta) (**g**) in human blastocyst-like structures. Scale bars, 100 μm . **h**, Absolute number of cells positive for OCT4, GATA3 and GATA4 (left) and ratios of cells belonging to individual lineages represented as percentage of total number of cells (right) in blastocyst-like structures (96 h) based on immunofluorescence. **i**, Representative immunofluorescence of the tight junction molecule ZO-1 (yellow), the adherence junction molecule CDH1 (magenta) and the apical domain molecule aPKC (cyan) in a representative human blastocyst-like structure. Scale bar, 50 μm .

[Source data](#)

Formation of blastocyst-stage analogues

Single-cell transcriptomics analysis showed that blastocyst-like structures formed only three distinct transcriptomic states (Fig. 2a, b, Extended Data Fig. 2a) marked by genes specific to the three founding lineages, including *GATA2* and *GATA3* (TE), *POU5F1* and *KLF17* (EPI), and *GATA4* and *SOX17* (PrE) (Fig. 2c, d, Extended Data Fig. 2b). Comparison with cells from blastocysts, in vitro cultured blastocysts and a gastrulation-stage embryo indicated that the cells in the blastocyst-like structures were transcriptionally similar to the blastocyst stage and distinct from post-implantation stages (Fig. 2e, f, Extended Data Fig. 2c–g). A higher-resolution clustering analysis (from resolution 0.02 to resolution 1) isolated one cluster of non-blastocyst-like cells with a gene-expression pattern reminiscent of post-implantation tissues¹⁵ (*GABRP*, *ISL1*, *APLNR* and *CRABP2*) (Extended Data Fig. 3a–c) that also appeared transcriptionally similar to amnion (annotated as non-neural ectoderm) and extra-embryonic mesoderm (Extended Data Fig. 3d–j). This sub-population constituted less than 3% of all sequenced cells (Extended Data Fig. 3i). Of note, we found that naive PSC culture also contained 5–6% similarly differentiated cells¹⁹ (Extended Data Fig. 3i). Bulk RNA-sequencing (RNA-seq) analysis showed that isolated trophoblast analogues (TROP2⁺) had an intermediate transcriptome between those of naive PSCs and post-implantation-like trophoblasts²⁰ (TSCs) (Extended Data Fig. 4a).

Furthermore, trophoblasts were enriched in blastocyst-stage TE transcripts¹¹ (*ESRRB*, *GRHL1*, *OVOL1*, *GATA2*, *GATA3*, *TBX3*, *KRT19*, *CGA*, *CGB5* and *CGB7*) but not in some post-implantation trophoblast markers¹¹ (*SIGLEC6* and *DPP4*) (Extended Data Fig. 4b, c). The transcriptome of isolated EPI analogues (TROP2⁻PDGFRA⁻) resembled that of naive PSCs (Extended Data Fig. 4a), was enriched in markers specific for blastocyst-stage EPI²¹ (*KLF17*, *ATG2A*, *SUSD2*, *TFCP2L1*, *DPPA2* and *PRDM14*), and differed from the transcriptome of primed PSCs (Extended Data Fig. 4a, d). Finally, isolated PrE analogues (PDGFRA⁺) had an intermediate transcriptome between those of naive PSCs and extraembryonic endoderm cell lines²² (nEND cells) (Extended Data Fig. 4a). PrE analogues were enriched in blastocyst-stage PrE markers (early blastocyst: *GATA6*, *MSX2* and *HNF4A*; late blastocyst: *PDGFRA*, *GATA4*, *SOXI7*, *HNF1B* and *FOXA2*) and downregulated in EPI genes (*ARGFX*, *PRDM14*, *SOX2*, *NANOG*, *DPPA2* and *POU5F1*), similar to during blastocyst development²¹ (Extended Data Fig. 4e). Blastocysts have the ability to establish stem cell lines²; similarly, blastocyst-like structures enabled de novo derivation of naive PSCs² (*NANOG*⁺*SOX2*⁺*OCT4*⁺*KLF17*⁺) (Extended Data Fig. 5a) that could form second-generation blastocyst-like structures (Extended Data Fig. 5b, c) and of TSCs²⁰ (*CDX2*⁻*GATA3*⁺*CK7*⁺) (Extended Data Fig. 5d) endowed with the capacity for rapid differentiation into syncytio trophoblasts (SCT) and extravillous trophoblasts (EVT) (over 3–6 days; Extended Data Fig. 5e–j). Of note, derivation of PrE cell lines from human blastocysts has not been reported. Thus, blastocyst-like structures formed blastocyst-stage cellular analogues (accounting for more than 97% of the cells sequenced).

Fig. 2: Human blastocyst-like structures form analogues of the three pre-implantation lineages.

 **figure 2**

a, b, Uniform manifold approximation and projection (UMAP) of the transcriptome of single cells originating from blastocyst-like structures (at 24, 60 and 96 h), naive PSCs, primed PSCs and TSCs (representing post-implantation cytotrophoblasts); individual cells are coloured on the basis of their origin (**a**) or their unsupervised

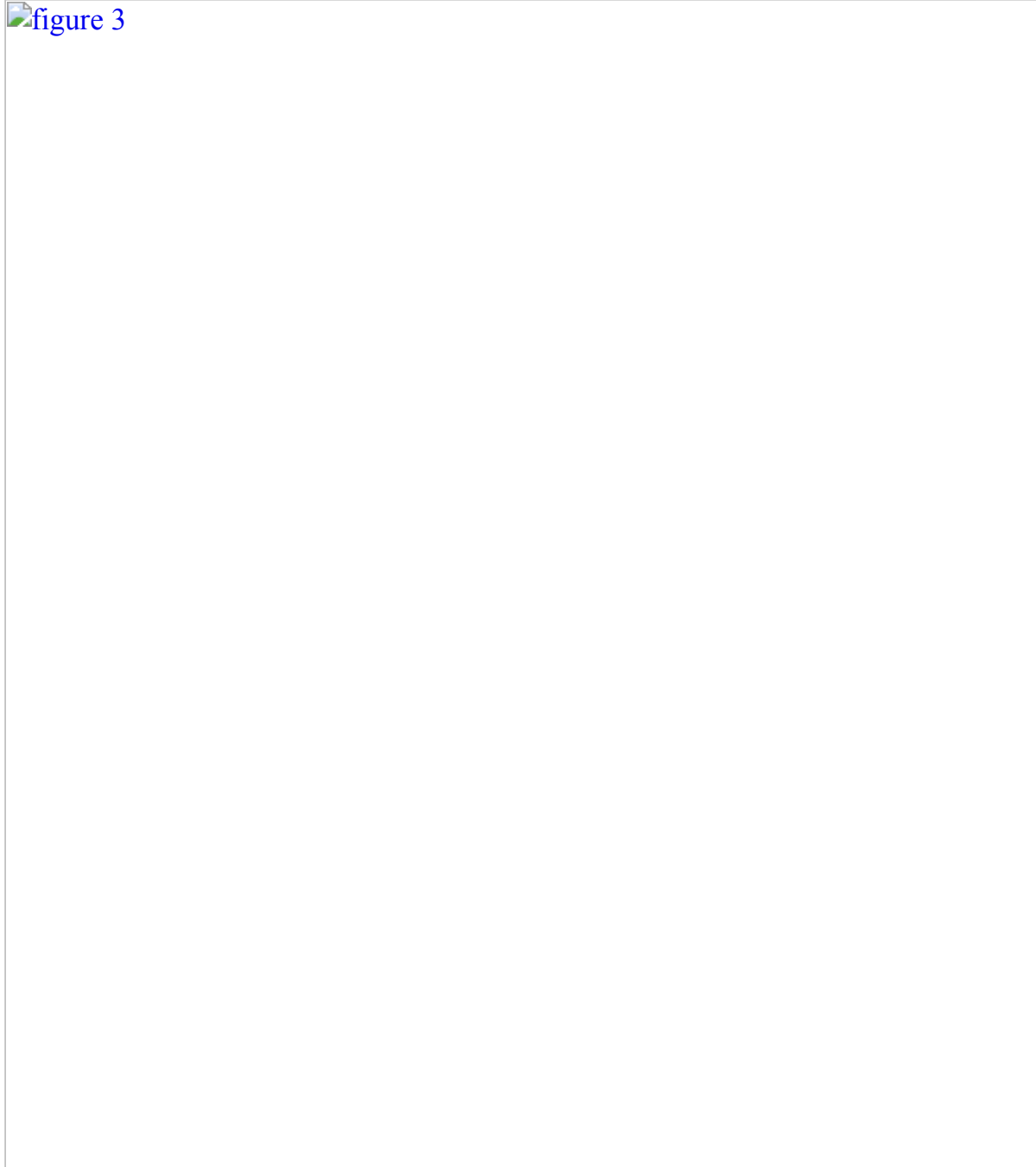
cluster affiliation (**b**). **c**, Expression level of markers of each blastocyst lineage. **d**, Unsupervised distance map generated using the top 30 genes that are enriched in clusters 0, 1 and 3 (defined in the UMAP in **b**). Note that this list includes epiblast markers specific to the blastocyst stage (for example, SUSD2, KLF17 and PRDM14). **e, f**, UMAP of single-cell transcriptome of cells from blastocyst-like structures, naive PSCs and primed PSCs integrated with published datasets from human embryos at pre-implantation, peri-implantation (in vitro cultured blastocysts) and gastrulation (Carnegie stage 7, that is, between embryonic days 16 and 19) stages. Individual cells are coloured on the basis of their origin in human embryos (**e**) or blastocyst-like structures or stem cells (**f**).

Hippo inhibition is essential

Knowledge about human blastocyst lineage segregation is limited (Fig. 3a). However, inhibition of the Hippo pathway is known to occur in peripheral cells upon acquisition of an apical domain, and is required to initiate TE specification¹² (Extended Data Fig. 6a). We tested whether blastocyst-like structures co-opted this mechanism. Of note, aPKC and F-actin expression domains appeared co-aligned in outer cells that also accumulated the Hippo downstream effector YAP1 in nuclei (Extended Data Fig. 6b, c). YAP1 nuclear location correlated with GATA2 and GATA3 expression, contrasted with NANOG expression, and became restricted to TE analogues¹² (Fig. 3b, Extended Data Fig. 6d, e). An aPKC inhibitor (CRT0103390)¹² largely prevented YAP1 nuclear accumulation, decreased the number of GATA3⁺ cells and prevented the formation of blastocyst-like structures (Extended Data Fig. 6f-h). Conversely, ligands of LPA receptors (LPA and NAEPA) that can inhibit the Hippo pathway enhanced the formation of blastocyst-like structures (Fig. 3c, Extended Data Fig. 6i). Because Hippo pathway inhibition frees YAP1 to enter the nucleus, we tested whether genetically engineered levels and functions of YAP1 could affect morphogenesis. Overexpression of wild-type or constitutively active forms of YAP1 (5SA) accelerated cavitation (Fig. 3d). The interaction between YAP1 and TEAD transcription factors is necessary for downstream gene regulation. Accordingly, over-expression of YAP1 with a mutation in the TEAD binding site (S94A) did not affect cavitation (Fig. 3d, Extended Data Fig. 6j), and verteporfin—which disrupts the YAP1–TEAD interaction—prevented the formation of blastocyst-like structures (Extended Data Fig. 6k). Cavity morphogenesis occurred through the apparent coalescence of multiple fluid-filled cavities²³ (Extended Data Fig. 6l). Aquaporin 3 (AQP3), the water transporter most highly expressed in human blastocysts¹¹, was initially visible in all cells (36 h) and was then restricted to TE analogues (96 h) (Extended Data Fig. 6m). Thus, similar to human blastocysts¹², TE specification and morphogenesis within these structures depends on aPKC, inhibition of the Hippo pathway, nuclear translocation of YAP1 and the ability of YAP1 to bind TEAD transcription factors.

Fig. 3: The three lineages form according to the sequence and time of blastocyst development.

 figure 3



a, Schematic depicting the sequential lineage specification of human blastocysts. **b**, Immunofluorescence of YAP1 (yellow) and GATA2 (cyan) in aggregates of naive PSCs cultured in PALLY medium for 60 h. Scale bar, 50 μ m. **c**, Dose-dependent effect of LPA on the yield of blastocyst-like structures. $n = 3$ independent microwell arrays; mean \pm s.d.; one-way analysis of variance (ANOVA) and Dunnett's multiple comparisons test. ** $P = 0.0016$, *** $P < 0.0001$. **d**, Effect of the overexpression of

different variants of YAP1 on cavitation events in early blastocyst-like structures. $n = 3$ experiments; mean \pm s.d.; one-way ANOVA and Tukey's multiple comparisons test. NS, not significant; *** $P = 0.0004$, **** $P = 0.00004$. e, Total cell numbers per lineage developing blastocyst-like structures at three time points of development (24, 60 and 96 h). Mean \pm s.d. EPI: $n = 11$ blastocyst-like structures at 24, 68 and 96 h; TE: $n = 8$ (24 h), $n = 14$ (48 h) and $n = 15$ (96 h) blastocyst-like structures; PrE: $n = 9$ (24 h), $n = 37$ (48 h) and $n = 9$ (96 h) blastocyst-like structures. f, Immunofluorescence of CDX2 (cyan), NR2F2 (magenta) and NANOG (yellow) in representative B4-stage human blastocyst (left) and blastocyst-like structures (middle). Quantification of the proportion of blastocyst-like structures with a preferentially polar NR2F2 expression pattern (axis) compared with a preferentially mural NR2F2 expression pattern (inverted axis) (right). $n = 4$ independent experiments with 4–12 blastocyst-like structures in each experiment; mean \pm s.d.; one-way ANOVA and Tukey's multiple comparisons test. * $P < 0.05$, *** $P < 0.001$. Scale bar, 50 μ m.

[Source data](#)

Adequate developmental sequence

In blastocysts, TE (GATA2 $^+$ DAB2 $^+$) and EPI (KLF17 $^+$ NANOG $^+$) cells appear first^{11,21} (5–6 dpf) and PrE cells (GATA6 $^+$ ADM $^+$) and polar TE cells (pTE) (CDX2 $^-$ NR2F2 $^+$) appear last²¹ (6–7 dpf). This sequence is recapitulated in the blastocyst-like structures. Trophoblasts (*DAB2* $^+$, *CDX2* $^+$, *GATA2* $^+$, *GATA3* $^+$) formed first (within 24 h) (Fig. 3e, Extended Data Fig. 7a), and changed the levels of transcripts related to PKC and Hippo signalling (*AKAP12*, *CAPZB*, *ULK4*, *MOB1A*, *AMOT*, *AMOTL2*, *LATS2* and *TEADI*) (Supplementary Table 1). At protein level, early TE-like cells were first YAP1^{nuclear}GATA2 $^+$ (at 24 h) and then CDX2 $^+$ GATA3 $^+$, while maintaining expression of KLF17 and OCT4, but not NANOG (at 60 h) (Extended Data Fig. 7b–d). Subsequently, OCT4 became undetectable¹¹ (Fig. 1g, Extended Data Fig. 1i). Genes associated with SMAD, ERK, Notch and Wnt signalling pathways were regulated during this process (Extended Data Fig. 7e,f, Supplementary Table 1). Finally, pTE analogues matured as marked by expression of *OVOL1*, *GREM2*, *CCR7*, *SP6* and *NR2F2* (Extended Data Fig. 7g–j), upregulation of NR2F2 and CCR7¹¹ and downregulation of CDX2 (Fig. 3f, Extended Data Fig. 7h,j). The transcriptome of EPI analogues maintained core blastocyst markers (*POU5F1*, *NANOG*, *KLF17*, *SUSD2*, *KLF4*, *ARGFX* and *GDF3*) (Fig. 3e, Extended Data Fig. 7k, l, Supplementary Table 1), while undergoing a progression characterized by regulation of Nodal (*NODAL*, *LEFTY1* and *LEFTY2*) and mTOR (*LAMTOR1*, *LAMTOR4*, *LAMTOR5*, *XBP1P1* (*XBP1*, also known as *SEC13* and *MLST8*) signalling-related genes, and of the X chromosome activation-related gene *XACT* (Extended Data Fig. 7k–m, Supplementary Table 1, cluster 4 versus cluster 0). At the protein

level, EPI analogues were marked by KLF17 and SUSD2, which are specifically highly expressed at the blastocyst stage (Extended Data Fig. 7l). PrE analogues appeared within 60 h and GATA4, OTX2 and SOX17 were detected¹¹ within 72 h (Fig. 3e, Extended Data Fig. 7n–p). Early PrE marker genes²¹ (*GATA6*, *LBH*, *ADM* and *LAMA1*) were uniformly expressed among the PrE analogues, while some late PrE marker genes (*CTSE*, *APOA1*, *PITX2* and *SLCO2A1*) were expressed only in a subpopulation of cells, suggesting a progression toward the late blastocyst stage¹¹ (Extended Data Fig. 7q). By 96 h, mature PrE analogues had regulated SMAD (*NODAL*, *BMP2*, *BMP6*, *GDF3*, *ID1* and *ID2*) and Wnt signalling-related transcripts (*WNT3*, *RSPO3* and *LBH*) and were enriched in transcripts controlling extracellular matrix organization (*LAMA1*, *LAMBI*, *LAMC1*, *COL4A1* and *COL4A2*), and endodermal and epithelial differentiation (Extended Data Fig. 7q, l, Supplementary Table 1, cluster 6 versus cluster 8). Because this model morphologically resembles the human blastocyst (see criteria in Methods), efficiently generates analogues of the three lineages with transcriptomes matching the blastocyst stage, and forms these analogues according to the sequence and approximate pace of blastocyst development, we refer to it as a human blastoid.

Distinct attachment to endometrial cells

At 7 dpf, the human blastocyst initiates implantation in utero through the attachment of its TE to a receptive endometrium (Fig. 4a, left). We tested whether blastoids could model this interaction by seeding endometrial organoids²⁴ in 2D to form an open-faced endometrial layer (OFEL) to facilitate the deposition of blastoids (Fig. 4a, right). Subpopulations of the OFEL were positive for acetylated α -tubulin, marking ciliated epithelial cells²⁴ (Extended Data Fig. 8a), and FOXA2, marking glandular epithelial cells (Extended Data Fig. 8b). The window of implantation is the period during which the uterus becomes receptive for blastocyst implantation. It opens upon exposure to oestrogen (E2) and progesterone (P4), and correlates with regulation of Wnt signalling²⁵. Accordingly, OFELs responded to E2, P4, cAMP and XAV939 by upregulating the expression of genes that mark the mid-secretory-phase endometrium (Extended Data Fig. 8c–e) and decreasing proliferation, which are hallmarks of receptivity²⁵ (Extended Data Fig. 8e, f). Notably, blastoids deposited onto non-stimulated OFELs did not attach; however, they did attach to and repel the endometrial cells of stimulated OFELs, as occurs in utero (Fig. 4b, Extended Data Fig. 8g, h). The contraceptive levonorgestrel impaired blastoid attachment (Extended Data Fig. 8j). We concluded that human blastoids are capable of interacting specifically with endometrial cells that have been made receptive.

Fig. 4: Human blastoids recapitulate aspects of implantation.

 **figure 4**

a, Left, schematic of the modelled implantation process. Right, OFEL priming assay using EPC/XAV939. E2, β -oestradiol; EPC, E2 + progesterone + cAMP. **b**, Representative phase-contrast images of blastoids (GFP^+) 24 h after deposition onto non-stimulated (top left) or stimulated (bottom left) OFELs. Scale bar, 100 μ m. Attachment efficiency of human blastoids (right). $n = 7$ independent experiments from 3 different donors; mean \pm s.d.; unpaired two-tailed t -test. $****P = 4.5 \times 10^{-8}$. **c**, Representative images of recently attached human blastoids (12 \pm 4 h). Top, the dashed delineates the inner cluster of blastoids formed from GFP^+ naive PSCs (also see Supplementary Video 3). Scale bar, 100 μ m. Bottom, $x-z$ plane of NR2F2 (magenta) and OCT4 (yellow) immunofluorescence in blastoids immediately after attachment. Scale bar, 5 μ m. **d**, Intensity profile of immunofluorescence of NR2F2 and OCT4 in blastoids immediately after attachment. $n = 10$. **e**, Left, representative phase-contrast images of trophospheres formed using 3 μ M SC144 (top) or 2 μ M XMU-MP-1 (middle), and aggregates of TSCs (bottom) deposited onto stimulated OFELs. Scale bar, 100 μ m. Right, attachment efficiency. $n = 3$ independent experiments; mean \pm s.d.; one-way ANOVA and Dunnett's multiple comparisons test. $****P < 0.0001$. **f**, Pregnancy test strips detecting secretion of CG β into the medium of unstimulated OFELs with unattached blastoids and stimulated OFELs with attached blastoids (48 h

on OFEL; see ELISA assay in Extended Data Fig. 10b). g, Immunofluorescence of OCT4 (yellow) and aPKC (grey) in human blastocysts (left) or blastoids (right) grown in post-implantation culture condition for 4 days, counterstained with phalloidin marking F-actin (cyan). Scale bars, 100 μ m. h, Number of cells positive for OCT4, GATA3 and GATA4 in blastoids grown in post-implantation culture for 6 days (time equivalent, day 13). $n = 5$. mean \pm s.d.

[Source data](#)

Epiblast signals gatekeep trophectoderm attachment

Human blastocysts attach to the endometrium via the pTE, which is defined by its contact with the EPI. Similarly, blastoids reproducibly initiated attachment through this region (Fig 4c, d, Extended Data Fig. 9a–c, Supplementary Videos 3, 4). We tested the role of the pTE–EPI interface by forming trophospheres devoid of EPI. IL-6 is highly expressed in the pTE and transcripts for its receptor (*IL6R* and *IL6ST* (also known as *GP130*)) and effector (*STAT3*) are present at high levels in the EPI (Extended Data Fig. 9d). Consistent with a role for STAT signalling in the EPI, the efficiency of blastoid formation increased with LIF concentration (Extended Data Fig. 9e), whereas the addition of a GP130 inhibitor (SC144) yielded trophospheres (Fig. 4e, Extended Data Fig. 9f). The presence of a potent inhibitor of the Hippo kinases MST1 and MST2 (XMU-MP-1) also yielded trophospheres (Fig. 4e, Extended Data Fig. 9g). The transcriptomes of these trophospheres reflected early and late blastocyst-stage TE (Extended Data Fig. 9h, i). Neither type of trophosphere attached to OFELs (Fig. 4e), and nor did aggregates of TSCs²⁰ that reflect post-implantation cytrophoblasts²⁶ (CDX2⁺CK7⁺) or aggregates of naive PSCs (Fig. 4e, Extended Data Fig. 9j, k). We thus conclude that signals from the EPI induce pTE maturation and endows it with the potential to interact with endometrial cells. This potential appears lost in TSCs reflecting a post-implantation stage. On the basis of transcriptome analysis and in utero data²⁵, we propose several pairs of molecules whose transcripts became more abundant upon endometrial cell stimulation and pTE analogue maturation (Extended Data Fig. 9l) that might mediate the first contact between blastocyst and uterus. Overall, we conclude that a polar-like TE state, whose maturation depends on EPI inductions, gatekeeps the interaction of the blastocyst with the endometrium. This interaction and subsequent maturation create a window of opportunity for blastocyst implantation.

Modelling post-stages on day 13

The blastoid morphology was stable for two days in peri-implantation culture conditions^{27,28} (Extended Data Fig. 10a). Clinical pregnancy is characterized by the

detection of chorionic gonadotropin- β hormone (CG β). Accordingly, upon attachment, blastoids formed trophoblasts expressing CG β at levels detectable using standard pregnancy tests and ELISA (Fig. 4f, Extended Data Fig. 10b). NR2F2 $^+$ pTE analogues proliferated and decreased CDX2 expression while upregulating the peri-implantation gene cytokeratin 7 (*KRT7* (a.k.a. *CK7*)) (Extended Data Fig. 10c, d). Some trophoblasts further differentiated into SCT and EVT expressing CG β and HLA-G, respectively (Extended Data Fig. 10e, f). EPI analogues maintained expression of OCT4 and SOX2, upregulated the primed pluripotency marker CD24 (Fig. 4g, Extended Data Fig. 10g) and patterned cortical F-actin as during post-implantation EPI epithelialization, and some blastoids cultured in vitro for 4 days past the equivalent of the blastocyst stage (day 7) formed pro-amniotic-like cavities enriched with F-actin, PODXL and aPKC (Fig. 4g, Extended Data Fig. 10h). A subpopulation in the periphery of the EPI analogue expressed CDX2 along with SOX2 or TFAP2C, suggestive of early amnion analogues (Extended Data Fig. 10i, j). Extra-embryonic endoderm analogues were characterized by restricted expression of OTX2¹¹ (Extended Data Figs. 7o, 10k). Upon prolonged culture (up to 6 days), the three lineages consistently expanded (Fig. 4h, Extended Data Fig. 10l, m) until a time equivalent of day 13, although, similar to blastocysts, their organization did not reflect that developmental stage.

Discussion

Human blastoids morphologically resemble the human blastocyst (criteria described in Methods), efficiently generate analogues of its three lineages with transcriptomes matching the human blastocyst stage, and form these analogues according to the sequence (TE and EPI, then pTE and PrE) and approximate pace (4 days) of blastocyst development. We therefore propose that this model is relevant for the study of human blastocyst development and implantation. Some initial parameters and end-point criteria that are useful to form and define these models^{5,6,7,8,9} are summarized in Supplementary Table 2. Mimicking the interaction between the epiblast and trophectoderm revealed that the epiblast induces the local maturation of polar trophectoderm and subsequently endows it with the capacity to attach onto stimulated endometrial cells. In future, human blastoids may be used to help identify therapeutic targets and contribute to preclinical modelling (for example, in vitro fertilization medium complements such as LPA and NAEPA or contraceptives such as SC144 (ref.³)). Considering the proportionality (balancing the benefits and harms) and subsidiarity (pursuing goals using the morally least problematic means) of human embryology, blastoids represent an ethical opportunity to complement research using embryos⁴.

Methods

Ethical approvals

The use of human embryos donated to research as surplus of IVF treatment was allowed by the French embryo research oversight committee (Agence de la Biomédecine) under approval number RE13-010 and RE18-010. All human pre-implantation embryos used in this study were obtained following informed consent from the couples who donated embryos and cultured at the Assisted Reproductive Technology unit of the University Hospital of Nantes, France, which are authorized to collect embryos for research under approval number AG110126AMP of the Agence de la Biomédecine. Human endometrium samples were obtained from patients who signed an informed consent form and protocols approved by the Ethics Committee of Royan Institute (IR.ACECR.ROYAN.REC. 1397.93) and of Shahid Beheshti University of Medical Sciences (IR.SBMU.MSP.REC. 1396.25). The Wicell line H9 was used under the agreement 20-WO-341 for a research program entitled ‘Modeling early human development: Establishing a stem cell based 3D in vitro model of human blastocyst (blastoids)’. Blastoid generation was approved by the Commission for Science Ethics of the Austrian Academy of Sciences. This work did not exceed a developmental stage normally associated with 14 consecutive days in culture after fertilization even though this is not forbidden by the ISSCR Guidelines as far as embryo models are concerned. All experiments complied with all relevant guidelines and regulations, including the 2021 ISSCR guidelines that forbid the transfer of human blastoids into any uterus⁴.

Culture of human naive pluripotent stem cells

Experiments were done using the following PSC lines; human ES cell lines: H9, Shef6 and HNES1. Induced pluripotent stem cell (iPSC) lines: cR-NCRM2 and niPSC 16.2.b. The H9 and H9-GFP lines reset to the naive state were provided by the laboratory of Y. Takashima. Other naive human ES cells and iPSCs were provided by the laboratory of A. Smith. Naive PSCs were cultured on gelatin-coated plates including a feeder layer of gamma-irradiated mouse embryonic fibroblasts (MEFs) in PXGL medium, as previously reported²⁹. PXGL medium is prepared using N2B27 basal medium supplemented with PD0325901(1 µM, MedChemExpress, HY-10254), XAV-939 (1 µM, MedChemExpress, HY-15147), Gö 6983 (2 µM, MedChemExpress, HY-13689) and human leukemia inhibitory factor (hLIF, 10 ng ml⁻¹, in-house made) as previously reported²⁹. N2B27 basal medium contained DMEM/F12 (50%, in house made), neurobasal medium (50%, in-house made), N-2 supplement (Thermo Fisher Science, 17502048), B-27 supplement (Thermo Fisher Science, 17504044), GultaMAX supplement (Thermo Fisher Science, 35050-038), non-essential amino acid, 2-mercaptoethanol (100 µM, Thermo Fisher Science, 31350010), and bovine serum albumin solution (0.45%, Sigma-Aldrich, A7979-50ML). Cells were routinely

cultured in hypoxic chambers (5% CO₂, 5% O₂) and passaged as single cells every three to four days. All cell lines had routinely tested negative for mycoplasma.

Culture of primed pluripotent embryonic stem cells

Primed H9 cells were cultured on Vitronectin XF (STEMCELL Technologies, 07180) coated plates (1.0 µg cm⁻²) using Essential 8 medium (prepared in-house).

Microwell arrays

Microwell arrays comprising microwells of 200 µm diameter were imprinted into 96-well plates as previously described^{30,31}.

Induction of blastoids and trophospheres

Naive PSCs were treated with Accutase (Biozym, B423201) at 37 °C for 5 min, followed by gentle mechanical dissociation with a pipette. After centrifugation, the cell pellet was resuspended in PXGL medium, supplemented with Y-27632 (10 µM, MedChemExpress, HY-10583). To exclude MEFs, the cell suspension was transferred onto gelatin-coated plates and incubated at 37 °C for 70 min. After MEF exclusion, the cell number was determined using a Countess automated cell counter (Thermo Fisher Scientific) and trypan blue staining to assess cell viability. The cells were then resuspended in N2B27 medium containing 10 µM Y-27632 (aggregation medium) and 3.0 × 10⁴ cells were seeded onto a microwell array included into a well of a 96-well plate and placed in a hypoxic chamber (5% CO₂, 5% O₂) for the whole period of blastoid or trophosphere formation. The cells were allowed to form aggregates inside the microwell for a period ranging from 0 to 24 h depending on the cell lines and based on their propensity for aggregation. Subsequently, the aggregation medium was replaced with PALLY medium (N2B27 supplemented with PD0325901 (1 µM), A 83-01 (1 µM, MedChemExpress, HY-10432), 1-oleoyl lysophosphatidic acid sodium salt (LPA)³² (500 nM, Tocris, 3854), hLIF (10 ng ml⁻¹) and Y-27632 (10 µM)). The PALLY medium was refreshed every 24 h. After 48 h, the PALLY medium was replaced with N2B27 medium containing 500 nM LPA and 10 µM Y-27632. At 96 h, a blastoid is defined based (1) on morphological similarities to B6 staged human blastocyst, as a structure composed of a monolayered cyst with an overall diameter of 150–250 µm comprising one inner cell cluster, and (2) on similarities to the molecular dynamic of human development as a structure that forms analogues of the three blastocyst cell lineages in the sequential and timely manner of a blastocyst. For example, >90% of morphologically adequate structures generated from the lines analysed formed >97% of analogues of three blastocyst-stage lineages (see Fig. 1h and Extended Data Fig. 3i). An exception is the line Shef6, which efficiently formed

morphologically correct structures but appeared less efficient at forming PrE analogues. See also Supplementary Table 2. Blastoids reproducibly formed at high efficiency and we did not observe differences based on the number of passages after resetting in PXGL culture conditions. The effect of LPA, NAEPA (Sigma-Aldrich, N0912) and Verteporfin (Selleck Chemicals Llc, S1786) on the yield of blastoid formation was assessed by culturing naive PSC aggregates in PALY medium (without LPA) complemented with molecules added every day from 0 to 96 h. The Verteporfin treatment was executed without exposure to the light. The effect of the aPKC inhibitor CRT0103390 (a gift from the laboratory of K. Niakan) was assessed by culturing naive PSC aggregates in PALLY medium complemented with 2 μ M CRT0103390 every day from 0 to 96 h. The formation of trophospheres was induced by culturing naive PSC aggregates in PALLY medium complemented with 2 μ M XMU-MP-1 (Med Chem Express, HY-100526) or 3 μ M SC-144 (Axon, 2324) every day from 0 to 96 h. The BSA concentration was titrated within the range of 0–0.3% for individual cell lines used for the formation of the blastoids and trophospheres. A step-by-step protocol is available on Protocol Exchange (<https://doi.org/10.21203/rs.3.pex-1639/v1>).

Derivation of cell lines from human blastoids

Derivation experiments were performed with blastoids cultured for 96 h as described in the previous section. Blastoids were individually transferred on gelatin-coated 96-well plates with feeder layers of gamma-irradiated MEFs. Naive PSCs were derived in PXGL medium². TSCs were derived in human TSC medium²⁰. After 24 h of culture on feeders, blastoids attached and, within one week, colonies were formed. Derivation was considered successful after three passages after blastoid transfer. For immunofluorescence assays, naive PSCs were transferred onto Geltrex (0.5 μ l cm⁻²)-coated coverslips, and TSCs were transferred onto fibronectin-coated coverslips (5 μ g ml⁻¹, Sigma Aldrich, 08012).

Trophoblast organoid formation

Organoid formation was performed with blastoid-derived TSC lines. Organoids were cultured as previously described³³ with some modifications. Colonies of TSCs were dissociated into single cells using 1× trypsin at 37 °C for 5 min. After centrifugation, 200,000 cells were resuspended in 150 μ l Matrigel (Corning, 356231). Droplets of 20 μ l per well were placed into a prewarmed 48-well cell culture plate and placed upside down into the incubator for 20 min. Organoids were cultured in 250 ml TOM medium (Advanced DMEM-F12, N2 supplement, B27 supplement minus vitamin a, PenStrep, N-acetyl-l-cysteine (1.25 mM), l-glutamine (2 mM), A83-01 (500 nM), CHIR99021 (1.5 uM), recombinant human EGF (50 ng ml⁻¹), 10% R-spondin 1 conditioned medium, recombinant human FGF2 (100 ng ml⁻¹), recombinant human HGF (50

ng ml⁻¹), PGE2 (2.5 µM). Medium was refreshed every other day. For SCT formation organoids were maintained in TOM medium until day 7.

2D trophoblast differentiations

The differentiation of blastoid derived TSCs was performed as described previously²⁰ with some modifications. TSC lines were adapted to Fibronectin coating (5 µg ml⁻¹, Sigma Aldrich, 08012) for at least three passages prior to the experiments. For EVT and SCT differentiation, cells were dissociated with TrypLE for 5 min at 37 °C and cells were seeded at a density of 55,000 cells per well onto 12-well plates. For SCT differentiation, the plates were precoated with 10 µg ml⁻¹ fibronectin and cultured in SCT medium (DMEM/F12, supplemented with 0.1 mM 2-mercaptoethanol, 0.5% penicillin-streptomycin, 1% ITS-X supplement, 7.5 mM A83-01, 2.5 mM Y27632, 4% KnockOut Serum Replacement and 2 mM forskolin) for 3 days. For EVT differentiation, plates were precoated with Matrigel and cells were cultured in EVT medium (DMEM/F12, supplemented with 0.1 mM 2-mercaptoethanol, 0.5% penicillin-streptomycin, 1% ITS-X supplement, 2% Matrigel, 7.5 mM A83-01, 2.5 mM Y27632, 4% KnockOut Serum Replacement and 100 ng ml⁻¹ NRG1). After three days, the medium was changed to EVT medium with 0.5% Matrigel and without NRG1. Cells were cultured until day 6.

Human pre-implantation embryos culture

Human embryos were thawed following the manufacturer's instructions (Cook Medical: Sydney IVF Thawing kit for slow freezing and Vitrolife: RapidWarmCleave or RapidWarmBlast for vitrification). Human embryos frozen at the 8-cell stage were loaded into a 12-well dish (Vitrolife: Embryoslide Ibidi) with non-sequential culture medium (Vitrolife G2 plus) under mineral oil (Origio: Liquid Paraffin) at 37 °C in 5% O₂/6% CO₂.

Plasmid construction

The cDNA sequence of hYAP1, hYAP1(5SA) and hYAP1(5SA + S94A) were amplified from the pQCXIH-Myc-YAP, pQCXIH-Myc-YAP-5SA and pQCXIH-Myc-YAP-S94A plasmids, respectively. These YAP plasmids³⁴ were gifts from K. Guan (Addgene #33091, #33093 and #33094). The individual cDNA sequences were cloned into pDONR211, followed by cloning into PB-TAC-ERP2 using Gateway (invitrogen) cloning strategy. PB-TAC-ERP2³⁵ was a gift from K. Woltjen (Addgene plasmid #80478). Complete sequences of the resulting plasmids are available upon request.

Cell transfection in human naive PSCs

pCAG-PBase (5 µg) and PB-TAC-YAP1-ERP (5 µg) were transfected by NEPA21 electroporation (Nepa Gene) into 5×10^4 cells in single-cell suspension.

Electroporated naive PSCs were plated on Geltrex (0.5 µl cm⁻², Thermo Fisher Science, A1413302)-coated 6-well plates with PXGL medium containing Y-27632 (10 µM). Puromycin (0.5 µg ml⁻¹, Sigma-aldrich, P7255) was added to PXGL medium from day 1 to day 3–4 to select transformed cells. pCAG-PBase was a gift from K. Woltjen.

YAP overexpression in naive PSC aggregates

The naive PSC aggregates were formed from naive H9 cell lines integrated with the doxycycline inducible cassette as described in the section above. The aggregates were cultured in PALLY medium with reduced LPA concentration (5 nM) from 0 h to 48 h along with 100 ng ml⁻¹ doxycycline. Higher LPA concentrations masked the effects of the genetic overexpression of the YAP1 variants. The number of cavitated aggregates was counted at 72 h.

Single-cell RNA-seq library preparation and sequencing

To avoid over-representation of TE cells, blastoids were collected, dissociated and the cell suspension was stained using antibodies against TROP2 and PDGFR α that mark trophoblasts and primitive endoderm, respectively. For the 96 h time point, blastoids were selectively picked up from the microwell arrays before the dissociation, according to the morphological criteria described above. On the contrary, for the 24 and 65 h time points, all structures, including the ones that will not develop into a blastoid, were included. Accordingly, this non-selective picking correlated with the presence of more off-target cells. Cells were FACS-sorted into 384-well-plates containing the lysis buffer for Smart-seq2 and immediately frozen. The antibody staining was exploited in order to harvest specific numbers of TROP2⁺, PDGFR α ⁺ and double-negative cells. The abutted FACS gates (DiVa 9.0.1) covered the whole spectrum and no blastoid cells were excluded. The H9 naive cells cultured on MEF were stained using an antibody against SUSD2, then FACS-sorted. Dead cells were excluded by DAPI staining. Smart-seq2 libraries were generated as described previously with minor optimization³⁶. Maxima H Minus reverse transcriptase (3 U per reaction, Thermo Fisher Science, EP0751) was used for the cDNA synthesis. The prepared libraries were sequenced on the S1 or SP flow cell using an Illumina Novaseq instrument in 50-bp paired-end mode.

Single-cell RNA-seq data analysis

Smart-Seq transcriptome sequencing experiments were analysed using genome sequence and gene annotation from Ensembl GRCh38 release 103 as reference. For gene-expression quantification RNA-seq reads were first trimmed using trim-galore v0.6.6 and thereafter aligned to the human genome using hisat2 v2.2.1. Uniquely mapping reads in genes were quantified using htseq-count v0.13.5 with parameter -s no. TPM estimates were obtained using RSEM v1.3.3 with parameter—single-cell-prior. Further analysis was performed in R v4.0.3 with Seurat v4.0.1. Based on initial evaluation of per-cell quality control metrics and outlier identification using the median absolute deviation algorithm, cells with $\leq 2,000$ detected genes or $\geq 12.5\%$ mitochondrial gene percentage were filtered out. Only genes detected in at least five cells were retained. Count-data were log-normalized, top 3,000 highly variable were selected, and standardization of per-gene expression values across cells was performed using NormalizeData, FindVariableFeatures and ScaleData data functions in Seurat. Principal component analysis (PCA) based on the standardized highly variable features was used for linear dimension reduction, a shared nearest neighbor (SNN) graph was constructed on the dimensionally reduced data, and the graph was partitioned using a SNN modularity optimization-based clustering algorithm at a range of resolutions using RunPCA, FindNeighbors and FindClusters from Seurat with default settings. Cluster marker and marker genes between identity groups were determined with the Wilcox likelihood-ratio test (two-sided) using the FindAllMarker and FindMarkers functions with *P*-value adjustment using Bonferroni correction and followed by filtering at a adjusted *P* value cut-off of 0.05. UMAP was used for visualization.

For integration of Smart-seq experiments from multiple sources we followed the previously described procedure¹⁰. Published data from E-MTAB-3929 (human preimplantation embryos³⁷ ranging from embryonic day 3 to 7), GSE109555 (in vitro cultured blastocysts³⁸) were downloaded, and data from Carnegie stage 7 embryo were kindly provided by the authors of the study³⁹. All the data was preprocessed to obtain per gene read counts using the same protocol as described for blastoid cells, in the case of GSE109555 including adaptations to accommodate UMI and CB information following the authors' instructions (https://github.com/WRui/Post_Implantation). For GSE109555 we used 1,000 cells randomly subsampled from the 3,184 high-quality single cells described in the original publication. Similar to ref. ¹⁰, we excluded cells belonging to haemogenic endothelial progenitors and erythroblasts. After evaluation of per-cell quality control metrics, and as in ref. ¹⁰, cells with $> 2,000$ detected genes and $< 12.5\%$ mitochondrial gene percentage were retained. Genes detected in at least five cells in any dataset were retained. log-normalization was performed using computeSumFactors in scran package v1.18.7, per-batch scaling normalization using multiBatchNorm in batchelor v1.6.3. Datasets were aligned using the fastMNN approach via SeuratWrappers v0.3.0 using the log-normalized batch-adjusted expression values. MNN low-dimensional coordinates were then used for clustering

and visualization by UMAP. The data processing and analysis pipelines are publicly available at https://github.com/RivronLab/Human_Blastoid_Kagawa_et_al-.

Bulk RNA-seq library preparation and sequencing

Bulk RNA-seq libraries were prepared using Smart-Seq2 protocol as previously described³⁶. For each sample, 50 cells were pooled together and prepared for sequencing. The libraries were then sequenced using an Illumina Novaseq 6000 with 50-bp paired end mode. For each sample, approximately 10 million reads were obtained.

Bulk RNA-seq data analysis

RNA-seq reads were first trimmed using trimgalore v0.5.0 and reads mapping to abundant sequences included in the iGenomes Ensembl GRCh38 bundle (rDNA, mitochondrial chromosome, phiX174 genome, adapter) were removed using bowtie2 v2.3.4.1 alignment. Remaining reads were analyzed using genome and gene annotation for the GRCh38/hg38 assembly obtained from Ensembl release 94. Reads were aligned to the genome using star v2.6.0c and reads in genes were counted with featureCounts (subread v1.6.2) and parameter -s 0. Differential gene-expression analysis on raw counts and variance-stabilized transformation of count data for heatmap visualization were performed using DESeq2 v1.18.1.

Culture of human trophoblast stem cells and aggregate formation

Experiments were performed using the human blastocyst-derived TSC line bTS5 provided by the laboratory of T. Arima. Cells were cultured on Laminin 511 (5 µg ml⁻¹, BioLamina, LN511) coated plates in TSC medium as previously described²⁰. Aggregates of TSCs were formed as follows. Colonies were dissociated into single cells using Accutase at 37 °C for 5 min. The cells were resuspended into TSC medium containing 10 µM Y-27632, and 3.0×10^4 cells were seeded onto a microwell array imprinted into a well of a 96-well plate. The same medium²⁰ was refreshed daily. After 72 h, the aggregates were used for both characterization and implantation experiments.

Endometrial organoid culture

Cryopreserved human endometrial organoids were provided by the H. Baharvand laboratory (Royan Institute) within the framework of collaboration agreements. Human endometrial organoids were established from healthy human donors following the protocol described previously^{24,40} with some modifications. In brief, organoids

were cultured in human endometrial expansion medium composed of 10% R-spondin 1 conditioned medium (in-house made) and 10% noggin-Fc-conditioned medium⁴¹ (in-house made), supplemented with 1× N2 supplement, 1× B27 supplement, 1× insulin-transferrin-selenium (in-house), Glutamax (1 µM), *N*-acetylcysteine (1.25 mM, Sigma-Aldrich, A7250), nicotinamide (2.5 mM, Sigma-Aldrich, 72340), EGF (50 ng ml⁻¹, Peprotech, 100-47), bFGF (2 ng ml⁻¹, Peprotech, 100-18B), HGF (10 ng ml⁻¹, Peprotech, 315-23), FGF10 (10 ng ml⁻¹, Peprotech, 100-26), A83-01 (500 nM) and SB202190 (10 µM, Tocris, 1264). Y-27632 (10 µM) was used in the first 2 days after passaging to prevent apoptosis. The medium was changed every 2 days and the organoids were passaged with TrypLE followed by mechanical dissociation every 7–9 days.

Hormonal stimulation of endometrial organoids and OFEL culture

Endometrial organoids were passaged as described in the previous section. The dissociated cells were resuspended in Matrigel supplemented with Y-27632 (10 µM), cell suspension was deposited in 48-well plates and were cultured in endometrial expansion medium for 2 days. The organoids were stimulated first with E2 (10 nM, Sigma-Aldrich, E2758) for 2 days, followed by the mixture of E2 (10 nM), P4 (1 µM, Sigma-Aldrich, P8783), and cAMP (250 µM, Biolog, B 007) with or without XAV939 (10 µM) (EPC or EPCX respectively) for 4 days. For OFEL culture, organoids were recovered from the matrigel droplets with ice-cold DMEM/F12 and mechanical pipetting. The organoids were dissociated using TrypLE and mechanically triturated to generate single cells and seeded at a density of 3–3.5 × 10⁴ cells per well into a 96-well glass bottom plate (Cellvis, P96-1.5H-N) and cultured for 2–3 days with stimulation. For contraceptive treatment, levonorgestrel⁴² (LNG) (10 µM, Sigma-Aldrich, PHR1850) was added every day to the medium after hormonal stimulation and continued until the end of the experiment.

In vitro implantation assay

Confluent OFELs were prepared for the implantation assay at least 2 h prior to the deposition of blastoids, trophospheres, naive PSCs or TSCs aggregates by washing the OFEL two times with DMEM/F12 and adding mIVC1 medium²⁸. Structures were then transferred onto the OFELs using a mouth pipette under an inverted microscope. After 24–48 h, the medium was removed, the well was washed with PBS, fixed using 4% formaldehyde for 30 min at room temperature and subsequently processed for immunofluorescence staining. The percentage of attached structures was reported as the percentage of total transferred structures.

In vitro culture of human blastoids in post implantation conditions

Human blastoids were selected using a mouth pipette, washed with CMRL1066 medium and transferred into suspension culture plates or 96-well plates coated with Matrigel containing pre-equilibrated media adapted from monkey blastocyst culture²⁷ with minor modifications as followed. For the first day, the culture medium was CMRL1066 supplemented with 10% (v/v) FBS, 1 mM l-glutamine (Gibco), 1× N2 supplement, 1× B27 supplement, 1 mM sodium pyruvate (Sigma) and 10 µM Y27632. After 24 h, half of the medium was replaced with a new medium including 5% Matrigel. After 48h, 50% of medium was replaced with a new medium supplemented with 20% (v/v) FBS and 5% Matrigel. After 72 h, half of the medium was replaced with a new medium supplemented with 30% (v/v) KSR and 5% Matrigel. Then, half of the medium was replaced every day and blastoids were cultured for up to 6 days. Cultures were fixed for staining after 4 and 6 days of in vitro culture with 4% PFA as mentioned above.

Human pre-implantation embryos

The use of human embryos donated to research as surplus of IVF treatment was allowed by the French embryo research oversight committee: Agence de la Biomédecine, under approval numbers RE13-010 and RE18-010. All human pre-implantation embryos used in this study were obtained from and cultured at the Assisted Reproductive Technology unit of the University Hospital of Nantes, France, which is authorized to collect embryos for research under approval number AG110126AMP of the Agence de la Biomédecine. Embryos used were initially created in the context of an assisted reproductive cycle with a clear reproductive aim and then voluntarily donated for research once the patients had fulfilled their reproductive needs or the embryos had tested positive for the presence of monogenic diseases. Informed written consent was obtained from both parents of all couples that donated spare embryos following IVF treatment. Before giving consent, people donating embryos were provided with all of the necessary information about the research project and the opportunity to receive counselling. No financial inducements were offered for donation. Molecular analysis of the embryos was performed in compliance with the guidelines of the embryo research oversight committee and The International Society for Stem Cell Research (ISSCR)⁴³.

RNA extraction, cDNA synthesis and RT-qPCR

RNA was extracted using the RNeasy mini kit (Qiagen, 74106) and cDNA synthesis was performed using the Superscript III (Invitrogen, 18080093) enzyme. qPCR reactions were performed using GoTaq qPCR Master Mix (Promega, A6001) on CFX384 Touch Real-Time PCR Detection System (Bio-rad). Quantification was performed using Microsoft Office Excel by applying the comparative cycle threshold

(C_t) method. Relative expression levels were normalized to GAPDH. The primers used for the qPCR analysis are listed in Supplementary Table 3.

ELISA assay for CG β detection

Medium from wells containing unattached or attached blastoids was collected and centrifuged to remove debris and stored at -80°C until use. The supernatant was subject to CG β ELISA (Abcam, ab178633), according to the manufacturer's instructions, alongside CG β standards.

Ligand–receptor analysis

The Cellinker web-platform was used to predict putative receptor–ligand interactions between polar TE and endometrial epithelial cells. Enriched genes in polar TE along with upregulated genes in stimulated OFELs were used as the query to search ligands and receptors in the database.

Immunohistochemistry

The samples were fixed with 4% formaldehyde for 30 min at room temperature. Post fixation, formaldehyde solution was removed and the samples were washed at least three times with PBS. The samples were then permeabilized and blocked using 0.3% Triton X-100 and 10% normal donkey serum in PBS for at least 60 min. The samples were then incubated overnight at 4°C with primary antibodies diluted in fresh blocking/permeabilization solution. The samples were washed with PBS containing 0.1% Triton X-100 (PBST) at least three times for 10 min each. The washing buffer was then replaced with Alexafluor tagged secondary antibodies (Abcam or Thermofisher scientific) along with a nuclear dye Hoechst-33342 (1:500 or 1:300 for 2D or 3D samples respectively, Life Technologies, H3570) diluted in PBST for 30 min in dark at room temperature. The samples were then washed with PBST three times for 10 min each. For human blastocysts, the samples were fixed at the B4 or B6 stage according to the grading system proposed by Gardner and Schoolcraft⁴⁴ or at B3 or B4 +72 h in vitro culture. Embryos were fixed with 4% paraformaldehyde for 10 min at room temperature and washed in PBS/BSA. Embryos were permeabilized and blocked in PBS containing 0.2% Triton-x100 and 10% FBS at room temperature for 60 min. Samples were incubated with primary antibodies overnight at 4°C . Incubation with secondary antibodies was performed for 2 h at room temperature along with Hoechst counterstaining. The samples were mounted for imaging in PBS in the wells of glass bottom micro slides (Ibidi, 81507). The details of antibodies and their dilutions along with stainings previously performed on human blastocysts (other studies) are provided in the Supplementary Tables 4, 5. EdU staining was done using Click-iT EdU Alexa

Fluor 647 Imaging Kit (Thermo Scientific, C10640) following the manufacturer's instructions.

Microscopy and image analysis

The phase-contrast images were acquired using Thermo Fisher scientific EVOS cell imaging system and inverted wide-field microscope Axio VertA1. The number of blastoids or cavitated structures were counted manually for each well. After 96 h, a blastoid is defined based on the morphological parameters as described in previous sections. The fluorescent images and time-lapse images were acquired using Olympus IX83 microscope with Yokogawa W1 spinning disk (Software: CellSense 2.3; camera: Hamamatsu Orca Flash 4.0) or Nikon Eclipse Ti E inverted microscope, equipped with a Yokogawa W1 spinning disc (Software: Visiview 4.5.0.7 ; camera: Andor Ixon Ultra 888 EMCCD). The confocal images were analysed and display images were exported using FIJI 1.53k or Bitplane Imaris 9.7.0 softwares. For cell counting, Bitplane Imaris software was used. Cell count parameters were set for size and fluorescence strength of voxels and then overall cell count data was obtained for each image using the Imaris spot function. Note that large cavities in blastoids increase the depth of the imaging field and cause poor signal from deeply located cells. Therefore, our counting data in Figs. [1h](#), [3g](#) could be underrepresented values, particularly in the case of trophectoderm cells. The quantification of the percentage of blastoids forming the NR2F2 axis was done manually. To do so, blastoids stained to detect NR2F2 expression were imaged using a confocal spinning disk microscope. The images were projected using a 3D-project function in FIJI. The blastoid was classified to have an axis when NR2F2 expression was restricted to its polar half with no expression or lower level of expression in the mural half. The inverted pattern of NR2F2 expression was classified as an invert axis. The blastoids with NR2F2 expression on their both polar and mural halves were classified to have no axis. Confocal immunofluorescence images of human blastocysts were acquired with a Nikon confocal microscope and a 20 \times mim or 25 \times silicon objective. Optical sections of 1 μ m-thick were collected. The images were processed using Fiji (<http://fiji.sc>) and Volocity 6.3 visualization softwares. Volocity software was used to detect and count nuclei.

Statistics and reproducibility

All the experiments were performed at least in three biological replicates unless specifically described in the Methods and the figure legends. Statistical analyses were performed using Graphpad prism 8.1.1 (330).

Reporting summary

Further information on research design is available in the [Nature Research Reporting Summary](#) linked to this paper.

Data availability

Single-cell RNA-seq and bulk RNA-seq data for human blastoids used in this study were deposited at the Gene Expression Omnibus under the accession number [GSE177689](#). [Source data](#) are provided with this paper.

References

1. 1.
Rivron, N. C. et al. Blastocyst-like structures generated solely from stem cells. *Nature* **557**, 106–111 (2018).
2. 2.
Guo, G. et al. Naive pluripotent stem cells derived directly from isolated cells of the human inner cell mass. *Stem Cell Rep.* **6**, 437–446 (2016).
3. 3.
Rivron, N. et al. Debate ethics of embryo models from stem cells. *Nature* **564**, 183–185 (2018).
4. 4.
Clark, A. T. et al. Human embryo research, stem cell-derived embryo models and in vitro gametogenesis: Considerations leading to the revised ISSCR guidelines. *Stem Cell Rep.* **16**, 1416–1424 (2021).
5. 5.
Liu, X. et al. Modelling human blastocysts by reprogramming fibroblasts into iBlastoids. *Nature* **591**, 627–632 (2021).
6. 6.
Yanagida, A. et al. Naive stem cell blastocyst model captures human embryo lineage segregation. *Cell Stem Cell* **28**, 1016–1022 (2021).
7. 7.

Yu, L. et al. Blastocyst-like structures generated from human pluripotent stem cells. *Nature* **591**, 620–626 (2021).

8. 8.

Sozen, B. et al. Reconstructing aspects of human embryogenesis with pluripotent stem cells. *Nat. Commun.* **12**, 5550 (2021).

9. 9.

Fan, Y. et al. Generation of human blastocyst-like structures from pluripotent stem cells. *Cell Discov.* **7**, 81 (2021).

10. 10.

Zhao, C. et al. Reprogrammed iBlastoids contain amnion-like cells but not trophectoderm. Preprint at <https://doi.org/10.1101/2021.05.07.442980> (2021).

11. 11.

Meistermann, D. et al. Integrated pseudotime analysis of human pre-implantation embryo single-cell transcriptomes reveals the dynamics of lineage specification. *Cell Stem Cell* **28**, 1625–1640.e6 (2021).

12. 12.

Gerri, C. et al. Initiation of a conserved trophectoderm program in human, cow and mouse embryos. *Nature* **587**, 443–447 (2020).

13. 13.

Rossant, J. Making the mouse blastocyst: past, present, and future. *Curr. Top. Dev. Biol.* **117**, 275–288 (2016).

14. 14.

Amita, M. et al. Complete and unidirectional conversion of human embryonic stem cells to trophoblast by BMP4. *Proc. Natl. Acad. Sci. USA* **110**, E1212–E1221 (2013).

15. 15.

Io, S. et al. Capturing human trophoblast development with naive pluripotent stem cells in vitro. *Cell Stem Cell* **28**, 1023–1039.e13 (2021).

16. 16.

Guo, G. et al. Human naive epiblast cells possess unrestricted lineage potential. *Cell Stem Cell* **28**, 1040–1056.e6 (2021).

17. 17.

Hardy, K., Handyside, A. H. & Winston, R. M. The human blastocyst: cell number, death and allocation during late preimplantation development in vitro. *Development* **107**, 597–604 (1989).

18. 18.

Lewis, W. H. & Gregory, P. W. Cinematographs of living developing rabbit-eggs. *Science* **69**, 226–229 (1929).

19. 19.

Messmer, T. et al. Transcriptional heterogeneity in naïve and primed human pluripotent stem cells at single-cell resolution. *Cell Rep.* **26**, 815–824.e4 (2019).

20. 20.

Okae, H. et al. Derivation of human trophoblast stem cells. *Cell Stem Cell* **22**, 50–63.e6 (2018).

21. 21.

Stirparo, G. G. et al. Integrated analysis of single-cell embryo data yields a unified transcriptome signature for the human pre-implantation epiblast. *Development* **145**, dev158501 (2018).

22. 22.

Linneberg-Agerholm, M. et al. Naïve human pluripotent stem cells respond to Wnt, Nodal, and LIF signalling to produce expandable naïve extra-embryonic endoderm. *Development* **146**, dev180620 (2019).

23. 23.

Dumortier, J. G. et al. Hydraulic fracturing and active coarsening position the lumen of the mouse blastocyst. *Science* **365**, 465–468 (2019).

24. 24.

Boretto, M. et al. Development of organoids from mouse and human endometrium showing endometrial epithelium physiology and long-term expandability. *Development* **144**, 1775–1786 (2017).

25. 25.

Wang, W. et al. Single-cell transcriptomic atlas of the human endometrium during the menstrual cycle. *Nat. Med.* **26**, 1644–1653 (2020).

26. 26.

Castel, G. et al. Induction of human trophoblast stem cells from somatic cells and pluripotent stem cells. *Cell Rep.* **33**, 108419 (2020).

27. 27.

Ma, H. et al. In vitro culture of cynomolgus monkey embryos beyond early gastrulation. *Science* **366**, eaax7890 (2019).

28. 28.

Xiang, L. et al. A developmental landscape of 3D-cultured human pre-gastrulation embryos. *Nature* **577**, 537–542 (2020).

29. 29.

Guo, G. et al. Epigenetic resetting of human pluripotency. *Development* **144**, 2748–2763 (2017).

30. 30.

Rivron, N. C. et al. Tissue deformation spatially modulates VEGF signaling and angiogenesis. *Proc. Natl. Acad. Sci. USA* **109**, 6886–6891 (2012).

31. 31.

Vrij, E. J. et al. 3D high throughput screening and profiling of embryoid bodies in thermoformed microwell plates. *Lab Chip* **16**, 734–742 (2016).

32. 32.

Yu, F.-X. et al. Regulation of the Hippo–YAP pathway by G-protein-coupled receptor signaling. *Cell* **150**, 780–791 (2012).

33. 33.
Turco, M. Y. et al. Trophoblast organoids as a model for maternal-fetal interactions during human placentation. *Nature* **564**, 263–267 (2018).
34. 34.
Zhao, B. et al. Inactivation of YAP oncprotein by the Hippo pathway is involved in cell contact inhibition and tissue growth control. *Genes Dev.* **21**, 2747–2761 (2007).
35. 35.
Kim, S.-I. et al. Inducible transgene expression in human iPS cells using versatile all-in-one piggyBac transposons. *Methods Mol. Biol.* **1357**, 111–131 (2016).
36. 36.
Picelli, S. et al. Full-length RNA-seq from single cells using Smart-seq2. *Nat. Protoc.* **9**, 171–181 (2014).
37. 37.
Petropoulos, S. et al. Single-cell RNA-seq reveals lineage and X chromosome dynamics in human preimplantation embryos. *Cell* **165**, 1012–1026 (2016).
38. 38.
Zhou, F. et al. Reconstituting the transcriptome and DNA methylome landscapes of human implantation. *Nature* **572**, 660–664 (2019).
39. 39.
Tyser, R. C. V. et al. Single-cell transcriptomic characterization of a gastrulating human embryo. *Nature* **600**, 285–289 (2021).
40. 40.
Turco, M. Y. et al. Long-term, hormone-responsive organoid cultures of human endometrium in a chemically defined medium. *Nat. Cell Biol.* **19**, 568–577 (2017).
41. 41.

Heijmans, J. et al. ER stress causes rapid loss of intestinal epithelial stemness through activation of the unfolded protein response. *Cell Rep.* **3**, 1128–1139 (2013).

42. 42.

Matsuo, M. et al. Levonorgestrel inhibits embryo attachment by eliminating uterine induction of leukemia inhibitory factor. *Endocrinology* **161**, bqz005 (2020).

43. 43.

Kimmelman, J. et al. New ISSCR guidelines: clinical translation of stem cell research. *Lancet* **387**, 1979–1981 (2016).

44. 44.

Gardner, D. K., Lane, M., Stevens, J., Schlenker, T. & Schoolcraft, W. B. Blastocyst score affects implantation and pregnancy outcome: towards a single blastocyst transfer. *Fertil. Steril.* **73**, 1155–1158 (2000).

45. 45.

Mischler, A. et al. Two distinct trophectoderm lineage stem cells from human pluripotent stem cells. *J. Biol. Chem.* **296**, 100386 (2021).

46. 46.

Jeschke, U. et al. The human endometrium expresses the glycoprotein mucin-1 and shows positive correlation for Thomsen–Friedenreich epitope expression and galectin-1 binding. *J. Histochem. Cytochem.* **57**, 871–881 (2009).

47. 47.

Zhang, Y. et al. Cellinker: a platform of ligand–receptor interactions for intercellular communication analysis. *Bioinformatics* **37**, 2025–2032 (2021).

Acknowledgements

This project has received funding from the European Research Council (ERC) under the European Union’s Horizon 2020 research and innovation programme (ERC-Co grant agreement no.101002317 ‘BLASTOID: a discovery platform for early human embryogenesis’). H.H.K. is supported by the Austrian Science Fund (FWF), Lise

Meitner Programme M3131-B. This project has also received funding from the ANR ‘BOOSTIVF’. L.D. thanks the iPSCDTC and MicroPICell core facilities. We thank Y. Takashima for sharing the H9 and H9-GFP cell lines; A. Smith, P. Andrews and G. Guo for sharing the HNES1, Shef6, niPSC 16.2b and cR-NCRM2 cell lines; H. Baharvand for sharing the endometrial organoids; K. Woltjen for sharing the PB-TAC-ERP2 and pCAG-PBase plasmids; K. Guan for sharing pQCXIH-Myc-YAP, pQCXIH-Myc-YAP-5SA, pQCXIH-Myc-YAP-S94A plasmids; J. M. Brickman for sharing the RNA isolated from PrE differentiated cells and nEND cells; S. Srinivas for sharing the single-cell RNA-seq data of peri-gastrulation embryo; A. Bykov and L. Cochella for technical assistance for SMARTSeq2 library preparation; and the NGS, Biooptic and Stem Cell facility at IMBA for critical assistance.

Author information

Author notes

1. These authors contributed equally: Harunobu Kagawa, Alok Javali, Heidar Heidari Khoei

Affiliations

1. Institute of Molecular Biotechnology of the Austrian Academy of Sciences (IMBA), Vienna BioCenter (VBC), Vienna, Austria

Harunobu Kagawa, Alok Javali, Heidar Heidari Khoei, Theresa Maria Sommer, Giovanni Sestini, Maria Novatchkova, Yvonne Scholte op Reimer & Nicolas Rivron

2. Institute of Molecular Pathology (IMP), Vienna Biocenter, Vienna, Austria

Maria Novatchkova

3. Université de Nantes, CHU Nantes, INSERM, Centre de Recherche en Transplantation et Immunologie, UMR 1064, ITUN, Nantes, France

Gaël Castel, Alexandre Bruneau, Jenna Lammers, Sophie Loubersac, Thomas Freour & Laurent David

4. Unit of Stem Cell Research, Cluster of Stem Cell and Developmental Biology, Department of Development and Regeneration, KU Leuven, (University of Leuven), Leuven, Belgium

Nina Maenhoudt & Hugo Vankelecom

5. CHU Nantes, Service de Biologie de la Reproduction, Nantes, France

Jenna Lammers, Sophie Loubersac & Thomas Freour

6. Université de Nantes, CHU Nantes, INSERM, CNRS, SFR Santé, FED 4203,
INSERM UMS 016, CNRS UMS 3556, Nantes, France

Laurent David

Contributions

H.K., A.J., H.H.K. and N.R. conceived the study; N.R. supervised the project; H.K., A.J., H.H.K., T.M.S. and N.R. designed the blastoid experiments; H.K., A.J., H.H.K., T.M.S. and Y.S.o.R. performed blastoid experiments; G.S., G.C. and M.N. performed the bioinformatic analysis of single-cell RNA-seq datasets; J.L., S.L. and T.F. managed human embryos donated for research in Nantes; A.B., J.L., S.L. and G.C. performed experiments on human embryos in Nantes; L.D. supervised experiments on human embryos in Nantes; H.H.K., N.M., H.V. and N.R. designed the experiments with endometrial organoids; N.R. hosted N.M. and G.C. in his laboratory; H.K., A.J., H.H.K., T.M.S., Y.S.o.R., G.C., A.B., N.M. and N.R. analysed data; N.R. wrote the manuscript with help from all of the authors.

Corresponding author

Correspondence to [Nicolas Rivron](#).

Ethics declarations

Competing interests

The Institute for Molecular Biotechnology, Austrian Academy of Sciences has filed patent application EP21151455.9 describing the protocols for human blastoid formation and for the blastoid–endometrium interaction assay. H.K., A.J., H.H.K. and N.R. are the inventors on this patent. All other authors declare no competing interests.

Peer review information

Nature thanks Jan Brosens, Jianping Fu, Insoo Hyun and the other, anonymous, reviewer(s) for their contribution to the peer review of this work.

Additional information

Publisher's note Springer Nature remains neutral with regard to jurisdictional claims in published maps and institutional affiliations.

Extended data figures and tables

[Extended Data Fig. 1 Naive hPSCs form human blastocyst-like structures comprising analogs of the three founding lineages.](#)

a. Phase contrast images of naive hPSCs cultured in PXGL medium and on MEF feeder layers. Scale bar: 50 µm. **b.** Time course phase contrast images of naive hPSCs aggregates cultured within microwell arrays either without LPA (PALY medium, **top**) or with 500 nM LPA (PALLY medium, **bottom**).

Scale bar: 200 μ m. **c.** Quantification of the effect of the initial cell numbers per microwell array on the yield of blastocyst-like structures. n=1 microwell arrays. **d.** Quantification of the effect of serial passaging of naive hPSCs on the yield of blastocyst-like structures. n=3 microwell arrays. mean \pm S.D. **e.** Quantification of the cell numbers per microwell at the time of seeding and in blastocyst-like structures at 96 h when cells are seeded at 3.0×10^4 cells per microwell array. n=190 microwells (seeding) and n=12 blastocyst-like structures (96 hrs.). **f.** Fluorescence staining of DNA using Hoechst in representative naive hPSCs aggregates over the course of formation of blastocyst-like structures (96 h, **left**). Scale bar: 50 μ m. Measurement of the distributed diameters of the structures over the course of formation of blastocyst-like structures (**right**). n=15, 31 and 11 for 0, 60 and 96 h, respectively. **g.** Pseudotime analysis of human pre-implantation development showing the expression of the TE markers *GATA2*, *GATA3*, *CDX2* and *TACSTD2*. Gene expression analysis was performed by using the public data analysis tool (<https://bird2cluster.univ-nantes.fr/demo/PseudoTimeUI/>). **h.** Immunofluorescence stainings for EPI marker NANOG (Yellow), TE marker CDX2 (Cyan) and primitive endoderm marker GATA4 (Magenta) in a representative B4-stage human blastocyst. Scale bar: 50 μ m. **i.** Immunofluorescence stainings for the EPI markers (Yellow) NANOG (**top**) and OCT4 (**bottom**); the TE markers (Cyan) CDX2 (**top**) and GATA3 (**bottom**); and the primitive endoderm marker (Magenta) GATA4 in five representative blastocyst-like structures. Counterstain with Hoechst (Grey) marking DNA. Scale bar: 50 μ m. **j.** Immunofluorescence staining for EPI marker OCT4 (yellow) and TE marker GATA2 (Cyan) in blastocyst-like structures. Scale bar: 100 μ m. **k.** Immunofluorescence staining for TE markers GATA3 (Cyan) and TROP2 (Magenta) in blastocyst-like structures. Scale bar: 100 μ m. **l.** Immunofluorescence staining for TE markers GATA3 (Cyan) and PrE marker GATA4 (Magenta) and PDGFR α (Yellow) in blastocyst-like structures. Scale bar: 100 μ m. **m.** Single optical section of immunofluorescence staining image for the tight junction molecule ZO-1 (Yellow), the adherence junction molecule CDH1 (Magenta), and the apical domain molecule aPKC (Cyan) in a representative human blastocyst-like structures. Scale bars: 50 μ m. **n.** Representative time points from a timelapse image of naive cell aggregates, cavitating into blastocyst-like structures while showing cycles of cavity inflation and deflation (**left**) -

quantification of blastocyst-like structures showing distinct frequencies of inflation and deflation (**right**). n=1 microwell arrays. Scale bar: 100 μ m. **o**. Phase contrast images of representative areas of microwell arrays showing blastocyst-like structures formed from different naive hPSCs and hiPSCs lines. n>3. Scale bar: 100 μ m. **p**. Quantification of the yield of blastocyst-like structures obtained from naive and primed H9 hPSCs. n=3 microwell arrays. mean \pm S.D.

[Source data](#)

Extended Data Fig. 2 Human blastocyst-like structures form analogs of pre-implantation lineages.

a. Flow cytometry analysis plot of cells isolated from blastocyst-like structures and stained for lineage-specific surface markers PDGFR α (PrE) and TROP2 (TE). The gates were used to sort analogs of EPI (double negative), TE (TROP2^{high}) and PrE (PDGFR α ^{high}) to subsequently process for single cell RNA sequencing. Note that the gates did not exclude any cells. This analysis was performed to correlate RNA measures, while ensuring a representation of all cell types. **b.** UMAPs of the transcriptome of single cells isolated from blastocyst-like structures and displaying the expression levels of genes specific for each of the three blastocyst lineages (TE - Trophectoderm, EPI - Epiblast, and PrE- Primitive endoderm). **c-g.** UMAPs of single cells isolated from both blastocyst-like structures and from embryos ranging from E3 to E19. **c.** Coloration of cells originating from *In Vitro Fertilization* (IVF) embryos isolated on day 3 (E3) to day 7 (E7). This period comprises only pre-implantation stage embryos. **d.** Coloration of cells originating from IVF embryos isolated on day 6 (E6) to day 12 (E12). These blastocysts (E6) were cultured *in vitro*. Note that this annotation reflects the number of days in culture rather than the developmental stages. **e.** Coloration of cells originating from gastrulation-stage embryo isolated on day 17 (E17) to 19 (E19). **f.** The expression levels of genes specific for each of the three blastocyst lineages (EPI, TE, and PrE). **g.** Coloration of cells displaying their unsupervised cluster affiliation.

Extended Data Fig. 3 Measurement of generation of off-target cells in human blastocyst-like structures and naive human pluripotent stem cells.

a, b. UMAP of clusters formed from cells isolated from blastocyst-like structures (high-resolution clustering of 1, x50 as compared to Fig. 2b) (**a**) and displaying the expression levels of genes specific for amnion lineage (**b**). **c.** Origin of the cells composing cluster 11. **d-h.** UMAPs of naive hPSCs, primed hPSCs, cells isolated from blastocyst-like structures and cells isolated from a CS7 staged human embryo. **d.** Coloration of embryo cells based on previously proposed annotations³⁹. **e.** Coloration of stem cells based on their origin. **f.** Display of the expression levels of genes specific for each of the three blastocyst lineages (EPI - Epiblast, TE - Trophectoderm, and PrE- Primitive endoderm). **g.** Coloration of individual cells based on their unsupervised cluster affiliation. **h.** Coloration of the cells previously identified as cluster 11 (see **a, b**). **i.** Quantification of the percentage of cells identified as abnormal based on the location in the UMAP in **h** (**top**) and on the cells annotations (**bottom**) for both naive hPSCs (**left**) and cells isolated from blastocyst-like structures (**right**). Similar results were obtained based on the location in the UMAP in (Extended Data Fig. 2c-e). **j.** Heatmap of previously proposed markers of different lineages differentially expressed in cells from blastocyst-like structures and gastrulation-stage embryo¹⁰.

Source data

Extended Data Fig. 4 Cells in human blastocyst-like structures are transcriptionally similar to pre-implantation lineages.

a. Principal component analysis (PCA) plot with PC1 vs PC2 (**top**) or PC1 vs PC3 (**bottom**) computed with top 500 variable gene in the bulk transcriptome of individual lineages of blastocyst-like structures (EPI, TE and PrE); stem cell lines: naive and primed hPSCs; hTSCs: blastocyst derived hTSCs (bTS5)²⁰, primed hPSC derived hTSCs (BAP¹⁴ and TM4 protocols⁴⁵; PrE like stem cell lines (RACL or nEND cells²²); naive PSC and TSCs rederived from blastocyst-like structures (see methods). **b.**

Heatmap of key blastocyst and post-implantation lineage markers differentially expressed between TE analogs ($TROP2^+$) of the blastocyst-like structures and hTSCs in their bulk transcriptome. **c.** Pseudotime analysis of human mature TE markers *CGB5*, *CGB7*, *CGB8* and *CGA*. Gene expression analysis was performed by using the public data analysis tool (<https://bird2cluster.univ-nantes.fr/demo/PseudoTimeUI/>). **d.** Heatmap of key pluripotency related genes differentially expressed between EPI analogs ($PDGFR^-/ TROP2^-$) in the blastocyst-like structures and primed hPSCs **e.** Heatmap of key pluripotency related genes or PrE markers differentially expressed between PrE analogs ($PDGFR\alpha^+$) in the blastocyst-like structures, naive PSC derived PrE-like cells and nEND cells.

Extended Data Fig. 5 Human blastocyst-like structures are permissive for derivation of stem cell lines.

a. Immunofluorescence staining for pluripotency factors NANOG (Yellow), OCT4 (Magenta), SOX2 (Cyan) and for naive pluripotency factor KLF17 (Yellow) in naive hPSC controls (**top**) and naive hPSCs derived from blastocyst-like structures (**bottom**). Scale bar: 100 μ m. **b.** Phase contrast images of blastocyst-like structures on microwell array formed from three rederived naive hPSC lines. Scale bar: 200 μ m. **c.** Immunofluorescence stainings for EPI marker (NANOG), TE marker (CDX2) and primitive endoderm marker (GATA4) in representative second-generation blastocyst-like structures. Scale bar: 100 μ m. **d.** Immunofluorescence staining for GATA3 (Cyan), post-implantation trophoblast marker CK7 (Magenta) and CDX2 (Yellow) in bTS5 hTSC (**top**) and hTSCs derived from blastocyst-like structures (**bottom**). Scale bar: 100 μ m. **e.** Phase contrast images of day 6 EVT differentiations from three hTSC lines derived from blastocyst-like structures. Scale bar: 150 μ m. **f.** Immunofluorescence stainings of trophoblast markers GATA3 (Cyan) and EVT marker HLA-G (Yellow) and CG β (Magenta) of day 6 EVT analogs from three hTSC lines, derived from blastocyst-like structures. Scale bar: 100 μ m. **g.** Phase contrast images of day 3 SCT analogs differentiated from three hTSC lines derived from blastocyst-like structures. Scale bar: 150 μ m. **h.** Immunofluorescence stainings for trophoblast markers GATA3 (Cyan) and SCT marker SDC1 (Yellow) and CG β (Magenta) of day 3 SCT analogs formed from hTSC line derived from blastocyst-like structure (Clone 1). Scale bar: 100 μ m. **i.**

Immunofluorescence stainings for CG β (Magenta) counterstained with Phalloidin (Cyan) and Hoechst marking Actin and DNA respectively (**left**), SDC (Yellow), CK7 (Magenta) (**right**) counterstained with Hoechst marking DNA of day 6 trophoblast organoids formed from hTSC lines derived from blastocyst-like structures (Clone 1). Scale bar: 50 μ m. **j.** Relative expression levels, as measured by RT-PCR, of day 6 EVT (**top**) and day 3 SCT analogs (**bottom**) with respective undifferentiated hTSCs lines derived from blastocyst-like structures. Expression levels were normalized to expression of *GAPDH*. n=1 biological replicate for three individual clones.

[Source data](#)

[Extended Data Fig. 6 The development of the human trophectoderm analog depends on aPKC and Hippo elements.](#)

a. A frame from time-lapse microscopy of B2 stage human blastocyst (**left**). Schematic showing the differential Hippo activity in inner and outer cells of developing blastocyst and the molecular regulators of the Hippo signalling pathway (**right**). **b.** Phalloidin fluorescence (Cyan) stainings for F-actin in naive hPSCs aggregates cultured in PALLY medium for 24 h (**top**) and 60 h (**bottom**). Counterstain with Hoechst marking DNA. Scale bar: 50 μ m. **c.** Immunofluorescence stainings for aPKC (Cyan) and YAP1 (Yellow) in aggregates of naive hPSCs cultured in PALLY medium for 24 h (**top**) and 60 h (**bottom**). Counterstain with Hoechst marking DNA. Scale bar: 50 μ m. **d.** Immunofluorescence stainings for YAP1 (Yellow) with GATA2 (Cyan) in aggregates of naive hPSCs cultured in PALLY medium for 24 h. Scale bar: 50 μ m. **e.** Immunofluorescence stainings for YAP1 (Yellow) and GATA3 (Cyan) (**top**) and YAP1 (Yellow) and NANOG (Cyan) (**bottom**) in naive hPSCs aggregates cultured in PALLY medium for 24 h (**left**) and 60 h (**right**). Counterstain with Hoechst marking DNA. Scale bar: 50 μ m. **f.** Immunofluorescence staining for YAP1 (Yellow) and GATA3 (Cyan) in blastocyst-like structures cultured without (**top**) or with an aPKC inhibitor (2 μ M CRT0103390, **bottom**). Counterstain with Hoechst marking DNA (Red). Insets: Individual and merge channels of YAP1 and GATA3 for a single optical section as well as maximum intensity projection of all the optical sections. Scale bar: 50 μ m. **g.** Quantification of the yield of

blastocyst-like structures upon the culture in PALLY medium or PALLY medium complemented with an aPKC inhibitor (2 μ M CRT0103390). n=3 independent microwell arrays; mean \pm S.D.; Two tailed unpaired t-test. *** is P=0.0002. **h.** Quantification of the percentage of GATA3 $^{+}$ cells in structures cultured in PALLY medium or in PALLY medium complemented with a aPKC inhibitor (2 μ M CRT0103390). n=7 blastocyst-like structures for the group cultured in PALLY medium and n=12 aggregates for the group cultured in PALLY medium complemented with CRT0103390. Representative results from three independent experiments. Mean \pm S.D.; Two-tailed unpaired t-test. **** is P=1.79e-08. **i.** Quantification of the dose dependent effect of the LPA receptor agonist NAEPA on the yield of blastocyst-like structures. The PALY medium (thus without LPA) was complemented with NAEPA. n=3 independent microwell arrays; mean \pm S.D.; one-way Anova and Tukey's multiple comparisons test. *** is P<0.0001. **j.** Phase contrast images of representative naive hPSC aggregates cultured in PALLY medium complemented with Doxycycline (100 ng/ml) for 72 h and overexpressing different variants of YAP1. The naive hPSCs aggregates were cultured with an adjusted PALLY medium characterized by a reduced LPA concentration (5 nM). Scale bar: 100 μ m. **k.** Measurement of the effect of Verteporfin (suppressor of the YAP1–TEAD complex) on the yield of blastocyst-like structures. n=3 independent microwell arrays; mean \pm S.D.; one-way Anova and Dunnett's multiple comparisons test. ** is p=0.0010, *** is p=0.00019, **** is P<0.0001. **l.** Phalloidin fluorescence staining of F-actin (Cyan) in naive hPSCs aggregates cultured in PALLY medium for 60 h. Counterstain with Hoechst marking DNA. Yellow arrows: Formation of cavities. Scale bar: 50 μ m. **m.** Immunofluorescence stainings for Aquaporin3 (AQP3, Cyan) and OCT4 (Yellow) in naive hPSCs aggregates cultured in PALLY medium for 36 (**left**) or 96 h (**right**, blastocyst-like structure stage). Scale bar: 50 μ m.

[Source data](#)

[**Extended Data Fig. 7 Blastocyst-like structures recapitulate the sequential specification of lineages occurring during blastocyst development.**](#)

a. Heatmap of the average count values in the expression of TE genes upon formation of the blastocyst-like structures TE analogs. **b-d.** Immunofluorescence stainings for GATA3 (Cyan) and OCT4 (Yellow) (**b**) or CDX2 (Cyan) and NANOG (Yellow) (**c**) or CDX2 (Cyan) and KLF17 (Yellow) (**d**) in naive hPSCs aggregates cultured in PALLY medium for 24 h (**top**) or 60 h (**bottom**). Scale bar: 50 µm. **e.** Gene ontology terms associated with the genes differentially regulated in the late TE analog of blastocyst-like structures (cluster 10) as compared to the early TE (cluster 2). **f.** Heatmap of average count values of Wnt, TGF-β and Notch signaling-associated genes in cells from cluster 4 (naive hPSCs), 10, 2 and 5 (TE analogs) and 7 (TSC). **g.** UMAPs of single cells isolated from blastocyst-like structures and displaying the expression levels of polar trophectoderm specific gene: NR2F2. **h.** Immunofluorescence staining for CDX2 (Cyan), NR2F2 (Magenta) and NANOG (Yellow) in blastocyst-like structures. Scale bar: 100 µm. **i.** UMAPs of single cells isolated from blastocyst-like structures and displaying the expression levels of polar trophectoderm specific gene: CCR7. **j.** Immunofluorescence stainings for CCR7 (Cyan) in a blastocyst-like structures. Counterstain with Hoechst marking DNA. Scale bar: 50 µm. **k.** Heatmap of average count values of top differentially regulated genes in cells from cluster 4 (naive hPSCs), 0 (EPI analogs) and 9 (primed hPSCs). **l.** Immunofluorescence staining for KLF17 (Cyan) and OCT4 (Yellow) or KLF4 (Cyan) and OCT4 (Yellow) (**top**) and SUSD2 (Cyan) and NANOG (Yellow) or IFI16 (Cyan) and KLF17 (Yellow) (**bottom**) in blastocyst-like structures. Counterstain with Hoechst marking DNA. Scale bar: 100 µm. **m.** UMAPs of single cells isolated from blastocyst-like structures and displaying the expression levels of X chromosome activation-related gene-*XACT*. **n.** Flow cytometry analysis plot of cells isolated from blastocyst-like structures cultured in PALLY medium for 60 h and stained for lineage-specific surface markers PDGFR α (PrE) and TROP2 (TE). **o, p.** Immunofluorescence stainings for OTX2 (Cyan), GATA4 (Magenta) and OCT4 (Yellow) (**o**) and SOX17 (Cyan) and GATA4 (Magenta) (**p**) in naive hPSCs aggregates cultured in PALLY medium for 60 h. Counterstain with Hoechst marking DNA. Scale bar: 50 µm. **q.** Heatmap of the average count values in the expression of PrE genes upon formation of the blastocyst-like structures PrE analogs. **r.** Heatmap of average count values of SMAD, MAPK and Wnt signaling-associated genes in cells from cluster 1, 6 (EPI analogs) and 8 (PrE analogs).

Source data

Extended Data Fig. 8 Human blastoids recapitulate aspects of implantation.

a. Immunofluorescence stainings for CDH1 (Magenta) and a ciliated cell marker acetylated α -tubulin (Yellow) in OFELs (**left**). Y-Z plane shows the apical location of the cilia (**right**). Scale bar: 50 μ m. **b.** Immunofluorescence staining for FOXA2 (Yellow) marking the endometrial glandular cells in OFELs. Scale bar: 50 μ m. **c.** Immunofluorescence staining for PAEP (Yellow) in non-stimulated (**left**) and stimulated (**right**) OFELs. **d.** qRT-PCR measurement of the expression levels of window-of-implantation markers in OFELs cultured with different media. Ctrl: Control medium, E: Estradiol, P: Progesterone, C: cAMP, X: XAV-939. Expression levels were normalized relative to the housekeeping gene GAPDH and the control condition. n = 2 independent experiments. The colors depict the data from 3 different donors. **e.** Heatmap of key cell cycle and secretory epithelial genes differentially expressed between stimulated and non-stimulated OFELs in bulk transcriptome. **f.** Staining for incorporated EdU (Red) reflective of cell proliferation in a stimulated OFEL (**left**). Scale bar: 50 μ m. Quantification of the number of EdU⁺ cells in non-stimulated and stimulated OFELs (**right**). Counterstain with Hoechst marking DNA. n=4 independent experiments. mean \pm S.D.; Unpaired two-tailed *t*-test, *** is P = 0.0009. **g.** Quantification of blastoid attachment onto OFELs prepared using endometrial organoids from 3 different donors. n=3 independent experiments for donor 1 and n=2 independent experiments for donor 2 and 3; mean \pm S.D.; Unpaired two-tailed *t*-test, ** is P = 0.0011. **h.** Immunofluorescence stainings for MUC1 (Magenta), a glycoprotein that highly expresses at the luminal epithelial surface of endometrium in the receptive phase⁴⁶, with an attached GFP+ blastoid (48 h after deposition onto an OFEL). Dashed lines indicate the area that trophoblast cells repelled endometrial cells. Scale bar: 200 μ m **i.** Quantification of blastoid attachment onto non-stimulated, stimulated OFELs, and OFELs additionally exposed to the contraceptive Levonorgestrel (LNG, 10 μ M). n=3 independent experiments. mean \pm S.D.; one-way Anova and Tukey's multiple comparisons test, * is P = 0.0211, *** is P = 0.0006.

Source data

Extended Data Fig. 9 Trophectoderm state is crucial for interaction with endometrium during implantation.

a. Representative images of human blastoids shortly after attachment to an OFEL. Dotted line outlines the inner cluster of blastoids that were formed using GFP⁺ naive hPSCs (**top**, also see Supplementary Video 3). Immunofluorescence stainings for NR2F2 (Magenta) and OCT4 (Yellow) in blastoids shortly after attachment to an OFEL (**bottom**). **b.** Immunofluorescence stainings for NR2F2 (Magenta) and OCT4 (Yellow) and respective fluorescence intensity profiles of representative blastoids immediately after attachment onto OFEL. Profiles were measured perpendicular to the plane of attachment (**right**). Line width, 10 µm. Y axis shows normalized intensity. **c.** Quantification of the distance between the first peak of fluorescence intensity profiles of NR2F2 and OCT4. n=10 attached blastoids. mean± S.D. **d.** Pseudotime analysis of human pre-implantation development showing the expression of *IL6*, *IL6R*, *GP130* and *STAT3*. Gene expression analysis is performed by using the public data analysis tool (<https://bird2cluster.univ-nantes.fr/demo/PseudoTimeUI/>). **e.** Quantification of the dose dependent effect of LIF on the yield of blastoids. n=2 (without Lif) and n=3 (all other conditions) independent experiments. mean± S.D. **f.** Immunofluorescence staining for NANOG (Yellow) and CDX2 (Cyan) (**left**), OCT4 (Yellow) and GATA3 (Cyan) (**middle**) and CDX2 (Cyan) and NR2F2 (Magenta) (**right**) in representative trophospheres formed from a blastoid exposed to SC144. Scale bar: 50 µm. **g.** Immunofluorescence staining for NANOG (Yellow) and CDX2 (Cyan) (**left**), OCT4 (Yellow) and GATA3 (Cyan) (**right**) in representative trophospheres formed from a blastoid exposed to XMU-MP-1. Scale bar: 50 µm. **h.** Heatmap of key lineage specific genes differentially expressed in bulk transcriptome of the trophectoderm of blastoids (TROP2 positive cells), trophospheres (SC144 or XMU) and TSCs (2D or 3D) compared to naive hPSCs. **i.** PCA plot computed using bulk transcriptome of blastoid cells, hPSCs (naive, primed or blastoid rederived naive cell lines), TSCs (bTS5, blastocyst rederived lines or human stem cell derived TSC like cells) and pluripotent stem cell derived primitive endoderm like cells (RACL or NACL cells). **j.** Immunofluorescence stainings for CDX2 (Cyan)

(left) and CK7 (Magenta) and GATA3 (Cyan) (right) in aggregates formed from bTS5 hTSCs. Counterstain with Hoechst marking DNA. Scale bar: 50 μ m. **k**. Representative phase contrast images of aggregates of naive hPSCs, deposited onto stimulated OFELs. Scale bar: 100 μ m. **l**. List of selected putative ligand-receptor pairs involved in cross-talk between polar trophectoderm and endometrial epithelial cells. The list was generated by in silico ligand receptor analysis of genes enriched in polar trophectoderm and stimulated OFEL, using Cellinker⁴⁷.

[Source data](#)

[Extended Data Fig. 10 Human blastoids recapitulate aspects of peri-implantation progression until day 13.](#)

a. Bright-field images of human blastoids (96 h) cultured for 4 additional days on a low attachment plate in post implantation culture condition (left). Each row shows a time series of an individual blastoid for 4 days. Note that, blastoids stably retain cavities at least for 2 days upon transferring to IVC media which has different osmolarity compared to the N2B27 media with PALLY. (See the [methods](#) for the composition of post implantation culture media.) Scale bar: 200 μ m. Quantification of percentage of blastoids retaining cavities on each day of postimplantation stage culture (right). n=2 independent experiments. **b.** Immunofluorescence staining for the syncytiotrophoblast-associated marker CG β (Magenta) in GFP $^+$ blastoids attached onto stimulated OFELs (48 h after deposition) (left). Counterstain with Hoechst marking DNA. Scale bar: 50 μ m. ELISA measurements of the concentration of the protein CG β secreted into the culture medium of unstimulated OFELs with unattached blastoids and stimulated OFELs with attached blastoids (24 and 48 h) (right). n=3 independent experiments. mean \pm S.D.; one-way Anova and Tukey's multiple comparisons test, *** is P = 0.00006. **c.** Immunofluorescence stainings for CDX2 (Cyan), NR2F2 (Magenta) and SOX2 (Yellow) in blastoids grown in postimplantation culture condition for 4 days. Scale bar: 100 μ m. **d.** Immunofluorescence stainings for OCT4 (Yellow), CK7 (Cyan) and GATA4 (Magenta) in blastoids grown in postimplantation culture condition for 4 days. Scale bar: 100 μ m. **e, f.** Immunofluorescence stainings for CG β (Magenta) and NR2F2 (Cyan) (e) or HLA-G (Magenta) and GATA3 (Cyan) (f), in blastoids grown

in postimplantation culture condition for 4 days (**e**) or 6 days (**f**). Counterstain with Hoechst marking DNA. Arrowhead points HLA-G positive EVT like cells. Scale bar: 100 µm. **g**. Immunofluorescence stainings for CD24 (Magenta) and SOX2 (Yellow) in blastoids grown in postimplantation culture condition for 6 days. Counterstain with Hoechst marking DNA. Scale bar: 100 µm. **h**. Immunofluorescence stainings for PODXL (Magenta) and SOX2 (Yellow) in blastoids grown in postimplantation culture condition for 4 days. Counterstain with Phalloidin marking F-actin (Cyan). Arrowhead points pro-amniotic-like cavity. Scale bar: 100 µm. **i-k**. Immunofluorescence stainings for SOX2 (Yellow), GATA3 (Cyan) and CDX2 (Magenta) (**i**), SOX2 (Yellow), CDX2 (Magenta) and TFAP2C (Cyan) (**j**), OCT4 (Yellow), GATA4 (Magenta) and OTX2 (Cyan) (**k**) in blastoids grown in postimplantation culture condition for 4 days. Counterstain with Hoechst marking DNA. Scale bar: 100 µm. **l**. Quantification of number of cells belonging to EPI, TE or PrE lineages in the blastoids cultured in postimplantation culture condition for four days on glass or OFEL. n=7 biological replicates. mean± S.D. **m**. Immunofluorescence stainings for OCT4 (Yellow), GATA3 (Cyan) and GATA4 (Magenta) in blastoids grown in postimplantation culture condition for 6 days corresponding to time equivalent of day 13 of cultured human blastocyst (**left**). Scale bar: 100 µm.

[Source data](#)

Supplementary information

[Reporting Summary](#)

[Supplementary Table 1](#)

Differentially expressed genes based on bulk and single-cell RNA-seq data. Tab1: Differentially expressed genes and enriched GO term are listed based on the comparison between PrE analogue cells isolated from blastoid and in vitro PrE stem cell culture (nEND and PrE cells: Linneberg-Agerholm et al., 2019). Tab2: Differentially expressed genes and enriched GO term are listed based on the comparison of TE analogue cells isolated from blastoid

against in vitro TSCs in 2D (Okae et al., 2018), or TE analogue cells derived from trophosphere induced by XMU-MT-1 treatment and the comparison between TE analogue cells derived from trophosphere induced by SC-144 and naive PSC. Differentially expressed genes are listed based on the comparison of TE analogue cells isolated from blastoid against TSCs in 3D culture or TSC converted from naive PSC in 2D culture condition (Guo et al., 2021). Tab3: Differentially expressed genes and enriched GO term are listed based on the comparison of different cluster of cells in UMAP generated by single-cell RNA seq. The tables contain the comparison between cluster 4 (naive PSC) and cluster 10 (early TE analogue), cluster 2 (mural TE analogue) and cluster 10 (early TE analogue), cluster 2 (mural TE analogue) and cluster 5 (polar TE analogue), cluster 1 (EPI analogue) and cluster 6 (EPI analogue), cluster 6 (EPI analogue) and cluster 8 (PrE analogue), and cluster 4 (naive PSC) and cluster 0 (EPI analogue). Tab4: List of reported marker genes for EPI, TE and PrE are summarized.

Supplementary Table 2

Summary of the reported parameters and criteria for different protocols reporting blastocyst-like structures. This table includes reported (a) cell lines, (b) initial cell state, (c) molecules for the formation of blastocyst-like structures, (d) time of formation of blastocyst-like structures, (e) morphometric criteria used to define a blastocyst-like structure, (f) mean efficiency, (g) sequence of lineage specification, (h) transcriptomic state of the cells forming the blastocyst-like structures (quoted text comes from the corresponding paper). As a reference, the time of blastocyst formation and some of its morphometric criteria were also included.

Supplementary Table 3

A list of primers used for RT-qPCR.

Supplementary Table 4

A list of primary antibodies used for immunofluorescence staining.

Supplementary Table 5

Details of stainings previously performed on human blastocysts. This table includes reported (a) lineage, (b) marker gene, (c–h) reference information, (i) figure in this paper.

Video 1

Live imaging of forming blastoids. Live imaging of forming blastoids within microwells and then fixed, immunostained using GATA3 and OCT4 antibodies, and subsequently imaged.

Video 2

Full chip live imaging of forming blastoids. Live imaging of a full microwell chip with forming blastoids.

Video 3

Human blastoid attachment to a hormonally stimulated layer of endometrial cells. Live imaging of a human blastoid undergoing attachment to a hormonally stimulated layer of endometrial cells.

Video 4

Human blastoid polarly attached to a hormonally stimulated layer of endometrial cells. Imaging of two human blastoids attached via the polar region to a hormonally stimulated layer of endometrial cells, and challenged by pipetting liquid in their vicinity.

Source data

Source Data Fig. 1

Source Data Fig. 3

Source Data Fig. 4

Source Data Extended Data Fig. 1

Source Data Extended Data Fig. 3

Source Data Extended Data Fig. 5

Source Data Extended Data Fig. 6

Source Data Extended Data Fig. 7

Source Data Extended Data Fig. 8

Source Data Extended Data Fig. 9

Source Data Extended Data Fig. 10

Rights and permissions

Open Access This article is licensed under a Creative Commons Attribution 4.0 International License, which permits use, sharing, adaptation, distribution and reproduction in any medium or format, as long as you give appropriate credit to the original author(s) and the source, provide a link to the Creative Commons license, and indicate if changes were made. The images or other third party material in this article are included in the article's Creative Commons license, unless indicated otherwise in a credit line to the material. If material is not included in the article's Creative Commons license and your intended use is not permitted by statutory regulation or exceeds the permitted use, you will need to obtain permission directly from the copyright holder. To view a copy of this license, visit <http://creativecommons.org/licenses/by/4.0/>.

Reprints and Permissions

About this article

Cite this article

Kagawa, H., Javali, A., Khoei, H.H. *et al.* Human blastoids model blastocyst development and implantation. *Nature* **601**, 600–605 (2022). <https://doi.org/10.1038/s41586-021-04267-8>

- Received: 12 February 2021
- Accepted: 18 November 2021
- Published: 02 December 2021
- Issue Date: 27 January 2022
- DOI: <https://doi.org/10.1038/s41586-021-04267-8>

Share this article

Anyone you share the following link with will be able to read this content:

[Get shareable link](#)

Sorry, a shareable link is not currently available for this article.

[Copy to clipboard](#)

Provided by the Springer Nature SharedIt content-sharing initiative

Further reading

- [Human embryos in a dish – modeling early embryonic development with pluripotent stem cells](#)
 - Xiukun Wang
 - Guang Hu

Cell Regeneration (2022)

- **A role model of human blastocysts**

- Kim Baumann

Nature Reviews Molecular Cell Biology (2021)

- **Embryo-like models shed fresh light on early human development**

- Sandeep Ravindran

Nature (2021)

A role model of human blastocysts

- Kim Baumann

Research Highlight 14 Dec 2021

This article was downloaded by **calibre** from <https://www.nature.com/articles/s41586-021-04267-8>

- Article
- [Published: 05 January 2022](#)

A naturally inspired antibiotic to target multidrug-resistant pathogens

- [Zongqiang Wang](#) ORCID: orcid.org/0000-0001-7121-0396¹,
- [Bimal Koirala](#) ORCID: orcid.org/0000-0003-1806-7935¹,
- [Yozen Hernandez](#) ORCID: orcid.org/0000-0003-3349-8856¹,
- [Matthew Zimmerman](#)²,
- [Steven Park](#)²,
- [David S. Perlin](#)² &
- [Sean F. Brady](#) ORCID: orcid.org/0000-0001-5967-8586¹

[Nature](#) volume 601, pages 606–611 (2022)

- 11k Accesses
- 1 Citations
- 241 Altmetric
- [Metrics details](#)

Subjects

- [Antibiotics](#)
- [Biosynthesis](#)
- [Natural products](#)

Abstract

Gram-negative bacteria are responsible for an increasing number of deaths caused by antibiotic-resistant infections^{1,2}. The bacterial natural product colistin is considered the last line of defence against a number of Gram-negative pathogens. The recent global spread of the plasmid-borne mobilized colistin-resistance gene *mcr-1* (phosphoethanolamine transferase) threatens the usefulness of colistin³. Bacteria-derived antibiotics often appear in nature as collections of similar structures that are encoded by evolutionarily related biosynthetic gene clusters. This structural diversity is, at least in part, expected to be a response to the development of natural resistance, which often mechanistically mimics clinical resistance. Here we propose that a solution to *mcr-1*-mediated resistance might have evolved among naturally occurring colistin congeners. Bioinformatic analysis of sequenced bacterial genomes identified a biosynthetic gene cluster that was predicted to encode a structurally divergent colistin congener. Chemical synthesis of this structure produced macolacin, which is active against Gram-negative pathogens expressing *mcr-1* and intrinsically resistant pathogens with chromosomally encoded phosphoethanolamine transferase genes. These Gram-negative bacteria include extensively drug-resistant *Acinetobacter baumannii* and intrinsically colistin-resistant *Neisseria gonorrhoeae*, which, owing to a lack of effective treatment options, are considered among the highest level threat pathogens⁴. In a mouse neutropenic infection model, a biphenyl analogue of macolacin proved to be effective against extensively drug-resistant *A. baumannii* with colistin-resistance, thus providing a naturally inspired and easily produced therapeutic lead for overcoming colistin-resistant pathogens.

This is a preview of subscription content

Access options

Subscribe to nature+

Get immediate online access to the entire Nature family of 50+ journals

\$29.99

monthly

[Subscribe](#)

Subscribe to Journal

Get full journal access for 1 year

\$199.00

only \$3.90 per issue

[Subscribe](#)

All prices are NET prices.

VAT will be added later in the checkout.

Tax calculation will be finalised during checkout.

Buy article

Get time limited or full article access on ReadCube.

\$32.00

[Buy](#)

All prices are NET prices.

Additional access options:

- [Log in](#)
- [Learn about institutional subscriptions](#)

Fig. 1: Discovery of macolacin.

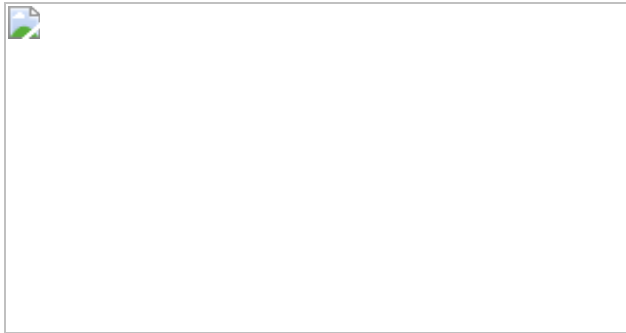


Fig. 2: Antibacterial activity of macolacin.

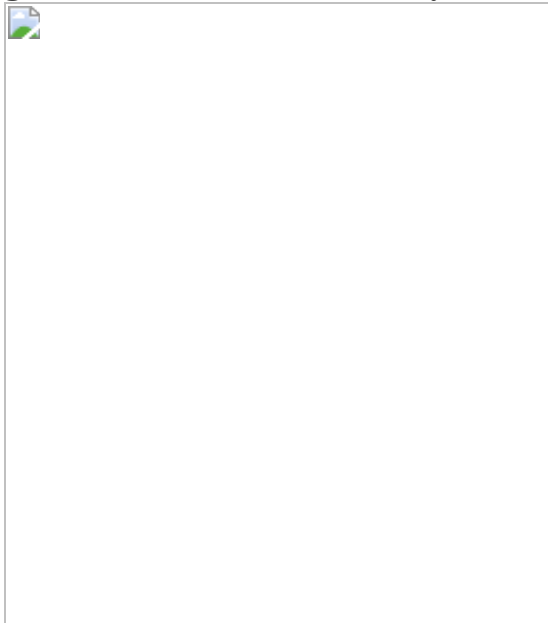
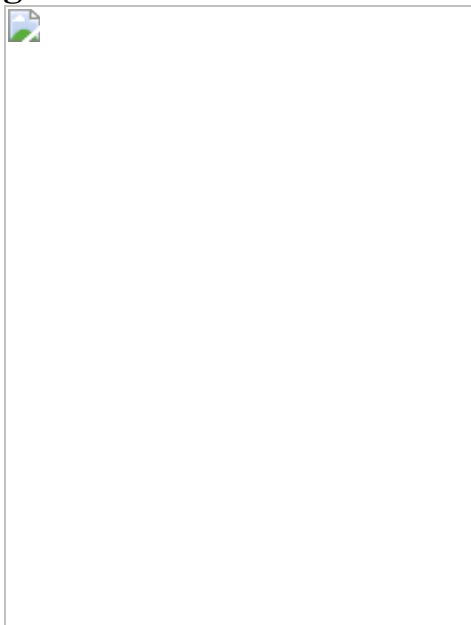


Fig. 3: In vitro and in vivo activity of biphenyl-macolacin.



Data availability

Publicly available DNA sequence data used in this study are referenced accordingly. The macolacin BGC sequence is available in GenBank with accession number NZ_CP018620.1. The website can be accessed through https://www.ncbi.nlm.nih.gov/nuccore/CP018620_1. Other accession numbers for polymyxin-like BGCs are included in Supplementary Table 2. NMR spectra for macolacin and diphenyl-macolacin are presented as [Supplementary Information](#). BGCs were collected from antiSMASH-db (v.2.0). The website can be accessed through <https://antismash-db.secondarymetabolites.org/>. [Source data](#) are provided with this paper.

References

1. 1.
Ventola, C. L. The antibiotic resistance crisis: part 1: causes and threats. *P. T.* **40**, 277–283 (2015).
2. 2.
Payne, D. J., Gwynn, M. N., Holmes, D. J. & Pompliano, D. L. Drugs for bad bugs: confronting the challenges of antibacterial discovery. *Nat. Rev. Drug Discov.* **6**, 29–40 (2007).
3. 3.
Deveson Lucas, D. et al. Emergence of high-level colistin resistance in an *Acinetobacter baumannii* clinical isolate mediated by inactivation of the global regulator H-NS. *Antimicrob. Agents Chemother.* **62**, e02442-17 (2018).
4. 4.
Aitolo, G. L., Adeyemi, O. S., Afolabi, B. L. & Owolabi, A. O. *Neisseria gonorrhoeae* antimicrobial resistance: past to present to

future. *Curr. Microbiol.* **78**, 867–878 (2021).

5. 5.

Tacconelli, E. et al. Discovery, research, and development of new antibiotics: the WHO priority list of antibiotic-resistant bacteria and tuberculosis. *Lancet Infect. Dis.* **18**, 318–327 (2018).

6. 6.

Imai, Y. et al. A new antibiotic selectively kills Gram-negative pathogens. *Nature* **576**, 459–464 (2019).

7. 7.

Biswas, S., Brunel, J. M., Dubus, J. C., Reynaud-Gaubert, M. & Rolain, J. M. Colistin: an update on the antibiotic of the 21st century. *Expert Rev. Anti Infect. Ther.* **10**, 917–934 (2012).

8. 8.

Liu, Y. Y. et al. Emergence of plasmid-mediated colistin resistance mechanism MCR-1 in animals and human beings in China: a microbiological and molecular biological study. *Lancet Infect. Dis.* **16**, 161–168 (2016).

9. 9.

Jeannot, K., Bolard, A. & Plesiat, P. Resistance to polymyxins in Gram-negative organisms. *Int. J. Antimicrob. Agents* **49**, 526–535 (2017).

10. 10.

Liu, Y. Y. et al. Structural modification of lipopolysaccharide conferred by *mcr-1* in Gram-negative ESKAPE pathogens. *Antimicrob. Agents Chemother.* **61**, e00580-17 (2017).

11. 11.

Schwarz, S. & Johnson, A. P. Transferable resistance to colistin: a new but old threat. *J. Antimicrob. Chemother.* **71**, 2066–2070 (2016).

12. 12.

Hameed, F. et al. Plasmid-mediated *mcr-1* gene in *Acinetobacter baumannii* and *Pseudomonas aeruginosa*: first report from Pakistan. *Rev. Soc. Bras. Med. Trop.* **52**, e20190237 (2019).

13. 13.

Tian, G. B. et al. MCR-1-producing *Klebsiella pneumoniae* outbreak in China. *Lancet Infect. Dis.* **17**, 577 (2017).

14. 14.

Rutledge, P. J. & Challis, G. L. Discovery of microbial natural products by activation of silent biosynthetic gene clusters. *Nat. Rev. Microbiol.* **13**, 509–523 (2015).

15. 15.

Sussmuth, R. D. & Mainz, A. Nonribosomal peptide synthesis – principles and prospects. *Angew. Chem. Int. Ed. Engl.* **56**, 3770–3821 (2017).

16. 16.

Stachelhaus, T., Mootz, H. D. & Marahiel, M. A. The specificity-conferring code of adenylation domains in nonribosomal peptide synthetases. *Chem. Biol.* **6**, 493–505 (1999).

17. 17.

Rabanal, F. & Cajal, Y. Recent advances and perspectives in the design and development of polymyxins. *Nat. Prod. Rep.* **34**, 886–908 (2017).

18. 18.

Li, J., Nation, R. & Kaye, K. (eds) *Polymyxin Antibiotics: From Laboratory Bench to Bedside Preface* **1145**, V–VI (Springer, 2019).

19. 19.

Tomm, H. A., Ucciferri, L. & Ross, A. C. Advances in microbial culturing conditions to activate silent biosynthetic gene clusters for novel metabolite production. *J. Ind. Microbiol. Biotechnol.* **46**, 1381–1400 (2019).

20. 20.

Chu, J. et al. Discovery of MRSA active antibiotics using primary sequence from the human microbiome. *Nat. Chem. Biol.* **12**, 1004–1006 (2016).

21. 21.

Chu, J., Vila-Farres, X. & Brady, S. F. Bioactive synthetic-bioinformatic natural product cyclic peptides inspired by nonribosomal peptide synthetase gene clusters from the human microbiome. *J. Am. Chem. Soc.* **141**, 15737–15741 (2019).

22. 22.

Chu, J. et al. Synthetic-bioinformatic natural product antibiotics with diverse modes of action. *J. Am. Chem. Soc.* **142**, 14158–14168 (2020).

23. 23.

Kang, K. N. et al. Colistin heteroresistance in *Enterobacter cloacae* is regulated by PhoPQ-dependent 4-amino-4-deoxy-l-arabinose addition to lipid A. *Mol. Microbiol.* **111**, 1604–1616 (2019).

24. 24.

McClerren, A. L. et al. A slow, tight-binding inhibitor of the zinc-dependent deacetylase LpxC of lipid A biosynthesis with antibiotic

activity comparable to ciprofloxacin. *Biochemistry* **44**, 16574–16583 (2005).

25. 25.

Moffatt, J. H. et al. Colistin resistance in *Acinetobacter baumannii* is mediated by complete loss of lipopolysaccharide production. *Antimicrob. Agents Chemother.* **54**, 4971–4977 (2010).

26. 26.

Wei, J.-R. et al. LpxK is essential for growth of *Acinetobacter baumannii* ATCC 19606: relationship to toxic accumulation of lipid A pathway intermediates. *mSphere* **2**, e00199–00117 (2017).

27. 27.

Richie, D. L. et al. Toxic accumulation of LPS pathway intermediates underlies the requirement of LpxH for growth of *Acinetobacter baumannii* ATCC 19606. *PLoS ONE* **11**, e0160918 (2016).

28. 28.

US Department of Health and Human Services. *Antibiotic Resistance Threats in the United States*; <https://www.cdc.gov/drugresistance/pdf/threats-report/2019-ar-threats-report-508.pdf> (2019).

29. 29.

Ling, Z. et al. Epidemiology of mobile colistin resistance genes *mcr-1* to *mcr-9*. *J. Antimicrob. Chemother.* **75**, 3087–3095 (2020).

30. 30.

Sakura, N. et al. The contribution of the N-terminal structure of polymyxin B peptides to antimicrobial and lipopolysaccharide binding activity. *Bull. Chem. Soc. Jpn* **77**, 1915–1924 (2004).

31. 31.

Tsubery, H., Ofek, I., Cohen, S. & Fridkin, M. N-terminal modifications of polymyxin B nonapeptide and their effect on antibacterial activity. *Peptides* **22**, 1675–1681 (2001).

32. 32.

Lutgring, J. D. et al. FDA-CDC antimicrobial resistance isolate bank: a publicly available resource to support research, development, and regulatory requirements. *J. Clin. Microbiol.* **56**, e01415-17 (2018).

33. 33.

Devarajan, P. Neutrophil gelatinase-associated lipocalin (NGAL): a new marker of kidney disease. *Scand. J. Clin. Lab. Invest. Suppl.* **241**, 89–94 (2008).

34. 34.

Wang, J., Ishfaq, M., Fan, Q., Chen, C. & Li, J. 7-hydroxycoumarin attenuates colistin-induced kidney injury in mice through the decreased level of histone deacetylase 1 and the activation of Nrf2 signaling pathway. *Front. Pharmacol.* **11**, 1146 (2020).

35. 35.

Bolignano, D. et al. Neutrophil gelatinase-associated lipocalin (NGAL) as a marker of kidney damage. *Am. J. Kidney Dis.* **52**, 595–605 (2008).

36. 36.

Blin, K. et al. The antiSMASH database version 2: a comprehensive resource on secondary metabolite biosynthetic gene clusters. *Nucleic Acids Res.* **47**, D625–D630 (2019).

37. 37.

Blin, K. et al. antiSMASH 5.0: updates to the secondary metabolite genome mining pipeline. *Nucleic Acids Res.* **47**, W81–W87 (2019).

38. 38.

Testing, E. C. O. A. S. *Recommendations for MIC Determination of Colistin (Polymyxin E) as Recommended by the Joint CLSI-EUCAST Polymyxin Breakpoints Working Group* (EUCAST, 2016).

39. 39.

Wikler, M. A. Methods for dilution antimicrobial susceptibility tests for bacteria that grow aerobically: approved standard. CLSI document M07-A7 (2006).

40. 40.

Bojkovic, J. et al. Characterization of an *Acinetobacter baumannii* lptD deletion strain: permeability defects and response to inhibition of lipopolysaccharide and fatty acid biosynthesis. *J. Bacteriol.* **198**, 731–741 (2015).

41. 41.

Carmichael, J., DeGraff, W. G., Gazdar, A. F., Minna, J. D. & Mitchell, J. B. Evaluation of a tetrazolium-based semiautomated colorimetric assay: assessment of chemosensitivity testing. *Cancer Res.* **47**, 936–942 (1987).

Acknowledgements

We thank the Y. Doi (pMQ124-*mcr-1* and pMQ124xlab-*mcr-1*) and J. M. Boll (*E. cloacae* 13047- Δ *phoP/Q* and *E. cloacae* 13047- Δ *phoP/Q*+*phoP/Q*) laboratories for providing strains and plasmids. We thank the CDC and FDA Antibiotic Resistance (AR) Isolate Bank for providing *A. baumannii* resistant strains (0282, 0286, 0287, 0295, 0296 and 0301). We thank the Comparative Bioscience Center at the Rockefeller University for

their help with the animal studies. This work was supported by the National Institutes of Health (1U19AI142731 and 5R35GM122559).

Author information

Affiliations

1. Laboratory of Genetically Encoded Small Molecules, The Rockefeller University, New York, NY, USA

Zongqiang Wang, Bimal Koirala, Yozen Hernandez & Sean F. Brady

2. Center for Discovery and Innovation, Hackensack Meridian Health, Nutley, NJ, USA

Matthew Zimmerman, Steven Park & David S. Perlin

Contributions

S.F.B. and Z.W. designed the study and analysed the data. Z.W. performed the biochemical experiments. B.K. performed the peptide synthesis. Z.W. and Y.H. performed the bioinformatic analysis. M.Z. performed the pharmacokinetic analysis. S.F.B., Z.W., S.P. and D.S.P. designed the animal study. All authors were involved in discussing the results. S.F.B. and Z.W. prepared the manuscript.

Corresponding author

Correspondence to [Sean F. Brady](#).

Ethics declarations

Competing interests

The authors declare no competing interests.

Peer review information

Nature thanks Gerry Wright and the other, anonymous, reviewer(s) for their contribution to the peer review of this work.

Additional information

Publisher's note Springer Nature remains neutral with regard to jurisdictional claims in published maps and institutional affiliations.

Extended data figures and tables

[Extended Data Fig. 1 Proposed macolacin biosynthetic pathway.](#)

The predicted biosynthetic scheme for macolacin based on detailed bioinformatic analysis of the *mac* BGC is depicted.

[Extended Data Fig. 2 Phylogenetic trees constructed from A-domain sequences associated with complete colistin and macolacin BGC.](#)

Phylogenetic trees constructed from A domain sequences associated with complete colistin and macolacin A BGC. **a)** A1 domain; **b)** A3 domain; **c)** A7 domain and **d)** A10 domain. Each A-domain sequence was extracted from the polymyxin-like BGCs was then aligned together with known characterized polymyxin BGCs (for example, MIBIG IDs: BGC0000408, BGC0001192, BGC0001153) using the MUSCLE alignment software. The resulting phylogenetic tree was visualized using iTOLv5 software. Red color represents hits in polymyxin clade. Blue color represents hits in macolacin clade.

[Extended Data Fig. 3 Structures of all synthetic macolacin derivate.](#)

Structural differences compared to macolacin are depicted in blue.

Extended Data Fig. 4 Cytotoxicity and pharmacokinetic evaluation of macolacin and biphenyl-macolacin.

a) Cytotoxicity of macolacin and biphenyl-macolacin against HEK293. Data are presented as means \pm SD. n = 3 technical replicates. **b)** Pharmacokinetic assessment of macolacin and biphenyl-macolacin. Total plasma concentrations of macolacin, biphenyl-macolacin or colistin versus time after administration of a single subcutaneous dose (10 mg/kg) to neutropenic mice. n = 2 biologically independent mice. Data are presented as mean of two independent assays. **c)** The level of serum NGAL in colistin or biphenyl-macolacin treated mice. Significant differences between groups were determined by one-way analysis of variance (ANOVA) (*P<0.05) (n = 6 biologically independent mice). Data are presented as means \pm SD. Vehicle vs. Colistin, P value = 0.0069; Vehicle vs. Biphenyl-macolacin, P value = 0.0104; Colistin vs. Biphenyl-macolacin, P value = 0.9773.

Source data

Extended Data Table 1 Macolacin A-domain specificity analysis.

Extended Data Table 2 MIC values for macolacin analogs with different lipid substituents.

Extended Data Table 3 MIC data for XDR *A. baumannii* with and without *mcr-1*.

Extended Data Table 4 SAR of amino acid differences between macolacin and colistin.

Extended Data Table 5 High-resolution mass spectrometry data for all syn-BNP peptides.

Supplementary information

Supplementary Information

Supplementary Tables 1 and 2 and Figs 1–4.

Reporting Summary

Source data

[Source Data Fig. 2](#)

[Source Data Fig. 3](#)

[Source Data Extended Data Fig. 4](#)

Rights and permissions

[Reprints and Permissions](#)

About this article

Cite this article

Wang, Z., Koirala, B., Hernandez, Y. *et al.* A naturally inspired antibiotic to target multidrug-resistant pathogens. *Nature* **601**, 606–611 (2022).
<https://doi.org/10.1038/s41586-021-04264-x>

- Received: 20 March 2021
- Accepted: 18 November 2021
- Published: 05 January 2022
- Issue Date: 27 January 2022
- DOI: <https://doi.org/10.1038/s41586-021-04264-x>

Share this article

Anyone you share the following link with will be able to read this content:

[Get shareable link](#)

Sorry, a shareable link is not currently available for this article.

[Copy to clipboard](#)

Provided by the Springer Nature SharedIt content-sharing initiative

Further reading

- [**A novel antibiotic from a bacterial arms race**](#)

- Megan Cully

Nature Reviews Drug Discovery (2022)

This article was downloaded by **calibre** from <https://www.nature.com/articles/s41586-021-04264-x>

| [Section menu](#) | [Main menu](#) |

- Article
- Open Access
- [Published: 07 December 2021](#)

Long-acting capsid inhibitor protects macaques from repeat SHIV challenges

- [Samuel J. Vidal](#)^{1,2} na1,
- [Elena Bekerman](#)³ na1,
- [Derek Hansen](#)³,
- [Bing Lu](#)³,
- [Kelly Wang](#)³,
- [Judy Mwangi](#)³,
- [William Rowe](#)³,
- [Federico Campigotto](#)³,
- [Jim Zheng](#)³,
- [Darryl Kato](#)³,
- [Abishek Chandrashekhar](#) ORCID: orcid.org/0000-0001-7821-5552¹,
- [Julia Barrett](#)¹,
- [Shivani Patel](#) ORCID: orcid.org/0000-0003-3475-1016¹,
- [Huahua Wan](#) ORCID: orcid.org/0000-0001-6958-9464¹,
- [Tochi Anioke](#)¹,
- [Noe B. Mercado](#) ORCID: orcid.org/0000-0001-7769-7326¹,
- [Joseph P. Nkolola](#)¹,
- [Melissa J. Ferguson](#)⁴,
- [William J. Rinaldi](#)⁴,
- [Christian Callebaut](#)³,
- [Wade Blair](#)³,
- [Tomas Cihlar](#)³,
- [Romas Gelezunas](#)³,
- [Stephen R. Yant](#) ³ &
- [Dan H. Barouch](#) ORCID: orcid.org/0000-0001-5127-4659^{1,5}

Nature volume 601, pages 612–616 (2022)

- 4306 Accesses

- 1 Citations
- 38 Altmetric
- [Metrics details](#)

Subjects

- [Drug development](#)
- [Retrovirus](#)

Abstract

Because no currently available vaccine can prevent HIV infection, pre-exposure prophylaxis (PrEP) with antiretrovirals (ARVs) is an important tool for combating the HIV pandemic^{1,2}. Long-acting ARVs promise to build on the success of current PrEP strategies, which must be taken daily, by reducing the frequency of administration³. GS-CA1 is a small-molecule HIV capsid inhibitor with picomolar antiviral potency against a broad array of HIV strains, including variants resistant to existing ARVs, and has shown long-acting therapeutic potential in a mouse model of HIV infection⁴. Here we show that a single subcutaneous administration of GS-CA1 provides long-term protection against repeated rectal simian–human immunodeficiency virus (SHIV) challenges in rhesus macaques. Whereas all control animals became infected after 15 weekly challenges, a single 300 mg kg⁻¹ dose of GS-CA1 provided per-exposure infection risk reduction of 97% for 24 weeks. Pharmacokinetic analysis showed a correlation between GS-CA1 plasma concentration and protection from SHIV challenges. GS-CA1 levels greater than twice the rhesus plasma protein-adjusted 95% effective concentration conferred 100% protection in this model. These proof-of-concept data support the development of capsid inhibitors as a novel long-acting PrEP strategy in humans.

[Download PDF](#)

Main

The HIV pandemic is a leading cause of morbidity and mortality worldwide⁵. Current strategies for HIV prevention include public health measures as well as vaccine development and improved pre-exposure prophylaxis (PrEP) uptake. Studies conducted by the Centre for the AIDS Programme of Research in South Africa (CAPRISA; trial 004)⁶, Pre-exposure Prophylaxis Initiative (iPrEx)⁷ and Partners PrEP⁸ have shown that tenofovir-based PrEP can reduce HIV transmission. Recent

real-world data confirm a significant population-level reduction in HIV-1 incidence in areas in which PrEP uptake is high^{9,10}. However, PrEP strategies reliant on frequent drug administration are limited by adherence, which reduces their real-world impact on HIV transmission^{11,12,13}. Long-acting PrEP agents may reduce the barriers associated with daily drug administration, frequent healthcare interactions and the stigma surrounding sexually transmitted infections including HIV³. As part of this approach, a long-acting formulation of the integrase strand-transfer inhibitor cabotegravir (CAB-LA), which is injected subcutaneously every 2 months, was shown to reduce HIV transmission in an HIV Prevention Trials Network (HPTN) study (HPTN 083)¹⁴.

The HIV capsid protein has multiple essential roles in the early and late stages of the viral replication cycle, making it an attractive target for antiretrovirals (ARVs)¹⁵. Lenacapavir (LEN, formerly GS-6207) is the first clinically validated HIV capsid inhibitor and displays picomolar antiviral activity against both wild-type virus and variants resistant to current ARVs¹⁶. LEN binds at a highly conserved interface between capsid protein monomers, which causes defects in capsid nuclear import, reduced virion production and aberrant capsid assembly. A long-acting formulation of LEN has been shown to have potent antiviral activity with a maximum 2.3 log₁₀ decline in HIV-1 RNA after 9 days of monotherapy¹⁷ and the potential for twice-yearly subcutaneous dosing in a phase 1b study¹⁸. GS-CA1, a structural analogue of LEN, has the same capsid-dependent multistage mechanism of action, similar binding affinity for different forms of HIV capsid (i.e., precursor, monomer, pentamer and hexamer), similar potency against both HIV and simian immunodeficiency virus (SIV), and a similar resistance profile. In addition, it has previously been demonstrated to have high preclinical efficacy in a humanized mouse model of HIV-1 treatment (Extended Data Table 1)⁴. However, long-term prophylactic efficacy of LEN or GS-CA1 has not previously been demonstrated. In this study, we assess the potential of a single dose of long-acting capsid inhibitor to offer protection against repeated challenges with simian–human immunodeficiency virus (SHIV) in rhesus macaques. GS-CA1 was chosen for this analysis because of its predicted higher rate of metabolic clearance in comparison to LEN and the associated accelerated washout phase after dose administration, which enables timely evaluation of the prophylactic efficacy of this compound class over a wide range of exposures.

GS-CA1 inhibits SHIV in macaque cells

GS-CA1 displayed potent in vitro anti-SHIV activity in peripheral blood mononuclear cells (PBMCs) isolated from three individual rhesus macaques of Indian origin (*Macaca mulatta*), with a mean 50% effective concentration (EC₅₀) of 0.72 nM (Fig. 1a and Extended Data Table 2). This compound also showed a mean Hill slope value

of 3.0 ± 0.7 in high-density antiviral dose–response curves measured against the HIV-1 IIIb strain in MT-4 cells, yielding a calculated 95% effective concentration (EC_{95}) of 1.91 nM when applied to the EC_{50} measured in SHIV-infected rhesus PBMCs. In vivo application showed that a large portion of the subcutaneously administered GS-CA1 became bound by plasma proteins, leaving less free drug available for antiviral effects. Competitive equilibrium dialysis was thus used to account for rhesus plasma protein binding to GS-CA1, resulting in a projected 15.8-fold decrease in free GS-CA1 concentration in vivo and yielding a rhesus protein-adjusted EC_{95} (pa EC_{95}) value of 30.2 nM.

Fig. 1: GS-CA1 exhibits potent antiviral activity in vitro and long-acting pharmacokinetics in rhesus macaques.

 figure 1



a, Representative antiviral dose–response curve for GS-CA1 in rhesus PBMCs acutely infected with SHIV-SF162P3. Data are shown as mean \pm s.d. from one of seven assays ($n = 3$ biological replicates each). **b**, Plasma GS-CA1 levels measured by mass spectrometry following a single subcutaneous administration of GS-CA1 dosed at 300 $mg\ kg^{-1}$ in three male rhesus macaques and at 100 $mg\ kg^{-1}$ in two male rhesus macaques. The bottom dotted line represents the assay limit of detection (LOD; 1 nM). The top dashed lines represent one and six times the rhesus pa EC_{95} for GS-CA1 (30.2 nM and 181.2 nM, respectively).

[Source data](#)

GS-CA1 shows long-acting plasma exposure

Low hepatic clearance is an essential attribute for a long-acting agent. Titration with 3H -labelled GS-CA1 was necessary to accurately measure the low turnover of GS-CA1 in primary rhesus hepatocytes and showed a predicted rate of hepatic clearance

of $0.071\text{ h}^{-1}\text{ kg}^{-1}$, or 2.9% of the hepatic extraction. These in vitro data suggest that GS-CA1 has the potential to sustain long-acting plasma exposure in rhesus macaques. To test this hypothesis and to select an appropriate GS-CA1 dose for the rhesus efficacy studies, we performed a pilot pharmacokinetic study with a single subcutaneous administration of a GS-CA1 formulation at two dose levels predicted to cover a broad range of plasma exposures over the projected length of the study. GS-CA1 was administered at 100 mg kg^{-1} and 300 mg kg^{-1} to two and three naive rhesus macaques of Indian origin, respectively, and its levels were monitored for 18 weeks. Plasma drug levels peaked in the concentration range of $1\text{--}3\text{ }\mu\text{M}$ by day 1 after dose administration, before decreasing to $0.4\text{--}1.1\text{ }\mu\text{M}$ by day 7 after dose administration. After this, GS-CA1 levels were maintained in excess of the rhesus paEC₉₅ value for at least 8 weeks and 14 weeks and in excess of six times the rhesus paEC₉₅ value for at least 1 week and 8 weeks for the 100 mg kg^{-1} and 300 mg kg^{-1} doses, respectively (Fig. 1b). Given that the mean target clinical exposure of LEN for HIV treatment is six times its paEC₉₅ in humans¹⁸, GS-CA1 doses of 300 mg kg^{-1} and 150 mg kg^{-1} were selected for the repeat SHIV challenge study to assess the reduction in transmission risk across rhesus-equivalent GS-CA1 exposures in excess of, equal to and below this clinically relevant target concentration.

GS-CA1 provides protection from SHIV challenges

We next conducted a study to evaluate the protective efficacy of a single administration of GS-CA1 against repeated, escalating-dose rectal SHIV-SF162P3 challenges in rhesus macaques (Fig. 2a). For this challenge study, 24 rhesus macaques of Indian origin were divided into 3 groups of 8 monkeys each with balanced sex and weight distributions. All animals received a single subcutaneous administration at week 0 in the scapular region. Animals in group 1 received the vehicle control, whereas those in groups 2 and 3 received GS-CA1 doses of 150 mg kg^{-1} and 300 mg kg^{-1} , respectively. Consistent with the pilot study, a single administration of GS-CA1 at both 150 mg kg^{-1} and 300 mg kg^{-1} achieved long-acting exposure. Specifically, peaks were reached at plasma GS-CA1 concentrations of $3.0\text{ }\mu\text{M}$ and $5.5\text{ }\mu\text{M}$ approximately 24 h and 42 h after dose administration, respectively, and GS-CA1 levels decreased slowly thereafter with a mean half-life of 287–317 h (Fig. 2b and Extended Data Table 3). The group receiving a dose of 300 mg kg^{-1} remained above the rhesus paEC₉₅ and six times above the rhesus paEC₉₅ for 14–16 weeks and 5–8 weeks, respectively, whereas the group receiving a dose of 150 mg kg^{-1} remained above these target concentrations for 8–15 weeks and 3–7 weeks, respectively. The variance in GS-CA1 pharmacokinetic parameters across animals was comparable to that observed with 900 mg of LEN in humans¹⁸, whereas the half-life and length of exposure above the corresponding $6\times$ paEC₉₅ threshold were lower than expected.

Fig. 2: Single-dose GS-CA1 confers long-term protection from repeated rectal SHIV challenge in rhesus macaques.

 figure 2



a, Study design. Rhesus macaques of Indian origin were treated with a single subcutaneous administration of vehicle control or GS-CA1 at week 0 followed by weekly intrarectal challenges with SHIV-SF162P3 in a dose-escalation scheme until all control animals were confirmed to be infected on week 15. **b**, Plasma GS-CA1 levels measured by mass spectrometry over time in rhesus macaques dosed once at 150 mg kg^{-1} or 300 mg kg^{-1} . The data for each group are shown as mean \pm s.d. from eight rhesus macaques. The bottom dotted line represents the assay LOD (1 nM). The top dashed lines represent one and six times the rhesus paEC₉₅ for GS-CA1 (30.2 nM and 181.2 nM, respectively). **c**, Kaplan–Meier plots showing the development of viraemia as assessed by RT–qPCR for plasma SHIV *gag* among rhesus macaques treated with a single subcutaneous administration of vehicle control ($n = 8$), GS-CA1 dosed at 150 mg kg^{-1} ($n = 8$) or GS-CA1 dosed at 300 mg kg^{-1} ($n = 8$).

[Source data](#)

To define the protective efficacy of GS-CA1, all animals received 15 weekly intrarectal SHIV-SF162P3 challenges in a dose-escalation protocol beginning at week 1 following GS-CA1 administration. Infection was assessed by quantifying viral *gag* RNA levels in the plasma by quantitative PCR with reverse transcription (RT–qPCR). To define the drug levels required for protection, we monitored plasma viraemia up to week 24 as GS-CA1 levels declined below therapeutic concentrations. Eight weekly intrarectal challenges at 30 times the median tissue culture infectious dose (TCID₅₀) resulted in infection of five of the eight vehicle-treated animals (Fig. 2c, Table 1 and Extended Data Fig. 1). Viral challenge dose escalation to 100 TCID₅₀ for 2 weeks yielded no additional infections, whereas further escalation to 300 TCID₅₀ resulted in infection of the remaining three control animals by week 15.

Table 1 Statistical analysis of the rhesus macaque challenge study

In contrast to the vehicle-treated group, the group receiving 300 mg kg⁻¹ GS-CA1 showed no viraemia until week 17 with this escalating-dose challenge protocol, when three of the eight monkeys became SHIV positive (Fig. 2c, Table 1 and Extended Data Fig. 1). The other five monkeys remained aviraemic until the end of the study, which translates to a 97% per-exposure risk reduction with the 300 mg kg⁻¹ dose ($P = 0.0001$, Cox proportional hazard regression analysis). The group that received a single administration of GS-CA1 at the reduced dose of 150 mg kg⁻¹ also exhibited fewer and delayed infections relative to the vehicle-treated control group. Specifically, no viraemia was detected until week 11, and two of the eight monkeys remained aviraemic until the end of the study, which represents an 87% per-exposure risk reduction ($P = 0.0038$). The median time to viraemia was 7.5 weeks in the vehicle-treated group and 16 weeks in the group receiving 150 mg kg⁻¹ GS-CA1; this point was not reached in the group receiving 300 mg kg⁻¹ GS-CA1 owing to an insufficient number of infections. The peak viral loads were significantly lower and the viral loads measured 7 weeks after infection showed a trend towards lower levels among the GS-CA1-treated animals as compared with the vehicle-treated control animals. This result could reflect a residual antiviral effect from subtherapeutic inhibitor levels (Extended Data Fig. 2).

We next performed immunological analyses in the GS-CA1-treated rhesus monkeys. First, we assessed the development of humoral immune responses against the SHIV envelope (Env) glycoprotein by enzyme-linked immunosorbent assay (ELISA). We detected binding antibody responses to Env at week 24 in all animals with SHIV viraemia but none in those without SHIV viraemia (Extended Data Fig. 3a). Second, we assessed the development of cellular immune responses against SHIV Gag polyprotein by enzyme-linked immune absorbent spot (ELISPOT) assay. We detected T cell responses to the Gag protein at week 19 in all but one animal with SHIV viraemia and in none of the animals without SHIV viraemia (Extended Data Fig. 3b).

These immunologic data suggest that the GS-CA1-treated animals that remained aviraemic during the study period were in fact protected from SHIV challenge.

Finally, we performed additional studies to confirm that our plasma viraemia measurements provided early detection of initial infection in the setting of GS-CA1 prophylaxis.

First, we performed intact proviral DNA analysis (IPDA) to detect integrated SHIV in a subset of infected animals treated with vehicle control or GS-CA1 with available PBMCs. Intact SHIV proviruses became detectable at the same time points at which plasma viraemia was detected in all cases except for a single GS-CA1-treated animal (K394) that showed very low-level intact provirus 1 week before detection of viraemia (Extended Data Table 4). Second, we determined the Env ELISA seroconversion time points for all infected animals and observed that viraemia preceded seroconversion in all cases (Extended Data Table 5). The median time to seroconversion from the onset of viraemia was 2.5 weeks (range, 1 to 13 weeks) in vehicle-treated control animals and 4 weeks (range, 1 to 5 weeks) in GS-CA1-treated animals, although the difference between the groups was not significant ($P = 0.80$, Mann–Whitney U test).

Protective levels of GS-CA1 in macaques

We next investigated the relationship between GS-CA1 plasma concentrations and protection against SHIV challenge. To facilitate exposure comparisons with other antivirals including LEN, we converted the concentrations for GS-CA1 to multiples of its rhesus paEC₉₅. To estimate the protective levels for GS-CA1, we focused on six animals that developed viraemia in the group receiving a dose of 150 mg kg⁻¹ and three animals that developed viraemia in the group receiving a dose of 300 mg kg⁻¹. Assuming a 2-week delay between rectal SHIV infection and detectable peripheral blood viraemia, we averaged the GS-CA1 exposure values 2 weeks before the first detectable viraemia among the infected animals. We estimated that mucosal infection occurred in the presence of 31.4 nM GS-CA1 on average, which is equal to the concentration of rhesus paEC₉₅ at a multiple of 1.0 (range, 0.4–1.6; Fig. 3a,b). Therefore, we estimated that, overall, all animals were fully protected in this model when the GS-CA1 plasma concentrations were more than twice the rhesus paEC₉₅ value for GS-CA1.

Fig. 3: Association between plasma GS-CA1 and protection from SHIV challenge.

 **figure 3**

a, Plasma levels of GS-CA1 measured by mass spectrometry among individual rhesus macaques ($n = 8$) treated with a 150 mg kg^{-1} dose over time. Black circles represent time points before the first detection of viraemia. Red circles represent time points including and after the first detection of viraemia. Grey shaded boxes represent serum Env ELISA seroconversion time points. The bottom dotted line represents the assay LOD (1 nM). The bottom and top dashed lines represent one and two times the rhesus paEC₉₅, respectively. **b**, Same data as in **a** for rhesus macaques treated with GS-CA1 at a dose of 300 mg kg^{-1} . No signal above the assay LOD was observed among the eight placebo-treated control animals throughout the study.

[Source data](#)

Plasma virus resistance analysis

To evaluate potential development of resistance against GS-CA1, particularly during the washout phase, we conducted longitudinal population-level sequence analysis of the SHIV *gag* region encoding capsid in rhesus plasma (Extended Data Fig. 4). As expected, plasma virus obtained from placebo-treated control animals encoded only wild-type capsid protein. Of the plasma virus samples analysed from the nine viraemic animals dosed with GS-CA1, 34 of 35 (97%) produced high-quality sequence reads, with wild-type capsid detected in all nine animals at the end of the study. Animal K342 in the low-dose (150 mg kg^{-1} GS-CA1) group showed transient prevalence of a capsid variant with substitution to alanine at Val11 (V11A; the numbering used here follows the HIV-1 HXB2 reference sequence) between study weeks 13 and 21. This V11A substitution, which is located far outside the GS-CA1-binding site in the capsid, disappeared by week 22 in this animal and is not associated with GS-CA1 resistance⁴.

Thus, no study animal showed emergence of variants associated with GS-CA1 resistance for the duration of this 24-week efficacy study.

Discussion

Long-acting PrEP regimens might overcome some of the current barriers to PrEP implementation, including the need for daily administration and frequent healthcare interaction. The HPTN 083 study recently demonstrated that long-acting ARV monotherapy agents such as CAB-LA can effectively reduce the rate of HIV-1 acquisition¹⁴. In the present study, we investigated whether a single administration of the capsid inhibitor GS-CA1 could provide long-term protection from repeated SHIV challenges in rhesus macaques. GS-CA1 provided significant protection from rectal infection after 15 repeat challenges, with complete protection achieved when GS-CA1 levels were more than twice the rhesus paEC₉₅.

Given the similar structural, mechanistic and long-acting properties of GS-CA1 and LEN, the preclinical GS-CA1 data in this study may inform the clinical development of LEN for PrEP. Our data show protection against rectal SHIV acquisition in macaques at plasma GS-CA1 exposures more than twice the rhesus paEC₉₅, which suggests that the current clinical formulation of LEN, conferring a mean exposure of more than six times human paEC₉₅ for at least 6 months after a single subcutaneous dose, might be sufficient for PrEP in humans. Nonetheless, the exposure threshold for prophylaxis against HIV acquisition with LEN in humans cannot be directly inferred from this escalating-dose preclinical study and will need to be defined in adequately powered clinical studies. Moreover, animal studies may underestimate exposures required for protection, as evident from the 4 of 12 incident infections among 2,243 analysed participants in the HPTN 083 study that occurred even though the target CAB-LA exposures were predicted preclinically to be efficacious^{19,20}. In future work, it will be important to evaluate the efficacy of long-acting capsid inhibitors by other routes of transmission (e.g., vaginal) to establish broader relevance to the populations at risk. Furthermore, a study incorporating mucosal biopsies could establish the pharmacokinetic relationship between plasma and tissue levels of GS-CA1 at the sites of infection.

The emergence of resistance mutations may be an important consideration during the implementation of any single-agent long-acting PrEP strategy. In the phase 3 HPTN 083 trial, 16 HIV seroconversions occurred among participants randomized to CAB-LA, including 4 baseline infections²⁰. Genotyping in 14 of these 16 cases revealed integrase mutations among 5 participants, although no resistance was observed among infections presumed to have occurred during the pharmacokinetic tail. Our preclinical study revealed no resistance mutations in the capsid protein among nine rhesus

macaques that were treated with GS-CA1 and became infected. However, the low-level resistance mutation Q67H in capsid (conferring a sixfold decrease in susceptibility to LEN¹⁶) was detected in 2 of 29 participants randomized to long-acting LEN monotherapy in a recent phase 1b study²¹. This mutation was detected 9 days after dose administration in at least one study participant in two of the LEN treatment arms among the five total receiving the lowest doses (20 mg and 50 mg) when the average LEN plasma concentrations measured 0.7 and 1.1 times the human paEC₉₅, respectively; both concentrations are considered to be subtherapeutic for HIV-1 treatment. These data suggest that large clinical studies will likely be necessary to fully characterize the potential emergence of resistance mutations among long-acting PrEP recipients.

In summary, our data demonstrate that a single subcutaneous administration of the capsid inhibitor GS-CA1 provides long-term protection against SHIV infection in rhesus macaques. Together with recent studies showing the potency and pharmacokinetics of LEN in people living with HIV, these data suggest that long-acting capsid inhibitors might offer an important and novel strategy for HIV prevention. A phase 3 clinical study to assess the safety and effectiveness of LEN for HIV PrEP has therefore been initiated (NCT04925752).

Methods

Drug and formulation

GS-CA1 and a generic internal small-molecule standard used for liquid chromatography coupled with mass spectrometry (LC–MS) experiments were both synthesized at Gilead Sciences and were subjected to standard quality control analysis. For the animal dosing studies, GS-CA1 was dissolved in vehicle (58.03% PEG 300, 27.1% water, 6.78% ethanol, 6.61% poloxamer 188, 1.48% sodium hydroxide) at 300 mg ml⁻¹, producing a clear, yellow–orange solution. The solution was stored at ambient temperature protected from light until dosing.

Metabolic stability of [³H]GS-CA1 in primary rhesus hepatocytes

A 500-μl suspension of human hepatocytes (1×10^6 cells per ml) and 0.25 μM [³H]GS-CA1 was prepared in Krebs–Henseleit buffer (KHB) medium and was incubated in a humidified incubator at 37 °C with 5% CO₂ in duplicate wells of a 24-well plate. Propranolol (1 μM final), a compound known to be efficiently metabolized by hepatocytes by oxidation and conjugation, was used as a positive control. A cell-free control was incubated in parallel as a negative control. Aliquots (100 μl) were removed after 0 h, 1 h, 3 h and 6 h and were then mixed with 200 μl quenching

solution, placed on a shaker for 10 min and centrifuged at 3,000g for 60 min. The supernatant was transferred to a new plate, diluted with 100 µl water and placed on a shaker for 10 min. Quantification of [³H]GS-CA1 and its metabolites was performed by radio flow chromatography using a PerkinElmer Radiomatic 625TR flow scintillation analyser with a 500-µl flow cell coupled to a Dionex Ultimate 3000 high-performance liquid chromatography (HPLC) system. PerkinElmer Ultima-Flo was used as the scintillation cocktail, which was mixed with the HPLC effluent at a ratio of 1:1. Sample (100 µl) was injected using a Leap Technologies CTC PAL autosampler. Separation was achieved on a Phenomenex Synergi Fusion-RP 80-Å pore size, 4-µm particle size, 150 × 4.6-mm column maintained at 32 °C. Mobile phase A consisted of 95% water, 5% acetonitrile and 0.1% trifluoroacetic acid (TFA). Mobile phase B consisted of 95% acetonitrile, 5% water and 0.1% TFA. Elution was achieved at a flow rate of 1 ml min⁻¹ by linear gradients: the initial condition was 2% B at 0 min, which was increased to 75% B over 45 min, held for 4 min at 75% B and then returned to the initial conditions. The column was allowed to re-equilibrate for 12 min between injections. Quantification was based on the radiochromatographic peak area using Dionex (Thermo Scientific) Chromeleon 6.8 software.

Cell culture

Freshly isolated PBMCs from three male rhesus macaque (*M. mulatta*) donors of Indian origin (HumanCells Biosciences) were cultured in RPMI-1640 cell culture medium (Life Technologies) supplemented with 10% heat-inactivated FBS (Hyclone), 2 mM glutamine and 100 U ml⁻¹ penicillin plus 100 µg ml⁻¹ streptomycin (complete RPMI). Before their use in the antiviral assays, rhesus PBMCs from three independent donors were pooled and activated at a density of 3 × 10⁶ cells per ml for 72 h at 37 °C by the addition of 1 µg ml⁻¹ phytohemagglutinin (PHA, Sigma-Aldrich) and 50 U ml⁻¹ recombinant human interleukin-2 (IL-2) (Roche Diagnostics).

Anti-SHIV antiviral assay in rhesus PBMCs

PHA/IL-2-stimulated rhesus PBMCs were infected in bulk culture with SHIV-SF162P3 at a concentration of 130 pg of p27 equivalent per million PBMCs. The cells were maintained in suspension by gently rocking the cultures mixed with virus inoculum for 3 h at 37 °C. The cells were then pelleted by centrifugation at 500g for 5 min, washed twice with complete RPMI to remove any unadsorbed virus and seeded into 96-well plates at a cell density of 2 × 10⁵ cells per well in 100 µl. Eight-point threefold serial dilutions of GS-CA1 were made in complete RPMI containing 50 U ml⁻¹ IL-2 and were added in triplicate to wells containing cells (100 µl per well). The cultures were incubated in a 5% CO₂ incubator at 37 °C for 7 days. Cell-free supernatants derived from the PBMC cultures were harvested 7 days after infection,

the amount of SHIV present was quantified using an SIV p27 antigen-capture ELISA assay (5436, Advanced Bioscience Laboratories) performed according to the manufacturer's protocol, and the data were acquired using SoftMax Pro 6.3.1 software (Molecular Devices). The mean EC₅₀ value for GS-CA1, which was determined from a total of seven assays performed in triplicate, was calculated from the dose-response curves using XLfit 5.5.0.5 software (IDBS) and was expressed graphically using GraphPad Prism 8.1.2 software. The Hill coefficient (*n*) for GS-CA1 was measured from the slope of the dose-response curves (*n* = 3.03 ± 0.69) and was used to derive the EC₉₅ value using the following equation: EC₉₅ = EC₅₀ × (95/5)^{1/*n*}.

Equilibrium dialysis shift assay

Rhesus plasma protein binding to GS-CA1 was determined by competitive equilibrium dialysis. Rhesus plasma (10%) was spiked with GS-CA1 (2 μM), and this mixture and blank RPMI cell culture medium containing 10% FBS (CCM) were placed into opposite sides of assembled dialysis cells; afterwards, incubations were performed in triplicate. After a 24-h equilibration period at 37 °C, samples were quenched with 4 volumes of 90% (vol/vol) acetonitrile and 10% (vol/vol) methanol containing internal standard. Then, they were quantified using the AB Sciex API 4000 LC–MS/MS system (GenTech Scientific) with electrospray ionization in positive mode and multiple-reaction monitoring and were analysed using Analyst 1.6.1 software. The fold change value in 100% rhesus plasma was then calculated using the plasma/CCM ratio after correcting for the sample dilution factor and the percentage of free fraction in the matrix. This shift value was multiplied by the calculated anti-SHIV EC₉₅ value for GS-CA1 to derive the corresponding rhesus plasma paEC₉₅.

Animals, drug administration and viral stocks

Studies involving the evaluation of GS-CA1 pharmacokinetics in naive male rhesus macaques of Indian origin were conducted at Covance Laboratories in a Laboratory Animal Care-accredited facility and were performed in strict compliance with all relevant ethical regulations. All study protocols were reviewed and approved by the Covance Laboratories Institutional Animal Care and Use Committee (IACUC). On day 0 of the study, rhesus monkeys were administered GS-CA1 dosed at 100 mg kg⁻¹ (*n* = 2) or 300 mg kg⁻¹ (*n* = 3) in the scapular region by subcutaneous injection using a syringe equipped with a 22-gauge needle. The GS-CA1 was prepared in a stock solution of 300 mg ml⁻¹; a maximum of 2 ml of the solution was injected into a single subcutaneous site. Whole blood was collected from each animal at designated time points, processed into plasma and then stored frozen at -80 °C for bioanalysis of GS-CA1 levels.

For the challenge study, 24 outbred rhesus macaques of Indian origin were assigned to the three study groups with even sex and weight distributions. All animals were housed at Alpha Genesis (Yemassee, SC), and all procedures were conducted in compliance with all relevant local, state and federal regulations and were approved by the Alpha Genesis IACUC. On week 0, the three groups were administered vehicle control, GS-CA1 dosed at 300 mg kg^{-1} or GS-CA1 dosed at 150 mg kg^{-1} in the scapular region by subcutaneous injection using a syringe equipped with a 22-gauge needle. The GS-CA1 was prepared in a stock solution of 300 mg ml^{-1} ; a maximum of 2 ml of solution was injected into a single subcutaneous site. The injection sites were monitored daily by veterinary staff for 3 days. Beginning in week 1, animals in all three groups were challenged by the intrarectal route with 1 ml of RPMI containing the specified dilution of a $3.62 \times 10^3 \text{ TCID}_{50}$ SHIV-SF162P3 stock. At each respective time point, the challenges were performed on the same day, using the same virus stock and inoculation method across the three groups. Whole blood was collected and processed into plasma and PBMCs as necessary to assess routine haematology, clinical chemistry, viral load and serology as well as for bioanalysis of drug levels. The animals were considered to be protected if they remained SHIV negative by plasma PCR assay and seronegative by enzyme immunoassay throughout the 15-week challenge phase and the 9-week follow-up.

Bioanalysis of GS-CA1 in macaque plasma

Rhesus plasma samples were stored frozen at -80°C . For analysis, the samples were thawed, and a 50- μl aliquot of each sample was treated with 200 μl acetonitrile containing a generic internal small-molecule standard. After precipitation of the protein component, a 100- μl aliquot of the supernatant was transferred to a clean 96-well plate and was mixed with 200 μl water. A 20- μl aliquot of the above solution was then injected into a Q-Exactive high-resolution mass spectrometer (Thermo Scientific) with electrospray ionization in positive mode. Quantification was performed with a Thermo Scientific Xcalibur 4.0.27.19 using accurate masses (<5 parts per million mass error; $[\text{M} + \text{H}]^+$ of 958.1853 for GS-CA1 and 758.3270 for the internal standard, respectively)^{22,23}. The lower and upper limits of quantification for GS-CA1 were 1 nM and 10,000 nM, respectively. Pharmacokinetic parameters, including the area under the plasma concentration–time curve from time 0 to the last quantifiable time point (AUC_{last}), the area under the plasma concentration–time curve from time 0 to infinity (AUC_{inf}), the maximum concentration (C_{max}), the time to reach the observed peak plasma concentration (t_{max}) and the terminal half-life ($t_{1/2}$), were determined by non-compartmental analysis using Phoenix WinNonlin 6.4 build 8.1.0.3530 software (Pharsight).

Plasma viral load assay

RNA was extracted from rhesus macaque plasma using a QIAcube high-throughput instrument and an IndiSpin QIAcube HT Pathogen kit (Qiagen). RNA standards using the SIV *gag* sequence were generated by AmpliCap-Max T7 High-Yield Message Maker kit (Cell Script) and were purified using an RNA Clean and Concentrator kit (Zymo Research). Log dilutions of the RNA were included with each RT–qPCR assay. Reverse transcription of standards and samples was performed using a Superscript III VILO kit (Invitrogen). qPCR was performed using forward primer 5'-GTCTGCGTCATCTGGTGCATT-3', reverse primer 5'-CACTAGGTGTCTGCACTATCTGTTT-3' and fluorescently labelled primer 5'-CTTCCTCAGTGTGTTCACTTTCTCTGCG-3' on a Quantstudio 6 Flex system (Applied Biosystems). The assay LOD was 200 copies *gag* per ml.

ELISA

Rhesus serum binding antibody titres against gp140 trimers were determined by ELISA. Ninety-six-well Maxisorp ELISA plates (Thermo Fisher Scientific) were coated overnight with 100 µl per well of 1 µg ml⁻¹ mosaic M gp140 protein in PBS and were then blocked for 2 h with blocker casein in PBS (Thermo Scientific). Macaque sera were added in threefold serial dilutions and were incubated for 1 h at room temperature. The plates were washed three times with PBS containing 0.05% Tween-20 and were then incubated for 1 h with a 1:1,000 dilution of a horseradish peroxidase (HRP)-conjugated goat anti-human secondary antibody (Jackson ImmunoResearch Laboratories). The plates were then washed three times with the above wash buffer and were developed using SureBlue tetramethylbenzidine (TMB) microwell peroxidase (KPL). Development was stopped by the addition of a stop solution (KPL), and the plates were then analysed at 450 nm with a Versamax ELISA microplate reader (Molecular Devices) using Softmax Pro 6.5.1 software. The ELISA endpoint titres were defined as the highest reciprocal serum dilution that yielded an OD_{450 nm} absorbance of >0.2. Seroconversion occurred when the OD_{450 nm} absorbance was greater than or equal to three times the value obtained at week 0 and the endpoint titre was greater than the assay LOD, which was 1:25.

IFN γ ELISPOT assay

T cell responses against the Gag polyprotein were determined in rhesus macaque PBMCs by ELISPOT assay. Ninety-six-well Multiscreen Immobilon-P plates (Millipore) were coated overnight with mouse anti-human interferon γ (IFN γ) antibody (BD Pharmingen) at 5 µg ml⁻¹. The plates were then washed three times with DPBS containing 0.25% Tween-20 and blocked with R10 (RPMI supplemented with 10% FBS and 1% penicillin–streptomycin) at 37 °C for 1 h. SIVmac239-derived Gag peptides (JPT) were plated at a concentration of 1 µg per well along with 200,000 rhesus macaque cells per well, and the cells and peptides were then incubated for 18–

24 h at 37 °C. All subsequent steps were performed at room temperature. The wells were washed nine times with the above wash buffer, cells were lysed with deionized water for 3 min and plates were then incubated with biotinylated rabbit anti-human IFNy antibody (U-Cytech) at a final concentration of 1 µg ml⁻¹ for 2 h. The wells were then incubated with streptavidin–alkaline phosphatase (Southern Biotech) at a final concentration of 2 µg ml⁻¹ for 2 h, washed five times with the above wash buffer and incubated with 5-bromo-4-chloro-3'-indolylphosphate *p*-toluidine salt (BCIP)/nitro-blue tetrazolium chloride (NBT) substrate solution (Thermo Scientific Pierce) for 7 min. The spot-forming cell (SFC) units were sent to ZellNet Consulting for quantification. The mock-stimulated background-subtracted median values were reported, and the assay LOD was 5 SFCs per 10⁶ PBMCs.

Intact proviral DNA assay

An SHIV-adapted version of IPDA (SHIV-IPDA) was used to determine the number of intact SHIV proviruses. Total genomic DNA was extracted from unfractionated PBMCs using a QIAamp DNA Mini kit (Qiagen). DNA quality and quantity were evaluated by spectrophotometry and fluorometry, respectively, and SHIV-IPDA was then performed on the isolated DNA. An in-depth description of SHIV-IPDA will be included in an upcoming manuscript by E. Fray et al. In brief, SHIV-IPDA consists of a three-component multiplex droplet digital PCR (ddPCR) reaction. The first is a SHIV proviral discrimination reaction targeting two conserved, frequently deleted regions of the SHIV genome to determine the intact provirus count; the second is a two-long terminal repeat (2-LTR) DNA circle reaction to determine 2-LTR circle counts; and the third is a copy reference/DNA shearing reaction targeting ribonuclease P/MRP subunit P30 (RPP30) to determine assay input cell equivalents and the DNA shearing index (DSI). All ddPCR reactions were performed using a Bio-Rad QX200 AutoDG ddPCR system with Bio-Rad ddPCR supermix for probes with no dUTP. After DSI correction and subtraction of intact 2-LTR circles, the intact proviral frequencies were reported per million input cells. The endpoint ddPCR data were collected using Bio-Rad QuantaSoft version 1.7.4.0917.

Plasma virus genotypic analysis

Total RNA was extracted from 50-µl plasma aliquots obtained from each viraemic monkey using the MagMAX-96 Viral RNA Isolation kit (Life Technologies) in conjunction with the Thermo Scientific KingFisher Flex automated extraction platform and were eluted in 60 µl AVE buffer. The portion of *gag* encoding capsid in each sample was then individually amplified by RT–PCR using a SuperScript IV One-Step RT–PCR System (Life Technologies) according to the manufacturer's recommended protocol. Amplification of the SHIV capsid-encoding region in each sample was performed using primers SIV-CA-F (5'-

CCAAAAACAAGTAGACCAACAG-3') and SIV-CA-R (5'-TGCAAAAGGGATTGGCAC-3'), and the products were subjected to population-level bulk sequencing at Elim Biopharmaceuticals using the same primer set. To identify codon changes, Sequencher version 4.9 (Gene Codes) was used to align DNA encoding sequences of the SHIV capsid for each sample with that of the parent virus obtained from each infected placebo-treated control animal. This provided a control for potential genetic drift that might have occurred during the 24-week efficacy study.

Statistical methods

Protection against acquired infection was analysed using Cox proportional hazard regression models based on the exact partial likelihood for discrete time expressed in weeks, which explicitly accounts for the time-varying viral challenge dose in the model. The hazard ratios with 95% confidence intervals for per-exposure relative reductions in acquisition risk were calculated for the GS-CA1-treated groups, and the results were compared with those for the vehicle-treated control group. Comparisons were considered statistically significant at a two-sided alpha level of 0.05 ($P < 0.05$). Statistical analyses were performed using GraphPad Prism version 8.1.2, SAS version 9.4 and R Studio software version 4.0.5.

Reporting summary

Further information on research design is available in the [Nature Research Reporting Summary](#) linked to this paper.

Data availability

All relevant data are available in the Article. Any additional data are available from the corresponding authors upon reasonable request. [Source data](#) are provided with this paper.

References

1. 1. World Health Organization. *Consolidated Guidelines on the Use of Antiretroviral Drugs for Treating and Preventing HIV Infection: Recommendations for a Public Health Approach*, 2nd ed. (World Health Organization Press, 2016).
2. 2.

Fonner, V. A. et al. Effectiveness and safety of oral HIV preexposure prophylaxis for all populations. *AIDS* **30**, 1973–1983 (2016).

3. 3.

Coelho, L. E., Torres, T. S., Veloso, V. G., Landovitz, R. J. & Grinsztejn, B. Pre-exposure prophylaxis 2.0: new drugs and technologies in the pipeline. *Lancet HIV* **6**, e788–e799 (2019).

4. 4.

Yant, S. R. et al. A highly potent long-acting small-molecule HIV-1 capsid inhibitor with efficacy in a humanized mouse model. *Nat. Med.* **25**, 1377–1384 (2019).

5. 5.

GBD 2019 Diseases and Injuries Collaborators. Global burden of 369 diseases and injuries in 204 countries and territories, 1990–2019: a systematic analysis for the Global Burden of Disease Study 2019. *Lancet* **396**, 1204–1222 (2020).

6. 6.

Abdoor Karim, Q. et al. Effectiveness and safety of tenofovir gel, an antiretroviral microbicide, for the prevention of HIV infection in women. *Science* **329**, 1168–1174 (2010).

7. 7.

Grant, R. M. et al. Preexposure chemoprophylaxis for HIV prevention in men who have sex with men. *N. Engl. J. Med.* **363**, 2587–2599 (2010).

8. 8.

Baeten, J. M. et al. Antiretroviral prophylaxis for HIV prevention in heterosexual men and women. *N. Engl. J. Med.* **367**, 399–410 (2012).

9. 9.

Grulich, A. E. et al. Population-level effectiveness of rapid, targeted, high-coverage roll-out of HIV pre-exposure prophylaxis in men who have sex with men: the EPIC-NSW prospective cohort study. *Lancet HIV* **5**, e629–e637 (2018).

10. 10.

Sullivan, P. S. et al. The impact of pre-exposure prophylaxis with FTC/TDF on HIV diagnoses, 2012–2016. Presented at the 22nd International AIDS Conference, Amsterdam, the Netherlands, 23–27 July 2018 (2018).

11. 11.

Anderson, P. L. et al. Emtricitabine-tenofovir concentrations and pre-exposure prophylaxis efficacy in men who have sex with men. *Sci. Transl. Med.* **4**, 151ra125 (2012).

12. 12.

Van Damme, L. et al. Preexposure prophylaxis for HIV infection among African women. *N. Engl. J. Med.* **367**, 411–422 (2012).

13. 13.

Marrazzo, J. M. et al. Tenofovir-based preexposure prophylaxis for HIV infection among African women. *N. Engl. J. Med.* **372**, 509–518 (2015).

14. 14.

Landovitz, R. J. et al. Cabotegravir for HIV prevention in cisgender men and transgender women. *N. Engl. J. Med.* **385**, 595–608 (2021).

15. 15.

Carnes, S. K., Sheehan, J. H. & Aiken, C. Inhibitors of the HIV-1 capsid, a target of opportunity. *Curr. Opin. HIV AIDS* **13**, 359–365 (2018).

16. 16.

Link, J. O. et al. Clinical targeting of HIV capsid protein with a long-acting small molecule. *Nature* **584**, 614–618 (2020).

17. 17.

Daar, E. et al. Dose–response relationship of subcutaneous long-acting HIV capsid inhibitor GS-6207. Presented at the 27th Conference on Retroviruses and Opportunistic Infections, Boston, MA, 8–11 March 2020 (2020).

18. 18.

Begley, R. et al. Lenacapavir sustained delivery formulation supports 6-month dosing interval. Presented at AIDS 2020: 23rd International AIDS Conference, virtual, 6–10 July 2020 (2020).

19. 19.

Andrews, C. D. et al. Long-acting integrase inhibitor protects macaques from intrarectal simian/human immunodeficiency virus. *Science* **343**, 1151–1154 (2014).

20. 20.

Marzinke, M. A. et al. Characterization of HIV infection in cisgender men and transgender women who have sex with men receiving injectable cabotegravir for HIV prevention: HPTN 083. *J. Infect. Dis.* <https://doi.org/10.1093/infdis/jiab152> (2021).

21. 21.

Margot, N. et al. Lenacapavir resistance analysis in a phase 1b clinical proof-of-concept study. Paper presented at 2020 HIV Drug Therapy Glasgow, virtual, 5–8 October 2020 (2020).

22. 22.

Ramanathan, R. et al. It is time for a paradigm shift in drug discovery bioanalysis: from SRM to HRMS. *J. Mass Spectrom.* **46**, 595–601 (2011).

23. 23.

Sturm, R. M., Jones, B. R., Mulvana, D. E. & Lowes, S. HRMS using a Q-Exactive series mass spectrometer for regulated quantitative bioanalysis: how, when, and why to implement. *Bioanalysis* **8**, 1709–1721 (2016).

Acknowledgements

We thank E. Bondzie, O. Sanborn, D. Sellers and K. Verrington for assistance with rhesus specimen processing and S. Suthram for assistance with statistical analysis. The study was funded by Gilead Sciences.

Author information

Author notes

1. These authors contributed equally: Samuel J. Vidal, Elena Bekerman

Affiliations

1. Center for Virology and Vaccine Research, Beth Israel Deaconess Medical Center, Harvard Medical School, Boston, MA, USA

Samuel J. Vidal, Abishek Chandrashekar, Julia Barrett, Shivani Patel, Huahua Wan, Tochi Anioke, Noe B. Mercado, Joseph P. Nkolola & Dan H. Barouch

2. Division of Infectious Diseases, Brigham and Women's Hospital and Massachusetts General Hospital, Harvard Medical School, Boston, MA, USA

Samuel J. Vidal

3. Gilead Sciences, Foster City, CA, USA

Elena Bekerman, Derek Hansen, Bing Lu, Kelly Wang, Judy Mwangi, William Rowe, Federico Campigotto, Jim Zheng, Darryl Kato, Christian Callebaut, Wade Blair, Tomas Cihlar, Romas Gelezunas & Stephen R. Yant

4. Alpha Genesis, Inc., Yemassee, SC, USA

Melissa J. Ferguson & William J. Rinaldi

5. Ragon Institute of MGH, MIT and Harvard, Cambridge, MA, USA

Dan H. Barouch

Contributions

J.M. designed and executed the preclinical metabolism studies. D.H. performed and analysed the antiviral assays. K.W. performed and analysed the equilibrium dialysis shift assays. D.K. oversaw GS-CA1 synthesis. W.R. supported drug formulation. B.L., J.Z., S.R.Y. and W.R. designed and analysed the GS-CA1 dose-range-finding studies in rhesus macaques. S.J.V., E.B., A.C., S.R.Y. and D.H.B. oversaw rhesus efficacy study execution with input from C.C., W.B. and T.C., and R.G., S.J.V. and J.B. performed rhesus specimen processing. S.J.V. and N.B.M. performed SHIV viral load measurements. H.W., T.A. and J.P.N. performed the Env ELISAs. S.P. performed the Gag ELISPOTs. W.J.R. and M.J.F. led the clinical care of the rhesus macaques. B.L., J.Z. and S.R.Y. analysed the plasma GS-CA1 concentrations. D.H. and S.R.Y. performed resistance analysis of the rhesus plasma virus. F.C. performed statistical

analysis. S.J.V., E.B., R.G., S.R.Y. and D.H.B. interpreted the data and wrote the manuscript with input from all authors.

Corresponding authors

Correspondence to [Stephen R. Yant](#) or [Dan H. Barouch](#).

Ethics declarations

Competing interests

E.B., D.H., B.L., K.W., J.M., W.R., F.C., J.Z., D.K., C.C., W.B., T.C., R.G. and S.R.Y. are employees of Gilead Sciences and received salary and stock ownership as compensation for their employment. The authors otherwise declare no potential conflicts of interest.

Additional information

Publisher's note Springer Nature remains neutral with regard to jurisdictional claims in published maps and institutional affiliations.

Extended data figures and tables

[Extended Data Fig. 1 Viral loads among vehicle- and GS-CA1-treated animals during the SHIV challenge study.](#)

a, Plasma SHIV viral loads measured by *gag* RT-qPCR among vehicle control rhesus macaques ($n = 8$) through week 24 following 15 weekly intrarectal challenges. **b**, Same data as **(a)** among rhesus macaques ($n = 8$) treated with a single 150 mg/kg subcutaneous injection of GS-CA1 at week 0. **c**, Same data as **(a)** and **(b)** among rhesus macaques ($n = 8$) treated with a single 300 mg/kg subcutaneous injection of GS-CA1 at week 0. Dotted lines represent the assay LOD (200 copies per ml).

[Extended Data Fig. 2 Peak and setpoint SHIV viral loads among infected rhesus macaques treated with vehicle control or GS-CA1.](#)

a, Peak plasma SHIV viral loads measured by *gag* RT-qPCR among infected rhesus macaques treated with vehicle control ($n = 8$), GS-CA1 dosed at 150 mg/kg ($n = 6$), or GS-CA1 dosed at 300 mg/kg ($n = 3$). **b**, Plasma SHIV viral loads 7 weeks post-infection (wpi) among the same groups as **(a)**. Dotted lines represent the assay LOD

(200 copies per ml). Solid lines represent group medians. P values reflect Kruskal-Wallis tests.

Extended Data Fig. 3 GS-CA1-treated rhesus macaques that remain aviremic do not show immunologic evidence of SHIV infection.

a, Week 24 anti-gp140 Env ELISA comparing viremic and aviremic animals in the vehicle control and GS-CA1 groups. Dotted line represents assay LOD (1:25 endpoint titer). **b**, Week 19 Gag ELISPOT comparing viremic and aviremic animals in the vehicle control and GS-CA1 groups. Data are represented as spot-forming cells (SFC) per 10^6 PBMCs. Dotted line represents the assay LOD (5 SFC per million PBMCs).

Extended data Fig. 4 Sequence analysis of study-emergent CA mutations.

a, Longitudinal CA sequence analysis of select plasma samples from viremic study animals. Samples with population-scale wild-type and V11A CA sequences are shaded grey and blue, respectively, whereas yellow boxes denote sequence failures. **b**, Alignment of HIV-1 (NL4.3 strain) and SHIV-SF162P3 CA amino-acid sequences. Shaded regions represent invariant residues, hashed lines denote sequence gaps, and red arrows highlight HIV-1 residues associated with GS-CA1 resistance (L56, N57, M66, Q67, K70, N74, T107). **c**, A single CA monomer (rendered as ribbons in cyan) within the HIV-1 CA hexamer-LEN crystal structure¹⁶, with notation of the CA N-terminal and C-terminal domains (CA_{NTD} and CA_{CTD}, respectively) and a GS-CA1 molecule (carbon atoms shown as green) docked at the LEN binding site. Location of the only CA variant (V11A) transiently detected by bulk sequencing is shown relative to all HIV-1 CA residues associated with bona fide in vitro GS-CA1 and LEN resistance (highlighted as sticks).

Extended Data Table 1 Comparison of the major structural and functional attributes for small molecule capsid inhibitors LEN and GS-CA1

Extended Data Table 2 Determination of the GS-CA1 rhesus paEC₉₅ in rhesus PMBCs

Extended Data Table 3 Pharmacokinetic parameters following a single subcutaneous administration of GS-CA1 in rhesus macaques

Extended Data Table 4 Detection of intact proviral SHIV DNA relative to viremia in the challenge study

Extended Data Table 5 Time from onset of viremia to seroconversion among infected rhesus macaques treated with vehicle control or GS-CA1

Supplementary information

Reporting Summary

Source data

[Source Data Fig. 1](#)

[Source Data Fig. 2](#)

[Source Data Fig. 3](#)

Rights and permissions

Open Access This article is licensed under a Creative Commons Attribution 4.0 International License, which permits use, sharing, adaptation, distribution and reproduction in any medium or format, as long as you give appropriate credit to the original author(s) and the source, provide a link to the Creative Commons license, and indicate if changes were made. The images or other third party material in this article are included in the article's Creative Commons license, unless indicated otherwise in a credit line to the material. If material is not included in the article's Creative Commons license and your intended use is not permitted by statutory regulation or exceeds the permitted use, you will need to obtain permission directly from the copyright holder. To view a copy of this license, visit <http://creativecommons.org/licenses/by/4.0/>.

[Reprints and Permissions](#)

About this article

Cite this article

Vidal, S.J., Bekerman, E., Hansen, D. *et al.* Long-acting capsid inhibitor protects macaques from repeat SHIV challenges. *Nature* **601**, 612–616 (2022).
<https://doi.org/10.1038/s41586-021-04279-4>

- Received: 02 June 2021
- Accepted: 24 November 2021
- Published: 07 December 2021
- Issue Date: 27 January 2022

- DOI: <https://doi.org/10.1038/s41586-021-04279-4>

Share this article

Anyone you share the following link with will be able to read this content:

[Get shareable link](#)

Sorry, a shareable link is not currently available for this article.

[Copy to clipboard](#)

Provided by the Springer Nature SharedIt content-sharing initiative

Further reading

- [**Refining HIV pre-exposure prophylactic agents**](#)

- M. Teresa Villanueva

Nature Reviews Drug Discovery (2022)

This article was downloaded by **calibre** from <https://www.nature.com/articles/s41586-021-04279-4>

| [Section menu](#) | [Main menu](#) |

- Article
- Open Access
- [Published: 23 November 2021](#)

A COVID-19 peptide vaccine for the induction of SARS-CoV-2 T cell immunity

- [Jonas S. Heitmann](#)^{1,2 na1},
- [Tatjana Bilich](#) [ORCID: orcid.org/0000-0002-8107-0419](#)^{1,2,3 na1},
- [Claudia Tandler](#)^{1,2,3 na1},
- [Annika Nelde](#) [ORCID: orcid.org/0000-0001-8504-8481](#)^{1,2,3},
- [Yacine Maringer](#) [ORCID: orcid.org/0000-0002-2197-8740](#)^{1,2,3},
- [Maddalena Marconato](#)¹,
- [Julia Reusch](#)¹,
- [Simon Jäger](#)^{1,4,5},
- [Monika Denk](#)³,
- [Marion Richter](#)³,
- [Leonard Anton](#)¹,
- [Lisa Marie Weber](#) [ORCID: orcid.org/0000-0001-9514-5218](#)¹,
- [Malte Roerden](#) [ORCID: orcid.org/0000-0001-7283-9778](#)^{2,3,6},
- [Jens Bauer](#) [ORCID: orcid.org/0000-0003-3731-2385](#)^{1,2,3},
- [Jonas Rieth](#)^{1,3},
- [Marcel Wacker](#)^{1,2,3},
- [Sebastian Hörber](#) [ORCID: orcid.org/0000-0002-5718-1530](#)⁷,
- [Andreas Peter](#)⁷,
- [Christoph Meisner](#)^{8,9},
- [Imma Fischer](#)⁸,
- [Markus W. Löffler](#)^{2,3,5,10,11},
- [Julia Karbach](#)¹²,
- [Elke Jäger](#)¹²,
- [Reinhild Klein](#)⁶,
- [Hans-Georg Rammensee](#)^{2,3,10},
- [Helmut R. Salih](#) [ORCID: orcid.org/0000-0002-6719-1847](#)^{1,2} &

- [Juliane S. Walz](#) ORCID: [orcid.org/0000-0001-6404-7391^{1,2,3,4,13}](https://orcid.org/0000-0001-6404-7391)

Nature volume 601, pages 617–622 (2022)

- 39k Accesses
- 2 Citations
- 528 Altmetric
- [Metrics details](#)

Subjects

- [Peptide vaccines](#)
- [Phase I trials](#)
- [SARS-CoV-2](#)
- [Viral infection](#)

Abstract

T cell immunity is central for the control of viral infections. CoVac-1 is a peptide-based vaccine candidate, composed of SARS-CoV-2 T cell epitopes derived from various viral proteins^{1,2}, combined with the Toll-like receptor 1/2 agonist XS15 emulsified in Montanide ISA51 VG, aiming to induce profound SARS-CoV-2 T cell immunity to combat COVID-19. Here we conducted a phase I open-label trial, recruiting 36 participants aged 18–80 years, who received a single subcutaneous CoVac-1 vaccination. The primary end point was safety analysed until day 56.

Immunogenicity in terms of CoVac-1-induced T cell response was analysed as the main secondary end point until day 28 and in the follow-up until month 3. No serious adverse events and no grade 4 adverse events were observed. Expected local granuloma formation was observed in all study participants, whereas systemic reactogenicity was absent or mild. SARS-CoV-2-specific T cell responses targeting multiple vaccine peptides were induced in all study participants, mediated by multifunctional T helper 1 CD4⁺ and CD8⁺ T cells. CoVac-1-induced IFN γ T cell responses persisted in the follow-up analyses and surpassed those detected after SARS-CoV-2 infection as well as after vaccination with approved vaccines.

Furthermore, vaccine-induced T cell responses were unaffected by current SARS-CoV-2 variants of concern. Together, CoVac-1 showed a favourable safety profile and induced broad, potent and variant of concern-independent T cell responses, supporting the presently ongoing evaluation in a phase II trial for patients with B cell or antibody deficiency.

[Download PDF](#)

Main

The coronavirus disease 2019 (COVID-19) pandemic caused by severe acute respiratory syndrome coronavirus 2 (SARS-CoV-2) is linked to the death of millions of people³. As predominantly individuals with medical comorbidities are severely affected⁴, vaccines inducing long-lasting immunity, particularly in high-risk populations, are needed^{5,6,7}.

CoVac-1 is a multi-peptide-based vaccine candidate designed to induce, upon a single vaccination, a broad and long-lasting SARS-CoV-2 T cell immunity resembling that acquired by natural infection, which is not affected by evolving viral variants of concern (VOCs). Thus, CoVac-1 is composed of multiple SARS-CoV-2 HLA-DR T cell epitopes derived from various viral proteins (spike, nucleocapsid, membrane, envelope and open reading frame 8 (ORF8)) that have been proven to be (1) frequently and HLA-independently recognized by T cells in convalescent individuals after COVID-19, (2) of pathophysiological relevance for T cell immunity to combat COVID-19, and (3) to mediate long-term immunity after infection^{1,2}. CoVac-1 vaccine peptides are adjuvanted with the novel Toll-like receptor (TLR) 1/2 agonist XS15 emulsified in Montanide ISA51 VG, which endorse activation and maturation of antigen-presenting cells and prevent vaccine peptides from immediate degradation, enabling the induction of a potent T cell response^{8,9,10}.

T cells have an important role for COVID-19 outcome and maintenance of SARS-CoV-2 immunity, even in the absence of humoral immune responses^{1,11,12,13,14,15,16,17,18,19}. Thus, the induction of SARS-CoV-2 T cell immunity is a central goal for vaccine development and of particular importance for patients with congenital or acquired B cell deficiencies. The latter comprise patients with cancer or treatment-related immunoglobulin deficiency, who develop only limited humoral immunity after infection or vaccination and persist with a high risk for a severe course of COVID-19^{20,21,22}.

Here we report the results of the open-label first-in-human phase I trial recruiting adults aged 18–80 years, to evaluate the safety, reactogenicity and immunogenicity of CoVac-1.

Participants

From 28 November 2020 to 15 January 2021, 12 healthy adults were enrolled in part I (age group 18–55 years), including sentinel dosing in the first participant. From 24

March 2021 to 1 April 2021, 24 adults were enrolled in part II (age group 56–80 years). Of part I and part II participants, 33% and 50%, respectively, were female participants. The median participant age was 38 (range 23–50) and 62 (range 56–70) years for part I and part II, respectively. All participants (pCoVs) received one dose of CoVac-1 on day 1 and were available for immunogenicity and safety analyses until day 28 (follow-up until month 3) and day 56, respectively (Extended Data Fig. 1). No major protocol violations occurred. Analyses of follow-up safety and long-term immunogenicity data (until month 6) are ongoing. Demographic and clinical characteristics of the participants are provided in Table 1.

Table 1 Characteristics of participants

Safety and reactogenicity

Data regarding solicited and unsolicited adverse events were available for all participants from diary cards (for 28 days after vaccination) and safety visits (until day 56). No participant discontinued the trial because of an adverse events. No serious adverse events and no grade 4 adverse events were reported. Reactogenicity in terms of solicited adverse events occurred in all participants (Fig. 1). Events were mild to moderate (grade 1–2) in 81% of participants. All participants showed expected formation of an induration (also called granuloma) at the injection site, which persisted beyond day 56. Severe adverse events (grade 3) comprised local erythema in 19%, accompanied by severe swelling in 6% of all participants. Grade 3 adverse events resolved within 2 days (median, range 1–7). Localized inguinal lymphadenopathy was reported by 22% of participants. Local skin ulceration at the vaccination site was reported by 25% of participants, with two participants in part II showing a grade 2 ulceration. Ulcerations in terms of small skin defects occurred between day 28 and day 56 and healed within 20 days (median, range 15–23) until day 56, none requiring any surgical intervention or drug treatment. No difference in local solicited adverse events was observed between part I and part II participants (Extended Data Table 1). No fever or other inflammatory systemic solicited adverse events were reported. Other systemic solicited adverse events occurred in 39% of all participants with no differences observed between part I and part II participants (Extended Data Table 1). All reported systemic solicited adverse events were mild, with transient fatigue being reported by 31% of participants.

Fig. 1: Local and systemic solicited adverse events.

 **figure 1**

a, b, Related local (**a**) and systemic (**b**) solicited adverse events within 56 days after vaccination. Severity was graded as mild (grade 1), moderate (grade 2) or severe (grade 3) based on the definition provided in Methods. Healthy adults 18–55 years of age were included in part I ($n = 12$), and participants 56–80 years of age were included in part II ($n = 24$). A detailed description of the data is presented in Extended Data Table 1.

[Source Data](#)

No clinically relevant changes in laboratory values were reported. In 31% of participants, acute phase reaction with elevated levels of C-reactive protein was observed.

Fifty-eight unsolicited adverse events occurred that were predominantly mild (81%; Extended Data Table 2). Viral re-activations (varicella zoster and herpes simplex virus) were reported by two participants (grade 2 or lower) in part II of the trial.

Until day 56, no SARS-CoV-2 infection or immune-mediated medical condition was observed in any participant.

Immunogenicity

Immunogenicity of CoVac-1 was determined in terms of CD4 $^{+}$ and CD8 $^{+}$ T cell responses to the six SARS-CoV-2 HLA-DR vaccine T cell epitopes as well as to

embedded HLA class I-binding peptides (Supplementary Table 1) using IFN γ enzyme-linked immunospot (ELISPOT) assays. T cell responses were assessed in all participants at baseline (day 1), on days 7, 14 and 28, as well as in the follow-up period on day 56 and month 3 after vaccination. None of the participants showed pre-existing SARS-CoV-2 T cell responses ex vivo at baseline. Vaccine-induced IFN γ T cell responses were observed in 100% of participants in part I and part II on day 28, showing a 200-fold or more and 100-fold or more increase (median calculated spot counts 2 (day 1) to 450 (day 28), and 2 (day 1) to 325 (day 28)) from baseline, respectively (Fig. 2a). Vaccine-induced T cell responses targeted multiple CoVac-1 peptides with a median 5 out of 6 peptides recognized by T cells of participants on day 28 (Fig. 2b, Extended Data Fig. 2). The CoVac-1 peptide P6_ORF8 derived from the ORF8 of SARS-CoV-2 showed most frequently induced T cell responses after vaccination (97%), followed by P5_mem and P4_env (both 94%), P3_spi (89%), P1_nuc (61%) and P2_nuc (58%; Extended Data Fig. 2). CoVac-1-induced T cell responses persisted in the follow-up analyses until month 3 in all participants.

Intensity of IFN γ T cell response decreased ex vivo in part I participants over time, but equivalent expandability of CoVac-1-induced T cells was observed in both part I and part II participants, at month 3 compared with day 28 post-vaccination (Extended Data Fig. 3a). The intensity of CoVac-1-induced IFN γ T cell responses in participants of part I and part II at day 28 and day 56 (pCoVs ($n = 24$), median 488 and 319 calculated spot counts, respectively) was up to 39 times higher than T cell responses against CoVac-1 vaccine peptides (median 13), as well as to previously described SARS-CoV-2-specific (median 29) and cross-reactive (median 35) T cell epitopes^{1,2} in age-matched human convalescent individuals after COVID-19 collected 16–52 days after positive SARS-CoV-2 real-time PCR (Fig. 2c, Supplementary Table 2). Titration with decreasing peptide concentrations (2.5 μ g ml $^{-1}$ to 0.1 ng ml $^{-1}$) revealed detection of CoVac-1 peptides by vaccine-induced T cells down to 1 ng ml $^{-1}$ (10 ng ml $^{-1}$ for 5 out of 5 pCoVs, 1 ng ml $^{-1}$ for 3 out of 5 pCoVs). This was lower than the detection limits of SARS-CoV-2-specific T cells in human convalescent individuals for CoVac-1 vaccine peptides (10 ng ml $^{-1}$ for 4 out of 5 human convalescent individuals, and 1 ng ml $^{-1}$ for 0 out of 5 human convalescent individuals), SARS-CoV-2-specific (10 ng ml $^{-1}$ for 5 out of 5 human convalescent individuals, and 1 ng ml $^{-1}$ for 0 out of 5 human convalescent individuals) and cross-reactive T cell epitopes (10 ng ml $^{-1}$ for 2 out of 5 human convalescent individuals, and 1 ng ml $^{-1}$ for 0 out of 5 human convalescent individuals; Extended Data Fig. 3b). The intensity of CoVac-1-induced IFN γ T cell responses (pCoVs, median of 488 calculated spot counts) exceeded spike-specific T cell responses induced by mRNA-based (median 141), adenoviral vector-based (median 24) and heterologous (median 98) vaccination assessed 18–42 days after the second vaccination (Extended Data Fig. 3c, Supplementary Table 3).

Fig. 2: CoVac-1-induced T cell responses.

 **figure 2**

a–c, CoVac-1-induced T cell responses assessed ex vivo by IFN γ ELISPOT assays using peripheral blood mononuclear cells from study participants of part I ($n = 12$) and part II ($n = 24$) collected before vaccination (day 1) and at different time points after vaccination (days 7, 14, 28 and 56) or from human convalescent individuals (HCs).

The intensity of T cell responses is depicted as cumulative calculated spot counts (mean spot count of technical replicates normalized to 500,000 cells minus the respective negative control) (a). The number of CoVac-1 T cell epitopes ($n = 6$) per participant that elicited a vaccine-induced T cell response (b). Intensities of CoVac-1-induced IFN γ T cell responses assessed ex vivo in part I and part II study participants (pCoVs; $n = 24$, day 28 and day 56, left y axis) compared with T cell responses detected in HCs (right y axis) against CoVac-1 vaccine peptides and previously published^{1,2} SARS-CoV-2-specific (spec) and cross-reactive (cross) T cell epitope compositions (ECs; CoVac-1 $n = 24$, cross EC $n = 27$, spec EC $n = 26$) (c). d, Frequencies of functional CoVac-1-induced CD4 $^{+}$ T cells in study participants before vaccination (day 1) and at day 28 following vaccination using ex vivo intracellular cytokines (IFN γ , TNF and IL-2) and surface marker staining (CD107a). The right graph displays the proportion of samples revealing difunctional (2), trifunctional (3) or tetrafunctional (4) T cells. Pos, positive. In a–d, the box plots or combined box-line plots show the median with 25th or 75th percentiles, and minimum and maximum whiskers. In a, b, d, two-sided Wilcoxon signed-rank test was used; in c, two-sided Mann–Whitney U-test was used. Healthy adults 18–55 years of age were included in part I, and participants 56–80 years of age were included in part II. pos, positive.

Source Data

In vitro expansion of CoVac-1-specific T cells revealed pre-existing low-frequency T cell responses to single-vaccine peptides at baseline in 61% of participants that could be boosted at least twofold by CoVac-1, as observed on day 28 in all but one participant (Extended Data Fig. 4).

CoVac-1-induced CD4 $^{+}$ T cells displayed a multifunctional T helper 1 (T_H1) phenotype with positivity for IFN γ , tumour necrosis factor (TNF), interleukin-2 (IL-2) and CD107a (Fig. 2d). The magnitude of CoVac-1-induced CD4 $^{+}$ T cell responses did not differ between part I and part II participants and was up to 40 times higher than SARS-CoV-2-specific CD4 $^{+}$ T cell responses of human convalescent individuals (0.42% versus 0.01% (median positive samples) CoVac-1-specific IFN γ $^{+}$ CD4 $^{+}$ T cells in part II participants versus human convalescent individuals, respectively; Fig. 2d, Extended Data Fig. 5a). The frequency of functional CD4 $^{+}$ T cells was increased up to 40-fold after in vitro expansion (17.9% versus 0.44% (median positive samples) of CoVac-1-specific TNF $^{+}$ CD4 $^{+}$ T cells in part I participants), reaching up to 15 times higher levels than expanded CoVac-1-specific T cells of human convalescent individuals (18.6% versus 1.23% (median positive samples) CoVac-1-specific TNF $^{+}$ CD4 $^{+}$ T cells in part II participants versus human convalescent individuals, respectively), indicating potent expandability of CoVac-1-induced T cells upon SARS-CoV-2 exposure (Extended Data Fig. 5b,c).

Vaccine-induced CD8⁺ T cell responses, identified after in vitro expansion by tetramer staining and IFN γ ELISpot assay with HLA-matched, CoVac-1-embedded, HLA class I peptides (Supplementary Table 1) were detected in 78% and 80% of participants in part I and 100% and 95% of participants in part II with matching HLA allotypes, respectively (Extended Data Fig. 6a, b). CoVac-1-induced CD8⁺ T cells showed a polyfunctional phenotype reflected by IFN γ , TNF, IL-2 and CD107a production or expression (Extended Data Fig. 6c).

No relevant differences were observed for immunogenicity parameters between part I and part II participants except for the frequency of IL-2⁺ CoVac-1-specific CD4⁺ T cells following 12-day in vitro expansion at day 28, which was increased in part II participants, and for the expandability of CoVac-1-induced T cells at the follow-up time points (day 56 and month 3), which was decreased in part II compared with part I participants (Extended Data Table 3).

In addition to T cell responses, the induction of low-concentration SARS-CoV-2 anti-spike IgG antibodies could be observed in two participants on day 28 (Extended Data Fig. 3d).

Impact of SARS-CoV-2 variants on CoVac-1

The impact of SARS-CoV-2 VOCs declared by the World Health Organization as of 1 October 2021 (B.1.1.7 (also known as Alpha), B.1.351 (also known as Beta), P.1 (also known as Gamma) and B.1.617.2 (also known as Delta)) on CoVac-1 was analysed comparing CoVac-1 peptides with the corresponding mutated regions of the respective source proteins described for each VOC (Supplementary Table 4). The sequences of 50% of vaccine peptides were not affected by any variant-defining or associated mutation^{23,24,25,26} (Supplementary Table 4). None of the mutations of P.1 and B.1.617.2 affect CoVac-1 vaccine peptides. Variant B.1.1.7 comprises two mutations affecting P2_nuc and P6_ORF8 with a single amino acid change, respectively. Two mutations of B.1.351 affect P3_spi with either one or two amino acid changes (Fig. 3a).

Fig. 3: Role of SARS-CoV-2 variants of concern on CoVac-1 peptides and immunogenicity.

 **figure 3**

a, Colour-coded mutations described for variants of concern are shown together with corresponding affected CoVac-1 peptides. **b, c**, Intensities of T cell responses (calculated spot counts) to CoVac-1 peptides as well as to the corresponding peptide pools comprising the CoVac-1-affecting mutations of B.1.1.7 and B.1.351 were assessed ex vivo by IFN γ ELISPOT assays using peripheral blood mononuclear cells from study participants of part I ($n = 12$) and part II ($n = 24$) collected on day 28 after vaccination (pCoVs) (**b**) or from HCs (**c**). Two-sided Mann–Whitney U -test was used.

Source Data

T cell responses to peptide pools comprising the B.1.1.7 and B.1.351 mutated peptides P2_nuc, P3_spi and P6_ORF8 were detectable in 100% of part I and part II participants with CoVac-1-induced T cell responses to P2_nuc, P3_spi and P6_ORF8 wild-type (WT) peptides (Fig. [3b](#)). Although the intensity of T cell responses to single-peptide variants (P3_spi and P6_ORF8) was reduced compared with WT peptides, the intensity of CoVac-1-induced T cell responses targeting the variant peptide pools was unaffected and at least 10-fold higher than T cell responses to WT and variant peptide pools observed in human convalescent individuals (median calculated spot counts 288 pCoVs B.1.1.7, 485 pCoVs B1.351, 13 WT human convalescent individuals, 14 B1.1.7 human convalescent individuals and 12 B.1.351 human convalescent individuals; Fig. [3c](#), Extended Data Fig. [7](#)).

Discussion

Our phase I trial shows that the CoVac-1 vaccine candidate has a favourable safety profile and induces potent T cell responses after a single vaccination. Local granuloma formation was observed in all study participants representing an expected and intended local reaction after Montanide-based vaccination^{9,27}, which enables continuous local stimulation of SARS-CoV-2-specific T cells required for induction of long-lasting T cell responses without systemic inflammation. Follow-up data until month 3 after vaccination showed persistence of T cell responses, which is in line with previous experience with XS15-adjuvanted peptide vaccinations⁸ and data from SARS-CoV-1 convalescent individuals, where T cell immunity persisted for up to 17 years¹⁶.

CoVac-1-induced T_H1 CD4 $^+$ T cell responses were complemented by multifunctional CD8 $^+$ T cells, counteracting the theoretical risk of vaccine-associated enhanced respiratory disease, which has been associated with a T_H2 -driven immune response²⁸.

The phenotype of CoVac-1-induced T cells resembles that acquired upon natural infection^{1,2,11,16}, but with higher magnitude than the SARS-CoV-2 T cell responses in human convalescent individuals as well as than spike-specific T cell responses induced by mRNA-based, vector-based and heterologous vaccination^{5,6,7,29}, substantiating the profound T cell immunity induced by CoVac-1. This is further supported by the high diversity of CoVac-1-induced T cells that target multiple vaccine peptides from different viral proteins, which is central for effective anti-viral defence^{1,30,31,32}. These broad T cell responses induced by CoVac-1 remain unaffected by current SARS-CoV-2 VOCs, which were associated with loss of neutralizing antibody capacity in convalescent individuals after COVID-19 and after vaccination^{33,34,35}.

In single participants, despite negative results in sequential SARS-CoV-2 PCRs, induction of SARS-CoV-2 anti-spike IgG antibodies was documented after vaccination. This might be due to CoVac-1-induced profound CD4 $^+$ T cell responses, which not only stimulate B cells upon virus encounter but also may boost pre-existing cross-reactive SARS-CoV-2 antibodies, which were reported in 3–15% of unexposed individuals³⁶.

T cell-mediated immunity and in particular CD4 $^+$ T cells are indispensable for the generation of protective antibody responses, reinforcement of CD8 $^+$ T cell responses^{37,38,39} as well as direct killing of virus-infected cells^{40,41}. The relevance of anti-viral T cell responses during acute infection and for long-term immunity has also been proven specifically for SARS-CoV-2^{1,2,13,14,15,16,17,18,19}. Moreover, cases of asymptomatic SARS-CoV-2 exposure, as well as reports from patients with congenital B cell deficiency document cellular immune responses without seroconversion,

providing evidence for T cell immunity in disease control even in the absence of neutralizing antibodies^{14,42}. Accordingly, CoVac-1 may well serve as a (complementary) vaccine to induce T cell immunity, particularly in elderly and immunocompromised individuals with impaired ability to mount sufficient immune responses after SARS-CoV-2 vaccination with currently approved vaccines^{20,21}.

Limitations of our trial include the small sample size, low ethnic diversity, as well as the non-equivalent time points of sample collection in the comparison of vaccine-induced and infection-induced SARS-CoV-2 T cells.

In conclusion, the safety and immunogenicity results of this trial indicate that CoVac-1 is a promising multi-peptide vaccine candidate for induction of profound SARS-CoV-2 T cell immunity, which builds the basis for a presently ongoing phase II study evaluating CoVac-1 in patients with congenital or acquired B cell defects, including patients with cancer after B cell-depleting therapy and disease-related immunoglobulin deficiency (NCT04954469).

Methods

Trial design and oversight

The phase I trial (ClinicalTrials.gov identifier: NCT04546841) was designed by and conducted at the Clinical Collaboration Unit (CCU) Translational Immunology, University Hospital Tübingen, Germany. Men as well as nonpregnant women aged 18–55 years, without any relevant pre-existing conditions and adults aged 56–80 years with stable medical conditions were included in part I and part II of the study, respectively. A detailed description of the inclusion and exclusion criteria can be found in the [Supplementary Information](#). Health status was based on medical history and clinical laboratory values, vital signs and physical examination at screening. Participants with a proven history of SARS-CoV-2 infection (real-time PCR or antibody test) were excluded. Before enrolment, all participants provided their written informed consent. As a safety measure, sentinel dosing of the first participant treated in part I was conducted with a follow-up period of 28 days after vaccination followed by a sponsor safety assessment before proceeding with the vaccination of further study participants. Safety assessment of the sentinel dosing participant is described in detail in the [Supplementary Information](#). The trial was open-label (no blinding) without a control arm (no randomization).

The trial was funded by the Ministry of Science, Research and the Arts Baden-Württemberg, Germany. The trial was approved by the Ethics Committee, University Tübingen (537/2020AMG1) and the Paul Ehrlich Institute and performed in

accordance with the International Council for Harmonization Good Clinical Practice guidelines.

Safety assessment to proceed to part II was performed by an independent data safety monitoring board (DSMB).

Trial vaccine and adjuvant

CoVac-1, developed and produced by the Good Manufacturing Practices (GMP) Peptide Laboratory of the Department of Immunology, University Tübingen, is a peptide-based vaccine comprising six HLA-DR-restricted SARS-CoV-2 peptides (Supplementary Table 1) derived from various SARS-CoV-2 proteins (spike, nucleocapsid, membrane, envelope and ORF8) and the adjuvant lipopeptide synthetic TLR1/2 ligand XS15⁸ (manufactured by Bachem AG) emulsified in Montanide ISA51 VG⁹ (manufactured by Seppic). CoVac-1 peptides represent dominant SARS-CoV-2 T cell epitopes (peptide-specific T cell responses detected in more than 50% and up to 100% of convalescent individuals after SARS-CoV-2 infection) validated in human convalescent individuals after SARS-CoV-2 infection to mediate long-term immunity^{1,2}. CoVac-1 peptides were predicted and validated to bind to multiple HLA-DR molecules (promiscuous binding)¹, which is important to enable HLA-independent induction of T cell responses by CoVac-1^{1,2,43}.

CoVac-1 HLA-DR T cell epitopes contain embedded HLA class I sequences for induction of both CD4⁺ and CD8⁺ T cell responses (Supplementary Table 1). CoVac-1 peptides were selected from viral non-surface proteins and their subunits or—in case of the spike protein-derived T cell epitope P3_spi—from buried (or hidden) amino acid sequences, which are not accessible for antibodies in their conformational state. The linear 15-amino acid peptides are characterized by a free N-terminal amino group and a free C-terminal carboxy group. All amino acid residues are in the l-configuration and were not chemically modified at any position. Synthetic peptides were manufactured by established solid-phase peptide synthesis procedures using Fmoc chemistry^{44,45}.

The novel adjuvant XS15 hydrochloride is a water-soluble synthetic linear, nine amino acid peptide with a palmitoylated N terminus (Pam₃Cys-GDPKHPKSF)⁸. Acting as a TLR1/2 ligand, XS15 strongly activates antigen-presenting cells⁸ and enables the induction of strong ex vivo CD8⁺ and T_H1 CD4⁺ responses to viral peptides, including SARS-CoV-2 T cell epitopes, in preliminary in vivo analyses in a human volunteer upon a single subcutaneous injection of XS15 mixed to uncoupled viral peptides in a water-in-oil emulsion with Montanide ISA51 VG^{8,10}. To our knowledge, this is the first report of the adjuvant XS15 being used in a human clinical trial. Montanide

ISA51 VG is a mixture of a highly purified mineral oil (Drakeol 6VR) and a surfactant (mannide monooleate). When mixed with an aqueous phase in a 50:50 ratio, it forms a water-in-oil emulsion. Such a Montanide-based water-in-oil emulsion has been used as vaccine adjuvant in multiple clinical trials^{9,27}, to build a depot at the vaccination site, thereby preventing vaccine peptides from immediate degradation and thus enhancing the immune response.

CoVac-1 peptides (250 µg per peptide) and XS15 (50 µg) are prepared as a water–oil emulsion 1:1 with Montanide ISA51 VG to yield an injectable volume of 500 µl. Each participant received one subcutaneous injection of the CoVac-1 vaccine in the lower abdomen on day 1.

The dosage of CoVac-1 vaccine peptides was determined based on results from various clinical trials evaluating peptide vaccines^{44,46,47,48,49,50,51} (including dose-finding studies for viral T cell epitopes), which showed significantly stronger immune responses to 250–500 µg versus 100 µg peptide dose, without significantly higher immune responses in the 1,000 µg versus 500 µg dose group⁴⁷. Similar T cell responses were induced with 250 µg and 500 µg peptide doses. Regarding safety, even doses up to 30 mg per peptide did not raise any concerns⁴⁸. On the basis of these data, the dose of 250 µg per peptide was used for CoVac-1 vaccine peptides.

The dosage of the TLR1/2 agonist XS15 was determined based on in vitro analyses of immune cell activation by TLR1/2. In these assays, 10 µg ml⁻¹ XS15 was shown to be the most efficient dose for the stimulation of immune cells. Considering the formation of a granuloma after subcutaneous injection of XS15 emulsified in Montanide ISA51 VG, which leads to a size-dependent decrease in XS15 concentration⁸, 50 µg XS15 was selected to achieve the desired dosage of 10 µg ml⁻¹ at the vaccination site. In a toxicity study in mice, 50 µg XS15 in Montanide ISA51 VG, applied subcutaneously, did not reveal any local or systemic toxicity beyond the long known and expected local toxicity of Montanide^{9,27}. For a more detailed description of the dosage rationale for the vaccine peptides and the adjuvant, please refer to the [Supplementary Information](#).

Safety assessment

Primary safety outcomes reflect the nature, frequency and severity of solicited adverse events until day 56 after vaccination. The documentation was facilitated by use of a volunteer diary (for 28 days after vaccination) and graded by the investigators according to a modified Common Terminology Criteria for Adverse Events (CTCAE) V5.0 grading scale (Supplementary Table 5). In addition, the number and percentage of participants with unsolicited events until day 56 were reported (documented according to CTCAE V5.0). Safety assessment included clinically significant changes

in laboratory values (haematology and blood chemistry), serious adverse events, and adverse events of special interest, which included desired induration (granuloma) formation, SARS-CoV-2 infection, COVID-19 manifestations and immune-mediated medical conditions (Supplementary Tables [6](#), [7](#)).

Immunogenicity assessment

Secondary outcome was the induction of CoVac-1-specific T cell responses to at least one of the CoVac-1 vaccine peptides evaluated on day 7, day 14 and day 28 by the IFN γ ELISPOT assay ex vivo and after in vitro T cell expansion (baseline day 1, before vaccination). Follow-up analyses of CoVac-1-induced T cell responses were performed on day 56 and month 3 after vaccination. The 12-day in vitro expansion of peptide-specific T cells was performed to enable detection of low-frequent, vaccine-induced and pre-existing SARS-CoV-2-specific T cells, as well as to prove the expandability of CoVac-1-induced T cells, which is of central importance for potent T cell response upon SARS-CoV-2 exposure. In this regard, the characterization of vaccine-induced CD8 $^{+}$ T cells was performed after 12-day in vitro expansion, due to the low frequency of peptide-specific CD8 $^{+}$ T cells observed ex vivo (Supplementary Table [8](#)). PBMCs were pulsed with CoVac-1 peptides ($5\text{ }\mu\text{g ml}^{-1}$ per peptide) and cultured for 12 days adding 20 U ml^{-1} IL-2 (Novartis) on days 3, 5 and 7. For IFN γ ELISPOT (ex vivo or after in vitro expansion), cells were stimulated with $1\text{ }\mu\text{g ml}^{-1}$ of HLA class I or $2.5\text{ }\mu\text{g ml}^{-1}$ of HLA-DR peptides and analysed in technical replicates. T cell responses were considered positive if the mean spot count was threefold or more higher than the mean spot count of the negative control and defined as CoVac-1-induced if the mean spot count post-vaccination was twofold or more higher than the respective spot count on day 1. CoVac-1-induced T cell responses were further characterized using tetramer ($5\text{ }\mu\text{g ml}^{-1}$), cell-surface marker and intracellular cytokine staining. For intracellular cytokine staining, cells were stimulated with $10\text{ }\mu\text{g ml}^{-1}$ per peptide. The gating strategy applied for the analyses of flow cytometry-acquired data is provided in Supplementary Fig. [1](#). Immunogenicity results were compared with human convalescent individuals with PCR-confirmed SARS-CoV-2 infection and healthy volunteers vaccinated with an approved mRNA-based or vector-based vaccine or received heterologous vaccination (Supplementary Tables [2](#), [3](#)). All assays were conducted in a blinded manner and are described in detail in the [Supplementary Information](#).

Statistical analysis

The sample size calculation (36 participants) of the trial was based on the assumption that incidence of serious adverse events associated with administration of CoVac-1 does not exceed a predetermined rate of 5%. Safety data are displayed by counting the

respective adverse event that has occurred at least once in a patient. The highest grading of this adverse event is indicated. Data are displayed as mean \pm s.d., box plots as median with 25% or 75% quantiles and minimum and maximum whiskers.

Continuous data were tested for distribution, and individual groups were tested by use of Fisher's exact test, unpaired Mann–Whitney *U*-test or paired Wilcoxon signed-rank test, all performed as two-sided tests. No adjustment for multiple testing was done. Details regarding the statistical analysis plan and sample size calculation are provided in the [Supplementary Information](#) and the protocol.

Reporting summary

Further information on research design is available in the [Nature Research Reporting Summary](#) linked to this paper.

Data availability

Data supporting the findings of this study including the study protocol and the statistical analysis plan are supplied as source data with this paper. Further data, including de-identified participant data, are available after final completion of the trial report and are shared according to data sharing guidelines on reasonable request to the corresponding author (J.S.W.).

References

1. 1.

Nelde, A. et al. SARS-CoV-2-derived peptides define heterologous and COVID-19-induced T cell recognition. *Nat. Immunol.* **22**, 74–85 (2021).

2. 2.

Bilich, T. et al. T cell and antibody kinetics delineate SARS-CoV-2 peptides mediating long-term immune responses in COVID-19 convalescent individuals. *Sci. Transl. Med.* **13**, eabf7517 (2021).

3. 3.

WHO. Weekly epidemiological update on COVID-19. *WHO* <https://www.who.int/docs/default-source/coronavirus/situation-reports/20201012-weekly-epi-update-9.pdf> (2021).

4. 4.

Zhou, F. et al. Clinical course and risk factors for mortality of adult inpatients with COVID-19 in Wuhan, China: a retrospective cohort study. *Lancet* **395**, 1054–1062 (2020).

5. 5.

Ramasamy, M. N. et al. Safety and immunogenicity of ChAdOx1 nCoV-19 vaccine administered in a prime-boost regimen in young and old adults (COV002): a single-blind, randomised, controlled, phase 2/3 trial. *Lancet* **396**, 1979–1993 (2021).

6. 6.

Polack, F. P. et al. Safety and efficacy of the BNT162b2 mRNA Covid-19 vaccine. *N. Engl. J. Med.* **383**, 2603–2615 (2020).

7. 7.

Baden, L. R. et al. Efficacy and safety of the mRNA-1273 SARS-CoV-2 vaccine. *N. Engl. J. Med.* **384**, 403–416 (2021).

8. 8.

Rammensee, H. G. et al. A new synthetic toll-like receptor 1/2 ligand is an efficient adjuvant for peptide vaccination in a human volunteer. *J. Immunother. Cancer* **7**, 307 (2019).

9. 9.

Aucouturier, J., Dupuis, L., Deville, S., Ascarateil, S. & Ganne, V. Montanide ISA 720 and 51: a new generation of water in oil emulsions as adjuvants for human vaccines. *Expert Rev. Vaccines* **1**, 111–118 (2002).

10. 10.

Rammensee, H. G. et al. Designing a SARS-CoV-2 T-cell-inducing vaccine for high-risk patient groups. *Vaccines* **9**, 428 (2021).

11. 11.

Rodda, L. B. et al. Functional SARS-CoV-2-specific immune memory persists after mild COVID-19. *Cell* **184**, 169–183.e17 (2021).

12. 12.

Long, Q. X. et al. Clinical and immunological assessment of asymptomatic SARS-CoV-2 infections. *Nat. Med.* **26**, 1200–1204 (2020).

13. 13.

Tan, A. T. et al. Early induction of functional SARS-CoV-2-specific T cells associates with rapid viral clearance and mild disease in COVID-19 patients. *Cell Rep.* **34**, 108728 (2021).

14. 14.

Soresina, A. et al. Two X-linked agammaglobulinemia patients develop pneumonia as COVID-19 manifestation but recover. *Pediatr. Allergy Immunol.* **31**, 565–569 (2020).

15. 15.

Dan, J. M. et al. Immunological memory to SARS-CoV-2 assessed for up to 8 months after infection. *Science* **371**, eabf4063 (2021).

16. 16.

Le Bert, N. et al. SARS-CoV-2-specific T cell immunity in cases of COVID-19 and SARS, and uninfected controls. *Nature* **584**, 457–462 (2020).

17. 17.

Grifoni, A. et al. Targets of T cell responses to SARS-CoV-2 coronavirus in humans with COVID-19 disease and unexposed individuals. *Cell* **181**, 1489–1501.e15 (2020).

18. 18.

Braun, J. et al. SARS-CoV-2-reactive T cells in healthy donors and patients with COVID-19. *Nature* **587**, 270–274 (2020).

19. 19.

Mateus, J. et al. Selective and cross-reactive SARS-CoV-2 T cell epitopes in unexposed humans. *Science* **370**, 89–94 (2020).

20. 20.

Herishanu, Y. et al. Efficacy of the BNT162b2 mRNA COVID-19 vaccine in patients with chronic lymphocytic leukemia. *Blood* **137**, 3165–3173 (2021).

21. 21.

Monin, L. et al. Safety and immunogenicity of one versus two doses of the COVID-19 vaccine BNT162b2 for patients with cancer: interim analysis of a prospective observational study. *Lancet Oncol.* **22**, 765–778 (2021).

22. 22.

Lee, L. Y. et al. COVID-19 mortality in patients with cancer on chemotherapy or other anticancer treatments: a prospective cohort study. *Lancet* **395**, 1919–1926 (2020).

23. 23.

Faria, N. R. et al. Genomics and epidemiology of the P.1 SARS-CoV-2 lineage in Manaus, Brazil. *Science* **372**, 815–821 (2021).

24. 24.

Andrew Rambaut et al. Preliminary genomic characterisation of an emergent SARS-CoV-2 lineage in the UK defined by a novel set of spike mutations. *Virological* <https://virological.org/t/preliminary-genomic-characterisation-of-an-emergent-sars-cov-2-lineage-in-the-uk-defined-by-a-novel-set-of-spike-mutations/563> (2020).

25. 25.

Mlcochova, P. et al. SARS-CoV-2 B.1.617.2 Delta variant replication and immune evasion. *Nature* **599**, 114–119 (2021).

26. 26.

Tegally, H. et al. Detection of a SARS-CoV-2 variant of concern in South Africa. *Nature* **592**, 438–443 (2021).

27. 27.

van Doorn, E., Liu, H., Huckriede, A. & Hak, E. Safety and tolerability evaluation of the use of Montanide ISA51 as vaccine adjuvant: a systematic review. *Hum. Vaccin. Immunother.* **12**, 159–169 (2016).

28. 28.

Lee, W. S., Wheatley, A. K., Kent, S. J. & DeKosky, B. J. Antibody-dependent enhancement and SARS-CoV-2 vaccines and therapies. *Nat. Microbiol.* **5**, 1185–1191 (2020).

29. 29.

Liu, X. et al. Safety and immunogenicity of heterologous versus homologous prime-boost schedules with an adenoviral vectored and mRNA COVID-19 vaccine (Com-COV): a single-blind, randomised, non-inferiority trial. *Lancet* **398**, 856–869 (2021).

30. 30.

Messaoudi, I., Guevara Patino, J. A., Dyall, R., LeMaoult, J. & Nikolich-Zugich, J. Direct link between mhc polymorphism, T cell avidity, and diversity in immune defense. *Science* **298**, 1797–1800 (2002).

31. 31.

Kiepiela, P. et al. CD8⁺ T-cell responses to different HIV proteins have discordant associations with viral load. *Nat. Med.* **13**, 46–53 (2007).

32. 32.

Bilich, T. et al. Preexisting and post-COVID-19 immune responses to SARS-CoV-2 in cancer patients. *Cancer Discov.* **11**, 1982–1995 (2021).

33. 33.

Emary, K. R. W. et al. Efficacy of ChAdOx1 nCoV-19 (AZD1222) vaccine against SARS-CoV-2 variant of concern 202012/01 (B.1.1.7): an exploratory analysis of a randomised controlled trial. *Lancet* **397**, 1351–1362 (2021).

34. 34.

Wang, Z. et al. mRNA vaccine-elicited antibodies to SARS-CoV-2 and circulating variants. *Nature* **592**, 616–622 (2021).

35. 35.

Wu, K. et al. Serum neutralizing activity elicited by mRNA-1273 vaccine. *N. Engl. J. Med.* **384**, 1468–1470 (2021).

36. 36.

Ng, K. W. et al. Preexisting and de novo humoral immunity to SARS-CoV-2 in humans. *Science* **370**, 1339–1343 (2020).

37. 37.

Shedlock, D. J. & Shen, H. Requirement for CD4 T cell help in generating functional CD8 T cell memory. *Science* **300**, 337–339 (2003).

38. 38.

Carvalho, L. H. et al. IL-4-secreting CD4⁺ T cells are crucial to the development of CD8⁺ T-cell responses against malaria liver stages. *Nat. Med.* **8**, 166–170 (2002).

39. 39.

Kemball, C. C. et al. The antiviral CD8⁺ T cell response is differentially dependent on CD4⁺ T cell help over the course of persistent infection. *J. Immunol.* **179**, 1113–1121 (2007).

40. 40.

van de Berg, P. J., van Leeuwen, E. M., ten Berge, I. J. & van Lier, R. Cytotoxic human CD4⁺ T cells. *Curr. Opin. Immunol.* **20**, 339–343 (2008).

41. 41.

Tsuji, M., Romero, P., Nussenzweig, R. S. & Zavala, F. CD4⁺ cytolytic T cell clone confers protection against murine malaria. *J. Exp. Med.* **172**, 1353–1357 (1990).

42. 42.

Gallais, F. et al. Intrafamilial exposure to SARS-CoV-2 associated with cellular immune response without seroconversion, France. *Emerg. Infect. Dis.* **27**, 113–121 (2021).

43. 43.

Tarke, A. et al. Comprehensive analysis of T cell immunodominance and immunoprevalence of SARS-CoV-2 epitopes in COVID-19 cases. *Cell Rep. Med.* **2**, 100204 (2021).

44. 44.

Hilf, N. et al. Actively personalized vaccination trial for newly diagnosed glioblastoma. *Nature* **565**, 240–245 (2019).

45. 45.

Platten, M. et al. A vaccine targeting mutant IDH1 in newly diagnosed glioma. *Nature* **592**, 463–468 (2021).

46. 46.

Rini, B. I. et al. IMA901, a multipeptide cancer vaccine, plus sunitinib versus sunitinib alone, as first-line therapy for advanced or metastatic renal cell carcinoma (IMPRINT): a multicentre, open-label, randomised, controlled, phase 3 trial. *Lancet Oncol.* **17**, 1599–1611 (2016).

47. 47.

Kran, A. M. et al. HLA- and dose-dependent immunogenicity of a peptide-based HIV-1 immunotherapy candidate (Vacc-4x). *Aids* **18**, 1875–1883 (2004).

48. 48.

Sato, Y. et al. Immunological evaluation of peptide vaccination for patients with gastric cancer based on pre-existing cellular response to peptide. *Cancer Sci.* **94**, 802–808 (2003).

49. 49.

Noguchi, M. et al. Induction of cellular and humoral immune responses to tumor cells and peptides in HLA-A24 positive hormone-refractory prostate cancer patients by peptide vaccination. *Prostate* **57**, 80–92 (2003).

50. 50.

Atsmon, J. et al. Safety and immunogenicity of multimeric-001-a novel universal influenza vaccine. *J. Clin. Immunol.* **32**, 595–603 (2012).

51. 51.

Feyerabend, S. et al. Novel multi-peptide vaccination in Hla-A2⁺ hormone sensitive patients with biochemical relapse of prostate cancer. *Prostate* **69**, 917–927 (2009).

Acknowledgements

We thank all of the participants of this trial and the members of the data safety monitoring board (P. Brossart, Bonn; H. Schild, Mainz; C. Wendtner, Munich); the technical and clinical staff of the CCU Translational Immunology, Department of Internal Medicine, University Hospital Tübingen; the team of the ‘Wirkstoffpeptid Labor’, Department of Immunology, Tübingen; the pharmacy of the University Hospital Tübingen; the data management team at the Institute for Clinical Epidemiology and Applied Biometry; the ‘Zentrum für Klinische Studien’ (particularly M. Walker) at the University Hospital Tübingen for support and coordination; and EMC Microcollections GmbH for provision of XS15. This work was supported by the Ministry of Science, Research and the Arts Baden-Württemberg, Germany (Sonderfördermassnahme COVID-19, TÜ17), Bundesministerium für Bildung und Forschung (BMBF, FKZ:01KI20130), the Robert Bosch Stiftung, the Deutsche Forschungsgemeinschaft (DFG, German Research Foundation, grant WA 4608/1-2), the Deutsche Forschungsgemeinschaft under Germany’s Excellence Strategy (grant EXC2180-390900677), the German Cancer Consortium (DKTK), the Wilhelm Sander Stiftung (grant 2016.177.2), the José Carreras Leukämie-Stiftung (grant DJCLS 05 R/2017), the Fortune Program of the University of Tübingen (Fortune number 2451-0-0) and the Ernst-Jung-Preis awarded to H.-G.R.

Author information

Author notes

1. These authors contributed equally: Jonas S. Heitmann, Tatjana Bilich, Claudia Tandler

Affiliations

1. Clinical Collaboration Unit Translational Immunology, German Cancer Consortium (DKTK), Department of Internal Medicine, University Hospital Tübingen, Tübingen, Germany

Jonas S. Heitmann, Tatjana Bilich, Claudia Tandler, Annika Nelde, Yacine Maringer, Maddalena Marconato, Julia Reusch, Simon Jäger, Leonard Anton, Lisa Marie Weber, Jens Bauer, Jonas Rieth, Marcel Wacker, Helmut R. Salih & Juliane S. Walz

2. Cluster of Excellence iFIT (EXC2180) “Image-Guided and Functionally Instructed Tumor Therapies”, University of Tübingen, Tübingen, Germany

Jonas S. Heitmann, Tatjana Bilich, Claudia Tandler, Annika Nelde, Yacine Maringer, Malte Roerden, Jens Bauer, Marcel Wacker, Markus W. Löffler, Hans-Georg Rammensee, Helmut R. Salih & Juliane S. Walz

3. Institute for Cell Biology, Department of Immunology, University of Tübingen, Tübingen, Germany

Tatjana Bilich, Claudia Tandler, Annika Nelde, Yacine Maringer, Monika Denk, Marion Richter, Malte Roerden, Jens Bauer, Jonas Rieth, Marcel Wacker, Markus W. Löffler, Hans-Georg Rammensee & Juliane S. Walz

4. Dr. Margarete Fischer-Bosch Institute of Clinical Pharmacology, Stuttgart, Germany

Simon Jäger & Juliane S. Walz

5. Department of Clinical Pharmacology, University Hospital Tübingen, Tübingen, Germany

Simon Jäger & Markus W. Löffler

6. Department of Hematology, Oncology, Clinical Immunology and Rheumatology, University Hospital Tübingen, Tübingen, Germany

Malte Roerden & Reinhild Klein

7. Institute for Clinical Chemistry and Pathobiochemistry, Department for Diagnostic Laboratory Medicine, University Hospital Tübingen, Tübingen, Germany

Sebastian Hörber & Andreas Peter

8. Institute for Clinical Epidemiology and Applied Biometry, University Hospital Tübingen, Tübingen, Germany

Christoph Meisner & Imma Fischer

9. Robert Bosch Hospital, Robert Bosch Society for Medical Research, Stuttgart, Germany

Christoph Meisner

10. German Cancer Consortium (DKTK) and German Cancer Research Center (DKFZ), partner site Tübingen, Tübingen, Germany

Markus W. Löffler & Hans-Georg Rammensee

11. Department of General, Visceral and Transplant Surgery, University Hospital
Tübingen, Tübingen, Germany

Markus W. Löffler

12. Department of Oncology and Hematology, Krankenhaus Nordwest, Frankfurt,
Germany

Julia Karbach & Elke Jäger

13. Robert Bosch Center for Tumor Diseases (RBCT), Stuttgart, Germany

Juliane S. Walz

Contributions

J.S.H., H.-G.R., H.R.S. and J.S.W. were involved in the design of the overall study and strategy. C.M., H.-G.R., I.F. and M.W.L. provided feedback on the study design. T.B., C.T., A.N., Y.M., M.Roerden, J.B., J.Rieth and M.W. performed the immunogenicity analyses. J.S.H., M.M., J.Reusch, S.J., L.A., L.M.W., S.H., A.P., J.K., E.J., R.K. and J.S.W. conducted patient data and sample collection, as well as medical evaluation and analysis. J.S.H., M.M., J.Reusch, S.J., H.R.S. and J.S.W. collected data as study investigators. C.M. and I.F. developed the statistical design and oversaw the data analysis. M.D. and M.Richter conducted GMP production of CoVac-1. J.S.H., T.B., C.T., M.W.L., H.R.S. and J.S.W. drafted the manuscript. All authors supported the review of the manuscript.

Corresponding author

Correspondence to [Juliane S. Walz](#).

Ethics declarations

Competing interests

The University Hospital Tübingen is in the process of applying for a patent application (EP 20 169 047.6) covering the SARS-CoV-2 T cell epitopes included in CoVac-1 that lists A.N., T.B., H.-G.R. and J.S.W as inventors. EMC Microcollections GmbH is in the process of applying for a patent application (DE102016005550.2) covering the

adjuvant XS15 included in CoVac-1 that lists H.-G.R. as an inventor. The other authors declare no competing interests.

Peer review information

Nature thanks Antonio Bertoletti and Julie Ledgerwood for their contribution to the peer review of this work. Peer review reports are available.

Additional information

Publisher's note Springer Nature remains neutral with regard to jurisdictional claims in published maps and institutional affiliations.

Extended data figures and tables

[Extended Data Fig. 1 Consort flow diagram of the trial.](#)

The 18 participants who were not enrolled did not meet the inclusion criteria at screening. All 36 enrolled participants received one dose of the CoVac-1 vaccine. Safety oversight to proceed to part II was performed by an independent safety monitoring committee and approved by the Paul Ehrlich Institute and the local Ethics Committee after an interim safety and immunogenicity analysis of study participants included in part I on day 28 after vaccine administration. n, number.

[Extended Data Fig. 2 Intensities of CoVac-1-induced T cell responses *ex vivo* assessed in IFN \$\gamma\$ ELISPOT assays.](#)

Heatmap of CoVac-1-induced T cell response intensities (calculated spots per 500,000 cells, color gradient blue) to single CoVac-1 peptides (nuc, nucleocapsid; spi, spike; env, envelope; mem, membrane; ORF, open reading frame) in *ex vivo* IFN γ ELISPOT assays using PBMCs from study participants (uniform participant number, UPN) of part I (n = 12) and part II (n = 24) before vaccination (day 1) and at different time points after vaccination (day 7, day 14, day 28).

[Source Data](#)

[Extended Data Fig. 3 Characterization of CoVac-1-induced immune responses.](#)

(a) CoVac-1-induced long-term T cell responses assessed *ex vivo* or after 12-day *in vitro* expansion (IVE) in study participants of part I and II at day 56 and month 3 after vaccination (compared to day 28) using IFN γ ELISPOT assays. Intensity of T cell responses is depicted as calculated spot counts (mean spot count of technical replicates normalized to 500,000 cells minus the respective normalized negative control). **(b)** Peptide titration in *ex vivo* IFN γ ELISPOT assays using PBMCs from study participants (pCoVs, n = 5, day 28) or from human COVID-19 convalescent donors (HCs, n = 5) with decreasing peptide concentrations (2.5 μ g mL $^{-1}$ to 0.1 ng mL $^{-1}$) of CoVac-1 (panel 1 and 2) or SARS-CoV-2 cross-reactive (panel 3) and SARS-CoV-2 specific (panel 4) epitope compositions (ECs). **(c)** Intensities of CoVac-1-induced IFN γ T cell responses assessed *ex vivo* in study participants of part I and part II (pCoVs, n = 24, day 28) compared to spike-specific T cell responses in healthy immunized donors after second vaccination with approved mRNA vaccines (n = 20), vector-based vaccines (n = 5), or heterologous vaccination (n = 5). **(d)** Anti-spike IgG antibody titers assessed on day 1 prior to vaccination and on day 28 after vaccination. Values < 0.1 were set to zero and values \geq 1.0 were considered positive. **(a, c)** Box plots or combined box-line plots show median with 25th or 75th percentiles, and min/max whiskers. **(a)** two-sided Wilcoxon signed-rank test, **(c)** two-sided Mann-Whitney U-test. no, number.

[Source Data](#)

Extended Data Fig. 4 Intensities of CoVac-1-induced T cell responses assessed in IFN γ ELISPOT assays after 12-day *in vitro* expansion.

Heatmap of preexisting (color gradient green) or CoVac-1-induced (color gradient blue) T cell response intensities (calculated spots per 500,000 cells) to single CoVac-1 peptides (nuc, nucleocapsid; spi, spike; env, envelope; mem, membrane; ORF, open reading frame) in IFN γ ELISPOT assays after 12-day *in vitro* expansion of PBMCs from study participants (uniform participant number, UPN) of part I (n = 12) and part II (n = 24) before vaccination (day 1) and at different time points after vaccination (day 7, day 14, day 28).

[Source Data](#)

Extended Data Fig. 5 CoVac-1-induced CD4 $^{\pm}$ T cell responses in human COVID-19 convalescents and study participants.

(a–c) Frequencies of CoVac-1-specific CD4 $^{\pm}$ T cells in **(a)** human convalescent samples (HCs) after SARS-CoV-2 infection analyzed *ex vivo* (n = 19) and **(b)** after 12-day *in vitro* expansion (n = 9), and **(c)** in study participants of part I (n = 11) and part II

(n = 24) after 12-day *in vitro* expansion of PBMCs collected prior to vaccination (day 1) or on day 28 following vaccine administration. Functionality of CD4⁺ T cells was assessed for upregulation of the degranulation marker CD107a and production of the T helper 1 (Th1) cytokines (IFN γ , TNF, and IL 2). (a–c) Box plots or combined box-line plots display median with 25th or 75th percentiles, and min/max whiskers, two-sided Wilcoxon signed-rank test, n.a., not applicable; no, number; pos, positive.

[Source Data](#)

Extended Data Fig. 6 CoVac-1-induced CD8 $^{\pm}$ T cell responses to HLA class I-restricted CoVac-1-embedded peptides and CoVac-1 peptides.

T cell responses to HLA class I-restricted SARS-CoV-2 peptides embedded within the CoVac-1 vaccine peptides (matching the HLA allotype of the respective participant) were assessed by (a) tetramer staining and (b) IFN γ ELISPOT assays after *in vitro* expansion of PBMCs from study participants (part I and II) obtained on day 28 after vaccination. Pie charts display number of samples with (a) specific T cells or (b) IFN γ T cell responses to CoVac-1-embedded peptides (pos, positive; neg, negative; n.a., not assessed). Dots represent frequencies of peptide-specific T cells shown for individual donors with detected T cell responses only. (c) Frequencies of functional CoVac-1-induced CD4⁺ T cells in study participants prior to vaccination (day 1) and at day 28 following vaccination using intracellular cytokine (IFN γ , TNF, and IL-2) and surface marker staining (CD107a). The right graph displays the proportion of samples revealing difunctional (2), trifunctional (3), or tetrafunctional (4) T cell responses. (a–c) Box plots or combined box-line plots show median with 25th or 75th percentiles, and min/max whiskers, two-sided Wilcoxon signed-rank test. no, number; pos, positive.

[Source Data](#)

Extended Data Fig. 7 Vaccine-induced IFN γ T cell response to CoVac-1 peptides affected by mutations of SARS-CoV-2 variants of concern (VOC).

CoVac-1-induced T cell response to the single wild-type (WT) CoVac-1 peptides (P2_nuc (nucleocapsid), P3_spi (spike), P6_ORF8 (open reading frame 8)) in comparison to corresponding peptides comprising mutations of B.1.1.7-Alpha and B.1.351-Beta VOC were assessed by *ex vivo* IFN γ ELISPOT assay for (a) P2_nuc, (b) P3_spi, and (c) P6_ORF8 using PBMCs from study participants (n = 4) collected on day 28 after CoVac-1 vaccination.

[Source Data](#)

Extended Data Table 1 Local and systemic solicited AEs compared between part I and II

Extended Data Table 2 Unsolicited AEs classified according to CTCAE V5.0

Extended Data Table 3 Comparison of immunogenicity between part I and part II

Supplementary information

Supplementary Information

The Supplementary Information contains: Supplementary Methods, Supplementary Study Results, Supplementary Tables 1–8 and Supplementary Fig. 1.

Reporting Summary

Study Protocol

This file contains the redacted study protocol and statistical analysis plan.

Peer Review File

Source data

Source Data Fig. 1

Source Data Fig. 2

Source Data Fig. 3

Source Data Extended Data Fig. 2

Source Data Extended Data Fig. 3

Source Data Extended Data Fig. 4

Source Data Extended Data Fig. 5

Source Data Extended Data Fig. 6

Source Data Extended Data Fig. 7

Rights and permissions

Open Access This article is licensed under a Creative Commons Attribution 4.0 International License, which permits use, sharing, adaptation, distribution and reproduction in any medium or format, as long as you give appropriate credit to the original author(s) and the source, provide a link to the Creative Commons license, and indicate if changes were made. The images or other third party material in this article are included in the article's Creative Commons license, unless indicated otherwise in a credit line to the material. If material is not included in the article's Creative Commons license and your intended use is not permitted by statutory regulation or exceeds the permitted use, you will need to obtain permission directly from the copyright holder. To view a copy of this license, visit <http://creativecommons.org/licenses/by/4.0/>.

Reprints and Permissions

About this article

Cite this article

Heitmann, J.S., Bilich, T., Tandler, C. *et al.* A COVID-19 peptide vaccine for the induction of SARS-CoV-2 T cell immunity. *Nature* **601**, 617–622 (2022).
<https://doi.org/10.1038/s41586-021-04232-5>

- Received: 17 August 2021
- Accepted: 11 November 2021
- Published: 23 November 2021
- Issue Date: 27 January 2022
- DOI: <https://doi.org/10.1038/s41586-021-04232-5>

Share this article

Anyone you share the following link with will be able to read this content:

[Get shareable link](#)

Sorry, a shareable link is not currently available for this article.

[Copy to clipboard](#)

Provided by the Springer Nature SharedIt content-sharing initiative

This article was downloaded by **calibre** from <https://www.nature.com/articles/s41586-021-04232-5>

| [Section menu](#) | [Main menu](#) |

- Article
- Open Access
- [Published: 07 December 2021](#)

Multi-omic machine learning predictor of breast cancer therapy response

- [Stephen-John Sammut](#) ORCID: [orcid.org/0000-0003-4472-904X^{1,2,3}](https://orcid.org/0000-0003-4472-904X),
- [Mireia Crispin-Ortuzar](#)^{1,na1},
- [Suet-Feung Chin](#) ORCID: [orcid.org/0000-0001-5697-1082^{1,na1}](https://orcid.org/0000-0001-5697-1082),
- [Elena Provenzano](#) ORCID: [orcid.org/0000-0003-3345-3965³](https://orcid.org/0000-0003-3345-3965),
- [Helen A. Bardwell](#)¹,
- [Wenxin Ma](#)⁴,
- [Wei Cope](#)¹,
- [Ali Dariush](#)^{1,5},
- [Sarah-Jane Dawson](#) ORCID: [orcid.org/0000-0002-8276-0374^{6,7}](https://orcid.org/0000-0002-8276-0374),
- [Jean E. Abraham](#)^{2,3},
- [Janet Dunn](#)⁸,
- [Louise Hiller](#)⁸,
- [Jeremy Thomas](#) ORCID: [orcid.org/0000-0002-4652-610X^{9,10}](https://orcid.org/0000-0002-4652-610X),
- [David A. Cameron](#)⁹,
- [John M. S. Bartlett](#)^{9,11,12},
- [Larry Hayward](#)⁹,
- [Paul D. Pharoah](#) ORCID: [orcid.org/0000-0001-8494-732X^{3,13}](https://orcid.org/0000-0001-8494-732X),
- [Florian Markowetz](#) ORCID: [orcid.org/0000-0002-2784-5308¹](https://orcid.org/0000-0002-2784-5308),
- [Oscar M. Rueda](#) ORCID: [orcid.org/0000-0003-0008-4884^{1,14}](https://orcid.org/0000-0003-0008-4884),
- [Helena M. Earl](#)^{2,3} &
- [Carlos Caldas](#) ORCID: [orcid.org/0000-0003-3547-1489^{1,2,3}](https://orcid.org/0000-0003-3547-1489)

Nature volume 601, pages 623–629 (2022)

- 15k Accesses
- 1 Citations
- 221 Altmetric

- [Metrics details](#)

Subjects

- [Breast cancer](#)
- [Chemotherapy](#)
- [Data integration](#)
- [Translational research](#)
- [Tumour biomarkers](#)

Abstract

Breast cancers are complex ecosystems of malignant cells and the tumour microenvironment¹. The composition of these tumour ecosystems and interactions within them contribute to responses to cytotoxic therapy². Efforts to build response predictors have not incorporated this knowledge. We collected clinical, digital pathology, genomic and transcriptomic profiles of pre-treatment biopsies of breast tumours from 168 patients treated with chemotherapy with or without HER2 (encoded by *ERBB2*)-targeted therapy before surgery. Pathology end points (complete response or residual disease) at surgery³ were then correlated with multi-omic features in these diagnostic biopsies. Here we show that response to treatment is modulated by the pre-treated tumour ecosystem, and its multi-omics landscape can be integrated in predictive models using machine learning. The degree of residual disease following therapy is monotonically associated with pre-therapy features, including tumour mutational and copy number landscapes, tumour proliferation, immune infiltration and T cell dysfunction and exclusion. Combining these features into a multi-omic machine learning model predicted a pathological complete response in an external validation cohort (75 patients) with an area under the curve of 0.87. In conclusion, response to therapy is determined by the baseline characteristics of the totality of the tumour ecosystem captured through data integration and machine learning. This approach could be used to develop predictors for other cancers.

[Download PDF](#)

Main

Neoadjuvant treatment, that is, systemic therapy (chemotherapy with or without targeted therapy) administered before surgery, is increasingly used in the management of breast cancer to improve rates of breast-conserving surgery and increase survival⁴. However, many patients do not have a good response^{3,5}. Features associated with response to neoadjuvant therapy have been derived from clinical⁶,

molecular^{7,8,9,10,11,12} and digital pathology analysis^{13,14}. However, these studies have been frequently small, combined data from patients receiving different treatments and used single platform profiling that fails to capture the complexity of the tumour ecosystem. Unsurprisingly, physicians continue to select patients for neoadjuvant therapies using empirical clinical risk-stratification¹⁵.

Tumour ecosystems are increasingly recognized as major determinants of treatment response² and we hypothesized that improved prediction models need to account for tumours as complex ecosystems, comprising communities of malignant clones within a microenvironment of stromal, vascular and immune cell types that are perturbed by therapy.

Here we characterized biological parameters extracted from a prospective neoadjuvant study that collected detailed pre-therapy tumour multi-omic data and associated these with eventual response. We found that malignant cell, immune activation and evasion features were associated with treatment response. These features, derived from clinicopathological variables, digital pathology and DNA and RNA sequencing, were used as input into an ensemble machine learning approach to generate predictive models. We validated the accuracy of the predictive models in independent, external cohorts and demonstrated that the best performers integrated clinicopathological and molecular data. The overall approach is widely applicable to other cancers and can be customized to include both fewer and newer features.

Multi-platform profiling of tumour biopsies

We prospectively enrolled 180 women with early and locally advanced breast cancer undergoing neoadjuvant treatment into a molecular profiling study (TransNEO) (Fig. 1, the cohort characteristics are summarized in [Supplementary Table 1](#)). Fresh-frozen pre-treatment core tumour biopsies were collected from 168 cases using ultrasound guidance (Extended Data Fig. 1). DNA and RNA were extracted and profiled by shallow whole-genome sequencing (168 samples), whole-exome sequencing (168 samples) and RNA sequencing (162 cases). The diagnostic core biopsy haematoxylin and eosin-stained slides from 166 cases were digitized. The tumours sampled ($n = 168$) included all major subtypes of breast cancer. Chemotherapy (block-sequential taxane and anthracycline) was administered for a median of 18 weeks (6 cycles) in 145 cases; 22 cases received a taxane (in combination with carboplatin in 3 cases and cyclophosphamide in 13 cases) and 1 case received an anthracycline in combination with cyclophosphamide. Two patients received only one cycle owing to drug toxicities ([Supplementary Table 1](#)). Patients with HER2⁺ tumours ($n = 65$) received a median of three cycles of anti-HER2 therapy in combination with a taxane. Response was assessed at surgery using the residual cancer burden (RCB) classification^{3,5} (Extended Data Fig. 2a, b). On completion of neoadjuvant treatment, in the 161 cases with RCB

assessment, 42 (26%) had a pathological complete response (pCR), 25 (16%) had a good response (RCB-I), 65 (40%) had a moderate response (RCB-II) and 29 (18%) had extensive residual disease (RCB-III).

Fig. 1: Overview of the study design.

 figure 1

Pre-therapy breast tumours from 168 patients were profiled using DNA sequencing and RNA sequencing (RNA-seq) and digital pathology analysis. Response was assessed on completion of neoadjuvant therapy using the RCB classification.

Individual pre-therapy clinical, molecular and digital pathology features associated with pCR were identified and integrated within machine learning models to predict responses, which were then validated in an independent dataset. sWGS, shallow whole-genome sequencing; WES, whole-exome sequencing.

Clinical phenotypes are limited predictors

The clinical features individually associated with pCR (Extended Data Fig. [2c, d](#); univariable logistic regression) included tumour grade (odds ratio (OR): 4.2, confidence interval (CI): 1.8–11, false discovery rate (FDR) = 0.009), ER⁻ receptor status (OR: 4.2, CI: 2–9.1, FDR = 0.002) and absence of lymph node involvement at diagnosis (OR: 3, CI: 1.4–6.6, FDR = 0.01). When all of these variables were combined by multiple logistic regression, only ER⁻ status was associated with pCR (OR: 3.8, CI: 1.6–9.2, FDR = 0.009), but there was response heterogeneity (for example, 55% of ER⁻ tumours did not attain pCR).

Genomic landscapes associate with response

Whole-exome sequencing ($n = 168$ tumours) identified 16,134 somatic mutations ([Supplementary Table 2](#)), with the highest frequency in driver genes, including *TP53* ($n = 96$, 57%), *PIK3CA* ($n = 44$, 26%), *GATA3* ($n = 16$, 10%) and *MAP3K1* ($n = 13$,

8%) (Extended Data Figs. 3, 4a). *TP53* mutations were associated with pCR (OR: 2.9, CI: 1.3–6.6, $P = 0.01$; Extended Data Fig. 4a), as previously reported⁷, whereas *PIK3CA* mutations were associated with residual disease (OR: 2.1, CI: 1.3–3.4, $P = 0.002$).

Tumour mutation burden was higher in tumours that attained pCR (median mutations per megabase pCR: 2.3, residual disease: 1.4, $P = 0.0005$) and monotonically associated with RCB class ($P = 0.004$; Fig. 2a). This was independent of computationally estimated tumour purity (Extended Data Fig. 4b). In subgroup analysis, the association was observed only in HER2⁻ ($P = 9 \times 10^{-6}$) tumours (Extended Data Fig. 4c). The clonal status of mutations¹⁶ also associated with response: tumours that failed to attain pCR had a higher percentage of subclonal mutations (Fig. 2b). Accordingly, tumours that attained pCR had higher predicted neoantigen burdens (median neoantigens pCR: 28, residual disease: 17, $P = 0.009$; Fig. 2c), and after stratification, this was observed only in HER2⁻ tumours ($P = 0.004$; Extended Data Fig. 4d).

Fig. 2: Genomic features monotonically associate with response to therapy.

 figure 2

a, b, Box plots showing monotonic association between RCB class: total tumour mutation burden (a) ($P = 0.004$, ordinal logistic regression; pCR versus RCB-II ** $P = 0.001$ and RCB-III *** $P = 0.0002$), and the percentage of subclonal mutations (b) (P

$= 0.02$, ordinal logistic regression; pCR versus RCB-I $**P = 0.007$, RCB-II $*P = 0.04$ and RCB-III $**P = 0.001$). **c**, Density curves showing distribution of neoantigens in tumours that attained pCR and RCB-III (monotonic association, $P = 0.03$, ordinal logistic regression; pCR versus RCB-III $*P < 0.05$). **d**, Associations between mutational signatures and pCR. Statistically significant associations obtained from logistic regression are shown in red (HRD: 3; APOBEC: 13). The measure of the centre is the parameter estimate, and the error bars represent 95% confidence intervals; the vertical dashed line corresponds to an odds ratio of 1. **e, f**, Box plots showing monotonic association between RCB class and HRD score (**e**) ($P = 0.00001$, ordinal logistic regression; pCR versus RCB-II $**P = 0.006$ and RCB-III $****P = 3 \times 10^{-6}$), and the percentage of copy number alterations (CNAs; **f**) ($P = 0.0002$, ordinal logistic regression; pCR versus RCB-I $*P = 0.01$, RCB-II $**P = 0.004$ and RCB-III $****P = 7 \times 10^{-5}$). In **a–f**, the number of patients with DNA sequencing data: 40 (for pCR), 24 (for RCB-I), 64 (for RCB-II) and 27 (for RCB-III). In **a, b, e, f**, the box bounds the interquartile range divided by the median, with the whiskers extending to a maximum of 1.5 times the interquartile range beyond the box. Outliers are shown as dots. Wilcoxon rank-sum tests; all P values are two-sided.

Analysis of mutational signatures¹⁷ (Fig. 2d) showed homologous recombination deficiency (HRD) and APOBEC signatures were associated with pCR across the entire cohort (HRD OR: 1.1, $P = 0.006$; APOBEC OR: 1.1, $P = 0.02$; logistic regression). Tumours that attained pCR had a greater contribution from non-clock signatures ($P = 0.002$; Extended Data Fig. 4e). Similarly, increasing HRD¹⁸ was monotonically associated with response ($P = 0.00001$; Fig. 2e) and associated with pCR in HER2[−] tumours ($P = 3 \times 10^{-6}$; Extended Data Fig. 4f).

Tumours that attained pCR had more copy number alterations and chromosomal instability was monotonically associated with RCB class ($P = 0.0002$; Fig. 2f, Extended Data Fig. 4g). To capture the ensemble of copy number alterations, which dominate the genomic landscapes, we stratified the pre-treated tumours into the 10 genomic driver-based integrative cluster (iC) subtypes¹⁹ (Extended Data Fig. 4h). iC10 tumours, mostly triple-negative with high prevalence of *TP53* mutations and copy number alterations, showed the strongest association with pCR. By contrast, tumours from indolent ER⁺ subtypes, iC3, iC7 and iC8 were unlikely to attain pCR. Two of the aggressive ER⁺ subtypes, iC2 (11q13/14 amplification) and iC6 (amplification of *ZNF703* at 8p12), also associated with lack of treatment response. We had previously reported a similar association for iC2 tumours²⁰.

In summary, tumours that attained pCR mostly came from more-aggressive iC subtypes, were enriched for *TP53* mutations, had higher tumour mutation burdens and neoantigen loads, had less-complex clonal architectures and were enriched for APOBEC and HRD signatures.

HLA class I allelic loss confers resistance

Loss of heterozygosity (LOH) over the HLA class I locus²¹ was identified in 29 cases and associated with residual disease (OR: 3.5, CI: 1.1–14.2, $P < 0.05$; logistic regression) independently of global LOH and copy number instability (Extended Data Fig. 4i). HLA LOH events were predicted to result in inability to present 30% of tumour neoantigens and 69% of LOH events targeted HLA alleles that presented an equal or greater number of neoepitopes than the retained allele. These data support a model in which some tumours appear to have immune escaped by losing copies of the HLA locus and these tumours are less likely to respond to treatment.

Tumour proliferation and immune signatures

We modelled response as a binary variable (pCR versus residual disease) and differential RNA expression analysis showed 2,071 genes underexpressed and 2,439 genes overexpressed in tumours attaining pCR ($FDR < 0.05$). pCR associated with overexpression of driver genes *CDKN2A*, *EGFR*, *CCNE1* and *MYC* and underexpression of *CCND1* (iC2), *ZNF703* (iC6) and *ESR1* (Fig. 3a). Gene set enrichment analysis on the MsigDB Hallmarks²² and Reactome²³ gene sets showed that proliferation and immune activation strongly associated with response (Fig. 3b, Extended Data Fig. 5a,b).

Fig. 3: Transcriptomic features associated with response to neoadjuvant therapy.

 figure 3



a, Expression of breast cancer driver genes associated with pCR. FC, fold change; RD, residual disease. **b**, MSigDB Hallmark gene sets associated with pCR. Response was predominantly associated with proliferative (green) and immune (brown) gene sets. **c**, Box plot showing association of GGI score with histological grade ($P = 5 \times 10^{-11}$) (left); density plots showing monotonic association ($P = 2 \times 10^{-5}$, ordinal logistic regression) between GGI score and RCB (pCR versus RCB-II ** $P = 0.01$ and RCB-III *** $P = 3 \times 10^{-5}$) (middle); and box plot showing monotonic association ($P = 0.0001$, ordinal logistic regression) between stem -cell enrichment score and RCB (pCR versus RCB-II * $P = 0.02$ and RCB-III *** $P = 7 \times 10^{-5}$) (right). The number of patients with RNA sequencing data: 39 (for pCR), 23 (for RCB-I), 62 (for RCB-II) and 25 (for RCB-III). **d**, Box plots showing monotonic associations between computationally estimated lymphocyte density and RCB ($P < 1 \times 10^{-10}$, ordinal logistic regression; $n = 153$ cases with digital pathology data; pCR versus RCB-II ** $P = 0.006$ and RCB-III *** $P = 0.0001$) (left); CYT score and RCB ($P = 0.001$; $n = 149$ cases with RNA sequencing data; pCR versus RCB-I * $P = 0.03$ and RCB-III ** $P = 0.001$) (middle); and Danaher CD8 T cell enrichment and RCB ($P = 0.0002$; $n = 149$ cases; pCR versus RCB-I * $P = 0.04$, RCB-II * $P = 0.04$ and RCB-III *** $P = 0.0003$) (right). **e**, 2D density plot showing the relationship between proliferation and immune activation across RCB classes. The number of cases in each quadrant is shown in white. **f**, The distribution of GGI and STAT1 scores across cohort (left). The shaded area represents samples with proliferation and immune enrichment values above the mean ($n = 45$ cases). The MSigDB Hallmarks pathways associated with residual disease in these 45 tumours (red represents overexpressed, and blue indicates underexpressed) (top right). Box plots showing association between T cell dysfunction (** $P = 0.006$ HER2 $^-$) and exclusion with response in these tumours are also shown (bottom right). EMT, epithelial-to-mesenchymal transition. In **c**, **d**, **f**, the box bounds the interquartile range divided by the median, with the whiskers extending to a maximum of 1.5 times the interquartile range beyond the box. Wilcoxon rank-sum tests; all P values are two-sided.

To further explore this association, we performed gene set variation analysis using the Genomic Grade Index (GGI) gene set²⁴ ([Supplementary Table 3](#)). The GGI gene set variation analysis score associated with tumour grade (Fig. [3c](#), left panel) and was monotonically associated with RCB class ($P = 2 \times 10^{-5}$; Fig. [3c](#), middle panel). Similar results were observed on enriching over an embryonic stem-cell metagene²⁵ ($P = 0.0001$; Fig. [3c](#), right panel), indicating that tumour dedifferentiation associates with response. In a subgroup analysis, this association was only observed in HER2 $^-$ tumours ($P = 4 \times 10^{-5}$; Extended Data Fig. [6a](#)), suggesting that efficacy of anti-HER2-targeted therapies is independent of proliferation. We also explored the utility of a taxane response metagene²⁶, computed as the difference in expression of proliferation

and ceramide metagenes: HER2⁻ tumours that attained pCR had higher enrichment scores ($P = 5 \times 10^{-7}$; Extended Data Fig. 6b).

The role of the tumour immune microenvironment (TiME) in predicting response was suggested by the automated scoring of digitally scanned core biopsy haematoxylin and eosin slides showing that lymphocytic density was a good predictor of pCR ($P = 0.0006$; Fig. 3d, left panel), in line with previous reports^{13,14}. The immune cytolytic activity score²⁷ was also monotonically associated with response across all tumours ($P = 0.001$; Fig. 3d, middle panel) and correlated with tumour lymphocytic density ($R^2 = 0.4$, $P = 1 \times 10^{-15}$).

These results motivated a detailed analysis of the TiME in pre-treatment biopsies using three different methods for RNA expression deconvolution (enrichment over Danaher gene sets²⁸, MCPcounter²⁹ and Immunophenoscore³⁰; Fig. 3d, right panel, Extended Data Fig. 7a–d). These analyses converged to reveal enrichment of both innate and adaptive immunity cell populations in ER⁺HER2⁻ and HER2⁺ tumours that attained pCR. Computationally estimated lymphocyte density also strongly correlated with the enrichment of many adaptive and innate immune components (Extended Data Fig. 7e). Immunologically active tumours were co-enriched for both cytotoxic and immunoinhibitory cell types and gene signatures (Extended Data Fig. 7d). The Danaher gene set enrichment also showed that mast cells were enriched in resistant tumours (enrichment score pCR: 2.1, residual disease: 3.4, $P = 0.0001$).

We then integrated proliferation (using GGI) and immune response in the pre-therapy tumours. We used the STAT1 gene expression module³¹ to represent immune response in a single score and computed correlations between GGI and STAT1 scores with RCB classes. Tumours that attained pCR mostly had high proliferation and high immune activation, with both signatures decreasing in a stepwise manner as the degree of residual disease increased (Fig. 3e). Similar findings were observed on analysing external data from the ISPY-I and NCT00455533 studies^{10,11} (Extended Data Fig. 7f).

In summary, in therapy-naive tumours, proliferation and immune response, both innate and adaptive, have combined effects that associate with sensitivity to treatment. In general, tumours that attain pCR tend to be highly proliferative and display evidence of an active TiME.

Immune dysfunction in resistant tumours

We noted that there were 26 of the 45 tumours with high GGI and STAT1 scores that failed to attain pCR. Differential gene expression analysis in these 45 cases (residual disease versus pCR) showed enrichment of epithelial-to-mesenchymal transition and downregulation of immune response pathways in tumours with residual disease (Fig.

[3f](#)). We hypothesized that an attenuated immune response could explain this and derived T cell dysfunction and T cell exclusion metrics using TIDE³² (Fig. [3f](#)). This showed that HER2⁻ tumours with residual disease had higher T cell dysfunction at diagnosis ($P = 0.006$) with no difference in T cell exclusion scores. The increased dysfunction was associated with enrichment of inhibitory natural killer CD56^{dim} cells ($P = 0.01$) and regulatory T cells ($P = 0.02$; Extended Data Fig. [8a](#)). Across the whole cohort, active T cell exclusion (Extended Data Fig. [8b](#)) was associated with poorer response: exclusion was higher in residual disease ($P = 0.02$), with increased enrichment of cancer-associated fibroblasts ($P = 0.009$) and M2 tumour-associated macrophages ($P = 0.0009$).

In summary, some tumours, despite being proliferative and with an enriched TiME, display features of T cell dysfunction and tend to be resistant to therapy.

Machine learning integrates multi-omic features

Above, we identified clinical, digital pathology, genomic and transcriptomic features present in the naive tumour ecosystem that associated with response to therapy, although individually none of these features performed robustly. This motivated the use of a machine learning framework (Fig. [4a](#)) to integrate features into a predictive model of pCR.

Fig. 4: Predicting response to therapy using a composite machine learning model.

 **figure 4**

a, Schematic of the machine learning framework. CV, cross validation. **b**, Feature importance calculated as the average z -score resulting from dropping each individual feature from the three components of the model and calculating the new area under the receiver operating characteristic curve (AUC). The importance of chemotherapy sequence features have been averaged into a ‘therapy sequence’ row for simplicity. ES cell, embryonic stem cell; TMB, tumour mutation burden. **c**, Receiver operating characteristic curves for the clinical (dashed) and fully integrated (continuous) models applied on the external validation cohort. The dotted line indicates random performance. FPR, false positive rate; TPR, true positive rate. **d**, AUCs for models with increasing levels of data integration. The continuous line on the foreground corresponds to the AUCs obtained from the external validation cohorts (filled markers), with bands representing the standard deviation estimated with bootstrap. The filled band on the background corresponds to the standard deviation of the AUCs obtained using cross-validation on the training dataset, with mean values represented by a dashed line. DigPath, digital pathology. **e**, Potential clinical impact of the pCR model, using data from the external validation confusion matrix (left). Bar plots show the number of patients that would be identified to be chemoresistant using operating thresholds of 0 and 2 false negatives (FN), using either the clinical or fully integrated models, respectively (right). ML, machine learning; NAT, neoadjuvant therapy.

A series of six pCR prediction models including different feature combinations were derived using: (1) clinical features only, and adding (2) DNA, (3) RNA, (4) DNA and RNA, (5) DNA, RNA and digital pathology, and (6) DNA, RNA, digital pathology and treatment. The number of predictive features totalled 34 (Fig. 4b, Extended Data Fig. 9a, b, [Supplementary Table 4](#)).

The models were based on a multi-step predictor pipeline. Inside the pipeline, features were first filtered by univariable selection and collinearity reduction, and then fed into an unweighted ensemble classifier³³. Each ensemble consisted of three algorithms acting in parallel: logistic regression with elastic net regularization, a support vector machine and a random forest. The three algorithm scores were then averaged to form the predictor (Extended Data Fig. 9c). A fivefold cross-validation scheme was used to optimize model hyperparameters (Methods and [Supplementary Methods](#)).

The fully trained models were tested for validation on an independent external cohort of 75 patients that received neoadjuvant therapy, either cases randomized to the control arm of the ARTemis clinical trial³⁴ or cases recruited into the Personalised Breast Cancer Programme (details listed in [Supplementary Table 5](#)). In the external cohort, the models achieved the following areas under the curve: 0.70 (clinical), 0.80 (clinical and DNA), 0.86 (clinical and RNA), 0.86 (clinical, DNA and RNA), 0.85 (clinical, DNA, RNA and digital pathology), 0.87 (fully integrated model (clinical, DNA, RNA, digital pathology and treatment)) (Fig. 4c, d, Extended Data Fig. 9d, e). The baseline clinical model, as implemented using our machine learning algorithms, performed similarly to other clinical predictors reported in larger datasets^{35,36}.

We explored the importance of the features used in the integrated training model and found that it used clinical phenotypes in combination with DNA, RNA and digital pathology features. The dominant features were age, lymphocyte density, and expression of *PGR*, *ESR1* and *ERBB2* (Fig. 4b, Extended Data Fig. 9b, [Supplementary Table 6](#)). In addition, the predictive model also used features associated with proliferation, immune activation and immune evasion. The fully integrated model relied on features obtained from all modalities of data, with RNA features having the largest contribution (Fig. 4b, Extended Data Fig. 9b).

Despite the models being trained using a binary response variable (pCR versus residual disease), an analysis of the predictor scores across both training and validation sets showed that these were highly correlated with RCB class, with a monotonic association observed (training: $P = 3 \times 10^{-10}$, validation: $P = 1 \times 10^{-6}$; Extended Data Fig. 10).

In a clinical workflow, the predictive models could be applied to candidates for neoadjuvant therapy; any predicted to have chemoresistant tumours should be considered for enrolment into clinical trials of novel therapies, as their prognosis is

poor if they are treated with standard-of-care therapies (Fig. 4e). We explored this in a simulation study and applied the confusion matrix obtained in the external validation cohorts on a total of 100 patients about to receive neoadjuvant therapy. If the criterion was that no patient guaranteed to obtain pCR should miss out on treatment (no false negatives), the clinical machine learning model would identify 15 non-responders, whereas the fully integrated machine learning model would increase this number to 31. By relaxing the false-negative threshold and allowing two false negatives, 24 (clinical model) and 52 (fully integrated model) patients who would not attain pCR would be correctly identified (Fig. 4e).

In summary, we used an ensemble machine learning approach that inputs multi-omic features from the pre-treatment biopsy to derive predictors of pCR. The models were externally validated demonstrating very good discrimination power.

Discussion

Human tumours are complex ecosystems formed in the malignant compartment by communities of clones and cell phenotypes, and in the tumour microenvironment by a very diverse array of stromal, vascular, innate and adaptive immune cell types^{1,2,37}. How these ecosystems are organized in breast cancer appears to be strongly associated with their genomic features³⁸. Therapy perturbs these tumour ecosystems and this is increasingly recognized as one of the main determinants of treatment response². Remarkably, efforts to identify features in untreated tumours that predict response to therapy have mostly ignored this.

Our findings showed that response is determined to a great degree by the baseline characteristics of the totality of the tumour ecosystem. Tumour proliferation emerged as a key determinant of response as reported previously^{9,26}. Genomic features that associated with response to chemotherapy in HER2⁻ tumours, and usually correlated with proliferation, included *TP53* mutations, tumour mutation burden, BRCA, HRD and APOBEC mutational signatures, and chromosomal instability. Remarkably, in HER2⁺ tumours, treated with chemotherapy and HER2-targeted antibodies, response appeared to be independent of proliferation. This observation was previously reported³⁹ and should motivate a search for the underlying mechanism. Clonal diversity and subclonal mutations were associated with residual disease. This has also been reported in oesophageal carcinoma⁴⁰, suggesting that clonally diverse tumours are more likely to contain or be able to select resistant subclones.

A central finding was that the TiME in treatment-naive tumours is a major determinant of response to therapy. Previous work in mouse models had shown that an effective response to chemotherapy requires an immunocompetent tumour microenvironment⁴¹.

Deconvolution of immune subpopulations using our RNA expression data suggested that both innate and adaptive immunity were already engaged in tumours that went on to have pCR. We previously reported digital pathology-derived lymphocytic density as an independent predictor of pCR^{13,14}, and here confirm this and also show that it strongly correlates with the cytolytic activity score (a surrogate for CD8 and natural killer cytotoxic cells). Pathologist-assessed infiltration of tumour lymphocytes has been reported by many groups as a predictor of response to chemotherapy⁴² and immunotherapy⁴³, and international guidelines for scoring exist⁴⁴. The direct role of the immune system in killing tumour cells as a result of chemotherapy, so-called chemotherapy-induced immunogenic cell death, has been proposed⁴⁵. We hypothesize that the presence of an engaged immune infiltrate in the tumour microenvironment in therapy-naive tumours mediates such chemotherapy-induced immunogenic cell death.

By contrast, a suppressed immune response in naive tumours associated with a propensity for poor response. HLA LOH was first implicated in immune evasion in lung cancer²¹ and we show here that it predicts poor response to therapy. T cell dysfunction⁴⁶ and exclusion⁴⁷ showed similar effects. The similarity of features predicting response to cytotoxic therapy compared with those reported to predict response to immune checkpoint inhibitors⁴⁸ raises the intriguing possibility that similar mechanisms of killing tumour cells are engaged.

We show that machine learning models for prediction of therapy response that combine clinical, molecular and digital pathology data significantly outperform those based on clinical variables. The high accuracy obtained in external validation suggests that the models are robust and may enable using molecular and digital pathology to determine therapy choice in future clinical trials, including in the adjuvant therapy setting. More generally, the framework highlights the importance of data integration in machine learning models for response prediction and could be used to generate similar predictors for other cancers.

Methods

Study population and tissue collection

We analysed breast tumours from patients with primary invasive cancer enrolled in the TransNEO study at Cambridge University Hospitals NHS Foundation Trust between 2013 and 2017. Appropriate ethical approval from the institutional review board (research ethics reference: 12/EE/0484) was obtained for the use of biospecimens with linked pseudo-anonymized clinical data. All patients provided informed consent for sample collection and all participants consented to the publication of research results.

Clinical data were collected in Microsoft Excel (as part of the office 365 suite) by data managers.

Pre-neoadjuvant and post-neoadjuvant chemotherapy specimens were handled following departmental standard operating procedures in accordance with international guidelines⁴⁹. RCB post-neoadjuvant therapy was assessed by experienced breast histopathologists (E.P. and J.T.) using the pathology protocol for assessment of RCB as provided on the MD Anderson RCB website (https://www.mdanderson.org/education-and-research/resources-for-professionals/clinical-tools-and-resources/clinical-calculators/calculators-rbc-pathology-protocol2.pdf?_ga=2.93785373.1680005878.1594213442-1702172112.1568299785). RCB assessment was not available in seven cases (Extended Data Fig. 1). PCR was defined as the absence of residual invasive cancer on haematoxylin and eosin (H&E) evaluation of the complete resected breast specimen and all sampled lymph nodes. Results for oestrogen receptor (ER) and HER2 status were extracted from pathology reports. ER and HER2 testing were performed in an accredited diagnostic laboratory and scored according to UK guidelines⁵⁰. ER staining was regarded as positive if the Allred score was more than 2. HER2 was regarded as positive if immunohistochemical staining was 3+, or if there was borderline 2+ staining with HER2 gene amplification on FISH (HER2 copy number ≥ 6.0 and/or HER2:CEP17 ratio ≥ 2).

Whole blood from all patients was collected before commencing neoadjuvant therapy in S-Monovette 7.5 ml EDTA tubes and centrifuged at 820g for 10 min at room temperature to partition plasma, buffy coat and erythrocytes. The buffy coat fraction was isolated and suspended in 10 ml of red cell lysis buffer (155 mM NH₄Cl, 10 mM KHCO₃ and 0.1 mM EDTA pH 7.4), centrifuged at 3,600g for 10 min at room temperature, followed by a further step of resuspension and centrifugation. The final cell pellet was suspended in 1 ml of phosphate-buffered saline, centrifuged at 10,000 r.p.m. for 5 min, isolated and frozen. Tumour tissue was collected before the initiation of neoadjuvant chemotherapy via an ultrasound-guided biopsy, flash-frozen in liquid nitrogen and stored at -80°C . Sectioning of the samples was performed on a cryostat (CM1520; Leica Biosystems). Following an initial 6- μm section taken for H&E staining, 20 30- μm sections were taken and 10 sections were placed in each of the two tubes containing either 180 μl ATL buffer or 700 μl of QIAzol for DNA or RNA extraction, respectively. The histology slides were stained with H&E, and tumour, stromal and immune infiltrate quantification was performed.

Nucleic acid processing and library preparation

Isolation of DNA from all buffy coat and sectioned tumour tissue samples was performed using the Qiagen DNeasy Blood and Tissue Kit (catalogue no. 69506).

DNA from tumour tissue was extracted using the manufacturer-recommended protocol. DNA quantification was performed using the Qubit Fluorometer (Invitrogen) and nucleic acid purity was assessed using the NanoDrop 8000 (Thermo Fisher Scientific). Normal and tumour DNA samples were normalized to a concentration of 5 ng/µl using a fluorescence-based method (Quant-IT dsDNA BR, Q33130, Thermo Fisher Scientific) and 50 ng of DNA used for exome library preparation. DNA libraries were constructed using the Illumina Nextera Rapid Capture Exome Library Preparation kit according to the manufacturer's protocol (Illumina document number: 15037436). The resulting whole-genome sequencing (WGS) libraries and captured whole-exome sequencing (WES) libraries were normalized and pooled, with each pool normalized to a molarity of 4 nM. Sequencing was performed on an Illumina HiSeq4000 instrument in 50-bp single-read mode (for shallow WGS (sWGS)) or 75-bp paired-end mode (for WES). Demultiplexing was performed using Illumina's bcl2fastq2 software using default options. Isolation of RNA from all tumour tissue samples was performed using the Qiagen miRNeasy Mini Kit (catalogue no. 217004). Tissue sections suspended in 700 µl of QIAzol were thawed and mixed by vortexing. Chloroform (140 µl) was added to each sample, vortexed and transferred to a heavy phase lock tube (Qiagen MaXtract, catalogue no. 129056). The samples were then spun at 12,000g for 15 min at 4 °C, following which the upper clear phase containing RNA was transferred to a 2-ml Eppendorf tube. Subsequent extraction was then performed using the Qiagen QIASymphony using the manufacturer-recommended protocol. RNA quantification was performed using the Qubit Fluorometer (Invitrogen) and assessment of the RNA integrity performed using the high-sensitivity RNA assays on the Agilent 4200 TapeStation Instrument. RNA samples were normalized to a concentration of 10 ng/µl and transcriptomic libraries were prepared using the Illumina TruSeq Stranded mRNA Library Preparation kit (catalogue no. 20020595) according to the manufacturer's protocol (Illumina document number: 1000000040498). Of each library, 5 nM was prepared and 94 samples were pooled per lane of sequencing on an Illumina HiSeq4000 system run in 75-bp paired-end mode. Demultiplexing was performed using bcl2fastq2 v.2.17 software (Illumina) using default options.

sWGS and WES pre-processing

For each exome paired FASTQ file, sequencing quality metrics were generated using the FastQC tool (version 0.11.7)

(<https://www.bioinformatics.babraham.ac.uk/projects/fastqc/>). Alignment to the GRCh37 decoy assembly of the human genome was performed using Novoalign (version 3.2.13) in paired-end mode with the following parameters enabled: (1) base quality recalibration, (2) trimming of Nextera adaptor sequence CTGTCTCTTATA, and (3) hard clipping of trailing bases with quality ≤ 20. sWGS data were processed similarly; however, Novoalign was run in single-read mode. Binary aligned sequencing (BAM) file merging, coordinate sorting and PCR and optical duplicate

marking were performed using Novosort (version 3.2.13). Local realignment around insertions and deletions was performed using the Genome Analysis Toolkit (GATK)⁵¹ programs RealignerTargetCreator and IndelRealigner. The performance of the library preparation as well as the quality of the sequencing data, target coverage metrics within exonic regions specified by the Nextera target BED file obtained from Illumina (Manifest version 1.2) were generated using Picard (version 2.17.0) CalculateHSMetrics. Median WES coverage was $\times 162$ for tumours and $\times 137$ for normal tissue. Median sWGS coverage was $\times 0.1$.

Variant calling

Germline variants were identified across all tumour and normal samples using GATK HaplotypeCaller (version 4.1.4) run in GVCF mode and filtered using GATK VariantRecalibrator. Somatic variant calling was performed using Mutect2 (version 4.1.4). A panel of normals was created by running Mutect2 in tumour-only mode on all normal samples and the resulting VCF files were merged using CreateSomaticPanelOfNormals. Mutect2 was run on each tumour–normal sample pair using this panel of normals and a database of germline variants present within gnomAD to improve somatic calling. Variant filtration was performed using FilterMutectCalls using default options. Mutations that were present at an allelic fraction (AF) of less than 1%, had coverage of less than $\times 25$ in both normal and tumour tissue exome data, were present in the gnomAD repository with a population prevalence greater than 1% and identified as lying within repetitive regions by ANNOVAR (version 599af129dbcf4e85a2da9832c4ae59898e2f3a9) were removed. Somatic variants were annotated using Ensembl Variant Effect Predictor (version 87)^{52,53}. The tumour mutation burden was computed as the sum of all mutations per tumour divided by the total number of bases sequenced in the genome (45.54 Mb). Breast cancer driver mutations were defined as those genes identified in previous publications^{54,55}.

Copy number calling

Genome binning and segmentation on low-pass sWGS data were performed using the R package QDNAseq (version 1.24)⁵⁶. Binning was performed across 100-kb windows and counts corrected for GC-rich regions as well as poorly mappable regions. sWGS data from normal tissues were used to correct for technical and germline artefacts. Segmentation was performed using the circular binary segmentation algorithm implemented in the R package DNAcopy (version 1.60)⁵⁷. Parental copy number quantification and estimation of tumour purity and ploidy were obtained using ASCAT (version 2.5.1)⁵⁸ using log ratios derived from QDNAseq and germline single-nucleotide polymorphisms obtained from HaplotypeCaller as input.

As recommended by the authors, the technology parameter gamma was set to 1 for WES data.

Clonal reconstruction

The CCF for each mutation was computed using the previously derived mathematical framework¹⁶:

$$\text{CCF} = \frac{\text{VAF} \cdot \text{CN}_{\text{normal}}}{(\text{VAF} \cdot \text{CN}_{\text{normal}}) + p \cdot (\text{CN}_{\text{tumour}} - \text{CN}_{\text{normal}})}$$

where VAF was the variant allele fraction for each mutation determined by exome sequencing, p was the tumour purity (computed using ASCAT), $\text{CN}_{\text{normal}}$ was the germline copy number state and $\text{CN}_{\text{tumour}}$ was the total copy number state at the mutant locus in the tumour. Point estimates for CCF and confidence intervals were computed using a binomial distribution modelled by the binconf function from the Hmisc R package (version 4.4) and a mutation was classified as clonal if the CCF 95% confidence interval overlapped 1, with all other mutations classified as subclonal.

Mutational signatures decomposition

Signature decomposition from the bulk exome sequencing mutation data was performed using the DeconstructSigs R package (version 1.8)⁵⁹, which uses the Wellcome Trust Sanger Institute Mutational Signature Framework as a reference and determines the linear combination of 30 pre-defined signatures by using a multiple logistic regression model with constraints to reconstruct the mutational profile of each tumour. Mutational signatures were solely identified in tumours with more than 10 mutations. To determine signature associations with response, each signature was \log_2 normalized using the exposure of signature 1 (age) as a reference. Associations between these normalized exposures and response were determined using logistic regression models.

HRD quantification

The scarHRD R package (version 0.1.1)¹⁸ was used to determine the levels of HRD present in the WES data, using the ASCAT allele-specific copy number as input. This tool inferred three components of HRD: telomeric allelic imbalance, LOH and the number of large-scale transitions, which were then summarized into an overall HRD score.

HLA typing, identification of HLA LOH and neoantigen calling

HLA typing was performed on the normal tissue sequencing data using the Polysolver tool (version 4)⁶⁰, which inferred the four-digit HLA type for each sample by using a Bayesian classifier to determine genotype. LOH over the HLA class I locus was determined by using the LOHHLA tool (downloaded from <https://bitbucket.org/mcgranahanlab/lohhla/src/master/> commit: 9d58c99)²¹, using as input ASCAT tumour purity and HLA genotyping data from PolySolver (version 4). Statistically significant HLA alleles with a copy number of less than 0.5 were assumed to be undergoing LOH. Neoantigen calling was performed by using the pVAC-tools (version 1.5.4) cancer immunotherapy suite⁶¹. Mutations identified on exome sequencing were translated into corresponding mutant proteins and a list of potential neoantigenic fragments containing the mutant protein generated by using a sliding window approach across the mutated locus, retaining epitopes of lengths 8–11 amino acids. These potentially antigenic fragments were analysed for binding affinity to the HLA class I molecules using the prediction software NetMHCpan version 3⁶², NetMHC version 4⁶³ and PickPocket version 1.1⁶⁴ bundled within the Immune Epitope Database resource⁶⁵. Neoantigens with a binding affinity score of less than 500 nM and that had a higher binding affinity than the corresponding wild-type sequences were retained. Further downstream filtering was done by retaining neoepitopes generated by transcripts that had an expression greater than 1 TPM.

iC10 classification

Classification of all tumours into one of the ten iC10 clusters^{19,66} was performed using the iC10 R package (version 1.5)²⁰, which took cellularity-corrected copy number log ratios obtained from QDNAseq and voom-normalized gene expression counts derived from the RNA sequencing (RNA-seq) data as input. The iC10 classification of tumours that did not have RNA-seq data was determined using the copy number data only. Associations with response were visualized using the mosaic function from the vcd R package (version 1.4-7).

RNA-seq pre-processing

FASTQ files for each sample generated from multiple sequencing lanes were merged and aligned using STAR version 2.5.2b⁶⁷, using an index generated from the GRCh37 decoy assembly of the human genome and a transcriptomic Gene Transfer Format (GTF) guide obtained from Ensembl Release 87. STAR was run in two-pass mode for sensitive novel junction discovery, in which the first pass performed a default mapping, and the second pass used the splice junctions detected in the first pass to perform a further round of alignment enhancement. This STAR BAM file was used for

differential expression and transcript counting. For variant calling, the BAM files generated by STAR were processed as per GATK best practices guidelines: PCR and optical duplicates were marked using Picard MarkDuplicates and following this, the GATK tool SplitNCigarReads was used to split reads having N CIGAR elements in separate sequence reads. Local realignment around insertions and deletions was performed using RealignerTargetCreator and IndelRealigner, using a calibration set derived from the 1000 Genomes project^{[68,69,70](#)}. Base quality recalibration across all variant sites was then performed using BaseRecalibrator. The tumour samples were sequenced to a median of 87 million reads.

RNA variant calling

Germline variants identified on exome sequencing were filtered by removing multi-allelic variants, indels, as well as mutations for which the minimum depth was less than 30× across all samples. The remaining germline variants were subsequently genotyped across all RNA samples and comparisons were done across homozygous germline variants only. The percentage median concordance across samples derived from a matched patient was 100%, whereas unrelated samples had a median concordance of 60%. Somatic variants detected on exome sequencing were genotyped in the RNA GATK BAM by using HaplotypeCaller in GENOTYPE_GIVEN_ALLELES mode. Mutations present in all samples for one patient were concatenated together, and a VCF was generated to guide HaplotypeCaller local reassembly and variant calling.

Gene and transcript abundance estimation

Gene expression estimation was performed on the STAR aligned BAM file using HTSeq (version 0.6.1p1)^{[71](#)} in read strand-aware union overlap resolution mode, where a read would only be assigned to a gene if it only overlapped within an exonic region of one gene, rather than multiple genes. Gene counts across all samples were merged into one counts matrix using R, and a trimmed mean of M-value (TMM) normalization performed across all samples using the edgeR R package (version 3.32.1)^{[72](#)} to correct for composition biases and make the transcript counts comparable across all samples^{[73,74](#)}. The library normalized counts were then transformed into fragment per kilobase millions (FPKMs) and then scaled to a total of a million counts, changing the unit of measure to transcripts per million (TPM)^{[75](#)}.

Differential expression

To identify sets of genes that were highly or lowly expressed given a set of experimental conditions (such as pCR versus residual disease) (Fig. [3a](#)), differential

expression was performed on the gene raw counts data obtained as described above using edgeR^{72,73}. The output of each model was a list of differentially expressed genes. Following the generation of a ranked list of differentially expressed genes for any comparison of interest, gene set enrichment was performed using the camera statistical method in edgeR; in brief, this method performed a competitive gene set test accounting for inter-gene correlation and tested whether genes were highly ranked relative to other genes in terms of differential expression⁷⁶. As input to this gene set enrichment analysis (GSEA) method, the annotated gene sets provided within the MSigDB version 6.1 were used^{22,77} (Fig. 3b). In addition, further enrichment over the Reactome database²³ (Extended Data Fig. 5) was performed using the ReactomePA R package (version v1.34)⁷⁸.

GSEA

GSVA and ssGSEA were performed using the GSVA R package (version 1.34)⁷⁹ on (1) the GGI gene set²⁴, (2) the core embryonic stem-cell-like module²⁵ and (3) the STAT1 immune signature³¹. The log-transformed TMM normalized TPM counts were used as input to the GSVA package. A high GSVA score (Fig. 3f, Extended Data Fig. 8a) was defined as any score above the mean value. We computed the paclitaxel response metagene²⁶, as the difference in expression of a mitotic metagene (geometric mean of *BUB1B*, *CDK1*, *AURKB* and *TTK* TPM expression) and a ceramide metagene (geometric mean of *UGCG* and *CERT1* expression).

Immune microenvironment characterization

The cytolytic activity score²⁷ was computed as the geometric mean of *GZMA* and *PRF1* (as expressed in TPM, 0.01 offset). Immune cell enrichment was performed using (1) MCPcounter²⁹ using voom-normalized RNA-seq counts as input, (2) enrichment over 14 cell types using 60 genes²⁸, using the log-transformed geometric mean of the TPM expression of cell-specific genes as input, and (3) z-score scaling of cancer immunity parameters³⁰ to classify four different immune processes (MHC molecules, immunomodulators, effector cells and suppressor cells), by generating z-score-normalized TPM gene expression for an input list of 162 genes. Heatmaps used to visualize the data were generated using the pheatmap R package (version 1.0.12) and unsupervised column hierarchical clustering based on the Euclidean distance performed. We used the TIDE algorithm (<http://tide.dfci.harvard.edu>)³² to derive T cell dysfunction and exclusion metrics. The input to TIDE was a log₂-transformed TPM matrix of counts, which was normalized by subtracting the average log₂ expression of all genes. The interplay between proliferation and immune activation across the four RCB classes (shown in Extended Data Fig. 7f) was validated by

performing GGI and STAT1 enrichment using a combined microarray dataset from the ISPY-I¹⁰ (GSE25066 and GSE32603) and NCT00455533 (ref. ¹¹) (GSE41998) trials, which were chosen for similar neoadjuvant therapy regimens, availability of core biopsy gene expression and RCB classification.

Digital pathology analysis

Whole-slide H&E images (scanned at a magnification of $\times 20$) were analysed using CellExtractor v1.0, an open-source platform developed for high-throughput analyses of histopathological images. The code was written in Python and used the OpenCV and OpenSlide library. Initially, full-face H&E scanned images were divided into several subregions. Each subregion was processed to remove the background using an adaptive threshold method. A distance matrix was calculated for individual foreground objects to de-blend overlapping objects during the watershed segmentation process. The latter produced binary images of cell masks from which cellular features such as centroids, shape descriptors, and pixel intensities were estimated. These features were used to train a two-level support vector machine-based classifier. During the first level, spurious detections such as artefacts, dirt and pen marks were separated from genuine detections. This was followed by a second level of classification to identify cancer cells, stromal cells and lymphocytes based on a training set of objects selected by a pathologist (W.C.) of approximately 1,000 objects for each category. Finally, on the basis of these classes, descriptive statistical parameters such as cellular fractions and densities were estimated. For each detected cell, density was obtained based on counting the number of nearest neighbours approach, that is, the density within the distance to the N th nearest neighbour calculated as follows: $\Sigma_N \text{ (pixel}^{-2}) = N / (\pi \times d_N^2)$ where d_N was the distance to the N th nearest neighbour within a density-defining population. A value of $N = 50$ was used to estimate the density parameter¹³. To ensure that the estimated density was not biased towards our choice of density parameter ($N = 50$), we calculated the density for N in range of 40–60, with 5-step increments. The results remained the same and were therefore independent of the choice of the number of neighbours.

Validation dataset

An external dataset comprising 75 patients treated with neoadjuvant therapy recruited to the Personalised Breast Cancer Programme (PBCP; research ethics reference: 18/EE/0251) study and the control arm of the ARTemis trial (research ethics reference: 08/H1102/104, EudraCT number: 2008-002322-11) was collated. All patients provided informed consent for sample collection and all participants consented to the publication of research results. These cases were selected due to the availability of

DNA, RNA and digital pathology data. Clinical and molecular details for these 75 cases are summarized in [Supplementary Table 5](#).

Statistical testing

All statistical tests in the exploratory analysis were performed using R version 4.0.3 and associated packages. All statistical tests described in this work were two-sided. Unless otherwise specified, all statistical comparisons were performed using cases that attained pCR as a comparator. Tests involving comparisons of distributions were done using ‘wilcox.test’ unless otherwise specified. Ordinal logistic regression models used the ordered RCB variable (pCR > RCB-I > RCB-II > RCB-III) as a response variable to determine monotonic associations and were modelled using the polr function from the MASS R package (version 7.3-54). To determine features associated with response, only cases that received at least one cycle of neoadjuvant chemotherapy and one cycle of anti-HER2 therapy (if HER2⁺) were used in the comparisons to avoid the confounding effect of suboptimal exposure to neoadjuvant therapy on response.

Derivation of a predictive model for relapse

Dataset and model training

The TransNEO dataset was used to train the machine learning pCR classification models. Hyperparameters were optimized using fivefold cross-validation in the training set to maximize the area under the receiver operating characteristic (AUC ROC) curve. The rest of the parameters were determined by setting the hyperparameters to their optimal values and refitting to the entire training cohort. To ensure robustness, we repeated the optimization process five times with different cross-validation seeds, effectively training five alternative predictors. Together, these five predictors constituted what we call the ‘model’: model predictions for new data are obtained by averaging the scores produced by the five predictors. Once trained and frozen, models were independently validated on an external dataset composed of $n = 75$ patients from the PBCP and ARTemis cohorts described previously.

Predictor architecture

The machine learning framework was built on Python (version 3.7.4) using the following libraries: scikit-learn (version 0.21.2), numpy (version 1.16.4), scipy (version 1.3), pandas (version 0.24.2) within a Singularity container (version 2.4.6-dist). Each predictor was built as an ensemble of three scikit-learn pipelines; in other words, the response prediction was calculated as the average of the scores produced by the three classification pipelines. Each pipeline contained four steps: collinearity

removal, k -best feature selection, scaling and classification. The first step removed all features with a mutual Pearson correlation above 0.8, retaining only the one with the highest correlation with the response variable. The second step removed all features that were not ranked within the top k according to their ANOVA F -value with respect to the binary response variable. The third step applied z -score scaling to the remaining features. The fourth step was the classification step, which consisted of a logistic regression⁸⁰ in the first pipeline, a support vector classifier⁸¹ in the second pipeline, and a random forest⁸² in the third pipeline. All hyperparameters were optimized using a randomized 1,000-step fivefold cross-validation search to maximize the AUC ROC curve. Logistic regression was implemented with elastic net regularization and SAGA solver, with C parameters between 10^{-3} and 10^3 , and L1 ratios between 0.1 and 1. The support vector classifier was allowed to have either radial basis function, sigmoid or linear kernels, with gamma parameters between 10^{-9} and 10^{-2} , and C parameters between 10^{-3} and 10^3 . Finally, the random forests were allowed to have between 5 and 100 (or the maximum number of) estimators, maximum features between 5% and 70% of the total, and minimum samples per split between 2 and 15. The final values of the hyperparameters obtained through the optimization procedure can be found in the [Supplementary Material](#).

Feature definitions

Models were trained on a combination of clinical, DNA, RNA, digital pathology and treatment features, as shown in Fig. 4a. Differences in treatment were captured using one-hot-encoded variables assessing whether the patient did or did not receive anthracycline or anti-HER2 treatment. A further set of variables captured whether taxane or anthracycline were given first. The complete list of features and their Spearman correlation matrix can be found in [Supplementary Table 4](#) and Extended Data Fig. 9a, respectively. The order in which features were added in successive models was determined by how widely available they typically are. Although the information required for treatment variables is normally accessible, they are highly correlated with HER2 status, and are therefore included mainly as a cautionary control mechanism. For the sake of the simplicity of the models, they were the last features to be added.

Data cleaning

In the training set, one patient who had clinically unevaluable tumour size was assumed to have a volume 10% larger than the largest present in the cohort. Four patients who were HER2⁺ who only received one cycle of trastuzumab, and two patients who were HER2⁻ who had only received one chemotherapy cycle were

removed from the training set. In the external validation datasets, missing treatment features were set to zero.

Testing

Models were applied on the test cohort and their respective ROC curves and AUCs were evaluated. In Fig. 4d, the standard deviation of the AUCs obtained in the training cross-validation (included as an optimistic performance estimation) was compared to the nominal test AUCs and the standard deviation of the AUCs obtained from 100 bootstrap replicas of the test datasets. In addition, 95% confidence intervals on each test AUC were obtained using the DeLong test⁸³ (Extended Data Fig. 9e). Adding digital pathology introduced a slight degradation of the performance due to the significant difference in the lymphocytic density observed in the training versus the external validation cohorts (Extended Data Fig. 9f). Precision-recall curves, average precision scores and areas under the precision-recall curve were obtained using standard sklearn implementations (Extended Data Fig. 9g).

Feature importance

Feature importances were determined for each algorithm (random forest, support vector classifier and logistic regression) after refitting on the full training cohorts. For consistency, we used an algorithm-agnostic methodology based on dropping each of the input features. We quantified the resulting change in AUC by means of a *z*-score,
$$\{z\}^i = \frac{\{\Delta AUC\}}{\sigma(AUC)}$$
 where z^i represents the *z*-score significance of the *i*th feature, and σ is the standard deviation of all the AUC changes. In Fig. 4b, we show the average *z*-score significances averaged across the three algorithms. In Extended Data Fig. 9b, we calculate signed *z*-score significances by removing the absolute value from the definition. The sign indicates whether the feature was adding value to the prediction (negative sign) or harming it (positive sign). In addition, the full list of features selected after the collinearity reduction and univariable selection steps for all the different models, as well as the logistic regression coefficients, can be found in the [Supplementary Material](#).

Reporting summary

Further information on research design is available in the [Nature Research Reporting Summary](#) linked to this paper.

Data availability

DNA and RNA sequencing data have been deposited at the European Genome-Phenome Archive (EGA), which is hosted by the EBI and the CRG, under accession number [EGAS00001004582](https://ega.ebi.ac.uk/study/EGAS00001004582).

Code availability

The R and Python source code used to run the analyses described in the article and to generate all figures is available at: <https://github.com/cclab-brca/neoadjuvant-therapy-response-predictor>.

References

1. 1.

Hanahan, D. & Weinberg, R. A. Hallmarks of cancer: the next generation. *Cell* **144**, 646–674 (2011).

2. 2.

Marusyk, A., Janiszewska, M. & Polyak, K. Intratumor heterogeneity: the Rosetta stone of therapy resistance. *Cancer Cell* **37**, 471–484 (2020).

3. 3.

Symmans, W. F. et al. Measurement of residual breast cancer burden to predict survival after neoadjuvant chemotherapy. *J. Clin. Oncol.* **25**, 4414–4422 (2007).

4. 4.

Asselain, B. et al. Long-term outcomes for neoadjuvant versus adjuvant chemotherapy in early breast cancer: meta-analysis of individual patient data from ten randomised trials. *Lancet Oncol.* **19**, 27–39 (2018).

5. 5.

Symmans, W. F. et al. Long-term prognostic risk after neoadjuvant chemotherapy associated with residual cancer burden and breast cancer subtype. *J. Clin. Oncol.* **35**, 1049–1060 (2017).

6. 6.

Candido dos Reis, F. J. et al. An updated PREDICT breast cancer prognostication and treatment benefit prediction model with independent validation. *Breast Cancer Res.* **19**, 58 (2017).

7. 7.

Bonnefoi, H. et al. TP53 status for prediction of sensitivity to taxane versus non-taxane neoadjuvant chemotherapy in breast cancer (EORTC 10994/BIG 1-00): a randomised phase 3 trial. *Lancet Oncol.* **12**, 527–539 (2011).

8. 8.

Yuan, H. et al. Association of PIK3CA mutation status before and after neoadjuvant chemotherapy with response to chemotherapy in women with breast cancer. *Clin. Cancer Res.* **21**, 4365–4372 (2015).

9. 9.

Callari, M. et al. Subtype-specific metagene-based prediction of outcome after neoadjuvant and adjuvant treatment in breast cancer. *Clin. Cancer Res.* **22**, 337–345 (2016).

10. 10.

Hatzis, C. et al. A genomic predictor of response and survival following taxane-anthracycline chemotherapy for invasive breast cancer. *JAMA* **305**, 1873–1881 (2011).

11. 11.

Horak, C. E. et al. Biomarker analysis of neoadjuvant doxorubicin/cyclophosphamide followed by ixabepilone or paclitaxel in early-stage breast cancer. *Clin. Cancer Res.* **19**, 1587–1595 (2013).

12. 12.

van 't Veer, L. J. et al. Gene expression profiling predicts clinical outcome of breast cancer. *Nature* **415**, 530–536 (2002).

13. 13.

Ali, H. R. et al. Computational pathology of pre-treatment biopsies identifies lymphocyte density as a predictor of response to neoadjuvant chemotherapy in breast cancer. *Breast Cancer Res.* **18**, 21 (2016).

14. Ali, H. R. et al. Lymphocyte density determined by computational pathology validated as a predictor of response to neoadjuvant chemotherapy in breast cancer: secondary analysis of the ARTemis trial. *Ann. Oncol.* **28**, 1832–1835 (2017).
15. NICE. Early and locally advanced breast cancer: diagnosis and management. NICE guideline [NG101]. NICE <https://www.nice.org.uk/guidance/ng101> (2018).
16. McGranahan, N. et al. Clonal status of actionable driver events and the timing of mutational processes in cancer evolution. *Sci. Transl. Med.* **7**, 283ra54 (2015).
17. Alexandrov, L. B. et al. Signatures of mutational processes in human cancer. *Nature* **500**, 415–421 (2013).
18. Sztupinszki, Z. et al. Migrating the SNP array-based homologous recombination deficiency measures to next generation sequencing data of breast cancer. *NPJ Breast Cancer* **4**, 16 (2018).
19. Curtis, C. et al. The genomic and transcriptomic architecture of 2,000 breast tumours reveals novel subgroups. *Nature* **486**, 346–352 (2012).
20. Ali, H. R. et al. Genome-driven integrated classification of breast cancer validated in over 7,500 samples. *Genome Biol.* **15**, 431 (2014).
21. McGranahan, N. et al. Allele-specific HLA loss and immune escape in lung cancer evolution. *Cell* **171**, 1259-1271.e11 (2017).
- 22.

Liberzon, A. et al. The Molecular Signatures Database (MSigDB) hallmark gene set collection. *Cell Syst.* **1**, 417–425 (2015).

23. 23.

Fabregat, A. et al. The Reactome Pathway Knowledgebase. *Nucleic Acids Res.* **46**, D649–D655 (2018).

24. 24.

Sotiriou, C. et al. Gene expression profiling in breast cancer: understanding the molecular basis of histologic grade to improve prognosis. *J. Natl Cancer Inst.* **98**, 262–272 (2006).

25. 25.

Wong, D. J. et al. Module map of stem cell genes guides creation of epithelial cancer stem cells. *Cell Stem Cell* **2**, 333–344 (2008).

26. 26.

Juul, N. et al. Assessment of an RNA interference screen-derived mitotic and ceramide pathway metagene as a predictor of response to neoadjuvant paclitaxel for primary triple-negative breast cancer: a retrospective analysis of five clinical trials. *Lancet Oncol.* **11**, 358–365 (2010).

27. 27.

Rooney, M. S., Shukla, S. A., Wu, C. J., Getz, G. & Hacohen, N. Molecular and genetic properties of tumors associated with local immune cytolytic activity. *Cell* **160**, 48–61 (2015).

28. 28.

Danaher, P. et al. Gene expression markers of tumor infiltrating leukocytes. *J. Immunother. Cancer* **5**, 18 (2017).

29. 29.

Becht, E. et al. Estimating the population abundance of tissue-infiltrating immune and stromal cell populations using gene expression. *Genome Biol.* **17**, 218 (2016).

30. 30.

Charoentong, P. et al. Pan-cancer immunogenomic analyses reveal genotype-immunophenotype relationships and predictors of response to checkpoint blockade. *Cell Rep.* **18**, 248–262 (2017).

31. 31.

Desmedt, C. et al. Biological processes associated with breast cancer clinical outcome depend on the molecular subtypes. *Clin. Cancer Res.* **14**, 5158–5165 (2008).

32. 32.

Jiang, P. et al. Signatures of T cell dysfunction and exclusion predict cancer immunotherapy response. *Nat. Med.* **24**, 1550–1558 (2018).

33. 33.

Ju, C., Bibaut, A. & van der Laan, M. J. The relative performance of ensemble methods with deep convolutional neural networks for image classification. *J. Appl. Stat.* **45**, 2800–2818 (2018).

34. 34.

Earl, H. M. et al. Efficacy of neoadjuvant bevacizumab added to docetaxel followed by fluorouracil, epirubicin, and cyclophosphamide, for women with HER2-negative early breast cancer (ARTemis): an open-label, randomised, phase 3 trial. *Lancet Oncol.* **16**, 656–666 (2015).

35. 35.

Jin, X. et al. A nomogram for predicting pathological complete response in patients with human epidermal growth factor receptor 2 negative breast cancer. *BMC Cancer* **16**, 606 (2016).

36. 36.

Lee, J. K. et al. Prospective comparison of clinical and genomic multivariate predictors of response to neoadjuvant chemotherapy in breast cancer. *Clin. Cancer Res.* **16**, 711–718 (2010).

37. 37.

Klemm, F. et al. Interrogation of the microenvironmental landscape in brain tumors reveals disease-specific alterations of immune cells. *Cell* **181**, 1643–

1660.e17 (2020).

38. 38.

Ali, H. R. et al. Imaging mass cytometry and multiplatform genomics define the phenogenomic landscape of breast cancer. *Nat. Cancer* **1**, 163–175 (2020).

39. 39.

Lesurf, R. et al. Genomic characterization of HER2-positive breast cancer and response to neoadjuvant trastuzumab and chemotherapy—results from the ACOSOG Z1041 (Alliance) trial. *Ann. Oncol.* **28**, 1070–1077 (2017).

40. 40.

Murugaesu, N. et al. Tracking the genomic evolution of esophageal adenocarcinoma through neoadjuvant chemotherapy. *Cancer Discov.* **5**, 821–831 (2015).

41. 41.

Michaud, M. et al. Autophagy-dependent anticancer immune responses induced by chemotherapeutic agents in mice. *Science* **334**, 1573–1577 (2011).

42. 42.

Denkert, C. et al. Tumor-associated lymphocytes as an independent predictor of response to neoadjuvant chemotherapy in breast cancer. *J. Clin. Oncol.* **28**, 105–113 (2010).

43. 43.

Loi, S., Schmid, P., Aktan, G., Karantza, V. & Salgado, R. Relationship between tumor infiltrating lymphocytes (TILs) and response to pembrolizumab (pembro)+chemotherapy (CT) as neoadjuvant treatment (NAT) for triple-negative breast cancer (TNBC): phase Ib KEYNOTE-173 trial. *Ann. Oncol.* **30**, iii2 (2019).

44. 44.

Salgado, R. et al. The evaluation of tumor-infiltrating lymphocytes (TILs) in breast cancer: recommendations by an International TILs Working Group 2014. *Ann. Oncol.* **26**, 259–271 (2015).

45. 45.

Green, D. R., Ferguson, T., Zitvogel, L. & Kroemer, G. Immunogenic and tolerogenic cell death. *Nat. Rev. Immunol.* **9**, 353–363 (2009).

46. 46.

Gajewski, T. F., Schreiber, H. & Fu, Y.-X. Innate and adaptive immune cells in the tumor microenvironment. *Nat. Immunol.* **14**, 1014–1022 (2013).

47. 47.

Joyce, J. A. & Fearon, D. T. T cell exclusion, immune privilege, and the tumor microenvironment. *Science* **348**, 74–80 (2015).

48. 48.

Cristescu, R. et al. Pan-tumor genomic biomarkers for PD-1 checkpoint blockade-based immunotherapy. *Science* **362**, eaar3593 (2018).

49. 49.

Provenzano, E. et al. Standardization of pathologic evaluation and reporting of postneoadjuvant specimens in clinical trials of breast cancer: recommendations from an international working group. *Mod. Pathol.* **28**, 1185–1201 (2015).

50. 50.

Royal College of Physicians. Pathology reporting of breast disease in surgical excision specimens incorporating the dataset for histological reporting of breast cancer. *RCPPath* https://www.rcpath.org/uploads/assets/693db661-0592-4d7e-9644357fbfa00a76/G148_BreastDataset-lowres-Jun16.pdf (2016).

51. 51.

McKenna, A. et al. The Genome Analysis Toolkit: a MapReduce framework for analyzing next-generation DNA sequencing data. *Genome Res.* **20**, 1297–1303 (2010).

52. 52.

Aken, B. L. et al. Ensembl 2017. *Nucleic Acids Res.* **45**, D635–D642 (2017).

53. 53.

McLaren, W. et al. The Ensembl Variant Effect Predictor. *Genome Biol.* **17**, 122 (2016).

54. 54.

Nik-Zainal, S. et al. Landscape of somatic mutations in 560 breast cancer whole-genome sequences. *Nature* **534**, 47–54 (2016).

55. 55.

Pereira, B. et al. The somatic mutation profiles of 2,433 breast cancers refines their genomic and transcriptomic landscapes. *Nat. Commun.* **7**, 11479 (2016).

56. 56.

Scheinin, I. et al. DNA copy number analysis of fresh and formalin-fixed specimens by shallow whole-genome sequencing with identification and exclusion of problematic regions in the genome assembly. *Genome Res.* **24**, 2022–2032 (2014).

57. 57.

Seshan V. E. & Olshen, A. B DNACopy: DNA copy number data analysis. *R package version 1.54.0* (2018).

58. 58.

Van Loo, P. et al. Allele-specific copy number analysis of tumors. *Proc. Natl Acad. Sci. USA* **107**, 16910–16915 (2010).

59. 59.

Rosenthal, R., McGranahan, N., Herrero, J., Taylor, B. S. & Swanton, C. DeconstructSigs: delineating mutational processes in single tumors distinguishes DNA repair deficiencies and patterns of carcinoma evolution. *Genome Biol.* **17**, 31 (2016).

60. 60.

Shukla, S. A. et al. Comprehensive analysis of cancer-associated somatic mutations in class I HLA genes. *Nat. Biotechnol.* **33**, 1152–1158 (2015).

61. 61.

Hundal, J. et al. pVAC-Seq: a genome-guided in silico approach to identifying tumor neoantigens. *Genome Med.* **8**, 11 (2016).

62. 62.

Nielsen, M. & Andreatta, M. NetMHCpan-3.0; improved prediction of binding to MHC class I molecules integrating information from multiple receptor and peptide length datasets. *Genome Med.* **8**, 33 (2016).

63. 63.

Lundegaard, C. et al. NetMHC-3.0: accurate web accessible predictions of human, mouse and monkey MHC class I affinities for peptides of length 8-11. *Nucleic Acids Res.* **36**, W509–W512 (2008).

64. 64.

Zhang, H., Lund, O. & Nielsen, M. The PickPocket method for predicting binding specificities for receptors based on receptor pocket similarities: application to MHC-peptide binding. *Bioinformatics* **25**, 1293–1299 (2009).

65. 65.

Vita, R. et al. The immune epitope database (IEDB) 3.0. *Nucleic Acids Res.* **43**, D405–D412 (2015).

66. 66.

Dawson, S.-J., Rueda, O. M., Aparicio, S. & Caldas, C. A new genome-driven integrated classification of breast cancer and its implications. *EMBO J.* **32**, 617–628 (2013).

67. 67.

Dobin, A. et al. STAR: ultrafast universal RNA-seq aligner. *Bioinformatics* **29**, 15–21 (2013).

68. 68.

DePristo, M. A. et al. A framework for variation discovery and genotyping using next-generation DNA sequencing data. *Nat. Genet.* **43**, 491–498 (2011).

69. 69.

Van der Auwera, G. A. et al. From FastQ data to high confidence variant calls: the Genome Analysis Toolkit best practices pipeline. *Curr. Protoc. Bioinformatics* **43**, 11.10.1–11.10.33 (2013).

70. 70.

Mills, R. E. et al. Natural genetic variation caused by small insertions and deletions in the human genome. *Genome Res.* **21**, 830–839 (2011).

71. 71.

Anders, S., Pyl, P. T. & Huber, W. HTSeq—a Python framework to work with high-throughput sequencing data. *Bioinformatics* **31**, 166–169 (2015).

72. 72.

Robinson, M. D., McCarthy, D. J. & Smyth, G. K. edgeR: a Bioconductor package for differential expression analysis of digital gene expression data. *Bioinformatics* **26**, 139–140 (2010).

73. 73.

McCarthy, D. J., Chen, Y. & Smyth, G. K. Differential expression analysis of multifactor RNA-seq experiments with respect to biological variation. *Nucleic Acids Res.* **40**, 4288–4297 (2012).

74. 74.

Robinson, M. D. & Oshlack, A. A scaling normalization method for differential expression analysis of RNA-seq data. *Genome Biol.* **11**, R25 (2010).

75. 75.

Li, B., Ruotti, V., Stewart, R. M., Thomson, J. A. & Dewey, C. N. RNA-seq gene expression estimation with read mapping uncertainty. *Bioinformatics* **26**, 493–500 (2010).

76. 76.

Wu, D. & Smyth, G. K. Camera: a competitive gene set test accounting for inter-gene correlation. *Nucleic Acids Res.* **40**, e133 (2012).

77. 77.

Subramanian, A. et al. Gene set enrichment analysis: a knowledge-based approach for interpreting genome-wide expression profiles. *Proc. Natl Acad. Sci. USA* **102**, 15545–15550 (2005).

78. 78.

Yu, G. & He, Q.-Y. ReactomePA: an R/Bioconductor package for reactome pathway analysis and visualization. *Mol. Biosyst.* **12**, 477–479 (2016).

79. 79.

Hänelmann, S., Castelo, R. & Guinney, J. GSVA: gene set variation analysis for microarray and RNA-seq data. *BMC Bioinformatics* **14**, 7 (2013).

80. 80.

Friedman, J., Hastie, T. & Tibshirani, R. Regularization paths for generalized linear models via coordinate descent. *J. Stat. Softw.* **33**, 1–22 (2010).

81. 81.

Cortes, C. & Vapnik, V. Support-vector networks. *Mach. Learn.* **20**, 273–297 (1995).

82. 82.

Breiman, L. Random Forests. *Mach. Learn.* **45**, 5–32 (2001).

83. 83.

Kazeev, N. Fast version of DeLong's method. *Yandex Data School* https://github.com/yandexdataschool/roc_comparison (2021).

Acknowledgements

S.-J.S. was supported by a Wellcome Trust PhD Clinical Training Fellowship (grant number 106566/Z/14/Z). M.C.-O. was supported by a Junior Research Fellowship from Trinity College, Cambridge, and a Borysiewicz Fellowship from the University of Cambridge. F.M. was supported by funding from Cancer Research UK (CRUK) (grant numbers A17197 and A19274). O.M.R. was supported by the NIHR Cambridge Biomedical Research Centre (BRC-1215-20014) and the Medical Research Council (UK; MC_UU_00002/16). C.C. was supported by funding from CRUK (grant numbers A17197, A27657 and A29580), an NIHR Senior Investigator Award (grant

number NF-SI-0515-10090) and a European Research Council Advanced Award (grant number 694620). The ARTemis molecular profiling dataset was funded in part by an unrestricted academic grant from F. Hoffman La Roche (grant administered by the University of Cambridge). The Programme received infrastructure funding from the CRUK Cambridge Centre and the Mark Foundation Institute for Integrated Cancer Medicine. We are grateful for the generosity of all the patients that donated samples for analysis; all the staff at the Cambridge Breast Cancer Research Unit for facilitating the collection and processing of samples; and the CRUK Cambridge Institute Core Facilities (Genomics, Bioinformatics, Histopathology and Biorepository) for support during the execution of this project.

Author information

Author notes

1. These authors contributed equally: Mireia Crispin-Ortuzar, Suet-Feung Chin

Affiliations

1. Cancer Research UK Cambridge Institute, University of Cambridge, Li Ka Shing Centre, Cambridge, UK

Stephen-John Sammut, Mireia Crispin-Ortuzar, Suet-Feung Chin, Helen A. Bardwell, Wei Cope, Ali Dariush, Florian Markowetz, Oscar M. Rueda & Carlos Caldas

2. Department of Oncology, University of Cambridge, Cambridge, UK

Stephen-John Sammut, Jean E. Abraham, Helena M. Earl & Carlos Caldas

3. CRUK Cambridge Centre, Cambridge Experimental Cancer Medicine Centre (ECMC) and NIHR Cambridge Biomedical Research Centre, University of Cambridge and Cambridge University Hospitals NHS Foundation Trust, Cambridge, UK

Stephen-John Sammut, Elena Provenzano, Jean E. Abraham, Paul D. Pharoah, Helena M. Earl & Carlos Caldas

4. School of Clinical Medicine, University of Cambridge, Cambridge, UK

Wenxin Ma

5. Institute of Astronomy, University of Cambridge, Cambridge, UK

Ali Dariush

6. Peter MacCallum Cancer Centre, Melbourne, Victoria, Australia

Sarah-Jane Dawson

7. Centre of Cancer Research and Sir Peter MacCallum Department of Oncology,
University of Melbourne, Melbourne, Victoria, Australia

Sarah-Jane Dawson

8. Warwick Clinical Trials Unit, University of Warwick, Coventry, UK

Janet Dunn & Louise Hiller

9. Edinburgh Cancer Research Centre, Western General Hospital, Edinburgh, UK

Jeremy Thomas, David A. Cameron, John M. S. Bartlett & Larry Hayward

10. Q2 Laboratory Solutions, Livingston, UK

Jeremy Thomas

11. Ontario Institute for Cancer Research, Toronto, Ontario, Canada

John M. S. Bartlett

12. Laboratory Medicine and Pathobiology, University of Toronto, Toronto, Ontario,
Canada

John M. S. Bartlett

13. Strangeways Research Laboratory, University of Cambridge, Cambridge, UK

Paul D. Pharoah

14. MRC Biostatistics Unit, University of Cambridge, Cambridge, UK

Oscar M. Rueda

Contributions

S.-J.S. and C.C. conceived the study, led data analysis and wrote the manuscript.
Tumour processing was led by S.-J.S. with input from S.-F.C., H.A.B. and W.M. E.P.

and J.T. provided histopathology expertise and calculated the RCB index. S.-J.S. created the bioinformatics analysis pipeline, performed all DNA and RNA analyses and identified univariable associations with response. W.C. and A.D. generated the digital pathology lymphocytic infiltration estimates. M.C.-O. and S.-J.S. developed and validated the machine learning models. O.M.R., P.D.P. and F.M. provided statistical advice and expertise. S.-J.D. wrote the TransNEO protocol. C.C. and J.E.A. contributed data from the Personalised Breast Cancer Programme for validation. H.M.E., J.E.A., J.D., L.Hiller, J.T., D.A.C., J.M.S.B., C.C. and L.Hayward are members of the ARTemis trial management group and contributed the data from the control arm of the trial for validation. All authors read and approved the manuscript.

Corresponding author

Correspondence to [Carlos Caldas](#).

Ethics declarations

Competing interests

C.C. is a member of the iMED External Science Panel for AstraZeneca, a member of the Scientific Advisory Board for Illumina and a recipient of research grants (administered by the University of Cambridge) from Genentech, Roche, AstraZeneca and Servier. M.C.-O. has received research funding from Lilly. All other authors declare no competing interests.

Peer review information

Nature thanks Beatrice Knudsen, Hatice Osmanbeyoglu and the other, anonymous, reviewer(s) for their contribution to the peer review of this work. Peer review reports are available.

Additional information

Publisher's note Springer Nature remains neutral with regard to jurisdictional claims in published maps and institutional affiliations.

Extended data figures and tables

[Extended Data Fig. 1 Summary of cases analysed within this study.](#)

180 women were recruited to the TransNEO neoadjuvant breast cancer study. Tumour profiling was performed in 168 cases and associations with response identified in 155 cases who received more than one cycle of neoadjuvant chemotherapy or targeted therapy. 147 cases had a complete molecular/digital pathology dataset, received more than one cycle of chemotherapy and targeted therapy and had an RCB assessment available: data from these cases were used to build a machine learning predictor of response to neoadjuvant therapy. Validation was performed across a cohort of 75 cases recruited to the ARTemis and Personalised Breast Cancer (PBCP) studies.

Extended Data Fig. 2 Calculation of the Residual Cancer Burden index and associations between clinical features and response.

a, Tumour and lymph node histological features used to calculate the continuous Residual Cancer Burden (RCB) index and categorical RCB class. Increasing RCB index denotes increasing burden of residual disease post-neoadjuvant therapy and increasing chemoresistance. **b**, Top: Box plots showing distribution of tumour and lymph node histological features in $n = 161$ cases with clinical data and RCB assessment across the RCB classes. The box bounds the interquartile range divided by the median, with the whiskers extending to a maximum of 1.5 times the interquartile range beyond the box. Outliers are shown as dots. Bottom: distribution of primary tumour score and lymph node score across RCB classes. **c**, Associations of clinical variables with pCR using simple and multiple logistic regression. Significant associations ($P < 0.05$, logistic regression) are shown in red. The measure of centre is the parameter estimate and error bars represent 95% confidence intervals. **d**, Distribution of tumour features across RCB classes: pre-operative staging (blue), pre-operative histological features (green), neoadjuvant therapy (red, T: taxane, A: anthracycline, aHER2: anti-HER2 therapy), surgical approach (red, WLE: wide local excision), post-operative tumour (ypT) and nodal (ypN) staging and lymphovascular invasion (purple) and PAM50 subtypes (yellow, A: Luminal A, B: Luminal B, Ba: Basal, H: HER2-enriched, N: Normal-like, U: Unknown). Tumours with RCB assessment and adequate therapy exposure only included (more than 1 cycle of chemotherapy or anti-HER2 therapy received, $n = 155$).

Extended Data Fig. 3 The somatic mutational driver landscape of tumours prior to neoadjuvant therapy.

Oncoprint showing somatic mutations in breast cancer driver gene identified using WES. Cases classified by RCB class. Multiple mutations in a case are denoted by a white \times . Truncating mutations (red) include nonsense, splice site and frame shift insertions and deletions. In-frame mutations (yellow) include in-frame insertions and deletions. Other mutations (green) include silent exonic mutations, 3' and 5' UTR flank mutations and intronic mutations.

Extended Data Fig. 4 Further associations between genomic features and response to neoadjuvant therapy.

a, Interaction plot showing co-occurrence of non-silent driver gene mutations and response. Associations between *TP53* and *PIK3CA* mutations and response shown in inset (logistic regression, red: positive, blue: negative, grey: not significant, error bars represent 95% confidence intervals). **b**, Pearson's product-moment correlations (R) between tumour purity and (left) tumour mutation burden and (right) %CNAs. The shaded area, in grey, represents the 95% confidence interval. **c**, Box plots showing associations between TMB and response, stratified by HER2 status. **d**, Box plots showing association between expressed neoantigen (NAg) load and response, stratified by HER2 status. **e**, Box plot showing monotonic association ($P = 0.005$, ordinal logistic regression) between exposure of non-clock signatures and RCB class. **f**, Box plots showing associations between HRD score and response, stratified by HER2 status. **g**, Box plots showing associations between %CNA and response, stratified by HER2 status. **c–g**, The box bounds the interquartile range divided by the median, with the whiskers extending to a maximum of 1.5 times the interquartile range beyond the box. Outliers are shown as dots. Wilcoxon rank sum tests, all P values two-sided. Number of cases analysed (n) = 155 (HER2- pCR = 22, RD (residual disease) = 76; HER2+ pCR = 18, RD = 39)). **h**, Associations between RCB class and iC10: Pearson residuals indicate overrepresentation of iC10 subtype with response (blue: overrepresentation, red: underrepresentation). **i**, Associations between HLA LOH, global LOH and global copy number alterations with pCR (logistic regression, red: positive association, blue: negative association). The measure of centre is the parameter estimate and error bars represent 95% confidence intervals.

Extended Data Fig. 5 Reactome pathways associated with response to neoadjuvant therapy.

a, b, Reactome pathway enrichment showing pathways associated with (a) pCR versus residual disease, (b) degree of residual disease following neoadjuvant therapy.

Extended Data Fig. 6 Associations between tumour proliferation and response.

a, Box plots showing associations between proliferation (GGI) GSVA scores across ER/HER subtypes. **b**, Top: Scatter plots showing the distribution of the mitotic and ceramide score components of a taxane response metagene within the HER2- and HER2+ cohorts. Bottom: Box plots showing association of the combined taxane response metagene score within the HER2- and HER2+ cohorts. In **a, b**, the box bounds the interquartile range divided by the median, with the whiskers extending to a

maximum of 1.5 times the interquartile range beyond the box. Outliers are shown as dots. Two-tailed Wilcoxon rank sum tests. Number of cases (*n*): ER-HER2-: 37, ER+HER2-: 57, HER2+: 55.

Extended Data Fig. 7 The relationship between tumour immune microenvironment and response.

a, PCA analysis on the abundance of tumour immune microenvironment components obtained through the deconvolution of RNA-seq data using Danaher's immune signatures (number of cases (*n*): pCR (green) = 39, RD (orange) = 110). **b, c**, Box plots showing associations between response and **(b)** Danaher immune cell enrichment and **(c)** MCPcounter immune cell enrichment across ER/HER subtypes. The box bounds the interquartile range divided by the median, with the whiskers extending to a maximum of 1.5 times the interquartile range beyond the box. Outliers are shown as dots. Two-tailed Wilcoxon rank sum tests. Number of cases (*n*): ER-HER2-: 37, ER+HER2-: 57, HER2+: 55. **d**, Heatmap showing unsupervised clustering of cancer immunity parameters across *n* = 149 cases with RNA sequencing data. **e**, Scatter plot showing association between computationally derived lymphocyte density and immune cell enrichment using Danaher's immune signatures across *n* = 147 cases with digital pathology and RNA sequencing data. Pearson's product-moment correlations (R) shown. The shaded area, in grey, represents the 95% confidence interval. **f**, 2D density plot validating relationship between GGI and STAT1 GSVA across RCB subgroups in two external microarray gene sets comprising 457 cases.

Extended Data Fig. 8 T-cell dysfunction and exclusion.

a, Box plots showing enriched inhibitory immune cell types (Danaher gene sets) in HER2- tumours with high GGI and STAT1 (number of cases (*n*): pCR = 12, RD = 16). **b**, Box plots showing association between components of T-cell exclusion score and response (number of cases (*n*): pCR = 39, RD = 110). CAF: Cancer associated fibroblasts, MDSC: Myeloid-derived suppressor cells. In **a, b**, the box bounds the interquartile range divided by the median, with the whiskers extending to a maximum of 1.5 times the interquartile range beyond the box. Outliers are shown as dots. Two-tailed Wilcoxon rank sum tests.

Extended Data Fig. 9 Machine learning model performance.

a, Correlation plot showing the results of unsupervised clustering between all the features explored. **b**, Signed feature importance split by algorithm. Negative numbers (blue) signify a decrease in AUC as a result of dropping, and therefore indicate that the feature improves the performance. **c**, Correlation of the three classification pipeline scores across the training dataset. Two-sided *P* values of all correlations < 2.2 x 10⁻¹⁶.

d, Receiver-operating characteristic curves for the clinical and integrated models applied on the external validation cohort. **e**, Comparison between AUCs of the clinical model and models with different levels of data integration. The measure of centre is the parameter estimate and error bars represent 95% DeLong confidence intervals. **f**, Association between lymphocyte density and treatment response in ARTemis patients with digital pathology and sequencing data (right, $n = 38$ cases) vs. patients with only digital pathology available (left, $n = 313$ cases). The box bounds the interquartile range divided by the median, with the whiskers extending to a maximum of 1.5 times the interquartile range beyond the box. Outliers are shown as dots. P values obtained from Wilcoxon rank sum tests. **g**, Precision-recall curves of the clinical and fully integrated models applied on the test cohorts. The average precision values are 0.46 (clinical model) and 0.68 (fully integrated model). The areas under the precision-recall curves are 0.43 (clinical model) and 0.67 (fully integrated model).

[Extended Data Fig. 10 Predictor score ordinally associated with RCB class.](#)

Box plots showing the distribution of predictor scores obtained by the six models across RCB classes in both training ($n = 147$ cases) and validation ($n = 75$ cases) sets. The box bounds the interquartile range divided by the median, with the whiskers extending to a maximum of 1.5 times the interquartile range beyond the box. Outliers are shown as dots. P values two-sided and obtained from FDR-corrected Wilcoxon rank sum tests.

Supplementary information

[Supplementary Information](#)

This file contains Supplementary Methods and Supplementary Tables 1 – 6.

[Reporting Summary](#)

[Peer Review File](#)

[Supplementary Tables 1 – 6](#)

This file contains Supplementary Tables 1 – 6. See below for Supplementary Table legends **Supplementary Table 1** Clinical metadata of 168 cases recruited to the TransNEO study. **Supplementary Table 2** Mutations identified within the WES data. **Supplementary Table 3** Tumour proliferation and immune metrics extracted from the RNA-seq data. **Supplementary Table 4** Complete list of features used to train the

models, their computation methods, and mean, minimum, and maximum values in the training dataset. **Supplementary Table 5** Clinical, molecular, and digital pathology metadata of validation cohort. **Supplementary Table 6** Ranked list of biological features including signed importance z-scores.

Rights and permissions

Open Access This article is licensed under a Creative Commons Attribution 4.0 International License, which permits use, sharing, adaptation, distribution and reproduction in any medium or format, as long as you give appropriate credit to the original author(s) and the source, provide a link to the Creative Commons license, and indicate if changes were made. The images or other third party material in this article are included in the article's Creative Commons license, unless indicated otherwise in a credit line to the material. If material is not included in the article's Creative Commons license and your intended use is not permitted by statutory regulation or exceeds the permitted use, you will need to obtain permission directly from the copyright holder. To view a copy of this license, visit <http://creativecommons.org/licenses/by/4.0/>.

Reprints and Permissions

About this article

Cite this article

Sammut, SJ., Crispin-Ortuzar, M., Chin, SF. *et al.* Multi-omic machine learning predictor of breast cancer therapy response. *Nature* **601**, 623–629 (2022).
<https://doi.org/10.1038/s41586-021-04278-5>

- Received: 30 July 2021
- Accepted: 23 November 2021
- Published: 07 December 2021
- Issue Date: 27 January 2022
- DOI: <https://doi.org/10.1038/s41586-021-04278-5>

Share this article

Anyone you share the following link with will be able to read this content:

[Get shareable link](#)

Sorry, a shareable link is not currently available for this article.

[Copy to clipboard](#)

Provided by the Springer Nature SharedIt content-sharing initiative

This article was downloaded by **calibre** from <https://www.nature.com/articles/s41586-021-04278-5>

| [Section menu](#) | [Main menu](#) |

- Article
- [Published: 05 January 2022](#)

Decoding gene regulation in the fly brain

- [Jasper Janssens](#) [ORCID: orcid.org/0000-0001-9264-0782](#)^{1,2} na1,
- [Sara Aibar](#) [ORCID: orcid.org/0000-0001-6104-7134](#)^{1,2} na1,
- [Ibrahim Ihsan Taskiran](#)^{1,2} na1,
- [Joy N. Ismail](#)^{1,2},
- [Alicia Estacio Gomez](#) [ORCID: orcid.org/0000-0001-6571-0757](#)³,
- [Gabriel Aughey](#)³,
- [Katina I. Spanier](#) [ORCID: orcid.org/0000-0002-1375-4157](#)^{1,2},
- [Florian V. De Rop](#)^{1,2},
- [Carmen Bravo González-Blas](#)^{1,2},
- [Marc Dionne](#) [ORCID: orcid.org/0000-0002-8283-1750](#)³,
- [Krista Grimes](#)³,
- [Xiao Jiang Quan](#)^{1,2},
- [Dafni Papasokrati](#)^{1,2},
- [Gert Hulselmans](#)^{1,2},
- [Samira Makhzami](#)^{1,2},
- [Maxime De Waegeneer](#) [ORCID: orcid.org/0000-0002-4535-3737](#)^{1,2},
- [Valerie Christiaens](#)^{1,2},
- [Tony Southall](#)³ &
- [Stein Aerts](#) [ORCID: orcid.org/0000-0002-8006-0315](#)^{1,2}

[Nature](#) volume **601**, pages 630–636 (2022)

- 17k Accesses
- 231 Altmetric

- [Metrics details](#)

Subjects

- [Cellular neuroscience](#)
- [Developmental neurogenesis](#)
- [Gene regulation](#)
- [Gene regulatory networks](#)

Abstract

The *Drosophila* brain is a frequently used model in neuroscience. Single-cell transcriptome analysis^{1,2,3,4,5,6}, three-dimensional morphological classification⁷ and electron microscopy mapping of the connectome^{8,9} have revealed an immense diversity of neuronal and glial cell types that underlie an array of functional and behavioural traits in the fly. The identities of these cell types are controlled by gene regulatory networks (GRNs), involving combinations of transcription factors that bind to genomic enhancers to regulate their target genes. Here, to characterize GRNs at the cell-type level in the fly brain, we profiled the chromatin accessibility of 240,919 single cells spanning 9 developmental timepoints and integrated these data with single-cell transcriptomes. We identify more than 95,000 regulatory regions that are used in different neuronal cell types, of which 70,000 are linked to developmental trajectories involving neurogenesis, reprogramming and maturation. For 40 cell types, uniquely accessible regions were associated with their expressed transcription factors and downstream target genes through a combination of motif discovery, network inference and deep learning, creating enhancer GRNs. The enhancer architectures revealed by DeepFlyBrain lead to a better understanding of neuronal regulatory diversity and can be used to design genetic driver lines for cell types at specific timepoints, facilitating their characterization and manipulation.

This is a preview of subscription content

Access options

Subscribe to nature+

Get immediate online access to the entire Nature family of 50+ journals

\$29.99

monthly

[Subscribe](#)

Subscribe to Journal

Get full journal access for 1 year

\$199.00

only \$3.90 per issue

[Subscribe](#)

All prices are NET prices.

VAT will be added later in the checkout.

Tax calculation will be finalised during checkout.

Buy article

Get time limited or full article access on ReadCube.

\$32.00

[Buy](#)

All prices are NET prices.

Additional access options:

- [Log in](#)
- [Learn about institutional subscriptions](#)

Fig. 1: Chromatin landscape of adult brain cell types.

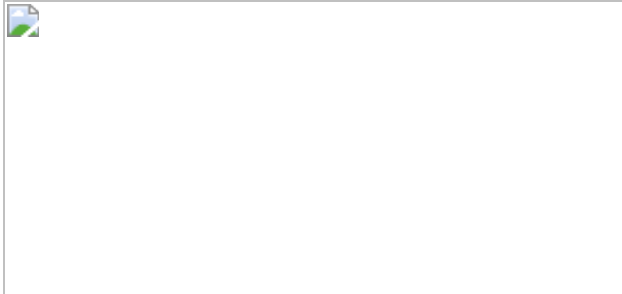


Fig. 2: Chromatin changes through neuronal development.



Fig. 3: Identification of regulators through multi-omic data integration.



Fig. 4: DL analysis unravels enhancer make-up.

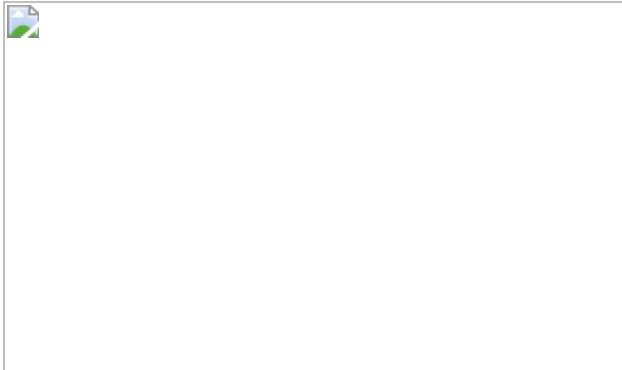
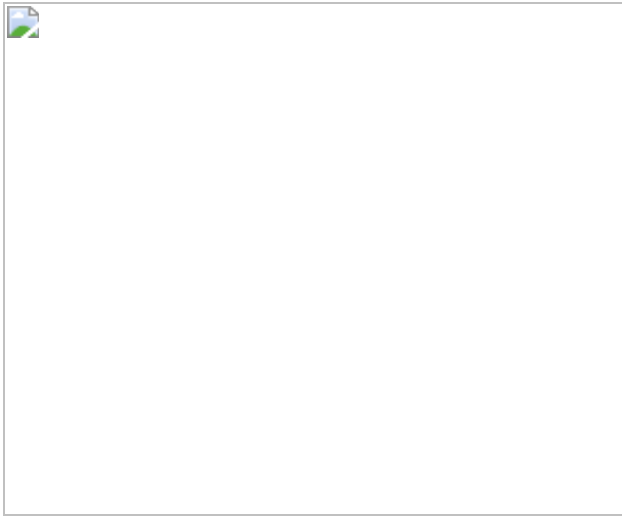


Fig. 5: eGRNs identify cell-type-specific activators and repressors.



Data availability

The data generated for this study have been deposited in NCBI's Gene Expression Omnibus and are accessible through GEO Series accession numbers [GSE163697](#) and [GSE181494](#) (DGRP lines). We also provide a dedicated website to browse the results of the analyses and processed data (<https://flybrain.aertslab.org>), which provides link-outs to the SCope session (http://scope.aertslab.org/#/Fly_Brain/), UCSC hub (<http://genome.ucsc.edu/cgi-bin/hgTracks?db=dm6&hubUrl=http://ucsctracks.aertslab.org/papers/FlyBrain/hub.txt>), the eGRNs in NDEx, the DeepExplainer plots of enhancers and other information. The following online databases were used: FlyBase (<https://flybase.org/>), FlyMine (<https://www.flymine.org/flymine>), icis-Target (<https://gbimod.kuleuven.be/apps/lcb/i-cisTarget/>), FlyLight (<https://flweb.janelia.org/cgi-bin/flew.cgi>), CIS-BP (<http://cisbp.ccbr.utoronto.ca/>), ENCODE (<https://www.encodeproject.org/> ENCF704WGH). The following publicly accessible datasets were also used: [GSE107451](#) (scRNA-seq adult brain), [GSE157202](#) (scRNA-seq larval brain), [GSE101581](#) (scATAC-seq embryo). The neural network is from Özel et al⁵.

Code availability

The updated version of cisTopic for scATAC-seq clustering and topic identification including warpLDA are available at GitHub (<https://github.com/aertslab/cisTopic>) with set-up instructions and a tutorial. The Nextflow pipeline for scRNA-seq analysis is available at GitHub (<https://github.com/vib-singlecell-nf/vsn-pipelines>) together with example config files and instructions. DeepFlyBrain is deposited in Kipoi (<https://kipoi.org/models/DeepFlyBrain>), and the Jupyter notebooks that can be used to train the model are provided in Supplementary Data 3–5. Enhancer gene links can be calculated using ScoMAP (<https://github.com/aertslab/ScoMAP>) and GENIE3 (<https://github.com/aertslab/GENIE3>). Trajectory analysis was performed using Monocle3 according to the package tutorials (<http://cole-trapnell-lab.github.io/monocle-release/monocle3>). Differential expression, accessibility and integration of RNA-seq and ATAC-seq was performed using Seurat v.3 (with vignettes and install instructions at <https://satijalab.org/seurat/>). TaDa analysis was performed using Perl scripts available at GitHub (https://github.com/tonysouthall/Peak_calling_DamID). Code for the website is available at GitHub (https://github.com/aertslab/FBD_App) and notebooks are available at GitHub (https://github.com/aertslab/fly_brain).

References

1. 1.
Li, H. et al. Classifying *Drosophila* olfactory projection neuron subtypes by single-cell RNA sequencing. *Cell* **171**, 1206–1220 (2017).
2. 2.
Davie, K. et al. A single-cell transcriptome atlas of the aging *Drosophila* brain. *Cell* **174**, 982–998 (2018).
3. 3.
Konstantinides, N. et al. Phenotypic convergence: distinct transcription factors regulate common terminal features. *Cell* **174**, 622–635 (2018).

4. 4.

Croset, V., Treiber, C. D. & Waddell, S. Cellular diversity in the *Drosophila* midbrain revealed by single-cell transcriptomics. *eLife* **7**, e34550 (2018).

5. 5.

Özel, M. N. et al. Neuronal diversity and convergence in a visual system developmental atlas. *Nature* **589**, 88–95 (2020).

6. 6.

Kurmangaliyev, Y. Z., Yoo, J., Valdes-Aleman, J., Sanfilippo, P. & Zipursky, S. L. Transcriptional programs of circuit assembly in the *Drosophila* visual system. *Neuron* **108**, 1045–1057 (2020).

7. 7.

Costa, M., Manton, J. D., Ostrovsky, A. D., Prohaska, S. & Jefferis, G. S. X. E. NBLAST: rapid, sensitive comparison of neuronal structure and construction of neuron family databases. *Neuron* **91**, 293–311 (2016).

8. 8.

Zheng, Z. et al. A complete electron microscopy volume of the brain of adult *Drosophila melanogaster*. *Cell* **174**, 730–743 (2018).

9. 9.

Scheffer, L. K. et al. A connectome and analysis of the adult *Drosophila* central brain. *eLife* **9**, e57443 (2020).

10. 10.

Jenett, A. et al. A GAL4-driver line resource for *Drosophila* neurobiology. *Cell Rep.* **2**, 991–1001 (2012).

11. 11.

Robie, A. A. et al. Mapping the neural substrates of behavior. *Cell* **170**, 393–406 (2017).

12. 12.

Ravenscroft, T. A. et al. *Drosophila* voltage-gated sodium channels are only expressed in active neurons and are localized to distal axonal initial segment-like domains. *J. Neurosci.* **40**, 7999–8024 (2020).

13. 13.

Konstantinides, N. et al. A comprehensive series of temporal transcription factors in the fly visual system. Preprint at <https://doi.org/10.1101/2021.06.13.448242> (2021).

14. 14.

Allen, A. M. et al. A single-cell transcriptomic atlas of the adult *Drosophila* ventral nerve cord. *eLife* **9**, e54074 (2020).

15. 15.

Doe, C. Q. Temporal patterning in the *Drosophila* CNS. *Annu. Rev. Cell Dev. Biol.* **33**, 219–240 (2017).

16. 16.

Estacio-Gómez, A., Hassan, A., Walmsley, E., Le, L. W. & Southall, T. D. Dynamic neurotransmitter specific transcription factor expression profiles during *Drosophila* development. *Biol. Open* **9**, bio052928 (2020).

17. 17.

Komiyama, T., Johnson, W. A., Luo, L. & Jefferis, G. S. X. E. From lineage to wiring specificity. POU domain transcription factors control

precise connections of *Drosophila* olfactory projection neurons. *Cell* **112**, 157–167 (2003).

18. 18.

Kurmangaliyev, Y. Z., Yoo, J., LoCascio, S. A. & Zipursky, S. L. Modular transcriptional programs separately define axon and dendrite connectivity. *eLife* **8**, e50822 (2019).

19. 19.

Schilling, T., Ali, A. H., Leonhardt, A., Borst, A. & Pujol-Martí, J. Transcriptional control of morphological properties of direction-selective T4/T5 neurons in *Drosophila*. *Development* **146**, dev169763 (2019).

20. 20.

Masserdotti, G., Gascón, S. & Götz, M. Direct neuronal reprogramming: learning from and for development. *Development* **143**, 2494–2510 (2016).

21. 21.

Aibar, S. et al. SCENIC: single-cell regulatory network inference and clustering. *Nat. Methods* **14**, 1083–1086 (2017).

22. 22.

Buenrostro, J. D. et al. Single-cell chromatin accessibility reveals principles of regulatory variation. *Nature* **523**, 486–490 (2015).

23. 23.

Bravo González-Blas, C. et al. cisTopic: *cis*-regulatory topic modeling on single-cell ATAC-seq data. *Nat. Methods* **16**, 397–400 (2019).

24. 24.

Kirilly, D. et al. A genetic pathway composed of Sox14 and Mical governs severing of dendrites during pruning. *Nat. Neurosci.* **12**, 1497–1505 (2009).

25. 25.

Atak, Z. K. et al. Interpretation of allele-specific chromatin accessibility using cell state-aware deep learning. *Genome Res.* **31**, 1082–1096 (2021).

26. 26.

Minnoye, L. et al. Cross-species analysis of enhancer logic using deep learning. *Genome Res.* **30**, 1815–1834 (2020).

27. 27.

Avet-Rochex, A., Maierbrugger, K. T. & Bateman, J. M. Glial enriched gene expression profiling identifies novel factors regulating the proliferation of specific glial subtypes in the *Drosophila* brain. *Gene Expr. Patterns* **16**, 61–68 (2014).

28. 28.

Crittenden, J. R., Skoulakis, E. M. C., Goldstein, E. S. & Davis, R. L. *Drosophila mef2* is essential for normal mushroom body and wing development. *Biol. Open* **7**, bio035618 (2018).

29. 29.

Minocha, S., Boll, W. & Noll, M. Crucial roles of Pox neuro in the developing ellipsoid body and antennal lobes of the *Drosophila* brain. *PLoS ONE* **12**, e0176002 (2017).

30. 30.

Davis, F. P. et al. A genetic, genomic, and computational resource for exploring neural circuit function. *eLife* **9**, e50901 (2020).

31. 31.

Naidu, V. G. et al. Temporal progression of *Drosophila* medulla neuroblasts generates the transcription factor combination to control T1 neuron morphogenesis. *Dev. Biol.* **464**, 35–44 (2020).

32. 32.

Lundberg, S. M. & Lee, S.-I. A unified approach to interpreting model predictions. *Advances in Neural Information Processing Systems* **30**, 4765–4774 (2017).

33. 33.

Shrikumar, A. et al. Technical note on transcription factor motif discovery from importance scores (TF-MoDISco) version 0.5.6.5. Preprint at <https://arxiv.org/abs/1811.00416> (2020).

34. 34.

Kaya-Okur, H. S. et al. CUT&Tag for efficient epigenomic profiling of small samples and single cells. *Nat. Commun.* **10**, 1930 (2019).

35. 35.

Southall, T. D. et al. Cell-type-specific profiling of gene expression and chromatin binding without cell isolation: assaying RNA Pol II occupancy in neural stem cells. *Dev. Cell* **26**, 101–112 (2013).

36. 36.

Mackay, T. F. C. et al. The *Drosophila melanogaster* Genetic Reference Panel. *Nature* **482**, 173–178 (2012).

37. 37.

Jacobs, J. et al. The transcription factor Grainy head primes epithelial enhancers for spatiotemporal activation by displacing nucleosomes. *Nat. Genet.* **50**, 1011–1020 (2018).

38. 38.

Southall, T. D., Davidson, C. M., Miller, C., Carr, A. & Brand, A. H. Dedifferentiation of neurons precedes tumor formation in *lola* mutants. *Dev. Cell* **28**, 685–696 (2014).

39. 39.

Yang, J., Ramos, E. & Corces, V. G. The BEAF-32 insulator coordinates genome organization and function during the evolution of *Drosophila* species. *Genome Res.* **22**, 2199–2207 (2012).

40. 40.

Trevino, A. E. et al. Chromatin accessibility dynamics in a model of human forebrain development. *Science* **367**, eaay1645 (2020).

41. 41.

Ma, S. et al. Chromatin potential identified by shared single-cell profiling of RNA and chromatin. *Cell* **183**, 1103–1116 (2020).

42. 42.

Cusanovich, D. A. et al. A single-cell atlas of in vivo mammalian chromatin accessibility. *Cell* **174**, 1309–1324 (2018).

43. 43.

Domcke, S. et al. A human cell atlas of fetal chromatin accessibility. *Science* **370**, eaba7612 (2020).

44. 44.

Lake, B. B. et al. Integrative single-cell analysis of transcriptional and epigenetic states in the human adult brain. *Nat. Biotechnol.* **36**, 70–80 (2018).

45. 45.

Preissl, S. et al. Single-nucleus analysis of accessible chromatin in developing mouse forebrain reveals cell-type-specific transcriptional regulation. *Nat. Neurosci.* **21**, 432–439 (2018).

46. 46.

Chen, S., Lake, B. B. & Zhang, K. High-throughput sequencing of the transcriptome and chromatin accessibility in the same cell. *Nat. Biotechnol.* **37**, 1452–1457 (2019).

47. 47.

Zhu, C. et al. An ultra high-throughput method for single-cell joint analysis of open chromatin and transcriptome. *Nat. Struct. Mol. Biol.* **26**, 1063–1070 (2019).

48. 48.

Avsec, Ž. et al. Base-resolution models of transcription-factor binding reveal soft motif syntax. *Nat. Genet.* **53**, 354–366 (2021).

49. 49.

Virtanen, P. et al. SciPy 1.0: fundamental algorithms for scientific computing in Python. *Nat. Methods* **17**, 261–272 (2020).

50. 50.

Gramates, L. S. et al. FlyBase at 25: looking to the future. *Nucleic Acids Res.* **45**, D663–D671 (2017).

51. 51.

Kang, H. M. et al. Multiplexed droplet single-cell RNA-sequencing using natural genetic variation. *Nat. Biotechnol.* **36**, 89–94 (2018).

52. 52.

Herrmann, C., Van de Sande, B., Potier, D. & Aerts, S. i-cisTarget: an integrative genomics method for the prediction of regulatory features and cis-regulatory modules. *Nucleic Acids Res.* **40**, e114 (2012).

53. 53.

Chen, J., Li, K., Zhu, J. & Chen, W. WarpLDA: a cache efficient O(1) algorithm for latent dirichlet allocation. *Proc. VLDB Endow.* **9**, 744–755 (2016).

54. 54.

Granja, J. M. et al. ArchR is a scalable software package for integrative single-cell chromatin accessibility analysis. *Nat. Genet.* **53**, 403–411 (2021).

55. 55.

De Waegeneer, M., Flerin, C. C., Davie, K. & Hulselmans, G. vib-singlecell-nf/vsn-pipelines: v0.26.1. *Zenodo* <https://doi.org/10.5281/ZENODO.3703108> (2021).

56. 56.

Wolf, F. A., Angerer, P. & Theis, F. J. SCANPY: large-scale single-cell gene expression data analysis. *Genome Biol.* **19**, 15 (2018).

57. 57.

Korsunsky, I. et al. Fast, sensitive and accurate integration of single-cell data with Harmony. *Nat. Methods* **16**, 1289–1296 (2019).

58. 58.

Van de Sande, B. et al. A scalable SCENIC workflow for single-cell gene regulatory network analysis. *Nat. Protoc.* **15**, 2247–2276 (2020).

59. 59.

Stanescu, D. E., Yu, R., Won, K.-J. & Stoffers, D. A. Single cell transcriptomic profiling of mouse pancreatic progenitors. *Physiol. Genom.* **49**, 105–114 (2017).

60. 60.

Stuart, T. et al. Comprehensive integration of single-cell data. *Cell* **177**, 1888–1902 (2019).

61. 61.

Li, H. et al. The Sequence Alignment/Map format and SAMtools. *Bioinformatics* **25**, 2078–2079 (2009).

62. 62.

Amemiya, H. M., Kundaje, A. & Boyle, A. P. The ENCODE blacklist: identification of problematic regions of the genome. *Sci. Rep.* **9**, 9354 (2019).

63. 63.

Ramírez, F. et al. deepTools2: a next generation web server for deep-sequencing data analysis. *Nucleic Acids Res.* **44**, W160–W165 (2016).

64. 64.

Zhang, Y. et al. Model-based analysis of ChIP-seq (MACS). *Genome Biol.* **9**, R137 (2008).

65. 65.

Shih, M.-F. M., Davis, F. P., Henry, G. L. & Dubnau, J. Nuclear transcriptomes of the seven neuronal cell types that constitute the *Drosophila* mushroom bodies. *G3* **9**, 81–94 (2019).

66. 66.

Corces, M. R. et al. An improved ATAC-seq protocol reduces background and enables interrogation of frozen tissues. *Nat. Methods* **14**, 959–962 (2017).

67. 67.

Aronesty et al. *ea-utils*: ‘Command-line tools for processing biological sequencing data’. <https://github.com/ExpressionAnalysis/ea-utils> (2011).

68. 68.

Imrichová, H., Hulselmans, G., Kalender Atak, Z., Potier, D. & Aerts, S. i-cisTarget 2015 update: generalized *cis*-regulatory enrichment analysis in human, mouse and fly. *Nucleic Acids Res.* **43**, W57–W64 (2015).

69. 69.

Aughey, G. N., Delandre, C., McMullen, J. P. D., Southall, T. D. & Marshall, O. J. FlyORF-TaDa allows rapid generation of new lines for in vivo cell-type-specific profiling of protein-DNA interactions in *Drosophila melanogaster*. *G3* **11**, jkaa005 (2021).

70. 70.

Marshall, O. J., Southall, T. D., Cheetham, S. W. & Brand, A. H. Cell-type-specific profiling of protein-DNA interactions without cell isolation using targeted DamID with next-generation sequencing. *Nat. Protoc.* **11**, 1586–1598 (2016).

71. 71.

Marshall, O. J. & Brand, A. H. *damidseq_pipeline*: an automated pipeline for processing DamID sequencing datasets. *Bioinformatics* **31**, 3371–3373 (2015).

72. 72.

Aerts, S. et al. Robust target gene discovery through transcriptome perturbations and genome-wide enhancer predictions in *Drosophila* uncovers a regulatory basis for sensory specification. *PLoS Biol.* **8**, e1000435 (2010).

73. 73.

Pedregosa, F. et al. Scikit-learn: machine learning in Python. *J. Mach. Learn. Res.* **12**, 2825–2830 (2011).

74. 74.

Kudron, M. M. et al. The ModERN resource: genome-wide binding profiles for hundreds of *Drosophila* and *Caenorhabditis elegans* transcription factors. *Genetics* **208**, 937–949 (2018).

75. 75.

Davis, C. A. et al. The Encyclopedia of DNA elements (ENCODE): data portal update. *Nucleic Acids Res.* **46**, D794–D801 (2018).

76. 76.

Shannon, P. et al. Cytoscape: a software environment for integrated models of biomolecular interaction networks. *Genome Res.* **13**, 2498–2504 (2003).

77. 77.

Quang, D. & Xie, X. DanQ: a hybrid convolutional and recurrent deep neural network for quantifying the function of DNA sequences. *Nucleic Acids Res.* **44**, e107 (2016).

78. 78.

Shrikumar, A., Greenside, P. & Kundaje, A. Learning important features through propagating activation differences. Preprint at *arXiv* (2019).

79. 79.

Bravo González-Blas, C. et al. Identification of genomic enhancers through spatial integration of single-cell transcriptomics and epigenomics. *Mol. Syst. Biol.* **16**, e9438 (2020).

80. 80.

Frith, M. C., Li, M. C. & Weng, Z. Cluster-Buster: finding dense clusters of motifs in DNA sequences. *Nucleic Acids Res.* **31**, 3666–3668 (2003).

81. 81.

Cao, J. et al. The single-cell transcriptional landscape of mammalian organogenesis. *Nature* **566**, 496–502 (2019).

82. 82.

Qiu, X. et al. Reversed graph embedding resolves complex single-cell trajectories. *Nat. Methods* **14**, 979–982 (2017).

83. 83.

Trapnell, C. et al. The dynamics and regulators of cell fate decisions are revealed by pseudotemporal ordering of single cells. *Nat. Biotechnol.* **32**, 381–386 (2014).

84. 84.

Harris, C. R. et al. Array programming with NumPy. *Nature* **585**, 357–362 (2020).

85. 85.

Cusanovich, D. A. et al. The *cis*-regulatory dynamics of embryonic development at single-cell resolution. *Nature* **555**, 538–542 (2018).

86. 86.

Seabold, S. & Perktold, J. Statsmodels: econometric and statistical modeling with Python. In *Proc. 9th Python Science Conf.* 92–96 (2010).

87. 87.

De Rop, F. V. et al. HyDrop: droplet-based scATAC-seq and scRNA-seq using dissolvable hydrogel beads. Preprint at <https://doi.org/10.1101/2021.06.04.447104> (2021).

Acknowledgements

We thank the staff at the Janelia FlyLight Project for publicly providing images and reporter lines to assess enhancer activity on the CNS in *Drosophila*; F. Pinto-Teixeira for providing the ato-Gal4 and acj6/TfAP-2 RNAi lines; and the members of the Aerts laboratory for discussions and for reading the manuscript. This work is funded by the following grants to S. Aerts: ERC Consolidator Grant (724226_cis-CONTROL), by the Special Research Fund (BOF) KU Leuven (grant C14/18/092) and the FWO (grants G0C0417N, G094121N). J.J., C.B.G.-B., F.V.D.R. and D.P. are supported by a PhD fellowship of The Research Foundation, Flanders (FWO, 1199518N; 11F1519N; 1S80920N; 1S75219N). 10x Chromium was partially made available through VIB Tech Watch Funding. Imaging, FACS and single-cell analyses were supported by the light microscopy, FACS and single-cell expertise units at the VIB-KU Leuven Center for Brain and Disease Research. Computing was performed at the Vlaams Supercomputer Center (VSC). Stocks obtained from the Bloomington *Drosophila* Stock Center were used in this study. The funders had no role in study design, data collection and analysis, decision to publish, or preparation of the manuscript.

Author information

Author notes

1. These authors contributed equally: Jasper Janssens, Sara Aibar, Ibrahim Ihsan Taskiran

Affiliations

1. VIB Center for Brain & Disease Research, Leuven, Belgium

Jasper Janssens, Sara Aibar, Ibrahim Ihsan Taskiran, Joy N. Ismail, Katina I. Spanier, Florian V. De Rop, Carmen Bravo González-Blas, Xiao Jiang Quan, Dafni Papasokrati, Gert Hulselmans, Samira Makhzami, Maxime De Waegeneer, Valerie Christiaens & Stein Aerts

2. Department of Human Genetics, KU Leuven, Leuven, Belgium

Jasper Janssens, Sara Aibar, Ibrahim Ihsan Taskiran, Joy N. Ismail, Katina I. Spanier, Florian V. De Rop, Carmen Bravo González-Blas, Xiao Jiang Quan, Dafni Papasokrati, Gert Hulselmans, Samira Makhzami, Maxime De Waegeneer, Valerie Christiaens & Stein Aerts

3. Department of Life Sciences, Imperial College London, London, UK

Alicia Estacio Gomez, Gabriel Aughey, Marc Dionne, Krista Grimes & Tony Southall

Contributions

S. Aerts, J.J., S. Aibar and I.I.T. conceived the study. J.J., S. Aibar, I.I.T. and D.P. performed computational analyses with assistance from K.I.S., C.B.G.-B., G.H. and M.D.W.; S.M. and V.C. performed scATAC-seq experiments. J.N.I., J.J. and S.M. performed FACS and omniATAC-seq. J.N.I., X.J.Q., J.J. and S.M. performed antibody staining and visualization. X.J.Q., V.C. and J.N.I. performed the cloning of selected enhancers. S.M. performed omniATAC on DGRP lines. J.N.I., J.J., and F.V.D.R. performed Hydrop-ATAC experiments. V.C. and J.N.I. performed CUT&Tag experiments. A.E.G., G.A. and T.S. performed TaDa experiments. M.D. and K.G. generated Mef2-Dam line. S. Aibar created the website with

assistance of G.H., D.P. and K.S.; S. Aerts, J.J., S. Aibar and I.I.T. wrote the manuscript.

Corresponding author

Correspondence to [Stein Aerts](#).

Ethics declarations

Competing interests

The authors declare no competing interests.

Peer review information

Nature thanks Andrew Adey and the other, anonymous, reviewer(s) for their contribution to the peer review of this work. Peer reviewer reports are available.

Additional information

Publisher's note Springer Nature remains neutral with regard to jurisdictional claims in published maps and institutional affiliations.

Extended data figures and tables

[Extended Data Fig. 1 Global analysis and adult clustering approaches.](#)

- a. UMAP of global cisTopic analysis (150k cells shown), coloured by region accessibilities near *elav* (red, neurons), *repo* (green, glia) and *dpn* (blue, neuroblasts). b. Overview of regions shown in a for representative cell types (Kenyon cells for neurons, Astrocytes for glia, optic lobe neuroblasts for neuroblasts). c. Distribution of cells per timepoint in the global UMAP. Timepoints jointly analysed in the upcoming sections

(green: early timepoints, blue: late timepoints) are grouped by borders. **d.** Spearman correlation of top 1000 variable regions across timepoints separating early timepoints (ET), middle timepoints (MT) and late timepoints (LT). **e.** UMAP after timepoint correction with Harmony (coloured by timepoint: ET in green, LT in blue). **f.** *t*-SNE of the 60k cells in the adult cell types analysis (LT). Central-brain only runs allow to annotate clusters according to their location (central brain (CB) and optic lobe (OL)). Subclustering was performed by splitting cells based in CB, OL and glia, note that Kenyon cells, plasmacytes and photoreceptors were not included. **g.** Subclustering of OL neurons leads to 58 subclusters, including a further split of T4/T5 neurons. **h.** Subclustering of CB neurons reveals 51 subtypes. Notice how the S-shaped separation of *pros*⁺ cells and *Imp*⁺ cells is retained. **i.** Subclustering of glia reveals 16 subtypes. **j.** Clustering 88k cells from 48h APF to adult, provides three extra clusters enriched for younger cells (young only: circle, young enriched: arrows), but does not increase the resolution of the adult cell types. **k.** Clustering using ArchR pipeline, on 56k cells from 48hAPF to adult, leading to 90 clusters. UMAPs are shown after Harmony batch effect correction. **l.** Heatmap showing the correspondence between clusters from cisTopic and ArchR. Note that cisTopic clusters are merged across age, in contrast to ArchR clusters, leading to multiple ArchR clustes (different ages) mapping to one cisTopic cluster).

Extended Data Fig. 2 Integration of scRNA-seq and snATAC-seq.

a. Calculation of gene-accessibility scores using a weighted sum of regions in the gene body and up to 5kb upstream of the TSS. Weights decrease exponentially with distance from the TSS (constant in the gene body), and increase with higher gini (variability) coefficients. **b.** Gene expression and gene accessibility display a similar pattern for many genes (6 examples shown), which can be used to transfer cell type annotations across modalities (black lines). **c.** Overview of used annotation methods. Main cell types are consistently detected with each method, while low confidence matches are method specific. **d.** Annotated *t*-SNE of the transcriptomes of 118k adult cells. **e.** Integrated *t*-SNE of scRNA-seq and snATAC-seq using Seurat's co-clustering. **f.** Gene set enrichment of marker genes

using AUCell on gene-accessibility matrix, revealing matches per cell type and per major cell type group (glia, optic lobe neurons, central brain neurons, Kenyon cells, photoreceptors and plasmacytocytes). **g.** Scatterplot showing the number of marker genes against the number of cells in the scRNA-seq dataset. Matched cell types between RNA and ATAC are coloured, unmatched are shown in grey. **h.** Scatterplot showing the number of marker genes in scRNA against the number of DARs for the matched cell types, with glia having the highest number for both. **i.** Heatmap of DARs per cluster. **j.** Bar plot showing the number of DARs per cluster.

[Extended Data Fig. 3 FAC-sorted cell types match single-cell aggregates.](#)

a. Overview of bulk ATAC-seq on three sorted Kenyon cell (KC) populations: (top) Confocal images of KC subtypes targeted with split-GAL4 lines (p: posterior, m: medial, d: dorsal); (middle) Average accessibility of the top 100 differential peaks from sorted cell types projected on the single-cell ATAC *t*-SNE; (bottom) Locus of three marker genes, showing similarity between bulk ATAC-seq (black) and the aggregated scATAC-seq profiles. **b–e.** Heatmap showing the Spearman's correlation of the FAC-sorted samples and single-cell aggregates over different sets of regions. Matching samples and aggregates are shown in bold. **f.** Subclustering of T4 and T5 neurons identifies the a/b and c/d subtypes, with differential regions near marker genes *TfAP-2* and *bi*. **g.** Locus of marker genes showing differential peaks between T4 and T5 neurons (top, *TfAP-2*, range: 0.8–252) and between a/b and c/d subtypes (bottom, *bi*, range: 0.2–120). **h.** Experimental overview: GH146 was used to drive GFP expression in OPNs, followed by FACS and scATAC-seq. **i.** UMAP showing 309 cells kept after filtering, forming 6 clusters. **j.** Visualization of gene accessibility near OPN markers, showing heterogeneity between clusters. **k.** 17k peaks were identified in the OPNs, of which 4.5k are unique, and of which 876 are near OPN marker genes (184 near highly expressed positive markers). These peaks were not found in the consensus peaks (CP) as shown in the tracks. **l.** Co-clustering UMAP of sorted OPNs and 10x scATAC data, with sorted OPNs shown in yellow (top), corresponding to cluster 37 which contains 10 cells of the 10x data, scattered from multiple clusters (bottom).

Extended Data Fig. 4 Chromatin landscapes of progenitors and developing neurons.

a. An SVM classifier was used to propagate the adult cell type labels to earlier stages in development. The classifier also included the progenitor cell types –from the developmental analysis– (purple and dark green colours). **b.** Proportion of cell types at each timepoint. **c.** Chromatin landscape for T1 neurons, shows a highly dynamic opening and closing of peaks during development. A core-set remains accessible at all times, of which a subset is specific to T1 neurons. **d.** Examples of regions with different developmental dynamics for T1 neurons. **e.** Bar plot showing the number of core-regions identified per cell type. Dark colours show specific core-regions (core-DARs). **f.** Number of DARs calculated per cell type (down sampled to 75 cells) for every timepoint, shows a decline over time. The arrow notes a small increase at 48h APF during synaptogenesis. The box plot marks the median (red line), upper and lower quartiles and 1.5× interquartile range (whiskers); outliers are shown individually, n=74,77,78,77,78,77,78,75,76 cell types. **g.** Progenitor cell types show specific marker accessibility, while neurons show accessibility in adult specific regions (*Awh*, *ey*). **h.** Number of DARs per cell type in the early development dataset, revealing a lower number for progenitors (purple shades). **i–j.** Trajectory from optic lobe neuroepithelium (ONE) to lamina progenitor cells (LPC) and optic lobe neuroblasts (OL NB) using **(i)** scATAC-seq and **(j)** scRNA-seq. Heatmap shows dynamic chromatin accessibility modules with enriched motifs (NES score shown) and line plot shows expression profiles for predicted master regulators. **k.** Specific comparison of different progenitor cell types detects thousands of differential regions, with motif enrichment of key TFs. **l.** *In vivo* reporter assay of a cloned ONE enhancer driving GFP. **m.** Optic lobe and central brain branches in 3D-UMAP. **n.** Central brain and VNC duality between *Imp* and *pros* traced through development. Standardized mean accessibility of *Imp* regions (n=128) and *pros* regions (n=166) is plotted for different developmental stages. Dati (AAAAAA) motifs and Pros ChIP-seq peaks (embryo, ModERN) are enriched in *Imp* regions where they are not expressed (grey) and vice versa, suggesting a chromatin closing role. **o.** AUCell enrichment scores of branch-specific regions for adult OL clusters (box plot marks the median (red line), upper and lower quartiles and 1.5×

interquartile range (whiskers); outliers are shown individually; number of cells between brackets). Candidate TFs expressed per branch are shown (TFs with matching motifs in bold).

Extended Data Fig. 5 Cistromes overview.

a. TF expression vs motif enrichment for a selection of TFs. **b.** Heatmap of number of regions per cell type which present motif enrichment for a TF, coloured according to the TF expression-motif enrichment correlation (red: positive correlation, blue: negative correlation). Note that in contrast to **c** this heatmap does not require the TF to be expressed in the given cell type. **c.** Dot-heatmap including all available "chromatin-opening" cistromes (full version of Fig. [3c](#)).

Extended Data Fig. 6 Deep learning predicts de novo key transcriptional activators and repressors.

a. *t*-SNE from the cisTopic analysis on the subset of 15 cell types used for the deep learning (DL) analysis. **b.** Accessibility of topic regions near marker genes. Calculated as the average region probability for topic-regions linked to each set of marker genes (markers from the transcriptome atlas). **c.** Comparison of topic coherence and DL classification performance (area under ROC-curve (auROC) for the classification of the left-out test regions). The topic coherence represents how likely the regions of the topic will co-occur (higher values are better). **d.** Box plot of TF motif enrichment in the topics (average enrichment score) split by the topic annotation (i.e., to one cell type, to multiple cell types, or marked as low contribution). The box plot marks the median, upper and lower quartiles and 1.5 \times interquartile range (whiskers); outliers are shown individually. Number of topics per category shown above plot. **e.** Topic heatmap showing cell-type specific topics. Bar plots show the number of regions per topic (cutoff p=0.995) and area under the precision recall curve (auPR) of the DL model. **f.** Contributions of the patterns identified by DeepFlyBrain to classify glial regions reveal activators and repressors (negative nucleotide importance). These motifs can be matched to known factors with concordant expression. **g–h.** Conservation of the regions centred by the motif (blue) or ATAC peak (orange) for **(g)** KC and **(h)** T neuron motif

instances. The location of the motifs is shown with dashed lines. **i.** Heatmap showing Jaccard index between TF binding site predictions from DL and regions from conventional motif discovery. **j.** Box plots showing higher conservation for overlapping regions compared to deep-learning only regions. The box plot marks the median, upper and lower quartiles and $1.5 \times$ interquartile range (whiskers); outliers are shown individually. Number of enhancers per category shown above plot. **k.** Box plots showing higher enhancer-gene link scores for overlapping regions compared to deep-learning only regions. The box plot marks the median, upper and lower quartiles and $1.5 \times$ interquartile range (whiskers); outliers are shown individually. Number of enhancers per category shown above plot. **l.** Bulk ATAC-seq was performed on brains of 44 different genotypes leading to the identification of caQTLs. caQTLs affecting each of 28k motifs (adjusted p-value of Fisher test versus difference of number of motifs increasing/decreasing accessibility, see [Methods](#)). Dots in the same colour affect similar motifs (black: not-significant). **m.** The fraction of caQTLs predicted to affect chromatin accessibility at different false positive rates (random SNPs). The 5% false positive rate is shown as a dashed grey line. **n–p.** Effect of SNPs in Mamo (**n**), Lola-PF (**o**) and Lola-N (**p**) motifs on chromatin accessibility. Top-left: DeepExplainer plot for the reference (G) and alternative allele (T), showing a loss of a repressor site for Mamo and Lola-N, and a gain of a repressor site for Lola-PF. Top-right: Candle plots showing predicted accessibility change caused by the SNP for different cell types (increase shown in blue, decrease in red). Bottom-left: Box plot showing bulk accessibility of 44 DGRP lines, split by genotype at this SNP, highlighting an increase in accessibility for the alternative allele. The box plot marks the median, upper and lower quartiles and $1.5 \times$ interquartile range (whiskers); all data points are shown. Number of genotypes associated with either reference (Ref) or alternative (Alt) alleles shown. Bottom-right: Single-cell aggregates over the SNP. **q.** Overexpression of lola isoform N (*lola-N*) in glia (repo driver) versus neurons (elav driver, control) leads to the closing of 250 regions with the GATC motif. **r.** Example of a region in perineurial glia (PNG) and subperineurial glia (SUB), that closes upon overexpression of *lola-N* in glia. The region is also part of the PNG eGRN (see Fig. [5](#)). **s.** caQTLs affecting DL motifs. Column nUP/nDw: Number of SNPs overlapping with the motif which produce an increase/decrease of

accessibility. The FDR is checked on 1000 random caQTLs with the same number of SNPs (i.e., *ey*: take 6 random caQTLs, 1000 times, and see how many of the 1k repetitions have at least 5 SNPs increasing accessibility).

Extended Data Fig. 7 Overview of TF binding and perturbation experiments.

- a.** Table showing a summary of all TF binding/perturbation experiments indicating number of affected regions, top motif enrichment and overlap with deep learning binding sites. **b.** CUT&Tag signal of Repo is enriched over predicted Repo binding sites. **c.** CUT&Tag signal of Ey is enriched over predicted Ey binding sites. **d.** Optimization of CUT&Tag for Ey, finding a combination of Pitstop and higher Tn5 concentration to increase the number of regions detected and improve motif enrichment. **e.** The genomic region near *trio* contains peaks for both glia and Kenyon cells, with predicted binding sites for Ey and Repo. Ey and Repo CUT&Tag data are normalized against each other, showing biases to the Ey side over Ey binding sites and to the Repo side over Repo binding sites.
- f.** TaDa coverage of Mef2 in optic lobe (Tm1) and Kenyon cells (left); and of Mef2 in γ -KC for predicted Mef2 regions in the optic lobe and the γ -KC. **g.** Venn diagrams showing overlap of TaDa experiments for Mef2 (left) and Acj6 (right). Motif enrichment is shown with Mef2 motifs enriched in all overlaps of Mef2, but no Acj6 enrichment in unique regions for acj6-TaDa. Strongest enrichments are found for common regions. **h.** Summary of RNAi results of Fig. 3f (knockdown in γ -KC and T4/T5 neurons). Bar plots show affected regions in both directions upon knock-down, with expected direction accentuated. Enriched motifs for the unexpected direction are shown. **i–k.** Results of hypergeometric tests of the overlap of TF knockdown affected regions for cistromes (**i**), cell-type specific cistromes (**j**) and deep learning binding sites (**k**). **l.** Mamo RNAi ATAC peaks from γ -KC are enriched for α/β Kenyon cell regions compared to WT or other knockdowns. **m.** Examples of three loci where Mamo RNAi has led to increased accessibility of α/β Kenyon cell regions in γ -KC.

Extended Data Fig. 8 Enhancers selected by accessible regions generate novel driver lines.

a. Peak in the overlap of two existing Kenyon Cell driver lines recapitulates KC expression. **b.** DeepExplainer view of the selected element from **(a)** showing Ey and Mef2 binding sites. **c.** Existing non-specific driver lines can be broken up in separate more specific drivers for KC and glia using cell-type specific ATAC-peak signals. **d.** In-silico overlap of ATAC-peak signals resembles that of in-vitro split-GAL4 lines for T4/T5 neurons. Images courtesy of the Janelia FlyLight Project. **e.** 63 adult enhancers were selected and cloned into a construct, flanked by gypsy insulators (GI) driving either direct GFP or GAL4 expression from the *Hsp70* promoter. Selected peaks have a median size of 580bp (direct) or 626 (Gal4). **f.** Overview of GFP expression in different cloned enhancers (GAL4 enhancers were crossed with UAS-nlsGFP). Red numbers point to enhancer-IDs (Supplementary Table 8). Green numbers are scores of enhancer activity in the predicted cell type (0: no activity, 1: low, 2: high). **g.** Bar plots showing validation rate for GFP expression within Kenyon cells (KC), optic lobe (OL), glia (G). Mixed (M) and Negative (N) bar plots are shown as controls. Dark colours mean high expression (2), light colours mean faint expression (1). **h.** ROC curve showing the performance of different metrics to predict OL activity of the 64 cloned enhancers (including developmental enhancer). **i.** ROC curve showing the performance of different metrics to predict glial activity of the 64 cloned enhancers (including developmental enhancer).

[Extended Data Fig. 9 DeepFlyBrain accurately predicts effects of mutations.](#)

a–e. Analysis of cloned enhancers near **(a)** *gish*, **(b)** *Appl*, **(c)** *Bx*, **(d)** *Pkc53e*, and **(e)** *CG15117*. Accessibility profiles of the loci, DL prediction scores for the WT and mutated (mut) sequences, nucleotide importance scores and in-silico saturation mutagenesis assays, and in vivo enhancer activity of the cloned sequences are shown as in Fig. 4a, b. **f, g.** *In vivo* enhancer activity and nuclei count of the WT region and the region with mutated repressors near **(f)** *sNPF* and **(g)** *Appl*. The expected nuclei count after destroying the repressors is shown as a dashed grey line (20% increase). The box plot marks the median, upper and lower quartiles and 1.5× interquartile range (whiskers); all data points are shown (one-sided Mann-Whitney U test). Number of measured brains shown.

Extended Data Fig. 10 Gene expression and region accessibility correlation can be exploited to build eGRNs, and classify TF roles according to their network activity.

a. Proportion of BEAF-32 ChIP-seq peaks that have a high-scoring BEAF-32 motif, and are accessible in the fly brain. Despite being performed on whole embryo (0-14 h, mixed sex), most of the motif containing peaks are ubiquitously accessible across the brain. **b.** Distance to the closest BEAF-32 peak with motif upstream and downstream of each gene. Most of the genes (86%) are within 50kb of a BEAF-32 peak (46% are between two peaks within 50kb, and 88% within 200kb). For genes further than 50kb, expanding the search space from 50kb to 200kb adds a median of 2 extra links. **c.** View of genes, topological associated domains (TADs), genomic regulatory blocks (GRBs), BEAF-32 ChIP-seq peaks and BEAF-32 defined search spaces near the locus of *Imp* (green), *ras* (red), *Ant2* (yellow) and *feo* (pink). The lowest track shows the search space for each gene (i.e., the region between the first two BEAF-32 peaks within 200kb of the transcript, skipping 500bp around the TSS. In case there are no peaks within 200kb, 50kb is kept as search space). **d.** Box plots showing higher correlation for enhancer-gene links contained within BEAF-32 domains compared to links outside. Links that cross boundaries have a higher anticorrelation. The box plot marks the median, upper and lower quartiles and 1.5× interquartile range (whiskers); outliers are shown individually.. Number of links per category is shown with one-sided Mann-Whitney U test. P-value below numerical precision equals 0. **e.** Overview of selected tracks in the *Pkc53E* locus; only the enhancer-gene links between two BEAF-32 peaks (green bar) are kept. The grey/blue regions on top are the pre-defined regulatory regions used for the analysis, dark blue indicates a region with link to the gene, grey regions are not differentially accessible. **f.** Regulatory region selection for *Pkc53E*; the inset shows accessibility of the top region versus gene expression (input to the random-forest), regions with a weight above the threshold are linked to the gene. On the right: t-SNEs showing the gene expression and accessibility, and the resulting network. **g.** Scatterplot showing the correlation (Pearson's r=0.4, two-sided test, p=0.001, n=64) between *in vivo* enhancer reporter activity (GFP score) and the strength of the enhancer-gene link (correlation). Linear regression and 95% confidence interval are shown. **h–i.** Correlation of gene expression

(h.) and TF gene expression **(i.)** with aggregated accessibility profiles at TSS, averaged gene-accessibility, and averaged accessibility of regions with positive links. Red line shows linear fit, with orange boundaries as the 95% confidence interval. Note the regions near the TSS that have high accessibility but do not lead to gene expression (highlighted in blue) and the increase in performance for the gene-accessibility score in the TF expression, while overall the highest correlation is reached with links. **j.** Overview of eGRN expression across different cell types. For each TF, the first row is TF expression, with below a heatmap value of normalized enrichment score of the eGRN (NES, gene-set enrichment analysis of eGRN target genes on genes ranked by FC in each cell type). Note that chromatin-repressing eGRNs are less validated, and represent lower confidence. **k.** Heatmap of number of genes in the TF-eGRNs (in all cell types) split by cistrome type and gene-link correlation (i.e., indicating potential activator/repressor roles). Canonical activators have most of their targets in opening-cistrome with positive-links. Most of the potential repressors are repressors of chromatin (e.g., closing enhancers), rather than opening repressive regions (i.e., regions with negative links). Only 4 TFs have a higher number of targets with the negative links: Fkh, Acj6, Oli and Ftz-f1 (cell-type dependent). TFs with an asterisk use 0.20 TF expression-motif correlation threshold. Bold highlights TFs with confirmed roles (in this study or previously known).

Extended Data Fig. 11 A resource of cell-type specific eGRNs.

- a.** γ -KC eGRN (motif-based) with key TFs in the middle. Genes marked as squares are also present in the DL-filtered eGRN (Fig. [5a](#)). **b.** Heatmap of Jaccard index between TF target regions in the γ -KC eGRN. **c.** eGRN T1 neurons (regions are coloured in blue shades, genes in red; regulatory TFs are in the center). **d.** Heatmap of Jaccard index between TF target regions in T1 eGRN. **e.** Heatmap of eGRN overlap (region based, Jaccard index) of all cell types and all TFs. Examples of eGRNs (*scro*, *TfAP-2*, *ey* and *Mef2*) are highlighted, showing co-clustering based on TF, and on cell type (genomic context). **f.** Regulatory network for KCs and perineurial glia, with colour showing the status of the network (average expression and accessibility). Presence of Mamo leads to repression of α/β -KC marker regions and genes, while Lola-N leads to repression of glial

marker regions and genes. **g.** eGRNs for different subtypes of Kenyon cells, T-neuron subclasses and glia are available for exploration on NDEx through <https://flybrain.aertslab.org/>. Link outs from the gene to FlyBase and UCSC allow to explore gene function and chromatin profiles with all nearby predicted enhancers coloured, while link outs from regions allow to inspect the region with DeepFlyBrain, to visualize nucleotide importances, while also linking to UCSC to view the genomic context with the selected region highlighted.

Extended Data Fig. 12 Enhancer switching is a prominent feature of development.

a. Heatmap showing 458 enhancers that undergo a switch from one cell type to another. Enhancers are grouped based on whether the switch is from (non)neuronal to (non)neuronal. Heatmap shows standardized average accessibility (RPGC): ET: early timepoints (larva-12h APF), MT: middle timepoints (24-48h APF), LT: late timepoints (72h APF-adult). **b.** Examples of enhancers that switch between cell types for different categories. Given that one region can contain multiple enhancers, it is hard to separate enhancer switches from shifters: the glia enhancer (right) shows a shift, where one peak goes down and an adjacent one becomes accessible. **c.** *t*-SNE from the cisTopic analysis on the subset of 18 cell types used for the deep learning (DL) analysis. **d.** Performance of the DL model for the different topics. **e.** Examples of topics linked to progenitor cell types (left) and to Kenyon cell subtypes (right). **f.** TF-MoDISco results for topics linked to progenitors (left) and to Kenyon cells (right), highlighting motifs of TFs expressed in those cell types. The motif for Ase shows negative nucleotide importances, suggesting a chromatin repressing role. **g.** *CG15117* enhancer switches from ensheathing glia (ENS) to T1 neurons. **h.** Bar plots showing predicted scores of the region for the developmental and adult DL model. **i-j.** DeepExplainer plot and in-silico mutagenesis plots of the *CG15117* enhancer calculated with (**i**) adult DL model and (**j**) development DL model. According to the models, the enhancer is repressed in adult ensheathing glia and developing T1 neurons by the same binding site (highlighted with orange box).

Supplementary information

Supplementary Information

Reporting Summary

Supplementary Data 1

FACS gating strategy: gating strategies used in the FACS runs performed on split-Gal4 lines (MB371B, MB418B and MB419B), and for the normal Gal4 lines (knockdown experiments: R16A06 and ato; TaDa: R74G01; sorted OPNs: GH146, sorted cell types: R16A06, R74G01 and ato) together with detailed results.

Supplementary Data 2–5

Supplementary Data 2: VSN config file to run the VSN Nextflow pipeline on the adult scRNA-seq data from Davie et al.². Supplementary Data 3: DeepFlyBrain training data containing a Jupyter notebook to train a DL model. Supplementary Data 4: DeepFlyBrain performance data containing a Jupyter notebook to determine the performance of the DL model. Supplementary Data 5: DeepFlyBrain scoring data and DeepExplainer plots containing a Jupyter notebook to score new regions and view nucleotide importance in the region.

Supplementary Tables

Supplementary Tables 1–11 and a guide of the Supplementary Tables.

Peer Review File

Rights and permissions

Reprints and Permissions

About this article

Cite this article

Janssens, J., Aibar, S., Taskiran, I.I. *et al.* Decoding gene regulation in the fly brain. *Nature* **601**, 630–636 (2022). <https://doi.org/10.1038/s41586-021-04262-z>

- Received: 30 December 2020
- Accepted: 17 November 2021
- Published: 05 January 2022
- Issue Date: 27 January 2022
- DOI: <https://doi.org/10.1038/s41586-021-04262-z>

Share this article

Anyone you share the following link with will be able to read this content:

[Get shareable link](#)

Sorry, a shareable link is not currently available for this article.

[Copy to clipboard](#)

Provided by the Springer Nature SharedIt content-sharing initiative

This article was downloaded by **calibre** from <https://www.nature.com/articles/s41586-021-04262-z>

- Article
- [Published: 19 January 2022](#)

Ageing exacerbates ribosome pausing to disrupt cotranslational proteostasis

- [Kevin C. Stein](#) [ORCID: orcid.org/0000-0002-0622-8319¹](#),
- [Fabián Morales-Polanco](#) [ORCID: orcid.org/0000-0002-7695-3081¹](#),
- [Joris van der Lienden](#) [ORCID: orcid.org/0000-0002-7012-2471¹](#),
- [T. Kelly Rainbolt¹](#) &
- [Judith Frydman](#) [ORCID: orcid.org/0000-0003-2302-6943^{1,2}](#)

[Nature](#) volume 601, pages 637–642 (2022)

- 10k Accesses
- 216 Altmetric
- [Metrics details](#)

Subjects

- [Biochemistry](#)
- [Protein folding](#)
- [Translation](#)

Abstract

Ageing is accompanied by a decline in cellular proteostasis, which underlies many age-related protein misfolding diseases^{1,2}. Yet, how ageing

impairs proteostasis remains unclear. As nascent polypeptides represent a substantial burden on the proteostasis network³, we hypothesized that altered translational efficiency during ageing could help to drive the collapse of proteostasis. Here we show that ageing alters the kinetics of translation elongation in both *Caenorhabditis elegans* and *Saccharomyces cerevisiae*. Ribosome pausing was exacerbated at specific positions in aged yeast and worms, including polybasic stretches, leading to increased ribosome collisions known to trigger ribosome-associated quality control (RQC)^{4,5,6}. Notably, aged yeast cells exhibited impaired clearance and increased aggregation of RQC substrates, indicating that ageing overwhelms this pathway. Indeed, long-lived yeast mutants reduced age-dependent ribosome pausing, and extended lifespan correlated with greater flux through the RQC pathway. Further linking altered translation to proteostasis collapse, we found that nascent polypeptides exhibiting age-dependent ribosome pausing in *C. elegans* were strongly enriched among age-dependent protein aggregates. Notably, ageing increased the pausing and aggregation of many components of proteostasis, which could initiate a cycle of proteostasis collapse. We propose that increased ribosome pausing, leading to RQC overload and nascent polypeptide aggregation, critically contributes to proteostasis impairment and systemic decline during ageing.

This is a preview of subscription content

Access options

Subscribe to nature+

Get immediate online access to the entire Nature family of 50+ journals

\$29.99

monthly

[Subscribe](#)

Subscribe to Journal

Get full journal access for 1 year

\$199.00

only \$3.90 per issue

[Subscribe](#)

All prices are NET prices.

VAT will be added later in the checkout.

Tax calculation will be finalised during checkout.

Buy article

Get time limited or full article access on ReadCube.

\$32.00

[Buy](#)

All prices are NET prices.

Additional access options:

- [Log in](#)
- [Learn about institutional subscriptions](#)

Fig. 1: Age-dependent ribosome pausing is conserved.

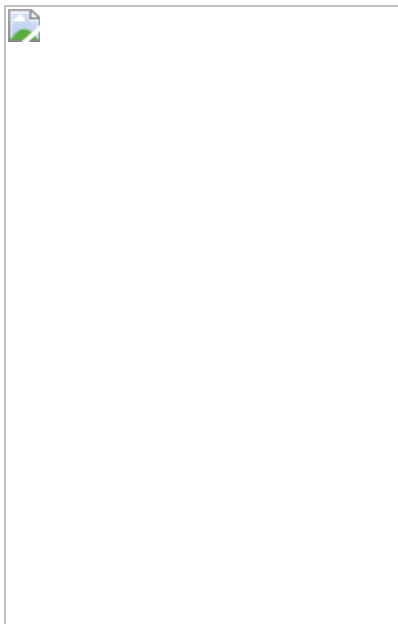


Fig. 2: Ageing exacerbates ribosome pausing at polybasic regions in yeast.

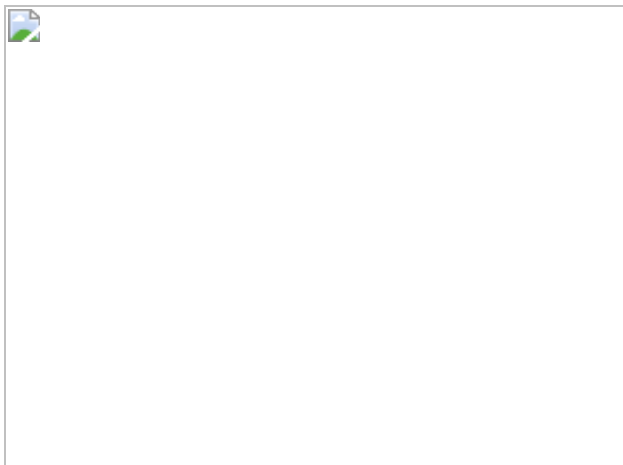


Fig. 3: Polybasic-driven age-dependent aggregation of truncated nascent polypeptides in yeast is mitigated in lifespan extension models.

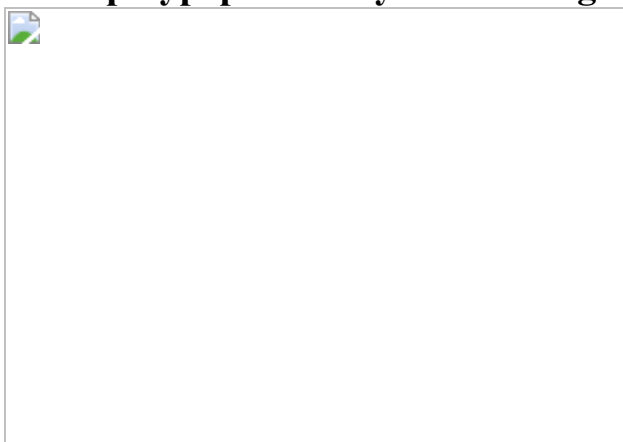


Fig. 4: Conserved mechanisms of age-dependent ribosome pausing and aggregation in worms.



Data availability

The datasets generated for this study have been deposited in NCBI's Gene Expression Omnibus (GEO) under GEO Series accession number [GSE152850](#). Additional datasets used in this study are also publicly available: [GSE139036](#) (disome profiling), [GSE69414](#) and [GSE52968](#) (Ribo-seq of yeast treated with 3-amino-1,2,4-triazole), ref. [62](#) (yeast chronological lifespan), ref. [6](#) (RQC flux), and refs. [37](#) and [65](#) (protein aggregation during *C. elegans* ageing).

Code availability

All customized Python or R scripts used for data processing and analysis are available from the corresponding author on request.

References

1. 1.

López-Otín, C., Blasco, M. A., Partridge, L., Serrano, M. & Kroemer, G. The hallmarks of aging. *Cell* **153**, 1194–1217 (2013).

2. 2.

Chiti, F. & Dobson, C. M. Protein misfolding, functional amyloid, and human disease. *Annu. Rev. Biochem.* **75**, 333–366 (2006).

3. 3.

Pechmann, S., Willmund, F. & Frydman, J. The ribosome as a hub for protein quality control. *Mol. Cell* **49**, 411–421 (2013).

4. 4.

Simms, C. L., Yan, L. L. & Zaher, H. S. Ribosome collision is critical for quality control during no-go decay. *Mol. Cell* **68**, 361–373 (2017).

5. 5.

Juszkiewicz, S. et al. ZNF598 is a quality control sensor of collided ribosomes. *Mol. Cell* **72**, 469–481 (2018).

6. 6.

Brandman, O. et al. A ribosome-bound quality control complex triggers degradation of nascent peptides and signals translation stress. *Cell* **151**, 1042–1054 (2012).

7. 7.

Balchin, D., Hayer-Hartl, M. & Hartl, F. U. In vivo aspects of protein folding and quality control. *Science* **353**, aac4354 (2016).

8. 8.

Jahn, T. R. & Radford, S. E. Folding versus aggregation: polypeptide conformations on competing pathways. *Arch. Biochem. Biophys.* **469**, 100–117 (2008).

9. 9.

Ciryam, P., Tartaglia, G. G., Morimoto, R. I., Dobson, C. M. & Vendruscolo, M. Widespread aggregation and neurodegenerative diseases are associated with supersaturated proteins. *Cell Rep.* **5**, 781–790 (2013).

10. 10.

Gingold, H. & Pilpel, Y. Determinants of translation efficiency and accuracy. *Mol. Syst. Biol.* **7**, 481 (2011).

11. 11.

Stein, K. C. & Frydman, J. The stop-and-go traffic regulating protein biogenesis: how translation kinetics controls proteostasis. *J. Biol. Chem.* **294**, 2076–2084 (2019).

12. 12.

Yu, C.-H. et al. Codon usage influences the local rate of translation elongation to regulate co-translational protein folding. *Mol. Cell* **59**, 744–754 (2015).

13. 13.

Pechmann, S. & Frydman, J. Evolutionary conservation of codon optimality reveals hidden signatures of cotranslational folding. *Nat. Struct. Mol. Biol.* **20**, 237–243 (2013).

14. 14.

Kudla, G., Murray, A. W., Tollervey, D. & Plotkin, J. B. Coding-sequence determinants of gene expression in *Escherichia coli*. *Science* **324**, 255–258 (2009).

15. 15.

Zhang, G., Hubalewska, M. & Ignatova, Z. Transient ribosomal attenuation coordinates protein synthesis and co-translational folding. *Nat. Struct. Mol. Biol.* **16**, 274–280 (2009).

16. 16.

Collart, M. A. & Weiss, B. Ribosome pausing, a dangerous necessity for co-translational events. *Nucleic Acids Res.* **48**, 1043–1055 (2020).

17. 17.

Chartron, J. W., Hunt, K. C. L. & Frydman, J. Cotranslational signal-independent SRP preloading during membrane targeting. *Nature* **536**, 224–228 (2016).

18. 18.

Pechmann, S., Chartron, J. W. & Frydman, J. Local slowdown of translation by nonoptimal codons promotes nascent-chain recognition by SRP in vivo. *Nat. Struct. Mol. Biol.* **21**, 1100–1105 (2014).

19. 19.

Stein, K. C., Kriel, A. & Frydman, J. Nascent polypeptide domain topology and elongation rate direct the cotranslational hierarchy of Hsp70 and TRiC/CCT. *Mol. Cell* **75**, 1117–1130 (2019).

20. 20.

Sitron, C. S. & Brandman, O. Detection and degradation of stalled nascent chains via ribosome-associated quality control. *Annu. Rev. Biochem.* **89**, 417–442 (2020).

21. 21.

Brandman, O. & Hegde, R. S. Ribosome-associated protein quality control. *Nat. Struct. Mol. Biol.* **23**, 7–15 (2016).

22. 22.

Dimitrova, L. N., Kuroha, K., Tatematsu, T. & Inada, T. Nascent peptide-dependent translation arrest leads to Not4p-mediated protein

degradation by the proteasome. *J. Biol. Chem.* **284**, 10343–10352 (2009).

23. 23.

Buhr, F. et al. Synonymous codons direct cotranslational folding toward different protein conformations. *Mol. Cell* **61**, 341–351 (2016).

24. 24.

Nedialkova, D. D. & Leidel, S. A. Optimization of codon translation rates via tRNA modifications maintains proteome integrity. *Cell* **161**, 1606–1618 (2015).

25. 25.

Kim, S. J. et al. Protein folding. Translational tuning optimizes nascent protein folding in cells. *Science* **348**, 444–448 (2015).

26. 26.

Willmund, F. et al. The cotranslational function of ribosome-associated Hsp70 in eukaryotic protein homeostasis. *Cell* **152**, 196–209 (2013).

27. 27.

Duttler, S., Pechmann, S. & Frydman, J. Principles of cotranslational ubiquitination and quality control at the ribosome. *Mol. Cell* **50**, 379–393 (2013).

28. 28.

Koplin, A. et al. A dual function for chaperones SSB-RAC and the NAC nascent polypeptide-associated complex on ribosomes. *J. Cell Biol.* **189**, 57–68 (2010).

29. 29.

Choe, Y.-J. et al. Failure of RQC machinery causes protein aggregation and proteotoxic stress. *Nature* **531**, 191–195 (2016).

30. 30.

Yonashiro, R. et al. The Rqc2/Tae2 subunit of the ribosome-associated quality control (RQC) complex marks ribosome-stalled nascent polypeptide chains for aggregation. *eLife* **5**, e11794 (2016).

31. 31.

Wu, C. C.-C., Peterson, A., Zinshteyn, B., Regot, S. & Green, R. Ribosome collisions trigger general stress responses to regulate cell fate. *Cell* **182**, 404–416 (2020).

32. 32.

Ishimura, R. et al. Ribosome stalling induced by mutation of a CNS-specific tRNA causes neurodegeneration. *Science* **345**, 455–459 (2014).

33. 33.

Bengtson, M. H. & Joazeiro, C. A. P. Role of a ribosome-associated E3 ubiquitin ligase in protein quality control. *Nature* **467**, 470–473 (2010).

34. 34.

Taylor, R. C. & Dillin, A. Aging as an event of proteostasis collapse. *Cold Spring Harb. Perspect. Biol.* **3**, a004440 (2011).

35. 35.

Ben-Zvi, A., Miller, E. A. & Morimoto, R. I. Collapse of proteostasis represents an early molecular event in *Caenorhabditis elegans* aging. *Proc. Natl Acad. Sci. USA* **106**, 14914–14919 (2009).

36. 36.

Steffen, K. K. & Dillin, A. A ribosomal perspective on proteostasis and aging. *Cell Metab.* **23**, 1004–1012 (2016).

37. 37.

Walther, D. M. et al. Widespread proteome remodeling and aggregation in aging *C. elegans*. *Cell* **161**, 919–932 (2015).

38. 38.

Pan, K. Z. et al. Inhibition of mRNA translation extends lifespan in *Caenorhabditis elegans*. *Aging Cell* **6**, 111–119 (2007).

39. 39.

Hansen, M. et al. Lifespan extension by conditions that inhibit translation in *Caenorhabditis elegans*. *Aging Cell* **6**, 95–110 (2007).

40. 40.

Reis-Rodrigues, P. et al. Proteomic analysis of age-dependent changes in protein solubility identifies genes that modulate lifespan. *Aging Cell* **11**, 120–127 (2012).

41. 41.

Narayan, V. et al. Deep proteome analysis identifies age-related processes in *C. elegans*. *Cell Syst.* **3**, 144–159 (2016).

42. 42.

Hu, Z. et al. Ssd1 and Gcn2 suppress global translation efficiency in replicatively aged yeast while their activation extends lifespan. *eLife* **7**, 4443 (2018).

43. 43.

Young, D. J., Guydosh, N. R., Zhang, F., Hinnebusch, A. G. & Green, R. Rli1/ABCE1 recycles terminating ribosomes and controls

translation reinitiation in 3'UTRs in vivo. *Cell* **162**, 872–884 (2015).

44. 44.

Guydosh, N. R. & Green, R. Dom34 rescues ribosomes in 3' untranslated regions. *Cell* **156**, 950–962 (2014).

45. 45.

Choi, J. et al. How messenger RNA and nascent chain sequences regulate translation elongation. *Annu. Rev. Biochem.* **87**, 421–449 (2018).

46. 46.

Schuller, A. P., Wu, C. C.-C., Dever, T. E., Buskirk, A. R. & Green, R. eIF5A functions globally in translation elongation and termination. *Mol. Cell* **66**, 194–205 (2017).

47. 47.

Meydan, S. & Guydosh, N. R. Disome and trisome profiling reveal genome-wide targets of ribosome quality control. *Mol. Cell* **79**, 588–602 (2020).

48. 48.

Gamble, C. E., Brule, C. E., Dean, K. M., Fields, S. & Grayhack, E. J. Adjacent codons act in concert to modulate translation efficiency in yeast. *Cell* **166**, 679–690 (2016).

49. 49.

Han, P. et al. Genome-wide survey of ribosome collision. *Cell Rep.* **31**, 107610 (2020).

50. 50.

Juszkiewicz, S., Speldewinde, S. H., Wan, L., Svejstrup, J. Q. & Hegde, R. S. The ASC-1 complex disassembles collided ribosomes. *Mol. Cell* **79**, 603–614 (2020).

51. 51.

Ikeuchi, K. et al. Collided ribosomes form a unique structural interface to induce Hel2-driven quality control pathways. *EMBO J.* **38**, e100276 (2019).

52. 52.

Shen, P. S. et al. Protein synthesis. Rqc2p and 60S ribosomal subunits mediate mRNA-independent elongation of nascent chains. *Science* **347**, 75–78 (2015).

53. 53.

Shao, S., Malsburg, von der, K. & Hegde, R. S. Listerin-dependent nascent protein ubiquitination relies on ribosome subunit dissociation. *Mol. Cell* **50**, 637–648 (2013).

54. 54.

Shao, S. & Hegde, R. S. Reconstitution of a minimal ribosome-associated ubiquitination pathway with purified factors. *Mol. Cell* **55**, 880–890 (2014).

55. 55.

Shao, S., Brown, A., Santhanam, B. & Hegde, R. S. Structure and assembly pathway of the ribosome quality control complex. *Mol. Cell* **57**, 433–444 (2015).

56. 56.

Juszkiewicz, S. & Hegde, R. S. Initiation of quality control during poly(A) translation requires site-specific ribosome ubiquitination. *Mol. Cell* **65**, 743–750 (2017).

57. 57.

Sundaramoorthy, E. et al. ZNF598 and RACK1 regulate mammalian ribosome-associated quality control function by mediating regulatory 40S ribosomal ubiquitylation. *Mol. Cell* **65**, 751–760 (2017).

58. 58.

Matsuo, Y. et al. Ubiquitination of stalled ribosome triggers ribosome-associated quality control. *Nat. Commun.* **8**, 159 (2017).

59. 59.

Tsuboi, T. et al. Dom34:hbs1 plays a general role in quality-control systems by dissociation of a stalled ribosome at the 3' end of aberrant mRNA. *Mol. Cell* **46**, 518–529 (2012).

60. 60.

Sitron, C. S. & Brandman, O. CAT tails drive on- and off-ribosome degradation of stalled polypeptides. *Nat. Struct. Mol. Biol.* **26**, 450–459 (2018).

61. 61.

Anisimova, A. S. et al. Multifaceted deregulation of gene expression and protein synthesis with age. *Proc. Natl Acad. Sci. USA* **117**, 15581–15590 (2020).

62. 62.

Powers, R. W., Kaerlein, M., Caldwell, S. D., Kennedy, B. K. & Fields, S. Extension of chronological life span in yeast by decreased TOR pathway signaling. *Genes Dev.* **20**, 174–184 (2006).

63. 63.

Fabrizio, P., Pozza, F., Pletcher, S. D., Gendron, C. M. & Longo, V. D. Regulation of longevity and stress resistance by Sch9 in yeast. *Science*

292, 288–290 (2001).

64. 64.

Kaeberlein, M. et al. Regulation of yeast replicative life span by TOR and Sch9 in response to nutrients. *Science* **310**, 1193–1196 (2005).

65. 65.

David, D. C. et al. Widespread protein aggregation as an inherent part of aging in *C. elegans*. *PLoS Biol.* **8**, e1000450 (2010).

66. 66.

Barros, G. C. et al. Rqc1 and other yeast proteins containing highly positively charged sequences are not targets of the RQC complex. *J. Biol. Chem.* **296**, 100586 (2021).

67. 67.

Brenner, S. The genetics of *Caenorhabditis elegans*. *Genetics* **77**, 71–94 (1974).

68. 68.

Winzeler, E. A. et al. Functional characterization of the *S. cerevisiae* genome by gene deletion and parallel analysis. *Science* **285**, 901–906 (1999).

69. 69.

Yofe, I. et al. One library to make them all: streamlining the creation of yeast libraries via a SWAp-Tag strategy. *Nat. Chem. Biol.* **13**, 371–378 (2016).

70. 70.

Huh, W.-K. et al. Global analysis of protein localization in budding yeast. *Nature* **425**, 686–691 (2003).

71. 71.

Hughes, A. L. & Gottschling, D. E. An early age increase in vacuolar pH limits mitochondrial function and lifespan in yeast. *Nature* **492**, 261–265 (2012).

72. 72.

Ingolia, N. T., Brar, G. A., Rouskin, S., McGeachy, A. M. & Weissman, J. S. The ribosome profiling strategy for monitoring translation in vivo by deep sequencing of ribosome-protected mRNA fragments. *Nat. Protoc.* **7**, 1534–1550 (2012).

73. 73.

Langmead, B., Trapnell, C., Pop, M. & Salzberg, S. L. Ultrafast and memory-efficient alignment of short DNA sequences to the human genome. *Genome Biol.* **10**, R25 (2009).

74. 74.

Love, M. I., Huber, W. & Anders, S. Moderated estimation of fold change and dispersion for RNA-seq data with DESeq2. *Genome Biol.* **15**, 550 (2014).

75. 75.

Dey, K. K., Xie, D. & Stephens, M. A new sequence logo plot to highlight enrichment and depletion. *BMC Bioinform.* **19**, 473 (2018).

76. 76.

Burtner, C. R., Murakami, C. J., Kennedy, B. K. & Kaeberlein, M. A molecular mechanism of chronological aging in yeast. *Cell Cycle* **8**, 1256–1270 (2009).

77. 77.

Huang, D. W., Sherman, B. T. & Lempicki, R. A. Systematic and integrative analysis of large gene lists using DAVID bioinformatics resources. *Nat. Protoc.* **4**, 44–57 (2009).

78. 78.

McCormick, M. A. et al. A comprehensive analysis of replicative lifespan in 4,698 single-gene deletion strains uncovers conserved mechanisms of aging. *Cell Metab.* **22**, 895–906 (2015).

Acknowledgements

We thank R. Aviner and M. Aguilar-Rangel for comments on the manuscript; members of the Frydman Laboratory for discussions and advice; J. Chartron, P. Dolan and K. Dalton for technical input; and J. Lim and J. Arribere for *C. elegans* expertise. *YTM1* and *HAT2* performed at the UCSF Center for Advanced Technology. K.C.S. was supported as a Glenn Foundation for Medical Research Postdoctoral Fellow and by NIH/NIA grant (T32AG047126). F.M.-P. was supported by The Pew Trusts in the Biomedical Sciences postdoctoral Award (00034104), and T.K.R was supported by the NIH/NIGMS National Research Service Award (F32GM120947). This work was supported by NIH grants GM056433 and AG054407 (to J.F.). J.F. is a CZ Biohub Investigator.

Author information

Affiliations

1. Department of Biology, Stanford University, Stanford, CA, USA

Kevin C. Stein, Fabián Morales-Polanco, Joris van der Lienden, T. Kelly Rainbolt & Judith Frydman

2. Department of Genetics, Stanford University, Stanford, CA, USA

Judith Frydman

Contributions

K.C.S. and J.F. designed the study. K.C.S. performed all of the experiments and computational analyses, with assistance from F.M.-P., J.L. and T.K.R. in carrying out the yeast reporter immunoblot and microscopy experiments. K.C.S. and J.F. wrote the manuscript with input from all authors.

Corresponding author

Correspondence to [Judith Frydman](#).

Ethics declarations

Competing interests

The authors declare no competing interests.

Peer review information

Nature thanks Andrew Dillin, Toshifumi Inada and the other, anonymous, reviewer(s) for their contribution to the peer review of this work.

Additional information

Publisher's note Springer Nature remains neutral with regard to jurisdictional claims in published maps and institutional affiliations.

Extended data figures and tables

[Extended Data Fig. 1 Decreased protein synthesis and translatome changes during chronological ageing of yeast.](#)

a, Survival curve of yeast during chronological ageing. $n = 3$ biological replicates with mean \pm s.e.m. **b – c**, Average ribosome occupancy at the **b**,

start and **c**, stop codons during yeast chronological ageing. The shaded region represents the 95% bootstrapped confidence interval. **d**, Polysome profiles of chronologically aged yeast at the indicated ages showing decreased population of polysomes during ageing. $n \geq 3$ biological replicates with representative profiles shown. **e**, Heat map of gene expression analysis of Ribo-seq data showing Pearson's correlation coefficient between all yeast samples. **f**, Volcano plot of differential gene expression shows widespread translatome changes for chronologically aged yeast. $n = 2,981$ total genes with 901 genes having increased ribosome occupancy (purple, > 2 fold up, adjusted $P < 0.05$, Benjamini-Hochberg method) and 1,033 genes having decreased ribosome occupancy (green, > 2 fold down, adjusted $P < 0.05$, Benjamini-Hochberg method) in Day 4 yeast cells relative to Day 0 yeast cells. **g**, Functional enrichment of differentially translated genes during ageing displaying representative gene ontology terms (adjusted $P < 0.1$, Benjamini-Hochberg method). See Supplementary Table 2 for complete, unfiltered results. **h**, Ribosome occupancy on ribosomal protein *RPL3* showing decreased translation during yeast ageing. **i**, Ribosome occupancy on the 5'UTR and coding sequence of *GCN4*, showing decreased occupancy at upstream ORFs and increased occupancy across the coding sequence during ageing. **j**, Scatter plot of average pause scores for each amino acid residue in coding sequences of young Day 0 and aged Day 4 yeast. **k**, Scatter plots of average pause scores for each amino acid residue in coding sequences of two biological replicates of Day 0 (left) and Day 4 (right) chronologically aged yeast.

Extended Data Fig. 2 Decreased protein synthesis and translatome changes during chronological ageing of worms.

a, Polysome profiles of adult worms at the indicated ages showing decreased population of polysomes during ageing. $n \geq 3$ biological replicates with representative profiles shown. **b – c**, Average ribosome occupancy at the **b**, start and **c**, stop codons of young Day 1 and aged Day 12 worms. The shaded region represents the 95% bootstrapped confidence interval. **d**, Heat map of gene expression analysis of Ribo-seq data showing Pearson's correlation coefficient between worm samples. **e**, Volcano plot of differential gene expression shows widespread translatome changes during worm ageing. $n = 8,341$ total genes with 621 genes having increased

ribosome occupancy (purple, > 2 fold up, adjusted $P < 0.05$, Benjamini-Hochberg method) and 655 genes having decreased ribosome occupancy (green, > 2 fold down, adjusted $P < 0.05$, Benjamini-Hochberg method) in Day 12 adult worms relative to Day 1 adult worms. **f**, Functional enrichment of differentially translated genes displaying representative gene ontology terms (adjusted $P < 0.1$, except for categories with number of genes < 20 where adjusted $P < 0.25$, Benjamini-Hochberg method). See Supplementary Table 2 for complete, unfiltered results. **g**, Ribosome occupancy on ribosomal protein *rps-3* showing decreased translation during ageing of worms. **h**, Scatter plot of average pause scores for each amino acid residue in coding sequences of Day 1 and Day 12 adult worms. **i**, Scatter plots of average pause scores for each amino acid residue in coding sequences of two biological replicates of Day 1 (left) and Day 12 (right) adult worms.

Extended Data Fig. 3 Age-dependent ribosome pausing.

a, Scatter plot of the average pause score for each amino acid residue in coding sequences of young WT yeast cells either untreated or treated with 3-amino-1,2,4-triazole (3-AT) from previously published Ribo-seq data⁴³. **b**, Amino acid residue frequency in the ribosomal A-site of statistically significant ribosome pause sites enriched in yeast cells treated with 3-AT⁴³, relative to the residue frequency in the transcriptome. **c**, Functional enrichment of genes with an age-dependent pause site in yeast displaying representative gene ontology terms (adjusted $P < 0.1$, Benjamini–Hochberg method). See Supplementary Table 2 for complete, unfiltered results. **d**, Functional enrichment of genes with an age-dependent pause site in worms displaying representative gene ontology terms (adjusted $P < 0.1$, Benjamini–Hochberg method). See Supplementary Table 2 for complete, unfiltered results. **e**, Investigating the association between age-dependent ribosome pausing and co-translational ubiquitination²⁷. Population $n = 937$ transcripts with a pause site, 3,145 transcripts without a pause site. $P = 0.002$, two-sided Fisher’s exact test. **f**, Codon frequency in the ribosomal A-site of age-dependent ribosome pause sites relative to the codon frequency in the transcriptome. $n = 271$ pause sites with Day 4 pause score > 6 in 232 genes. **g – i**, Peptide motif associated with greater ribosome pausing in the indicated age comparisons.

Extended Data Fig. 4 Association of age-dependent ribosome pausing in yeast with disome formation.

a, Peptide motif associated with disome formation in young cells⁴⁷. **b**, Ribosome occupancy on *HAT2* with age-dependent ribosome pausing at position 188 with Trp in the A-site. **c**, Occupancy of monosomes and disomes on *HAT2* from disome footprint profiling of young cells⁴⁷. **d – h**, Average ribosome occupancy in young and aged yeast, with a lagging ribosome peak present in aged cells, at **d**, the position where disomes were most enriched in each transcript in young cells⁴⁷; **e**, inhibitory codon pairs previously associated with ribosome pausing⁴⁸ and disome formation⁴⁷; and **f – h**, tripeptide motifs previously associated with disome formation⁴⁷. The shaded region represents the 95% bootstrapped confidence interval.

Extended Data Fig. 5 Age-dependent ribosome pausing at polybasic regions.

a – b, Average ribosome occupancy at polybasic regions of **a**, monosomes and **b**, disomes in young WT yeast⁴⁷ showing length-dependent pausing and collisions. **c**, Average ribosome occupancy at polybasic regions consisting of 3 (left) or 5 (right) consecutive Lys or Arg (K/R) for young Day 0 and aged Day 4 yeast. $n = 3,729$ sites of 3 K/R in 2,198 genes, and 159 sites of 5 K/R in 152 genes. The shaded region represents the 95% bootstrapped confidence interval. Arrow indicates a putative increase in ribosome collision events with age at regions with 5 K/R. **d – e**, Average ribosome occupancy at polybasic regions of **d**, young Day 0 and **e**, aged Day 4 yeast. Also see panel c and Fig. 2c and 2d. **f**, Ribosome occupancy on *SIS1* with inset highlighting ribosome pausing and collision (arrow) at stretch of 6 K/R within a 10 residue window.

Extended Data Fig. 6 Age-dependent aberrant translation and aggregation of truncated nascent polypeptides in yeast.

a, Immunoblot of young Day 0 and aged Day 4 yeast of the indicated strains harboring the no-insert *GFP-RFP* control reporter. Truncated and full-length products are noted. $n \geq 3$ biological replicates with

representative example shown. For gel source data, see Supplementary Fig. 1. **b**, Increased formation of truncated polypeptides in chronologically aged yeast is not due to acidification of the media or respiratory conditions. Immunoblot of young Day 0 and aged Day 4 WT yeast harboring the *GFP-R12-FLAG-HIS3* ribosome pausing reporter and grown in standard media containing 2% glucose as carbon source, media buffered to pH 6.0, or media containing 3% glycerol. $n \geq 3$ biological replicates with representative example shown. For gel source data, see Supplementary Figure 2. **c**, Depletion of media nutrients during yeast chronological ageing does not increase formation of truncated polypeptides. Immunoblot of *GFP-K12-FLAG-HIS3* ribosome pausing reporter from young Day 0 and aged Day 4 WT or *ltn1Δ* yeast, as well as after swapping media (i.e. young Day 0 yeast cells grown in “aged” media from Day 4 cells). $n \geq 3$ biological replicates with representative example shown. For gel source data, see Supplementary Fig. 2. **d – f**, Fluorescence microscopy examining puncta formation in young (Y) Day 0 and aged (A) Day 4 yeast of WT and RQC mutant cells harboring **d**, GFP-RFP, or **e**, the ribosome pausing reporter with 12 K inserted between *GFP* and *RFP*. $n \geq 3$ biological replicates with representative examples shown. Scale bar: 3 μ m. **f**, Associated quantification of GFP^+RFP^- puncta from $n \geq 200$ cells from 3 biological replicates with mean \pm SEM. For cells harboring the K12 reporter: WT: $P = 2.2\text{e}^{-4}$, *ltn1Δ*: $P = 1.3\text{e}^{-4}$; *rqc2Δ*: $P = 9.6\text{e}^{-5}$, *hel2Δ*: $P = 1.7\text{e}^{-6}$, two-sided Welch’s *t*-test. **g**, Immunoblot of young Day 0 and aged Day 4 *ltn1Δ* yeast harboring the *GFP-K12-FLAG-HIS3* ribosome pausing reporter and probed with αGFP and αFLAG antibodies. Truncated, full-length, and high-molecular weight (HMW) species are noted. $n \geq 3$ biological replicates with representative example shown. An asterisk around 50 kDa indicates a non-specific band from αFLAG antibody. For gel source data, see Supplementary Fig. 2.

Extended Data Fig. 7 Age-dependent ribosome pausing, aberrant translation, and aggregation of endogenous yeast proteins and reporters.

a, Immunoblot of young Day 0 and aged Day 4 yeast harboring GFP-tagged *YTM1* that is either N-terminally tagged to monitor co-translational

products or C-terminally tagged to monitor post-translational degradation products. $n = 3$ biological replicates with representative example shown. For gel source data, see Supplementary Fig. 3. **b**, Fluorescence microscopy and quantification of GFP⁺ puncta of GFP-tagged *YTM1* in young and aged WT and *ltn1Δ* yeast cells. $n \geq 200$ cells from 3 biological replicates with representative examples shown and mean \pm s.e.m. WT N-term: $P = 2.0\text{e}^{-4}$; *ltn1Δ* N-term: $P = 2.3\text{e}^{-5}$; *ltn1Δ* C-term: $P = 2.8\text{e}^{-4}$, two-sided Welch's *t*-test. Scale bar: 3 μm . **c**, Immunoblot of young Day 0 and aged Day 4 yeast harboring N-terminally GFP-tagged *HAT2* showing increased truncated co-translational products during ageing. $n = 3$ biological replicates with representative example shown. For gel source data, see Supplementary Fig. 3. **d**, Quantification of GFP⁺RFP⁺ puncta in *hel2Δ* cells using the indicated reporter. $n \geq 200$ cells from 3 biological replicates with mean \pm s.e.m. K12: $P = 7.0\text{e}^{-4}$; R12: $P = 2.5\text{e}^{-4}$, two-sided Welch's *t*-test. **e**, Ribosome occupancy across the stalling reporter *GFP-K12-FLAG-HIS3* (left) and the no-insert control (right) of young Day 0 and aged Day 4 yeast, showing increased occupancy in 3' end of the stalling reporter coding sequence during ageing.

[Extended Data Fig. 8 Association of extended lifespan with improved RQC flux and reduced ribosome pausing and collision.](#)

a, RQC flux was assessed based on the abundance of the *GFP-R12-HIS3* ribosome pausing reporter⁶. RQC flux of the following four groups of genes was compared to yeast strains with deficient RQC (i.e. strains with reporter GFP abundance greater than 3 standard deviations above the mean of the total collection;⁶ $n = 39$): 1) long-lived CLS strains (strains with a chronological lifespan greater than 1 standard deviation above the mean of the total collection;⁶² $n = 150$, $P = 7.3\text{e}^{-22}$), 2) genes involved in the TOR pathway ($n = 31$, $P = 2.8\text{e}^{-20}$), 3) long-lived CLS strains not involved in the TOR pathway ($n = 142$, $P = 9.3\text{e}^{-23}$), and 4) long-lived RLS strains⁷⁸ ($n = 201$, $P = 1.3\text{e}^{-21}$). Statistical analysis was performed using two-sided Wilcoxon rank-sum tests. **b**, Heat map of gene expression analysis of Ribo-seq data showing Pearson's correlation coefficient between all yeast samples. **c**, Average ribosome occupancy at age-dependent pause sites ($n =$

5,951 sites in 937 genes) in the indicated strains, with the distribution of pause scores in aged (A) Day 4 WT and *sch9Δ* yeast cells on the right ($P = 2.5e^{-77}$, two-sided Wilcoxon rank-sum test). **d**, Peptide motif associated with positions in the translatome where ribosome pausing is greater in aged Day 4 WT yeast relative to aged Day 4 *sch9Δ* yeast. **e**, Average ribosome occupancy in WT and *sch9Δ* yeast at polybasic regions consisting of 6 consecutive Lys or Arg (K/R). $n = 60$ K/R sites in 58 genes. The shaded region represents the 95% bootstrapped confidence interval. Arrow indicates a putative increase in ribosome collision events. **f**, Ribosome occupancy on *HAT2* (top) and *YTM1* (bottom) in the indicated yeast strains around age-dependent ribosome pause sites (*HAT2*: position 188 with Trp in the A-site; *YTM1*: a stretch of 5 consecutive K/R). **g**, Fluorescence microscopy of GFP⁺RFP⁻ puncta formation in young (Y) Day 0 and aged (A) Day 4 yeast of WT and *sch9Δ* cells harboring the indicated reporter. $n \geq 3$ biological replicates with representative examples shown. Scale bar: 3 um. **h**, Immunoblot of young Day 0 and aged Day 4 yeast of WT or *sch9Δ* cells harboring the indicated reporter. Truncated and full-length products are noted. $n \geq 3$ biological replicates with representative example shown. For gel source data, see Supplementary Fig. 4. **i**, Relative gene expression of RQC machinery in the translatome of WT or *sch9Δ* cells comparing aged Day 4 yeast to young Day 0 yeast. ns = not significant; WT / *sch9Δ* cells: *ASC1*: $P = 4.1e^{-40} / 9.8e^{-26}$, *HEL2*: $P = 0.002 / 1.3e^{-4}$, *LTN1*: $P = 0.006 /$ ns, *RQC2*: $P = 1.2e^{-9} / 2.0e^{-20}$, two-sided Wald test with Benjamini-Hochberg correction.

Extended Data Fig. 9 Sequence specificity of age-dependent ribosome pausing in worms.

a, Amino acid residue frequency in the ribosomal P- and E-sites of age-dependent ribosome pause sites relative to the residue frequency in the transcriptome. $n = 587$ pause sites with Day 12 pause score > 10 in 437 genes. P-site Arg: $P = 0.01$, E-site Arg: $P = 0.04$, two-sided Fisher's exact test. **b**, Codon frequency in the ribosomal A-site of age-dependent ribosome pause sites relative to the codon frequency in the transcriptome. $n = 587$ pause sites with Day 12 pause score > 10 in 437 genes. **c – e**, Peptide motif associated with greater ribosome pausing in the indicated age comparisons.

f, Ribosome occupancy on *K12C11.6* with ribosome pausing at position 62 with Trp in the ribosomal active site. **g**, Average ribosome occupancy at polybasic regions consisting of 4 (left) or 5 (right) consecutive Lys or Arg (K/R). $n = 1,396$ sites of 4 K/R in 1,720 genes, and 369 sites of 5 K/R in 348 genes. The shaded region represents the 95% bootstrapped confidence interval.

Extended Data Fig. 10 Association of age-dependent aggregation and ribosome pausing in worms.

a, Investigating the association between age-dependent ribosome pausing and aggregation⁶⁵. Population $n = 742$ proteins with pause site, 6,219 proteins without a pause site. $P = 1.6e^{-23}$, two-sided Fisher's exact test. **b**, Enrichment of polybasic regions (4 or more consecutive Lys or Arg, and 2 or more consecutive Arg) in age-dependent aggregated proteins from two different datasets^{37,65}, and those proteins that also have age-dependent ribosome pausing. Walther, et al.: 4+ Lys/Arg: $P = 0.01$ (aggregate) and $P = 0.03$ (pause + agg.), 2+ Arg: $P = 4.9e^{-6}$ (aggregate) and $P = 4.8e^{-5}$ (pause + agg.); David, et al.: 4+ Lys/Arg: $P = 0.05$ (aggregate) and $P = 0.04$ (pause + agg.), 2+ Arg: $P = 0.02$ (aggregate) and $P = 0.01$ (pause + agg.), two-sided Fisher's exact test. **c**, Comparing the functional enrichment within aggregated proteins⁶⁵ to those that also have age-dependent ribosome pausing, displaying representative gene ontology terms (adjusted $P < 0.05$, Benjamini-Hochberg correction). Categories related to proteostasis are highlighted. Also see Supplementary Table 2. **d**, Aggregate abundance³⁷ over time of tRNA synthetases exhibiting both age-dependent aggregation and ribosome pausing. **e**, Relative gene expression of worm RQC orthologs (yeast ortholog in parentheses) in the translatome in aged Day 12 adult worms compared to young Day 1 worms. ns = not significant, *K04D7.1*: $P = 1.2e^{-14}$, *K07A12.1*: $P = 3.9e^{-18}$, *Y82E9BR.18*: $P = 5.4e^{-7}$, two-sided Wald test with Benjamini-Hochberg correction. **f**, Aggregate abundance³⁷ over time of worm RQC orthologs.

Supplementary information

Supplementary Information

Supplementary Discussion, elaborating on the implications of our study, and Supplementary Figs. 1–4, showing the uncropped source data of our immunoblotting experiments.

Reporting Summary

Supplementary Table 1

Age-dependent pause sites in worms and yeast. The age-dependent pause sites that were identified as having a statistically significant increase in ribosome pausing during ageing.

Supplementary Table 2

Gene Ontology analysis. The unfiltered gene ontology terms associated with (1) differential gene expression during ageing; (2) genes containing an age-dependent pause site; and (3) worm genes associated with age-dependent protein aggregation.

Supplementary Table 3

Polybasic regions in worms and yeast. The regions of 3, 4, 5 or 6+ consecutive Lys (K) or Arg (R) residues identified in coding sequences.

Rights and permissions

Reprints and Permissions

About this article

Cite this article

Stein, K.C., Morales-Polanco, F., van der Lienden, J. *et al.* Ageing exacerbates ribosome pausing to disrupt cotranslational proteostasis. *Nature* **601**, 637–642 (2022). <https://doi.org/10.1038/s41586-021-04295-4>

- Received: 01 August 2020
- Accepted: 01 December 2021
- Published: 19 January 2022
- Issue Date: 27 January 2022
- DOI: <https://doi.org/10.1038/s41586-021-04295-4>

Share this article

Anyone you share the following link with will be able to read this content:

[Get shareable link](#)

Sorry, a shareable link is not currently available for this article.

[Copy to clipboard](#)

Provided by the Springer Nature SharedIt content-sharing initiative

This article was downloaded by **calibre** from <https://www.nature.com/articles/s41586-021-04295-4>

- Article
- Open Access
- [Published: 05 January 2022](#)

Structural insights into inhibitor regulation of the DNA repair protein DNA-PKcs

- [Shikang Liang](#) [ORCID: orcid.org/0000-0002-6930-7882¹](#),
- [Sherine E. Thomas](#)¹ [nAff3](#),
- [Amanda K. Chaplin](#)^{1,4},
- [Steven W. Hardwick](#) [ORCID: orcid.org/0000-0001-9246-1864²](#),
- [Dimitri Y. Chirgadze](#) [ORCID: orcid.org/0000-0001-9942-0993²](#) &
- [Tom L. Blundell](#) [ORCID: orcid.org/0000-0002-2708-8992¹](#)

[Nature](#) volume 601, pages 643–648 (2022)

- 13k Accesses
- 37 Altmetric
- [Metrics details](#)

Subjects

- [Cryoelectron microscopy](#)
- [Drug development](#)
- [Kinases](#)
- [Small molecules](#)

Abstract

The DNA-dependent protein kinase catalytic subunit (DNA-PKcs) has a central role in non-homologous end joining, one of the two main pathways that detect and repair DNA double-strand breaks (DSBs) in humans^{1,2}. DNA-PKcs is of great importance in repairing pathological DSBs, making DNA-PKcs inhibitors attractive

therapeutic agents for cancer in combination with DSB-inducing radiotherapy and chemotherapy³. Many of the selective inhibitors of DNA-PKcs that have been developed exhibit potential as treatment for various cancers⁴. Here we report cryo-electron microscopy (cryo-EM) structures of human DNA-PKcs natively purified from HeLa cell nuclear extracts, in complex with adenosine-5'-(γ -thio)-triphosphate (ATP γ S) and four inhibitors (wortmannin, NU7441, AZD7648 and M3814), including drug candidates undergoing clinical trials. The structures reveal molecular details of ATP binding at the active site before catalysis and provide insights into the modes of action and specificities of the competitive inhibitors. Of note, binding of the ligands causes movement of the PIKK regulatory domain (PRD), revealing a connection between the p-loop and PRD conformations. Electrophoretic mobility shift assay and cryo-EM studies on the DNA-dependent protein kinase holoenzyme further show that ligand binding does not have a negative allosteric or inhibitory effect on assembly of the holoenzyme complex and that inhibitors function through direct competition with ATP. Overall, the structures described in this study should greatly assist future efforts in rational drug design targeting DNA-PKcs, demonstrating the potential of cryo-EM in structure-guided drug development for large and challenging targets.

[Download PDF](#)

Main

DNA double-strand breaks (DSBs) are the most toxic form of DNA damage. Two major pathways, homologous recombination (HR) and non-homologous end joining (NHEJ), repair DSBs¹. HR requires DNA end resection and is active during the S and G2 phases of the cell cycle, when a sister chromatid is available as a repair template⁵. By contrast, NHEJ directly ligates DNA ends efficiently in the absence of any template².

DSBs lead to increased genome instability and trigger cell death. This is widely exploited in the treatment of cancer in both radiotherapy using ionizing radiation (IR) and chemotherapy using topoisomerase II inhibitors^{2,3}. However, intrinsic DNA damage response and repair provide tumour cells with some protection. The pathological DSBs caused by IR and topoisomerase II inhibitors are mainly repaired by NHEJ, which requires DNA-dependent protein kinase (DNA-PK), comprising the DNA-dependent protein kinase catalytic subunit (DNA-PKcs) and a Ku70–Ku80 heterodimer^{6,7,8}. DNA-PKcs, which belongs to the phosphoinositide 3-kinase (PI3K)-related protein kinase (PIKK) family, has a central role in the regulation of NHEJ⁹. In combination with IR or genotoxic chemotherapy, inhibition of DNA-PK kinase activity can improve cancer therapy⁴. There have been many efforts to develop small-molecule inhibitors targeting the ATP-binding site of DNA-PKcs, informed by early

studies of synthetic small-molecule PI3K inhibitors¹⁰. The older-generation DNA-PK inhibitors, including CC115, KU-0060648, LY294002, LY3023414, NU7026 and NU7441, are effective, but all have different limited selectivity against PI3K and PIKK members (especially mTOR and PI3K γ). The newer-generation inhibitors, developed from large-scale screening, include VX-984, M3814 and AZD7648, which have better selectivity for DNA-PKcs^{4,10,11}.

So far, to our knowledge, no structures have been published of DNA-PKcs in complex with ATP or any inhibitor. This has limited understanding of both ATP binding to DNA-PKcs and the mode of action of the inhibitors, including drug candidates, and has posed a major hurdle to lead development. Here we report structures of DNA-PKcs in complex with adenosine-5'-(γ -thio)-triphosphate (ATP γ S) and other inhibitors, including the broad-spectrum PI3K inhibitor wortmannin, the older-generation DNA-PKcs selective inhibitor NU7441 and the newer-generation AZD7648 and M3814, which are in clinical trials. The structures allow understanding of DNA-PKcs binding to ATP before substrate binding and catalysis, the modes of action of the inhibitors and the mechanisms by which they achieve specificity. They also provide structural guidance for future drug design targeting DNA-PKcs, demonstrating the great potential of cryo-EM in structure-based drug discovery.

DNA-PKcs in complex with ATP γ S-(Mg²⁺)₂

DNA-PKcs purified from HeLa cell nuclear extract was incubated with ATP γ S and loaded onto a previously prepared grid with a support film of homemade single-layer graphene oxide (Extended Data Fig. 1). The overall resolution of the DNA-PKcs–ATP γ S complex is 3.40 Å with the local resolution of the catalytic core region better than 3 Å, showing clear density for the modelling of ATP γ S with two Mg²⁺ ions and demonstrating a similar structure to that of the homologue mTOR (Fig. 1a and Extended Data Fig. 2a)¹². The p-loop (residues 3729–3735) interacts closely with the phosphate groups of ATP γ S. Central to this is the interaction between the β -phosphate and the main chain NH group of Arg3733, together with the side chain of Ser3731. Lys3753 interacts with the α -phosphate of ATP γ S. Asn3927, Asp3941 and Glu3756 together coordinate the Mg²⁺ ions. The γ -phosphate of ATP γ S points towards the substrate-binding site. The ‘hinge loop’ between the N-lobe and C-lobe, together with the two lobes, constitutes a hydrophobic surface, formed by the side chains of Leu3751, Tyr3791, Trp3805, Leu3806 and Ile3940 and the main chain of Glu3804, to which the adenine moiety of ATP γ S can bind. Thus, ATP γ S and the Mg²⁺ ions bind in the ATP-binding groove of DNA-PKcs, coordinating the N- and C-lobes, including the p-loop, activation loop and catalytic loop of the kinase. Conformational changes include the outward rotation of both Trp3805 and Met3929, opening the pocket to accommodate ATP (Fig. 1b)¹³, and coordinated movements of α -helices in the head

unit of the protein (Fig. 1c). Notably, the PRD (residues 4009–4039) does not interfere with the interaction of DNA-PKcs with ATP and Mg²⁺. However, the α -helix of the PRD (residues 4009–4023) of DNA-PKcs is moved away from the substrate-binding site following ATP binding, partly relieving the blockage by PRD of the substrate-binding site required for subsequent catalysis (Fig. 1c).

Fig. 1: ATP γ S–(Mg²⁺)₂ interaction with and regulation of DNA-PKcs.

 figure 1



a. Coulomb potential map of the DNA-PKcs–ATP γ S–(Mg²⁺)₂ complex. The expanded view shows ATP γ S–(Mg²⁺)₂ binding in the ATP-binding groove. ATP γ S (light grey), together with two Mg²⁺ ions (fluorescent green), coordinates the N- and C-lobes, especially the p-loop (plum), catalytic loop (chocolate) and activation loop (azure) of DNA-PKcs (grey). The γ -phosphate group points towards the substrate-binding site. The top left image shows the clear Coulomb potential map for modelling of ATP γ S–

$(\text{Mg}^{2+})_2$, while the schematic representation below highlights the three units of DNA-PKcs and detailed composition of the head unit. **b**, Opening of the ATP-binding groove entrance. The residues on both sides of the ATP-binding groove entrance, Trp3805 and Met3929, exhibit an outward rotation that allows docking of the adenine moiety of ATP γ S. Apo DNA-PKcs (Protein Data Bank (PDB), [6ZFP](#)) is coloured pink with a mesh surface. **c**, ATP γ S– $(\text{Mg}^{2+})_2$ regulation on the PRD. PRD blocks the substrate-binding site. When ATP binds, PRD is tilted and moves away from its position in the apo structure.

DNA-PKcs in complex with inhibitors

DNA-PKcs was incubated with several DNA-PKcs inhibitors with different specificities (wortmannin, NU7441, AZD7648 and M3814), to investigate protein–ligand interactions (Supplementary Table 1). The overall resolutions of the structures range from 2.96 Å to 3.33 Å. In all the structures, the kinase core has the highest local resolution, allowing the inhibitors to be unequivocally modelled (Fig. 2a).

Fig. 2: ATP competitive inhibitors (wortmannin, NU7441, AZD7648 and M3814) and their modes of binding to DNA-PKcs.

 **figure 2**

a, Inhibitors investigated and their corresponding Coulomb potential maps. **b**, Binding of wortmannin (green) to the ATP-binding site, where it is covalently modified by the primary amine group of Lys3753. **c**, Binding of NU7441 (blue) to the ATP-binding site. **d**, Binding of AZD7648 (purple) to the ATP-binding site. **e**, Binding of M3814 (cyan) to the ATP-binding site. DNA-PKcs is shown in grey.

Wortmannin is one of the early DNA-PK inhibitors used for kinase inhibition¹⁴. In the cryo-EM structure, wortmannin packs on one side, mainly against the N-lobe of DNA-PKcs (Leu3751, Ile3803 and Trp3805), while on the other side it packs against the C-lobe (Met3929 and Asp3940) (Fig. [2b](#)). One edge of the compound is facing the deep

pocket of the ATP-binding site, and the opposite edge is exposed to solvent. The primary amine (ε -amino group) of Lys3753 forms a covalent C–N bond with C19 in the furan ring of wortmannin (Fig. 2a), irreversibly inhibiting kinase activity. The ATP-binding site of DNA-PKcs has close structural complementarity to wortmannin. The C14 methyl resides in a pocket formed by Leu3751, Ile3803 and Trp3805, while the C10 methyl fits into a pocket formed by Met3729, Pro3735 and Leu3751 (Fig. 2b). There is no density corresponding to the acetoxy group attached to C11 of wortmannin, as was observed in the published structure of wortmannin in complex with porcine PI3K γ (Extended Data Fig. 3a)¹⁵.

Compared with wortmannin, NU7441 is a more selective inhibitor, developed from the earlier inhibitors NU7026 and LY294002, which were derived from the broad-spectrum protein kinase flavonoid inhibitor quercetin¹⁶. The chromone core and morpholino ring of NU7441 bind in the centre of the deepest pocket formed by Leu3751, Tyr3791, Ile3803, Trp3805, Leu3806, Ile3940 and Met3929, within which O1 and O27 of NU7441 form hydrogen bonds with the peptide backbones of Asp3941 and Leu3806 (Fig. 2c). The dibenzothiophene group interacts with the N-lobe and docks in the hydrophobic groove of Met3729, Pro3735 and Leu3751 (Fig. 2c).

AZD7648 is a recently developed DNA-PK inhibitor shown to be highly selective and to enhance the efficacy of doxorubicin and IR^{11,17}. Moreover, AZD7648 was identified as a potential combinational therapy with the PARP inhibitor olaparib and is currently under clinical trial for advanced malignancies (trial identifier, [NCT03907969](#))¹¹. The developers of AZD7648 took advantage of a previously published crystal structure of AZD7648 bound to PI3K γ ¹⁷. In the DNA-PKcs–AZD7648 complex, the compound binds the hinge loop (Fig. 2d). The triazolopyridine moiety with a methyl group lies in the deep hydrophobic pocket formed by Tyr3791, Ile3803, Leu3806 and Ile3940. The purine moiety docks in the narrow tunnel formed by Trp3805, Leu3806 and Met3929. Similarly to the PI3K γ –AZD7648 complex, the N3 hydrogen of AZD7648 (the aniline NH) forms bonds with the backbone oxygen of Glu3804 and N7 accepts the hydrogen from the backbone NH group of Leu3806 (ref. [17](#)). N6 in the triazolopyridine moiety also binds to the backbone NH group of Asp3941. There is a further hydrogen bond in the case of DNA-PKcs–AZD7648: N5 forms a bond with the primary amine group of Lys3753. Comparison of the two structures shows a 90° rotation of the indole ring for Trp812 in PI3K γ relative to Trp3805 in DNA-PKcs, which in DNA-PKcs not only provides a better hydrophobic binding surface but also aligns nicely to the AZD7648 purine ring, leading to a π stacking interaction that enhances affinity (Extended Data Fig. 3b).

M3814 (peposertib or nedisertib) is another recently developed DNA-PK selective inhibitor^{18,19}. Preclinical studies have revealed its synergy with radiotherapy and chemotherapies using doxorubicin and etoposide²⁰. The compound was shown to be

well tolerated with modest efficacy in unselected tumours in phase 1 clinical trial results (trial identifier, [NCT02316197](#))¹⁹; M3814 is currently in four phase 2 clinical trials targeting different cancers (trial identifiers, [NCT03770689](#), [NCT04068194](#), [NCT04071236](#) and [NCT04172532](#)). According to our structure, the quinazoline and morpholino moieties of the compound fit well into the deepest, largely hydrophobic pocket formed by the side chains of Leu3751, Tyr3791, Val3793, Ile3803, Trp3805, Leu3806, Ile3938 and Ile3940 and the main chains of Glu3804 and Asp3941 (Fig. 2e). The chloro-fluorobenzene ring rotates by ~60° and points towards the N-lobe, facing the side chains of Met3729, Ser3731, Pro3735, Leu3751 and Lys3753. The remaining moiety containing the pyridazine ring then rotates back to be almost parallel to the quinazoline plane, lying in the groove of Met3729, Trp3805, Thr3811, Asn3926 and Met3929.

Comparison of binding modes

All the inhibitors studied target the ATP-binding groove of DNA-PKcs, overlapping with the ATPγS-binding site (Fig. 3). Among them, wortmannin has the maximum overlap. Compared with ATPγS, wortmannin has greater complementarity to the binding site (Fig. 3a), binding deeper into the ATP adenine-moiety pocket, with its two protruding methyl groups fitting better into the hydrophobic pocket on the surface of the N-lobe.

Fig. 3: Comparisons of the binding modes among ATPγS–(Mg²⁺)₂ and the four inhibitors.

 figure 3

a, Comparison of the binding modes of ATPγS–(Mg²⁺)₂ and wortmannin in DNA-PKcs. Top, binding conformations of ATPγS–(Mg²⁺)₂ (light grey, ATPγS; fluorescent green, Mg²⁺ ions) and wortmannin (green). Bottom, conformational differences in the binding groove of DNA-PKcs between ATPγS–(Mg²⁺)₂ (grey) and wortmannin (green). **b**, Comparison of the binding modes of ATPγS–(Mg²⁺)₂ and NU7441 in

DNA-PKcs. Top, binding conformations of ATP γ S–(Mg $^{2+}$)₂ and NU7441 (blue). Bottom, conformational differences in the binding groove of DNA-PKcs between ATP γ S–(Mg $^{2+}$)₂ and NU7441 (blue). **c**, Comparison of the binding modes of ATP γ S–(Mg $^{2+}$)₂ and AZD7648 in DNA-PKcs. Top, binding conformations of ATP γ S–(Mg $^{2+}$)₂ and AZD7648 (purple). Bottom, conformational differences at the binding groove of DNA-PKcs between ATP γ S–(Mg $^{2+}$)₂ and AZD7648 (purple). **d**, Comparison of the binding modes of ATP γ S–(Mg $^{2+}$)₂ and M3814 in DNA-PKcs. Top, binding conformations of ATP γ S–(Mg $^{2+}$)₂ and M3814 (cyan). Bottom, conformational differences at the binding groove of DNA-PKcs between ATP γ S–(Mg $^{2+}$)₂ and M3814 (cyan).

NU7441 binds quite differently from ATP γ S to the ATP-binding groove. The chromone core and the morpholino ring of NU7441 bind to the pocket occupied by the adenine moiety and α -phosphate group of ATP γ S (Fig. [3b](#)). The dibenzothiophene moiety overlaps with the ATP γ S ribose and inserts into the groove between the p-loop and the hinge loop, which is formed by the 120° inward swinging of Met3729.

In the case of AZD7648, the triazolopyridine moiety with a methyl group docks deeper than the adenine moiety of ATP γ S in the same pocket (Fig. [3c](#)). While the tetrahydropyran ring occupies the same space as the ATP γ S ribose, the purine ring of AZD7648 fits nicely into the empty groove between Trp3805 and Met3929.

M3814 has the least overlap with ATP γ S in the binding groove. The quinazoline and morpholine parts reach deeper into the pocket of the adenine moiety and α -phosphate group of ATP γ S (Fig. [3d](#)). Moreover, when the compound binds, the side chain of Trp3805 moves inwards, changing the open adenine-binding site to an enclosed hydrophobic pocket, in which the morpholine ring of M3814 is fully accommodated. The chloro-fluorobenzene ring overlaps with the ATP γ S α -phosphate and points towards the N-lobe, causing an uplift of the p-loop and the region around Lys3753. The pyridazine ring is adjacent to the ATP γ S ribose but closer to the C-lobe, where Asn3926 rotates towards M3814 to form a small groove for docking of the drug.

The different inhibitors result in varying conformational changes that each modify the surface properties to optimize binding interactions with the ligand. There are two key regions of conformational change. One is the p-loop, where the conformation is guided by the residues with their side chains facing the ATP-binding groove. In apo DNA-PKcs, the position of the p-loop is restrained by the flanking β -sheets and the electrostatic interaction between Arg3733 and Asp3587 (Fig. [4a](#)). The conformations of Met3729, Ser3731 and Pro3735 change according to the different chemical properties of the ligands, resulting in an up–down movement of the p-loop like a ‘spring leaf’. This movement induces corresponding conformational changes in the

flanking β -sheets that are passed on to the hydrophobic core of the DNA-PKcs head region (Fig. 4b). The resulting conformational changes of DNA-PKcs, especially the movement of the PRD, appear concerted (Fig. 4c). The other key region of conformational change is at Trp3805 on the hinge loop, which guards the entrance to the main pocket (Fig. 4b). The indole side chain of Trp3805 contributes to the stacking effects and hydrophobic interactions with ligands, and its movement impacts the architecture of the binding site.

Fig. 4: Conformational changes resulting from binding of ATP γ S–(Mg $^{2+}$)₂ and competitive inhibitors.

 figure 4



a, The p-loop conformation in apo DNA-PKcs (pink) is fixed by the flanking β -sheets and the electrostatic interaction between Arg3733 and Asp3587. **b**, Two views, related by rotation of 120°, of the effect of binding different ligands on the conformation of the p-loop. These conformational changes resemble the movement of a spring leaf. The corresponding movement of the flanking β -sheets transmits a conformational

change to the core DNA-PKcs kinase region. Grey, ATP γ S; green, wortmannin; blue, NU7441; purple, AZD7648; cyan, M3814. **c**, Orthogonal views of the p-loop conformations regulating the conformation of the DNA-PKcs kinase region, including the PRD.

Ligand regulation and future development

Understanding of the mechanism of DNA-PKcs in DNA repair has recently been advanced through structural studies using crystallography and cryo-EM^{13,21,22,23,24,25,26}. However, technical challenges and limitations have been the major hurdle in biochemical and structural investigations. The structure of DNA-PKcs–ATP γ S–(Mg²⁺)₂ described here shows how ATP γ S and two Mg²⁺ ions occupy the ATP-binding groove, coordinating the p-loop, activation loop and catalytic loop. The presence of ATP γ S–(Mg²⁺)₂ results in movement of the PRD to partly relieve the blockage of the substrate-binding site before catalysis. This is consistent with the observation that DNA-PKcs can be active in vitro in the absence of assembly of the DNA-PK holoenzyme and explains why the kinase activity of the C terminus of DNA-PKcs is not stimulated by Ku70–Ku80 and DNA²⁷. Together with the structures of the DNA-PKcs–inhibitor complexes, this reveals that PRD conformation can be regulated by spring leaf-like p-loop movements. Moreover, we obtained a structure for the DNA-PK–ATP γ S–(Mg²⁺)₂ complex at a medium resolution of 4.3 Å (Extended Data Fig. 4a, b). In this structure, the kinase domain of DNA-PKcs fits nicely into the corresponding region of the map of DNA-PK–ATP γ S–(Mg²⁺)₂, indicating that the binding modes of the ligands in the single polypeptide chain of DNA-PKcs and the holoenzyme are similar. Moreover, we conducted electrophoretic mobility shift assays (EMSA) to confirm that the inhibitors do not stop formation of the DNA-PK holoenzyme (Extended Data Fig. 4d). In addition, structural and single-molecule studies have demonstrated that binding of ligands does not affect dimerization of the long-range NHEJ complex involving DNA-PKcs^{24,28}. Therefore, DNA-PKcs inhibitors should not structurally disturb high-order complex formation. They function via direct ATP competition.

Current drug candidates have been successfully developed from large-scale screening targeting the ATP-binding site, but molecular details of the modes of action of such candidates have been unclear^{4,10}. In our structures, all inhibitors investigated are less elongated than ATP and do not extend beyond the position of the α -phosphate group. However, the inhibitors more effectively target the deep hydrophobic pocket where the adenine moiety of ATP is located. The inhibitors all have large hydrophobic groups that bind deeply into this pocket, achieving high occupancy. It appears that the occupancy level of the pocket is related to selectivity: NU7441, AZD7648 and M3814

display higher occupancy than wortmannin. Comparisons between the older-generation inhibitor NU7441 and the newer-generation inhibitors AZD7648 and M3814 indicate that selectivity can also be improved by exploring the entrance tunnel between the N- and C-lobes and the peripheral region on the C-lobe (Fig. 3c,d). Comparison of the structures of DNA-PKcs–ligand complexes with those of mTOR–ligand complexes demonstrates that inhibitor specificity is related to the p-loop conformation and composition (Extended Data Fig. 2a–c). The ligand-binding pockets of DNA-PKcs and mTOR are highly similar, with the main differences lying in the p-loops (Extended Data Fig. 2b). In DNA-PKcs, the p-loop is closer to the C-lobe than it is in mTOR. Together with the extended side chain of Met3729, the p-loop of DNA-PKcs creates a narrower path to the binding pocket, the effect of which can be visualized through comparison of ATP γ S–(Mg $^{2+}$)₂ binding modes (Supplementary Fig. 2a,b). While the adenine moieties overlap nicely in the two structures, the ribose moiety and phosphate groups have different binding modes due to p-loop differences (Extended Data Fig. 2b).

Future inhibitor development can also be guided using our in-house hotspot-mapping program²⁹. Hotspots can be defined as areas within the protein that make an essential contribution to the overall binding of small molecules³⁰. The predicted hotspot map of the catalytic core of DNA-PKcs exhibits a large apolar region at the centre, juxtaposed with polar hydrogen-bond donor and acceptor regions (Extended Data Fig. 5a). The hydrophobic core overlaps with the adenosine moiety of ATP γ S as well as the central heterocyclic scaffold of the inhibitors described in this study. Strong polar regions can be observed adjacent to this hydrophobic core, close to the p-loop, and overlap with the ATP phosphate group-binding site (Extended Data Fig. 5a). A second polar hotspot region is seen at the edge of the ATP pocket close to the catalytic loop. Of note, the more selective inhibitors examined in this study, AZD7648 and M3814, have functional groups that engage this region (Extended Data Fig. 5a,b). The polar contacts mediated by the side chain of Thr3811 and the backbone carbonyl of Asn3926 here allow compounds AZD7648 and M3814, respectively, to adopt a binding mode distinct from those of ATP, wortmannin and NU7441 by extending outside the ATP-binding groove (Extended Data Fig. 5b). It is tempting to speculate that interactions at this part of the ATP pocket, close to the catalytic loop, could further contribute to selective inhibition of DNA-PKcs in addition to the p-loop conformation. Therefore, introducing functional groups to engage Asn3926, Asn3927, Thr3811 and Thr3809 in this region of the active site may potentially help further enhance selective inhibition of DNA-PKcs.

Furthermore, now that it is possible to obtain high-resolution structures for DNA-PKcs–ligand complexes routinely (Extended Data Fig. 6), structure-guided drug discovery can exploit other specific pockets of DNA-PKcs in the development of allosteric inhibitors or proteolysis-targeting chimeric (PROTAC) drugs with enhanced

potency and selectivity^{31,32}. Degradation of DNA-PKcs eliminates not only its kinase activity but also the stage provided for downstream NHEJ and DNA damage response signalling^{13,32,33}. However, PROTAC drugs cannot be guaranteed to be beneficial as previous studies have shown that inhibiting kinase activity has more potent effects than knockdown or knockout³⁴. Nevertheless, with optimized sample preparation and the reported cryo-EM structures, future drugs could be further developed to target allosteric sites instead of, or in addition to, the conserved kinase catalytic core, to achieve better specificity for DNA-PKcs.

Methods

Purification of DNA-PKcs

DNA-PKcs was purified natively from HeLa cell nuclear extracts (Ipracell) as previously described²¹. The entire purification process was conducted at 4 °C, and samples were kept on ice. Frozen pellets of nuclear extract were thawed and dialysed in precooled buffer (20 mM HEPES pH 7.6, 100 mM NaCl, 10% glycerol (vol/vol), 0.5 mM EDTA, 2 mM MgCl₂, 5 mM DTT, 0.2 mM PMSF), and purification of DNA-PKcs was carried out in four steps of ion exchange chromatography in the sequential order of HiTrap Q, HiTrap Heparin, Mono-S and Mono-Q columns. A salt gradient of 0.1 M to 1 M NaCl was used to elute DNA-PKcs from the columns. A final gel filtration step with a Superose-6 column was used to check size, and the buffer was exchanged to the final storage buffer (20 mM HEPES pH 7.6, 200 mM NaCl, 0.5 mM EDTA, 2 mM MgCl₂, 5 mM DTT). Purified DNA-PKcs was snap frozen in liquid nitrogen and stored at –80 °C.

Sample preparation and cryo-EM data acquisition

DNA-PKcs was incubated on ice for 1 h with 1 mM target ligand (ATPγS, wortmannin, NU7441, AZD7648 or M3814) and then loaded onto a Quantifoil R1.2/1.3 grid with graphene oxide. For the homemade single-layer graphene oxide, the grids were previously glow discharged for 120 s at a current of 15 mA and the graphene oxide preparation was based on the previous protocol of Bokori-Brown et al.³⁵. Protein samples were left to adhere for 20 s and later blotted and plunge-frozen in liquid ethane using the FEI Vitrobot Mark IV system (ThermoFisher Scientific) at 4 °C and 100% humidity. The grids were transferred to a Titan Krios electron microscope operating at a voltage of 300 kV with a K3 direct electron detector (Gatan) at the cryo-EM facility of the Department of Biochemistry, University of Cambridge. All datasets were collected in super-resolution counting mode with a magnification of × 130,000.

Image processing and model refinement

In general, data were processed using Warp and cryoSPARC^{36,37,38}. CTF correction, motion correction and particle autoselection were carried out using Warp. The selected particles were then subjected to cryoSPARC ab initio reconstruction to remove ice, contamination and aggregated or degraded protein components and generate the initial three-dimensional model of the complex. The nice class from ab initio reconstruction was selected and optimized through iterative rounds of heterogeneous refinement in cryoSPARC to further remove bad particles. The final optimized class of particles was then further refined using homogeneous refinement, global CTF refinement and non-uniform refinement in cryoSPARC. All reported resolutions were determined based on the ‘gold standard’ of 0.143 for the Fourier shell correlation criterion³⁹. To model the complexes, our previously published cryo-EM structure of apo DNA-PKcs (PDB, [6ZFP](#)) was used as an initial template for the protein¹³. The template was first rigid-body-fitted into the maps in CHIMERA and CHIMERAX followed by real-space refinement in PHENIX^{40,41,42}. The ligand was then modelled into the corresponding density in an EM map in COOT, followed by further refinement rounds in PHENIX and model building in COOT^{42,43}.

Reporting summary

Further information on research design is available in the [Nature Research Reporting Summary](#) linked to this paper.

Data availability

Cryo-EM maps have been deposited in the Electron Microscopy Data Bank under accession numbers [EMDB-13062](#) (DNA-PKcs in complex with NU7441), [EMDB-13064](#) (DNA-PKcs in complex with ATPγS), [EMDB-13067](#) (DNA-PKcs in complex with wortmannin), [EMDB-13068](#) (DNA-PKcs in complex with AZD7648), [EMDB-13069](#) (DNA-PKcs in complex with M3814) and [EMDB-13443](#) (DNA-PK in complex with ATPγS). Model coordinates have been deposited in the Protein Data Bank under accession numbers [7OTM](#) (DNA-PKcs in complex with NU7441), [7OTP](#) (DNA-PKcs in complex with ATPγS), [7OTV](#) (DNA-PKcs in complex with wortmannin), [7OTW](#) (DNA-PKcs in complex with AZD7648) and [7OTY](#) (DNA-PKcs in complex with M3814). The Hotspots application programming interface (API) is available from <https://github.com/prcurran/hotspots> under an MIT license, dependent on the commercial CSD Python API.

References

1. 1.

Jackson, S. P. & Bartek, J. The DNA-damage response in human biology and disease. *Nature* **461**, 1071–1078 (2009).

2. 2.

Lieber, M. R. The mechanism of double-strand DNA break repair by the nonhomologous DNA end-joining pathway. *Annu. Rev. Biochem.* **79**, 181–211 (2010).

3. 3.

O'Connor, M. J. Targeting the DNA damage response in cancer. *Mol. Cell* **60**, 547–560 (2015).

4. 4.

Mohiuddin, I. S. & Kang, M. H. DNA-PK as an emerging therapeutic target in cancer. *Front. Oncol.* **9**, 635 (2019).

5. 5.

Sung, P. & Klein, H. Mechanism of homologous recombination: mediators and helicases take on regulatory functions. *Nat. Rev. Mol. Cell Biol.* **7**, 739–750 (2006).

6. 6.

Yang, F., Teves, S. S., Kemp, C. J. & Henikoff, S. Doxorubicin, DNA torsion, and chromatin dynamics. *Biochim. Biophys. Acta Rev. Cancer* **1845**, 84–89 (2014).

7. 7.

Davis, A. J., Chen, B. P. C. & Chen, D. J. DNA-PK: a dynamic enzyme in a versatile DSB repair pathway. *DNA Repair* **17**, 21–29 (2014).

8. 8.

Chang, H. H. Y., Pannunzio, N. R., Adachi, N. & Lieber, M. F. R. Non-homologous DNA end joining and alternative pathways to double-strand break repair. *Nat. Rev. Mol. Cell Biol.* **18**, 495–506 (2017).

9. 9.

Jette, N. & Lees-Miller, S. P. The DNA-dependent protein kinase: a multifunctional protein kinase with roles in DNA double strand break repair and mitosis. *Prog. Biophys. Mol. Biol.* **117**, 194–205 (2015).

10. 10.

Harnor, S. J., Brennan, A. & Cano, C. Targeting DNA-dependent protein kinase for cancer therapy. *ChemMedChem* **12**, 895–900 (2017).

11. 11.

Fok, J. H. L. et al. AZD7648 is a potent and selective DNA-PK inhibitor that enhances radiation, chemotherapy and olaparib activity. *Nat. Commun.* **10**, 5065 (2019).

12. 12.

Yang, H. et al. MTOR kinase structure, mechanism and regulation. *Nature* **497**, 217–223 (2013).

13. 13.

Chaplin, A. K. et al. Dimers of DNA-PK create a stage for DNA double-strand break repair. *Nat. Struct. Mol. Biol.* **28**, 13–19 (2021).

14. 14.

Boulton, S., Kyle, S., Yalçintepe, L. & Durkacz, B. W. Wortmannin is a potent inhibitor of DNA double strand break but not single strand break repair in Chinese hamster ovary cells. *Carcinogenesis* **17**, 2285–2290 (1996).

15. 15.

Walker, E. H. et al. Structural determinants of phosphoinositide 3-kinase inhibition by wortmannin, LY294002, quercetin, myricetin, and staurosporine. *Mol. Cell* **6**, 909–919 (2000).

16. 16.

Hardcastle, I. R. et al. Discovery of potent chromen-4-one inhibitors of the DNA-dependent protein kinase (DNA-PK) using a small-molecule library approach. *J. Med. Chem.* **48**, 7829–7846 (2005).

17. 17.

Goldberg, F. W. et al. The discovery of 7-methyl-2-[(7-methyl[1,2,4]triazolo[1,5-*a*]pyridin-6-yl)amino]-9-(tetrahydro-2*H*-pyran-4-yl)-7,9-dihydro-8*H*-purin-8-one (AZD7648), a potent and selective DNA-dependent protein kinase (DNA-PK) inhibitor. *J. Med. Chem.* **63**, 3461–3471 (2020).

18. 18.

Zenke, F. T. et al. Pharmacologic inhibitor of DNA-PK, M3814, potentiates radiotherapy and regresses human tumors in mouse models. *Mol. Cancer Ther.* **19**, 1091–1101 (2020).

19. 19.

van Bussel, M. T. J. et al. A first-in-man phase 1 study of the DNA-dependent protein kinase inhibitor pebosertib (formerly M3814) in patients with advanced solid tumours. *Br. J. Cancer* **124**, 728–735 (2021).

20. 20.

Wise, H. C. et al. Activity of M3814, an oral DNA-PK inhibitor, in combination with topoisomerase II inhibitors in ovarian cancer models. *Sci. Rep.* **9**, 18882 (2019).

21. 21.

Sibanda, B. L., Chirgadze, D. Y., Ascher, D. B. & Blundell, T. L. DNA-PKcs structure suggests an allosteric mechanism modulating DNA double-strand break repair. *Science* **355**, 520–524 (2017).

22. 22.

Chen, X. et al. Structure of an activated DNA-PK and its implications for NHEJ. *Mol. Cell* **81**, 801–810 (2021).

23. 23.

Sharif, H. et al. Cryo-EM structure of the DNA-PK holoenzyme. *Proc. Natl Acad. Sci. USA* **114**, 7367–7372 (2017).

24. 24.

Chen, S. et al. Structural basis of long-range to short-range synaptic transition in NHEJ. *Nature* <https://doi.org/10.1038/s41586-021-03458-7> (2021).

25. 25.

Yin, X., Liu, M., Tian, Y., Wang, J. & Xu, Y. Cryo-EM structure of human DNA-PK holoenzyme. *Cell Res.* **27**, 1341–1350 (2017).

26. 26.

Chaplin, A. K. et al. Cryo-EM of NHEJ supercomplexes provides insights into DNA repair. *Mol. Cell* **81**, 3400–3409 (2021).

27. 27.

Davis, A. J., Lee, K. J. & Chen, D. J. The N-terminal region of the DNA-dependent protein kinase catalytic subunit is required for its DNA double-stranded break-mediated activation. *J. Biol. Chem.* **288**, 7037–7046 (2013).

28. 28.

Graham, T. G. W., Walter, J. C. & Loparo, J. J. Two-stage synapsis of DNA ends during non-homologous end joining. *Mol. Cell* **61**, 850–858 (2016).

29. 29.

Radoux, C. J., Olsson, T. S. G., Pitt, W. R., Groom, C. R. & Blundell, T. L. Identifying interactions that determine fragment binding at protein hotspots. *J. Med. Chem.* **59**, 4314–4325 (2016).

30. 30.

Hajduk, P. J., Huth, J. R. & Tse, C. Predicting protein druggability. *Drug Discov.* **10**, 1675–1682 (2005).

31. 31.

Lai, A. C. & Crews, C. M. Induced protein degradation: an emerging drug discovery paradigm. *Nat. Rev. Drug Discov.* **16**, 101–114 (2017).

32. 32.

Sun, X. et al. Protacs: great opportunities for academia and industry. *Signal Transduct. Target. Ther.* **4**, 64 (2019).

33. 33.

Liang, S. et al. Stages, scaffolds and strings in the spatial organisation of non-homologous end joining: insights from X-ray diffraction and cryo-EM. *Prog. Biophys. Mol. Biol.* **163**, 60–73 (2020).

34. 34.

Menolfi, D. & Zha, S. ATM, ATR and DNA-PKcs kinases—the lessons from the mouse models: inhibition ≠ deletion. *Cell Biosci.* **10**, 8 (2020).

35. 35.

Bokori-Brown, M. et al. Cryo-EM structure of lysenin pore elucidates membrane insertion by an aerolysin family protein. *Nat. Commun.* **7**, 11293 (2016).

36. 36.

Tegunov, D. & Cramer, P. Real-time cryo-electron microscopy data preprocessing with Warp. *Nat. Methods* **16**, 1146–1152 (2019).

37. 37.

Punjani, A., Rubinstein, J. L., Fleet, D. J. & Brubaker, M. A. CryoSPARC: algorithms for rapid unsupervised cryo-EM structure determination. *Nat. Methods* **14**, 290–296 (2017).

38. 38.

Punjani, A., Brubaker, M. A. & Fleet, D. J. Building proteins in a day: efficient 3D molecular structure estimation with electron cryomicroscopy. *IEEE Trans. Pattern Anal. Mach. Intell.* **39**, 706–718 (2017).

39. 39.

Rosenthal, P. B. & Henderson, R. Optimal determination of particle orientation, absolute hand, and contrast loss in single-particle electron cryomicroscopy. *J. Mol. Biol.* **333**, 721–745 (2003).

40. 40.

Pettersen, E. F. et al. UCSF Chimera—a visualization system for exploratory research and analysis. *J. Comput. Chem.* **25**, 1605–1612 (2004).

41. 41.

Pettersen, E. F., et al. UCSF ChimeraX: structure visualization for researchers, educators, and developers. *Protein Sci.* **30**, 70-82 (2021).

42. 42.

Afonine, P. V. et al. Real-space refinement in PHENIX for cryo-EM and crystallography. *Acta Crystallogr. D* **74**, 531–544 (2018).

43. 43.

Emsley, P., Lohkamp, B., Scott, W. G. & Cowtan, K. Features and development of Coot. *Acta Crystallogr. D* **66**, 486–501 (2010).

Acknowledgements

We thank L. Cooper and the cryo-EM facility in the Biochemistry Department, University of Cambridge, for their help with sample preparation, screening and data collection. We thank Q. Wu, T. Ochi and T.M. De Oliveira for discussion on NHEJ and DNA-PKcs. We thank B. Mao, J. He, T. Dendooven, M. Ma and B. Luisi for advice and discussion on support film and sample preparation. We are also grateful for an Investigator Award from the Wellcome Trust (200814/Z/16/Z; 2016–) for support of this research. S.E.T. has been funded by the Cystic Fibrosis Trust (RG92393) and Fondation Botnar (grant project no. 6063).

Author information

Author notes

1. Sherine E. Thomas

Present address: Department of Pathology, University of Cambridge, Cambridge, UK

Affiliations

1. Department of Biochemistry, University of Cambridge, Cambridge, UK

Shikang Liang, Sherine E. Thomas, Amanda K. Chaplin & Tom L. Blundell

2. Cryo-EM Facility, Department of Biochemistry, University of Cambridge, Cambridge, UK

Steven W. Hardwick & Dimitri Y. Chirgadze

3. Leicester Institute for Structural and Chemical Biology, Department of Molecular and Cell Biology, University of Leicester, Leicester, UK

Amanda K. Chaplin

Contributions

S.L. and A.K.C. purified the protein. S.L. prepared the cryo-EM samples, collected and processed the cryo-EM data and modelled the protein structures. S.E.T. provided expertise with structure modelling and hotspot analysis. S.W.H. and D.Y.C. helped collect data and provided expertise on cryo-EM structure analysis. S.L. wrote the first draft of the manuscript. T.L.B. directed the study, provided advice and edited the manuscript. All authors commented on the final version of the manuscript.

Corresponding authors

Correspondence to [Shikang Liang](#) or [Tom L. Blundell](#).

Ethics declarations

Competing interests

The authors declare no competing interests.

Peer review information

Nature thanks the anonymous reviewers for their contribution to the peer review of this work.

Additional information

Publisher's note Springer Nature remains neutral with regard to jurisdictional claims in published maps and institutional affiliations.

Extended data figures and tables

Extended Data Fig. 1 Home-made graphene oxide grid for DNA-PKcs/ATP γ S-Mg $^{2+}$ ₂ complex.

a, TEM image of grid hole with suspended graphene oxide on. **b**, Cryo-EM micrograph of DNA-PKcs/ ATP γ S-Mg $^{2+}$ ₂ complex. **c**, Fourier transform of b with the graphene oxide reciprocal lattice circled in white dashed line. The graphene-oxide grid is replicated for the DNA-PKcs/complex studies.

Extended Data Fig. 2 Comparisons between DNA-PKcs and mTOR in complex with ligands.

a, Comparison of ATP γ S-Mg $^{2+}$ ₂ binding in the ligand binding grooves of DNA-PKcs and mTOR (PDB entry: 4JSP)¹². The PIKK regulatory domain (PRD) of mTOR is lifted and removed completely from the substrate-binding site while the PRD of DNA-PKcs still docks there, although it is lifted compared to apo DNA-PKcs. DNA-PKcs/ATP γ S-Mg $^{2+}$ ₂ complex is coloured grey while mTOR/ATP γ S-Mg $^{2+}$ ₂ is coloured orange. PRDs of DNA-PKcs and mTOR are circled in dashed lines. **b**, Close-up view of the ligand-binding pocket of DNA-PKcs and mTOR. Residues contributing to the pocket are highly conserved between DNA-PKcs and mTOR. The major differences lie in the p-loop, including residue composition and loop conformation. The residues that differ are labeled in the figure. Compared to that of mTOR, the p-loop of DNA-PKcs is positioned more inward and closer to the C-lobe, leaving a narrower channel for the ligands to enter. Moreover, DNA-PKcs p-loop pushes the ligands more toward the C-lobe as the ribose moiety and the phosphate groups of ATP γ S-Mg $^{2+}$ ₂ rotate towards the C-lobe compared to those of mTOR. The adenine moieties overlay well as the deep hydrophobic pockets are highly structurally similar. **c**, Comparison of mTOR in complex with specific inhibitor Torin2 (PDB code: 4JSX) and pp242 (PDB code: 4JT5) and DNA-PKcs in complex with specific inhibitor AZD7648 and M3814 and close-up view. The major differences are in the p-loop conformations. Moreover, among the few residues that differ, Met3729 of DNA-PKcs is more extended compared to the Ile2163 of mTOR at the equivalent position and acts as the gatekeeper. Moreover, it affects the conformation of DNA-PKcs p-loop when different ligands bind. DNA-PKcs in complex with AZD7648 is coloured purple, DNA-PKcs in complex with M3814 is coloured cyan, mTOR in complex with Torin2 is coloured salmon and mTOR in complex with pp242 is coloured olive.

Extended Data Fig. 3 ATP competitive inhibitors in complex with homologues of DNA-PKcs.

a, Comparison of wortmannin binding on the ATP binding groove of porcine PI3K γ (PDB entry: 1E7U) and DNA-PKcs¹⁵. The Lys 833 of porcine PI3K γ and Lys 3753 of DNA-PKcs react with the furan ring of wortmannin to form a covalent C-N bond and irreversibly inhibit the kinase activity. **b**, Comparison of AZD7648 binding on ATP binding groove of PI3K γ (PDB entry: 6T3C) and DNA-PKcs¹⁷. The 90° rotation of the indole ring from PI3K γ Trp 812 to DNA-PKcs Trp 3805 provides a better surface and strong stacking effect for the binding of AZD7648. The porcine PI3K γ /Wortmannin complex is coloured brown. The PI3K γ /AZD7648 complex is coloured olive.

Extended Data Fig. 4 Ligand binding in the same pocket of DNA-PKcs in higher-order complexes without structurally affecting the assemblies.

a, The Coulomb potential map of DNA-PK holoenzyme in complex with ATP γ S- Mg^{2+} ₂. **b**, Close-up view of the DNA-PKcs kinase domain in the DNA-PK/ATP γ S- Mg^{2+} ₂ Coulomb potential map with the model of the kinase domain of the DNA-PKcs/ATP γ S- Mg^{2+} ₂ complex docked in. **c**, Close-up view of the Coulomb potential map of NHEJ long-range complex (EMD-23510) and the related kinase domain model (PDB: 7LT3), which includes the ligand binding of ADP²⁴. **d**, EMSA/gel shift assay of Ku70/80, DNA-PKcs and DNA-PKcs inhibitor with DNA (replicated three times). For gel source data, see Supplementary Figure 1.

Extended Data Fig. 5 Hotspot analysis for further structure-guided inhibitor development.

a, Hotspot map of DNA-PKcs ATP binding site contoured at 14. The apolar, donor and acceptor hotspot regions are depicted as yellow, blue and red surfaces with the key contributing residues shown as brown, salmon and blue lines respectively. ATP γ S- Mg^{2+} ₂ is shown in green stick-ball representation with inhibitors wortmannin (grey), NU7441 (pink), AZD7648 (blue) and M3814 (brown) overlaid. **b**, Surface electrostatic representation of DNA-PKcs in complex with ATP γ S (green stick-ball) and inhibitors wortmannin (grey), NU7441 (pink), AZD7648 (blue) and M3814 (yellow) overlaid as lines. AZD7648 and M3814 are seen extending to the edge of the ATP pocket due to unique interactions with residues near the catalytic loop, not seen with the other two inhibitors. Additional lead optimization may involve elaborating compounds to utilize interactions on the catalytic loop (blue arrow) and base of C-lobe (green arrow). Growing compounds further into the groove (yellow arrow) occupied by the activation loop, thereby engaging additional polar and electrostatic contacts, allows extension further away from the ATP binding site.

Extended Data Fig. 6 Cryo-EM data processing of the DNA-PKcs/ligand complexes.

a, Cryo-EM data processing of the DNA-PKcs/ATP γ S-Mg $^{2+}$ ₂ complex. **b**, Cryo-EM data processing of the DNA-PKcs/wortmannin complex. **c**, Cryo-EM data processing of the DNA-PKcs/NU7441 complex. **d**, Cryo-EM data processing of the DNA-PKcs/AZD7648 complex. **e**, Cryo-EM data processing of the DNA-PKcs/M3814 complex.

Supplementary information

Supplementary Information

This file contains Supplementary Tables 1 and 2, Supplementary Fig. 1 and supplementary references.

Reporting Summary

Rights and permissions

Open Access This article is licensed under a Creative Commons Attribution 4.0 International License, which permits use, sharing, adaptation, distribution and reproduction in any medium or format, as long as you give appropriate credit to the original author(s) and the source, provide a link to the Creative Commons license, and indicate if changes were made. The images or other third party material in this article are included in the article's Creative Commons license, unless indicated otherwise in a credit line to the material. If material is not included in the article's Creative Commons license and your intended use is not permitted by statutory regulation or exceeds the permitted use, you will need to obtain permission directly from the copyright holder. To view a copy of this license, visit <http://creativecommons.org/licenses/by/4.0/>.

Reprints and Permissions

About this article

Cite this article

Liang, S., Thomas, S.E., Chaplin, A.K. *et al.* Structural insights into inhibitor regulation of the DNA repair protein DNA-PKcs. *Nature* **601**, 643–648 (2022). <https://doi.org/10.1038/s41586-021-04274-9>

- Received: 02 June 2021
- Accepted: 19 November 2021
- Published: 05 January 2022
- Issue Date: 27 January 2022
- DOI: <https://doi.org/10.1038/s41586-021-04274-9>

Share this article

Anyone you share the following link with will be able to read this content:

[Get shareable link](#)

Sorry, a shareable link is not currently available for this article.

[Copy to clipboard](#)

Provided by the Springer Nature SharedIt content-sharing initiative

This article was downloaded by **calibre** from <https://www.nature.com/articles/s41586-021-04274-9>

| [Section menu](#) | [Main menu](#) |

- Article
- [Published: 08 December 2021](#)

Architecture of the chloroplast PSI–NDH supercomplex in *Hordeum vulgare*

- [Liangliang Shen](#) [ORCID: orcid.org/0000-0003-0868-3283](#)^{1,2} na1,
- [Kailu Tang](#)³ na1,
- [Wenda Wang](#) [ORCID: orcid.org/0000-0002-1842-8633](#)¹ na1,
- [Chen Wang](#)³,
- [Hangjun Wu](#)⁴,
- [Zhiyuan Mao](#)^{1,2},
- [Shaoya An](#)^{3,4},
- [Shanghai Chang](#)⁴,
- [Tingyun Kuang](#) [ORCID: orcid.org/0000-0002-1885-4210](#)¹,
- [Jian-Ren Shen](#) [ORCID: orcid.org/0000-0003-4471-8797](#)^{1,5},
- [Guangye Han](#) [ORCID: orcid.org/0000-0003-3373-2008](#)¹ &
- [Xing Zhang](#) [ORCID: orcid.org/0000-0002-6776-326X](#)^{3,4,6}

[Nature](#) volume 601, pages 649–654 (2022)

- 5747 Accesses
- 27 Altmetric
- [Metrics details](#)

Subjects

- [Bioenergetics](#)

- [Cryoelectron microscopy](#)
- [Photosystem I](#)

Abstract

The chloroplast NADH dehydrogenase-like (NDH) complex is composed of at least 29 subunits and has an important role in mediating photosystem I (PSI) cyclic electron transport (CET)^{1,2,3}. The NDH complex associates with PSI to form the PSI–NDH supercomplex and fulfil its function. Here, we report cryo-electron microscopy structures of a PSI–NDH supercomplex from barley (*Hordeum vulgare*). The structures reveal that PSI–NDH is composed of two copies of the PSI–light-harvesting complex I (LHCI) subcomplex and one NDH complex. Two monomeric LHCI proteins, Lhca5 and Lhca6, mediate the binding of two PSI complexes to NDH. Ten plant chloroplast-specific NDH subunits are presented and their exact positions as well as their interactions with other subunits in NDH are elucidated. In all, this study provides a structural basis for further investigations on the functions and regulation of PSI–NDH-dependent CET.

This is a preview of subscription content

Access options

Subscribe to nature+

Get immediate online access to the entire Nature family of 50+ journals

\$29.99

monthly

[Subscribe](#)

Subscribe to Journal

Get full journal access for 1 year

\$199.00

only \$3.90 per issue

[Subscribe](#)

All prices are NET prices.

VAT will be added later in the checkout.

Tax calculation will be finalised during checkout.

Buy article

Get time limited or full article access on ReadCube.

\$32.00

[Buy](#)

All prices are NET prices.

Additional access options:

- [Log in](#)
- [Learn about institutional subscriptions](#)

Fig. 1: Overall architecture of the PSI–NDH supercomplex of barley.

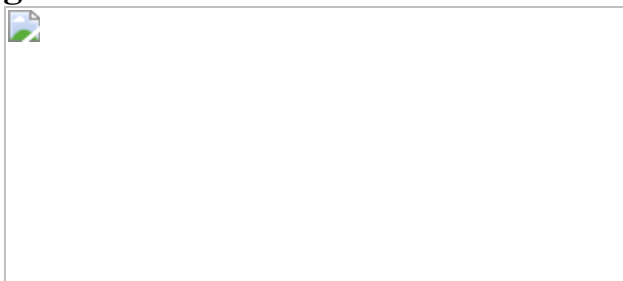


Fig. 2: Structures of Lhca5 and Lhca6 from the PSI–LHCI-1 and PSI–LHCI-2 complexes.

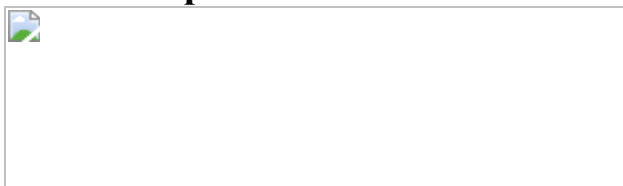


Fig. 3: Structure of the NDH complex from barley.

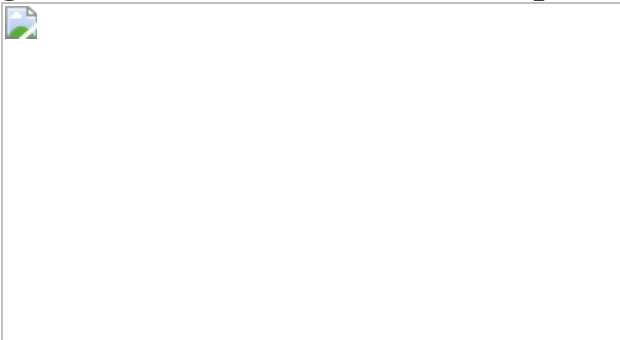
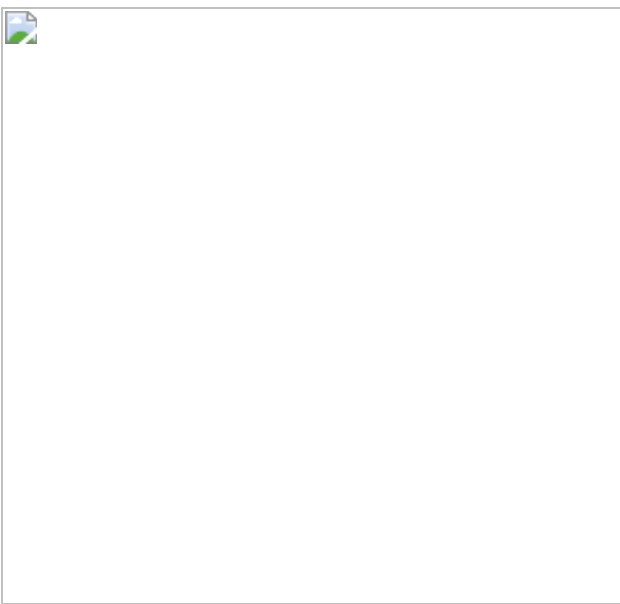


Fig. 4: Interactions between PSI–LHCI and NDH and a functional model for PSI–NDH-mediated CET.



Data availability

The cryo-EM density map and atomic models have been deposited in the Electron Microscopy Data Bank and the Protein Data Bank for the PSI–NDH supercomplex structure at 4.4-Å resolution (EMDB ID code [31498](#) and PDB ID code [7F9O](#)), the PSI–LHCI-1 supercomplex structure at 3.40-Å resolution (EMDB ID code [31348](#) and PDB ID code [7EW6](#)), the PSI–LHCI-2 supercomplex structure at 3.88-Å resolution (EMDB ID code [31350](#) and PDB ID code [7EWK](#)) and the NDH supercomplex structure at 3.70-Å resolution (EMDB ID code [31307](#) and PDB ID code [7EU3](#)). For gel source images and mass spectrometry data, see the [Supplementary Information](#). Source data are provided with this paper.

References

1. 1.

Shikanai, T. Central role of cyclic electron transport around photosystem I in the regulation of photosynthesis. *Curr. Opin. Biotech.* **26**, 25–30 (2014).

2. 2.

Yamori, W. & Shikanai, T. Physiological functions of cyclic electron transport around photosystem I in sustaining photosynthesis and plant growth. *Annu. Rev. Plant Biol.* **67**, 81–106 (2016).

3. 3.

Shikanai, T. Regulation of photosynthesis by cyclic electron transport around photosystem I. *Adv. Bot. Res.* **96**, 177–204 (2020).

4. 4.

Munekage, Y. et al. Cyclic electron flow around photosystem I is essential for photosynthesis. *Nature* **429**, 579–582 (2004).

5. 5.

Johnson, G. N. Physiology of PSI cyclic electron transport in higher plants. *Biochim. Biophys. Acta* **1807**, 384–389 (2011).

6. 6.

Miyake, C. Alternative electron flows (water-water cycle and cyclic electron flow around PSI) in photosynthesis: molecular mechanisms and physiological functions. *Plant Cell Physiol.* **51**, 1951–1963 (2010).

7. 7.

Munekage, Y. et al. PGR5 is involved in cyclic electron flow around photosystem I and is essential for photoprotection in *Arabidopsis*. *Cell* **110**, 361–371 (2002).

8. 8.

DalCorso, G. et al. A complex containing PGRL1 and PGR5 is involved in the switch between linear and cyclic electron flow in *Arabidopsis*. *Cell* **132**, 273–285 (2008).

9. 9.

Shikanai, T. et al. Directed disruption of the tobacco *ndhB* gene impairs cyclic electron flow around photosystem I. *Proc. Natl Acad. Sci. USA* **95**, 9705–9709 (1998).

10. 10.

Burrows, P. A., Sazanov, L. A., Svab, Z., Maliga, P. & Nixon, P. J. Identification of a functional respiratory complex in chloroplasts through analysis of tobacco mutants containing disrupted plastid *ndh* genes. *EMBO J.* **17**, 868–876 (1998).

11. 11.

Kofer, W., Koop, H. U., Wanner, G. & Steinmüller, K. Mutagenesis of the genes encoding subunits A, C, H, I, J and K of the plastid NAD(P)H-plastoquinone-oxidoreductase in tobacco by polyethylene glycol-mediated plastome transformation. *Mol. Gen. Genet.* **258**, 166–173 (1998).

12. 12.

Shikanai, T. Chrloroplast NDH: a different enzyme with a structure similar to that of respiratory NADH dehydrogenase. *Biochim. Biophys. Acta* **1857**, 1015–1022 (2016).

13. 13.

Peltier, G., Aro, E.-M. & Shikanai, T. NDH-1 and NDH-2 plastoquinone reductases in oxygenic photosynthesis. *Annu. Rev. Plant Biol.* **67**, 55–80 (2016).

14. 14.

Peng, L., Shimizu, H. & Shikanai, T. The chloroplast NAD(P)H dehydrogenase complex interacts with photosystem I in *Arabidopsis*. *J. Biol. Chem.* **283**, 34873–34879 (2008).

15. 15.

Peng, L., Fukao, Y., Fujiwara, M., Takami, T. & Shikanai, T. Efficient operation of NAD(P)H dehydrogenase requires the supercomplex formation with photosystem I via minor LHCl in *Arabidopsis*. *Plant Cell* **21**, 3623–3640 (2009).

16. 16.

Peng, L. & Shikanai, T. Supercomplex formation with photosystem I is required for the stabilization of the chloroplast NADH dehydrogenase-like complex in *Arabidopsis*. *Plant Physiol.* **155**, 1629–1639 (2011).

17. 17.

Kouřil, R. et al. Structural characterization of a plant photosystem I and NAD(P)H dehydrogenase supercomplex. *Plant J.* **77**, 568–576 (2014).

18. 18.

Otani, T., Kato, Y. & Shikanai, T. Specific substitutions of light-harvesting complex I proteins associated with photosystem I are required for supercomplex formation with chloroplast NADH dehydrogenase-like complex. *Plant J.* **94**, 122–130 (2018).

19. 19.

Qin, X., Suga, M., Kuang, T. & Shen, J.-R. Structural basis for energy transfer pathways in the plant PSI–LHCI supercomplex. *Science* **348**, 989–995 (2015).

20. 20.

Mazor, Y., Borovikova, A., Caspy, I. & Nelson, N. Structure of the plant photosystem I supercomplex at 2.6 Å resolution. *Nat. Plants* **3**, 17014 (2017).

21. 21.

Wang, J. et al. Structure of plant photosystem I–light harvesting complex I supercomplex at 2.4 Å resolution. *J. Integr. Plant Biol.* **63**, 1367–1381 (2021).

22. 22.

Laughlin, T. G., Bayne, A. N., Trempe, J. F., Savage, D. F. & Davies, K. M. Structure of the complex I-like molecule NDH of oxygenic photosynthesis. *Nature* **566**, 411–414 (2019).

23. 23.

Schuller, J. M. et al. Structural adaptations of photosynthetic complex I enable ferredoxin-dependent electron transfer. *Science* **363**, 257–260 (2019).

24. 24.

Pan, X. et al. Structural basis for electron transport mechanism of complex I-like photosynthetic NAD(P)H dehydrogenase. *Nat. Commun.* **11**, 610 (2020).

25. 25.

Zhang, C. et al. Structural insights into NDH-1 mediated cyclic electron transfer. *Nat. Commun.* **11**, 888 (2020).

26. 26.

Pan, X. et al. Structure of the maize photosystem I supercomplex with light-harvesting complexes I and II. *Science* **360**, 1109–1113 (2018).

27. 27.

Shimizu, H. et al. CRR23/NdhL is a subunit of the chloroplast NAD(P)H dehydrogenase complex in *Arabidopsis*. *Plant Cell Physiol.* **49**, 835–842 (2008).

28. 28.

Yamamoto, H., Sato, N. & Shikanai, T. Critical role of NdhA in the incorporation of the peripheral arm into the membrane-embedded part of the chloroplast NADH dehydrogenase-like complex. *Plant Cell Physiol.* **62**, 1131–1145 (2021).

29. 29.

Ishikawa, N. et al. NDF6: a thylakoid protein specific to terrestrial plants is essential for activity of chloroplastic NAD(P)H dehydrogenase in *Arabidopsis*. *Plant Cell Physiol.* **49**, 1066–1073 (2008).

30. 30.

Yabuta, S. et al. Three PsbQ-like proteins are required for the function of the chloroplast NAD(P)H dehydrogenase complex in *Arabidopsis*. *Plant Cell Physiol.* **51**, 866–876 (2010).

31. 31.

Yamamoto, H., Peng, L., Fukao, Y. & Shikanai, T. An Src homology 3 domain-like fold protein forms a ferredoxin binding site for the chloroplast NADH dehydrogenase-like complex in *Arabidopsis*. *Plant Cell* **23**, 1480–1493 (2011).

32. 32.

Sirpio, S. et al. Novel nuclear-encoded subunits of the chloroplast NAD(P)H dehydrogenase complex. *J. Biol. Chem.* **284**, 905–912 (2009).

33. 33.

Takabayashi, A. et al. Three novel subunits of *Arabidopsis* chloroplastic NAD(P)H dehydrogenase identified by bioinformatic and reverse genetic approaches. *Plant J.* **57**, 207–219 (2009).

34. 34.

Ishihara, S. et al. Distinct functions for the two PsbP-like proteins PPL1 and PPL2 in the chloroplast thylakoid lumen of *Arabidopsis*. *Plant Physiol.* **145**, 668–679 (2007).

35. 35.

Suorsa, M. et al. Two proteins homologous to PsbQ are novel subunits of the chloroplast NAD(P)H dehydrogenase. *Plant Cell Physiol.* **51**, 877–883 (2010).

36. 36.

Kato, Y., Sugimoto, K. & Shikanai, T. NDH–PSI supercomplex assembly precedes full assembly of the NDH complex in chloroplast. *Plant Physiol.* **176**, 1728–1738 (2018).

37. 37.

Kato, Y., Odahara, M. & Shikanai, T. Evolution of an assembly factor-based subunit contributed to a novel NDH–PSI supercomplex formation in chloroplasts. *Nat. Commun.* **12**, 3685 (2021).

38. 38.

Sirpiö, S., Holmström, M., Battchikova, N. & Aro, E. M. AtCYP20-2 is an auxiliary protein of the chloroplast NAD(P)H dehydrogenase complex. *FEBS Lett.* **583**, 2355–2358 (2009).

39. 39.

Otani, T., Yamamoto, H. & Shikanai, T. Stromal loop of Lhca6 is responsible for the linker function required for the NDH–PSI supercomplex formation. *Plant Cell Physiol.* **58**, 851–861 (2017).

40. 40.

Quiles, M. J., Albacete, M. E., Sabater, B. & Cuello, J. Isolation and partial characterization of the NADH dehydrogenase complex from barley chloroplast thylakoids. *Plant Cell Physiol.* **37**, 1134–1142 (1996).

41. 41.

Ikeuchi, M. & Inoue, Y. A new 4.8-kDa polypeptide intrinsic to the PS II reaction center, as revealed by modified SDS–PAGE with improved resolution of low-molecular-weight proteins. *Plant Cell Physiol.* **29**, 1233–1239 (1988).

42. 42.

Manaresi, E. et al. Chemiluminescence western blot assay for the detection of immunity against parvovirus B19 VP1 and VP2 linear epitopes using a videocamera based luminograph. *J. Virol. Methods* **81**, 91–99 (1999).

43. 43.

Schorb, M., Haberbosch, I., Hagen, W. J., Schwab, Y. & Mastronarde, D. N. Software tools for automated transmission electron microscopy. *Nat. Methods* **16**, 471–477 (2019).

44. 44.

Zheng, S. Q. et al. MotionCor2: anisotropic correction of beam-induced motion for improved cryo-electron microscopy. *Nat. Methods* **14**, 331–332 (2017).

45. 45.

Punjani, A., Rubinstein, J. L., Fleet, D. J. & Brubaker, M. A. cryoSPARC: algorithms for rapid unsupervised cryo-EM structure determination. *Nat. Methods* **14**, 290–296 (2017).

46. 46.

Grigorieff, N. & Harrison, S. C. Near-atomic resolution reconstructions of icosahedral viruses from electron cryo-microscopy. *Curr. Opin. Struct. Biol.* **21**, 265–273 (2011).

47. 47.

Scheres, S. H. RELION: implementation of a Bayesian approach to cryo-EM structure determination. *J. Struct. Biol.* **180**, 519–530 (2012).

48. 48.

Pettersen, E. F. et al. UCSF Chimera—a visualization system for exploratory research and analysis. *J. Comput. Chem.* **25**, 1605–1612 (2004).

49. 49.

Biasini, M. et al. SWISS-MODEL: modelling protein tertiary and quaternary structure using evolutionary information. *Nucleic Acids Res.* **42**, W252–W258 (2014).

50. 50.

Emsley, P., Lohkamp, B., Scott, W. G. & Cowtan, K. Features and development of Coot. *Acta Crystallogr D Biol. Crystallogr.* **66**, 486–501 (2010).

51. 51.

Adams, P. D. et al. PHENIX: a comprehensive Python-based system for macromolecular structure solution. *Acta Crystallogr D Biol.*

Crystallogr. **66**, 213–221 (2010).

52. 52.

Pettersen, E. F. et al. UCSF ChimeraX: structure visualization for researchers, educators, and developers. *Protein Sci.* **30**, 70–82 (2021).

Acknowledgements

We thank C. Ma from the Protein Facility (School of Medicine, Zhejiang University) for providing the platform for sample purification, X. Meng in the Center of Biomedical Analysis (Tsinghua University) for protein mass spectrometry analysis and W. Tang from the Institute of Botany (CAS) for instrumental support in sample preparation. The project was funded by the National Key R&D Program of China (2020YFA0907600, 2018YFA0507700, 2017YFA0503700, 2017YFA0504803, 2019YFA0906300, 2021YFA1300403), the Strategic Priority Research Program of CAS (XDA26050402, XDB17000000), the Key Research Program of Frontier Sciences of CAS (QYZDY-SSW-SMC003), the Youth Innovation Promotion Association of CAS (2020081), the CAS Interdisciplinary Innovation Team (JCTD-2020-06), the CAS Project for Young Scientists in Basic Research (YSBR-004), the Fundamental Research Funds for the Central Universities (2018XZZX001–13) and JSPS KAKENHI (JP17H06434).

Author information

Author notes

1. These authors contributed equally: Liangliang Shen, Kailu Tang, Wenda Wang

Affiliations

1. Photosynthesis Research Center, Key Laboratory of Photobiology, Institute of Botany, Chinese Academy of Sciences, Beijing, China

Liangliang Shen, Wenda Wang, Zhiyuan Mao, Tingyun Kuang, Jian-Ren Shen & Guangye Han

2. University of Chinese Academy of Science, Beijing, China

Liangliang Shen & Zhiyuan Mao

3. Department of Biophysics and Department of Pathology of Sir Run Run Shaw Hospital, Zhejiang University School of Medicine, Hangzhou, China

Kailu Tang, Chen Wang, Shaoya An & Xing Zhang

4. Center of Cryo-Electron Microscopy, Zhejiang University School of Medicine, Hangzhou, China

Hangjun Wu, Shaoya An, Shenghai Chang & Xing Zhang

5. Institute for Interdisciplinary Science and Graduate School of Natural Science and Technology, Okayama University, Okayama, Japan

Jian-Ren Shen

6. Liangzhu Laboratory, Zhejiang University Medical Center, Hangzhou, China

Xing Zhang

Contributions

X.Z., J.-R.S. and G.H. conceived the project. L.S., Z.M. and G.H. performed the sample preparation and characterization. K.T., C.W., S.C. and S.A. collected the cryo-EM data. X.Z., S.C. and H.W. processed the cryo-EM data and reconstructed the cryo-EM density map. L.S., K.T. and H.W. prepared figures. W.W. built the structure model and refined the structure. L.S., W.W., G.H., J.-R.S. and X.Z. analysed the structure. L.S., K.T., W.W., T.K., G.H., J.-R.S. and X.Z. jointly wrote the manuscript. All authors discussed and commented on the results and the manuscript.

Corresponding authors

Correspondence to [Jian-Ren Shen](#), [Guangye Han](#) or [Xing Zhang](#).

Ethics declarations

Competing interests

The authors declare no competing interests.

Peer review information *Nature* thanks Roman Kouril, Toshiharu Shikanai and the other, anonymous, reviewer(s) for their contribution to the peer review of this work. Peer reviewer reports are available.

Additional information

Publisher's note Springer Nature remains neutral with regard to jurisdictional claims in published maps and institutional affiliations.

Extended data figures and tables

[Extended Data Fig. 1 Sample preparation and characterization of the PSI-NDH supercomplex from barely.](#)

a, Separation of the PSI-NDH supercomplex by sucrose density gradient (SDG) centrifugation from barley thylakoids. The band of PSI-NDH was indicated by a black arrow. **b**, Size-exclusion chromatographic elution profile of the PSI-NDH fraction isolated by SDG with a Superose 6 Increase 10/300 GL column (flow rate: $100 \mu\text{l min}^{-1}$) performed at 4°C and monitored by absorption at 280 nm. **c**, Room-temperature absorption spectrum of the PSI-NDH obtained from the size-exclusion chromatography. For comparison, the spectrum of PSI-LHCI was also shown. The spectra were normalized based on the absorption maximum at 680 nm (indicated by a black arrow). The absorption value at 280 nm (indicated by a red arrow) of PSI-NDH is higher than that of PSI-LHCI,

indicating a larger ratio of protein to chlorophylls (Chls) in PSI-NDH than that in PSI-LHCI. **d**, SDS-PAGE analysis of the thylakoid membrane and purified PSI-NDH from barley (For gel source data, see Supplementary Figure 1). Lane 1: marker; lane 2: thylakoid membranes; lane 3: PSI-NDH after size-exclusion chromatography. Samples were loaded onto lane 2 and lane 3 at 20 µg of Chl per lane. The bands were stained by Coomassie Brilliant Blue (CBB). **e**, Silver staining profiles of the SDS-PAGE gel of the purified PSI-NDH from barley. Lane 1: marker; lane 2 and lane 3: PSI-NDH after size-exclusion chromatography loaded at 20 µg and 10 µg of Chl, respectively. The proteins of the CBB and silver staining bands in panels **d** and **e** were identified based on mass spectrometry analysis (see Source Data files 1 and 2) and labeled on the right side. **f**, Western-blotting analysis of thylakoid membrane and PSI-NDH supercomplex using the antibodies against NdhB and PnsB5. The polypeptide samples were separated by SDS-PAGE and stained with CBB (left), and polypeptides in the gels were electrophoretically transferred to a polyvinylidene fluoride membrane and detected with antibodies against NdhB (middle) or PnsB5 (right). Lane 1: pre-stained marker; lane 2: thylakoid membrane; lane 3: PSI-NDH after size-exclusion chromatography; lane 4: unstained marker. Samples were loaded onto SDS-PAGE at 5 µg of Chl per lane. The primary antibody against PnsB5 was custom-made by Genscript, and the primary antibody against NdhB (AS164064) and the horseradish peroxidase (HRP)-conjugated secondary antibody (Goat Anti Rabbit IgG) (AS09602) were purchased from Agrisera. Data shown in this figure is repeated more than three times, and all resulted in the same results.

[Source data](#)

[Extended Data Fig. 2 Data collection and image processing.](#)

a, Flow chart of the cryo-EM data processing of the overall PSI-NDH supercomplex and local-refinement of PSI-LHCI-1, PSI-LHCI-2 and NDH sub-complexes from the four datasets (dataset 1–4). All data were collected on a K2 summit direct electron detector. **b**, Gold standard FSC curves of the final 3D reconstruction of the PSI-NDH supercomplex. **c**, Local resolution distributions of PSI-NDH generated with Relion.

Extended Data Fig. 3 Cryo-EM density maps of protein subunits and typical cofactors in the PSI-NDH supercomplex of barley.

The protein subunits are shown as cartoon and colored differently as indicated. The locations of each subunit in the supercomplex are depicted in the surface representations above each subunit. Carotenoids and lipids are represented by sticks, and the cryo-EM density maps of each subunit and cofactors are depicted in gray meshes.

Extended Data Fig. 4 Comparisons of the structure of the PSI-LHCI moieties from the barley PSI-NDH supercomplex with PSI-LHCI from pea and maize with top views from the stromal side.

a, b, Structural comparisons of barley PSI-LHCI-1 (blue) with pea PSI-LHCI (purple, PDB code: [4XK8](#)) (**a**) and maize PSI-LHCI-LHCII (cyan, PDB code: [5ZJI](#)) (**b**). Structural differences in the C-terminal region of Lhca1 are highlighted with black dashed boxes, and enlarged in the right side. **c, d**, Pigment comparisons of barley PSI-LHCI-1 (blue) with pea PSI-LHCI (purple, PDB code: [4XK8](#)) (**c**) and maize PSI-LHCI-LHCII (cyan, PDB code: [5ZJI](#)) (**d**). **e, f**, Structural comparisons of barley PSI-LHCI-2 (green) with pea PSI-LHCI (purple, PDB ID: 4XK8) (**e**) and maize PSI-LHCI-LHCII (cyan, PDB code: 5ZJI) (**f**). Structural differences in the C-terminal region of Lhca1 and the AC loop region of Lhca2/Lhca6 are highlighted with black dashed boxes, and enlarged in the right side. **g, h**, Pigment comparisons of barley PSI-LHCI-2 (green) with pea PSI-LHCI (purple, PDB ID: 4XK8) (**g**) and maize PSI-LHCI-LHCII (cyan, PDB code: 5ZJI) (**h**). The protein subunits are shown as ribbon models and pigments are shown as sticks in **a-h**. For clarity, the phytol tails of the Chls are omitted. The pigments with different arrangements between the different structures and the pigments bound to the pea or maize subunits but are missed in the barley PSI in (**c**), (**d**), (**g**), (**h**) are highlighted with black and red dashed cycles, respectively.

Extended Data Fig. 5 Structural comparisons of Lhca5 and Lhca6 from barley with Lhca4 and Lhca2 of pea and maize.

a, Comparisons of Lhca5 from barley PSI-NDH (green) with Lhca4 from pea PSI-LHCI (PDB code: 4XK8, purple) and maize PSI-LHCI (PDB code: 5ZJI, cyan). **b**, Comparisons of Lhca6 from barley PSI-NDH (red) with Lhca2 from pea PSI-LHCI (PDB code: 4XK8, purple) and maize PSI-LHCI (PDB code: 5ZJI, cyan). The Lhcas are shown with ribbon models, whereas the pigments and lipids are shown as sticks and colored as that of the protein subunits respectively. Different regions between the three homologues subunits are highlighted by black dashed boxes. The phytol chains of all Chls were omitted for clarity.

Extended Data Fig. 6 Multiple sequence alignments of Lhca5/Lhca6 from barley (*Hordeum vulgare*) with Lhca4/Lhca2 from pea (*Pisum sativum*) and maize (*Zea mays*).

a, Sequence alignment of Lhca5 from barley with Lhca4 from pea (*PS*) and maize (*ZM*). **b**, Sequence alignment of Lhca6 from barley with Lhca2 from pea (*PS*) and maize (*ZM*). Secondary structures are shown above the sequences. The AC loop involved in the interactions within NDH is marked with red solid line underneath the sequences in **b**.

Extended Data Fig. 7 Structural comparisons of NDH and its typical subunits from barley (*Hordeum vulgare*) with those of NDH-1L of the thermophilic cyanobacterium *T. elongatus*.

a, Structural comparison between the NDH moiety of PSI-NDH and the cyanobacterial NDH-1L (PDB ID: [6L7O](#)). **b-h**, Structural comparisons of the typical subunits NdhA (**b**), NdhB (**d**), NdhC (**e**), NdhD (**f**), NdhF (**g**), and NdhG (**h**) between barley and *T. elongatus* (PDB ID: [6L7O](#)). The structural differences between two homologues subunits are highlighted by black dashed boxes. The electron density map of the N-terminal loop of NdhA of barley and its interactions with the surface of PnsL2 is shown in (**c**). **i**, Structural comparison between PnsB4 of barley and NdhP of *T. elongatus* (PDB ID: [6L7O](#)). The extra extensions of the C-terminus and N-

terminus found in PnsB4 were highlighted by black dashed boxes. In all panels, subunits in barley NDH are shown in same color as in Fig. 3a, and subunits in the cyanobacterial NDH-1L are shown in grey.

Extended Data Fig. 8 Interactions among different subunits in NDH.

a, Interactions between the PnsB4 helix inserted inside PnsB1 with PnsB5. **b**, Interactions between PnsL3 and NdhF mediated through the N-terminal region of PnsB4, and interactions between the N-terminal region of PnsL3 with NdhD. **c**, Interactions between the transmembrane regions of PnsB5 with PnsB4. The NdhB/D/F subunits are shown in the surface model. **d**, Interactions of the long N-terminal loop of PnsB5 with NdhD and NdhF. **e**, Interactions between PnsB1 and the horizontal helix of NdhF in the stromal side. **f**, Interactions of PnsL4 with PnsL1 and PnsL2 mediated through the luminal helices of NdhG. The luminal helices of NdhG are shown in surface model. **g**, Interactions of PnsL2 with NdhA, NdhB, NdhC, NdhE, NdhG and PnsL4. **h**, Interactions of PnsL5 with PnsL4, NdhB and NdhD. **i**, Interactions between NdhF loop^{TM13-TM14} and PnsB2, PnsB3. **j**, Interactions between NdhF loop^{TM15-TM16} and PnsB2 as well as between the NdhF horizontal helix and PnsB3.

Extended Data Fig. 9 Structures of the plant-chloroplast-specific (PCS)-subunits PnsB3, PnsL1, PnsL2 and PnsL3 of NDH from barley (*Hordeum vulgare*), and sequence alignments of PnsL1/PnsL2/PnsL3 from barley (HV) NDH with PsbP/PsbQ from *Spinacia oleracea* (SO).

a, The structure of barley PnsB3. The Fe-S cluster and four coordinated cysteine residues are shown in ball-and-sticks. **b**, The local environment of the Fe-S cluster of PnsB3 in the NDH complex. **c**, Superposition of the barley PnsL1 and spinach PsbP structures (PDB ID: [3JCU](#)). **d**, Superposition of the barley PnsL2 and spinach PsbQ structures (PDB ID: [3JCU](#)). **e**, Superposition of the barley PnsL3 and spinach PsbQ structures (PDB ID: [3JCU](#)). **f**, Sequence alignment of PnsL1 with spinach PsbP. **g**,

Sequence alignment of PnsL2 with spinach PsbQ. **h**, Sequence alignment of PnsL3 with spinach PsbQ.

Extended Data Fig. 10 Structure and localization of USP in the barley PSI-NDH supercomplex.

a, Surface representation of the PSI-NDH supercomplex structure. The regions involving USP are highlighted by a red dashed box and a black box, and enlarged in the middle of the figure. USP is located at the surface of membrane subunits NdhB, NdhE, NdhF and NdhG, and connected to the PnsB1 subunit. Interactions between the C-terminus of USP and Lhca5 are depicted in the right side of the panel. **b**, Western-blotting analysis of thylakoid membrane and PSI-NDH supercomplex using the antibody against PGR5 and PGRL1 (see Supplementary Fig. 2 for gel source data). The polypeptide samples were separated by SDS-PAGE and stained with CBB (left), and detected with antibodies against PGR5 (middle) and PGRL1 (right). Lane 1: pre-stained marker; lane 2: thylakoid membrane; lane 3: PSI-NDH after size-exclusion chromatography; lane 4: unstained marker. Samples of 5 µg of Chl were loaded per lane. Data shown in this figure is repeated more than three times, and all resulted in the same results.

Extended Data Table 1 Cryo-EM data collection and processing statistics, and list of PSI-NDH subunits identified in barley in the present study

Extended Data Table 2 Cofactors associated with each subunit of PSI-NDH from barley identified in the present study

Supplementary information

Supplementary Information

This file contains Supplementary Discussion, Supplementary Figs. 1 and 2, and supplementary references.

Reporting Summary

Source Data Extended Data Fig. 1

Rights and permissions

Reprints and Permissions

About this article

Cite this article

Shen, L., Tang, K., Wang, W. *et al.* Architecture of the chloroplast PSI–NDH supercomplex in *Hordeum vulgare*. *Nature* **601**, 649–654 (2022). <https://doi.org/10.1038/s41586-021-04277-6>

- Received: 13 July 2021
- Accepted: 23 November 2021
- Published: 08 December 2021
- Issue Date: 27 January 2022
- DOI: <https://doi.org/10.1038/s41586-021-04277-6>

Share this article

Anyone you share the following link with will be able to read this content:

[Get shareable link](#)

Sorry, a shareable link is not currently available for this article.

[Copy to clipboard](#)

Provided by the Springer Nature SharedIt content-sharing initiative

This article was downloaded by **calibre** from <https://www.nature.com/articles/s41586-021-04277-6>

| [Section menu](#) | [Main menu](#) |

- Matters Arising
- [Published: 26 January 2022](#)

The Living Planet Index does not measure abundance

- [Mikael Puurtinen](#) ORCID: [orcid.org/0000-0003-3340-2762^{1,2}](https://orcid.org/0000-0003-3340-2762),
- [Merja Elo^{1,2}](#) &
- [Janne S. Kotiaho^{1,2}](#)

[Nature](#) volume **601**, pages E14–E15 (2022)

- 889 Accesses
- 8 Altmetric
- [Metrics details](#)

Subjects

- [Biodiversity](#)
- [Policy](#)

[Matters Arising](#) to this article was published on 26 January 2022

The [Original Article](#) was published on 18 November 2020

arising from B. Leung et al. *Nature* <https://doi.org/10.1038/s41586-020-2920-6> (2020)

This is a preview of subscription content

Access options

Subscribe to nature+

Get immediate online access to the entire Nature family of 50+ journals

\$29.99

monthly

[Subscribe](#)

Subscribe to Journal

Get full journal access for 1 year

\$199.00

only \$3.90 per issue

[Subscribe](#)

All prices are NET prices.

VAT will be added later in the checkout.

Tax calculation will be finalised during checkout.

Buy article

Get time limited or full article access on ReadCube.

\$32.00

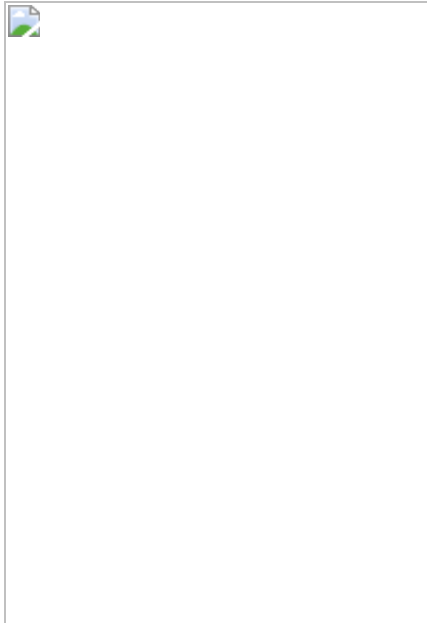
[Buy](#)

All prices are NET prices.

Additional access options:

- [Log in](#)
- [Learn about institutional subscriptions](#)

Fig. 1: Numerical examples illustrating the relationship between population trends and percentage change in total abundance, arithmetic average of proportional change, and the LPI.



Data availability

All data generated or analysed during this study are included in this published article.

References

1. 1.

Almond, R. E. A., Grooten, M. & Petersen, T. (eds) *Living Planet Report 2020 – Bending the Curve of Biodiversity Loss* (WWF, 2020).

2. 2.

Leung, B. et al. Clustered versus catastrophic global vertebrate declines. *Nature* **588**, 267–271 (2020).

3. 3.

Buckland, S. T., Studeny, A. C., Magurran, A. E., Illian, J. B. & Newson, S. E. The geometric mean of relative abundance indices: a biodiversity measure with a difference. *Ecosphere* **2**, 1–15 (2011).

4. 4.

McRae, L., Deinet, S. & Freeman, R. The diversity-weighted living planet index: controlling for taxonomic bias in a global biodiversity indicator. *PLoS ONE* **12**, e0169156 (2017).

5. 5.

Leung, B., Greenberg, D. A. & Green, D. M. Trends in mean growth and stability in temperate vertebrate populations. *Divers. Distrib.* **23**, 1372–1380 (2017).

6. 6.

Marconi, V., McRae, L., Deinet, S., Ledger, S. & Freeman, F. in *Living Planet Report 2020 – Bending the Curve of Biodiversity Loss* (eds Almond, R. E. A., Grooten, M. & Petersen, T.) (WWF, 2020).

7. 7.

Daskalova, G. N., Myers-Smith, I. H. & Godlee, J. L. Rare and common vertebrates span a wide spectrum of population trends. *Nat. Commun.* **11**, 4394 (2020).

8. 8.

Daskalova, G. N. et al. Landscape-scale forest loss as a catalyst of population and biodiversity change. *Science* **368**, 1341–1347 (2020).

9. 9.

IPBES. *Summary for Policymakers of the Global Assessment Report on Biodiversity and Ecosystem Services of the Intergovernmental Science-Policy Platform on Biodiversity and Ecosystem Services* (IPBES Secretariat, 2019).

10. 10.

van Strien, A. J., Soldaat, L. L. & Gregory, R. D. Desirable mathematical properties of indicators for biodiversity change. *Ecol. Indic.* **14**, 202–208 (2012).

Author information

Affiliations

1. Department of Biological and Environmental Science, University of Jyväskylä, Jyväskylä, Finland

Mikael Puurtinen, Merja Elo & Janne S. Kotiaho

2. School of Resource Wisdom, University of Jyväskylä, Jyväskylä, Finland

Mikael Puurtinen, Merja Elo & Janne S. Kotiaho

Contributions

M.P. initiated the comment and led the writing process. All authors contributed to the text and approved the final manuscript.

Corresponding author

Correspondence to [Mikael Puurtinen](#).

Ethics declarations

Competing interests

The authors declare no competing interests.

Additional information

Publisher's note Springer Nature remains neutral with regard to jurisdictional claims in published maps and institutional affiliations.

Rights and permissions

[Reprints and Permissions](#)

About this article

Cite this article

Puurtinen, M., Elo, M. & Kotiaho, J.S. The Living Planet Index does not measure abundance. *Nature* **601**, E14–E15 (2022).
<https://doi.org/10.1038/s41586-021-03708-8>

- Received: 13 January 2021
- Accepted: 03 June 2021
- Published: 26 January 2022
- Issue Date: 27 January 2022
- DOI: <https://doi.org/10.1038/s41586-021-03708-8>

Share this article

Anyone you share the following link with will be able to read this content:

[Get shareable link](#)

Sorry, a shareable link is not currently available for this article.

[Copy to clipboard](#)

Provided by the Springer Nature SharedIt content-sharing initiative

This article was downloaded by **calibre** from <https://www.nature.com/articles/s41586-021-03708-8>

| [Section menu](#) | [Main menu](#) |

- Matters Arising
- [Published: 26 January 2022](#)

Reply to: The Living Planet Index does not measure abundance

- [Brian Leung](#) [ORCID: orcid.org/0000-0002-8323-9628](#)^{1,2},
- [Anna L. Hargreaves](#)¹,
- [Dan A. Greenberg](#)³,
- [Brian McGill](#)⁴,
- [Maria Dornelas](#) [ORCID: orcid.org/0000-0003-2077-7055](#)⁵ &
- [Robin Freeman](#)⁶

[Nature](#) volume 601, page E16 (2022)

- 409 Accesses
- 1 Altmetric
- [Metrics details](#)

Subjects

- [Ecology](#)

The [Original Article](#) was published on 26 January 2022

replying to M. Puurtinen et al. *Nature* <https://doi.org/10.1038/s41586-021-03708-8> (2022)

This is a preview of subscription content

Access options

Subscribe to nature+

Get immediate online access to the entire Nature family of 50+ journals

\$29.99

monthly

[Subscribe](#)

Subscribe to Journal

Get full journal access for 1 year

\$199.00

only \$3.90 per issue

[Subscribe](#)

All prices are NET prices.

VAT will be added later in the checkout.

Tax calculation will be finalised during checkout.

Buy article

Get time limited or full article access on ReadCube.

\$32.00

[Buy](#)

All prices are NET prices.

Additional access options:

- [Log in](#)
- [Learn about institutional subscriptions](#)

References

1. 1.

Puurtinen, M., Elo, M. & Kotiaho, J. S. The Living Planet Index does not measure abundance. *Nature* <https://doi.org/10.1038/s41586-021-03708-8> (2021).

2. 2.

Leung, B. et al. Clustered versus catastrophic global vertebrate declines. *Nature* **588**, 267–271 (2020).

Author information

Affiliations

1. Department of Biology, McGill University, Montreal, Quebec, Canada

Brian Leung & Anna L. Hargreaves

2. Bieler School of Environment, McGill University, Montreal, Quebec, Canada

Brian Leung

3. Department of Biological Sciences, Simon Fraser University, Burnaby, British Columbia, Canada

Dan A. Greenberg

4. School of Biology and Ecology and Mitchell Center for Sustainability Solutions, University of Maine, Orono, ME, USA

Brian McGill

5. Centre for Biological Diversity, University of St Andrews, St Andrews, UK

Maria Dornelas

6. Indicators and Assessments Unit, Institute of Zoology, Zoological Society of London, London, UK

Robin Freeman

Contributions

B.L. wrote the response. A.L.H. and D.A.G. helped with writing, editing and discussing ideas. B.M., M.D. and R.F. discussed ideas and did some editing.

Corresponding author

Correspondence to [Brian Leung](#).

Ethics declarations

Competing interests

The authors declare no competing interests.

Additional information

Publisher's note Springer Nature remains neutral with regard to jurisdictional claims in published maps and institutional affiliations.

Rights and permissions

[Reprints and Permissions](#)

About this article

Cite this article

Leung, B., Hargreaves, A.L., Greenberg, D.A. *et al.* Reply to: The Living Planet Index does not measure abundance. *Nature* **601**, E16 (2022).
<https://doi.org/10.1038/s41586-021-03709-7>

- Published: 26 January 2022
- Issue Date: 27 January 2022
- DOI: <https://doi.org/10.1038/s41586-021-03709-7>

Share this article

Anyone you share the following link with will be able to read this content:

[Get shareable link](#)

Sorry, a shareable link is not currently available for this article.

[Copy to clipboard](#)

Provided by the Springer Nature SharedIt content-sharing initiative

[Clustered versus catastrophic global vertebrate declines](#)

- Brian Leung
- Anna L. Hargreaves
- Robin Freeman

Article 18 Nov 2020

This article was downloaded by **calibre** from <https://www.nature.com/articles/s41586-021-03709-7>

- Matters Arising
- [Published: 26 January 2022](#)

Shifting baselines and biodiversity success stories

- [Zia Mehrabi](#) ORCID: [orcid.org/0000-0001-9574-0420¹](https://orcid.org/0000-0001-9574-0420) &
- [Robin Naidoo](#) ORCID: [orcid.org/0000-0003-3872-0962^{2,3}](https://orcid.org/0000-0003-3872-0962)

[Nature](#) volume **601**, pages E17–E18 (2022)

- 675 Accesses
- 8 Altmetric
- [Metrics details](#)

Subjects

- [Biodiversity](#)
- [Environmental impact](#)

[Matters Arising](#) to this article was published on 26 January 2022

The [Original Article](#) was published on 18 November 2020

arising from B. Leung et al. *Nature* <https://doi.org/10.1038/s41586-020-2920-6> (2020)

This is a preview of subscription content

Access options

Subscribe to nature+

Get immediate online access to the entire Nature family of 50+ journals

\$29.99

monthly

[Subscribe](#)

Subscribe to Journal

Get full journal access for 1 year

\$199.00

only \$3.90 per issue

[Subscribe](#)

All prices are NET prices.

VAT will be added later in the checkout.

Tax calculation will be finalised during checkout.

Buy article

Get time limited or full article access on ReadCube.

\$32.00

[Buy](#)

All prices are NET prices.

Additional access options:

- [Log in](#)
- [Learn about institutional subscriptions](#)

References

1. 1.
Almond, R. E. A., Grooten, M. & Petersen, T. (eds) *Living Planet Report 2020 – Bending the Curve of Biodiversity Loss* (WWF, 2020).
2. 2.
Leung, B. et al. Clustered versus catastrophic global vertebrate declines. *Nature* **588**, 267–271 (2020).
3. 3.
Deinet, S. et al. *Wildlife Comeback in Europe: The Recovery of Selected Mammal and Bird Species* (final report to Rewilding Europe by ZSL, BirdLife International and the European Bird Census Council) (2013).
4. 4.
Ceballos, G., Ehrlich, P. R. & Dirzo, R. Biological annihilation via the ongoing sixth mass extinction signaled by vertebrate population losses and declines. *Proc. Natl Acad. Sci. USA* **114**, E6089–E6096 (2017).
5. 5.
Pauly, D. Anecdotes and the shifting baseline syndrome of fisheries. *Trends Ecol. Evol.* **10**, 430 (1995).
6. 6.
Daskalova, G. N., Myers-Smith, I. H. & Godlee, J. L. Rare and common vertebrates span a wide spectrum of population trends. *Nat. Commun.* **11**, 4394 (2020).

7. 7.

Setiawan, R. et al. Preventing global extinction of the Javan rhino: tsunami risk and future conservation direction. *Conserv. Lett.* **11**, e12366 (2018).

8. 8.

Mondol, S., Bruford, M. W. & Ramakrishnan, U. Demographic loss, genetic structure and the conservation implications for Indian tigers. *Proc. R. Soc. Lond. B* **280**, 20130496 (2013).

9. 9.

Milner-Gulland, E. J. & Beddington, J. R. The exploitation of elephants for the ivory trade: An historical perspective. *Proc. R. Soc. Lond. B* **252**, 29–37 (1993).

10. 10.

Casas-Marce, M. et al. Spatiotemporal dynamics of genetic variation in the iberian lynx along its path to extinction reconstructed with ancient DNA. *Mol. Biol. Evol.* **34**, 2893–2907 (2017).

11. 11.

Chase, M. J. et al. Continent-wide survey reveals massive decline in African savannah elephants. *PeerJ* **4**, e2354 (2016).

12. 12.

Jhala, Y. V., Qureshi, Q. & Nayak, A. K. (eds) *Status of Tigers, Co-Predators and Prey in India 2018. Summary Report* (National Tiger Conservation Authority, Government of India, New Delhi & Wildlife Institute of India, 2019).

13. 13.

Sanderson, E. W. et al. The ecological future of the North American bison: conceiving long-term, large-scale conservation of wildlife. *Conserv. Biol.* **22**, 252–266 (2008).

Author information

Affiliations

1. Sustainability Innovation Lab at Colorado and the Environmental Studies Program, University of Colorado Boulder, Boulder, CO, USA

Zia Mehrabi

2. Institute for Resources Environment and Sustainability, University of British Columbia, Columbia, Canada

Robin Naidoo

3. WWF-US, Washington, DC, USA

Robin Naidoo

Contributions

Z.M. and R.N. contributed equally to this work.

Corresponding authors

Correspondence to [Zia Mehrabi](#) or [Robin Naidoo](#).

Ethics declarations

Competing interests

The authors declare no competing interests.

Additional information

Publisher's note Springer Nature remains neutral with regard to jurisdictional claims in published maps and institutional affiliations.

Rights and permissions

[Reprints and Permissions](#)

About this article

Cite this article

Mehrabi, Z., Naidoo, R. Shifting baselines and biodiversity success stories. *Nature* **601**, E17–E18 (2022). <https://doi.org/10.1038/s41586-021-03750-6>

- Received: 04 December 2020
- Accepted: 20 June 2021
- Published: 26 January 2022
- Issue Date: 27 January 2022
- DOI: <https://doi.org/10.1038/s41586-021-03750-6>

Share this article

Anyone you share the following link with will be able to read this content:

[Get shareable link](#)

Sorry, a shareable link is not currently available for this article.

[Copy to clipboard](#)

Provided by the Springer Nature SharedIt content-sharing initiative

This article was downloaded by **calibre** from <https://www.nature.com/articles/s41586-021-03750-6>

| [Section menu](#) | [Main menu](#) |

- Matters Arising
- [Published: 26 January 2022](#)

Reply to: Shifting baselines and biodiversity success stories

- [Brian Leung](#) ORCID: orcid.org/0000-0002-8323-9628^{1,2},
- [Anna L. Hargreaves](#)¹,
- [Dan A. Greenberg](#)³,
- [Brian McGill](#)⁴ &
- [Maria Dornelas](#) ORCID: orcid.org/0000-0003-2077-7055⁵

Nature volume **601**, page E19 (2022)

- 296 Accesses
- 2 Altmetric
- [Metrics details](#)

Subjects

- [Ecology](#)

The [Original Article](#) was published on 26 January 2022

replying to Z. Mehrabi & R. Naidoo *Nature* <https://doi.org/10.1038/s41586-021-03750-6> (2022)

This is a preview of subscription content

Access options

Subscribe to nature+

Get immediate online access to the entire Nature family of 50+ journals

\$29.99

monthly

[Subscribe](#)

Subscribe to Journal

Get full journal access for 1 year

\$199.00

only \$3.90 per issue

[Subscribe](#)

All prices are NET prices.

VAT will be added later in the checkout.

Tax calculation will be finalised during checkout.

Buy article

Get time limited or full article access on ReadCube.

\$32.00

[Buy](#)

All prices are NET prices.

Additional access options:

- [Log in](#)
- [Learn about institutional subscriptions](#)

References

1. 1.

Mehrabi, Z. & Naidoo, R. Shifting baselines and biodiversity success stories. *Nature* <https://doi.org/10.1038/s41586-021-03750-6> (2021).

2. 2.

Leung, B. et al. Clustered versus catastrophic global vertebrate declines. *Nature* **588**, 267–271 (2020).

Author information

Affiliations

1. Department of Biology, McGill University, Montreal, Quebec, Canada

Brian Leung & Anna L. Hargreaves

2. Bieler School of Environment, McGill University, Montreal, Quebec, Canada

Brian Leung

3. Department of Biological Sciences, Simon Fraser University, Burnaby, British Columbia, Canada

Dan A. Greenberg

4. School of Biology and Ecology and Mitchell Center for Sustainability Solutions, University of Maine, Orono, ME, USA

Brian McGill

5. Centre for Biological Diversity, University of St Andrews, St Andrews, UK

Maria Dornelas

Contributions

B.L. wrote the response. A.L.H. and D.A.G. helped with writing, editing and discussing ideas. B.M. and M.D. discussed ideas and did some editing. R. Freeman, who was an author on the original paper, could not be contacted for this Reply.

Corresponding author

Correspondence to [Brian Leung](#).

Ethics declarations

Competing interests

The authors declare no competing interests.

Additional information

Publisher's note Springer Nature remains neutral with regard to jurisdictional claims in published maps and institutional affiliations.

Rights and permissions

[Reprints and Permissions](#)

About this article

Cite this article

Leung, B., Hargreaves, A.L., Greenberg, D.A. *et al.* Reply to: Shifting baselines and biodiversity success stories. *Nature* **601**, E19 (2022). <https://doi.org/10.1038/s41586-021-03749-z>

- Published: 26 January 2022
- Issue Date: 27 January 2022
- DOI: <https://doi.org/10.1038/s41586-021-03749-z>

Share this article

Anyone you share the following link with will be able to read this content:

[Get shareable link](#)

Sorry, a shareable link is not currently available for this article.

[Copy to clipboard](#)

Provided by the Springer Nature SharedIt content-sharing initiative

[Clustered versus catastrophic global vertebrate declines](#)

- Brian Leung
- Anna L. Hargreaves
- Robin Freeman

Article 18 Nov 2020

This article was downloaded by **calibre** from <https://www.nature.com/articles/s41586-021-03749-z>

- Matters Arising
- [Published: 26 January 2022](#)

Emphasizing declining populations in the Living Planet Report

- [Gopal Murali](#)^{1,2 na1},
- [Gabriel Henrique de Oliveira Caetano](#)^{1,2 na1},
- [Goni Barki](#)^{2,3 na1},
- [Shai Meiri](#) [ORCID: orcid.org/0000-0003-3839-6330](#)^{4 na2} &
- [Uri Roll](#) [ORCID: orcid.org/0000-0002-5418-1164](#)^{2 na2}

[Nature](#) volume **601**, pages E20–E24 (2022)

- 741 Accesses
- 20 Altmetric
- [Metrics details](#)

Subjects

- [Conservation biology](#)
- [Macroecology](#)
- [Population dynamics](#)

[Matters Arising](#) to this article was published on 26 January 2022

The [Original Article](#) was published on 18 November 2020

arising from B. Leung et al. *Nature* <https://doi.org/10.1038/s41586-020-2920-6> (2020)

This is a preview of subscription content

Access options

Subscribe to nature+

Get immediate online access to the entire Nature family of 50+ journals

\$29.99

monthly

[Subscribe](#)

Subscribe to Journal

Get full journal access for 1 year

\$199.00

only \$3.90 per issue

[Subscribe](#)

All prices are NET prices.

VAT will be added later in the checkout.

Tax calculation will be finalised during checkout.

Buy article

Get time limited or full article access on ReadCube.

\$32.00

[Buy](#)

All prices are NET prices.

Additional access options:

- [Log in](#)
- [Learn about institutional subscriptions](#)

Fig. 1: The effects of three different extreme population removal strategies to assess the sensitivity of overall growth rates.

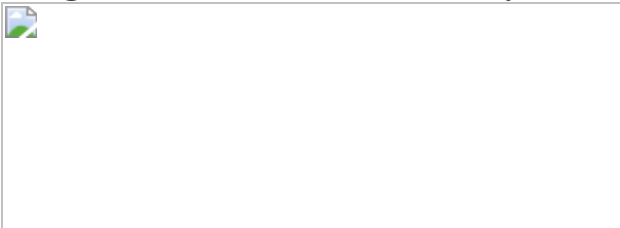
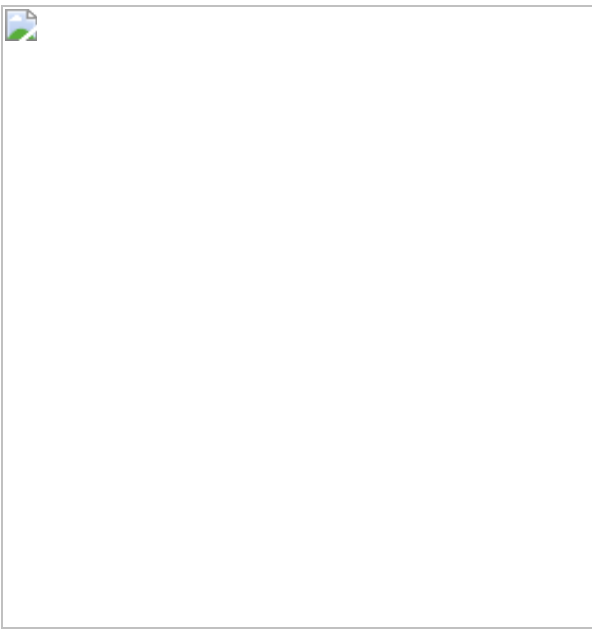


Fig. 2: The probability of LPI populations' sampling location to be inside protected areas for given species range overlap with protected areas.



Data availability

The Living Planet Database is available from the LPI website (<https://livingplanetindex.org>). The Protected Area maps are available at the World Database of Protected Area (<https://www.protectedplanet.net>).

Species range size was obtained from the IUCN, BirdLife databases (<https://www.iucnredlist.org>; <https://www.birdlife.org>) and from Roll et al.¹⁰ for reptiles.

Code availability

The R codes associated with the study are provided in the [Supplementary Information](#).

References

1. 1.

Almond, R. E. A., Grooten, M. & Peterson, T. *Living Planet Report 2020—Bending the Curve of Biodiversity Loss* (World Wildlife Fund, 2020).

2. 2.

Harrison, I. et al. The freshwater biodiversity crisis. *Science* **362**, 1369–1369 (2018).

3. 3.

He, F. et al. The global decline of freshwater megafauna. *Global Change Biol.* **25**, 3883–3892 (2019).

4. 4.

Pacourea, N. et al. Half a century of global decline in oceanic sharks and rays. *Nature* **589**, 567–571 (2021).

5. 5.

Leung, B. et al. Clustered versus catastrophic global vertebrate declines. *Nature* **588**, 267–271 (2020).

6. 6.

Loh, J. et al. The Living Planet Index: using species population time series to track trends in biodiversity. *Philos. Trans. R. Soc. B* **360**, 289–295 (2005).

7. 7.

Caughley, G. Directions in conservation biology. *J. Anim. Ecol.* 215–244 (1994).

8. 8.

Watson, J. E., Dudley, N., Segan, D. B. & Hockings, M. The performance and potential of protected areas. *Nature* **515**, 67–73 (2014).

9. 9.

Gray, C. L. et al. Local biodiversity is higher inside than outside terrestrial protected areas worldwide. *Nat. Commun.* **7**, 12306 (2016).

10. 10.

Roll, U. et al. The global distribution of tetrapods reveals a need for targeted reptile conservation. *Nat. Ecol. Evol.* **1**, 1677–1682 (2017).

Acknowledgements

This work was supported by the Israel Science Foundation (grant no. 406/19).

Author information

Author notes

1. These authors contributed equally: Gopal Murali, Gabriel Henrique de Oliveira Caetano, Goni Barki
2. These authors jointly supervised this work: Shai Meiri, Uri Roll

Affiliations

1. Jacob Blaustein Center for Scientific Cooperation, The Jacob Blaustein Institutes for Desert Research, Ben-Gurion University of the Negev, Midreshet Ben-Gurion, Israel
Gopal Murali & Gabriel Henrique de Oliveira Caetano
2. Mitrani Department of Desert Ecology, The Jacob Blaustein Institutes for Desert Research, Ben-Gurion University of the Negev, Midreshet Ben-Gurion, Israel
Gopal Murali, Gabriel Henrique de Oliveira Caetano, Goni Barki & Uri Roll
3. Albert Katz International School for Desert Studies, The Jacob Blaustein Institutes for Desert Research, Ben-Gurion University of the Negev, Midreshet Ben-Gurion, Israel
Goni Barki
4. School of Zoology & The Steinhardt Museum of Natural History, Tel Aviv University, Tel Aviv, Israel
Shai Meiri

Contributions

All of the authors conceived the study. G.H.d.O.C. downloaded LPI data and conducted sensitivity analyses. G.H.d.O.C., G.B. and G.M. assembled and analysed the dataset. All of the authors drafted and substantially revised the manuscript.

Corresponding author

Correspondence to [Uri Roll](#).

Ethics declarations

Competing interests

The authors declare no competing interests.

Additional information

Publisher's note Springer Nature remains neutral with regard to jurisdictional claims in published maps and institutional affiliations.

Extended data figures and tables

[Extended Data Fig. 1 The probability of LPI populations' sampling location to be inside protected areas for given species range overlap with protected areas \(by taxon\).](#)

Taxon was included as an interaction with the overlap area. The solid red line represents a generalized linear mixed model with the binomial fit and dashed lines 95% confidence interval. The black line represents the expected slope of 1 if populations were sampled at random in the species' range. The histograms represent the proportion of overlap of species ranges with protected areas. Red, LPI locations found within protected areas; blue, LPI location found outside protected areas.

[Extended Data Fig. 2 The probability of LPI populations' sampling location to be inside protected areas for given species range overlap with protected areas \(by realm–domain combination\).](#)

Realm-domain combination was included as interaction with overlap area. The solid red line represents a generalized linear mixed model with the binomial fit and dashed lines 95% confidence interval. The black line represents the expected slope of 1 if populations were sampled at random in the species' range. The histograms represent the proportion of overlap of species ranges with protected areas. Red, LPI locations found within protected areas; blue, LPI location found outside protected areas.

Supplementary information

Supplementary Information

Supplementary Methods, Supplementary Table 1 and Supplementary References, and the R code.

Reporting Summary

Rights and permissions

Reprints and Permissions

About this article

Cite this article

Murali, G., de Oliveira Caetano, G.H., Barki, G. *et al.* Emphasizing declining populations in the Living Planet Report. *Nature* **601**, E20–E24 (2022). <https://doi.org/10.1038/s41586-021-04165-z>

- Received: 14 January 2021
- Accepted: 06 October 2021
- Published: 26 January 2022
- Issue Date: 27 January 2022

- DOI: <https://doi.org/10.1038/s41586-021-04165-z>

Share this article

Anyone you share the following link with will be able to read this content:

[Get shareable link](#)

Sorry, a shareable link is not currently available for this article.

[Copy to clipboard](#)

Provided by the Springer Nature SharedIt content-sharing initiative

This article was downloaded by **calibre** from <https://www.nature.com/articles/s41586-021-04165-z>

| [Section menu](#) | [Main menu](#) |

- Matters Arising
- [Published: 26 January 2022](#)

Reply to: Emphasizing declining populations in the Living Planet Report

- [Brian Leung](#) [ORCID: orcid.org/0000-0002-8323-9628^{1,2}](#),
- [Anna L. Hargreaves¹](#),
- [Dan A. Greenberg³](#),
- [Brian McGill⁴](#),
- [Maria Dornelas](#) [ORCID: orcid.org/0000-0003-2077-7055⁵](#) &
- [Robin Freeman⁶](#)

[Nature](#) volume **601**, pages E25–E26 (2022)

- 298 Accesses
- 2 Altmetric
- [Metrics details](#)

Subjects

- [Ecology](#)

The [Original Article](#) was published on 26 January 2022

replying to G. Murali et al. *Nature* <https://doi.org/10.1038/s41586-021-04165-z> (2022)

This is a preview of subscription content

Access options

Subscribe to nature+

Get immediate online access to the entire Nature family of 50+ journals

\$29.99

monthly

[Subscribe](#)

Subscribe to Journal

Get full journal access for 1 year

\$199.00

only \$3.90 per issue

[Subscribe](#)

All prices are NET prices.

VAT will be added later in the checkout.

Tax calculation will be finalised during checkout.

Buy article

Get time limited or full article access on ReadCube.

\$32.00

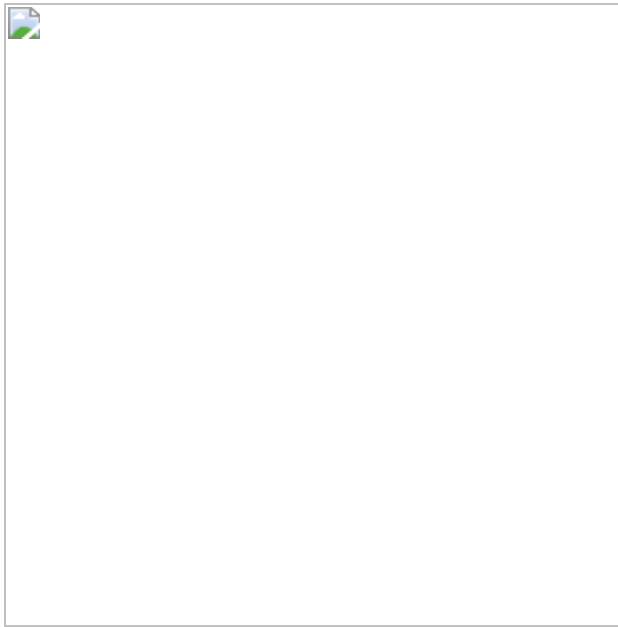
[Buy](#)

All prices are NET prices.

Additional access options:

- [Log in](#)
- [Learn about institutional subscriptions](#)

Fig. 1: Simulation analysis showing effect of a small 2.5% asymmetry on LPI.



References

1. 1.

Murali, G. et al. Emphasizing declining populations in the Living Planet Report. *Nature* <https://doi.org/10.1038/s41586-021-04165-z> (2022).

2. 2.

Leung, B. et al. Clustered versus catastrophic global vertebrate declines. *Nature* **588**, 267–271 (2020)

3. 3.

Almond, R. E. A., Grooten, M. & Peterson, T. *Living Planet Report 2020—Bending the Curve of Biodiversity Loss* (World Wildlife Fund, 2020)

4. 4.

Daskalova, G. N., Myers-Smith, I. H. & Godlee, J. L. Rare and common vertebrates span a wide spectrum of population trends. *Nat. Commun.* **11**, 4394 (2020).

5. 5.

Leung, B., Greenberg, D. A. & Green, D. M. Trends in mean growth and stability in temperate vertebrate populations. *Divers. Distrib.* **23**, 1372–1380 (2017).

Acknowledgements

This work was supported by a Natural Sciences and Engineering Research Council (NSERC) Discovery grant to B.L.

Author information

Affiliations

1. Department of Biology, McGill University, Montreal, Quebec, Canada

Brian Leung & Anna L. Hargreaves

2. Bieler School of Environment, McGill University, Montreal, Quebec, Canada

Brian Leung

3. Department of Biological Sciences, Simon Fraser University, Burnaby, British Columbia, Canada

Dan A. Greenberg

4. School of Biology and Ecology and Mitchell Center for Sustainability Solutions, University of Maine, Orono, ME, USA

Brian McGill

5. Centre for Biological Diversity, University of St Andrews, St Andrews, UK

Maria Dornelas

6. Indicators and Assessments Unit, Institute of Zoology, Zoological Society of London, London, UK

Robin Freeman

Contributions

B.L. wrote the response. A.C.H. and D.A.G. helped with writing, editing and discussing ideas. B.M. and M.D. discussed ideas with some editing. R.F. contributed discussions to the original manuscript².

Corresponding author

Correspondence to [Brian Leung](#).

Ethics declarations

Competing interests

The authors declare no competing interests.

Additional information

Publisher's note Springer Nature remains neutral with regard to jurisdictional claims in published maps and institutional affiliations.

Supplementary information

Reporting Summary

Rights and permissions

Reprints and Permissions

About this article

Cite this article

Leung, B., Hargreaves, A.L., Greenberg, D.A. *et al.* Reply to: Emphasizing declining populations in the Living Planet Report. *Nature* **601**, E25–E26 (2022). <https://doi.org/10.1038/s41586-021-04166-y>

- Published: 26 January 2022
- Issue Date: 27 January 2022
- DOI: <https://doi.org/10.1038/s41586-021-04166-y>

Share this article

Anyone you share the following link with will be able to read this content:

[Get shareable link](#)

Sorry, a shareable link is not currently available for this article.

[Copy to clipboard](#)

Provided by the Springer Nature SharedIt content-sharing initiative

Clustered versus catastrophic global vertebrate declines

- Brian Leung
- Anna L. Hargreaves
- Robin Freeman

Article 18 Nov 2020

This article was downloaded by **calibre** from <https://www.nature.com/articles/s41586-021-04166-y>.

| [Section menu](#) | [Main menu](#) |

- Matters Arising
- [Published: 26 January 2022](#)

Do not downplay biodiversity loss

- [Michel Loreau](#) [ORCID: orcid.org/0000-0002-0122-495X¹](#),
- [Bradley J. Cardinale²](#),
- [Forest Isbell](#) [ORCID: orcid.org/0000-0001-9689-769X³](#),
- [Tim Newbold](#) [ORCID: orcid.org/0000-0001-7361-0051⁴](#),
- [Mary I. O'Connor⁵](#) &
- [Claire de Mazancourt¹](#)

[Nature](#) volume **601**, pages E27–E28 (2022)

- 1458 Accesses
- 47 Altmetric
- [Metrics details](#)

Subjects

- [Biodiversity](#)

[Matters Arising](#) to this article was published on 26 January 2022

The [Original Article](#) was published on 18 November 2020

arising from B. Leung et al. *Nature* <https://doi.org/10.1038/s41586-020-2920-6> (2020)

This is a preview of subscription content

Access options

Subscribe to nature+

Get immediate online access to the entire Nature family of 50+ journals

\$29.99

monthly

[Subscribe](#)

Subscribe to Journal

Get full journal access for 1 year

\$199.00

only \$3.90 per issue

[Subscribe](#)

All prices are NET prices.

VAT will be added later in the checkout.

Tax calculation will be finalised during checkout.

Buy article

Get time limited or full article access on ReadCube.

\$32.00

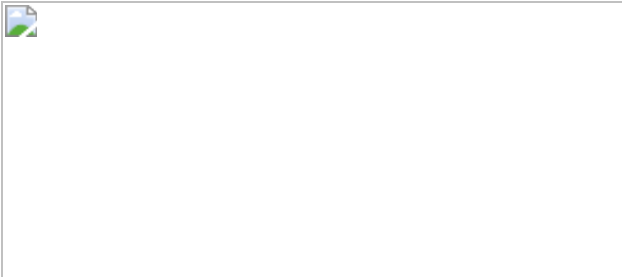
[Buy](#)

All prices are NET prices.

Additional access options:

- [Log in](#)
- [Learn about institutional subscriptions](#)

Fig. 1: The methodology adopted by Leung et al.¹ would not detect global climate change.



Data availability

Data used to produce Fig. 1 are freely available from <https://data.giss.nasa.gov/gistemp/>.

References

1. 1.

Leung, B. et al. Clustered versus catastrophic global vertebrate declines. *Nature* **588**, 267–271 (2020).

2. 2.

McRae, L., Deinet, S. & Freeman, R. The diversity-weighted Living Planet Index: controlling for taxonomic bias in a global biodiversity indicator. *PLoS ONE* **12**, e0169156 (2017).

3. 3.

Koricheva, J. & Gurevitch, J. Uses and misuses of meta-analysis in plant ecology. *J. Ecol.* **102**, 828–844 (2014).

4. 4.

Cardinale, B. J., Gonzalez, A., Allington, G. R. H. & Loreau, M. Is local biodiversity in decline or not? A summary of the debate over analysis of species richness time trends. *Biol. Conserv.* **219**, 175–183 (2018).

5. 5.

Inger, R. et al. Common European birds are declining rapidly while less abundant species' numbers are rising. *Ecol. Lett.* **18**, 28–36 (2015).

6. 6.

Rosenberg, K. V. et al. Decline of the North American avifauna. *Science* **366**, 120–124 (2019).

7. 7.

Gonzalez, A. et al. Estimating local biodiversity change: a critique of papers claiming no net loss of local diversity. *Ecology* **97**, 1949–1960 (2016).

8. 8.

Scholes, R. J. et al. Toward a global biodiversity observing system. *Science* **321**, 1044–1045 (2008).

Acknowledgements

M.L. and C.d.M. acknowledge support from the TULIP Laboratory of Excellence (ANR-10-LABX-41).

Author information

Affiliations

1. Theoretical and Experimental Ecology Station, CNRS, Moulis, France

Michel Loreau & Claire de Mazancourt

2. Department of Ecosystem Science and Management, Penn State University, University Park, PA, USA

Bradley J. Cardinale

3. Department of Ecology, Evolution and Behavior, University of Minnesota, St. Paul, MN, USA

Forest Isbell

4. Centre for Biodiversity and Environment Research, Department of Genetics, Evolution and Environment, University College London, London, UK

Tim Newbold

5. Biodiversity Research Centre and Department of Zoology, University of British Columbia, Vancouver, British Columbia, Canada

Mary I. O'Connor

Contributions

M.L. designed the work and wrote the first draft of the manuscript. C.d.M. analysed the climate change data. All authors contributed to idea development and manuscript revisions.

Corresponding author

Correspondence to [Michel Loreau](#).

Ethics declarations

Competing interests

The authors declare no competing interests.

Additional information

Publisher's note Springer Nature remains neutral with regard to jurisdictional claims in published maps and institutional affiliations.

Supplementary information

[Reporting Summary](#)

Rights and permissions

[Reprints and Permissions](#)

About this article

Cite this article

Loreau, M., Cardinale, B.J., Isbell, F. *et al.* Do not downplay biodiversity loss. *Nature* **601**, E27–E28 (2022). <https://doi.org/10.1038/s41586-021-04179-7>

- Received: 12 January 2021
- Accepted: 07 October 2021
- Published: 26 January 2022
- Issue Date: 27 January 2022
- DOI: <https://doi.org/10.1038/s41586-021-04179-7>

Share this article

Anyone you share the following link with will be able to read this content:

[Get shareable link](#)

Sorry, a shareable link is not currently available for this article.

[Copy to clipboard](#)

Provided by the Springer Nature SharedIt content-sharing initiative

This article was downloaded by **calibre** from <https://www.nature.com/articles/s41586-021-04179-7>

| [Section menu](#) | [Main menu](#) |

- Matters Arising
- [Published: 26 January 2022](#)

Reply to: Do not downplay biodiversity loss

- [Brian Leung](#) [ORCID: orcid.org/0000-0002-8323-9628](#)^{1,2},
- [Anna L. Hargreaves](#)¹,
- [Dan A. Greenberg](#)³,
- [Brian McGill](#)⁴,
- [Maria Dornelas](#) [ORCID: orcid.org/0000-0003-2077-7055](#)⁵ &
- [Robin Freeman](#)⁶

[Nature](#) volume 601, pages E29–E31 (2022)

- 580 Accesses
- 3 Altmetric
- [Metrics details](#)

Subjects

- [Ecology](#)

The [Original Article](#) was published on 26 January 2022

replying to M. Loreau et al. *Nature* <https://doi.org/10.1038/s41586-021-04179-7> (2022)

This is a preview of subscription content

Access options

Subscribe to nature+

Get immediate online access to the entire Nature family of 50+ journals

\$29.99

monthly

[Subscribe](#)

Subscribe to Journal

Get full journal access for 1 year

\$199.00

only \$3.90 per issue

[Subscribe](#)

All prices are NET prices.

VAT will be added later in the checkout.

Tax calculation will be finalised during checkout.

Buy article

Get time limited or full article access on ReadCube.

\$32.00

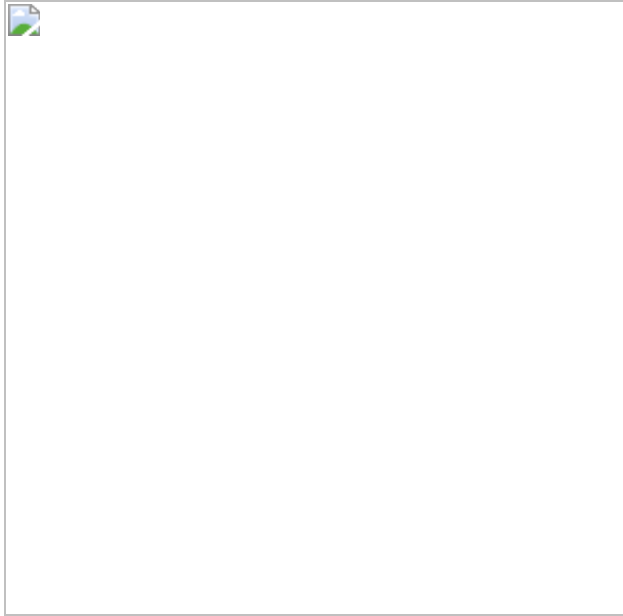
[Buy](#)

All prices are NET prices.

Additional access options:

- [Log in](#)
- [Learn about institutional subscriptions](#)

Fig. 1: Mean log annual growth rates as a function of the number of yearly abundance estimates in each time series.



Data availability

Data can be accessed from the Living Planet Index database (www.livingplanetindex.org/).

References

1. 1.

Loreau, M. et al. Do not downplay biodiversity loss. *Nature* <https://doi.org/10.1038/s41586-021-04179-7> (2022).

2. 2.

Leung, B. et al. Clustered versus catastrophic global vertebrate declines. *Nature* **588**, 267–271 (2020).

3. 3.

Antão, L. H. et al. Temperature-related biodiversity change across temperate marine and terrestrial systems. *Nat. Ecol. Evol.* **4**, 927–933 (2020).

4. 4.

Leung, B., Greenberg, D. A. & Green, D. M. Trends in mean growth and stability in temperate vertebrate populations. *Divers. Distrib.* **23**, 1372–1380 (2017).

5. 5.

Daskalova, G. N., Myers-Smith, I. H. & Godlee, J. L. Rare and common vertebrates span a wide spectrum of population trends. *Nat. Commun.* **11**, 4394 (2020).

6. 6.

Murali, G. et al. Emphasizing declining populations in the Living Planet Report. *Nature* <https://doi.org/10.1038/s41586-021-04165-z> (2022).

7. 7.

Leung, B., et al. Reply to: Emphasizing declining populations in the Living Planet Report. *Nature* <https://doi.org/10.1038/s41586-021-04166-y> (2022).

8. 8.

Dornelas, M., et al. A balance of winners and losers in the Anthropocene. *Ecol. Lett.* **22**, 847–854 (2019).

9. 9.

Hilborn, R. Faith based fisheries. *Fisheries* **31**, 554–555 (2006).

Acknowledgements

This work was supported by a Natural Sciences and Engineering Research Council (NSERC) Discovery grant to B.L.

Author information

Affiliations

1. Department of Biology, McGill University, Montreal, Quebec, Canada

Brian Leung & Anna L. Hargreaves

2. Bieler School of Environment, McGill University, Montreal, Quebec, Canada

Brian Leung

3. Department of Biological Sciences, Simon Fraser University, Burnaby, British Columbia, Canada

Dan A. Greenberg

4. School of Biology and Ecology and Mitchell Center for Sustainability Solutions, University of Maine, Orono, ME, USA

Brian McGill

5. Centre for Biological Diversity, University of St Andrews, St Andrews, UK

Maria Dornelas

6. Indicators and Assessments Unit, Institute of Zoology, Zoological Society of London, London, UK

Robin Freeman

Contributions

B.L. wrote the response. A.L.H. and D.A.G. helped with writing, editing and discussing ideas. B.M. and M.D. discussed ideas and helped with editing. R.F. contributed discussions to the original manuscript².

Corresponding author

Correspondence to [Brian Leung](#).

Ethics declarations

Competing interests

The authors declare no competing interests.

Additional information

Publisher's note Springer Nature remains neutral with regard to jurisdictional claims in published maps and institutional affiliations.

Supplementary information

[**Reporting Summary**](#)

Rights and permissions

[**Reprints and Permissions**](#)

About this article

Cite this article

Leung, B., Hargreaves, A.L., Greenberg, D.A. *et al.* Reply to: Do not downplay biodiversity loss. *Nature* **601**, E29–E31 (2022).
<https://doi.org/10.1038/s41586-021-04180-0>

- Published: 26 January 2022
- Issue Date: 27 January 2022
- DOI: <https://doi.org/10.1038/s41586-021-04180-0>

Share this article

Anyone you share the following link with will be able to read this content:

[Get shareable link](#)

Sorry, a shareable link is not currently available for this article.

[Copy to clipboard](#)

Provided by the Springer Nature SharedIt content-sharing initiative

[Clustered versus catastrophic global vertebrate declines](#)

- Brian Leung
- Anna L. Hargreaves
- Robin Freeman

Article 18 Nov 2020

This article was downloaded by **calibre** from <https://www.nature.com/articles/s41586-021-04180-0>

Amendments & Corrections

- **Publisher Correction: Host immunomodulatory lipids created by symbionts from dietary amino acids** [09 January 2022]
Publisher Correction •
- **Publisher Correction: Collective durotaxis along a self-generated stiffness gradient in vivo** [12 January 2022]
Publisher Correction •

- Publisher Correction
- [Published: 09 January 2022](#)

Publisher Correction: Host immunomodulatory lipids created by symbionts from dietary amino acids

- [Sungwhan F. Oh](#) [ORCID: orcid.org/0000-0002-0280-7903](#)^{1,2} na1,
- [T. Praveena](#)³ na1,
- [Heebum Song](#)⁴,
- [Ji-Sun Yoo](#) [ORCID: orcid.org/0000-0003-3100-0794](#)²,
- [Da-Jung Jung](#)²,
- [Deniz Erturk-Hasdemir](#)¹,
- [Yoon Soo Hwang](#)⁴,
- [ChangWon C. Lee](#) [ORCID: orcid.org/0000-0001-7534-0526](#)¹,
- [Jérôme Le Nours](#)³,
- [Hyunsoo Kim](#)⁴,
- [Jesang Lee](#)⁴,
- [Richard S. Blumberg](#) [ORCID: orcid.org/0000-0002-9704-248X](#)⁵,
- [Jamie Rossjohn](#) [ORCID: orcid.org/0000-0002-2020-7522](#)^{3,6,7},
- [Seung Bum Park](#) [ORCID: orcid.org/0000-0003-1753-1433](#)⁴ &
- [Dennis L. Kasper](#) [ORCID: orcid.org/0000-0001-8808-5333](#)¹

Nature volume **601**, page E32 (2022)

- 1051 Accesses
- 6 Altmetric

- [Metrics details](#)

Subjects

- [Mass spectrometry](#)
- [Microbiology](#)
- [Mucosal immunology](#)
- [Chemical synthesis](#)
- [X-ray crystallography](#)

The [Original Article](#) was published on 10 November 2021

[Download PDF](#)

Correction to: *Nature* <https://doi.org/10.1038/s41586-021-04083-0> published online 10 November 2021

In the version of this Article initially published, a typo appeared in the third sentence of the “SB2217 induces unique NKT cell signalling” subsection of the main text. The typo appeared as “*Erg*” 1–3 rather than “*Egr*” for the gene names in the corrected sentence now reading “Differentially expressed genes with SB2217 treatment include those encoding several canonical NKT cell cytokines such as IL-2, IL-4 and IL-13 as well as the multiple immunoregulatory genes *Egr1*, *Egr2*, *Egr3*, *Lrrc32* (which encodes a TGF- β activator), *Socs1* and *Cish* (Fig. 3d).”

The original Article has been corrected online.

Author information

Author notes

1. These authors contributed equally: Sungwhan F. Oh, T. Praveena

Affiliations

1. Department of Immunology, Blavatnik Institute of Harvard Medical School, Boston, MA, USA

Sungwhan F. Oh, Deniz Erturk-Hasdemir, ChangWon C. Lee & Dennis L. Kasper

2. Center for Experimental Therapeutics and Reperfusion Injury, Department of Anesthesiology, Perioperative and Pain Medicine, Brigham and Women's Hospital, Boston, MA, USA

Sungwhan F. Oh, Ji-Sun Yoo & Da-Jung Jung

3. Infection and Immunity Program & Department of Biochemistry and Molecular Biology, Biomedicine Discovery Institute, Monash University, Clayton, Victoria, Australia

T. Praveena, Jérôme Le Nours & Jamie Rossjohn

4. CRI Center for Chemical Proteomics, Department of Chemistry, Seoul National University, Seoul, Republic of Korea

Heebum Song, Yoon Soo Hwang, Hyunsoo Kim, Jesang Lee & Seung Bum Park

5. Division of Gastroenterology, Hepatology and Endoscopy, Department of Medicine, Brigham and Women's Hospital, Boston, MA, USA

Richard S. Blumberg

6. Australian Research Council Centre of Excellence in Advanced Molecular Imaging, Monash University, Clayton, Victoria, Australia

Jamie Rossjohn

7. Institute of Infection and Immunity, Cardiff University School of Medicine, Heath Park, Cardiff, UK

Jamie Rossjohn

Corresponding authors

Correspondence to [Sungwhan F. Oh](#), [Jamie Rossjohn](#), [Seung Bum Park](#) or [Dennis L. Kasper](#).

Rights and permissions

[Reprints and Permissions](#)

About this article

Cite this article

Oh, S.F., Praveena, T., Song, H. *et al.* Publisher Correction: Host immunomodulatory lipids created by symbionts from dietary amino acids. *Nature* **601**, E32 (2022). <https://doi.org/10.1038/s41586-021-04276-7>

- Published: 09 January 2022
- Issue Date: 27 January 2022
- DOI: <https://doi.org/10.1038/s41586-021-04276-7>

Share this article

Anyone you share the following link with will be able to read this content:

[Get shareable link](#)

Sorry, a shareable link is not currently available for this article.

[Copy to clipboard](#)

Provided by the Springer Nature SharedIt content-sharing initiative

| [Section menu](#) | [Main menu](#) |

- Publisher Correction
- [Published: 12 January 2022](#)

Publisher Correction: Collective durotaxis along a self-generated stiffness gradient *in vivo*

- [Adam Shellard ORCID: orcid.org/0000-0002-7609-9049¹](#) &
- [Roberto Mayor ORCID: orcid.org/0000-0001-9053-9613¹](#)

Nature volume **601**, page E33 (2022)

- 637 Accesses
- 1 Altmetric
- [Metrics details](#)

Subjects

- [Cell biology](#)
- [Developmental biology](#)

The [Original Article](#) was published on 08 December 2021

[Download PDF](#)

Correction to: *Nature* <https://doi.org/10.1038/s41586-021-04210-x>
Published online 8 December 2021

In the version of this article initially published, there were errors in the second through fourth panel labels of Fig. 4c. The text “Push + Sdfl” should have appeared in purple, not cyan, while “Control” should have appeared in cyan, not purple.

The corrections have been made to the online version of the article.

Author information

Affiliations

1. Department of Cell and Developmental Biology, University College London, London, UK

Adam Shellard & Roberto Mayor

Corresponding author

Correspondence to [Roberto Mayor](#).

Rights and permissions

[Reprints and Permissions](#)

About this article

Cite this article

Shellard, A., Mayor, R. Publisher Correction: Collective durotaxis along a self-generated stiffness gradient in vivo. *Nature* **601**, E33 (2022).
<https://doi.org/10.1038/s41586-021-04367-5>

- Published: 12 January 2022
- Issue Date: 27 January 2022

- DOI: <https://doi.org/10.1038/s41586-021-04367-5>

Share this article

Anyone you share the following link with will be able to read this content:

[Get shareable link](#)

Sorry, a shareable link is not currently available for this article.

[Copy to clipboard](#)

Provided by the Springer Nature SharedIt content-sharing initiative

This article was downloaded by **calibre** from <https://www.nature.com/articles/s41586-021-04367-5>

| [Section menu](#) | [Main menu](#) |